

Johan Hoffman and Claes Johnson

Computational Turbulent Incompressible Flow

SPIN Springer's internal project number, if known

Applied Mathematics: Body & Soul Vol 4

October 20, 2006

Springer

To our families

Preface

Applied Mathematics: Body&Soul is a mathematics education reform program including a series of books, together with associated educational material and open source software freely available from the project web page at www.bodysoulmath.org.

Body&Soul reflects the revolutionary new possibilities of mathematical modeling opened by the modern computer in the form of *Computational Calculus (CC)*, which is now changing the paradigm of mathematical modeling in science and technology with new methods, questions and answers, as a modern form of the classical calculus of Leibniz and Newton.

The Body&Soul series of books presents CC in a synthesis of computational mathematics (Body) and analytical mathematics (Soul) including applications. Volumes 1-3 [36] give a modern version of calculus and linear algebra including computation starting at a basic undergraduate level, and subsequent volumes on a graduate level cover different areas of applications with focus on computational methods:

- Volume 4: Computational Turbulent Incompressible Flow.
- Volume 5: Computational Thermodynamics.
- Volume 6: Computational Dynamical Systems.

The present book is Volume 4, with Volumes 5 and 6 to appear in 2007 and further volumes on solid mechanics and electro-magnetics being planned. A gentle introduction to the Body&Soul series is given in [63].

The overall goal of the Body&Soul project may be formulated as the *Automation of Computational Mathematical Modeling (ACMM)* involving the key steps of automation of (i) discretization, (ii) optimization and (iii) modeling. The objective of ACMM is to open for massive use of CC in science, engineering, medicine, and other areas of application. ACMM is realized in the *FEniCS project* (www.fenics.org), which may be seen to represent the top software part of Body&Soul.

The automation of discretization (i) involves automatic translation of a given differential equation in standard mathematical notation into a discrete

system of equations, which can be automatically solved using numerical linear algebra to produce an approximate solution of the differential equation. The translation is performed using adaptive stabilized finite element methods, which we refer to as General Galerkin or G2 with the adaptivity based on a posteriori error estimation by duality and the stabilization representing a weighted least squares control of the residual.

The automation of optimization (ii) is performed similarly starting from the differential equations expressing stationarity of an associated Lagrangian. Finally, one can couple modeling to optimization by seeking from an Ansatz a model with best fit to given data.

The present Vol 4 may be viewed as a test of the functionality of the general technique for ACMM based on G2. In this book we apply G2 implemented in FEniCS to the specific problem of solving the incompressible Euler and Navier–Stokes (NS) equations computationally. The challenge includes computational simulation of turbulent flow, since solutions of the Euler and NS equations in general are turbulent, and thus the challenge in particular includes the open problem of computational turbulence modeling.

We show in the book that G2 passes this test successfully: By direct application of G2 to the Euler and NS equations, we can on a PC compute quantities of interest in turbulent flow in the form of mean values such as drag and lift, up to tolerances of interest. G2 does not require any user specified turbulence model or wall model for turbulent boundary layers; by the direct application of G2 to the Euler or NS equations, we avoid introducing Reynolds stresses in averaged NS equations requiring turbulence models. Instead the weighted least squares stabilization of G2 automatically introduces sufficient turbulent dissipation on the finest computational scales and thus acts as an automatic turbulence model including friction boundary conditions as wall model. Furthermore, the adaptivity of G2 ensures that the flow is automatically resolved by the mesh where needed. G2 thus opens for the *Automation of Computational Fluid Dynamics*, which could be an alternative title of this book.

Applying G2 to the Euler and NS equations opens a vast area for exploration, which we demonstrate by resolving several scientific mysteries, including d'Alembert's paradox of zero drag in inviscid flow, the 2nd Law of thermodynamics and transition to turbulence. We also uncover several secrets of fluid dynamics including secrets of ball sports, flying, sailing and racing.

In particular we are led to a new computational foundation of thermodynamics based on deterministic microscopical mechanics producing deterministic mean value outputs coupled with indeterminate pointwise outputs, in which the 2nd Law is a consequence of the 1st Law. The new foundation of thermodynamics is not based on microscopical statistics as the statistical mechanics foundation pioneered by Boltzmann, and thus offers a rational scientific basis of thermodynamics based on computation, without the mystery of the 2nd Law in the statistical approach. We believe the new computational approach also may give insight to physics following the idea that Nature in

one way or the other is performing an analog computation when evolving in time from one moment to the next. We initiate the development of the new foundation in this volume and expand in Vol 5.

We are also led to a new computational approach to basic mathematical questions concerning existence and uniqueness of solutions of the Euler and NS equations, for which analytical methods have not shown to be productive. In particular we show the usefulness of the new concepts of *approximate weak solutions* and *weak uniqueness*, through which we may mathematically describe turbulent solutions with non-unique point values but unique mean values.

In short, we show that G2 opens to new insights into both mathematics, physics and mechanics with an amazingly rich range of possible applications. The main message of this book thus is that of a breakthrough: Using G2 one can simulate turbulent flow on a standard PC with a 2 GHz processor and 1-2 Gb memory computing on adaptive meshes with $10^5 - 10^6$ mesh points in space (but not less). We thus show that G2 simulation leads not only to images and movies, which are fun (and instructive) to watch, but also to new insights into the rich physical world of turbulence as well as the mathematics of turbulence.

The book is a test not only of the functionality of G2/FEniCS for simulation of turbulent flow, but also of the functionality of the Body&Soul educational program: The book is at the research front of computational turbulence, while it can be digested with the CC basis of Body&Soul Vol 1-3. If we are correct, and experience will tell, then masters programs in computational science and engineering based on Body&Soul may reach the very forefront of research, and in particular give a flying start for PhD studies. This is made possible by the amazing power of CC using only basic tools of calculus combined with computing.

We hope the reader will have a good productive time reading the book and also trying out the G2 FEniCS software on old and new challenges. For inspiration a vast material of G2 simulations of turbulent flows is available on the web page of the book at www.bodysoulmath.org.

The authors would like to thank the participants of the 2006 Geilo Winter School in Computational Mathematics, who offered valuable comments on the manuscript, and who helped in tracking down some of the mistakes.

The first author would like to acknowledge the joint work with Prof. Jonathan Goodman at the Courant Institute in developing the mesh smoothing algorithm of Section 32.5.

The main source of mathematicians pictures is the MacTutor History of Mathematics archive, other pictures are taken from what is assumed to be the public domain, or otherwise the sources are stated in the picture captions.

Stockholm and Göteborg,
April 2006

*Johan Hoffman
Claes Johnson*

Contents

Part I Overview

1	Main Objective	3
1.1	Computational Turbulent Incompressible Flow	3
2	Mysteries and Secrets	29
2.1	Mysteries	29
2.2	Secrets	30
3	Turbulent Flow and History of Aviation	33
3.1	Leonardo da Vinci, Newton and d'Alembert	33
3.2	Cayley and Lilienthal	34
3.3	Kutta, Zhukovsky and the Wright Brothers	34
4	The Euler Equations	39
4.1	Foundation of Fluid Dynamics	39
4.2	Derivation of the Euler Equations	40
4.3	The Euler Equations as a Continuum Model	41
4.4	Incompressible Flow	42
5	The Incompressible Euler and Navier–Stokes Equations	43
5.1	The Incompressible Euler Equations	43
5.2	The Incompressible Navier–Stokes Equations	44
5.3	What is Viscosity?	44
5.4	What is Heat Conductivity?	46
5.5	Friction Boundary Conditions	46
5.6	Einstein's Ideal	46
5.7	Euler and NS as Dynamical Systems	47

6	Triumph and Failure of Mathematics	49
6.1	Triumph: Celestial Mechanics	49
6.2	Failure: Potential Flow	50
7	Laminar and Turbulent Flow	51
7.1	Reynolds	51
7.2	Applications and Reynolds Numbers	53
8	Computational Turbulence	57
8.1	Are Turbulent Flows Computable?	57
8.2	Typical Outputs: Drag and Lift	58
8.3	What about Boundary Layers?	59
8.4	Approximate Weak Solutions: G2	59
8.5	G2 Error Control and Stability	60
8.6	What about Mathematics of Euler and NS?	60
8.7	When is a Flow Turbulent?	61
8.8	G2 vs Physics	61
8.9	Computability and Predictability	62
9	A First Study of Stability	65
9.1	The Linearized Euler Equations	65
9.2	Flow in a Corner or at Separation	66
9.3	Couette Flow	69
9.4	Resolution of Sommerfeld's Mystery	70
9.5	Reflections on Stability and Perspectives	70
10	d'Alembert's Mystery and Bernoulli's Law	73
10.1	Introduction	73
10.2	Bernoulli, Euler, Ideal Fluids and Potential Solutions	74
10.3	d'Alembert's Mystery	74
10.4	A Vector Calculus Identity	75
10.5	Bernoulli's Law	75
10.6	Potential Flow around a Circular Cylinder	76
10.7	Zero Drag/Lift of Potential Flow	76
10.8	Ideal Fluids and Vorticity	78
10.9	d'Alembert's Computation of Zero Drag/Lift	78
10.10A	Reformulation of the Momentum Equation	79
11	Prandtl's Resolution of d'Alembert's Mystery	81
11.1	Quotation from a Standard Source	81
11.2	Quotation from Prandtl's 1904 report	82
11.3	Discussion of Prandtl's Resolution	83

12	New Resolution of d'Alembert's Mystery	87
12.1	Introduction	87
12.2	Drag of a Circular Cylinder	87
12.3	The Role of the Boundary Layer	92
12.4	Analysis of Instability of the Potential Solution	92
12.5	Sum up of the New Resolution	94

Part II Mathematics of Turbulence

13	Turbulence and Chaos	97
13.1	Introduction	97
13.2	Weather as Deterministic Chaos	97
13.3	Predicting the Temperature in Málilla	99
13.4	Chaotic Dynamical System	99
13.5	The Harmonic Oscillator as a Chaotic System	101
13.6	Randomness and Foundations of Probability	102
13.7	NS Chaotic rather than Random	106
13.8	Observability vs Computability	107
13.9	Lorenz System	107
13.10	Lorenz, Newton and Free Will	109
13.11	Algorithmic Information Theory	110
13.12	Statistical Mechanics and Roulette	111
14	A \$1 Million Prize Problem	113
14.1	The Clay Institute Impossible \$1 Million Prize	113
14.2	Towards a Possible Formulation	114
14.3	Well-Posedness According to Hadamard	115
14.4	ϵ -Weak Solutions	116
14.5	Existence of ϵ -Weak Solutions by Regularization	118
14.6	Output Sensitivity and the Dual Problem	119
14.7	Reformulation of the Prize Problem	120
14.8	The Standard Approach to Uniqueness	122
15	Weak Uniqueness by Computation	123
15.1	Introduction	123
15.2	Uniqueness of c_D and c_L	124
15.3	Non-Uniqueness of $D(t)$	126
15.4	Stability of the Dual Solution with Respect to Time Sampling .	128
15.5	Conclusion	128
16	Existence of ϵ-Weak Solutions by G2	131
16.1	Introduction	131
16.2	The Basic Energy Estimate for the Navier–Stokes Equations .	132
16.3	Existence by G2	133

16.4 A Posteriori Output Error Estimate for G2	135
17 Stability Aspects of Turbulence in Model Problems	137
17.1 The Linearized Dual Problem	137
17.2 Rotating Flow	138
17.3 A Model Dual Problem for Rotating Flow	140
17.4 A Model Dual Problem for Oscillating Reaction	141
17.5 Model Dual Problem Summary	142
17.6 The Dual Solution for Bluff Body Drag	143
17.7 Duality for a Model Problem	143
17.8 Ensemble Averages and Input Variance	144
18 A Convection-Diffusion Model Problem	147
18.1 Introduction	147
18.2 Pointwise vs Mean Value Residuals	147
18.3 Artificial Viscosity From Least Squares Stabilization	149
19 G2 for Euler	151
19.1 Introduction	151
19.2 EG2 as a Model of the World	153
19.3 Solution of the Euler Equations by G2	153
19.4 Drag of a Square Cylinder	154
19.5 Instability of the Potential Solution	156
19.6 Temperature	162
19.7 G2 as Dissipative Weak Solutions	164
19.8 Comparison with Viscous Regularization	164
19.9 Finite Limit of Turbulent Dissipation	165
19.10 The 2nd Law of Thermodynamics	165
19.11A Global Form of the 2nd Law	166
19.12 Understanding a Basic Fact	167
19.13 Proof that EG2 is a Dissipative Weak Solution	167
20 Summary of Mathematical Aspects	169
20.1 Outputs of ϵ -weak Solutions	169
20.2 Chaos and Turbulence	170
20.3 Computational Turbulence	171
20.4 Irreversibility	171

Part III Secrets

21 Secrets of Ball Sports	175
21.1 Introduction	175
21.2 Dimples of a Golf Ball: Drag Crisis	175
21.3 Topspin in Tennis: Magnus Effect	176
21.4 Roberto Carlos: Magnus Effect	178

21.5 Pitching: Drag Crisis and Magnus Effect	180
22 Secrets of Flight	181
22.1 Generation of Lift	181
22.2 Simulation of Take-off	182
22.3 More on Generation of Drag	188
22.4 A Critical View on Kutta-Zhukovsky	188
22.5 The Challenge	189
23 Secrets of Sailing	191
23.1 The Sail	191
23.2 The Keel	192
23.3 The Challenge	193
24 Secrets of Racing	195
24.1 Downforce	195
24.2 The Wheels	196
24.3 Drag and Fuel Consumption	197

Part IV Computational Method

25 Reynolds Stresses In and Out	201
25.1 Introducing Reynolds Stresses	201
25.2 Removing Reynolds Stresses	202
26 Smagorinsky Viscosity In and Out	203
26.1 Introducing Smagorinsky Viscosity	203
26.2 Removing Smagorinsky Viscosity	204
27 Friction Boundary Condition as Wall Model	207
27.1 A Skin Friction Wall Model	207
28 G2 for Navier-Stokes Equations	209
28.1 Introduction	209
28.2 Development of G2	210
28.3 The Incompressible Navier-Stokes Equations	211
28.4 G2 as Eulerian $cG(p)dG(q)$	211
28.5 Neumann Boundary Conditions	213
28.6 No Slip and Slip Boundary Conditions	213
28.7 Outflow Boundary Conditions	213
28.8 Shock Capturing	213
28.9 Basic Energy Estimate for $cG(p)dG(q)$	214
28.10 G2 as Eulerian $cG(1)dG(0)$	214
28.11 Eulerian $cG(1)cG(1)$	215
28.12 Basic Energy Estimate for $cG(1)cG(1)$	216

28.13	Slip with Friction Boundary Conditions	216
29	A Discrete Solver	219
29.1	Fixed Point Iteration Using Multigrid/GMRES.....	219
30	G2 as Adaptive DNS/LES	221
30.1	An A Posteriori Error Estimate	221
30.2	Proof of the A Posteriori Error Estimate	223
30.3	Interpolation Error Estimates	223
30.4	G2 as Adaptive DNS/LES	225
30.5	Computation of Multiple Output	226
30.6	Mesh Refinement	227
31	Implementation of G2 with FEniCS	229
31.1	The FEniCS Project	229
32	Moving Meshes and ALE Methods	231
32.1	Introduction	231
32.2	G2 Formulation	231
32.3	Free Boundary	233
32.4	Laplacian Mesh Smoothing	233
32.5	Mesh Smoothing by Local Optimization	234
32.6	Object in a Box	235
32.7	Sliding Mesh	238

Part V Flow Fundamentals

33	Bluff Body Flow	245
33.1	Introduction	245
33.2	Drag and Lift	246
33.3	An Alternative Formula for Drag and Lift	246
33.4	A Posteriori Error Estimation	247
33.5	Surface Mounted Cube	250
33.5.1	The drag coefficient c_D	250
33.5.2	Dual solution and a posteriori error estimates	253
33.5.3	Comparison with reference data	253
33.6	Flow Past a Car	254
33.7	Square Cylinder	257
33.7.1	Computing mean drag: time vs. phase averages.....	257
33.7.2	Dual solution and a posteriori error estimates	261
33.7.3	Comparison with reference data	263
33.8	Circular Cylinder	264
33.8.1	Comparison with reference data	265
33.8.2	Dual solution and a posteriori error estimates	275
33.9	Sphere	275

33.9.1 Comparison with reference data	275
33.9.2 Dual solution and a posteriori error estimates	276
34 Boundary Layers	279
34.1 Introduction	279
34.2 Flat Plate Laminar Boundary Layer	280
34.3 Skin Friction for Laminar Boundary Layers	280
34.4 Skin Friction for Turbulent Boundary Layers	281
34.5 Computing Skin Friction by G2	282
34.6 Summary	283
35 Separation	285
35.1 Introduction	285
35.2 Simulation of Blood Flow	285
35.3 Drag Reduction for a Square Cylinder	286
35.4 Drag Crisis	286
35.5 Drag Crisis for a Circular Cylinder	290
35.6 EG2 and Turbulent Euler Solutions	292
35.7 The Dual Problem for EG2	293
35.8 EG2 for a Circular Cylinder	295
35.9 The Magnus Effect	296
35.10 Flow Past an Airfoil	298
35.11 Flow Due to a Cylinder Rolling Along Ground	298
36 Transition to Turbulence	305
36.1 Modal and Non-Modal Schools	305
36.2 Difficulties of Experimental Transition Studies	306
36.3 Possibilities of Computational Transition	307
36.4 The Challenge	307
36.5 Modal and Non-Modal Perturbation Growth	308
36.6 Different Perturbations and Threshold Levels	308
36.7 Analytical Stability of the Linearized NS	309
36.7.1 Worst Case Exponential Perturbation Growth	310
36.7.2 Linear perturbation growth in shear flow	311
36.8 Computational Transition in Shear Flows	313
36.9 Couette Flow	314
36.9.1 Linear Perturbation Growth	314
36.9.2 Periodic Span-wise Boundary Conditions	322
36.9.3 Random Force Perturbation	323
36.10 Poiseuille Flow - Reynolds Experiment	327
36.11 Taylor-Görtler Perturbations	329
36.12 Unstable Jet Flow	329
36.13 Test for Optimal Perturbations	330
36.14 A Critical Review of Classical Theory	334
36.15 Comparison with Bifurcation towards Stability	337

36.16An ODE-Model for Transition	337
36.17A Bifurcating ODE-Model	340
36.18Summary	342

Part VI Loschmidt's Mystery

37 Thermodynamics	347
37.1 Objective	347
37.2 What is Thermodynamics?	348
37.3 EG2 as a Model of Thermodynamics	348
37.4 The Classical Laws of Thermodynamics	349
37.5 What is the Role of the 2nd Law?	350
38 Joule's 1845 Experiment	351
38.1 The Experiment	351
39 Compressible Euler in 1d	357
39.1 The Compressible Euler Equations in 1d	357
39.2 Euler is Formally Reversible	358
39.3 All Wrong	358
39.4 The 2nd Law in Local Form	359
39.5 The 2nd Law in Global Form	360
39.6 Irreversibility by the 2nd Law	361
39.7 Compression and Expansion	361
40 Burgers' Equation	363
40.1 A Model of the Euler Equations	363
40.2 The Rankine-Hugoniot Condition	364
40.3 Rarefaction wave	364
40.4 Shock	365
40.5 Weak solutions may be non-unique	366
40.6 The 2nd Law for Burgers' Equation	367
40.7 Destruction of Information	367
41 Compressible Euler in 3d	369
41.1 The 2nd Law in Local Form	369
41.2 Incompressible Flow	370
41.3 The 2nd Law in Global Form	370
41.4 Irreversibility by the 2nd Law	371
41.5 Trend Towards Equilibrium by the 2nd Law	371
41.6 Comparison with Classical Entropy	372
41.7 Heat Capacities and the Gas Constant	372

42 EG2 for Compressible Flow	375
42.1 G2 for the Compressible Euler Equations	375
42.2 EG2 Satisfies the 2nd Law	376
42.3 EG2 and the Classical Entropy	376
43 Philosophy of EG2	377
43.1 Dijkstra's Vision	377
43.2 The Role of Least Squares Stabilization in G2	378
43.3 Aspects of Irreversibility	379
43.4 Imperfect Nature and Mathematics?	381
43.5 A New Paradigm of Computation	382
43.6 The Clay Prize Problem Again	382
44 Does God Really Play Dice?	383
44.1 Einstein and Modern Physics	383
44.2 Boltzmann and Statistical Mechanics	384
44.3 Summary	386
References	389
Index	395

Part I

Overview

1

Main Objective

Turbulence is one of the principal unsolved problems of physics today.The real challenge, it seems to us, is that no adequate model for turbulence exists today.... The equations of motion have been analyzed in great detail, but it is still next to impossible to make accurate quantitative predictions without relying heavily on empirical data. (Tennekes and Lumley in A First Course in Turbulence, 1994).

1.1 Computational Turbulent Incompressible Flow

This book is Vol 4 of the Body&Soul series and is devoted to *computational fluid dynamics* with focus on *turbulent incompressible flow*. In this first Part I we give a glimpse of the central themes of the book, which are developed in detail in Part II on mathematical aspects, Part III revealing secrets of fluid flow in basic applications, Part IV on computational aspects, Part V on fundamental aspects of fluid flow and a concluding Part VI leading into thermodynamics of turbulent compressible flow. In the forthcoming Vol 5 of the Body&Soul series, we continue to make a synthesis of incompressible and compressible fluid dynamics as *Computational Thermodynamics*.

A *fluid* may appear in the form of a liquid like water or a gas like air. Water is virtually *incompressible*; the relative change in volume for each atmosphere in pressure is less than 10^{-6} . Air can be viewed to be incompressible as long as the flow speed is well below the speed of sound, that is for flow speeds less than say 300 kilometers per hour (200 miles per hour).

Turbulence in fluid flow represents a basic phenomenon of our world of crucial importance in a wide range of phenomena in Nature and technical applications. Turbulent flow has a complex, seemingly chaotic, variation in space and time on a wide range of scales from small to large, and typically appears for fluids with *small viscosity*, such as air and water.

The basic mathematical models for fluid flow, incompressible and compressible, are given by the the *Euler equations* and the *Navier–Stokes equa-*

tions expressing conservation of mass, momentum and energy. The Euler equations model the flow of a fluid with zero viscosity, referred to as an *ideal fluid*, and were formulated by Euler in 1755. The Navier–Stokes equations model the flow of a fluid with positive viscosity, and were formulated during 1821–45 by Navier, Stokes, Poisson and Saint-Venant, assuming the fluid to be *Newtonian*, with the viscous forces depending linearly on velocity strains.

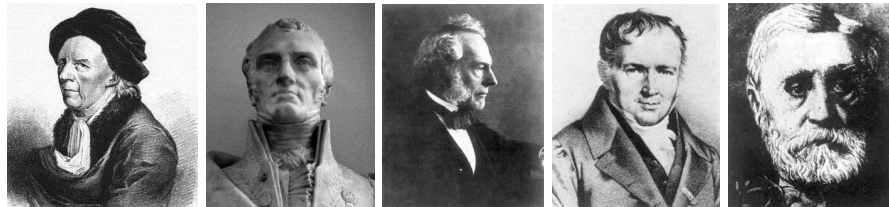


Fig. 1.1. Leonhard Euler (1707–1783), Claude Louis Marie Henri Navier (1785–1836), George Gabriel Stokes (1819–1903), Siméon Denis Poisson (1781–1840), and Adhémar Jean Claude Barré de Saint-Venant (1797–1886).

We all have practical experience of fluid motion and the concept of *viscosity* for fluids with large viscosity such as heavy oil or tooth paste, and fluids with small viscosity such as air and water. The Navier–Stokes equations appear to be an accurate mathematical model of fluid flow with varying viscosity from small to large, including in particular turbulent flow for fluids with small viscosity. There are also non-Newtonian fluids with a nonlinear dependence of the viscosity, typically fluids with large viscosity such as polymers.

The basic mathematical models for turbulence thus appear to be known since very long, but nevertheless turbulence is viewed as the basic open problem of classical mechanics. How can it be? The main reason is that the progress of solving the Navier–Stokes equations using analytical mathematical methods to obtain quantitative information about turbulent flow, has been very slow or rather non-existent, because the complexity of turbulent solutions to the Navier–Stokes equations defy analytical representations. Even basic qualitative mathematical questions concerning existence and uniqueness of solutions represent open problems seemingly inaccessible to analytical mathematical treatment using classical methods of calculus and functional analysis.

The main objective of this book is to show that it is possible to accurately simulate turbulent fluid flow by solving the Euler or Navier–Stokes equations computationally using solid mathematical principles, in simple geometries on a PC, and in complex geometries on clusters of PCs. The main objective is thus to demonstrate that *computational turbulence* now is available for massive use in a wide range of applications.

We will show that the objective may be reached by solving the Euler and Navier–Stokes equations using a *finite element method* which we refer to as *General Galerkin* or *G2* for short. G2 is a *Galerkin method* seeking a solution

in a finite element space with residual orthogonal to a set of finite element test functions combined with a *weighted least squares* control of the residual. G2 is *adaptive* with

- *automatic turbulence modeling,*
- *automatic error control.*

The adaptivity is based on solving a linearized dual problem to obtain sensitivity in output or quantities of interest in terms of the residual and the finite element mesh size.

As a preview of the book, below we present some G2 computations including solutions of associated linearized dual problems.

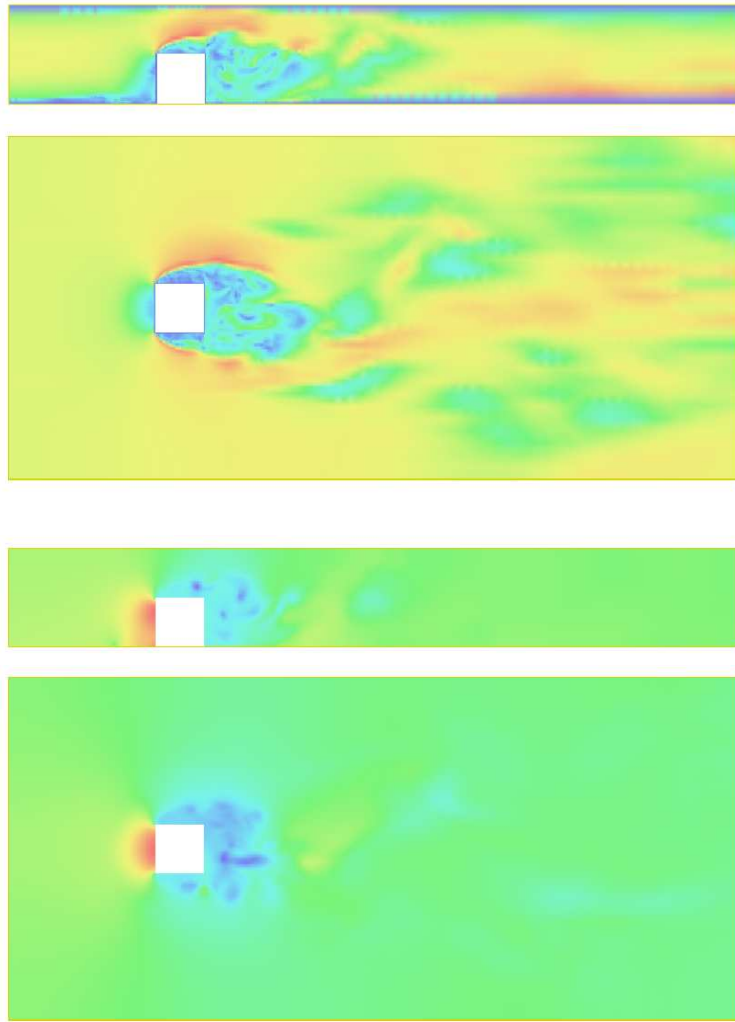


Fig. 1.2. From Chapter 15: Surface mounted cube: velocity $|U|$ (upper) and pressure P (lower), in the x_1x_2 -plane at $x_3 = 3.5H$ and in the x_1x_3 -plane at $x_2 = 0.5H$.

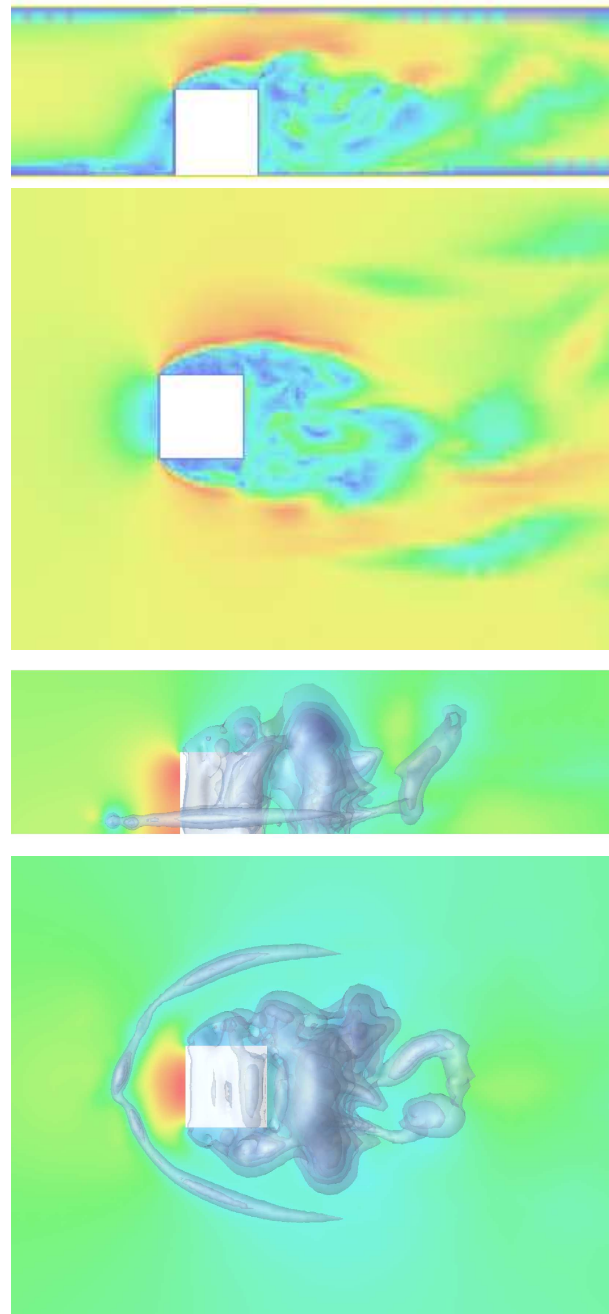


Fig. 1.3. From Chapter 33: Surface mounted cube: Magnitude of velocity (upper), and pressure color map, with iso-surfaces for negative pressure, illustrating the horse shoe vortex.

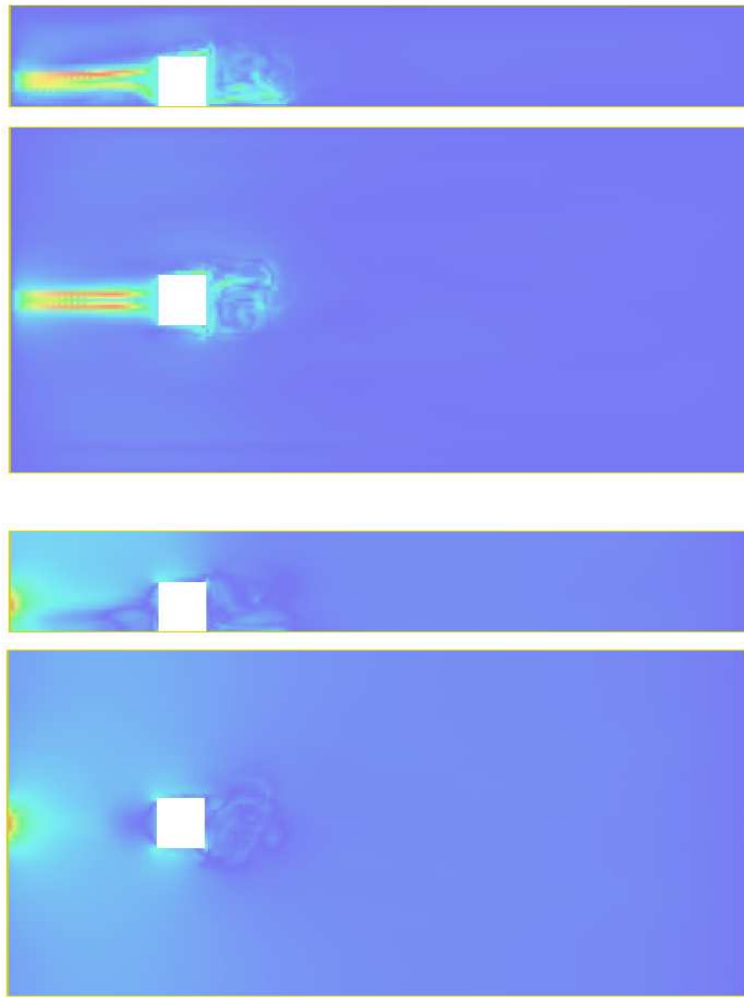


Fig. 1.4. From Chapter 15: Surface mounted cube: dual velocity $|\varphi_h|$ (upper), and dual pressure $|\iota_h|$ (middle), in the x_1x_2 -plane at $x_3 = 3.5H$ and in the x_1x_3 -plane at $x_2 = 0.5H$.

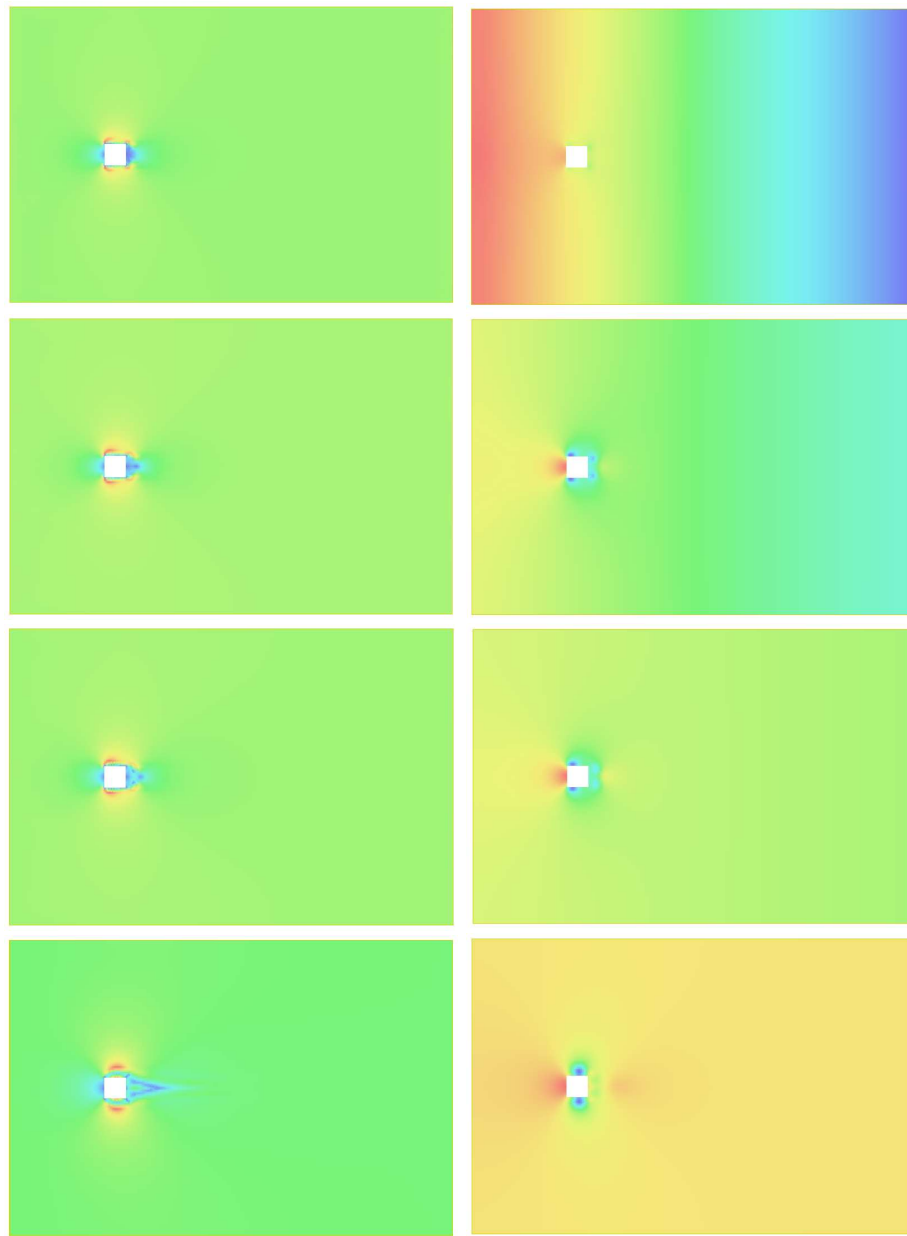


Fig. 1.5. From Chapter 19: Magnitude of the computed velocity (left) and pressure (right) corresponding to zero initial data, for time steps 4,6,8,32.

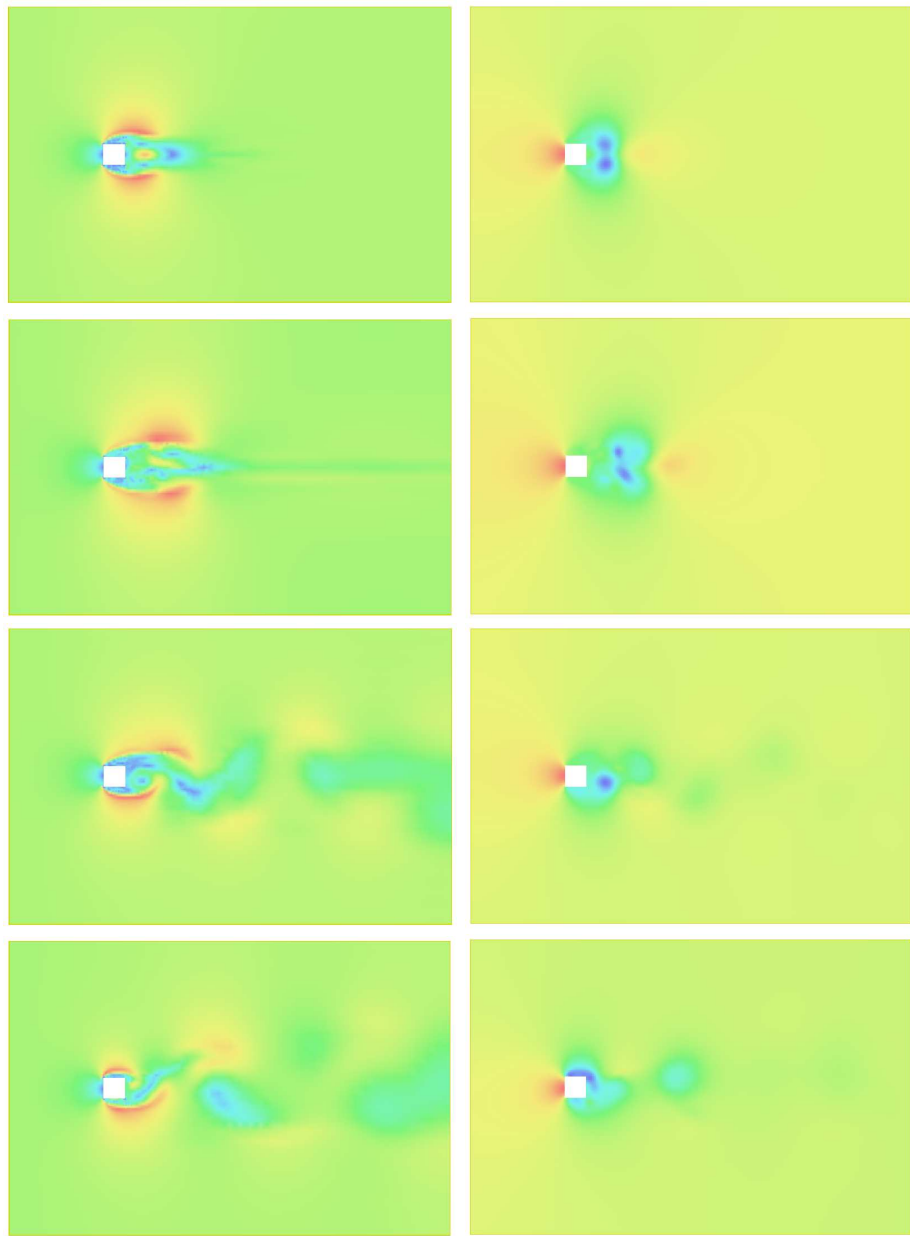


Fig. 1.6. From Chapter 19: Magnitude of the computed velocity (left) and pressure (right) corresponding to zero initial data, for time steps 64,128,704,1024.

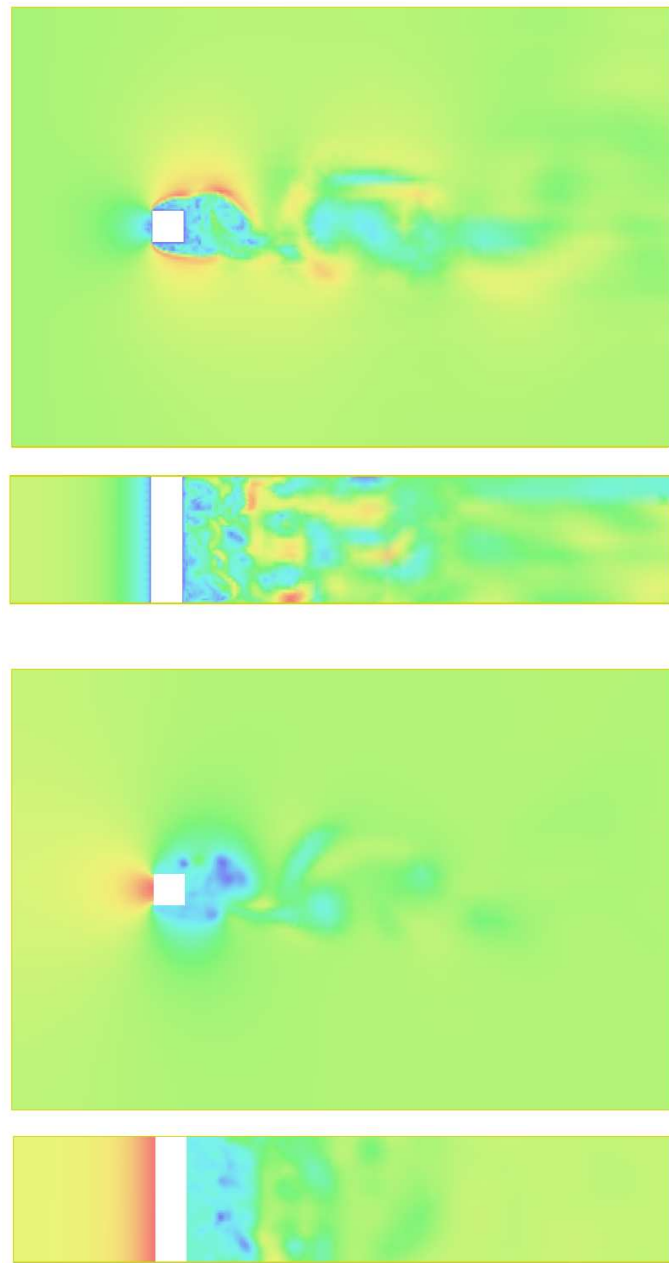


Fig. 1.7. From Chapter 33: Velocity $|U|$ (upper), and pressure P (lower), in the x_1x_2 -plane at $x_3 = 2D$.

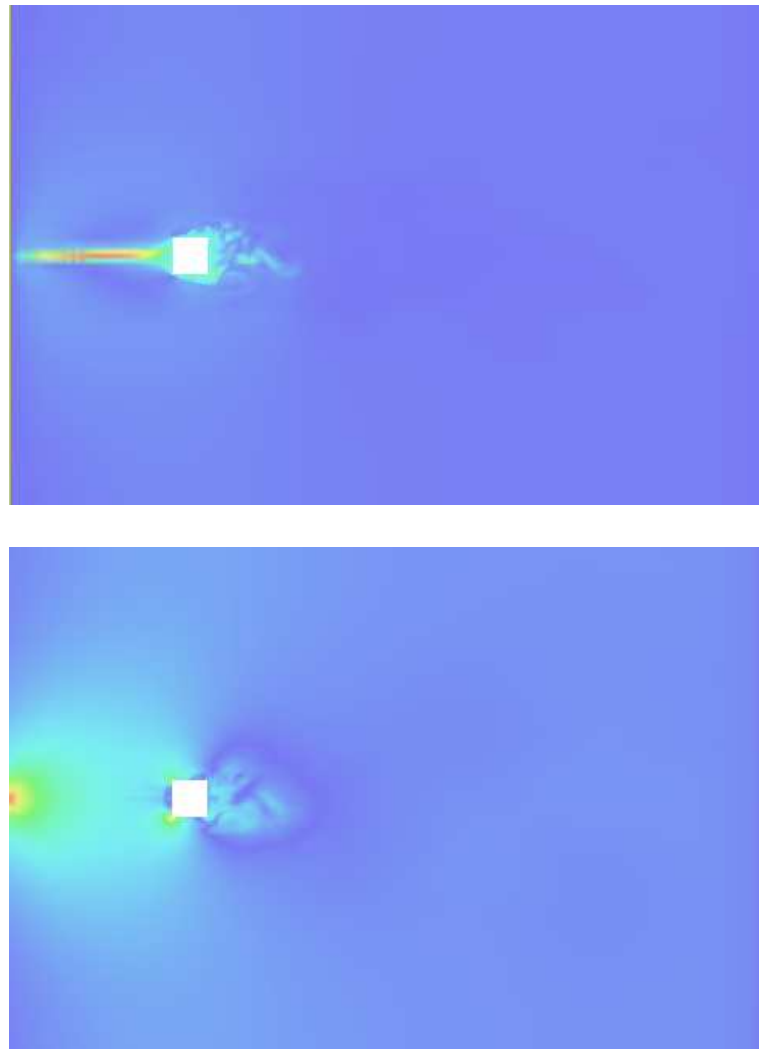


Fig. 1.8. From Chapter 33: Square cylinder: dual velocity $|\varphi_h|$ (upper), and dual pressure $|\iota_h|$ (lower), in the x_1x_3 -plane at $x_2 = 7D$ and in the x_1x_2 -plane at $x_3 = 2D$.

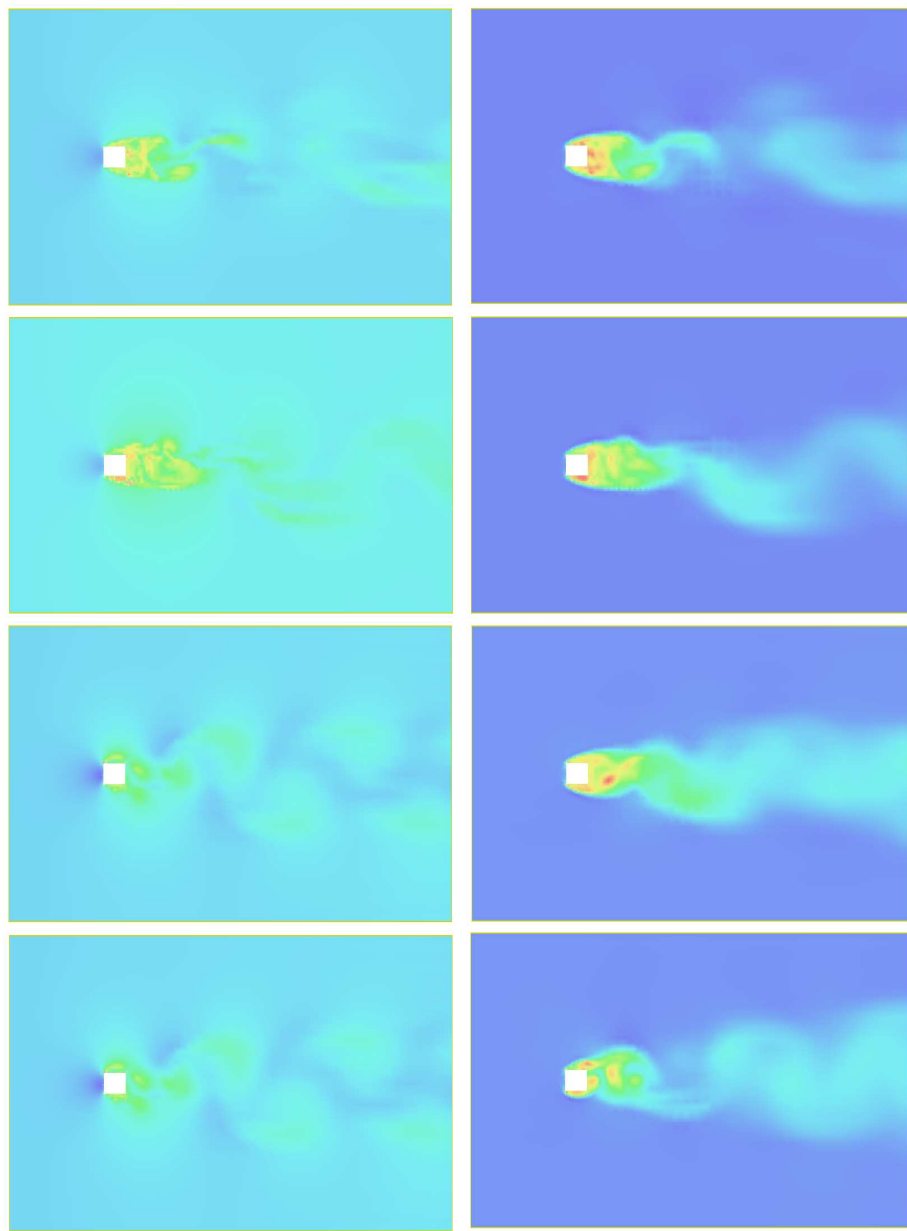


Fig. 1.9. From Chapter 19: Total energy e (left) and temperature T (right); $t = 4.5, 5.5, 11, 16$.

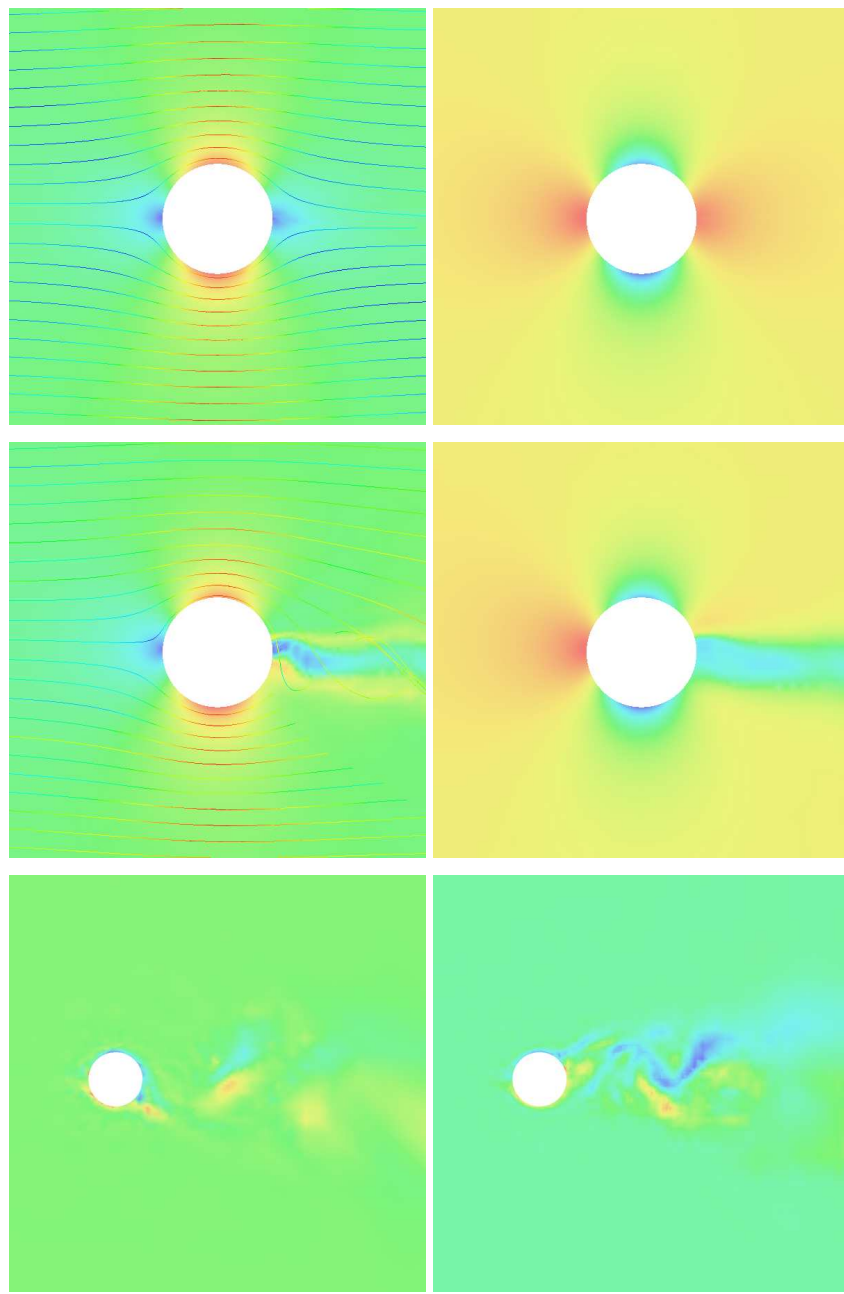


Fig. 1.10. From Chapter 12 and Chapter 35: Flow past a circular cylinder; velocity and pressure for the potential solution and a G2 turbulent solution (upper), and out of paper vorticity of the G2 solution at two different times, in two different sections parallel to the x_1x_2 -plane (lower).

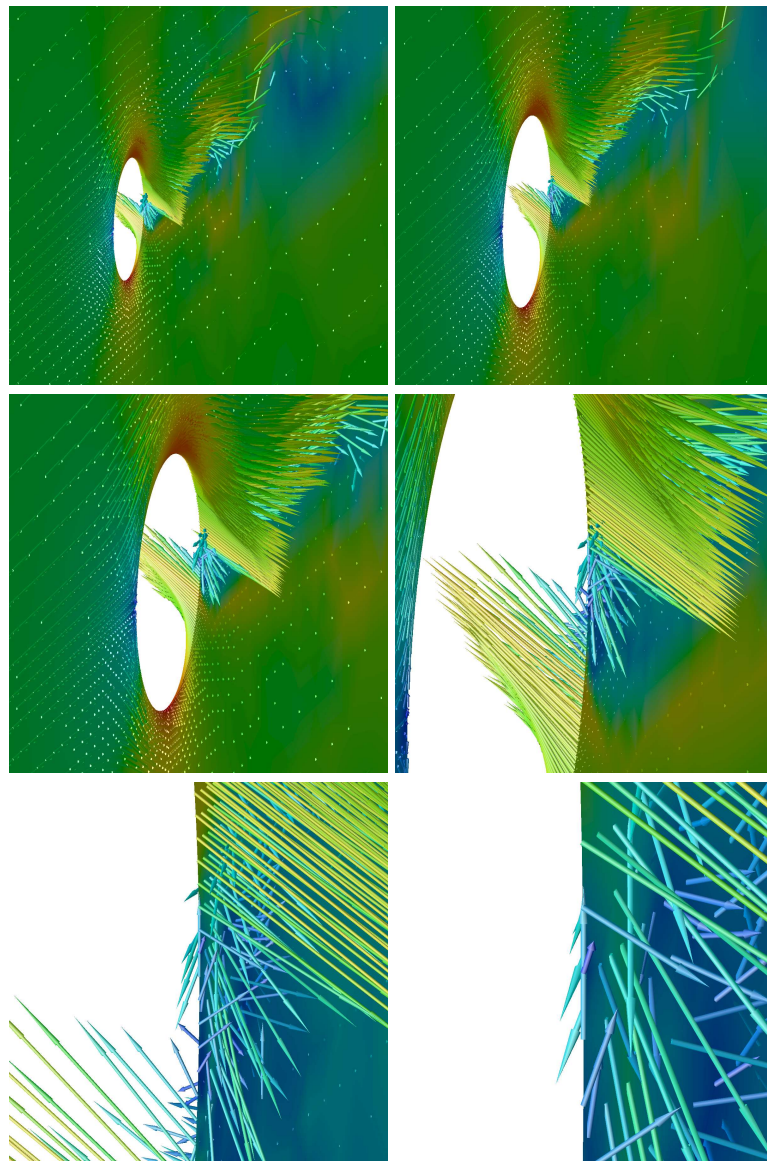


Fig. 1.11. From Chapter 12: Snapshot of the velocity in a G2 computation illustrating the single separation point.

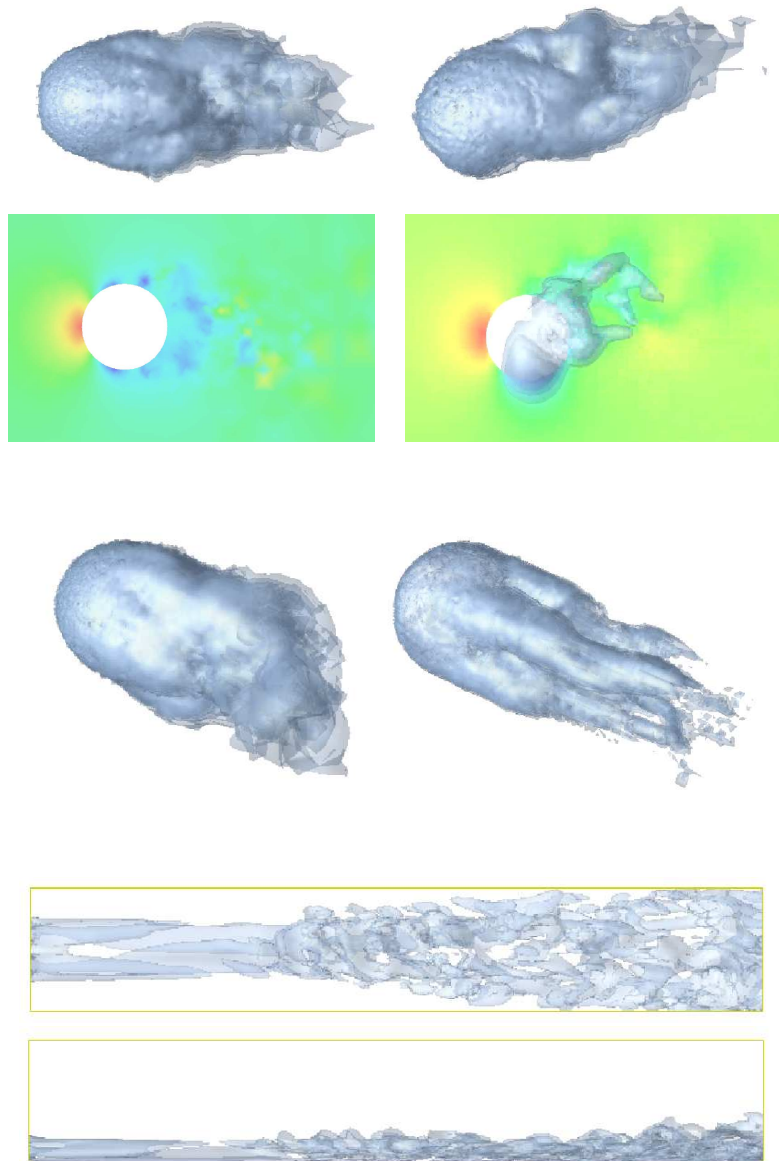


Fig. 1.12. From Chapter 21 and Chapter 36: Pressure for a still and a rotating sphere (upper), and vorticity for a sphere before and after drag crisis (middle), and transition to turbulence in a boundary layer computation (lower).

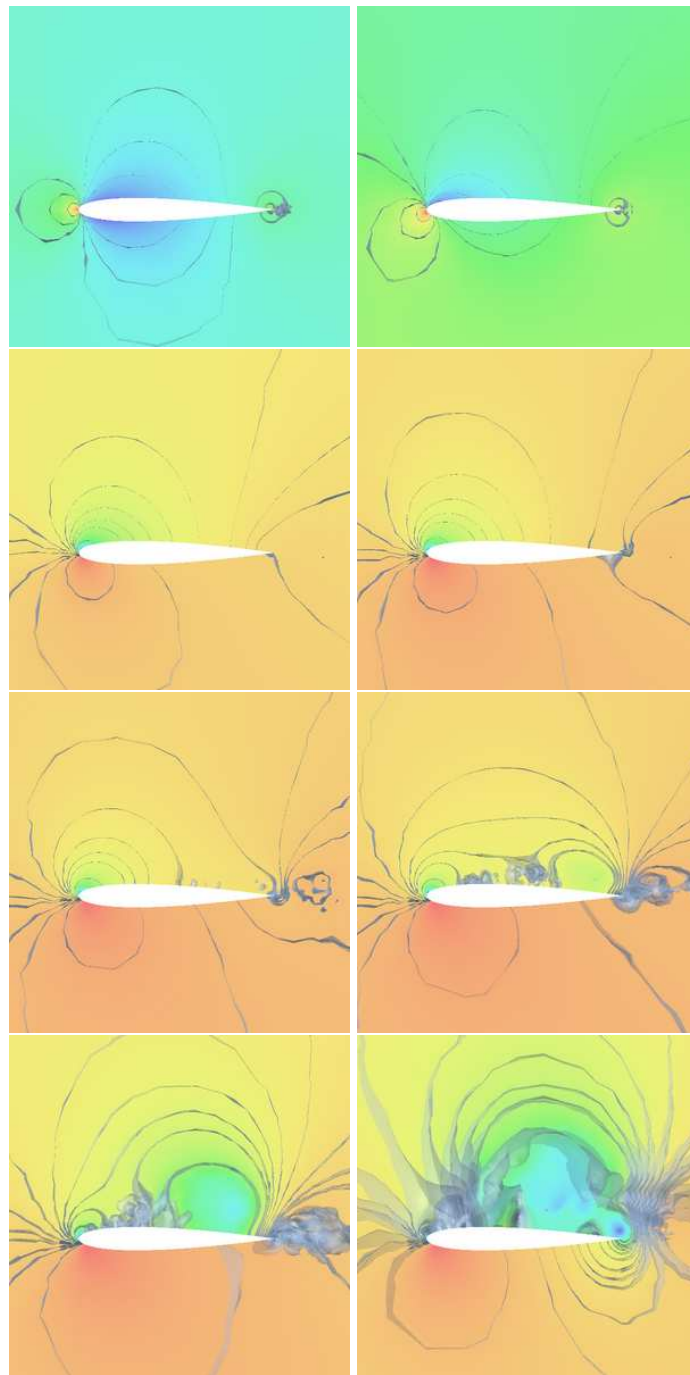


Fig. 1.13. From Chapter 22: Pressure for a 3d wing using EG2, with increasing angle of attack; 0,4,12,14,16,18,20, and 22°.

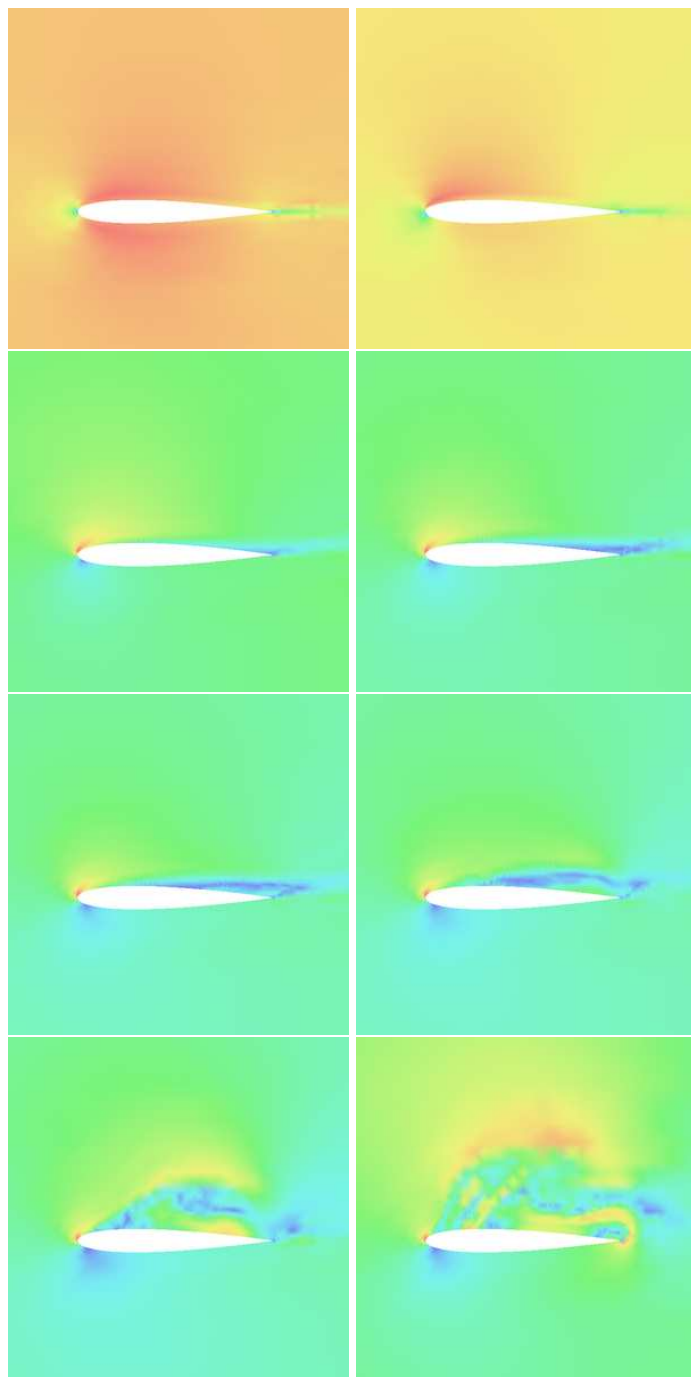


Fig. 1.14. From Chapter 22: Magnitude of the velocity for a 3d wing using EG2, with increasing angle of attack; 0,4,12,14,16,18,20, and 22° .

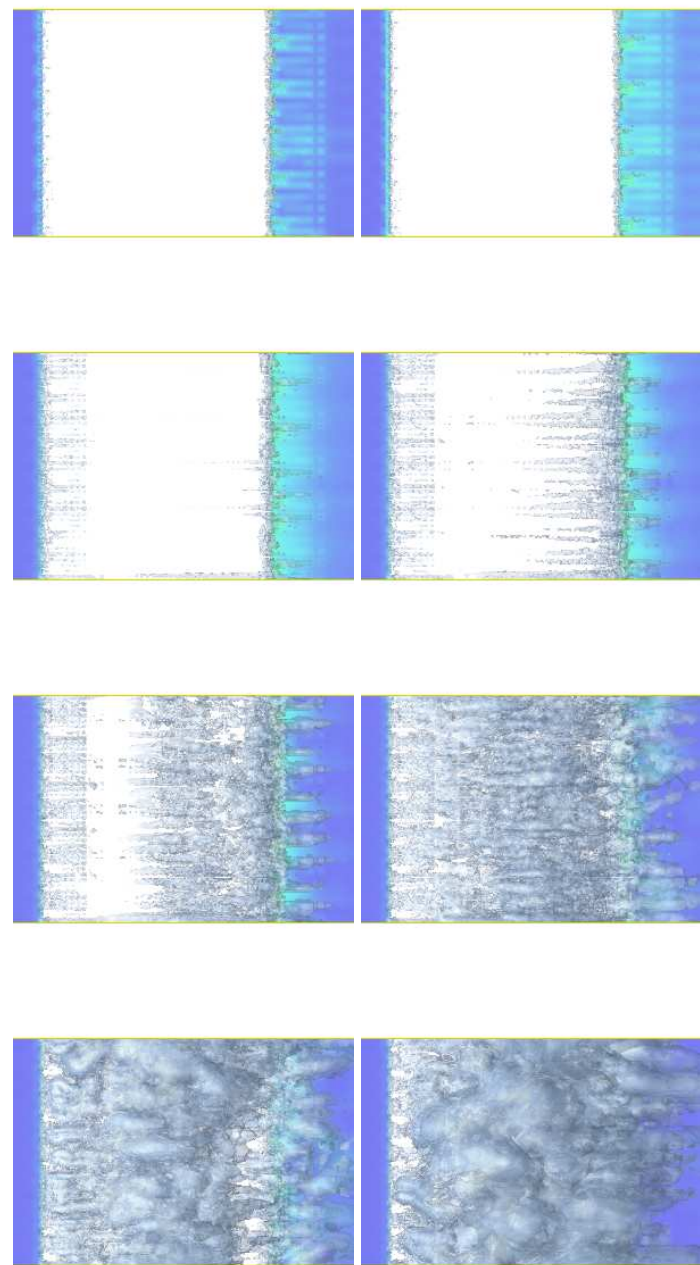


Fig. 1.15. From Chapter 22: Magnitude of first 2 vorticity components $|(\omega_1, \omega_2)|$ for a 3d wing using EG2 (with the third component in the direction of the wing), with increasing angle of attack; 0,4,12,14,16,18,20, and 22° .

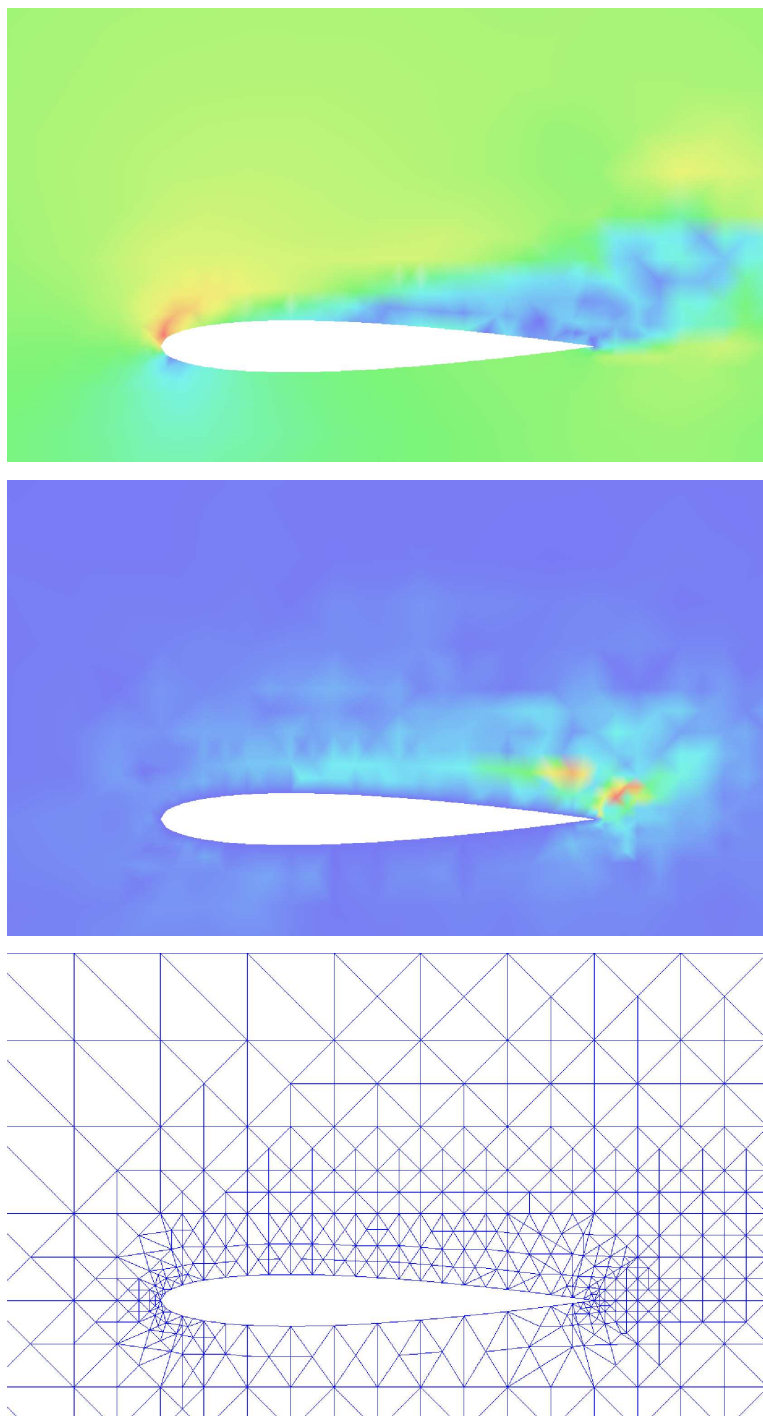


Fig. 1.16. From Chapter 35: Adaptive mesh refinement for the flow past a NACA 0012: magnitude of the velocity (upper), dual solution (middle) representing sensitivity information related to the computation of lift and drag, and a corresponding (coarse) mesh under refinement (lower).

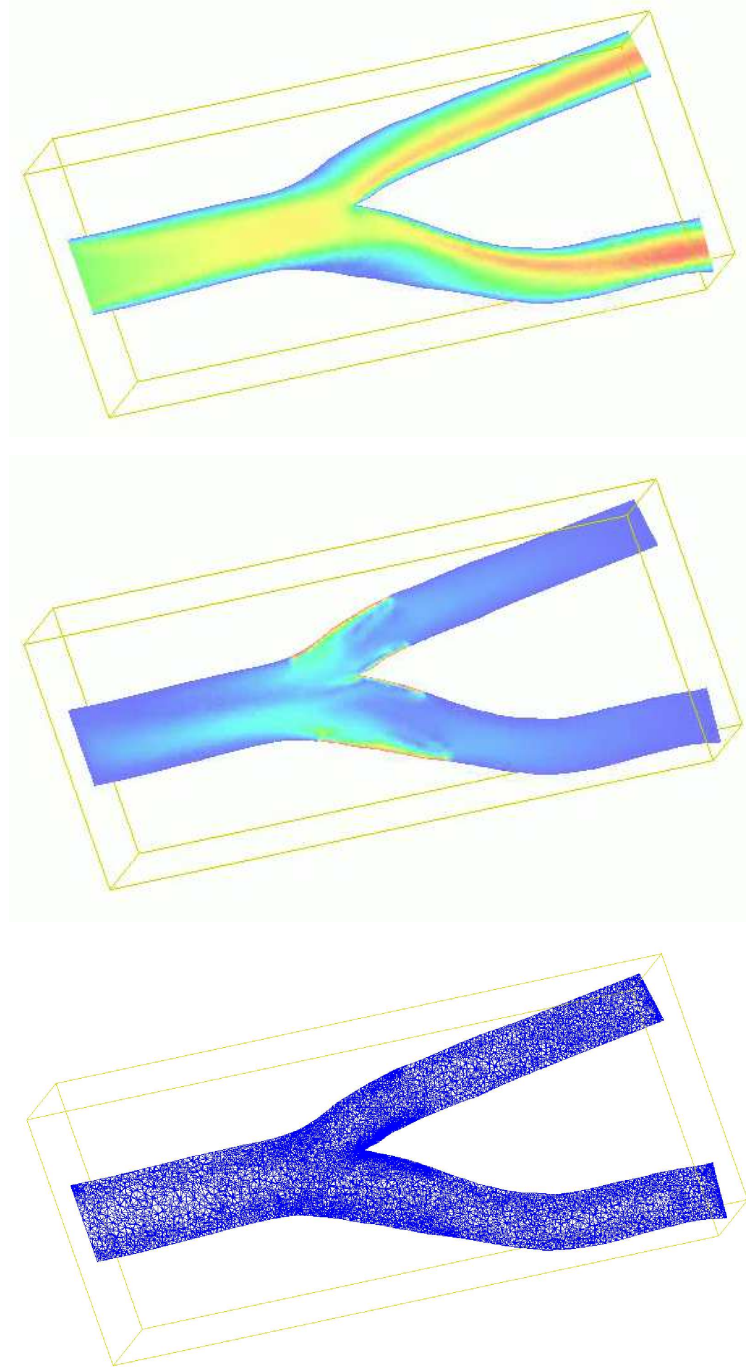


Fig. 1.17. From Chapter 35: Midsections showing snapshots of a G2 simulation of the blood flow in a realistic bifurcation model of a human carotid bifurcation (upper), the dual solution corresponding to the computational error in wall shear stress (middle), and the corresponding mesh (lower). Geometrical model produced by K. Perktold, TUG Graz, developed from an experimental cast (D. Liepsch, FH Muenich).

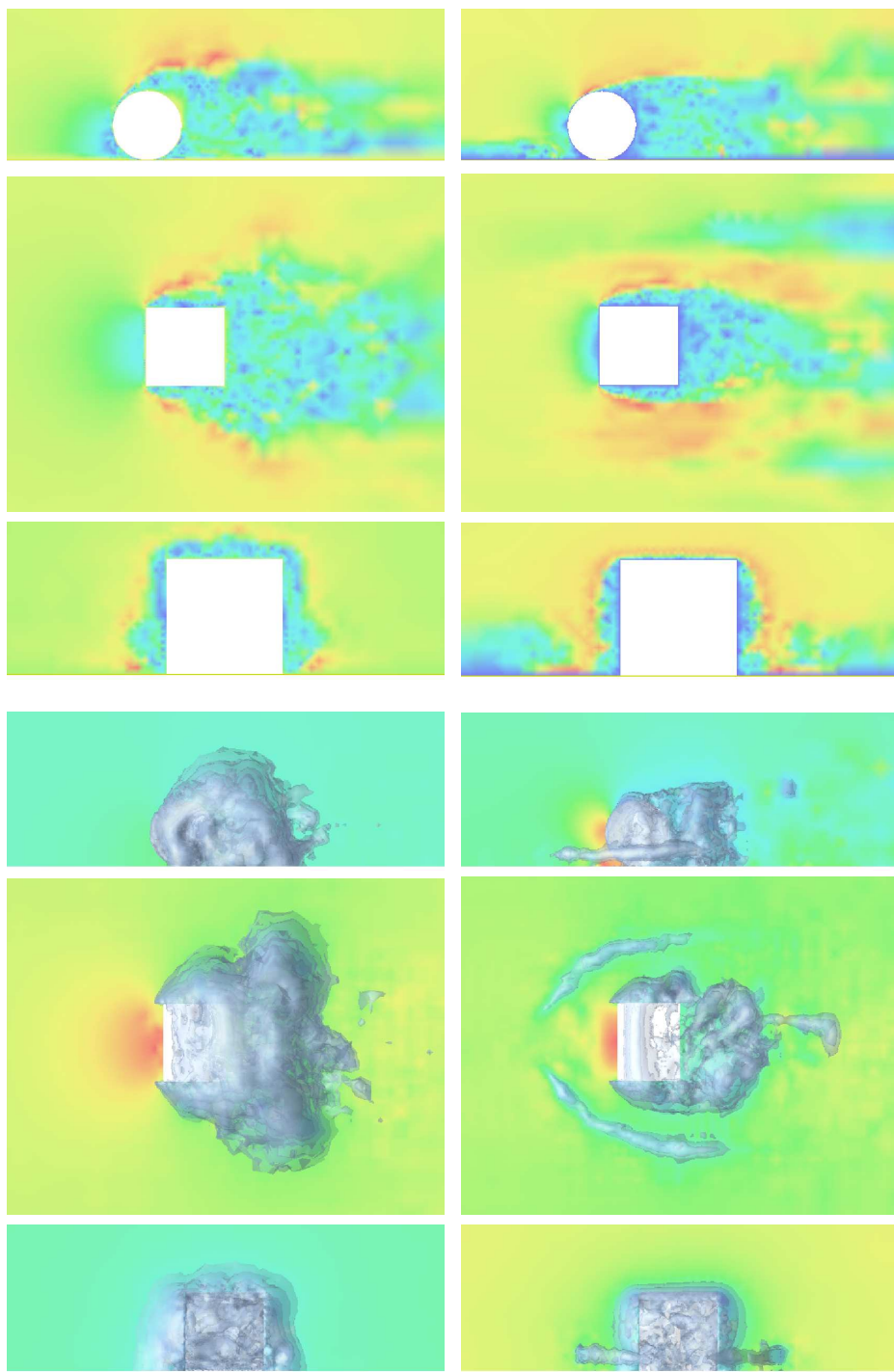


Fig. 1.18. From Chapter 35: Snapshots of magnitude of velocity (upper) and pressure and iso-surfaces of negative pressure (lower), for rotating (left) and stationary (right) cylinder, in the x_1x_2 -, x_1x_3 -, and x_2x_3 -planes, through the center of the cylinder.

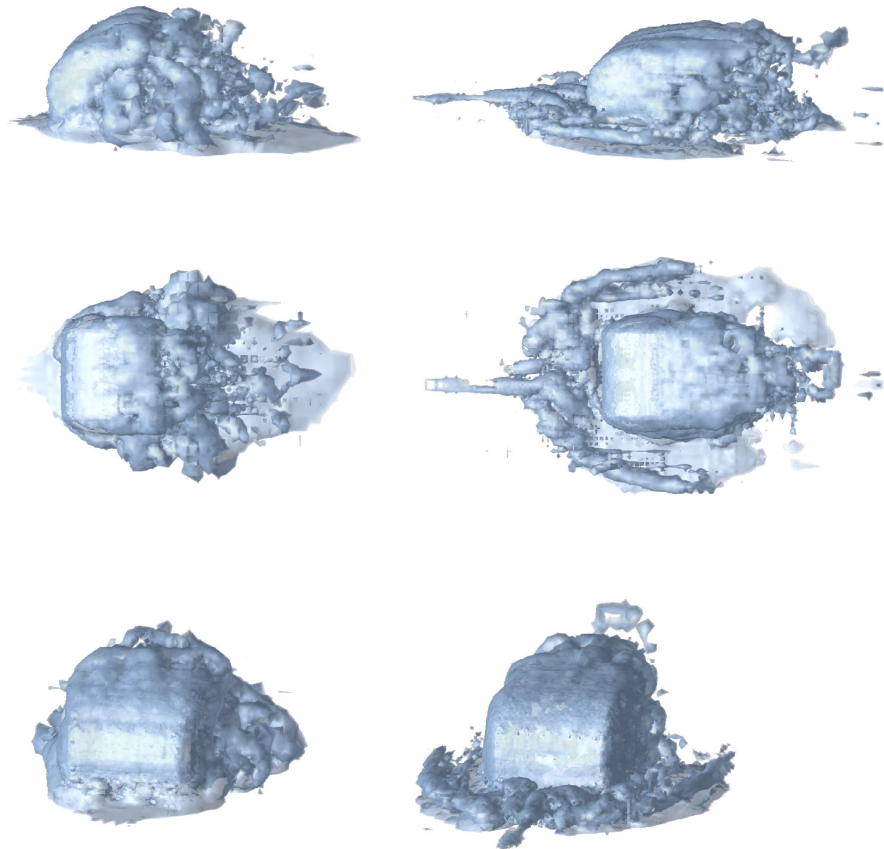


Fig. 1.19. From Chapter 24: G2 solutions of the flow past a wheel: snapshots of magnitude of the vorticity for the rotating (left) and the stationary (right) cylinder.

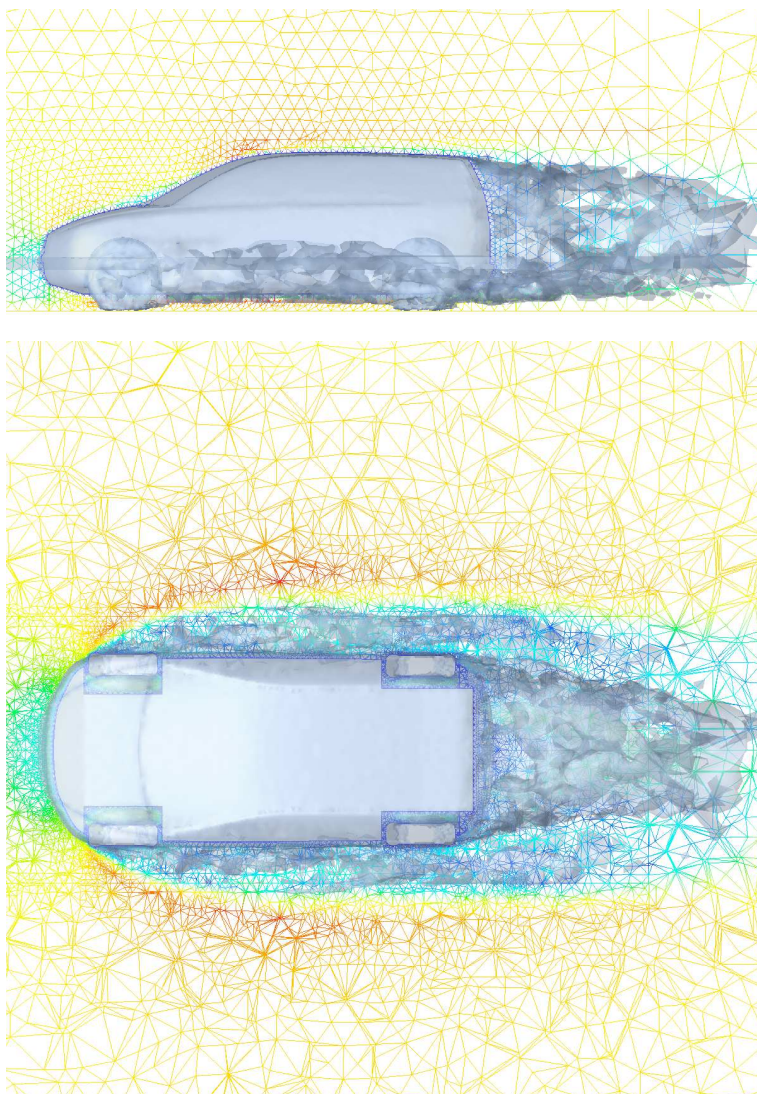


Fig. 1.20. From Chapter 33: G2 solution of the turbulent flow around a car (geometry courtesy of Volvo Car Corporation).

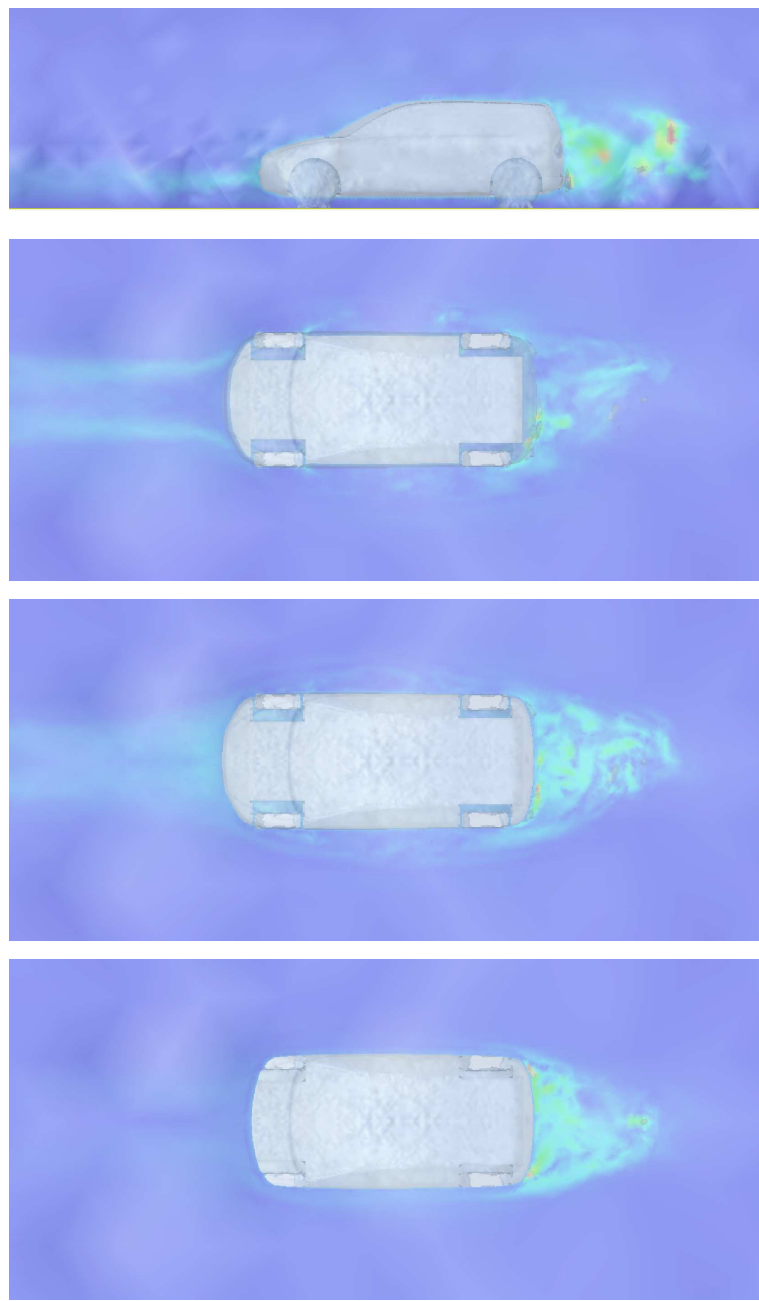


Fig. 1.21. From Chapter 33: dual solution with respect to drag around a car (geometry courtesy of Volvo Car Corporation).

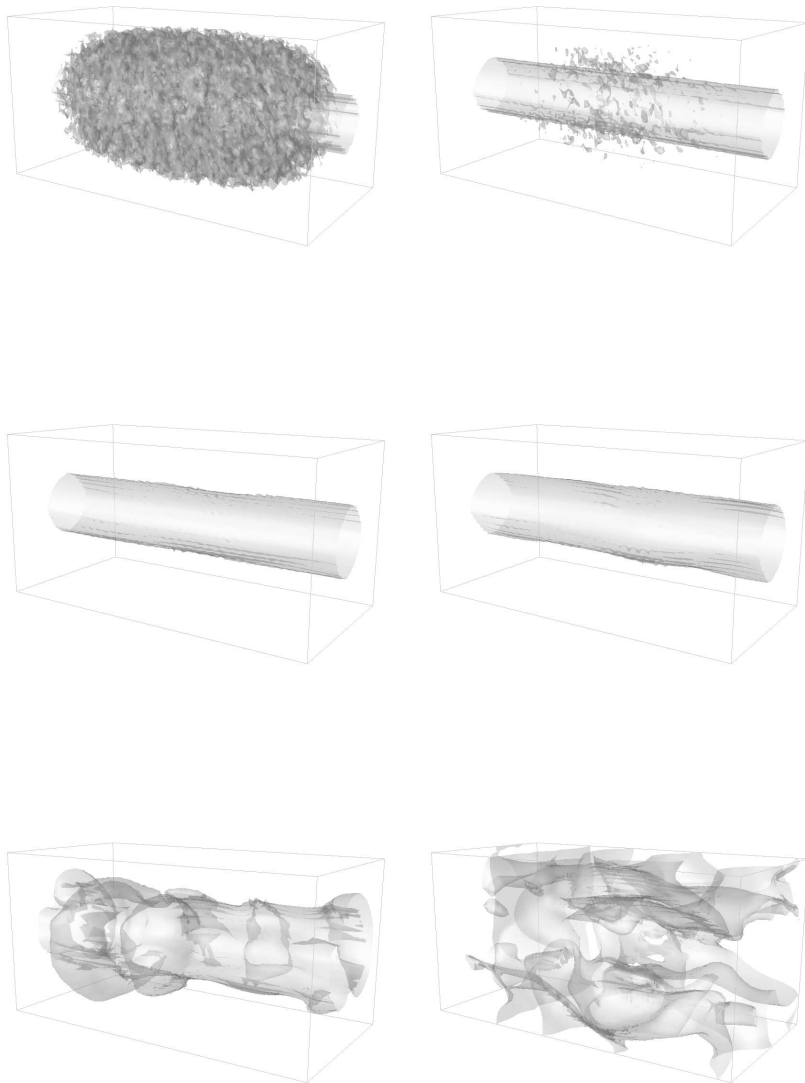


Fig. 1.22. From Chapter 36: streamwise velocity iso-surfaces for $|u_1| = 0.02$ in jet flow (random initial perturbation) for $t = 0, 2, 5, 7, 10, 15$

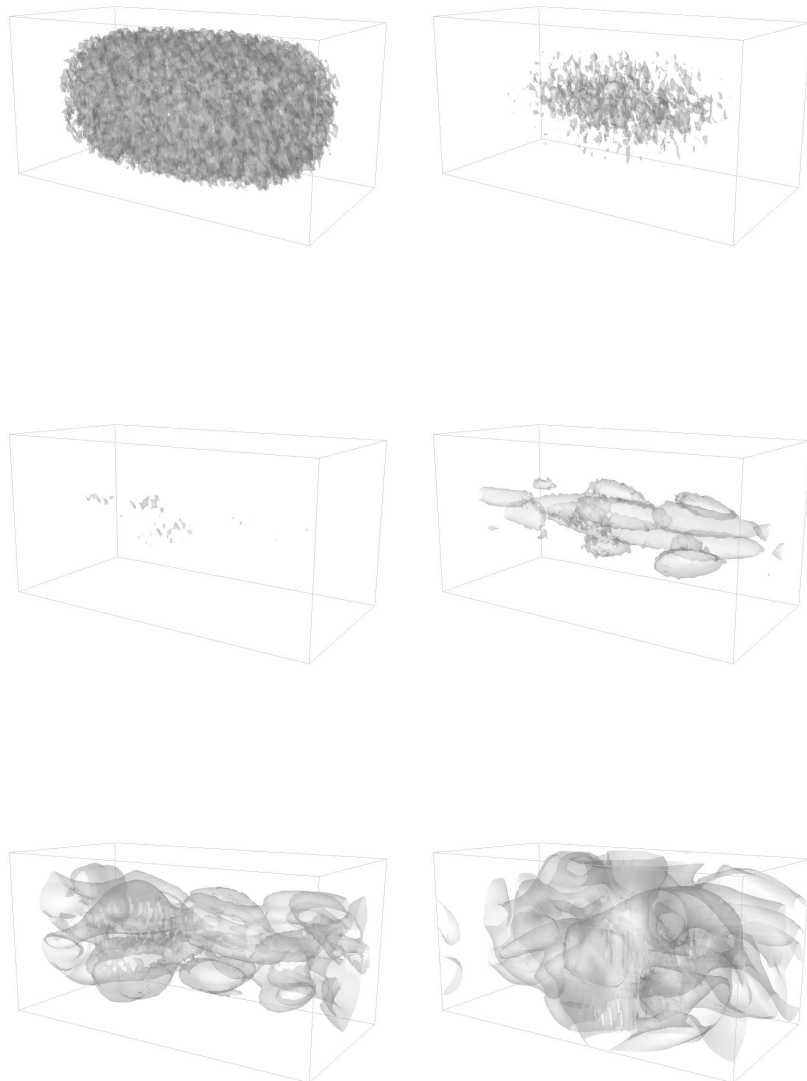


Fig. 1.23. From Chapter 36: Transversal velocity iso-surfaces for $|u_2| = 0.02$ in jet flow (random initial perturbation) for $t = 0, 2, 5, 7, 10, 15$

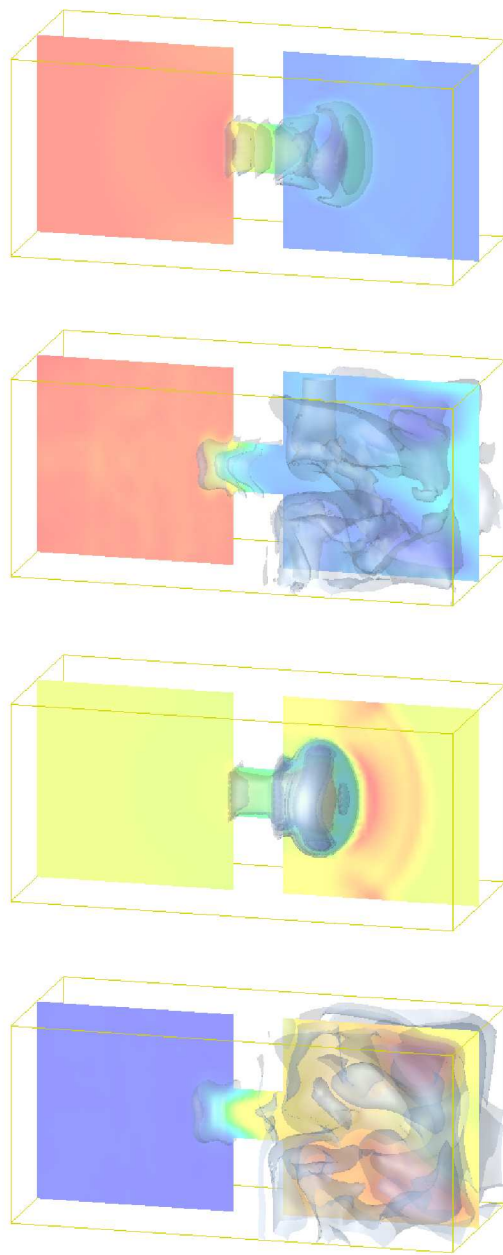


Fig. 1.24. From Chapter 38: EG2 simulation of the Joule-Thomson experiment: snapshots of density (upper 2 figures) and temperature (lower 2 figures) at 2 different time instants.

Mysteries and Secrets

...the whole procedure was an act of despair because a theoretical interpretation had to be found at any price, no matter how high that might be...
(Planck on the statistical mechanics basis of his radiation law)

Sommerfeld's very exhaustive discussion of Couette flow led to the conclusion that this type of flow remains stable for all viscosities. For a time, after this negative result had been obtained, it was thought that the method of small oscillations was unsuitable for the theoretical solution of the problem of transition to turbulence. It transpired later that this view was not justified, because Couette flow is a very special and restricted example.
(Schlichting in Boundary Layer Theory, p 465, McGraw-Hill 1979)

2.1 Mysteries

We shall also demonstrate the usefulness of computational turbulence in basic science by resolving the following unsolved mysteries, which have haunted scientists over centuries:

- d'Alembert's Mystery: Zero drag of inviscid flow,
- Loschmidt's Mystery: Violation of the 2nd law of thermodynamics,
- Sommerfeld's Mystery: Stability of Couette flow.

All these mysteries reflect *paradoxes*, where phenomena predicted by mathematics are not at all observed in reality. Since science is supposed to be rational and based on mathematics, paradoxes are catastrophic for the credibility of science, and thus have to be resolved (or covered up), in one way or the other, at any price.

In d'Alembert's Mystery formulated in 1752 [29], mathematics predicts that a body may move through a fluid with zero (very small) viscosity, like air and water, with zero (very small) resistance or *drag*. But everybody knows that this is impossible; the drag increases roughly quadratically with the velocity and becomes very substantial for higher velocities.

In Loschmidt's Mystery formulated in 1876 [84], mathematics of systems with zero viscosity predicts that time reversal and a perpetuum mobile is possible. But everybody knows that time is always moving forward and that a perpetuum mobile is impossible, as expressed by the 2nd law of thermodynamics.

In Sommerfeld's Mystery from 1908 [104], mathematics predicts that the simplest of all flows, Couette flow with a stationary linear velocity profile, is stable and thus should exist. But nobody has ever observed this flow in a fluid with small viscosity.

The cover up of d'Alembert's Mystery is to blame the assumption of zero viscosity for the erroneous prediction: In reality there is always some possibly very very small viscosity (of some nature), which changes everything. We will below argue that such explanations are not scientifically satisfactory and we shall instead present a new resolution based on computational turbulence in the inviscid Euler equations.

The cover up of Loschmidt's Mystery is to introduce statistical mechanics based on microscopic games of roulette. We will below argue that such an explanation is cumbersome scientifically, and we shall instead present a new resolution demonstrated through computational turbulence in the Euler equations.

The cover up of Sommerfeld's Mystery is to say that a linear velocity profile is too simple for the mathematical theory to apply, which evidently is not scientifically satisfactory either. We will below computationally study Couette flow and we will find that it is not stable, just as observed. After this experience we will be able to theoretically understand, using mathematics and avoiding the pitfall of Sommerfeld, *why* Couette flow is not stable.

2.2 Secrets

As applications of computational turbulence we shall uncover (some of the) secrets of the following activities based on turbulent incompressible flow of air and water:

- ball sports,
- flying,
- sailing,
- racing.

In all ball sports including football (soccer), baseball, tennis, golf and table-tennis, the player that can control the spin of the ball to give it a desired curved path, has an important advantage. The fluid mechanics giving the spinning ball a curved path, depending on the direction of the spin, is referred to as the *Magnus effect* which creates a *lift* force perpendicular to the direction of motion and spin. Below we will study aerodynamics of ball sports

computationally including the dependence on the spin, speed and the roughness of the surface of the ball. Of course, the flow of air around a spinning ball is turbulent.

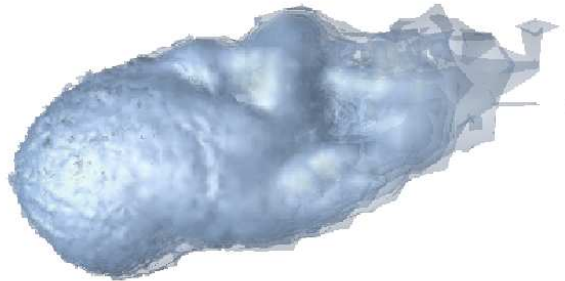


Fig. 2.1. Turbulent flow around a spinning ball.

To understand why flying is possible, we will below simulate the turbulent flow around a wing, and this way uncover how the necessary lift and unavoidable drag is generated. We shall also see that without computational turbulence it is impossible to mathematically predict lift and drag, in particular at take-off and landing, where the *angle of attack* of the wing against the flow is large and the flow is very turbulent. We shall thus compute the turbulent flow around a wing at different angles of attack and discover that the flow features are very different for the low angle of attack at cruising speed and the high angle of attack at take-off and landing. We shall see that classical analytical mathematical methods may give fairly reasonable predictions for (very) long wings at small angles of attack, but not so for normal wings and/or large angles of attack. To cruise at 30 000 feet is one thing, and to take off and land a completely different game.

Sailing is similar to flying from a fluid mechanics point of view, with the sail when going against the wind acting like a wing giving a lift force pulling the sail and boat against the wind but also tilting the boat. Needless to say, the flow of air around a sail is turbulent, and thus computational turbulence certainly opens new insights into the art of sailing and how to win Americas Cup. Also the keel of a sailing boat acts like a wing and gives a pull partly balancing the side force from the sail.

Modern cars are designed to have small drag, since fuel consumption directly couples to drag, and for racing cars also the lift is of concern since a flying racing car is hard to control. Computational turbulence offers new possibilities of car design, since traditional experimental testing of prototypes in wind tunnels is very slow and costly.

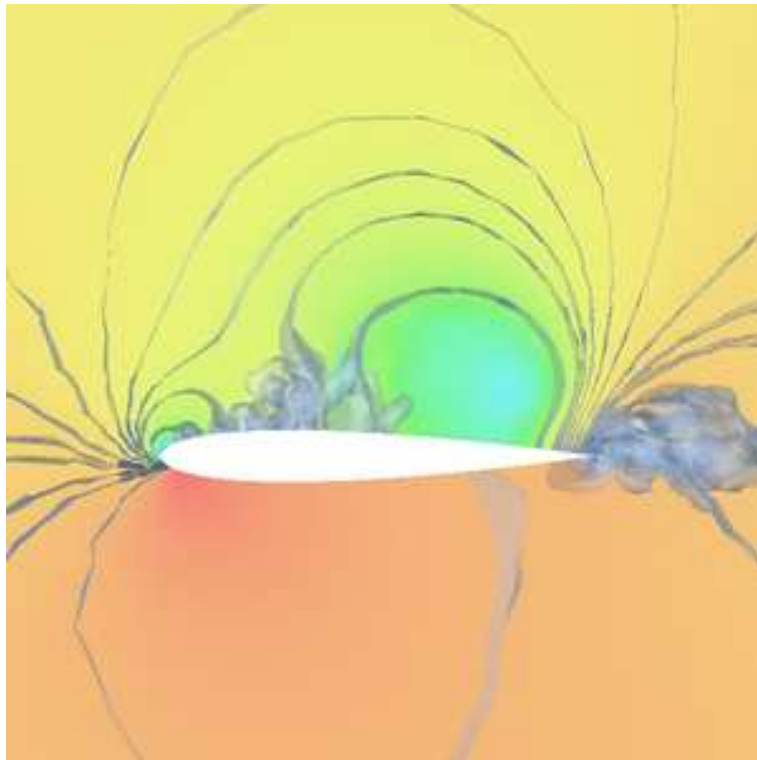


Fig. 2.2. Turbulent flow around a wing.

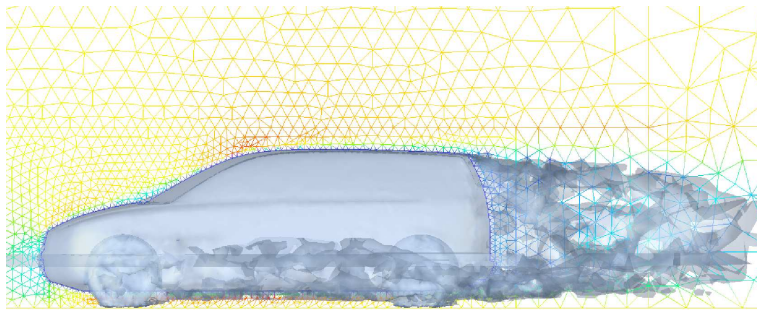


Fig. 2.3. Turbulent flow around a car (geometry courtesy of Volvo Car Corporation).

3

Turbulent Flow and History of Aviation

I feel perfectly confident, however, that this noble art will soon be brought home to man's general convenience, and that we shall be able to transport ourselves and families, and their goods and cattle, more securely by air than by water, and with a velocity of from 20 to 100 miles per hour. (George Cayley 1809)

3.1 Leonardo da Vinci, Newton and d'Alembert

Is it conceivable that with proper mathematics, humans would have been flying, at least gliders (without engine), several hundred years before this actually came true in the late 19th century? Well, let's face some facts.

The idea of flying, like the birds, goes back at least to Greek mythology about the inventor and master craftsman Daedalus, who built wings for himself and his son Icarus in order to escape from imprisonment in the Labyrinth of Knossos on the island of Crete.

Leonardo da Vinci made impressive and comprehensive investigations into aerodynamics collected into his *Treatise on the Flight of Birds* from 1505, and designed a large variety of devices for muscle-powered human flight. After extensive testing da Vinci concluded that even if both arms and legs got involved through elaborate mechanics, human power was insufficient to get off the ground.

Newton confirmed these experiences by calculating the lift of a tilted flat plate, representing a wing, in a horizontal stream of "air particles" hitting the plate from below, to obtain a disappointingly small (erroneous) value of the lift.

Newton's result was further supported by d'Alembert's Mystery predicting that both the drag and the lift of a body traveling through air would be close to zero, clearly at variance with many early observations of birds flying long distances even without flapping their wings. d'Alembert built his computations of drag (and lift) on particular solutions to the Euler equations

referred to as *potential solutions*, with the velocity given as the gradient of a potential satisfying Laplace's equation. But nobody could come up with any kind of resolution of the mystery before Ludwig Prandtl, called the Father of Modern Fluid Dynamics, in a short note from 1904 suggested a resolution based on boundary layer effects from vanishingly small viscosity, which still today remains the accepted resolution of the mystery. As already indicated, we shall below present computational evidence that Prandtl's resolution is not credible and instead put forward a new scientifically more satisfactory resolution.

3.2 Cayley and Lilienthal

Despite the pessimistic predictions by Newton and d'Alembert, the 29 years old engineer George Cayley (uncle of the mathematician Arthur Cayley) in 1799 sketched the by now familiar configuration of an airplane with fixed cambered wings and aft horizontal and vertical tails, and also investigated the characteristics of airfoils using a whirling arm apparatus. Cayley outlined his ideas about the principles of flying in *On Aerial Navigation* (1809). But Cayley did not produce any mathematical description of the motion of an aircraft and thus had no quantitative basis for designing airplanes. In 1849 Cayley built a large glider, along the lines of his 1799 design, and tested the device with a 10-year old boy aboard. The glider carried the boy aloft on at least one short flight.

The next major step was taken by the German engineer Otto Lilienthal, who made careful experiments on the lift and drag of wings of different shapes and designed various gliders, and himself made 2000 more or less successful flights starting from a little (artificial) hill, see Fig 3.1, before he broke his neck in 1896 after the glider had stalled 15 meter above ground.

3.3 Kutta, Zhukovsky and the Wright Brothers

Stimulated by Lilienthal's successful flights and his widely spread book *Bird Flight as the Basis of Aviation* from 1899, the mathematician Martin Kutta in his thesis from 1902 modified the erroneous classical potential flow solution by including a new term corresponding to a rotating flow around the wing with the strength of the vortex determined so that the combined flow velocity became zero at the trailing edge of the wing. This *Kutta condition* reflected the observation of Lilienthal that the flow should come off the wing smoothly, at least for small angles of attack. The strength of the vortex was equal to the *circulation* around the wing of the velocity, which was also equal to the lift. Kutta could this way predict the lift of various airfoils with a precision of practical interest. But the calculation assumed the flow to be fully two-dimensional and the wings to be very long and became inaccurate for shorter wings and large angles of attack.

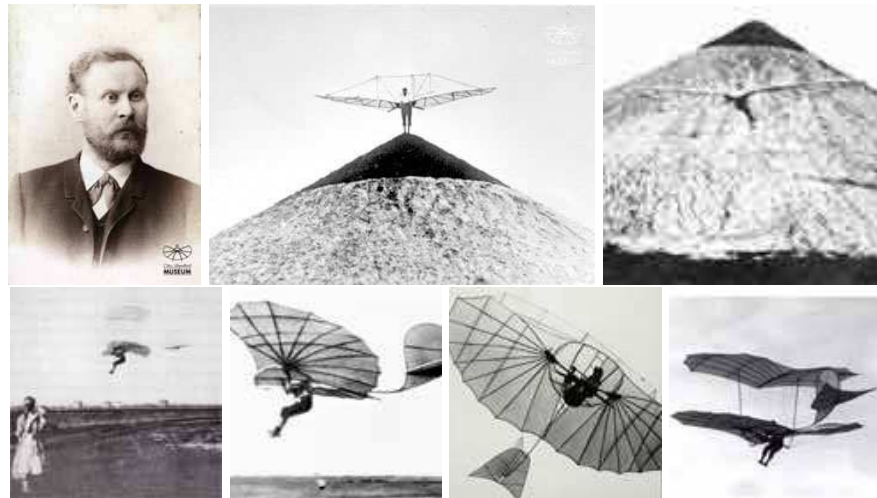


Fig. 3.1. Otto Lilienthal (1848–1896), some of the 137 known photos from 1891 to 1896. To document the development of his flight technique he was regularly joined by photographers during his flight practice (photos from Archive Otto-Lilienthal-Museum: www.lilienthal-museum.de).

The first successful powered controlled flight was performed by the brothers Orville and Wilbur Wright on December 17 1903 on the windy fields of Kitty Hawk, North Carolina, with Orville winning the bet to be the pilot of the *Flyer* and Wilbur watching on ground, see Fig 3.2. In the words of the Wright brothers from Century Magazine, September 1908:

The flight lasted only twelve seconds, a flight very modest compared with that of birds, but it was, nevertheless, the first in the history of the world in which a machine carrying a man had raised itself by its own power into the air in free flight, had sailed forward on a level course without reduction of speed, and had finally landed without being wrecked. The second and third flights were a little longer, and the fourth lasted fifty-nine seconds, covering a distance of 852 feet over the ground against a twenty-mile wind.

The modern era of aviation had started.

The mathematician Nikolai Zhukovsky, called the Father of Russian Aviation, in 1906 independently derived the same mathematics for computing lift as Kutta, after having observed several of Lilienthal's flights, which he presented before the Society of Friends of the Natural Sciences in Moscow as: *The most important invention of recent years in the area of aviation is the flying machine of the German engineer Otto Lilienthal.* Zhukovsky also purchased one of the eight gliders which Lilienthal sold to members of the public.

Kutta and Zhukovsky thus could modify the mathematical potential theory of lift of a wing to give reasonable results, but of course could not give anything but a very heuristic justification of their Kutta-Zhukovsky condition

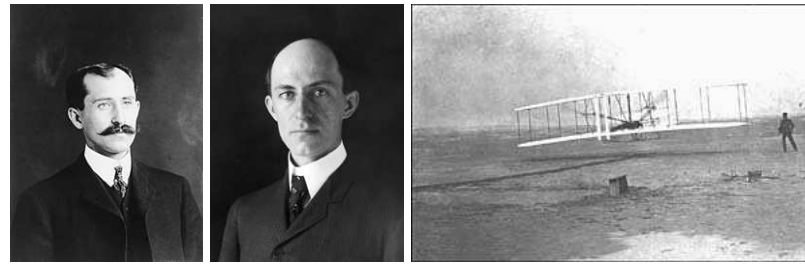


Fig. 3.2. Orville Wright (1871–1948) and Wilbur Wright (1867–1912) and the lift-off at Kitty Hawk, North Carolina, the 17th December 1903.

of zero velocity at the trailing edge of the wing, and could not treat realistic wings in three dimensions. Further, their modified potential solutions were not turbulent at all, so their calculations would seem merely like happy coincidences (knowing ahead the correct answer to obtain). We will return below in more detail to the basic problem of lift and drag of wings in turbulent flow.

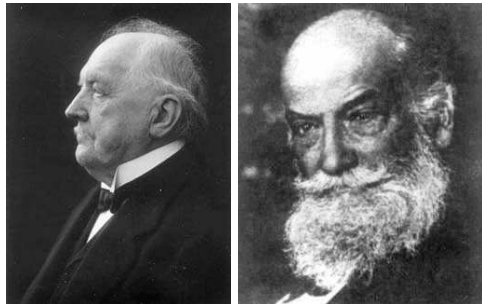


Fig. 3.3. Martin Kutta (1867–1944) and Nikolai Egorovich Zhukovsky (1847–1921).

Today computational methods open new possibilities of solving the equations for fluid flow using the computational power of modern computers. Thus, for the first time the mathematical fluid models of Euler and Navier–Stokes may come to a real use, which opens new revolutionary possibilities of computational simulation and prediction of fluid flow in science and technology. The range of possible applications is incredibly rich! For example, it is now becoming possible to simulate the turbulent flow around an entire aircraft and thus systematically investigate questions of stability and control, which caused severe head-ache for the Wright brothers, as well as the designers of the modern Swedish jet fighter JAS Gripen. Actually, both the 1903 Wright *Flyer* airplane, with a forward canard instead of an aft tail, and the JAS are unstable and require careful control to fly. The instability of the fighter is intentional allowing quick turns, but the Wrights later replaced the canard with the conventional aft tail to improve stability. The stability of an airplane

is similar to that of a boat, with the important design feature being the relative position of the center of gravity and the center of the forces from the fluid (center of buoyancy for a boat), with the center of gravity ahead (below) giving stability, cf. Chapter 71 in Body&Soul Vol 3 [36].



Fig. 3.4. The 1903 Wright *Flyer* and JAS Gripen (JAS photo from <http://www.gripen.com/.>)

It is remarkable that 400 years passed between Leonardo da Vinci's investigations and the largely similar ones by Lilienthal. Why did it take so long time from almost success to success? Can we blame the erroneous mathematics of Newton and d'Alembert for the delay? Or was the reason that the (secret) writings of da Vinci were made public with a delay of 300 years? We leave the question open.

The Euler Equations

However sublime are the researches on fluids which we owe to Messrs Bernoulli, Clairaut and d'Alembert, they flow so naturally from my two general formulae that one cannot sufficiently admire this accord of their profound meditations with the simplicity of the principles from which I have drawn my equations ... (Euler 1752)

4.1 Foundation of Fluid Dynamics

Fluid dynamics as a scientific discipline starts with the *Euler equations* expressing conservation of mass, momentum and total energy as a system of partial differential equations. We now formulate these equations for an inviscid fluid enclosed in a fixed (open) domain Ω in three-dimensional space \mathbb{R}^3 with boundary Γ over a time interval $[0, \hat{t}]$ with initial time zero and final time \hat{t} . An inviscid fluid ($\nu = 0$) is also said to be an *ideal fluid*. We thus assume that there are no viscous forces (inviscid flow) and we also assume that there is no heat flow from conduction (zero heat conductivity).

We seek the *density* ρ , *momentum* $m = \rho u$, with $u = (u_1, u_2, u_3)$ the *velocity*, and the *total energy* e as functions of $(x, t) \in \Omega \cup \Gamma \times [0, \hat{t}]$, where $x = (x_1, x_2, x_3)$ denotes the coordinates in \mathbb{R}^3 and u_i is the velocity in the x_i -direction. The Euler equations for $\hat{u} \equiv (\rho, m, e)$ read with $Q = \Omega \times I$ and $I = (0, \hat{t}]$:

$$\begin{aligned} \dot{\rho} + \nabla \cdot (\rho u) &= 0 && \text{in } Q, \\ \dot{m}_i + \nabla \cdot (m_i u) + p_{,i} &= f_i && \text{in } Q, \quad i = 1, 2, 3, \\ \dot{e} + \nabla \cdot (eu + pu) &= 0 && \text{in } Q, \\ u \cdot n &= 0 && \text{on } \Gamma \times I, \\ \hat{u}(\cdot, 0) &= \hat{u}^0 && \text{in } \Omega, \end{aligned} \tag{4.1}$$

where $p = p(x, t)$ is the *pressure* of the fluid, $p_{,i} = \partial p / \partial x_i$ is the partial derivative with respect to x_i , the dot indicates differentiation with respect to time, n denotes the outward unit normal to Γ and $f = (f_1, f_2, f_3)$ is a

given *volume force* (like gravity) acting on the fluid, and $\hat{u}^0 = \hat{u}^0(x)$ represent initial conditions. Further, the total energy $e = k + \theta$, where $k = \rho|u|^2/2$ is the *kinetic energy*, with $|u|^2 \equiv u_1^2 + u_2^2 + u_3^2$, and $\theta = \rho T$ is the *internal energy* with T the *temperature* scaled so that $c_v = 1$, where c_v is the heat capacity under constant volume.

The boundary condition $u \cdot n = 0$ is a *slip boundary condition* requiring the normal velocity $u \cdot n$ to vanish corresponding to an impenetrable boundary with zero friction. Below we will consider other boundary conditions, including inflow and outflow boundary conditions and non-zero friction.

Further,

$$\nabla \cdot v = \sum_{i=1}^3 v_{i,i}$$

denotes the divergence of $v = (v_1, v_2, v_3)$, while the gradient of a scalar function w will be denoted by $\nabla w = (w_{,1}, w_{,2}, w_{,3})$.

There are five equations in the Euler system (4.1), while the number of unknowns including the pressure is six, and so we need one more equation. This equation may be a *state equation for a compressible gas* expressing the pressure p as a function of density ρ and temperature T , e.g. the *state equation* $p = (\gamma - 1)\rho T$ of a *perfect gas*, where $\gamma = c_p$ is the *adiabatic index* with c_p the heat capacity under constant pressure, and $(\gamma - 1)$ is the *gas constant*. The additional equation may alternatively express that the fluid is *incompressible* in the form $\nabla \cdot u = 0$ in Q .

For a perfect gas, the *speed of sound* c is given by $c^2 = \gamma(\gamma - 1)T$, and the *Mach number* is defined as $M = |u|/c$, with u the velocity of the gas. We assume in this book that the fluid is incompressible with constant density. This is an approximation up to a variation in density of size M^2 , so that for $M < 0.3$ the variation would be less than say 10 %. Traveling through air thus corresponds to velocities less than 300 km/h (200 mph), which is applicable to most cars, small airplanes, or even jumbo-jets at start and landing. Water can be viewed to be incompressible in most applications.

The extension of the Euler equations to include viscous forces and heat flow by conduction are referred to as the *Navier–Stokes equations*. The Navier–Stokes and Euler equations describe a very rich complex world of fluid dynamics.

In this book we focus mainly on incompressible inviscid or viscous flow, and open to compressible flow in the last chapter, which we continue in Body&Soul Vol 5 on Computational Thermodynamics.

4.2 Derivation of the Euler Equations

We now show that the Euler equations (4.1) express conservation of mass, momentum and total energy in the *conservation variables* (ρ, m, e) . To this

end consider a fixed small volume V in Ω with boundary S . Mass conservation implies that

$$\int_V \dot{\rho} dx = \frac{\partial}{\partial t} \int_V \rho dx = - \int_S (\rho u) \cdot n ds,$$

expressing that the rate of increase of total mass in the fixed volume V is equal to the rate of inflow through the boundary S . The Divergence Theorem (see e.g. B&S Vol 3 [36]) states that

$$\int_V \nabla \cdot (\rho u) dx = \int_S (\rho u) \cdot n ds,$$

and we thus conclude that

$$\int_V \dot{\rho} dx + \int_V \nabla \cdot (\rho u) dx = 0$$

for all volumes V . Assuming that the integrands are continuous, we thus obtain the equation for mass conservation $\dot{\rho} + \nabla \cdot (\rho u) = 0$.

We obtain the differential equation expressing conservation of each component of the momentum m_i similarly, noting that by Newtons 2nd law the rate of change of momentum is given by the corresponding component $-p_{,i}$ of the pressure gradient ∇p with increasing pressure retarding the flow, combined with a volume force f_i . Finally, the equation expressing conservation of total energy e is obtained noting that the rate of change of the total energy is given by the work pu .

4.3 The Euler Equations as a Continuum Model

The Euler equations represent a *continuum model* with formally no smallest scale, since there is no smallest scale of the set of real numbers \mathbb{R} . In reality we solve the Euler equations in *finite precision computation* using the G2 finite element method with finite mesh size h , which may vary in space and time. We may think of the finite precision as effectively computing with a fixed number of digits (e.g. double precision with about 16 digits) instead of computing with real numbers with infinitely many digits with infinite precision (which is impossible). Typical meshes have a mesh size of 10^{-2} on the unit cube with 10^6 mesh points. A gas has about 10^{24} molecules per mole, and thus the values of density, momentum and energy at each mesh point represent mean values of about 10^{18} molecules, thus mean values over incredibly many "fluid particles".

A computational *particle model* of a gas accounting for the position and velocity of each of the 10^{24} particles in each mole, is inconceivable on any kind of thinkable computer. Thus, only continuum models can be used for macroscopic phenomena of fluid flow.

4.4 Incompressible Flow

In an incompressible fluid the density ρ does not change if we follow the motion of the fluid particles of the flow. We can express this fact in the differential equation form

$$D_u \rho \equiv \dot{\rho} + u \cdot \nabla \rho = 0,$$

where $D_u \rho$ is the *convective derivative* of ρ with respect to the velocity u . We obtain the convective derivative by computing the change in time following the *trajectory* $x(t)$ of a fluid particle satisfying the differential equation $\dot{x}(t) = u(x, t)$. Differentiating $\rho(x(t), t)$ with respect to time, we obtain by the chain rule:

$$\frac{d}{dt} \rho(x(t), t) = (\dot{\rho} + \dot{x} \cdot \nabla \rho)(x(t), t) = D_u \rho(x(t), t).$$

Since mass conservation reads $D_u \rho + \rho \nabla \cdot u = 0$, we conclude that the velocity u in incompressible flow is characterized by the equation

$$\nabla \cdot u = 0, \quad \text{in } Q. \tag{4.2}$$

The Incompressible Euler and Navier–Stokes Equations

Various liquids carried by virtue of their own weight from various points to form a pool of various liquids at a point of accumulation. (Lawrence Weiner, conceptual artist describing in words a piece of art instead of realizing it physically, 1978)

In a reasonable theory there are no dimensionless numbers whose values are only empirically determinable. (Einstein)

5.1 The Incompressible Euler Equations

We now specialize the Euler equations (4.1) for $\hat{u} = (\rho, u, e)$ to incompressible flow assuming constant density $\rho = 1$:

$$\begin{aligned}\nabla \cdot u &= 0 && \text{in } Q, \\ \dot{u} + (u \cdot \nabla)u + \nabla p &= f && \text{in } Q, \\ \dot{e} + \nabla \cdot (eu + pu) &= 0 && \text{in } Q, \\ u \cdot n &= 0 && \text{on } \Gamma \times I, \\ u(\cdot, 0) &= u^0 && \text{in } \Omega, \\ e(\cdot, 0) &= e^0 && \text{in } \Omega,\end{aligned}\tag{5.1}$$

where we write the momentum equation in vector form noting that by incompressibility and constant unit density $\nabla \cdot (m_i u) = u \cdot \nabla u_i + u_i \nabla \cdot u = (u \cdot \nabla)u_i$. The equation of mass conservation and the momentum equations give four equations for the four unknowns (u, p) . Formally we can thus solve for (u, p) in the first two equations and then separately solve for the total energy e with (u, p) given.

We thus start out considering the reduced system in (u, p) which we will also refer to as the Euler equations for incompressible flow:

$$\begin{aligned}\dot{u} + (u \cdot \nabla)u + \nabla p &= f && \text{in } Q, \\ \nabla \cdot u &= 0 && \text{in } Q, \\ u \cdot n &= 0 && \text{on } \Gamma \times I, \\ u(\cdot, 0) &= u^0 && \text{in } \Omega,\end{aligned}\tag{5.2}$$

where to conform to common notational practice we changed the order of the equations for mass conservation and momentum.

5.2 The Incompressible Navier–Stokes Equations

We now generalize to the Navier–Stokes equations including viscous forces modeled in the form of a Laplacian term $-\nu\Delta u$ in the momentum equation, where $\nu > 0$ is a constant coefficient of viscosity. We thus assume the fluid to be *Newtonian* with viscous stresses depending linearly on velocity gradients. We shall below scrutinize the general concept of viscosity and the particular assumption of a Newtonian fluid. For now we assume that the viscous force is modeled by the term $-\nu\Delta u$ in the momentum equation, with further justification in Section 28.3.

The Navier–Stokes equations (NS) for a Newtonian fluid enclosed in a fixed volume Ω in \mathbb{R}^3 read:

$$\begin{aligned}\dot{u} + (u \cdot \nabla)u - \nu\Delta u + \nabla p &= f, && \text{in } Q, \\ \nabla \cdot u &= 0, && \text{in } Q, \\ u &= 0, && \text{on } \Gamma \times I, \\ u(\cdot, 0) &= u^0, && \text{in } \Omega,\end{aligned}\tag{5.3}$$

where now all components of the velocity u are prescribed to be zero on the boundary Γ , not only the normal velocity $u \cdot n$ as in the Euler equations. The boundary condition $u = 0$ is referred to as a *no slip boundary condition* or *homogeneous Dirichlet boundary condition* for the velocity u . We consider other boundary conditions below including inflow and outflow boundary conditions and friction boundary conditions.

5.3 What is Viscosity?

In fact, viscosity closely couples to turbulence and thus the viscosity in NS would rather represent a *turbulent viscosity* $\nu = \nu(u)$ with a possibly very complex dependence on the velocity u ; with a non-constant ν the viscous term would rather take the form $-\nabla \cdot (\nu \nabla u)$. But if indeed ν depends on u and we cannot determine how, then the NS equations would seem to be useless for predictions, even using computational methods.

So how are we going to handle this problem? Well, first we recall that we focus on the case of *small viscosity*. The first idea that comes up is then of course to assume that the viscosity is so small that we can put it equal to zero, which gives us the Euler equations. This is the classical approach of Euler which however led to d'Alembert's Mystery, and thus had to be abandoned as if the great scientist Euler was incorrect. We will show that Euler was not stupid at all; in fact Euler's solution to the tricky problem of finding a proper

(small) viscosity by simply setting the viscosity to zero, is very elegant and far-reaching. But to come to this satisfactory conclusion we have to solve the Euler equations computationally, and not try analytical methods.

Next we assume that ν is non-vanishing, but still small, so that we are facing NS equations. We shall below see that solving NS equations computationally we have to use a mesh with a certain mesh size h , and we shall see that the computational method itself introduces an effect which can be viewed as a mesh dependent *artificial viscosity* ν_h . Now, if $\nu_h > \nu$, then the true viscosity ν will be overshadowed by the artificial viscosity ν_h , which means that the precise value of ν becomes irrelevant. And the smaller ν is, the bigger is the chance that it will be overshadowed by the artificial viscosity ν_h , so that we do not have to determine ν accurately; it would be sufficient just to know that ν is (sufficiently) small.

Of course, we expect the solution $(u, p) = (u_\nu, p_\nu)$ to depend on ν , and in order for a computation with an artificial viscosity $\nu_h > \nu$ to have some predictive value, it is necessary that the *output* or *quantity of interest* from the solution (u_ν, p_ν) is not critically depending on the precise value of ν . We shall below see that this may indeed be true in many cases if the output is a mean value in space-time such as a *drag coefficient* $c_D(\nu)$ measuring the total force of a body moving through a fluid with viscosity ν . Thus, we shall see that $c_D(\nu)$ varies quite slowly with ν , which means that we do not have to know ν very precisely (which certainly helps when determining ν), or that we effectively can compute with an artificial viscosity ν_h and only need to know that $\nu < \nu_h$. Thus, the good news is that for turbulent flow with small viscosity, in many cases we do not need to specify the viscosity very precisely, which would be very difficult.

We shall also study cases with a critical dependence on (small) viscosity, including the so-called *drag crisis* reflecting that the resistance of e.g. a cylinder of unit diameter and speed moving through a fluid, quite suddenly drops by more than 50% as ν decreases to about 10^{-6} to raise again for smaller ν .

As indicated, we shall see that simply assuming $\nu = 0$, in a case where we know that the viscosity is small but not exactly how small, will take us quite far. This follows the initial ingenious idea of Euler of studying ideal fluids with zero viscosity, but we shall see that to arrive at this peak, we will have to pass through the deep valley of d'Alembert's Mystery.

To sum up: Turbulence occurs in fluids with small viscosity ν and typical outputs may have a weak dependence on ν . This means that we do not need precise information on ν ; in many cases we may effectively set $\nu = 0$ following Euler, or knowing just one binary digit of ν may be enough. Thus turbulent flow is difficult because of its complexity, but may be easy because precise information on the viscosity is not needed. This is favorable for computation, because complexity is handled by brute computational power, while the viscosity advantage remains.

5.4 What is Heat Conductivity?

We have seen that in the Euler equations we assume no flow of heat by conduction, which we may express as setting the coefficient of *heat conductivity* to zero. We will see that nevertheless heat will flow in turbulent fluid flow, not by conduction but by convection with the fluid. In turbulent flow heat energy thus will have a tendency to spread out (by turbulent convection), and if we don't see the turbulent motion of the fluid we may attribute the flow of heat to some form of conduction with a certain coefficient of heat conductivity. We understand that in turbulent flow the *effective coefficient of heat conduction* may be a very complex function of the flow, and thus impossible to determine.

We will see in G2 simulations of the Euler equations that we can directly compute the heat flow (by turbulent convection). This way we are thus relieved from the difficult task of finding an effective heat conductivity, since the objective of determining such a coefficient is to compute the heat flow.

To sum up, we are led to the conclusion that the classical need of determining coefficients of viscosity and heat conductivity in order to compute viscous stresses and heat flow, disappears in turbulent flow with small viscosity and heat conductivity, since the fluid motion and heat flow is directly computable from the Euler equations. We believe this is an elegant mathematical solution of a very difficult if not impossible practical problem.

5.5 Friction Boundary Conditions

We start our studies in Chapter 9 considering the Euler equations with slip boundary conditions, following the historical development of fluid dynamics, to discover several surprising facts. Later we shall also discuss *friction boundary conditions* for the Euler equations with the tangential stress coupled to the tangential velocity with a friction parameter, with slip corresponding to zero friction. We will view the friction boundary conditions as a simple so-called *wall model* for the flow in a *turbulent boundary layer* close to the boundary, with the friction parameter depending on the Reynolds number.

We will find that we may simulate flows with very large Reynolds numbers using the Euler equations with proper friction boundary conditions, without computationally (fully) resolving the boundary layer. Computational solution of the Euler equations thus will become extremely useful all along Euler's original plans, which resurrects Euler's model after a long dark age of discredit caused by d'Alembert's Mystery.

5.6 Einstein's Ideal

We note that the given data for NS equations is represented by (Ω, I, f, u^0) together with the viscosity ν , which we refer to as a *parameter*, and $\hat{u} = (u, p)$

is the corresponding solution which we seek. The specification of the data (Ω, I, f, u^0) is usually clear, while the determination of the viscosity ν (or Reynolds number) is much less clear, as we have seen.

In the Euler equations we set the viscosity ν to zero (and heat conductivity as well) with the intention to model fluid flow with very small viscosity. The Euler equations represent the *ideal of Einstein*, namely a *model without any (dimensionless) parameter*, such as the Reynolds number. We shall see below that we may predict quantitative properties of fluid from the Euler equations only supplying the data (Ω, I, f, u^0) but not any viscosity. We may thus predict the drag of body in a flow with small viscosity by only supplying the shape of the body as data! This is like predicting the circumference ($= 2\pi r$) of a circle supplying only the radius r of the circle as data.

Einstein dreamed about forming his equations of general relativity without any parameter, but was forced to put in a *cosmological constant* (to model a static universe), which he declared was his "biggest blunder". But the Euler equations for incompressible flow is a true example of Einstein's ideal model.

But is it really possible to make predictions about the flow of a fluid without knowing the viscosity of the fluid, only knowing that the viscosity is small? In the book we shall show that this is possible, but not in the classical way that led to catastrophe assuming that the effect of viscosity was zero, but in a new non-trivial way building on the observation that outputs of turbulent flows may have a weak dependence on viscosity!

5.7 Euler and NS as Dynamical Systems

The Euler and NS equations are examples of a *dynamical system* of the general form of an initial value problem $\dot{u}(t) = g(u(t))$ for $t \in (0, \hat{t}]$, $u(0) = u^0$, where $g(v)$ is a given function of v , u^0 is a given initial value, and $t \rightarrow u(t)$ is the solution defined on $[0, \hat{t}]$. We say that the function $v \rightarrow g(v)$ expresses the *law of the dynamical system*. We also refer to a solution $t \rightarrow u(t)$ as a *trajectory* of the dynamical system. In a dynamical system of this form time changes continuously over an interval of time from an initial time 0 to a final time \hat{t} . If g is bounded, then a solution $u(t)$ is continuous in time.

Triumph and Failure of Mathematics

No part of the aim of normal science is to call forth new sorts of phenomena; indeed those that will not fit the box are often not seen at all. Nor do scientists normally aim to invent new theories, and they are often intolerant of those invented by others. Instead, normal-scientific research is directed to the articulation of those phenomena and theories that the paradigm already supports. (Thomas Kuhn in *The Structure of Scientific Revolutions*, 1962)

The field of hydrodynamic phenomena which can be explored with exact analysis is more and more increasing. (Zhukovsky, 1911)

6.1 Triumph: Celestial Mechanics

In the famous treatise *Celestial Mechanics* in five volumes published during 1799–1825, Laplace formulated Newton's theory of gravitation in the form $-\Delta\phi = \rho$, where ϕ is the *gravitational potential* and ρ the *mass distribution*. Knowing the mass distribution, e.g. one heavy point mass representing the Sun, surrounded by lighter point masses representing the planets, that is, knowing $\rho(x)$ at a given time instant, one can solve for $\phi(x)$ and obtain the gravitational force field $F(x) = \nabla\phi(x)$, from which the acceleration of the masses can be determined using Newton's Law $F = ma$, where m is the mass and a the acceleration. From the acceleration, the velocity and motion of the masses can then be determined. Laplace could thus summarize celestial mechanics in the differential equation $-\Delta\phi = \rho$, and in particular this way prove Newton's inverse square law, which Newton just assumed to be true. Laplace could thus, and also did, predict the positions of the planets many years ahead from knowing their present positions and velocities. This is probably the most important triumph of mathematics all times, and gave mathematics and science an enormous boost.



Fig. 6.1. Isaac Newton (1643–1727), Pierre-Simon Laplace (1749–1827), and Jean Le Rond d'Alembert (1717–1783).

6.2 Failure: Potential Flow

The triumph for mathematics in celestial mechanics starting with Newton, stimulated mathematicians of the 18th and 19th centuries to try the same approach for fluid mechanics, with the hope of summarizing also this scientific discipline in the form $\Delta\phi = 0$, with ϕ now a *velocity potential* with $\nabla\phi$ representing the flow velocity. The prospects seemed really good: In this form one could represent a variety of ideal, *stationary* (time-independent), incompressible, *irrotational* flows as potential flows. We recall that a flow velocity u is irrotational if $\nabla \times u = 0$, which holds if $u = \nabla\phi$.

We know that potential flows had been studied already by d'Alembert in the mid 18th century and d'Alembert had published his paradox in 1752: A body of any shape can move through a lightly viscous fluid like water without any drag! Of course nobody could believe this, which from start gave mathematical fluid mechanics a strange reputation among the many practitioners of hydraulic engineering, which probably has lasted into our days. The challenge is to change this unfortunate situation.

The same mathematical equation, Laplace's equation, which was so amazingly successful in celestial mechanics, thus was a complete failure in fluid mechanics, and evidently mathematics and fluid mechanics lived a long time with a very disturbing paradox. How could that be?

As indicated, we present below a new resolution of d'Alembert's Mystery to illustrate basics aspects of fluid flow, including stability and transition to turbulence.

Laminar and Turbulent Flow

Il y a toujours sur ma strophe ou sur ma page
un peu de l'ombre du nuage et de la salive de la mer;
ma pensée flotte et va et vient, comme dénouée par toute
cette gigantesque oscillations de l'infini. (Victor Hugo)

In my boyhood I had the advantage of the constant guidance of my father,
also a lover of mechanics, and a man of no mean attainments in mathematics
and its application to physics. (Reynolds)

7.1 Reynolds

The NS equations give an accurate description of a great variety of fluid flows including both *laminar flow* with ordered flow features and *turbulent flow* with unordered seemingly chaotic fluid dynamics.

The onset of turbulence in laminar flow was studied experimentally by Osborne Reynolds in the 1880s. By injecting dye in a flow through a transparent pipe of a certain length, Reynolds could trace streamlines of the flow through the pipe, and thus observe the straight streamlines of laminar inlet flow starting to fluctuate into irregular motion downstream. Reynolds thus could study *transition* from laminar to turbulent flow, see Fig. 7.1.

Reynolds tried to find a connection between transition and the *Reynolds number* $Re \equiv \frac{UL}{\nu}$, where U represents a characteristic flow velocity and L a characteristic length scale. Reynolds found that transition occurred if Re was large enough (usually in the range $10^2 - 10^3$), but his hope to determine a *critical value of Re*, above which transition would always occur and never below, turned out to be elusive. We will explain in Chapter 36 below in a detailed study of transition, why this is impossible. In short, the reason is that transition occurs if a product of perturbation growth and perturbation level is above a certain threshold, and only the perturbation growth can be connected to Re . In Reynolds' experiments the perturbation level varied from one day to the other, and thus the transition could occur at a certain Re one

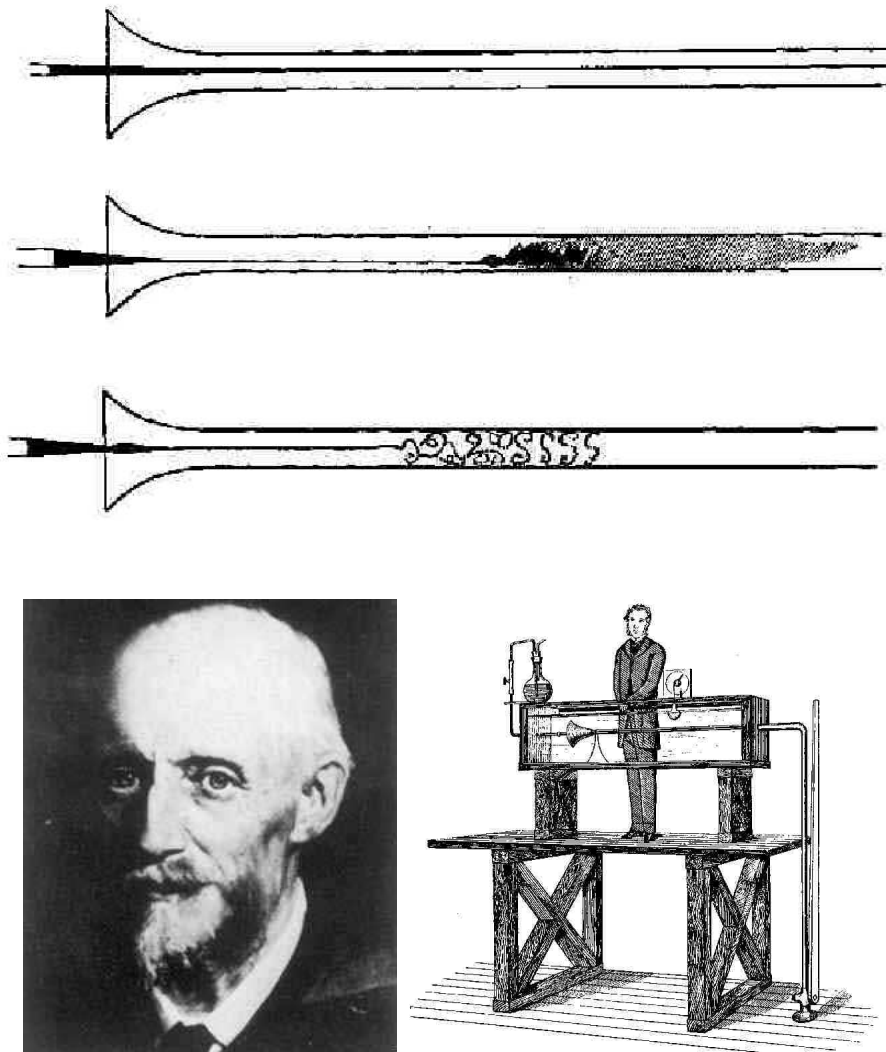


Fig. 7.1. "This is a definite relation of the exact kind for which I was in search. Of course without integration the equations only gave the relation without showing at all in what way the motion might depend upon it. It seemed, however, to be certain, if the eddies were due to one particular cause, that integration would show the birth of eddies to depend on some definite value of UL/ν " (Osborne Reynolds, 1842–1912).

day, but not the next. Therefore Reynolds' idea of a critical value of Re for transition will have to be abandoned.

As a consequence, there is no precise value of Re indicating the presence of turbulence in a given flow, but most flows exhibit turbulent flow features for $Re \geq 10^3$, because perturbations are always present in both practice and controlled experiments, albeit on different levels. Kolmogorov conjectured in his famous 1941-articles [75, 76, 74] that turbulent flow features occur on a range of length scales down to a smallest scale, which may be estimated to be of size $Re^{-3/4}$ (or $\nu^{3/4}$), normalizing to $U = L = 1$. We can thus use the rough size of Re to indicate the qualitative nature of a given flow, such as the presence and scale features of turbulent flow.

7.2 Applications and Reynolds Numbers

Important applications concern fluid flow around *bluff bodies*, such as the flow of air around a car, a jumbo-jet at take off/landing or the sail of a sailing boat, or the flow of water around a super-tanker or a sailing boat, which all represent incompressible partly turbulent flows at large Reynolds numbers: $Re \approx 10^6$ for a car traveling at 60 mph, $Re \approx 10^8$ for a jumbo jet or a super-tanker at cruising speed, while $Re \approx 10^{10}$ might be relevant in meteorology. In bluff body flow, turbulence typically appears in a *boundary layer* close to the surface of the body, and in a *wake* attaching to the rear of the body, while the flow elsewhere is laminar, see Fig. 7.2. Typically the boundary layer is laminar on the body surface facing the flow, with streamlines following the surface, until *separation* away from the surface into recirculating turbulent flow. For very high Re ($\sim 10^6$) the boundary layer may undergo transition to turbulence before separation, resulting in a delayed separation of the boundary layer, corresponding to a drastically reduced volume of the wake, and thus also a reduction of the drag force, referred to as *drag crisis*.

In everyday life, we can observe separating laminar/turbulent bluff body flow around a boat, a stone in a river, or a car in the case of light rain or mist when the flow pattern becomes visible, see Fig. 7.2–7.3.

In this book we focus on flows with *medium* (say $Re \approx 10^2 - 10^4$) over *large* (say $Re \approx 10^4 - 10^6$) to *very large* (say $Re > 10^7$) Reynolds numbers involving both laminar and turbulent flow features, which appear in many important applications. For short we refer to such flows as *turbulent flows*. Such flows typically have surfaces separating laminar and turbulent flow, see Fig. 7.2. For very large Reynolds numbers we use the Euler equations, formally corresponding to $Re = \infty$.

Normalizing to $U = L = 1$, we thus focus on flows with medium small viscosity ($\nu \approx 10^{-2} - 10^{-4}$), over small ($\nu \approx 10^{-4} - 10^{-6}$) to very small viscosity or zero viscosity ($\nu = 0$), that is, we focus on *small viscosity*. We shall see that the precise value of the small viscosity, or the large Reynold's number, in many cases is irrelevant. As indicated, this relieves us from the

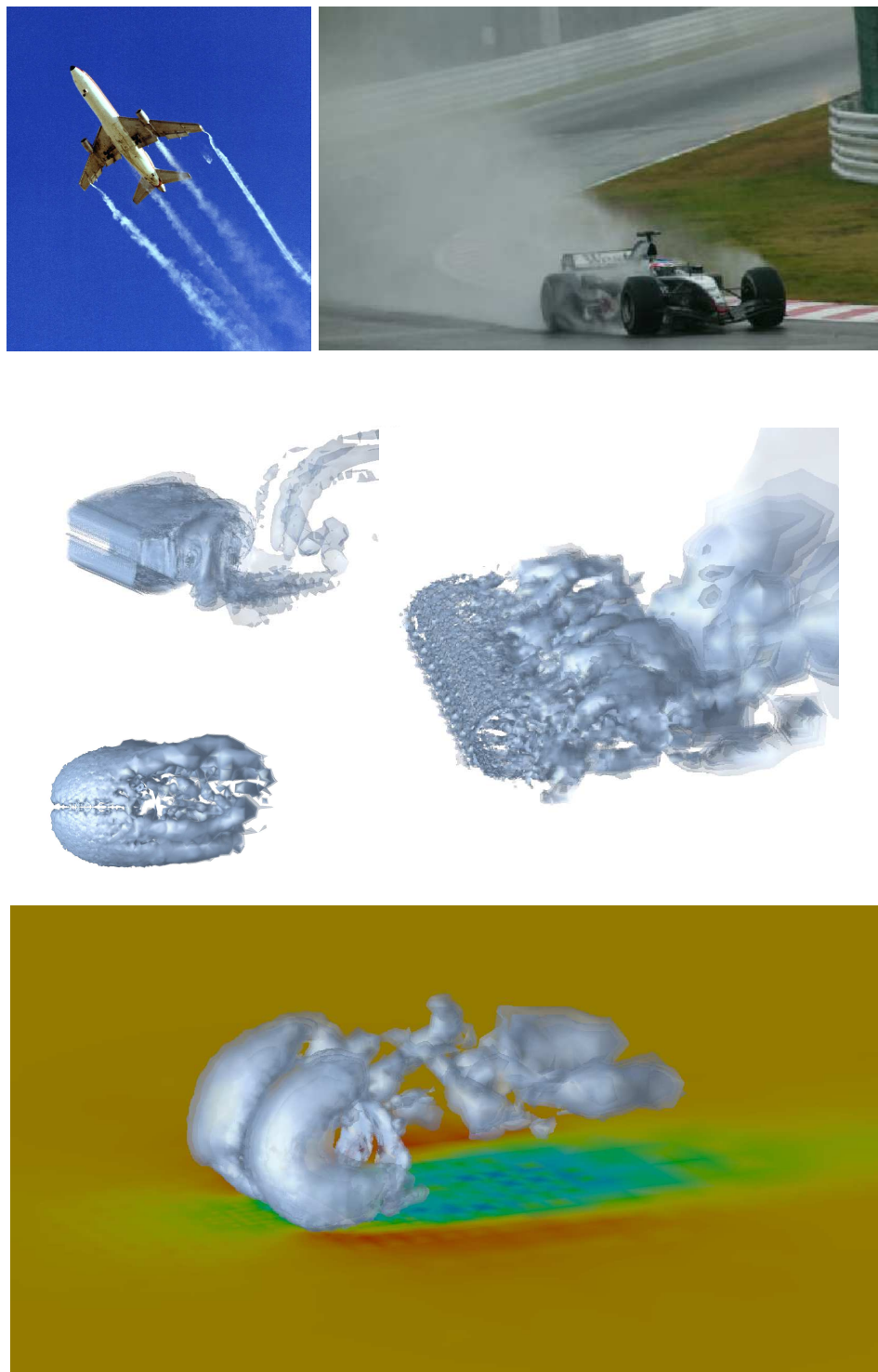


Fig. 7.2. Lockheed L-1011 and F1 racing car (upper), vorticity in computations of flow past square and circular cylinders and a sphere, transversal velocities in a boundary layer computation, and in a computation of flow past cylinder rolling along ground (modeling a wheel).

difficult (or simply impossible) task of determining a precise value of the viscosity ν to put into the NS equations.

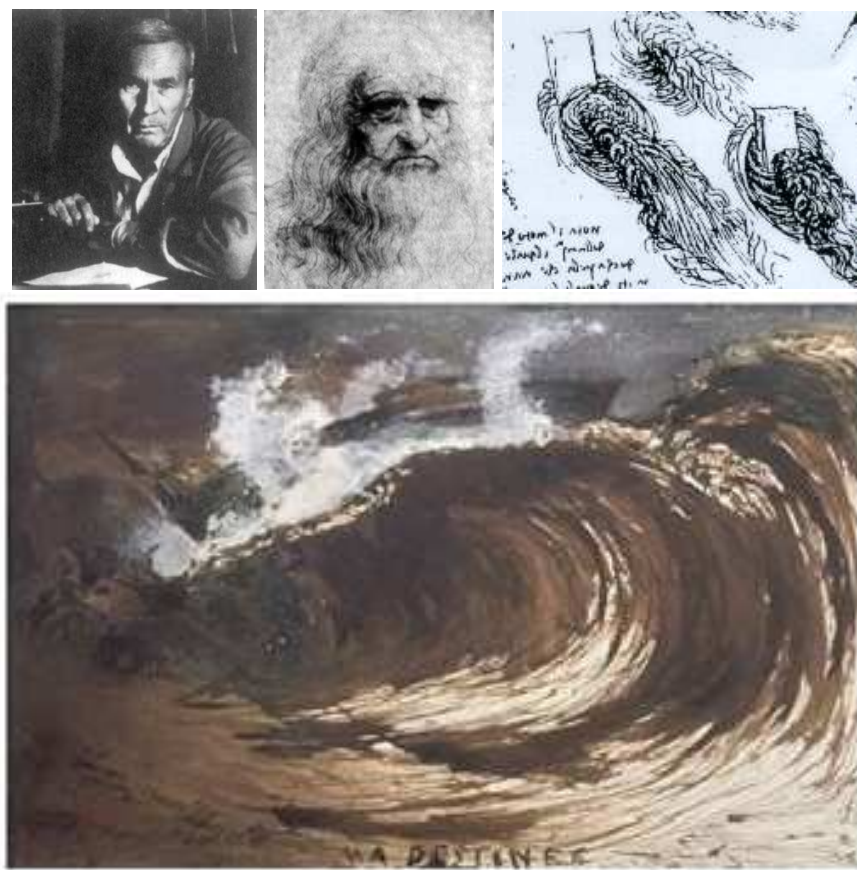


Fig. 7.3. Andrey Nikolaevich Kolmogorov (1903–1987), and Leonardo da Vinci (1452–1519) with a sketch of turbulent wakes behind bluff bodies, and “My Destiny” by Victor Hugo. Inscription on the ship; FRACTA SED INVICTA.

Computational Turbulence

I am an old man now, and when I die and go to heaven there are two matters on which I hope for enlightenment. One is quantum electrodynamics, and the other is the turbulent motion of fluids. And about the former I am rather optimistic. (Horace Lamb, 1932)

Consider a transport airplane with a 50-meter-long fuselage and wings with a chord length (the distance from the leading to the trailing edge) of about five meters. If the craft is cruising at 250 meters per second at an altitude of 10,000 meters, about 10 quadrillion (10^{16}) grid points are required to simulate the turbulence near the surface with reasonable detail. (Parviz Moin and John Kim in Scientific American 1997)

8.1 Are Turbulent Flows Computable?

The main question addressed in this book is the following: Can we compute solutions to the Euler or NS equations in the case of turbulent flow? Or shorter: Are turbulent flows computable?

Recalling the dimensional analysis of Kolmogorov, it would appear that to pointwise resolve all the scales of a turbulent flow in a *Direct Numerical Simulation DNS*, would seem to require of the order Re^3 mesh points in space-time, assuming the smallest scale in space and time is $Re^{-3/4}$ and that $U = L = \hat{t} = 1$. Thus, already a flow at $Re = 10^6$ would seem to require at least $Re^3 = 10^{18}$ mesh points in space-time for pointwise representation, which is beyond the capacity of any foreseeable computer. Not to speak of Euler with $Re = \infty$! This reflects a common expert opinion as expressed above by Moin and Kim [87].

Does this mean that we have to give up, and simply conclude that turbulent flows are not computable? The answer is yes if we ask for pointwise accurate computations in space-time. This not only because the number of mesh points would be overwhelming, but also because in fact pointwise values of a turbulent flow are not well defined, but fluctuate in a seemingly chaotic

way. So even if we could compute with 10^{18} mesh points, we should not expect to be able to get pointwise accurate solutions for turbulent flow.

In fact, as we will see below, mathematical existence of pointwise solutions can neither be proved nor expected, and pointwise accurate computed solutions thus seem to be pure fiction. We may phrase this as an impossibility of obtaining solutions $\hat{u} = (u, p)$ to the NS or Euler equations written in the form $R(\hat{u}) = 0$, with the residual $R(\hat{u})$ being zero pointwise in space-time. If true this would certainly be shocking to the large community of mathematicians trying to prove existence of pointwise solutions, but would not in principle disturb a computational mathematician familiar with the fact that computational solutions usually have non-zero residuals. However, we shall see that the pointwise residuals in computational simulations of turbulent flow usually are far from being small, and facing this evidence also many computational mathematicians should become nervous. In particular, these results challenge the traditional idea of DNS as a computation with small pointwise error.

The natural way out of this obvious dilemma is to ask for less, that is to seek to compute hopefully well-defined *mean values* in space-time, instead of ill-defined *point values*. This means that as *quantities of interest*, or *observables*, or simply *outputs*, we shift from pointwise to different mean value quantities.

We further introduce a quantitative quality measure in the form of a *tolerance* indicating the desired precision in a chosen output. We also measure *computational cost*, in terms of e.g. computing time and memory requirements on a certain system. The main problem addressed in this book can now be formulated as follows:

- (P) What outputs of turbulent flows are computable to what tolerance to what cost?

We present answers to this problem, and in particular we show that we can compute outputs for turbulent flows of interest in a large variety of applications using the computational power of a PC on meshes with 100 000-500 000 mesh points. These results are new and should have important consequences concerning the use of computational methods for simulation of fluid flow.

8.2 Typical Outputs: Drag and Lift

A typical quantity of interest may be the *drag coefficient* c_D or the *lift coefficient* c_L of a bluff body, which are mean values in time of the total fluid force acting on the body in the direction of the flow and perpendicular to the flow, respectively. The drag and lift coefficients thus represent global mean values in space-time. Some car manufacturers like to present the c_D of a certain car as an indication of fuel economy (for example $c_D < 0.3$). For a jumbo-jet a decrease in drag with one percent could save \$400 million in fuel cost over a 25 year life span.

As a main contribution of this book, we show that mean values such as c_D and c_L are computable by G2 on a PC within a day (in 2006) up to a tolerance of a few percent.

We also show that as the mean values become more local in space or time, the computational work to reach the same tolerance increases, so that in particular point values are uncomputable.

8.3 What about Boundary Layers?

We shall see that for flows with small viscosity it is not necessary to resolve all boundary layers, to accurately predict outputs such as drag and lift. We shall see that by using slip or friction boundary conditions we avoid having to resolve all boundary layers, while with adaptivity crucial details such as separation may be captured without an excessive number of mesh points. Effectively, this means that we may reduce from the impossible $> 10^{16}$ to possible $< 10^8$ number of mesh points for a complete aircraft. The reduction from impossible to possible is opened by G2 adaptivity with automatic turbulence modeling including slip/friction boundary conditions.

8.4 Approximate Weak Solutions: G2

When we relax outputs to mean values, we open to relax to a *weak solution concept*, where we ask that $((R(\hat{u}), \hat{v})) \approx 0$, where $((\cdot, \cdot))$ is a scalar product in space-time and \hat{v} varies over a set of (smooth) *test functions*. We thus relax twofold from requiring *exact* satisfaction of $R(\hat{u}) = 0$ in a *pointwise* sense, to *approximate* satisfaction $R(\hat{u}) \approx 0$ in a *weak* sense, that is, $((R(\hat{u}), \hat{v})) \approx 0$ for all test functions \hat{v} with the meaning of \approx made precise below. Accordingly, we say that a function \hat{u} satisfying $R(\hat{u}) \approx 0$ in a weak sense, is an *approximate weak solution*.

Our main problem can now be reformulated as follows:

- (P1) What is the error in output of approximate weak solutions?

To answer this question amounts to finding the effect of a nonzero residual on the output error, which as we will see can be expressed as a question of *stability* of an associated *dual problem*.

In this book we compute approximate weak solutions using a Galerkin finite element method, where we seek an approximate solution \hat{U} in a finite element space satisfying $((R(\hat{U}), \hat{v})) = 0$ for a set of finite element test functions \hat{v} . More precisely, we use a *General Galerkin method* with a certain *strong* control of the residual in a *weighted least squares* sense, which we refer to as G2. We may thus view a G2 solution \hat{U} as an approximate weak/strong solution of the NS or Euler equations. We shall see that the weighted least squares control corresponds to an *automatic turbulence model*, relieving us

from the (very difficult or probably in general impossible) task of finding a correct turbulence model.

8.5 G2 Error Control and Stability

In general terms, we will be able to estimate an output error of a G2 solution \hat{U} by a product $S\epsilon$, where ϵ measures the size of the residual $R(\hat{U})$ in the weak sense and S is a *stability factor* which measures certain norms of the solution of the dual problem with data depending on the output. The computational goal is then to achieve $S\epsilon \leq TOL$, where TOL is the tolerance.

We shall see that for turbulent solutions the residual $R(\hat{U})$ of a G2 solution \hat{U} may be small in the weak sense, while $R(\hat{U})$ is large in the pointwise sense, and the stability factor S may be of moderate size for a mean-value output like drag and lift. Altogether, we shall thus see that it is possible to satisfy the *stopping criterion* $S\epsilon \leq TOL$ with tolerances of practical interest and mesh sizes affordable on a PC.

An output with strong sensitivity will have a very large stability factor S , and one way of expressing the chaotic nature of a pointwise output of a turbulent flow is to say that the corresponding stability factor is so large that we can never make the residual so small that $S\epsilon \leq TOL$. Effectively we may say that this corresponds to $S = \infty$, and therefore it is impossible to choose $\epsilon > 0$ so that $S\epsilon \leq TOL$. In this case it does not help to choose $\epsilon = 0$, since $S\epsilon$ is not well defined if $S = \infty$ and $\epsilon = 0$. The result is that we have to give up the idea of a pointwise well defined solution to the NS equations in the case of turbulent flow.

Stability factors obviously play a central role in this book since they directly couple to errors in outputs, and a central theme of the book is accordingly the computation of stability factors. And we will be very happy to find that stability factors for mean-value outputs are of moderate size and not too large!

8.6 What about Mathematics of Euler and NS?

The mathematician Jean Leray proved in 1934 existence of an exact weak solution to the NS equations satisfying $((R(\hat{U}), \hat{v})) = 0$ for all test functions \hat{v} (corresponding to $\epsilon = 0$), by using methods from functional analysis. Leray referred to his weak solutions as turbulent solutions. This is still today the only analytical mathematical existence result for the general form of the NS equations! Leray did not prove any result on uniqueness of weak solutions of NS equations. Since uniqueness directly couples to stability, this means that effectively Leray did not consider the aspect of stability and in particular not the question of *output uniqueness* or *weak uniqueness*, which for turbulent flows has to replace pointwise uniqueness: We can estimate the difference in

output of two approximate weak solutions by $S\epsilon$ if ϵ bounds the two residuals, so that the output will be unique up to $S\epsilon$.

For the Euler equations not even existence of an exact weak solution has been proved mathematically. Thus the analytical mathematics for the Euler and NS equations has remained severely incomplete over a long time, with little progress.

Our results indicate that approximate weak solution and output uniqueness are suitable concepts for the Euler and NS equations, while traditional analytical mathematical techniques working with exact weak solutions without output uniqueness, are not. We will discuss these aspects in more detail below when presenting the Clay Institute Millenium \$1 million Prize Problem asking for existence and uniqueness of solutions to the NS equations.

8.7 When is a Flow Turbulent?

In G2 computations we will identify turbulence by the fact that the G2 least squares stabilization is not small signifying that the pointwise residual is large. Typically, this situation prevails under mesh refinement which reflects that the smallest scales of the physical flow are not computationally resolved, not even on the finest mesh.

8.8 G2 vs Physics

Changing from the classical setting with pointwise residuals and outputs to the new setting of global mean value outputs and G2 weak/strong residuals, suggests a new perspective on mathematical modeling of fundamental phenomena such as turbulent fluid flow. We remarked above that residuals of approximate weak solutions of the NS equations may be large pointwise but small in a mean value sense. We may view a pointwise large NS residual as a local violation of Newtons 2nd law and incompressibility, which we could view as a local non-equilibrium. An approximate weak solution would thus represent fluid dynamics in global equilibrium but local non-equilibrium.

Experimentally we would not be able to distinguish such “imperfect fluid dynamics” from “perfect fluid dynamics” in equilibrium pointwise, since we can only observe mean values. Mathematically we would be able to rationalize “imperfect fluid dynamics” by proving existence of approximate weak solutions, but probably not “perfect fluid dynamics” requiring exact solutions with pointwise vanishing residual. The scientific study of fluid dynamics would thus concern “imperfect fluid dynamics”, while “perfect fluid dynamics” would belong to metaphysics. We add more substance to this picture below. In particular we propose a solution of the classical paradox of irreversibility in reversible systems based on finite precision computation.

The same type of reasoning may apply to other fundamental mathematical models of mechanics and physics such as the Schrödinger equation for the quantum mechanics of atoms and molecules. Solutions of the Schrödinger equation are called wave functions and have an incredibly rich structure with one separate copy of \mathbb{R}^3 for each electron and nucleus. It is impossible to experimentally or computationally determine this structure pointwise even for small clusters of atoms, and thus the existence of a world ruled by “perfect quantum mechanics” could again be questioned. This connects to the question of how it can be that an electron is smart enough to solve its own \mathbb{R}^3 version of the Schrödinger equation to determine what to do? Maybe the answer is that single electrons simply aren’t that smart and thus leave large pointwise residuals, while clusters of electrons can do better and have small residuals in a mean value sense, all of which could be viewed to correspond to some kind of “imperfect quantum mechanics”.

8.9 Computability and Predictability

Using the NS equations to simulate fluid flow, we obtain contributions to the error in output from the following sources: (i) computation, (ii) data and (iii) modeling. In this book we focus on output errors from computation and we also discuss errors from data, which includes Ω , f , u_0 , ν , while we leave out errors from modeling related to the assumptions of incompressibility and constant density. In a forthcoming volume we consider compressible and variable density flows.

We will below connect the general concept of *predictability* to the quality of output based on the quality of given data, that is, predictability will connect to error in output resulting from error in data. Further, we will connect *computability* to output error from computation.

It is natural to expect that aspects of predictability and computability closely couple, because both connect to stability or *perturbation growth* in the model. Stability factors measure the sensitivity in output to perturbations from computation, data and modeling. Large stability factors indicate strong sensitivity.

We will further use the general concept of *reliability* to signify that the output error is below a certain *tolerance TOL*. We may thus indicate the reliability of a computation of a drag coefficient c_D by stating that $c_D = 1.5 \pm TOL$, or $|c_D - 1.5| \leq TOL$, where $TOL = 0.1$.

Using the NS equations to make predictions, it may be natural to speak of a total prediction error in output including errors from both data and computation. Usually however, we connect predictability to output error from data, and computability to output error from computation.

We have indicated that in turbulent flow pointwise values in space-time of velocity-pressure are not predictable/computable to any tolerance of interest. The main question of this book thus concerns the predictability and

computability of mean values in space-time of turbulent flow up to tolerances of interest.

The reader is encouraged to download Dolfin [1] and try its Euler/NS solver on some problems in the book, and of course other problems. There are many waiting to be solved.

A First Study of Stability

...do steady flow ever occur in Nature, or have we been pursuing fantasy all along? If steady flows do occur, which ones occur? Are they stable, or will a small perturbation of the flow cause it to drift to another steady solution, or even an unsteady one? The answer to none of these questions is known.
 (Marvin Shinbrot in Lectures on Fluid Mechanics, 1970)

9.1 The Linearized Euler Equations

As already indicated, a main theme of this book is the stability of fluid flow. Stability concerns the growth of perturbations in the flow. Since fluid flow is well described by the Euler and NS equations, stability concerns the growth of perturbations of solutions of the Euler and NS equations. Focusing here on Euler, suppose that \hat{u} and \hat{w} are two solutions to the Euler equations (5.2) with different initial data u^0 and w^0 . We are interested in the difference $\hat{v} = (v, q) = \hat{u} - \hat{w}$ for time $t > 0$ knowing that $v^0 = u^0 - w^0$. Subtracting the two versions of the Euler equations, we obtain the following system, which we may refer to as the *linearized Euler equations*:

$$\begin{aligned}\dot{v} + (u \cdot \nabla)v + (v \cdot \nabla)w + \nabla q &= 0 && \text{in } \Omega \times I, \\ \nabla \cdot v &= 0 && \text{in } \Omega \times I, \\ v \cdot n &= 0 && \text{on } \Gamma \times I, \\ v(\cdot, 0) &= u^0 - w^0 && \text{in } \Omega,\end{aligned}\tag{9.1}$$

We may view this as a linear system for \hat{v} with u a given convection velocity, and ∇w a given reaction coefficient. The growth properties of $\hat{v}(t)$ in time expresses the stability, and these properties directly couple to the reaction term $(v \cdot \nabla)w$ with ∇w as reaction coefficient in matrix form, while the convection term $(u \cdot \nabla)v$ intuitively does not seem to influence the growth of \hat{v} , since it just “shifts v around”. We expect the eigenvalues of ∇w to connect to the growth properties of \hat{v} , with eigenvalues with positive real part corresponding to eigenmodes with exponential decay and with negative real part to eigenmodes of exponential growth.

Because of the incompressibility, the trace of ∇w will be zero, and thus the sum of the eigenvalues will also be zero, and thus we normally have eigenvalues with real parts of both signs. Thus normally we expect to see some exponential growth, unless all the eigenvalues are purely imaginary or zero. We thus expect perturbations of Euler solutions to grow exponentially, and thus any Euler solution would be expected to be unstable! In particular, a stationary solution given by an analytical formula would be expected to be unstable.

We notice that the stability connects to the growth properties of \hat{v} which may be studied assuming the perturbations to be small so that effectively we may choose $w = u$. To study the stability of a given solution \hat{u} , we would thus study the linearized Euler equations (9.1) with $w = u$.

We now proceed to give two basic examples illustrating basic features of the flow of an ideal fluid, which are also relevant for fluids with small viscosity. We thus present two analytical stationary solutions to the Euler equations, and we will of course discover that they are both unstable. We will kill any hopes of the reader by reminding that an unstable solution has no permanence, and thus will have no interest from a practical point of view; it simply does not “exist” and cannot be observed. We would thus be led to the conclusion that making predictions about fluid flow based on an analytical solution of the Euler or NS equations (with small viscosity) would be impossible. This would seem to indicate pretty grim perspectives for analytical mathematics in fluid dynamics. We will give evidence below indicating that this is not overly pessimistic. Of course, we will counter by showing that on the other hand computational mathematics has excellent possibilities of generating information of value, by computational solution of the Euler or NS equations.

9.2 Flow in a Corner or at Separation

We consider the linear velocity $u(x, t) = (2x_1, -2x_2, 0)$ in the half-plane $\{x_1 > 0\}$, with streamlines according to Fig 9.1. We easily check that (u, p) solves the Euler equation, with $p = -2(x_1^2 + x_2^2)$. This is the potential solution for an incompressible ideal fluid in the corner of the quarter-plane $\{x_1, x_2 > 0\}$, or at a separation point at the origin considering the half-plane $\{x_1 > 0\}$, see Fig 9.2. We will explain below, why it is referred to as a potential solution. Incidentally, this potential solution is also a solution to the NS equations for any viscosity, in particular for small viscosities.

To study the stability of this potential flow we study the perturbation equation (9.1) with $w = u$ and we are thus led to study the matrix ∇u , which we find to be diagonal with diagonal $(2, -2, 0)$, thus with one positive (stable) and one negative (unstable) eigenvalue. We conclude that the potential flow of an incompressible ideal fluid at a separation point is unstable, in fact exponentially unstable.

We will return to this observation below. Already here we can indicate some (far-reaching) consequences. Consider the flow around a body, e.g. a

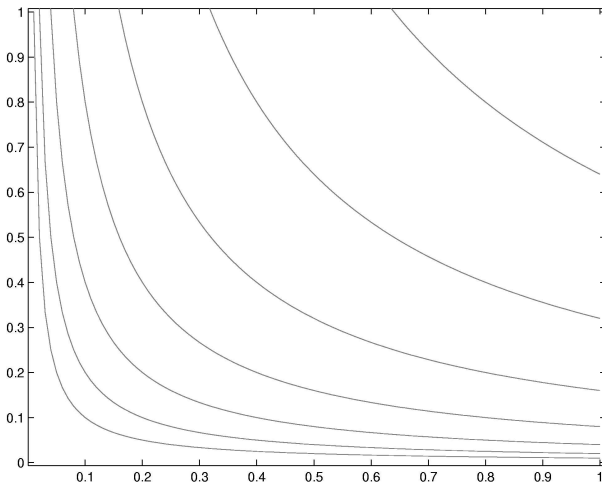


Fig. 9.1. Potential solution at a corner.

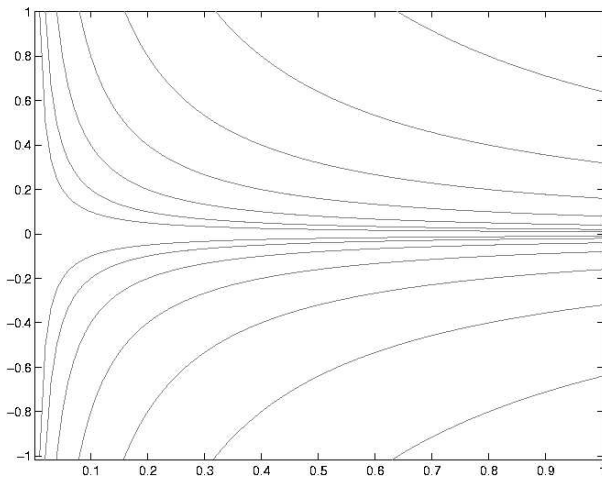


Fig. 9.2. Potential solution at a separation point.

circular cylinder with axis along the x_3 -axis in a flow in the direction of the x_1 -axis. This could model the water flow around the pillar of a bridge standing on the bottom of a deep river. We could then imagine a stationary solution with streamlines around the pillar, e.g. according to Fig 9.3 (we will write down the corresponding analytical solution formula in Chapter 10 below). We notice that any such flow will necessarily have a separation point somewhere at the back of the cylinder, where the flow would look like the potential solution just given. Necessarily! We conclude that any such stationary flow will be unstable and hence would be impossible to observe. If we observe the flow

around a pillar of a bridge, we must see something different. We will show what below.

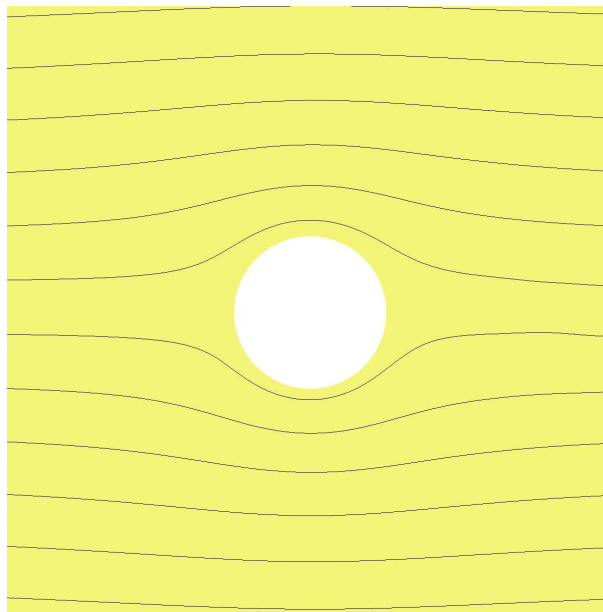


Fig. 9.3. Streamlines for the potential solution of a circular cylinder.

Having now observed that the sum of the eigenvalues of the reaction coefficient in the linearized Euler equations is always equal to zero, we understand that most solutions to the Euler equations must be unstable! The flow at a separation point just studied was just one example. If someone comes to us with a formula for the analytical solution to the Euler equations, we would be able, with very high probability, to say that the solution must be unstable and thus can never be observed and thus would not have any predictive value. Right?

From this experience, we could be led to conclude that there is something seriously wrong with the Euler equations, so that we should never speak about this equation, and of course never try to find any solutions. We shall see below that this conclusion is wrong: We will see that the Euler equations is a very valuable model with lots of predictive value but we will have to qualify what we mean by *solving the Euler equations*. We shall see that this occupies an essential part of this book.

9.3 Couette Flow

Is there some flow velocity u with the eigenvalues of $\nabla u = 0$ all having zero real part? Yes, there is a basic flow pattern with this property, which is *Couette flow* given by $u(x) = (ax_2, 0, 0)$ and $p = 0$ with $a > 0$ a constant, which is a stationary solution of both the Euler and NS equations. It represents *parallel shear flow* in the x_1 -direction, which may occur inside a flow or in a boundary layer along a boundary at $x_2 = 0$. The streamlines are parallel to the x_1 -axis and the u_1 velocity increases linearly with x_2 . The coefficient a controls the strength of the shear layer with the shear force given by $\nu \partial u_1 / \partial x_2 = \nu a$. This is the simplest possible model solution to both the Euler and NS equations representing stationary parallel shear flow, see Fig. 9.4. Of course, for Euler we would have $\nu = 0$, so the shear force would be zero. But $u(x)$ would anyway be a solution to the Euler equations.

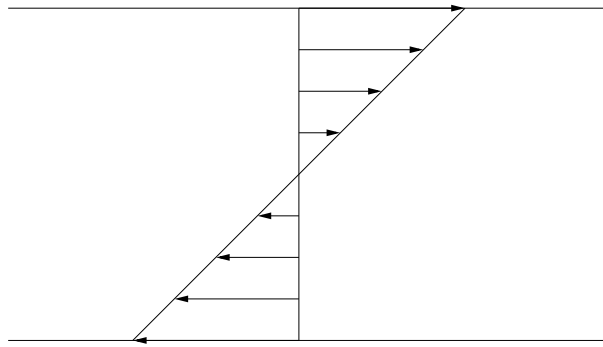


Fig. 9.4. Couette flow: parallel shear flow.

Is Couette flow a stable solution to Euler? Well, we compute and find that $\nabla u = (0, a, 0; 0, 0, 0; 0, 0, 0)$ with the rows separated by semi-colon. Obviously, the eigenvalues are all zero, so there are no exponentially unstable modes, but the presence of the off-diagonal coefficient a allows for linear growth in t with slope a . This is referred to as *non-modal growth*, occurring because the matrix ∇u is non-normal (in particular non-symmetric) with degenerate eigenmodes. More precisely, we expect to see that $v_1(t) \sim t a v_2^0$. If a is large, then this will correspond to considerable growth of the perturbation \hat{v} , and thus would signify an unstable Couette flow. Now, in a boundary layer of thickness δ we would have $a \sim 1/\delta$, and we would thus conclude that Couette flow in a boundary layer would be unstable.

9.4 Resolution of Sommerfeld's Mystery

We are now prepared to resolve, at least in principle, Sommerfeld's Mystery from 1908. We will return with more details in Chapter 36 below.

Couette flow with velocity $u = (x_2, 0, 0)$ is a solution to NS for $\nu \geq 0$ including the Euler equations with $\nu = 0$. We may assume that $\nabla u = (\nu, 1, 0; 0, \nu, 0; 0, 0, \nu)$ with the ν on the diagonal representing the viscous term. The three-fold eigenvalue of this matrix is equal to $\nu \geq 0$, and we already noticed that this means that there are no exponentially unstable modes.

If we now forget about the non-modal linear growth, we could be led to the conclusion that Couette flow is stable. This is what Sommerfeld did! But we cannot forget the non-modal growth, because it may be large! More precisely, as shown in Chapter 36, the growth is proportional to $1/\nu$, and thus a small initial transversal perturbation in u_2 and u_3 of size ν may grow to a perturbation of size 1 in u_1 and thereby change ∇u to have exponentially unstable modes leading to transition to turbulence. We will see this happening in front of our eyes in Chapter 36.

Sommerfeld thus made the mistake of applying a result valid for symmetric matrices to a case with a non-symmetric matrix. This shows that even a great mathematician can make elementary mistakes, and how important it is to properly understand a mathematical result and the assumptions it is based on. Sommerfeld's mistake passed undiscovered through several generations of fluid dynamicists, and was questioned first in the 1960s and then only by a few. Most textbooks in fluid mechanics still today present Sommerfeld's erroneous conclusions [106], and the debate in the fluid dynamics community between a minority of proponents of non-modal analysis and a majority following Sommerfeld is still going on. We enter this debate in Chapter 36 and the reader may choose side: non-modal or modal?

9.5 Reflections on Stability and Perspectives

We have presented two simple stationary analytical solutions to the Euler and NS equations, and we have shown that both solutions are unstable. From this experience we could easily be led to the suspicion that it would be hard to find *any* solution to the Euler/NS equations that is stable. In computations we will below see that if we initiate the flow with one of these simple solutions, then the flow will quickly develop into a completely different time-dependent, in fact turbulent, solution.

We see that the effect of the instability of solutions to the Euler/NS equations is the development of a fluctuating time-dependent turbulent solution. Since the flow is unstable, it will always have to change from one state to another; it simply cannot find any stable stationary configuration. It is like a flag in the wind, which is never in a flat stationary state, but is always changing from one state to another in a fluctuating seemingly chaotic way. It

is clearly impossible to predict the exact position of a flag over a time interval which is not very short, yet there is some kind of repetitive behavior in the motion of a flag, but the motion is not periodic, rather sort of “turbulent”.

We see similar phenomena in the evolution of the Weather; always changing in a way which is more or less predictable a couple of days ahead but not much more, but always with some mix of rain and sunshine and with certain mean values predictable over longer time. In fact, models for the weather look like the Euler/NS equations, and we will return to basic aspects of weather prediction below connecting to the Euler/NS equations.

We shall see that outputs from computed turbulent solutions fit with observations. We will in fact be able by a posteriori error estimation to assess the precision in the outputs. In the a posteriori error estimation we solve (dual) linearized Euler or NS equations linearized at a computed solution and compute the relevant stability factors and find that these factors are not very large. We will thus be able to make accurate predictions of certain outputs by computing solutions to the Euler or NS equations, and thus we can reach our main goal: prediction by computation.

What we just said seems to contain a contradiction: We first said that the linearized Euler/NS equations seemed to be exponentially unstable, so that solutions would “blow up” exponentially, even when linearized at very simple basic solutions. On the other hand we claimed that we could solve the (dual) linearized Euler/NS equations without blow-up reflecting that stability factors are not very large, when linearized at a complex turbulent solution. How can this be? Exponential blow-up for simple solutions but no blow-up for complex turbulent solutions! We will discuss this remarkable phenomenon below and give some mathematical justification. Roughly speaking the secret reflects effects of *cancellation* in a fluctuating turbulent flow, which are not present in the case of the simple stationary solutions studied above. It is probable that this aspect of stability also is crucial for phenomena in Nature to be functional and not completely chaotic and may explain why Nature is complex; simple solutions are unstable and only complex solutions can be realized and have some permanence!

We may thus say that it is the complexity that makes turbulent solutions to the Euler/NS equations computable. But the cancellation of perturbations in this complex flow is also some kind of “miracle”, a miracle which gives permanence, stability and thus computability of certain outputs.

Below we will, in our discussion of d'Alembert's Mystery, give more evidence that predictions from analytical solutions (without stability analysis) may be completely wrong. We spend some time and effort on this kind of “wrong mathematics” because it occupies an important part of the history of fluid dynamics, and because one can learn something even from completely wrong arguments, by proper understanding of exactly what is wrong.

d'Alembert's Mystery and Bernoulli's Law

Thus, I do not see, I admit, how one can satisfactorily explain by theory the resistance of fluids. On the contrary, it seems to me that the theory, in all rigor, gives in many cases zero resistance; a singular paradox which I leave to future Geometers for elucidation. (d'Alembert)

In classical hydrodynamics the motion of non-viscous fluids is chiefly discussed. For the motion of viscous fluids, we have the differential equation (NS) whose evaluation has been well confirmed by physical observations. As for solutions of this differential equation, we have, aside from unidimensional problems like those given by Lord Rayleigh, only the ones in which inertia of the fluid is disregarded (Stokes equations) or plays no important role. The bi-dimensional and dimensional problems, taking viscosity and inertia into account (NS), still await solution. (Prandtl in *Motion of fluids with very little viscosity* 1904)

10.1 Introduction

We recall the Euler equations for incompressible inviscid flow:

$$\begin{aligned} \dot{u} + (u \cdot \nabla) u + \nabla p &= 0 && \text{in } \Omega \times I, \\ \nabla \cdot u &= 0 && \text{in } \Omega \times I, \\ u \cdot n &= g && \text{on } \Gamma \times I, \\ u(\cdot, 0) &= u^0 && \text{in } \Omega. \end{aligned} \tag{10.1}$$

We here set the volume force $f = 0$, and assume the non-homogeneous slip boundary condition $u \cdot n = g$, with n the outward unit normal to Γ , and g a given function. We assume that $\int_{\Gamma} g \, ds = 0$, so that the boundary condition is compatible with the incompressibility condition $\nabla \cdot u = 0$ in Ω , in view of the divergence theorem stating that

$$\int_{\Omega} \nabla \cdot u \, dx = \int_{\Gamma} u \cdot n \, ds.$$

It may seem natural to expect that the Euler equations model the flow of a fluid with very small viscosity (or very high Reynold's number). We shall below see that this statement is largely true, if interpreted in the right way. However, we shall now show that this idea has a serious flaw, if interpreted in the wrong way, which in particular was done during the initial mathematical studies of fluid mechanics by even the great masters of the 18th century.

10.2 Bernoulli, Euler, Ideal Fluids and Potential Solutions

The Euler equations were formulated by Euler in 1755 [38] building on Daniel Bernoulli's Hydrodynamik from 1738 and Johann Bernoulli's (father of Daniel) Hydraulica, and thus predated the NS equations by almost 100 years.

In particular, Euler derived Bernoulli's Law for stationary incompressible inviscid irrotational flow from the Euler equations. We shall present Euler's derivation below.

The initial studies by the Bernoulli's and Euler thus concerned ideal fluids, with the terminology suggesting that these studies would be fundamental: In the ideal world there would be ideal fluids behaving in an ideal way. Of course, the hope was that the newly invented Calculus would be the ideal tool to uncover the secrets of this ideal World.

In particular, the interest focused on stationary potential solutions with the velocity $u = \nabla\phi$, where the potential ϕ is a harmonic function satisfying Laplace's equation $\Delta\phi = 0$ in the domain of the fluid together with the Neumann boundary condition $\frac{\partial\phi}{\partial n} = u \cdot n = g$. Obviously, such a velocity is both *irrotational* ($\nabla \times u = 0$) and divergence free ($\nabla \cdot u = 0$). We show below that if $u = \nabla\phi$ with $\Delta\phi = 0$, then there is a pressure p such that (u, p) solves the stationary Euler equations. By solving Laplace's equation, one can thus construct stationary irrotational solutions to the Euler equations, and thus fluid mechanics seems to be open for exploration by Calculus, with all its capabilities of producing harmonic functions. Unfortunately for Calculus (but fortunately for science, since potential solutions are pretty boring), these hopes were almost instantly ruined by the discovery that this type of ideal fluid theoretical predictions almost always were in complete disagreement with observations and thus had no scientific value.

10.3 d'Alembert's Mystery

This was pointed out by d'Alembert in 1752 in his famous paradox [29], comparing the Calculus prediction of zero drag/lift of an inviscid potential solution, with the undeniable observations of non-zero drag/lift in nearly inviscid fluids such as air and water. We shall present d'Alembert's Mystery below. We shall also propose a (new) solution to the mystery: Briefly speaking, we will



Fig. 10.1. Daniel Bernoulli (1700–1782), his father Johann Bernoulli (1667–1748), and Joseph-Louis Lagrange (1736–1813).

show that the zero drag/lift inviscid potential solution is not stable and instead a turbulent approximate solution develops, which has non-zero drag/lift. Our resolution of the mystery is different from the standard solution by Prandtl from 1904, which claims that even the slightest viscosity changes the flow completely due to the presence of no-slip boundary layers. We will present more material further below to open for the reader to judge which solution of the mystery may be closest to the truth. Of course, we do not claim that boundary layers never influence the flow and drag/lift, but we give evidence that for very small viscosity (very large Reynold's number), Prandtl's no-slip boundary layers may not be the true reason why non-zero drag/lift develops.

10.4 A Vector Calculus Identity

In our study of potential solutions we shall use the following identity, which may be verified by direct computation: If $u = (u_1, u_2, u_3)$ is differentiable, then

$$\frac{1}{2} \nabla |u|^2 = (u \cdot \nabla)u + u \times (\nabla \times u). \quad (10.2)$$

10.5 Bernoulli's Law

Let now $u = \nabla\phi$ with $\Delta\phi = 0$ in the domain Ω of the fluid together with the Neumann boundary condition $\frac{\partial\phi}{\partial n} = u \cdot n = g$ on Γ . Let us next define the pressure p by the equation

$$\frac{1}{2}|u|^2 + p = C \quad \text{in } \Omega, \quad (10.3)$$

where C is a constant. Taking the gradient of both sides of (10.3) and using (10.2) recalling that $\nabla \times u = 0$, we find that (u, p) satisfies

$$(u \cdot \nabla)u + \nabla p = 0, \quad \nabla \cdot u = 0 \quad \text{in } \Omega, \quad (10.4)$$

and we thus refer to (u, p) as a stationary *potential solution* to the Euler equations with $f = 0$, noting that by construction $u \cdot n = g$ on Γ . We have already remarked that a potential velocity is irrotational. We note further that the pressure in the Euler equations (with velocity boundary conditions) is only determined up to a constant, which explains the presence of the (arbitrary) constant C in Bernoulli's Law.

Conversely, we see that a stationary irrotational solution (u, p) of the Euler equations (10.1), also satisfies (10.3), which we refer to as *Bernoulli's Law*. We thus see that for stationary potential solutions, the stationary Euler equations and Bernoulli's Law boil down to the same thing, all according to Euler. The same conclusion was reached by Lagrange, who showed that Bernoulli's Law is the exact differential of the Euler equations.

From Bernoulli's Law follows that for a potential solution (u, p) , the pressure p is large where the speed $|u|$ is small, and vice versa.

10.6 Potential Flow around a Circular Cylinder

Consider an infinitely long cylinder of diameter 1 oriented along the x_3 axis and immersed in an inviscid fluid filling \mathbb{R}^3 with velocity $(1, 0, 0)$ at infinity, see Fig. 10.2. We now construct a corresponding potential solution $u = \nabla\phi$ by using Calculus, where we assume that $u_3 = 0$, and seek a function $\phi(x_1, x_2)$ which is harmonic outside the disc $x_1^2 + x_2^2 \leq 1$ occupied by the cylinder, such that $\frac{\partial\phi}{\partial n} = 0$ on the boundary of the disc.

We find that ϕ is equal to the real part of the analytic function $w(z) = z + \frac{1}{z}$ with $z = x_1 + ix_2$ and i the imaginary unit, that is,

$$\phi(x_1, x_2) = (r + \frac{1}{r}) \cos(\beta), \quad (10.5)$$

where $(x_1, x_2) = (r \cos(\beta), r \sin(\beta))$ is expressed in polar coordinates (r, β) . We verify readily that ϕ is harmonic outside the disc, because ϕ is the real part of an analytic function, and that $\frac{\partial\phi}{\partial n} = 0$ on the boundary of the disc. Further, one can show by a little more work that $\lim_{x_1^2 + x_2^2 \rightarrow \infty} \nabla\phi(x_1, x_2) = (1, 0, 0)$, so that the potential solution satisfies the uniform flow condition far away from the cylinder. In Fig 10.2 we plot the streamlines of u , which are the level curves of the imaginary part $(r - \frac{1}{r}) \sin(\beta)$ of $w(z)$.

We have now constructed a potential flow solution around the cylinder, which intuitively looks quite convincing: the flow opens up to go around the cylinder and then closes, pretty much as one may naively expect. Right?

10.7 Zero Drag/Lift of Potential Flow

Let us now compute the drag of the potential flow around the cylinder, that is the net force on the cylinder in the x_1 direction from the pressure acting on the

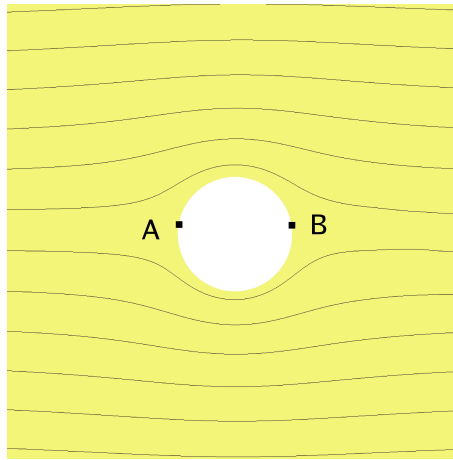


Fig. 10.2. Potential flow around a cylinder

boundary of the cylinder. To this end we note that the flow speed $|u|$ evidently is symmetric with respect to both the x_1 and the x_2 -axis, because the flow after/below the cylinder is evidently a mirror image of the flow before/above the cylinder. From Bernoulli's Law we then deduce that also the fluid pressure is symmetric before/after and above/below. This means that the pressure around the cylinder balances out to zero, that is, there is no net force from the flow on the cylinder: The drag is zero and evidently also the lift which is the net force in the x_2 -direction. We see in particular that the pressure is high at the stagnation point A with zero speed opposing the flow, and that this high pressure is balanced by an equally large pressure in the opposite direction at the stagnation point B at the back of the cylinder. And so it goes for all symmetrically placed points on the boundary. One can easily generalize this result to a body of arbitrary (non-symmetric) shape, subject to potential flow which is uniform at infinity, we give the proof in the last section of this chapter.

This is d'Alembert's Mystery: Potential flow uniform at infinity has zero drag/lift. But massive experimental evidence indicates substantial non-zero drag even if the flow is very slightly viscous such as air and water. The first such experiments were performed by d'Alembert himself in order to present his paradox. Further, with zero lift, flying would be impossible, again at variance with everybody's experience.

So how is science/mathematics to deal with d'Alembert's Mystery? Evidently, something must be wrong with the potential solution. But what? Is it the assumption about inviscid flow, which is essentially Prandtl's explanation? Or is there a different explanation? To find this out let us solve the Euler equations computationally using G2, instead of using analytical mathematics, and see what we get. Before we plunge into this adventure, let us give another

highlight of Calculus applied to the Euler equations, which is as misleading as the zero drag/lift of a potential solution.

10.8 Ideal Fluids and Vorticity

Taking the vorticity of the momentum equation in (10.1), we obtain with a direct computation using e.g. (10.2), the following equation for the vorticity $\omega \equiv \nabla \times u$:

$$\dot{\omega} + (u \cdot \nabla) \omega - (\omega \cdot \nabla) u = 0 \quad \text{in } \Omega \times I. \quad (10.6)$$

This may be viewed as a linear convection-reaction equation for the propagation of the vorticity ω with the fluid velocity u being given. Multiplying by ω and integrating by parts with respect to x , we obtain

$$\frac{d}{dt} \int_{\Omega} \omega^2(x, t) dx + \frac{1}{2} \int_{\Gamma} u \cdot n \omega^2(s, t) ds \leq G \int_{\Omega} \omega^2(x, t) dx$$

if the gradient of the velocity ∇u is bounded by the constant G , where Γ is the boundary of Ω . It follows that if ω vanishes in Ω at initial time $t = 0$, and no vorticity is convected into Ω through the boundary Γ where $u \cdot n < 0$, then $\omega(t)$ vanishes in Ω for all $t > 0$. We are thus led to the conclusion that in an ideal fluid with bounded velocity gradient, vorticity cannot be created. In the computational example with an ideal fluid which we present below, nevertheless vorticity seems to be generated. The only way out of this deadlock is that the assumption of a bounded velocity gradient is not verified, that is, that the underlying Euler solution (u, p) is not a pointwise solution.

10.9 d'Alembert's Computation of Zero Drag/Lift

We recall d'Alembert's (erroneous) computation of zero drag: Suppose there is a stationary pointwise solution (u, p) to the Euler equations of inviscid incompressible flow around a bluff body in a horizontal channel oriented in the x_1 -direction, with the velocity u irrotational, i.e., $\nabla \times u = 0$. Integrating the momentum equation over the domain, we obtain by partial integration, considering the first component

$$0 = \int_{\Gamma_b} p n_1 ds + \int_{\Gamma_{in}} (u \cdot n u_1 + p n_1) ds + \int_{\Gamma_{out}} (u \cdot n u_1 + p n_1) ds$$

where Γ_{in} and Γ_{out} denote the inflow and outflow boundaries of the channel, and Γ_b denotes the boundary of the immersed body. Assuming now that the velocity is equal on in and outflow, which is natural if the channel is long, by Bernoulli's law (stating that $|u|^2/2 + p$ is constant), the pressure will be as well, and thus the inflow and outflow terms will cancel and therefore the drag $\int_{\Gamma_b} p n_1 ds$ will be zero.

Obviously, zero drag of a bluff body contradicts experience: All bluff bodies show substantial drag with the major contribution coming from the pressure distribution around the body with high pressure up front and low pressure in the back, and not from viscosity. In particular, we can attribute only a small part of the drag to viscosity and thus experience clearly indicates substantial drag for inviscid flow. But d'Alembert's computation shows zero drag.

We shall now in a concrete example see in Chapters 11–12 that the trouble with Alembert's computation of zero drag is that the pointwise laminar solution simply does not exist as a stable solution, which makes the computation meaningless. Instead a turbulent approximate solution develops and this solution has a substantial drag close to that for a solution of the NS equations with large Reynolds number.

10.10 A Reformulation of the Momentum Equation

Using the identity (10.2) we can rewrite the Euler momentum equation as follows, assuming $f = 0$

$$\dot{u} - u \times \omega + \nabla\left(\frac{1}{2}|u|^2 + p\right) = 0, \quad (10.7)$$

a formulation which is sometimes used. In particular, we derive from this equation Bernoulli's Law for stationary irrotational flow.

Prandtl's Resolution of d'Alembert's Mystery

By denying scientific principles, one may maintain any paradox.
(Galileo Galilei)

11.1 Quotation from a Standard Source

To get the proper perspective, we present the standard view on the resolution of d'Alembert's Mystery as the one suggested by Prandtl in the short report *Motion of fluids with very little viscosity* read before the Third International Congress of Mathematicians at Heidelberg in 1904, in the form of some quotations from the standard source [92]:

Ludwig Prandtl's discovery of the boundary layer is regarded as one of the most important breakthroughs in fluid mechanics of all time and has earned Prandtl the title of Father of Modern Fluid Mechanics.

Before Prandtl's description of the boundary layer in 1904, there was no lack of interest in the dynamics of fluids due to the practical problems of nautical engineering, ballistics, and hydraulics. Throughout the 18th and 19th century the top physicists and mathematicians of Europe examined flows from a mathematical point of view. Much of this work was to construct potential flows, i.e., incompressible, irrotational flows, over bodies. Examples recognizable to most undergraduates are flows over circular cylinders and other flows involving source-sink superpositions. Although the mathematics was elegant and the flows aesthetically pleasing, it was recognized that such flows failed to mimic "real" flows seen in Nature. Furthermore, it was known since the time of d'Alembert that potential flows frequently resulted in zero drag; a prediction in clear contradiction with everyday experience!

What were these mathematicians to do? Thanks to Coulomb and Stokes, they were aware that a no-slip condition should be applied at solid bodies (we now realize that this condition holds at all fluid boundaries). However, standard external flow problems are ill-posed when the potential flow equations are

combined with the no-slip condition. The correct approach would be to abandon the inviscid (small viscosity) approximation and solve the full Navier–Stokes equations. Stokes had done this himself for the problem of creeping flow around a sphere and derived a non-zero expression for the drag. However, the Stokes flow does not generate the large scale separation seen in most day-to-day flows and the predicted drag is always much less than what is measured for things like cannon balls and marbles in air and water. The reason for these discrepancies is the neglect of the fluid inertia in the creeping flow approximation. To include these terms is a daunting task, even today.

Thus, as the 19th century came to a close, a universal and practical application of fluid mechanics seemed far off. Prandtl's contribution was to realize that we can view the flow as being divided into two regions. The bulk of the flow can be regarded as a potential flow essentially the same as that studied by the mathematicians. Only in a small region near the body do viscous effects dominate. This thin layer is known as the boundary layer. Conceptually, Prandtl's boundary layer is the reason the potential flow theory is compatible with the exact physics. Furthermore, certain details of the structure of the boundary layer are the key to understanding both flow separation and the physical mechanism behind the Kutta condition. That is, a proper understanding of the boundary layer allows us to understand how a (vanishingly) small viscosity and a (vanishingly) small viscous region can modify the global flow features. Thus, with one insight Prandtl resolved d'Alembert's paradox and provided fluid mechanists with the physics of both lift and form drag.

11.2 Quotation from Prandtl's 1904 report

We follow up with some paragraphs from Prandtl's 1904 report which appeared in English translation as Technical Memorandum 452 of the National Advisory Committee for Aeronautics in 1928 [93]:

It is known, however, that the solutions of the Euler equations generally agree very poorly with experience. I will recall only the Dirichlet sphere which, according to the theory, should move without friction.

I have now set myself the task to investigate systematically the laws of motion of a fluid whose viscosity is assumed to be very small. The viscosity is supposed to be so small that it can be disregarded wherever there are no great velocity differences nor accumulative effects. This plan has proved to be very fruitful, in that, on the one hand, it produces mathematical formulas. which enable a solution of the problem and, on the other hand, the agreement with observations promises to be very satisfactory.

The most important aspect of the problem is the behavior of the fluid on the surface of the solid body, assuming that the fluid adheres to the surface and that, therefore, the velocity is either zero or equal to the velocity of the body. In the thin transition layer, the great velocity differences will then produce noticeable effects in spite of the small viscosity.

The most important practical results of these investigations is that, in certain cases, the flow separates from the surface at a point entirely determined by external conditions. A fluid layer, which is set in rotation by the friction on the wall, is thus forced into the free fluid.

On the one hand, we have the free fluid, which can be treated as non-viscous, while, on the other hand, we have the transition layers on the solid boundaries, impart their characteristic impress on the free flow by the emission of turbulent layers.

No. 7-10 show the flow around a cylindrical obstacle. No. 7 shows the beginning of the separation; Nos. 8-9, subsequent stages. No. 10 shows the permanent condition. The wake of turbulent water behind the cylinder swings back and forth, whence the momentary unsymmetrical appearance (referring to the pictures in Fig. 11.2).



Fig. 11.1. Ludwig Prandtl (1875–1953).

11.3 Discussion of Prandtl's Resolution

The main point of Prandtl's resolution of the d'Alembert's Mystery is that boundary layers always exist at solid boundaries, even if the viscosity is very small, and that by the strong velocity difference in the boundary layer, vorticity is created in the layer and is then ejected into the fluid. The important feature is the direction of the vortex generation according to Prandtl, which is parallel to the surface and perpendicular to the streamwise direction corresponding to “tripping” the flow by friction in the boundary layer. We refer to vorticity in this direction as *transversal vorticity*. The accepted resolution of the mystery according to Prandtl is thus that transversal vorticity is generated in the boundary layer, even if the viscosity is very small, and this vorticity generation changes the global patterns of the flow, allowing non-zero

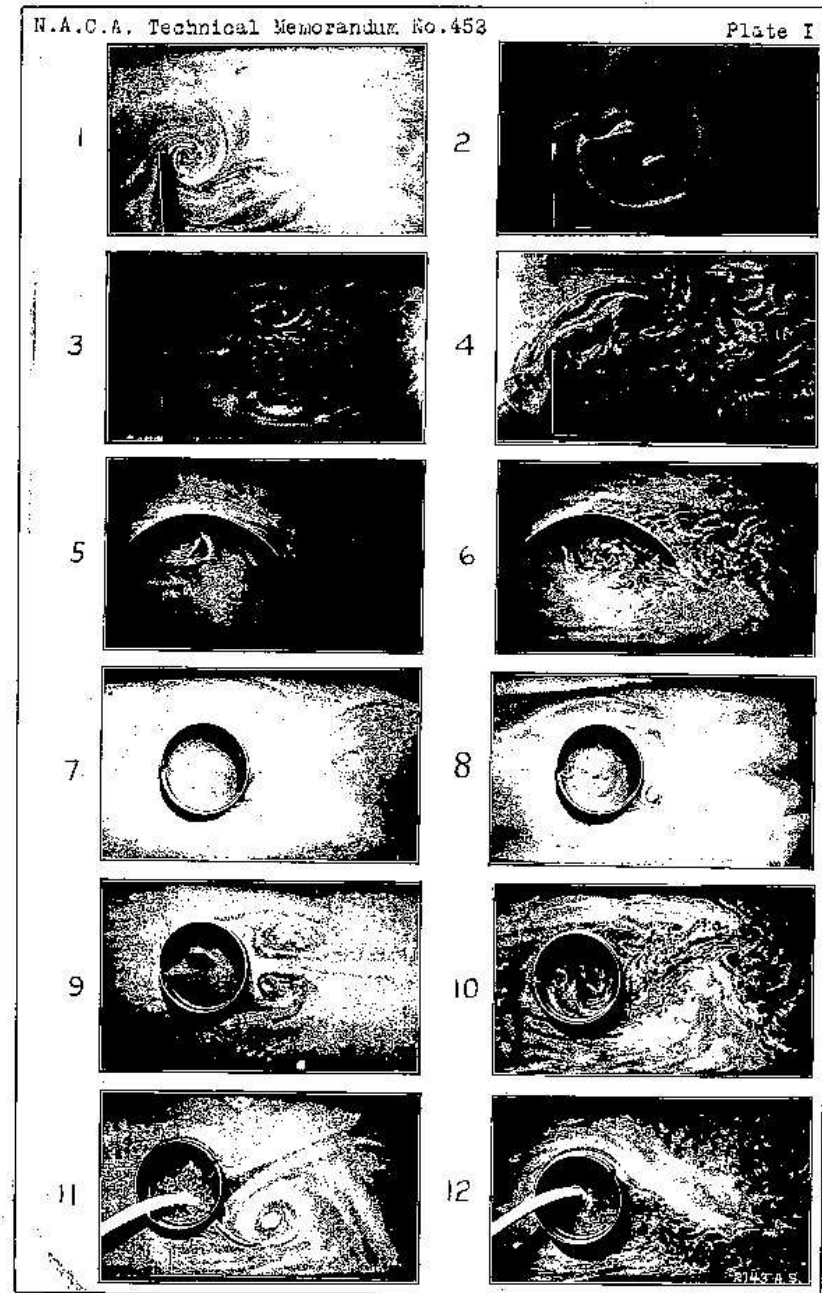


Fig. 11.2. Pictures 1–12 from Prandtl's Technical Memorandum 452.

drag to develop. Prandtl thus claims that the potential solution does not occur in practice, but instead a different (turbulent) solution develops from the generation of transversal vorticity in the boundary layer.

We will below show that Prandtl's view on the potential solution is correct, but we will question his explanation by transversal vorticity generation by showing the importance of instead generation of vorticity in the streamwise direction reflecting the stability analysis in Chapter 9.

Another important aspect concerns the separation points: It is clear from Fig 5 and 6 that Prandtl believes that *there must be two* separation points, although his remark on No. 10 ("*The wake of turbulent water behind the cylinder swings back and forth, whence the momentary unsymmetrical appearance.*"), indicates that he *can see only one* swinging back and forth. We will below show that with very small viscosity, there is in fact only one separation point (in each section perpendicular to the cylinder axis), which fits with Prandtl's experiment, but is contrary to Prandtl's analysis.

Altogether, we will thus present a resolution of the mystery, which is fundamentally different from the accepted resolution by Prandtl.

12

New Resolution of d'Alembert's Mystery

How wonderful that we have met with a paradox. Now we have some hope of making progress. (Nils Bohr)

12.1 Introduction

In this chapter we present a new resolution of d'Alembert's Mystery [61]. We do this by showing computationally that the zero-drag potential solution is unstable, and will therefore not be realized physically, and instead a turbulent approximate solution with substantial drag develops. We show that the drag results from the low pressure inside tubes of strong vorticity in the streamline direction reflecting vorticity generation according to the stability analysis of Chapter 9. Our resolution is different from the accepted solution by Prandtl from 1904 based on boundary layer effects of vanishing viscosity. We believe that our solution is more to the point in the case of vanishing (small) viscosity. We leave to the reader to judge which solution is more accurate.

12.2 Drag of a Circular Cylinder

We now show results of a G2 computational simulation of the flow around a circular cylinder with axis oriented in the x_3 -direction in a long channel oriented in the x_1 -direction, subject to a uniform inflow velocity $(1, 0, 0)$ according to Fig. 12.1. This computation is presented in detail in [55]. We choose the initial velocity equal to zero, and see a potential solution with almost zero drag developing in a couple of time steps, but if we continue the computation we see that the potential solution undergoes transition to a turbulent solution with large drag and a lot of vorticity behind the cylinder.

There is only one separation point (in each transversal section), see Fig. 12.2, which oscillates up and down, and we observe the generation of

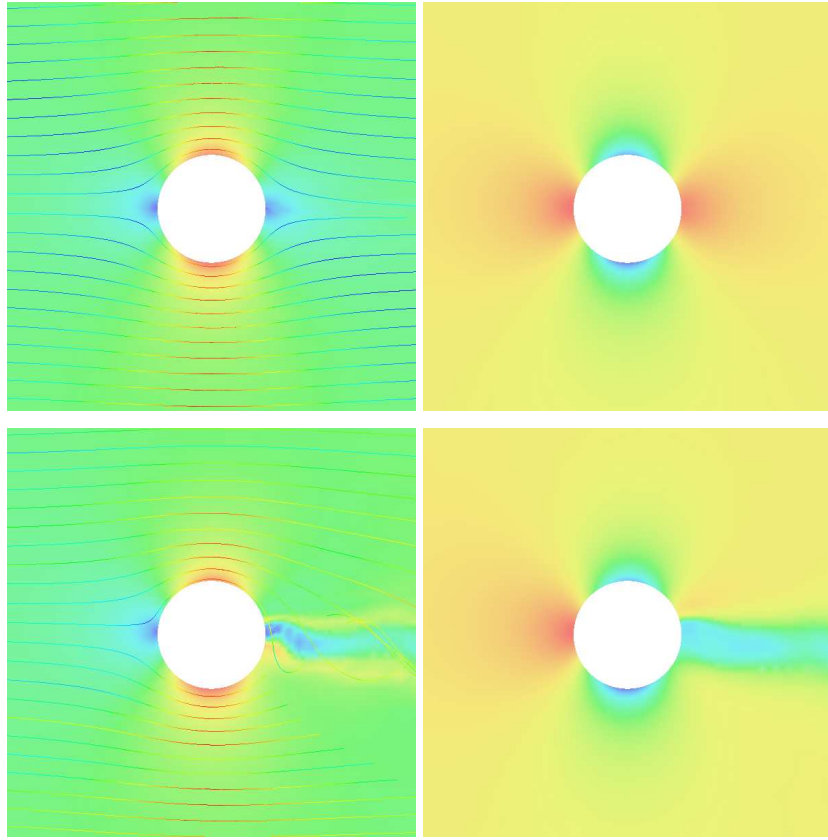


Fig. 12.1. Flow past a circular cylinder; velocity (left) and pressure (right), for the potential solution (upper) and a G2 turbulent solution (lower).

vortex tubes in the streamwise direction inside which the pressure is low generating substantial drag, see Fig. 12.3-12.6. In particular, we note that the transversal vorticity component ω_3 mainly develops downstream the cylinder, whereas the streamwise vorticity is generated at the separation point.

We thus observe the following key features of the Euler solution:

1. No boundary layer prior to separation.
2. Only one separation point, which oscillates up and down.
3. Strong generation of vorticity in the streamwise direction at the separation point.

These main features are completely different from those suggested by Prandtl based boundary layers before separation at two points and generation of transversal vorticity by tripping the flow.

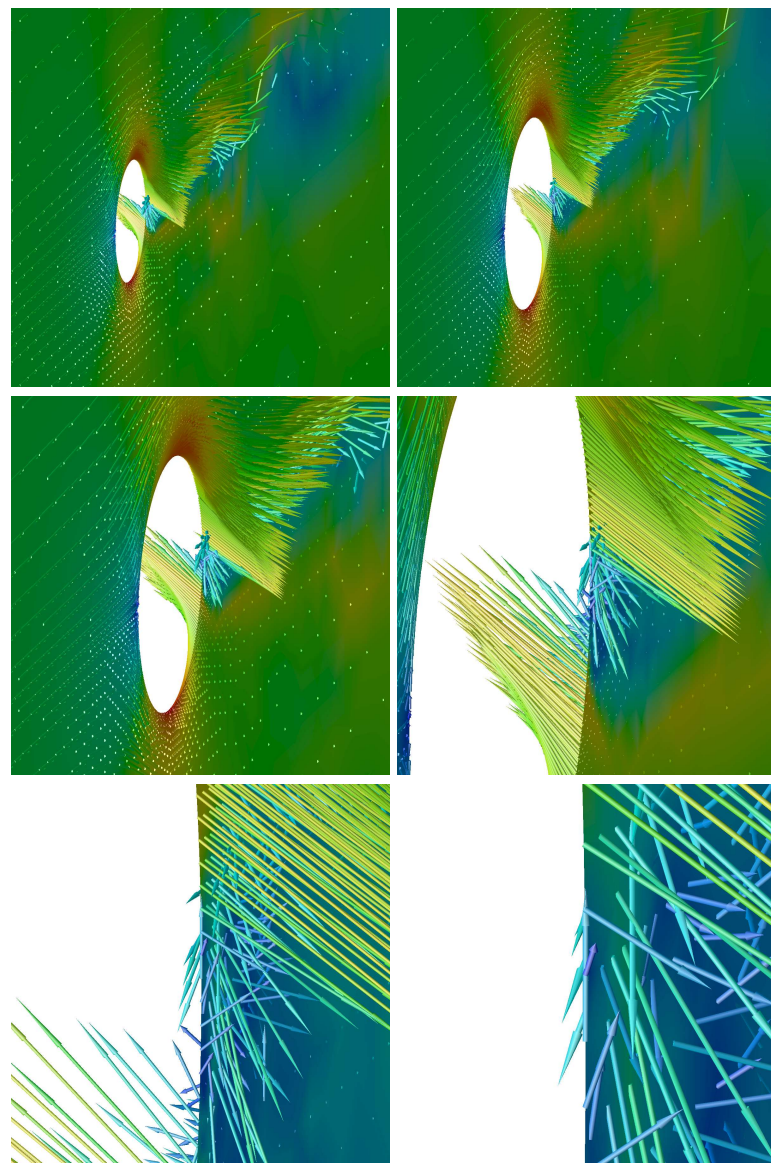


Fig. 12.2. Snapshot of the velocity in a G2 computation illustrating the single separation point.

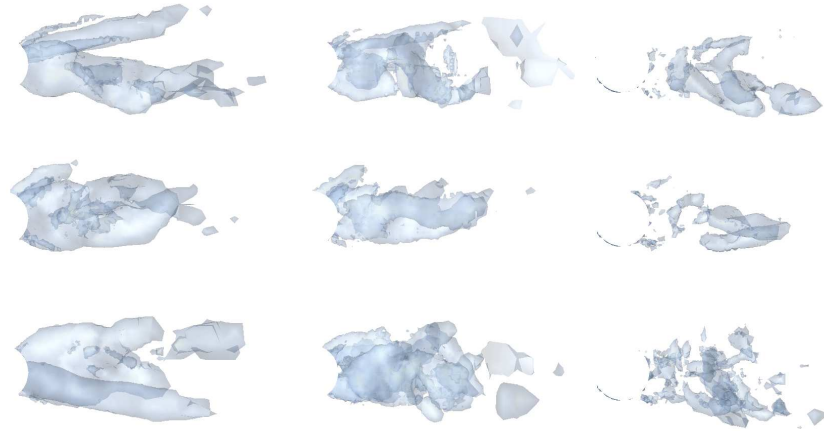


Fig. 12.3. G2 simulation using a mesh with mesh size h ; iso-surfaces for strong vorticity ($\sim h^{-1/2}$): $|\omega_1|$ (left), $|\omega_2|$ (middle) and $|\omega_3|$ (right), at three times $t_1 < t_2 < t_3$ (upper, middle, lower), in the x_1x_2 -plane.

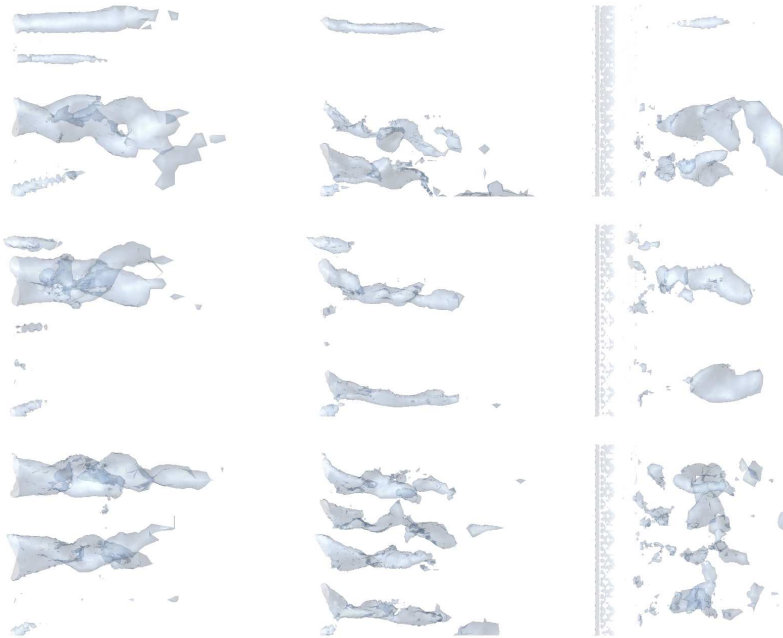


Fig. 12.4. G2 simulation using a mesh with mesh size h ; iso-surfaces for strong vorticity ($\sim h^{-1/2}$): $|\omega_1|$ (left), $|\omega_2|$ (middle) and $|\omega_3|$ (right), at three times $t_1 < t_2 < t_3$ (upper, middle, lower), in the x_1x_3 -plane.

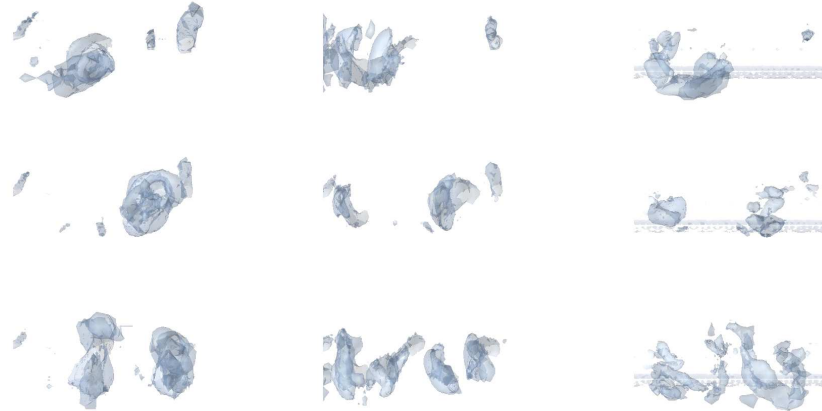


Fig. 12.5. G2 simulation using a mesh with mesh size h ; iso-surfaces for strong vorticity ($\sim h^{-1/2}$): $|\omega_1|$ (left), $|\omega_2|$ (middle) and $|\omega_3|$ (right), at three times $t_1 < t_2 < t_3$ (upper, middle, lower), in the x_2x_3 -plane.

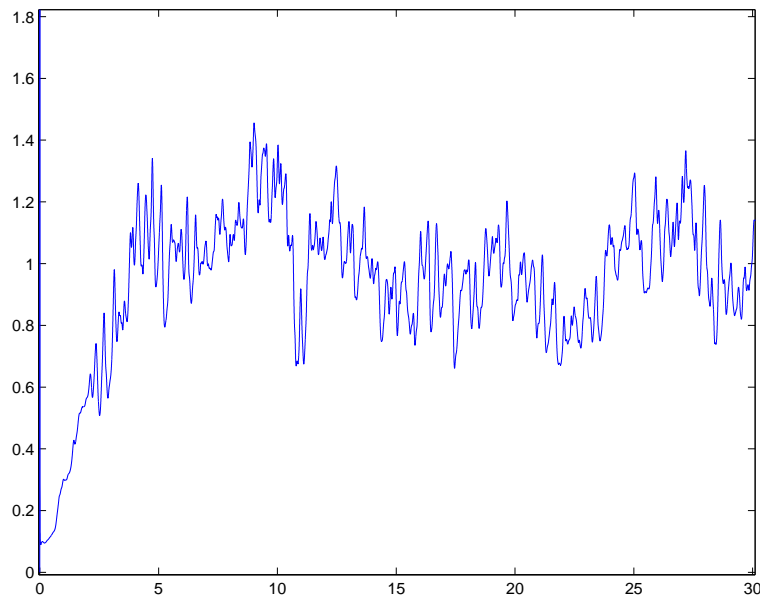


Fig. 12.6. Time series of c_D for a G2 solution to the Euler equations.

12.3 The Role of the Boundary Layer

We now comment on a critical aspect connecting to Prandtl's analysis, namely the role of the boundary layer. An Euler solution with slip boundary condition has no boundary layer, while a NS solution will have a turbulent boundary layer. Prandtl claims that the NS boundary layer will have a global effect on the drag even under vanishing viscosity, while we claim that the effect will vanish with the viscosity, so that a slip boundary condition will serve as a good model for very small viscosity.

We then start from the observation that the effective *skin friction* F from a turbulent boundary layer from experiments appears to decay with the viscosity as $F \sim \nu^{0.2}$, see e.g. [99]. If now the turbulent NS boundary layer has thickness d and an effective turbulent viscosity $\hat{\nu}$, then we will have $F \sim \hat{\nu}/d$ since the tangential velocity gradient in the normal direction $\sim 1/d$. Further, the total turbulent dissipation $\hat{\epsilon}$ in the layer will satisfy $\hat{\epsilon} \sim \hat{\nu}d^{-2}d = \hat{\nu}/d$, and thus $\hat{\epsilon} \sim F \sim \nu^{0.2}$. This indicates that the global effect of the boundary layer decays like $\nu^{0.2}$, and thus will vanish for vanishing viscosity.

We notice that one may argue that the intensity of the transversal vorticity in the turbulent boundary layer will be $\sim 1/d$, and thus the total vorticity generated in the boundary layer would be ~ 1 . We believe Prandtl may have taken this as evidence that the boundary layer vorticity generation would have a global effect and could change the drag. We believe this was a mistake since only strong vorticity can cause substantial turbulent dissipation and change the drag, because of the coupling to a small viscosity in turbulent dissipation. We conclude that the global influence on e.g. the drag of the boundary layer is proportional to the skin friction and thus vanishes with vanishing viscosity.

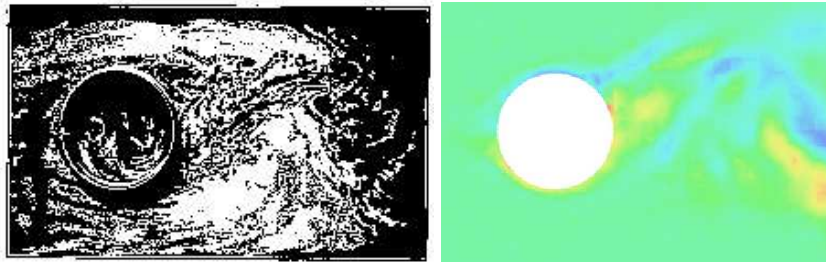


Fig. 12.7. Vorticity in turbulent flow past a circular cylinder: Prandtl's experiment (left), and a G2 solution without boundary layer (right).

12.4 Analysis of Instability of the Potential Solution

The stability analysis below indicates that strong vorticity in the x_1 -direction should be generated at the separation point, which is clearly observed in the

computations, and which in particular reflects the instability of the potential solution.

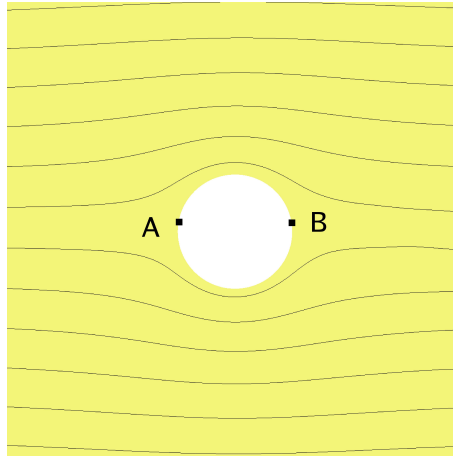


Fig. 12.8. Streamlines for the potential solution of a circular cylinder.

We have observed strong generation of streamwise velocity at the separation point for a circular cylinder, which we now support by analytical evidence. We then focus on the potential solution with velocity $u(x)$ given as the gradient of the real part $\phi(x_1, x_2) = (r + \frac{1}{r}) \cos(\beta)$ of the analytic function $w = z + \frac{1}{z}$ with $z = x_1 + ix_2$, see Fig. 12.8. The stability is governed by (i) the linearized Euler equations (9.1), or (ii) the vorticity equations:

$$\dot{\omega} + (u \cdot \nabla)\omega - (\omega \cdot \nabla)u = 0, \quad \text{in } \Omega \times I, \quad (12.1)$$

which we may view as a linear convection-reaction equation for the propagation of the vorticity ω with the fluid velocity u being given. In both cases (i)-(ii) the crucial term is the reaction term with $\pm \nabla u$ acting as coefficient in a linear convection-reaction problem. We now compute ∇u near the rear separation point B given by $z = 1$. We then write

$$w(z) = z - 1 + 1 + \frac{1}{z - 1 + 1} \approx 1 + (z - 1)^2$$

and thus have

$$\phi(x_1, x_2) \approx 1 + (x_1 - 1)^2 - x_2^2$$

and

$$u(x) \approx (2(x_1 - 1), -2x_2, 0)$$

and thus the vorticity equation takes the following approximate form close to B :

$$\begin{aligned}\dot{\omega}_1 + (u \cdot \nabla) \omega_1 &= 2\omega_1 \\ \dot{\omega}_2 + (u \cdot \nabla) \omega_2 &= -2\omega_2 \\ \dot{\omega}_3 + (u \cdot \nabla) \omega_3 &= 0\end{aligned}\tag{12.2}$$

We see that ω_1 is exponentially increasing with rate $\exp(2t)$, which indicates that the potential flow solution is exponentially unstable: Strong vorticity will be generated at the separation point.

12.5 Sum up of the New Resolution

We sum up our combined observation from computation and analysis as follows: The potential solution with zero drag is unstable and will not be realized in reality. Instead a turbulent Euler solution develops with strong vorticity and substantial drag. The turbulent Euler solution has no boundary layer prior to separation, which fits with the observation that the skin friction in NS vanishes with vanishing viscosity indicating that the boundary layer has no influence on a global quantity such as drag. This is our resolution of d'Alembert's Mystery.

Part II

Mathematics of Turbulence

13

Turbulence and Chaos

God does not throw dice. (Einstein)

We ought to regard the present state of the universe as the effect of its antecedent state and as the cause of the state that is to follow. An intelligence knowing all the forces acting in nature at a given instant, as well as the momentary positions of all things in the universe, would be able to comprehend in one single formula the motions of the largest bodies as well as the lightest atoms in the world, provided that its intellect were sufficiently powerful to subject all data to analysis; to it nothing would be uncertain, the future as well as the past would be present to its eyes. (Laplace)

13.1 Introduction

In this part we develop certain basic aspects of turbulence of mathematical nature. We start by considering weather prediction exhibiting features of *chaos*, *randomness*, *observability* and *computability* of relevance to turbulence. We then take a look at the Clay Institute \$1 million prize problem on the existence and regularity of exact solutions to the NS equations, representing a current goal of mathematics research on the NS equations. We open new lines of mathematical thought by introducing the concepts of ϵ -*weak solutions*, and *weak uniqueness* or *output uniqueness* reflecting stability features of turbulent flow. We end with a study of G2 for the Euler equations and open to a study of the 2nd Law of thermodynamics and irreversibility, which is continued in Part VI.

13.2 Weather as Deterministic Chaos

We start with the concept of *deterministic chaos* originating from the work of the meteorologist Edward Lorenz on the unpredictable nature of the weather, initiated in the early 1960s [83]. It is natural to make this connection because

weather predictions are routinely made by computational solution of systems of differential equations similar to the NS equations modeling the turbulent motion of air and moisture in the atmosphere of the Earth.

We shall use the term *chaotic dynamical system* to describe dynamical systems for which pointwise values in space/time are very sensitive to perturbations and thus unpredictable, while certain mean values in space/time are less sensitive and thus predictable. We shall see that the NS equations is an example of a chaotic dynamical system in this sense.

We recall that we consider dynamical systems of the form $\dot{u} = g(u)$, where the given function $u \rightarrow g(u)$ represents the law of the system. We thus consider *deterministic systems* following a deterministic law, and a chaotic dynamical system expresses deterministic chaos. The unpredictability of point values thus results from the strong sensitivity to perturbations, and not from any randomness in the given law. The law of a chaotic system is often of simple form, without any presence of randomness.

To illustrate the difference between pointwise values and mean values, we may consider the problem of predicting the weather, or more precisely the temperature, at a specific location in space. Guide books often present, for given locations, predictions of monthly mean temperatures for the different months of the year, but never 24h daily mean temperatures for all the days of the year. This indicates that monthly mean values are predictable to a tolerance of interest, while 24h daily mean values are not.

A daily mean value is an average over short time, which we may refer to as a pointwise value in time, while we may refer to a monthly mean value simply as a mean value. We may then say that mean values appear to be predictable to a tolerance of interest while point values are not.

It is a common observation that predictions of the daily weather more than 3-6 days ahead (depending on the general weather situation) are very unreliable. Lorenz connected the unpredictability to strong sensitivity to perturbations with the question: “Does the flap of a butterfly’s wings in Brazil set off a tornado in Texas?” In predictions of daily weather it is observed that perturbations may double every 12-48 hour depending on the model, and thus make predictions over more than say a week unreliable because of the considerable uncertainty in both data and modeling.

Obviously, the size of the tolerance is an important aspect of predictability: To predict a July mean value up to 10°C is of little interest, while a tolerance of 1°C may be the best we can ever hope for. So, the difference between interest or no interest may be just one order of magnitude. We shall meet this aspect below when computing drag and lift coefficients.

To say that a daily mean temperature is unpredictable up to a tolerance of say 1°C , does of course not mean that the daily mean temperature a specific day of July at a specific location is not determined up to 1°C , but only that its value may effectively be anything between say 10°C and 30°C , and that we cannot predict more than a few days ahead what the actual value might be.

13.3 Predicting the Temperature in Målilla

As an illustration we focus on the little village Målilla in the county of Småland in southern Sweden, for which data are available from the Swedish Institute of Meteorology SMHI. In Fig. 13.1 we display daily, weekly, and monthly mean temperatures over the years 1988–1995, and we also show the yearly mean values of the temperature in southern Sweden for the period 1860–2003. We see that the variation of the daily temperatures is $\pm 10^\circ\text{C}$, of weekly averages $\pm 7^\circ\text{C}$, monthly averages $\pm 4^\circ\text{C}$, and yearly averages $\pm 2^\circ\text{C}$.

We may say that there are many possible daily temperature curves in Målilla which differ significantly ($\pm 10^\circ\text{C}$), and it seems impossible to predict which curve the actual temperature in Målilla will follow a particular year.

On the other hand, the variation of monthly averages over the different daily temperature curves is significantly smaller, and seems predictable to a tolerance of $\pm 4^\circ\text{C}$. Further, taking the monthly mean value of any of the many possible daily temperature curves will give a good approximation of the common monthly mean value for all the curves. To compute monthly averages is thus not necessarily a matter of statistics, where we would compute ensemble averages over many different daily temperature curves.

13.4 Chaotic Dynamical System

Lorenz connected the term chaos to strong pointwise sensitivity to perturbations, and noticed that many systems including pinball machines, planetary motion and the weather may show features of strong pointwise sensitivity to perturbations, and thus according to Lorenz show features of chaos. This is no surprise of course; everybody is familiar with the possibility that small perturbations may have large pointwise effects.

What made chaos to such a hot topic in the 1980s, was the seemingly paradoxical concept of *order in chaos*: in a system behaving pointwise in an irregular chaotic unpredictable manner, there may still be some aspects that are predictable. The challenge then becomes to identify these aspects, that is, to identify the order in the disorder or chaos.

The intriguing aspect of a chaotic system such as the weather, is that some quantities appear to be truly unpredictable, like a daily temperature, but there are also other quantities, such as a monthly average temperature, which may be predictable to a tolerance of interest.

We are thus led to identify a dynamical system as *chaotic* if the following two conditions are satisfied:

- (1) pointwise quantities are strongly sensitive to perturbations and therefore unpredictable.
- (2) Certain quantities of interest are moderately sensitive to perturbations and thus predictable.

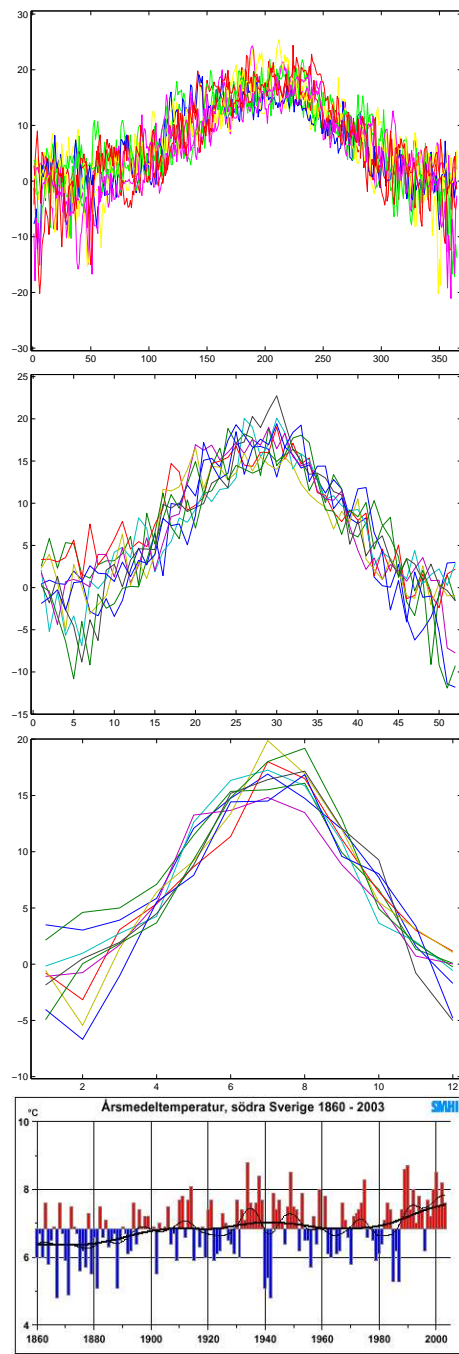


Fig. 13.1. Mean temperatures for Målilla in Sweden over the years 1988–1995, 24 hour mean, weekly mean, monthly mean, and also yearly mean temperatures for southern Sweden over the years 1860–2003.

Typically, the quantities of interest are more or less local mean values in space-time of individual trajectories or solutions to the dynamical system, but may also be other quantities reflecting certain aspects of the solution.

The nature of the order in chaos of course is of prime importance. Much of the mathematical work on chaos has been geared towards global aspects such as *attractors* approached by all trajectories after long time. We focus on aspects of order in chaos that can be captured by mean values in space/time, which are not necessarily very long, like monthly mean values of daily temperatures. We do this by computational methods which open new possibilities of identifying more precise expressions of order than analytical methods.

A main new contribution of this book is evidence that turbulent flow is chaotic in the above sense: pointwise quantities are unpredictable with strong sensitivity to perturbations, while certain mean value quantities in space-time of interest are predictable with moderate sensitivity to perturbations.

The notion of a chaotic system may seem to be paradoxical in the following sense: In a chaotic system (like the weather) individual trajectories are unpredictable (like the daily temperature in Málilla), yet certain mean values of interest of such unpredictable trajectories indeed may be predictable to tolerances of interest (like monthly mean value temperatures). We can also formulate the paradox: How can it be that certain mean values of a pointwise incorrect individual trajectory may be correct? If our daily trajectory is all wrong, how come that we are able to live normal lives over many years? We will unfold the paradox below, not as simple matter of statistics (because it is not), but as a subtle matter of cancellation.

We may express the essence of a chaotic system alternatively as follows: Each individual trajectory represents *one possible* trajectory out of *many possible* trajectories and we cannot predict which trajectory out of the many possible ones the system will actually follow. There are many possible developments of the daily weather over the next month and we cannot predict which possibility will be realized. However, certain mean value outputs vary little over the different possible trajectories, which effectively makes certain mean value outputs predictable. In Málilla there are many possible daily temperature variations, which are all very different, but their monthly mean values are all similar.

Another example: The trajectories of life for different human beings are all vastly different, but certain mean value quantities may have smaller variation (many human lives are quite alike in certain aspects).

13.5 The Harmonic Oscillator as a Chaotic System

A basic model of physics is the harmonic oscillator with angular frequency $\omega > 0$:

$$\ddot{u}(t) + \omega^2 u(t) = 0 \quad \text{for } 0 < t \leq \hat{t},$$

with solution $u(t) = \cos(\omega t)$ satisfying the initial conditions $u(0) = 1$, $\dot{u}(0) = 0$. We claim that if ω is large, then this is a chaotic system. How can it be? Isn't the harmonic oscillator the most ordered, predictable and non-chaotic system that is thinkable? Well, let us consider the output $u(\hat{t})$ where \hat{t} is the given final time. A change from \hat{t} to $\hat{t} + \delta\hat{t}$ will change the output by the amount $\omega\delta\hat{t}\sin(\omega\hat{t})$, which may be far from small even if $\delta\hat{t}$ is small, since ω is large. Thus the output $u(\hat{t})$ is strongly sensitive to perturbations in \hat{t} , and thus unpredictable, so that the harmonic oscillator satisfies (1) in the requirement of a chaotic system, if ω is large.

Next, let us now for a small positive $\Delta\hat{t}$ consider the output

$$M_{\Delta\hat{t}}(u) = \frac{1}{\Delta\hat{t}} \int_{\hat{t}-\Delta\hat{t}}^{\hat{t}} u(t) dt = \frac{1}{\omega\Delta\hat{t}} (\sin(\omega\hat{t}) - \sin(\omega(\hat{t} - \Delta\hat{t}))),$$

which is a mean value in time close to the final time \hat{t} . Clearly, $|M_{\Delta\hat{t}}(u)| \leq \frac{2}{\omega\Delta\hat{t}}$, and thus $M_{\Delta\hat{t}}(u) \approx 0$ if $\omega\Delta\hat{t}$ is large, which does not change under perturbations of \hat{t} . We conclude that if $\omega\Delta\hat{t}$ is large, then the mean-value $M_{\Delta\hat{t}}(u) \approx 0$ is not at all sensitive to perturbations in the data \hat{t} and is therefore predictable, and thus also (2) is satisfied. Evidently, there is some order in the pointwise chaos of the harmonic oscillator at high frequency.

We conclude that the harmonic oscillator with large frequency may be viewed to be a chaotic system: The solution is pointwise unpredictable but a mean value in time is predictable. We understand that the reason for this effect is the oscillatory nature of the solution $u(t) = \cos(\omega t)$, creating substantial cancellation in the integral defining the mean value. We shall below meet the same crucial feature in turbulence.

We may say that the order of the harmonic oscillator is built into the law of the dynamical system itself: $\ddot{u} + \omega^2 u = 0$, which expresses Newtons 2nd law for a unit mass connected to the origin with a Hookean spring with spring constant ω^2 . This is clearly a very simple law which should impose some order, and certainly does, although pointwise outputs evidently become unpredictable if the spring is stiff with ω large and the oscillation is fast. Similarly, the NS equations express Newtons 2nd law for a Newtonian fluid combined with incompressibility, and so we may expect some order in the chaos of turbulence as well.

13.6 Randomness and Foundations of Probability

One may attempt to describe a dynamical system to be *random* if only (1) is satisfied but not (2). A random system would then be a system which deterministically would be fully unpredictable; not even mean values in space/time would be deterministically predictable. Knowing one solution trajectory of a random system would say nothing about other possible trajectories, not

even about mean values. One might have the impression that the ideal objects of study in probability and statistics would be such deterministically unpredictable systems, but as we will see this does not appear to be a correct viewpoint.

As a possible example of a random system, let us consider the process of *coin-tossing*, which is studied with probabilistic methods in any text on probability or statistics. The assumption is that it is impossible to predict the outcome of head or tail of a single coin toss. As a compensation the notion of *probability* is introduced aimed at describing that tossing the coin *many times* will show approximately an equal number of heads and tails (if there is nothing wrong with the coin). One would thus associate a probability of 1/2 to both head and tail.

From a deterministic point of view the process of coin tossing may be described by the equations of motion for a rotating coin based on Newtons 2nd law, that is as a dynamical system based on a simple law as we have discussed. This system is very sensitive to perturbations in e.g. initial conditions, which makes it satisfy condition (1). A simplified model for coin tossing is the harmonic oscillator with the solution $u(t)$ describing the rotation of the coin during the tossing, with the outcome being say head if $u(\hat{t}) > 0$ and tail if $u(\hat{t}) < 0$, where \hat{t} is the final time when the coin hits the table (and $u(\hat{t}) = 0$ would correspond to the unlikely outcome that the coin ends up balancing vertically on its perimeter). We may here assume that we always initiate the coin with the same initial conditions $u(0) = 1$ and $\dot{u}(0) = 0$ say, and the unpredictable nature of the outcome of the tossing would then correspond to small perturbations in the choice of final time \hat{t} , as in the above study of the harmonic oscillator. Viewing coin tossing this way would correspond to viewing it as a deterministic chaotic dynamical system with continuous time, for which a pointwise output in time would be unpredictable, but for which a mean value in time would be predictable. The predictability of the mean value in time would then result from carefully following one single coin toss and observing that half of the time of the toss the coin would have heads up.

However, in probability theory coin tossing is instead viewed as a process with discrete time, where the coin *jumps* from an initial state $u(0)$ at initial time 0 to a final state $u(\hat{t})$ at final time \hat{t} . Here time appears to be *discrete* with only two values 0 and \hat{t} , and the motion of the coin under a continuous change of time is not observed. It is like closing the eyes during the toss and to only open them at the end of the toss to observe the outcome. The assumption is now made that it is impossible to say anything about a single coin toss, representing a jump from $u(0)$ to $u(\hat{t})$. To say anything about properties of the coin or the process of coin tossing, we would have to toss the coin many times corresponding to *ensembles of solutions* from which we can experimentally compute mean values and probabilities. Alternatively, for an *ideal coin* one could use probability theory based on (in this case very simple) combinatorics, noting that for an ideal toss of an ideal coin head and tail represent 2 equally possible outcomes, to compute the the probability for each outcome to be 1/2.

For a *real coin* (possibly a bit non-symmetric) tossed by real people, only the experimental method of tossing the coin many times would be seem to be available, and to determine any slight bias would require many thousands of coin tosses. In both practical experiments and probabilistic mathematics, we would then be working with *ensemble mean values* over many tosses and not mean values in time of a single toss.

The mathematical statistician Persi Diaconis [31, 25] tried to get around costly experiments with real people tossing coins many times by instead recording the motion of a coin tossed by a simple coin-tossing machine with a high-speed camera. From the video Diaconis could predict that in 51 cases out of 100 the coin would land on the same side it started. This result was also supported by a mathematical analysis of the equations of motion of the coin indicating that the amount of bias depended on one single parameter, the angle between the normal to the coin and the angular momentum. Diaconis concluded that “coin tossing is physics and not random”. This is precisely our own standpoint!

Of course, using a deterministic approach, we would instead try computational simulation using a realistic model of a flipping coin based on Newtons 2nd law, with the advantage that it would be cheap and quick (if you have the software for the modeling and computation). Using computation we could thus be able to mimic Diaconis two methods, by either simulating the outcomes of many coin tosses with slightly different data and computing corresponding ensemble averages, or by carefully recording the motion of the coin in a few experiments and (somehow) drawing conclusions about the probability of head or tail by the very motion of the coin. In both cases we would, following the leading probabilist Diaconis, view coin tossing as a deterministic chaotic dynamical system, rather than taking a probabilistic view. In particular, we would this way directly see a connection between ensemble mean values and time mean values: A time mean value at final time may be viewed either as a mean value in time over a discrete set of uniformly distributed quadrature points of a single coin toss, or as an ensemble mean value corresponding to randomly chosen quadrature points corresponding to randomly chosen final times, and the two mean values should be approximately the same. It would further seem natural to expect the randomly chosen final times to be smoothly distributed as a reflection of the strong sensitivity of the final time to perturbations in e.g. initial data. This would follow from the idea of Poincaré [91] that the scales of the initial data perturbations would be larger than the very small scales of initial data resulting in different outputs reflecting the strong sensitivity. Of course, this idea connects to the idea of Leibniz and Laplace of “equally possible” outcomes.

Viewing coin tossing as deterministic chaos would connect to what is referred to as an *objectivist* point of view in probability theory advocated by Popper, where the probability of coin tossing with a certain coin would reflect the physics of that particular coin under tossing, or the *propensity* of the coin, also connecting to *single-case probability*. The experimental approach corre-

sponds to the *frequentist* interpretation where the probability of head is the frequency of heads over ensembles of many tosses.



Fig. 13.2. Gottfried Wilhelm von Leibniz (1646–1716): "I say therefore that the existent is the being which is compatible with most things, or the most possible being, so that all coexistent things are equally possible." Pierre-Simon Laplace (1749–1827): "The theory of chance consists in reducing all the events of the same kind to a certain number of cases equally possible...". Jules Henri Poincaré (1854–1912): "... it may happen that small differences in the initial conditions produce very great ones in the final phenomena."

Now, are there dynamical systems which are random but not chaotic? Assuming that a dynamical system is defined by some deterministic law, it would seem quite impossible that there would be no reflection whatsoever of this law as some kind of order in the variation in time of system trajectories. The only way we could get a random system would then be to build in the randomness into the law of the system, which would then no longer be deterministic. So maybe after all there are no dynamical systems based on deterministic laws which are random, but only chaotic systems with some order or fully deterministic systems with a lot of order?

Could it be that if we find some order in a system we believe is random, such as some ensemble mean values approaching some limit as the size of the ensemble grows, corresponding to a central limit theorem or law of large numbers in probability theory, this order in fact signifies that the system is chaotic instead of random. If we view space-time mean values as some kind of ensemble mean values, we may get support for such a suspicion. With this perspective the order in the randomness of coin tossing would have the same origin as the order in coin tossing as a chaotic dynamical system, namely Newtons 2nd law underlying the process of coin tossing, which regulates the propensity of the coin.

If we observe pointwise unpredictable outputs of a certain system, and we do not search and find predictable mean value outputs, then we could come to believe that the system is random and not chaotic. If we then as probabilists observe some predictability of ensemble mean values of this system,

then we would probably connect this to some *Law of Chance*. However, as non-probabilists we might instead from the observed order suspect that we are in fact dealing with a deterministic chaotic system based on some law, and we could then find motivation to search for a law defining the system. The observed order would then express the order built into the chaotic system by its law, rather than some (mysterious) Law of Chance.

13.7 NS Chaotic rather than Random

At any rate, the NS equations do not seem to represent a random dynamical system with solutions jumping around unpredictably like tossed coins in a probabilistic setting. Therefore, we avoid using probability theory and statistics in this book. We thus use a deterministic approach and not a probabilistic one. We do this not only because we do not master probabilistic methods, but also because we do not see any reasons to approach turbulence using such methods, because we are dealing with a dynamical system with a known simple law: Newtons 2nd law. We consider dynamical systems with pointwise outputs being unpredictable and certain space-time mean value outputs being predictable and we do not have to proceed to ensemble mean values. This way we avoid the serious problem of obtaining input data needed in a statistical approach. The data we need is deterministic input data for the NS equations (f, u^0, Ω, I, ν) , which we can regard as mean values, but not data on statistical distributions such as covariances, which may be extremely difficult to obtain.

To handle uncertainties in data we use a deterministic approach based on duality, where we compute sensitivities in output to perturbations in input, only requiring a rough estimate of the variance, thus again avoiding detailed statistics.

We sum up this discussion by pinpointing an important difference between a chaotic and a random system as follows: If we have access to only one trajectory of a chaotic dynamical system, we may still get correct information about certain mean values in space-time. In contrast, from knowing only one trajectory of a random system, we can conclude nothing. In the standard setting of discrete time it is impossible to draw some conclusion about the property of a coin by throwing it once. To get information from a random system we need ensembles of many trajectories from which we can form ensemble mean values. We have to throw the coin many times to get statistical information concerning its properties.

This is a key point directly coupling to computational work. To compute information about a random system, we have to use *Monte Carlo simulation* corresponding to computing many trajectories and taking ensemble mean values. Alternatively, randomness may be modeled in a deterministic system with new independent variables, which is also computationally costly. In a chaotic system like turbulent flow, it may be sufficient to compute one trajectory

and take mean values in space-time. Obviously the difference in amount of computational work may be enormous.

Computing solutions of a chaotic system generates seemingly random pointwise output from deterministic input, which could be viewed as some kind of a random number generation, and we could analyze the output using statistical methods. By computation we could thus generate data for statistics. We may say that computation is cheap while acquiring data by measurement in general is expensive, and thus computations could help tackle a main difficulty of statistics, namely how to collect statistical data.

As a final comment on chaotic vs random, we remind that the trajectory of the life of a certain person may be viewed to be chaotic in the sense that it is unpredictable pointwise, but this does not mean that it is random. In fact each life trajectory follows a certain logic (laws) and is far from being random (most of the time). A person taking all the time random decisions will not live long.

13.8 Observability vs Computability

The same questions of predictability/computability of mean values vs point values in space-time, seem to arise in connection with many basic mathematical models containing *macro*-states in the form of mean values of *micro*-states, such as the Schrödinger equations or Boltzmann's equations. In these cases the macro-states may correspond to *observables* such as energy levels or temperature, which are quantities which can be reliably measured and which represent mean values of micro-states in the form of point-valued wave functions or velocity distributions. In these models many different micro-states may produce the same mean value macro-state, and the pointwise values of the micro-states may not be observables nor predictable/computable. We may say that only God may have a correct knowledge about the micro-states, while we as human beings can only hope to observe/predict/compute macro-states. Or with another metaphor: We can never get full information about the thoughts of another person, but sometimes we may get some gross idea of the state of mind of that person and predict the action of that person (up to some tolerance of interest).

13.9 Lorenz System

Lorenz studied a dynamical system in the form of a 3×3 system $\dot{u} = f(u)$ of ordinary differential equations with

$$f(u) = (-10u_1 + 10u_2, 28u_1 - u_2 - u_1u_3, -\frac{8}{3}u_3 + u_1u_2).$$

One may view *Lorenz system* as a very simple model for the NS equations obtained by a Galerkin method with 3 trigonometric basis functions. One may thus view Lorenz system as a model for the evolution of the weather. Lorenz showed that solutions of the Lorenz system are very sensitive to perturbations, e.g. small perturbations in initial data, which makes it impossible to predict/compute the solution pointwise correctly over longer time. More precisely, using double precision it seems impossible to accurately compute over a time interval longer than 50 time units [82]. Lorenz thus in a very simple model problem gave an explanation of the observed impossibility of predicting the daily weather more than about 3-5 days ahead depending on the weather conditions.

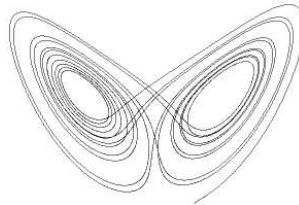


Fig. 13.3. A Lorenz trajectory.

Lorenz system has a stationary point at the origin, which is unstable, and two slightly unstable stationary points P_1 and P_2 away from the origin. A trajectory of a solution to the Lorenz system repeatedly shifts from orbiting P_1 to P_2 and back again and the number of revolutions around each point seems to vary in an irregular “chaotic” way, see Fig 13.3. However, a plot of a solution trajectory is beautiful and partly very ordered, reflecting that there is some “order in chaos”. A solution of the Lorenz system viewed as a weather model, may represent a succession of weather periods with alternating periods of high and low pressure with the lengths of the periods varying irregularly.

So what could then be the order of the Lorenz system, other than that expressed by the beautiful “butterfly” order of a typical trajectory? One may expect that over long time the number of revolutions around P_1 and that around P_2 will be approximately the same. In Fig 13.4 we plot these numbers as functions of time for a trajectory computed over long time. Such a trajectory is not pointwise correct but would rather have to be viewed as an ensemble of trajectories over shorter time which are pointwise correct. At any rate we see that the number of revolutions around P_1 and P_2 are approximately the same.

Summing up, turbulent flow shows features of chaos in the sense that pointwise quantities are not predictable/computable, which reflects strong pointwise sensitivity to perturbations, but certain mean values are predictable/computable, which reflects less sensitivity of mean values, and thus some “order in chaos”.

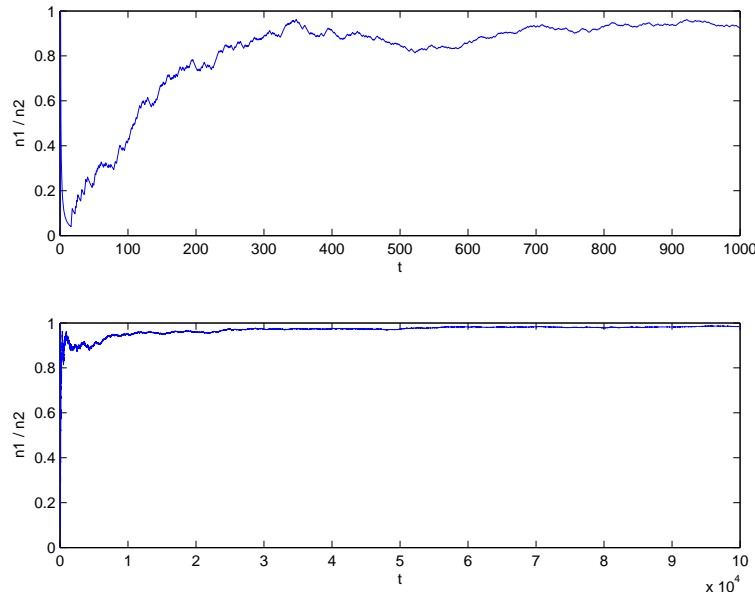


Fig. 13.4. Number of rotations around P1 and P2 for a Lorenz trajectory (computations by Anders Logg, TTI Chicago).

Lorenz connected chaos to pointwise unpredictability, reflecting strong pointwise sensitivity to perturbations. However, Lorenz did not emphasize the other aspect of chaos which we are proposing, namely predictability of certain mean values reflecting moderate sensitivity to perturbations, which distinguishes a chaotic system from a random system.

13.10 Lorenz, Newton and Free Will

The reason Lorenz system attracted so much attention was the discovery that a seemingly innocent system of ordinary differential equations such as the Lorenz system with constant coefficients and quadratic non-linearities, could have pointwise unpredictable solutions. The interest came from the apparent contradiction with the Newtonian view of the Universe as a dynamical system governed by Laws of Nature like Newton's Law of Gravitation, for which the future could be determined if the initial conditions were known to sufficient precision. The eternal philosophical question concerned the possible coexistence of Newtonian mechanics with the idea of a *free will*. If the future was determined by the past, there would be no free will. The Newtonian view now seemed to break down if not even in such a simple system like the Lorenz system, the future was well determined from the past.

Of course, the understanding that small causes could have a large effect is present in Newtonian mechanics, the simplest example being the inverted pendulum, which is very sensitive to small perturbations in an initial top position at rest. So, in fact, there is no contradiction between Newtonian mechanics and the free will: If a small cause can have a large effect, the future is not pre-determined (as we all know), but can be influenced by something like a free will.

Summing up, there are two seemingly paradoxical phenomena, which after all are not paradoxical, but perfectly normal and understandable: (i) A dynamical system expressing simple laws may have very complex pointwise chaotic solutions. (ii) There may be some order in the chaos generated by a dynamical system expressing simple laws.

The NS equations builds on simple laws, and have pointwise chaotic unpredictable solutions, while some mean values seem to be predictable and ordered.

13.11 Algorithmic Information Theory

In algorithmic information theory one makes the distinction between the length of a computer program (list of instructions), and the length of the output of the program. A computer program for the solution of a dynamical system building on a simple law, like the NS equations, may be short, but the output in the form of a turbulent solution may be long, that is require a lot of memory to store pointwise, and thus require a lot of computational work to produce.

A chaotic system would then be a system with short instruction and long computation producing long pointwise output, from which reliable short mean value output could be obtained. A chaotic system would thus transform short input to short mean value output by passing through long pointwise output, obtained by long computation, following short instruction. Such a chaotic system requires little data and instruction but a lot of computation, which is favorable because data and instruction are both expensive in general, while computation is cheap. In contrast, a random system would require long data and/or instruction and thus would be expensive.

The basic mathematical models of mechanics and physics such as the equations by Schrödinger, Maxwell and Navier-Stokes, all combine short instruction/data with long computation, while mathematical models in biology and economics generally require long instruction/data. The “unreasonable effectiveness of mathematics in the natural sciences” according to Wigner, may be rooted in this difference.

13.12 Statistical Mechanics and Roulette

Boltzmann invented statistical mechanics in the scientific dead-lock caused by Loschmidt's Mystery of irreversibility in reversible Hamiltonian systems. Einstein in the later half of his life seriously questioned science based on microscopic games of roulette like statistical mechanics, as expressed in his famous "God does not play dice". Einstein was not stupid, but his critique was obviated by referring to senility, and statistical mechanics is today viewed as a basis of physics, including quantum mechanics with its probabilistic "Copenhagen interpretation" of the Schrödinger wave function.

However, basing mechanics on microscopic games of roulette has a very high scientific price: First, it is impossible to experimentally verify the basic assumptions of microscopic statistics, because the microscopics is not open to inspection (by definition). Secondly, the basic idea of cause-effect in science, has to be given up: the microscopic particles are supposed to "jump" randomly without any cause.

As an alternative to statistical mechanics we propose a new basis of thermodynamics which we refer to as EG2, which is a computational version of the basic laws of conservation of mass, momentum and energy, see Chapter 19. We can describe EG2 as a model with *deterministic mean-value outputs* based on *deterministic microscopics*, for which point value outputs are indeterminate. Thus in short, EG2 models output mean-value determinism coupled with output pointwise indeterminism based on microscopic determinism. EG2 thus may be viewed as a complex game of roulette in which pointwise outcomes are indeterminate but mean values are determinate.

In contrast, statistical mechanics is based on microscopic indeterminism. To simulate microscopic games of roulette it appears that one would need microscopics of microscopics, since a game of roulette necessarily is complex, which is against all logic. With this basic motivation we side up with Einstein in his skepticism of statistical mechanics (and he is not alone among famous scientists): Maybe after all, he was not senile when he so clearly expressed his doubts?

We present more aspects on statistical mechanics in Part VI of this book.

A \$1 Million Prize Problem

Leray viewed mathematics as a tool for modelling, and drew his inspiration from problems in mechanics and physics, such as fluid dynamics and wave propagation. He was fond of explaining how the road from mathematics to applications is two-way, and how a purely mathematical theorem (concerning, for instance, the existence and uniqueness of solutions of systems of partial differential equations) might have profound physical implications.
(Ivar Ekeland on Jean Leray)

Is it by accident that the deepest insight into turbulence came from Andrei Kolmogorov, a mathematician with a keen interest in the real world? (Uriel Frisch)

Some proofs command assent. Others woo and charm the intellect. They evoke delight and an overpowering desire to say, "Amen, Amen". (John William Strutt (Lord Rayleigh) 1842–1919)

14.1 The Clay Institute Impossible \$1 Million Prize

At the 2000 Millennium shift, the *Clay Mathematics Institute* presented seven \$1 million prize problems, as a reflection of the 23 problems formulated by the famous mathematician Hilbert at the second International Congress of Mathematicians in 1900 in Paris. The prize problems represent open important problems of mathematics of today.

One of the prize problems concerns the *existence, uniqueness* and *regularity* of (pointwise) solutions to the NS equations for incompressible flow, that is, precisely the equations (5.3) at focus in this book.

This *Prize Problem* has resisted the attacks of the sharpest mathematical minds for many decades. Of course, with our experience from the previous chapters, it may be natural to connect the difficulty to the presence of turbulent solutions which are not pointwise well-defined in space-time. This was pointed out by Jean Leray, who in 1934 proved the *existence of weak solutions*, or *turbulent solutions* in the terminology used by Leray, which satisfy

the NS equations in an average sense, that is with the residual tested against a suitable set of smooth test functions, as indicated above.

Proving uniqueness and regularity (which means that the solutions can be differentiated many times and satisfies the NS equations pointwise in space-time) of Leray's weak solutions, would give the \$1 million prize. But nobody has been able to come up with such a proof. Leray himself probably did not even attempt to prove uniqueness nor regularity of his weak solutions, because turbulent solutions do not seem to have these qualities.

This leads to the suspicion that the Prize Problem is simply impossible to solve: The NS equations seem to have turbulent solutions and such solutions cannot be expected to be neither pointwise uniquely defined nor regular. So it appears that this is a safe formulation of the Prize Problem for which the prize will never have to be handed out, but this was probably not the intention by the Clay Institute.

We shall see below that the Euler equations in general lack pointwise as well as weak exact solutions, but admit approximate weak solutions, which carry important information.

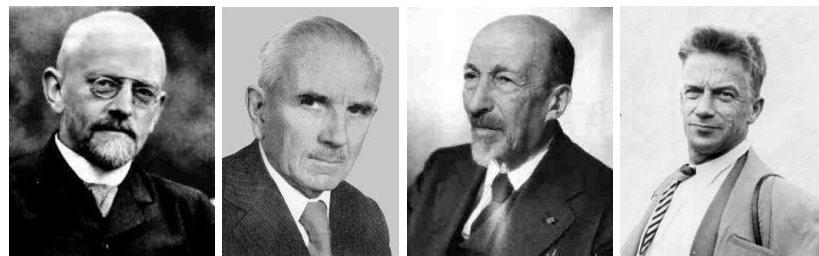


Fig. 14.1. The mathematician David Hilbert (1862–1943), Jean Leray (1906–98) who proved existence of weak solutions, Jacques Salomon Hadamard (1865–1963) who first studied well-posedness of differential equations, and Sergei Lvovich Sobolev (1908–1989) who introduced many fundamental concepts in functional analysis underlying the study of partial differential equations.

14.2 Towards a Possible Formulation

We will now suggest a new formulation of the Prize Problem, which may not be impossible to solve. In this formulation we relax the uniqueness question to uniqueness of certain mean value outputs rather than pointwise uniqueness of solutions, and we do not request a proof of regularity.

To formulate the Prize Problem in this new setting, we will be led to extend the solution concept not only to Leray's weak solutions, but further to *approximate weak solutions* in quantitative form, as already indicated above.

The basic ideas follows a standard approach in *Functional Analysis* and can be concisely expressed as follows: Writing as above the NS equations in pointwise form as $R(\hat{u}) = 0$ with $\hat{u} = (u, p)$, we view $R(\cdot)$ as a *residual* vanishing pointwise for the solution \hat{u} . In this setting we seek a *strong solution* \hat{u} which can be differentiated and thus satisfies the equation $R(\hat{u}) = 0$ pointwise in space-time.

We now first relax the requirements on \hat{u} , and define \hat{u} to be a *weak solution* if

$$((R(\hat{u}), \hat{v})) = 0,$$

for all *test functions* \hat{v} in a *test space* \hat{V} with norm $\|\cdot\|_{\hat{V}}$ consisting of suitably pointwise differentiable functions, and $R(\hat{u})$ is assumed to belong to a space dual to \hat{V} , and $((\cdot, \cdot))$ denotes a duality pairing. Effectively this means that we relax the regularity requirements on the solution \hat{u} and only ask the equation $R(\hat{u})$ to be satisfied in some average sense depending on the test space \hat{V} . Typically, $((\cdot, \cdot))$ corresponds to a L_2 inner product in space-time and $((R(\hat{u}), \hat{v}))$ is formally obtained by pointwise multiplication of $R(\hat{u})$ by the test function \hat{v} and integration in space-time. It is the integration in space-time combined with the regularity requirements put on the test functions that relaxes the strong formulation $R(\hat{u}) = 0$ to the weak formulation $((R(\hat{u}), \hat{v})) = 0$ for all $\hat{v} \in \hat{V}$.

Next we relax further and define \hat{u} to be an ϵ -*weak solution* if

$$|((R(\hat{u}), \hat{v}))| \leq \epsilon \|\hat{v}\|_{\hat{V}} \quad \forall \hat{v} \in \hat{V},$$

where ϵ is a (small) positive number. This means that for an ϵ -weak solution \hat{u} , we require the residual $R(\hat{u})$ to be smaller than ϵ in a weak norm which is dual to the strong norm of \hat{V} . Choosing $\epsilon = 0$ would then bring us back to Leray's concept of an *exact weak solution*. Note that we here do not specify precisely the space of functions where we seek the solution \hat{u} , but of course we require that \hat{u} is such that $((R(\hat{u}), \hat{v}))$ is well defined for all $\hat{v} \in \hat{V}$, or that $R(\hat{u})$ belongs to the dual space of \hat{V} .

The final step is now to choose an output quantity of interest and seek to estimate the difference in output of two ϵ -weak solutions. This will lead us to introduce a certain linearized problem and measure its stability properties by a certain stability factor S . The difference in output of two ϵ -weak solutions will then be estimated by $2\epsilon S$.

Before proceeding to present details of the new possible formulation of the Prize Problem, we connect to the concept of well-posedness according to Hadamard.

14.3 Well-Posedness According to Hadamard

The general question of uniqueness directly couples to a question about *well-posedness* of a set of differential equations, as first studied by the French mathematician Jacques Salomon Hadamard. A set of partial differential equations

(like the NS equations) is *well-posed* if small variations in data (like initial data) result in small variations in the solution (at a later time). Hadamard stated that only well-posed mathematical models could be meaningful: if very small changes in data could cause large changes in the solution, it would clearly be impossible to reach the basic requirement in science of reproducibility.

The question of well-posedness may alternatively be viewed as a question of *sensitivity to perturbations*. A problem with very strong sensitivity to perturbations would not be well-posed in the Hadamard sense. Now Hadamard proved the well-posedness of some basic partial differential equations like the Poisson equation, but he did not state any result for the NS equations.

Of course, believing that solutions to the NS equations may be turbulent, and observing the seemingly pointwise chaotic nature of turbulence, we could not expect the NS equations to be well-posed in a pointwise sense: we would expect to see a very strong pointwise sensitivity to small perturbations. But, of course it would be most natural to ask if certain mean values may be less sensitive, so that the NS equations would be well-posed in the sense of such mean values. This is what we will do. The stability factor S may then be viewed to measure the well-posedness of certain mean values in the sense of Hadamard. Surprisingly maybe, this appears to be a new concept, which one may describe as *output uniqueness of approximate weak solutions* as compared to (non-existent) pointwise uniqueness of strong solutions.

14.4 ϵ -Weak Solutions

We now define the concept of ϵ -weak solutions of the NS equations (5.3) in detail. We define for $\hat{v} = (v, q) \in \hat{V}$

$$\begin{aligned} ((R(\hat{u}), \hat{v})) &\equiv ((\dot{u}, v)) + (u(0), v(0)) + ((u \cdot \nabla u, v)) - ((\nabla \cdot v, p)) \\ &\quad + ((\nabla \cdot u, q)) + ((\nu \nabla u, \nabla v)) - (u^0, v(0)) - ((f, v)), \end{aligned} \tag{14.1}$$

where we choose

$$\hat{V} = \{\hat{v} = (v, q) \in H^1(Q)^4 : v = 0 \text{ on } \Gamma \times I\}$$

and $((\cdot, \cdot))$ is the $L_2(Q)^m$ inner product with $m = 1, 3$ (or a suitable duality pairing) over the space-time domain $Q = \Omega \times I$, and (\cdot, \cdot) is the $L_2(\Omega)^3$ inner product. Here $H^1(Q)$ denotes the Sobolev space of functions defined on Q with first order derivatives in space-time in $L_2(Q)$, and $H^1(Q)^2 = H^1(Q) \times H^1(Q)$ et cet. In order for all the terms in the definition of $((R(\hat{u}), \hat{v}))$ to be defined, we thus ask (for example) that $u \in L_2(I; H_0^1(\Omega)^3)$, $(u \cdot \nabla)u \in L_2(I; H^{-1}(\Omega)^3)$, $\dot{u} \in L_2(I; H^{-1}(\Omega)^3)$, $p \in L_2(I; L_2(\Omega))$, $f \in L_2(I; H^{-1}(\Omega)^3)$, where $H_0^1(\Omega)$ is the usual Sobolev space of vector functions being zero on the boundary Γ and square integrable together with their first order derivatives over Ω , with dual $H^{-1}(\Omega)$. As usual, $L_2(I; X)$ with X a Hilbert space denotes the

Hilbert space of functions $v : I \rightarrow X$ which are square integrable, with norm $\|v\|_{L_2(I;X)} = (\int_X \|v(t)\|_X^2)^{1/2}$.

We note that we could have chosen \hat{V} differently, asking for more or less smoothness; e.g. we may demand more smoothness and ask \hat{V} to be a subset of the Sobolev space $H^2(Q)^4$ of vector functions with square integrable second order derivatives. The choice of \hat{V} we made above fits into the G2 formulation to be given below.

We now define \hat{u} to be an ϵ -weak solution if

$$|(R(\hat{u}), \hat{v})| \leq \epsilon \|\hat{v}\|_{\hat{V}} \quad \forall \hat{v} \in \hat{V}, \quad (14.2)$$

where $\|\cdot\|_{\hat{V}}$ denotes the $H^1(Q)^4$ -norm. We may here without loss of generality put in requirements on some smoothness of \hat{u} , e.g. that $\hat{u} \in \hat{V}$, or even the more stringent requirement that $R(\hat{u}) \in L_2(Q)^4$, with $R(\hat{u})$ the residual of (5.3). This is because we use a concept of approximate weak solution, which allows us to smooth an approximate weak solution with minimal smoothness requirements to get a smooth approximate weak solution. This reflects that for any function $v \in L_2(Q)$, there is a smooth function v_ϵ (e.g. in $H^1(Q)$), such that $\|v - v_\epsilon\| \leq \epsilon$, where $\|\cdot\|$ is the $L_2(Q)$ -norm. We also note that the initial condition $u(0) = u^0$ is imposed approximately through the variational formulation (14.1).

We now finally define \hat{W}_ϵ to be the set of ϵ -weak solutions (in \hat{V}) for a given $\epsilon > 0$. Equivalently, we may say that $\hat{u} \in \hat{V}$ is an ϵ -weak solution if

$$\|R(\hat{u})\|_{\hat{V}'} \leq \epsilon,$$

where $\|\cdot\|_{\hat{V}'}$ is the dual norm of \hat{V} . This is a weak norm measuring mean values of $R(\hat{u})$ with decreasing weight as the size of the mean value decreases. Point values of $R(\hat{u})$ are thus measured very lightly. As indicated, we could go to an even weaker solution concept, for example by replacing H^1 by H^2 .

We could also alternatively define \hat{W}_ϵ to be the set of functions \hat{u} such that $((R(\hat{u}), \hat{v})) = \epsilon \|\hat{v}\|_{\hat{V}}$ for all $\hat{v} \in \hat{V}$, with $= \epsilon$, but we prefer here the first definition with $\leq \epsilon$.

Formally, we would obtain the equation

$$((R(\hat{u}), \hat{v})) = 0$$

by multiplying the NS equation by \hat{v} , that is, integrating in space-time the sum of the momentum equation multiplied by v and the incompressibility equation multiplied by q . Thus, a pointwise solution \hat{u} to the NS equations would be an ϵ -weak solution for all $\epsilon \geq 0$, while an ϵ -weak solution for $\epsilon > 0$ may be viewed as an approximate weak solution, but not as an approximate pointwise solution, because its pointwise residual may be large as well as $\|R(\hat{u})\|_{L_2(Q)}$, while $\|R(\hat{u})\|_{\hat{V}'}$ is small.

Note that we may view an ϵ -weak solution \hat{u} to be a pointwise defined solution, like a finite element solution, for which the residual $R(\hat{u})$ is small in the weak \hat{V}' -norm, but not in the $L_2(Q)$ -norm.

14.5 Existence of ϵ -Weak Solutions by Regularization

There is a great variety of so called regularized NS equations for which it is possible to prove existence of pointwise solutions using standard methods of mathematical analysis. The regularization could be imposed by a higher-order diffusion term like the biLaplacian with a small coefficient acting on the velocity, or replacing the velocity-independent Newtonian viscosity ν by a viscosity $\hat{\nu}$ depending on the norm of the velocity gradient with e.g.

$$\hat{\nu} = \nu + h^2 |\nabla u|^\alpha,$$

where $|\nabla u|^\alpha = \sum_i |\nabla u_i|^\alpha$, $\alpha \geq 1$ and h acts as a (small) scaling parameter. For such regularized NS equations it is possible to prove the existence and uniqueness of solutions (see e.g [81, 51]).

The question is then if such regularized solutions would be ϵ -weak solutions, with an ϵ tending to zero with the regularization? In general we would be able to answer this question by yes, if we just use a sufficiently weak solution concept. The easiest case to analyze is regularization with the biLaplacian, corresponding to introducing the additional viscous term $((\kappa \Delta u, \Delta v))$ in the weak form of the NS equations, where $\kappa > 0$ is a small regularization parameter. We denote the corresponding regularized solution by \hat{u}_κ , which can be proved to exist by standard methods. By a basic energy estimate, we would have that $((\kappa \Delta u_\kappa, \Delta u_\kappa)) \leq C$, where C would depend only on data. Computing $((R(\hat{u}_\kappa), \hat{v}))$ we would get by Cauchy's inequality, assuming $C = 1$ for simplicity,

$$|((R(\hat{u}_\kappa), \hat{v}))| = |((\kappa \Delta u_\kappa, \Delta v))| \leq \sqrt{\kappa} \|\hat{v}\|_{L_2(I; H^2(\Omega)^3)}$$

so that \hat{u}_κ would be an $\sqrt{\kappa}$ -weak solution with the norm of \hat{V} including the $L_2(I; H^2(\Omega)^3)$ -norm on the velocities.

Further, the original proof of Leray [79] produces a solution which is an ϵ -weak solution for $\epsilon = 0$, if we impose on \hat{V} a slightly stronger norm on the velocities than $L_2(I; H^1(\Omega)^3)$, see [79, 81].

By introducing the notion of an ϵ -weak solution to the NS equations with a suitable choice of norms on the test functions, it is thus possible to prove existence of solutions using standard methods of mathematical analysis. Below, we shall computationally construct ϵ -weak solutions using the G2 finite element method (under a certain minor assumption). In general, for a computed G2 solution \hat{U} , we can by evaluating the residual $R(\hat{U})$ determine the corresponding ϵ .

To sum up, we may say that the question of existence of ϵ -weak solutions of the NS equations is easy to settle, analytically or computationally. By relaxing the requirements on the solution we have made the existence question easy to answer positively. We now turn to the real issue.

14.6 Output Sensitivity and the Dual Problem

Suppose now the quantity of interest, or output, related to a given velocity u is a scalar quantity of the form

$$M(\hat{u}) = ((\hat{u}, \hat{\psi})), \quad (14.3)$$

where $\hat{\psi} \in L_2(Q)$ is a given weight function, which represents a mean-value in space-time. In typical applications the output could be a drag or lift coefficient in a bluff body problem. In this case the weight $\hat{\psi}$ is a piecewise constant in space-time. More generally, $\hat{\psi}$ may be a piecewise smooth function corresponding to a mean-value output.

We now seek to estimate the difference in output of two different ϵ -weak solutions $\hat{u} = (u, p)$ and $\hat{w} = (w, r)$. We thus seek to estimate a certain form of *output sensitivity* of the space \hat{W}_ϵ of ϵ -weak solutions. To this end, we introduce the following linearized dual problem of finding $\hat{\varphi} = (\varphi, \iota) \in \hat{V}$ such that

$$a(\hat{u}, \hat{w}; \hat{v}, \hat{\varphi}) = ((\hat{v}, \hat{\psi})), \quad \forall \hat{v} \in \hat{V}_0, \quad (14.4)$$

where $\hat{V}_0 = \{\hat{v} \in \hat{V} : v(\cdot, 0) = 0\}$, and

$$\begin{aligned} a(\hat{u}, \hat{w}; \hat{v}, \hat{\varphi}) &\equiv ((\dot{v}, \varphi)) + ((u \cdot \nabla v, \varphi)) + ((v \cdot \nabla w, \varphi)) \\ &\quad - ((\nabla \cdot \varphi, q)) + ((\nabla \cdot v, \iota)) + ((\nu \nabla v, \nabla \varphi)), \end{aligned}$$

with u and w acting as coefficients, and $\hat{\psi}$ is given data.

This is a linear convection-diffusion-reaction problem in variational form, with u acting as the convection coefficient and ∇w as the reaction coefficient, and the time variable runs “backwards” in time with initial value $(\varphi(\cdot, \hat{t}) = 0)$ given at final time \hat{t} imposed by the variational formulation. The reaction coefficient ∇w may be large and highly fluctuating, and the convection velocity u may also be fluctuating.

Choosing now $\hat{v} = \hat{u} - \hat{w}$ in (14.4), we obtain

$$((\hat{u}, \hat{\psi})) - ((\hat{w}, \hat{\psi})) = a(\hat{u}, \hat{w}; \hat{u} - \hat{w}, \hat{\varphi}) = ((R(\hat{u}), \hat{\varphi})) - ((R(\hat{w}), \hat{\varphi})), \quad (14.5)$$

and thus we may estimate the difference in output as follows:

$$|M(\hat{u}) - M(\hat{w})| \leq 2\epsilon \|\hat{\varphi}\|_{\hat{V}}. \quad (14.6)$$

By defining the *stability factor* $S(\hat{u}, \hat{w}; \hat{\psi}) = \|\hat{\varphi}\|_{\hat{V}}$, we can write

$$|M(\hat{u}) - M(\hat{w})| \leq 2\epsilon S(\hat{u}, \hat{w}; \hat{\psi}), \quad (14.7)$$

and by defining

$$S_\epsilon(\hat{\psi}) = \sup_{\hat{u}, \hat{w} \in \hat{W}_\epsilon} S(\hat{u}, \hat{w}; \hat{\psi}), \quad (14.8)$$

we get

$$|M(\hat{u}) - M(\hat{w})| \leq 2\epsilon S_\epsilon(\hat{\psi}), \quad (14.9)$$

which expresses output uniqueness of \hat{W}_ϵ .

Clearly, $S_\epsilon(\hat{\psi})$ is a decreasing function of ϵ and we may expect $S_\epsilon(\hat{\psi})$ to tend to a limit $S_0(\hat{\psi})$ as ϵ tends to zero. For small ϵ , we thus expect to be able to simplify (14.9) to

$$|M(\hat{u}) - M(\hat{w})| \leq 2\epsilon S_0(\hat{\psi}). \quad (14.10)$$

Depending on $\hat{\psi}$, the stability factor $S_0(\hat{\psi})$ may be small, medium, or large, reflecting different levels of output sensitivity, with $S_0(\hat{\psi})$ increasing as the mean value becomes more local. Normalizing, we may expect the output $M(\hat{u}) \sim 1$, and then one would need $2\epsilon S_0(\hat{\psi}) < 1$ in order for two ϵ -weak solutions to have a similar output.

Estimating $S_0(\hat{\psi})$ in terms of the data $\hat{\psi}$, using a standard argument based on multiplication by an integrating factor, would give a bound of the form $S_0(\hat{\psi}) \leq e^{G\hat{t}}$, where G a pointwise bound of $|\nabla w|$. In a turbulent flow with $Re = 10^6$, we may have $G \sim 10^3$, and with $\hat{t} = 10$ we would have $S_0(\hat{\psi}) \leq e^{G\hat{t}} \sim e^{10000}$, which is an incredibly large number, larger than a *googol* = 10^{100} . It would be inconceivable to have $\epsilon < 10^{-100}$ and thus the output of an ϵ -weak solution would not seem to be well defined.

However, computing the dual solution corresponding to drag and lift coefficients in turbulent flow at $Re = 10^6$, we find values of $S_0(\hat{\psi})$ which are much smaller, in the range $S_0(\hat{\psi}) \approx 10^3$, for which it is possible to choose ϵ so that $2\epsilon S_0(\hat{\psi}) < 1$, with the corresponding outputs thus being well defined (up to a certain tolerance). We attribute the fact that $\hat{\phi}$ and derivatives thereof are not exponentially large, to cancellation effects from the oscillating reaction coefficient ∇w . We shall study this aspect in model form more closely below. However, the cancellation effects seem to be impossible to account for by analytical methods, because (i) knowledge of the underlying flow velocity u is necessary and (ii) the flow velocity has a complexity defying analytical description. The only way to get this knowledge is to compute the velocity, and introducing computation, we may as well compute the dual solution to get a computational hopefully reasonably accurate estimate of $S_0(\hat{\psi})$, instead of using a worst case estimate of no value at all. In practice, there is a lower limit for ϵ , typically given by the maximal computational cost, and thus $S_0(\hat{\psi})$ effectively determines the computability of different outputs.

Note that we may view W_ϵ to be a set of *possible (ϵ -weak) solutions* sharing a similar output up to the corresponding stability factor.

14.7 Reformulation of the Prize Problem

We now consider a couple of different possible alternative formulations of the Prize Problem. One could simply be our formulations (P) or (P1) from Chapter 1. It seems that these problems could only be answered on a case by

case basis, so the Prize would have to be reformulated as a collection of say 1000 \$1000 prizes, one for each case. In this book we cover a certain number of these cases of key interest in applications.

We may compare with the following purely qualitative formulation which could fit into a tradition of “pure” mathematics dealing with exact solutions:

- (P2) What outputs of Leray’s weak solutions are unique?

In this book we present evidence indicating that (P2) is impossible to answer, because of its purely qualitative nature. Instead we propose the quantitative formulation (P1) involving approximate weak solutions. We could also formulate this problem as a problem of stability or sensitivity as follows:

- (P3) Determine output sensitivity of ϵ -weak solutions with $\epsilon > 0$, that is, estimate the stability factor $S_\epsilon(\hat{\psi})$ for $\epsilon > 0$ for different flows and different outputs (and different norms for the test functions).

We have seen above that the difference in output given by a function $\hat{\psi}$ of two ϵ -weak solutions is at most $2\epsilon S_\epsilon(\hat{\psi})$, which reflects the output sensitivity in quantitative form. We may thus answer (P1) by answering (P3). One may refer to (P3) as a question of *weak uniqueness* as a short for *output sensitivity of approximate weak solutions*.

We remind the reader again that a Leray weak solution corresponds to a ϵ -weak solution with $\epsilon = 0$. If $S_0(\hat{\psi}) < \infty$, one could in purely qualitative form argue that $\epsilon S_\epsilon(\hat{\psi}) = 0$ for $\epsilon = 0$, and output uniqueness of Leray solutions would follow. However, as we said above, if $S_0(\hat{\psi})$ is very large, this conclusion could be misleading, because multiplication of 0 by ∞ is ill defined. We thus would conclude that (P2) may not be a mathematically sound formulation, while the quantitative version (P3) should be.

In this book we thus only consider ϵ -weak solutions with $\epsilon > 0$. In fact the concept of an 0-weak solution does not make much sense, since already a weak solution is some kind of approximate solution in the pointwise sense. We may then as well choose $\epsilon > 0$, and refrain from the possibly “pathological” case $\epsilon = 0$!

In this book we address (P1), or (P3), using adaptive finite element methods with a posteriori error estimation. As indicated above the a posteriori error estimate results from an *error representation* expressing the output error as a space-time integral of the *residual* of a computed solution multiplied by *weights* which relate to derivatives of the solution of an associated *dual problem*. The weights express *sensitivity* of a certain output with respect to the residual of a computed solution, and their size determine the degree of computability of a certain output: The larger the weights are, the smaller the residual has to be and the more work is required. In general the weights increase as the size of the mean value in the output decreases, indicating increasing computational cost for more local quantities. The stability factor $S_0(\hat{\psi})$ is a certain space-time norm of the weights, and gives a scalar measure of the output sensitivity.

In the next chapter we present computational evidence in a bluff body problem that the drag coefficient c_D , which is a mean value in time of the drag force, is computable to a reasonable tolerance at a reasonable computational cost affordable on a PC, while the value of the drag force at a specific point in time appears to be uncomputable even at a very high computational cost.

14.8 The Standard Approach to Uniqueness

The standard approach to uniqueness of NS solutions goes as follows: Suppose \hat{u} and \hat{w} are two classical pointwise solutions to the NS equations (5.3). Subtracting the two versions of the NS equations, we obtain the following equation for the difference $\hat{v} = (v, q) = \hat{u} - \hat{w}$:

$$\begin{aligned}\dot{v} + (u \cdot \nabla)v + (v \cdot \nabla)w - \nu\Delta v + \nabla q &= 0 && \text{in } \Omega \times I, \\ \nabla \cdot v &= 0 && \text{in } \Omega \times I, \\ v &= 0 && \text{on } \Gamma \times I, \\ v(\cdot, 0) &= u^0 - w^0 && \text{in } \Omega,\end{aligned}\quad (14.11)$$

Multiplying the momentum equation by v and integrating, we obtain for $t \in I$

$$\frac{1}{2} \frac{d}{dt} \|v(\cdot, t)\|^2 + \nu \|\nabla v(\cdot, t)\|^2 = -((v \cdot \nabla)w, v), \quad (14.12)$$

where (\cdot, \cdot) and $\|\cdot\|$ denote the scalar product and norm in $L_2(\Omega)^m$ for $m = 1, 3$, and we used the fact that since $\nabla \cdot u = 0$, we have $((u \cdot \nabla)v, v) = 0$. Estimating the right hand side by $G\|v\|^2$, where G as above is a pointwise bound for ∇w , we obtain the following standard stability estimate:

$$\|v(\cdot, \hat{t})\| \leq \exp(G\hat{t}) \|u^0 - w^0\|.$$

We noted above that this estimate is void of content from any practical point of view if G is large. Now, intense efforts over many years have been made to come up with alternative stability estimates involving only bounds on w and not ∇w . This is possible using various *Sobolev estimates* as e.g in [81], but will involve moving the derivative in $((v \cdot \nabla)w, v)$ instead to v and then require using the ν -term in (14.12) in a stability estimate, and thus bring in an exponential factor with exponent depending on negative powers of ν , which again will be very large for high Reynolds numbers corresponding to small ν .

There is a classical type uniqueness result of this form stating uniqueness if $w \in L_q(I; L_p(\Omega))$ with $\frac{3}{p} + \frac{2}{q} = 1$ [81]. Since one can actually guarantee that $w \in L_q(I; L_p(\Omega))$ with $\frac{3}{p} + \frac{2}{q} = \frac{3}{2}$, it would seem that uniqueness would lie around the corner, but again the presence of a very large exponential factor means that this is only an illusion.

The net result seems to be that any conceivable stability estimate of classical type based on norm estimation of the crucial term $((v \cdot \nabla)w, v)$, which does not use the oscillating character of the reaction coefficient ∇w , would necessarily involve very large stability factors and would thus be of no real value, according to our point of view.

Weak Uniqueness by Computation

There's no sense in being precise when you don't even know what you're talking about. (John von Neumann)

Ces relations se déduisent d'ailleurs des équations de Navier–Stokes à l'aide d'intégration par parties...j'ai pu démontrer le suivant: les relations en question possèdent toujours *au moins une solution*...Peut-être cette solution est-elle trop peu régulière pour posséder à tout instant des dérivées secondes bornées; alors elle n'est pas, au sens propre du terme, une solution des équations de Navier–Stokes; je propose de dire qu'elle en constitue "*une solution turbulente*" (Leray 1934).

15.1 Introduction

To compute approximations of a stability factor $S_\epsilon(\hat{\psi})$ defined by two ϵ -weak solutions \hat{u} and \hat{w} approximately, we replace both \hat{u} and \hat{w} as coefficients in the dual problem by a computed ϵ -weak solution \hat{U} , such as a finite element solution, and then compute an approximate dual velocity $\hat{\varphi}_h$ to get $S_\epsilon(\hat{\psi}) \approx S_h(\hat{U}; \hat{\psi}) \equiv \|\hat{\varphi}_h\|_{\hat{V}}$. We may then study $S_h(\hat{U}; \hat{\psi})$ as we refine the mesh size h , and we may extrapolate to $h = \nu$ to get an approximation of $S_0(\hat{\psi})$, assuming that $h = \nu$ would correspond to a small ϵ . If the extrapolated value is not too large, then we would have evidence of output uniqueness, and if the extrapolated value is very large, we would get indication of output non-uniqueness. As a crude test of largeness it may be natural to use $S_0(\hat{\psi}) >> \nu^{-1/2}$.

If the output is a mean value, then $\|\hat{\varphi}_h\|_{\hat{V}}$ will typically grow slowly with decreasing h . We may take this slow growth as evidence that it is possible to replace both \hat{u} and \hat{w} by \hat{U} in the computation of the solution of the dual problem: a near constancy indicates a desired robustness to (possibly large) perturbations of the coefficients \hat{u} and \hat{w} .

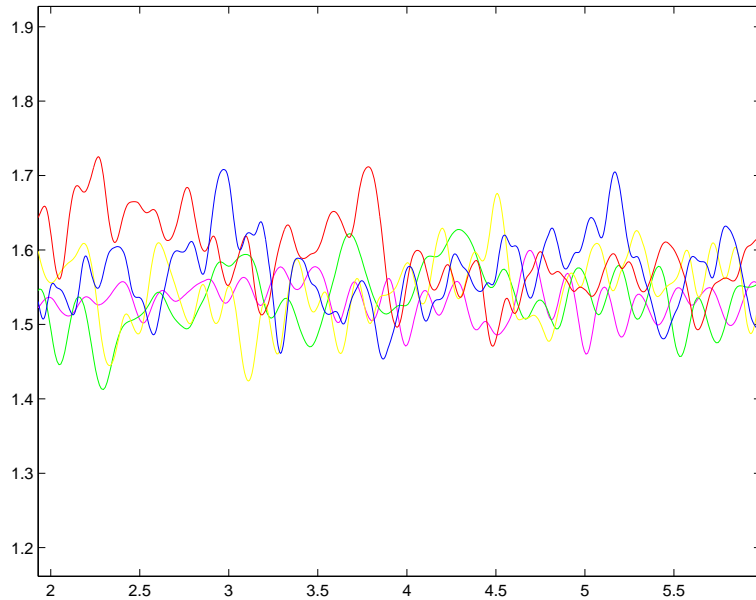


Fig. 15.1. Drag $D(t)$ (normalized) for a surface mounted cube, as a function of time, for 5 computational meshes.

15.2 Uniqueness of c_D and c_L

The computational example is a bluff body benchmark problem, which is presented in more detail in Chapter 33. We compute the mean value in time of drag and lift forces on a surface mounted cube in a rectangular channel, from an incompressible fluid governed by the NS equations (5.3), at $Re = 40\,000$ based on the cube side length and the bulk inflow velocity. We compute the mean values over a time interval of a length corresponding to 40 cube side lengths, which we take as approximations of c_D and c_L defined as (normalized) mean values over very long time.

The incoming flow is laminar time-independent with horse-shoe vortex upstream the cube and a laminar boundary layer on the front surface of the body, which separates and develops a turbulent time-dependent wake attaching to the rear of the body. The flow is thus very complex with a combination of laminar and turbulent features including boundary layers and a large turbulent wake, see Figure 15.2.

The dual problem corresponding to c_D has boundary data of unit size for φ_h on the cube in the direction of the mean flow, acting on the time interval underlying the mean value, and zero boundary data elsewhere. A snapshot of the dual solution corresponding to c_D is shown in Figure 15.3, and in Figure 15.4 we plot $S_h(\hat{U}; \hat{\psi})$ as a function of h^{-1} for a range of adaptively

refined computational meshes, with h the smallest element diameter in the mesh.

We find that $S_h(\hat{U}; \hat{\psi})$ shows a slow logarithmic growth, and extrapolating we find that $S_\nu(\hat{U}; \hat{\psi}) \sim \nu^{-1/2}$. We take this as evidence of computability and weak uniqueness of c_D , and we obtain similar results for the lift coefficient c_L .

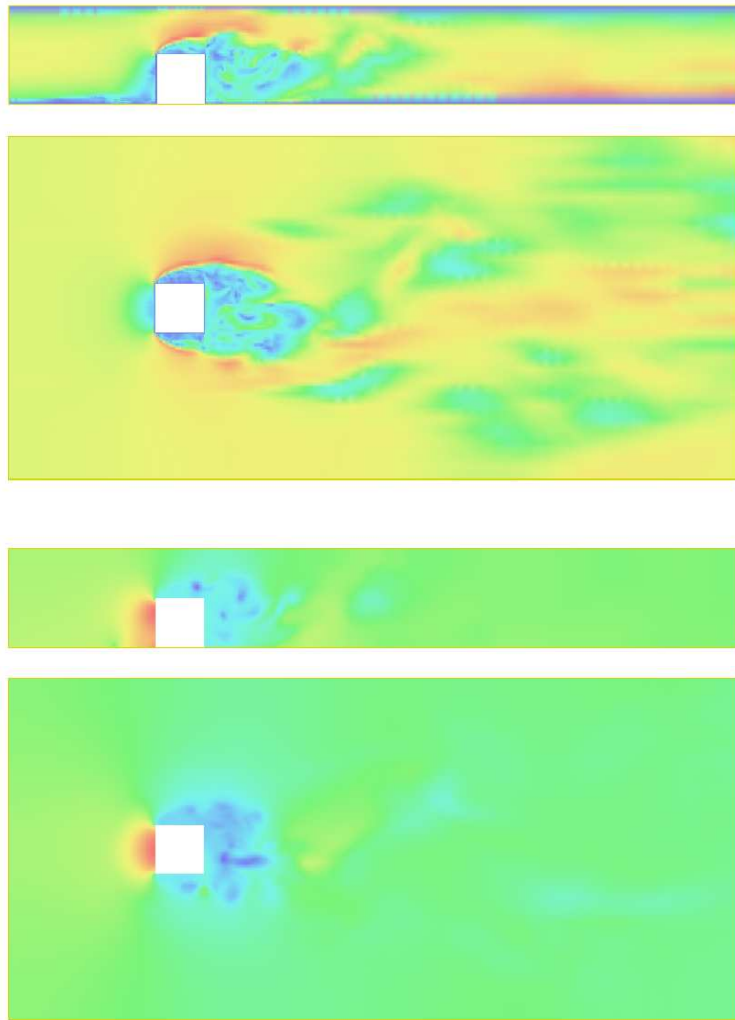


Fig. 15.2. Surface mounted cube: velocity $|U|$ (upper) and pressure P (lower), in the x_1x_2 -plane at $x_3 = 3.5H$ and in the x_1x_3 -plane at $x_2 = 0.5H$.

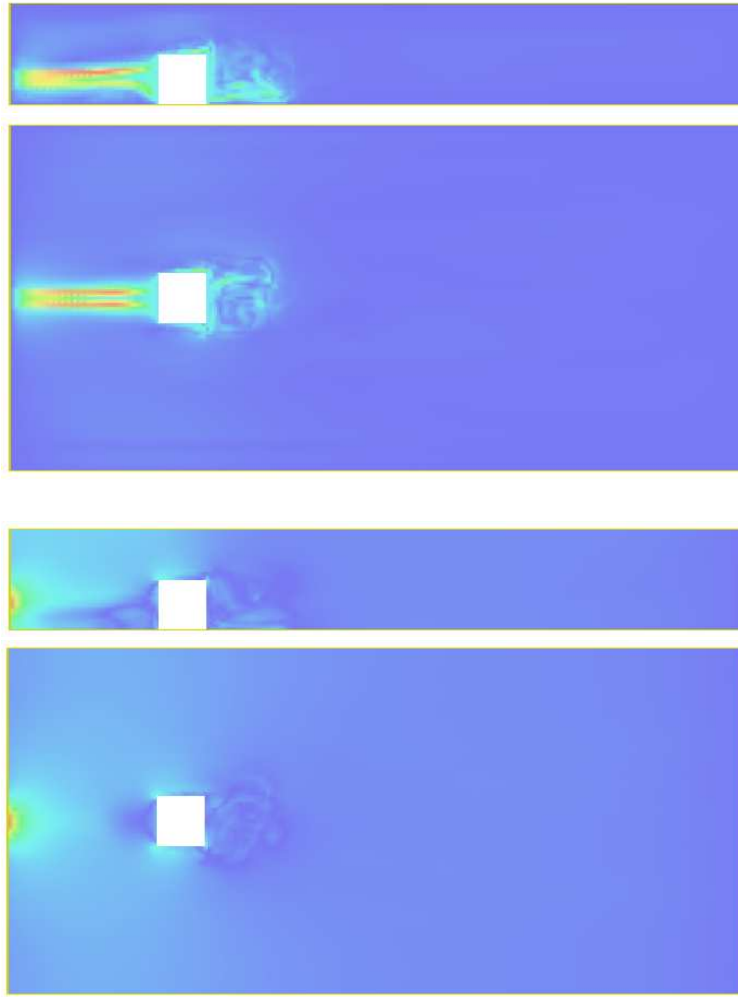


Fig. 15.3. Surface mounted cube: dual velocity $|\varphi_h|$ (upper), and dual pressure $|\iota_h|$ (middle), in the x_1x_2 -plane at $x_3 = 3.5H$ and in the x_1x_3 -plane at $x_2 = 0.5H$.

15.3 Non-Uniqueness of $D(t)$

We now investigate the computability and weak uniqueness of the normalized drag force $D(t)$ at a specific time t . In Figure 15.1 we show the variation in time of $D(t)$ computed on different meshes, and we notice that $D(t)$ for a given t does not appear to converge with decreasing h : The best we can say seems to be that $1.3 \leq D(t) \leq 1.7$.

We now choose one of the finer meshes corresponding to $h^{-1} \approx 500$, and we compute the dual solution corresponding to a mean value of $D(t)$ over a

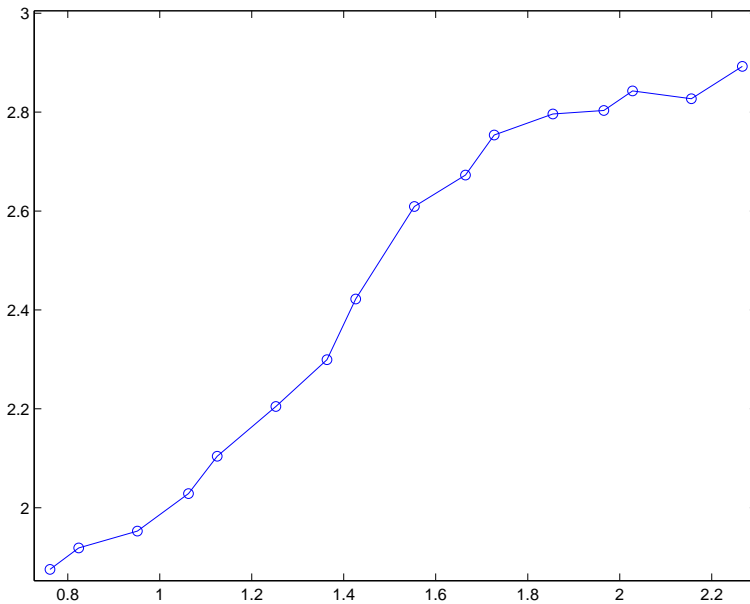


Fig. 15.4. \log_{10} - \log_{10} -plot of $S_h(\hat{U}; \hat{\psi})$ as a function of $1/h$.

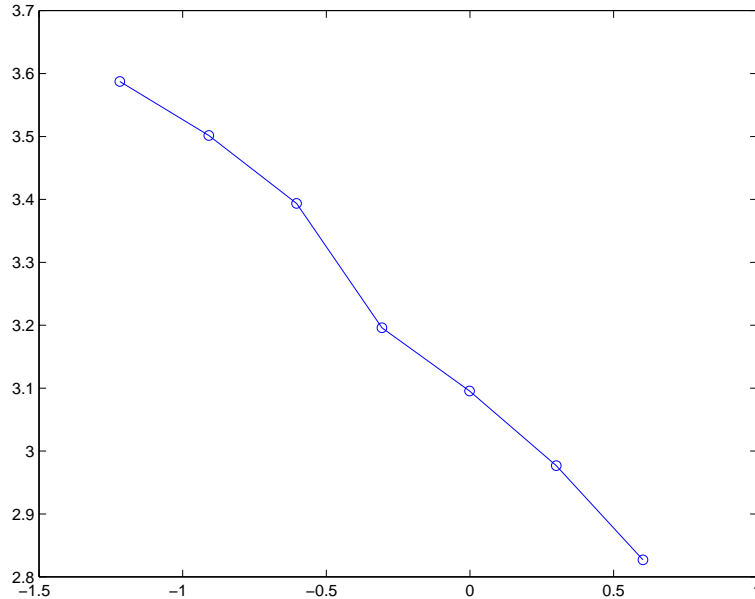


Fig. 15.5. $S_h(\hat{U}; \hat{\psi})$ corresponding to computation of the mean drag force (normalized) over a time interval $[\hat{t}_0, \hat{t}]$, as a function of the interval length $|\hat{t} - \hat{t}_0|$ (\log_{10} - \log_{10} -plot).

time interval $[\hat{t}_0, \hat{t}]$, where we let $\hat{t}_0 \rightarrow \hat{t}$. We thus seek to compute the point value $D(\hat{t})$.

In Figure 15.5 we find a growth of $S_h(\hat{U}; \hat{\psi})$ similar to $|\hat{t} - \hat{t}_0|^{-1/2}$, as we let $\hat{t}_0 \rightarrow \hat{t}$. The results show that for $|\hat{t} - \hat{t}_0| = 1/16$ we have $S_h(\hat{U}; \hat{\psi}) \approx 10\nu^{-1}$, and extrapolation of the computational results indicate further growth of $\tilde{S}_0(\hat{\psi})$, as $\hat{t}_0 \rightarrow \hat{t}$ and $h \rightarrow \nu$. We take this as evidence of non-computability and weak non-uniqueness of $D(\hat{t})$.

15.4 Stability of the Dual Solution with Respect to Time Sampling

To get an idea of the dependence of stability factors on the primal solution \hat{U} used to compute the dual solution, we sample the coefficients in the dual problem with different frequencies in time and compute the corresponding dual solutions. In Table 5.1 we display different norms of the dual solution $\hat{\varphi}_h$ and notice that different sampling frequencies give very similar stability factors, and in Fig. 15.6 we plot snapshots of different dual solutions, again very similar.

freq.	$\ \varphi_h\ $	$\ \nabla \varphi_h\ $	$\ \hat{\varphi}_h\ _{\hat{V}}$
8	7.99	646	652
4	8.04	658	663
4*	8.14	679	684
2	8.23	693	698
1	8.35	744	749

Table 15.1. Surface mounted cube: Norms of the dual solution φ_h linearized at a primal velocity U sampled with different frequencies (normalized by the inflow velocity $U_\infty = 1$), with “4*” being a translated sampling of “4” with the same frequency.

15.5 Conclusion

We have given computational evidence of weak uniqueness of mean values such as c_D and c_L and weak non-uniqueness of a momentary value $D(t)$ of the total drag. In the computations we observe this phenomenon as a continuous degradation of computability (increasing stability factor $S_0(\hat{\psi})$) as the length of the time interval underlying the mean value decreases to zero. Effectively we seem to be able to compute c_D and c_L up to a tolerance of roughly 0.05 taking mean values in time of length 10, while the variation of a momentary value $D(t)$ may be almost a factor 10 larger. Thus the distinction

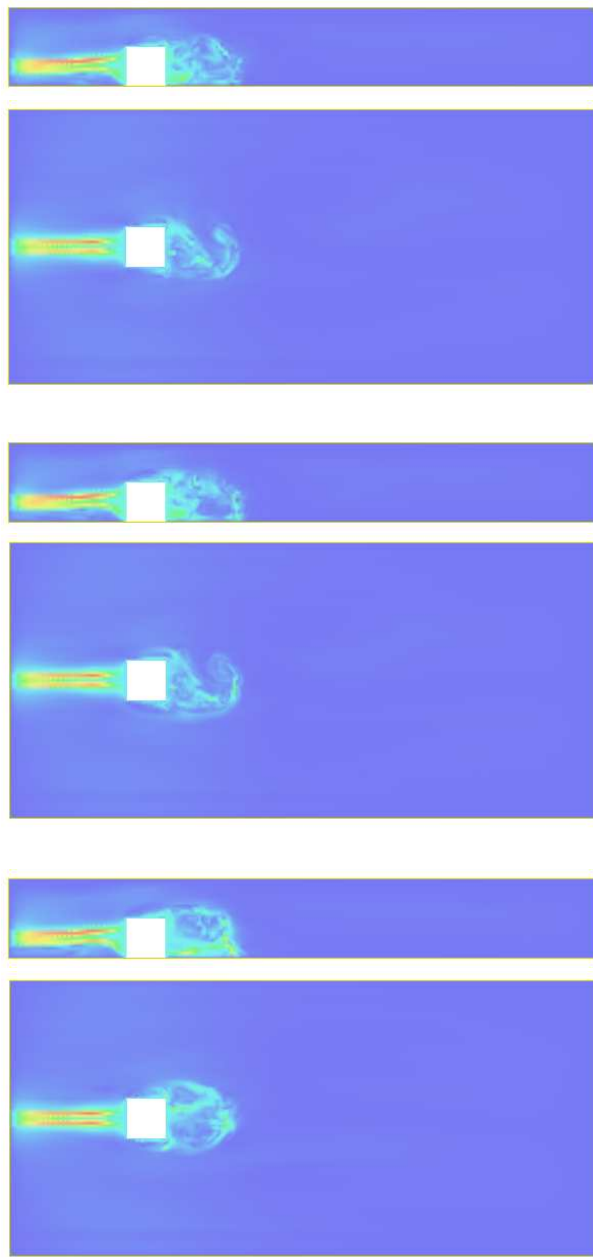


Fig. 15.6. Surface mounted cube: snapshots of the dual velocity $|\varphi_h|$ sampled 4 times per time unit (upper), 2 times per time unit (middle), and once per time unit (lower), corresponding to “4”, “2”, and “1”, in Table 15.1, in the x_1x_2 -plane at $x_3 = 3.5H$ and in the x_1x_3 -plane at $x_2 = 0.5H$.

between computability (or weak uniqueness) and non-computability (weak non-uniqueness) may in practice be just one order of magnitude in output error, rather than a difference between 0 and 1 (or ∞).

Of course, this is what you may expect to see in a quantified computational world, as compared to an ideal mathematical world. In particular, we are led to measure residuals of approximate weak solutions, rather than working with the exact weak solutions of Leray with zero residuals. A such quantified mathematical world is in fact richer than an ideal zero residual world, and thus may be more accessible.

Existence of ϵ -Weak Solutions by G2

One may be tempted to believe that physical laminar flows correspond to smooth mathematical solutions (of the Navier–Stokes equations) and turbulent flows to non-smooth solutions (Oseen in Hydrodynamik ...).

On peut vérifier en outre que l'énergie cinétique totale du liquide reste bornée; mais il ne semble pas possible de déduire de ce fait que le mouvement lui-même reste régulier; j'ai même indiqué une raison qui me fait croire à l'existence de mouvements devenant irréguliers au bout d'un temps fini; je n'ai malheureusement pas réussi à forger un exemple d'une telle singularité (Leray 1934).

We will now discuss in a little more detail the Struggle for Existence.(Darwin)

16.1 Introduction

We now show that we may construct ϵ -weak solutions of the NS equations using stabilized Galerkin finite element methods in the form of G2. We do this in order to highlight a basic property of a G2 solution, which is designed so as to have a small residual in a weak sense, and thus may pass as an ϵ -weak solution for a certain ϵ depending on the mesh size. We do not here give full details of the formulation of G2, e.g. concerning the use of continuous or discontinuous Galerkin for the time stepping, but focus on the basic role of the stabilization in G2, and give a complete description of G2 in Chapter 28.

In the discussion of the Clay Prize Problem we commented that an alternative way of proving existence of ϵ -weak solutions is to first prove existence for suitably regularized NS equations, which is possible using standard methods of mathematical analysis, and to then prove that a regularized solution passes as an ϵ -weak solution for some ϵ depending on the regularization, which tends to zero with the regularization.

16.2 The Basic Energy Estimate for the Navier–Stokes Equations

We start by deriving a basic stability estimate of energy type for the velocity u of the NS equations (5.3), assuming for simplicity that $f = 0$. This is about the only analytical a priori estimate known for the NS equations. We thus formally assume existence of a (pointwise) solution (u, p) , and derive a bound for the velocity u in terms of given data.

Scalar multiplication of the momentum equation by u and integration with respect to x gives

$$\frac{1}{2} \frac{d}{dt} \int_{\Omega} |u|^2 dx + \nu \sum_{i=1}^3 \int_{\Omega} |\nabla u_i|^2 dx = 0,$$

because by partial integration (with boundary terms vanishing),

$$\int_{\Omega} \nabla p \cdot u dx = - \int_{\Omega} p \nabla \cdot u dx = 0$$

and

$$\int_{\Omega} (u \cdot \nabla) u \cdot u dx = - \int_{\Omega} (u \cdot \nabla) u \cdot u dx - \int_{\Omega} \nabla \cdot u |u|^2 dx$$

so that

$$\int_{\Omega} (u \cdot \nabla) u \cdot u dx = 0. \quad (16.1)$$

Integrating next with respect to time, we obtain the following basic a priori stability estimate for $\hat{t} > 0$ in terms of the L_2 -norm of the initial velocity u^0 :

$$E_{\nu}(u) \equiv \frac{1}{2} \|u(\cdot, \hat{t})\|^2 + D_{\nu}(u, \hat{t}) = \frac{1}{2} \|u^0\|^2, \quad (16.2)$$

where

$$D_{\nu}(u, \hat{t}) = \nu \sum_{i=1}^3 \int_0^{\hat{t}} \|\nabla u_i\|^2 dt,$$

and where $\|\cdot\|$ denotes the $L_2(\Omega)$ -norm. This estimate gives a bound on the kinetic energy of the velocity with $D_{\nu}(u, \hat{t})$ representing the total *dissipation* from the viscosity of the fluid over the time interval $[0, \hat{t}]$. We see that the growth of this term with time corresponds to a decrease of the velocity (momentum) of the flow (with $f = 0$).

The characteristic feature of a turbulent flow is that $D_{\nu}(u, \hat{t})$ is comparatively large, while in a laminar flow with ν small, $D_{\nu}(u, \hat{t})$ is small. With $D_{\nu}(u, \hat{t}) \sim 1$ in a turbulent flow and $|\nabla u|$ uniformly distributed, we may expect to have pointwise

$$|\nabla u_i| \sim \nu^{-1/2}. \quad (16.3)$$

16.3 Existence by G2

To generate approximate weak solutions of the NS equations, we use a finite element method of the form (assuming for simplicity $f = 0$): Find $\hat{U} \equiv \hat{U}_h \in \hat{V}_h$, where $\hat{V}_h \subset \hat{V}$ is a finite dimensional subspace of piecewise polynomial functions defined on a computational mesh in space-time of mesh size h , such that

$$((R(\hat{U}), \hat{v})) + ((hR(\hat{U}), R(\hat{v}))) = 0, \quad \forall \hat{v} \in \hat{V}_h, \quad (16.4)$$

where $R(\hat{w}) \equiv (R_1(\hat{w}), R_2(w))$, $\hat{w} = (w, r)$ and

$$\begin{aligned} R_1(\hat{w}) &= \dot{w} + U \cdot \nabla w + \nabla r - \nu \Delta w, \\ R_2(w) &= \nabla \cdot w, \end{aligned} \quad (16.5)$$

with element-wise definition of second order terms. We here interpret a convection term $((U \cdot \nabla w, v))$ as

$$\frac{1}{2}((U \cdot \nabla w, v)) - \frac{1}{2}((U \cdot \nabla v, w))$$

which is literally true if $\nabla \cdot U = 0$. With this interpretation we will have $((U \cdot \nabla U, U)) = 0$, which corresponds to (16.1), even if the divergence of the finite element velocity U does not vanish exactly. With this interpretation we obtain choosing $\hat{v} = \hat{U}$ in (16.4) (still assuming $f = 0$):

$$E_\nu(U) + ((hR(\hat{U}), R(\hat{U}))) = \frac{1}{2} \|u^0\|^2. \quad (16.6)$$



Fig. 16.1. Richard Courant (1888–1972) introduced the finite element method in 1922, in an existence proof of a version of the Riemann mapping theorem. Boris Grigorievich Galerkin (1871–1945), Russian engineer who introduced the finite element method as a computational tool.

The finite element method (16.4) is a stabilized Galerkin method with the term $((R(\hat{U}), v))$ corresponding to Galerkin's method and the term

$((hR(\hat{u}), R(\hat{v})))$ corresponding to a weighted residual least squares method with stabilizing effect expressed in (16.6). We also refer to this method as *General Galerkin* or *G2*, and we thus refer to \hat{U} as a *G2-solution*. The existence of a discrete solution $\hat{U} \equiv \hat{U}_h \in V_h$ follows by Brouwer's fixed point theorem combined with the stability estimate (16.6).

We now return to the main objective of this chapter of showing the existence of ϵ -weak solutions to the NS equations. For all $\hat{v} \in \hat{V}$, we have with $\hat{v}^h \in \hat{V}_h$ a standard interpolant of v satisfying $\|h^{-1}(\hat{v} - \hat{v}^h)\| \leq C_i \|\hat{v}\|_{\hat{V}}$, using also (16.4),

$$\begin{aligned} ((R(\hat{U}), \hat{v})) &= ((R(\hat{U}), \hat{v} - \hat{v}^h)) - ((hR(\hat{U}), R(\hat{v}^h))) \\ &\leq C_i \|hR(\hat{U})\| \|\hat{v}\|_{\hat{V}} + M(U) \|hR(\hat{U})\| \|\hat{v}\|_{\hat{V}}, \end{aligned} \quad (16.7)$$

where $M(U)$ is a pointwise bound of the velocity $U(x, t)$, and $C_i \approx 1$ is an interpolation constant. It follows that the G2-solution \hat{U} is an ϵ -weak solution with

$$\epsilon = (C_i + M(U)) \|hR(\hat{U})\| \leq \sqrt{h}(C_i + M(U)) \|u^0\|,$$

since from the energy stability estimate $\|\sqrt{h}R(\hat{U})\| \leq \|u^0\|$.

Assuming now that $M(U) = M(U_h)$ is bounded with $h > 0$, and letting $C_i + M(U) \leq C$, it follows that \hat{U} is an ϵ -weak solution with $\epsilon = C\sqrt{h}$, assuming $\|u^0\| \leq 1$. More generally, we may say that a G2 solution \hat{U} is an ϵ -weak solution with $\epsilon = C\|hR(\hat{U})\|$.

We have now demonstrated the existence of an ϵ -weak solution to the NS equations for any ϵ , assuming that the maximum computed velocity is bounded (or grows slower than $h^{-1/2}$). More generally, we have shown that a G2-solution \hat{U} is an ϵ -weak solution with $\epsilon = C_U \|hR(\hat{U})\|$ with $C_U = C_i + M(U)$. Computing \hat{U} , we can compute $\epsilon = C_U \|hR(\hat{U})\|$ and thus determine the corresponding ϵ .

We conclude that coming up with ϵ -weak solutions to the NS equations is easy, if we use G2 and a computer (and find that C_U grows slower than $h^{-1/2}$).

We now turn to the question of estimation of the error in output of G2-solutions, which of course as above will bring in the corresponding stability factor.

Remark. In estimating above $((R(\hat{U}), \hat{v} - \hat{v}^h))$ we did not properly account for the diffusion term $((\nu \nabla U, \nabla(v - v^h)))$. Doing so would introduce an additional term which most easily can be estimated by a term of the form $C\sqrt{\nu} \|\hat{v}\|_{\hat{V}}$, and to bound this term as above we would need that $\nu \leq h$. Since ν often is smaller than 10^{-4} for the problems we focus on in this book, this would not be restrictive in most cases. For larger ν we can turn the argument around in a different way, but we do not here enter into details.

16.4 A Posteriori Output Error Estimate for G2

We now let \hat{u} be an ϵ -weak solution of the NS equations and let \hat{U} be a G2-solution, which we just showed can be viewed to be an ϵ_{G2} -weak solution, with $\epsilon_{G2} = C_U \|hR(\hat{U})\| >> \epsilon$.

As above we get the following a posteriori error estimate for a mean-value output given by a function $\hat{\psi}$:

$$|M(\hat{u}) - M(\hat{U})| \leq (\epsilon + C_U \|hR(\hat{U})\|) S_{\epsilon_{G2}}(\hat{\psi}), \quad (16.8)$$

where $S_{\epsilon_{G2}}(\hat{\psi})$ is the corresponding stability factor defined as above. Obviously the size of the stability factor $S_{\epsilon_{G2}}(\hat{\psi})$ is crucial for computability: the stopping criterion is evidently (assuming ϵ small):

$$C_U \|hR(\hat{U})\| S_{\epsilon_{G2}}(\hat{\psi}) \leq TOL,$$

where $TOL > 0$ is a tolerance. If $S_{\epsilon_{G2}}(\hat{\psi})$ is too large, or TOL is too small, then we may not be able to reach the stopping criterion with available computing power, and the computability is out of reach.

Stability Aspects of Turbulence in Model Problems

Merkwürdig ist auch das Versagen der Eindeutigkeitsbeweise in drei Dimensionen. Diese Fragen sind immer noch nicht befriedigend erklärt. Es ist schwer zu glauben daß die Anfangswertaufgabe zäher Flüssigkeiten für $n = 3$ mehr als eine Lösung haben könnte, und der Erledigung der Eindeutigkeitsfrage sollte mehr Aufmerksamkeit geschenkt werden. (E. Hopf)

17.1 The Linearized Dual Problem

We have seen that the predictability/computability of a given flow (solution $\hat{u} = (u, p)$ of the NS equations) is determined by the stability properties of the corresponding linearized dual problem. We may thus say that the secret of computational modeling of turbulent flow is hidden in the stability properties of the dual problem, which takes the following form when linearized around the given velocity u , if we for simplicity leave out the pressure part of the dual solution: Given ψ find φ such that

$$-\dot{\varphi} - u \cdot \nabla \varphi + \nabla u^\top \varphi - \nu \Delta \varphi = \psi \quad \text{on } [0, \hat{t}], \quad \varphi(\hat{t}) = 0,$$

where $(\nabla u^\top \varphi)_j = \sum_{i=1}^3 u_{i,j} \varphi_i$. This is a linear convection-diffusion-reaction problem with convection velocity u and reaction coefficient matrix ∇u and data ψ . We are interested in the stability properties of the dual problem which concern the size of the stability factor $S = \|\varphi\|/\|\psi\|$ where $\|\cdot\|$ represent some norms, usually different, for φ and ψ . The stability factor S expresses the sensitivity of an output related to ψ .

We now seek to estimate the size of the stability factor S for different data ψ corresponding to different outputs. We seek qualitative understanding and are thus ready to simplify. In reality, of course we just compute the stability factor S and we do not need to understand anything, but we here seek some rationale behind the computed values for S .

We then assume that the norm of $\|\varphi\|$, which typically involves derivatives of φ , can be reflected through the size of φ itself through the coupling to

the viscous term in the dual equation. Effectively, we may then leave out the viscous term. Further, we note that the size of the dual solution φ does not seem to be much affected by the convection, since convection only shifts φ in space but does not change its size. In contrast, the reaction term with coefficient ∇u^\top obviously may change the size of φ , and thus may affect the size of S . We thus focus on the stability properties of the reaction problem:

$$-\dot{\varphi} + A\varphi = \psi \quad \text{on } [0, \hat{t}], \quad \varphi(\hat{t}) = 0,$$

where the matrix $A = \nabla u^\top$ depends on (x, t) . We are interested in the size of the dual solution φ for different ψ . In a turbulent flow A may have large coefficients which may change rapidly with (x, t) . In general we may expect that the growth properties of φ connect to the spectrum of A with exponential growth corresponding to eigenvalues with negative real part, exponential decay to eigenvalues with positive real part, and oscillations corresponding to the imaginary part of conjugate pairs of eigenvalues.

Let us now freeze x and let $\lambda_i(t)$, $i = 1, 2, 3$, be the eigenvalues of $A(x, t)$. By (approximate) incompressibility of u and the fact that the sum of the eigenvalues of a matrix is equal to the sum of its diagonal elements, we have that

$$\sum_{i=1}^3 \text{Real part}(\lambda_i) \approx 0,$$

see Fig. 17.1, and thus we may expect that the exponential growth and decay from the real parts of the eigenvalues will balance with no net growth, if we let φ convect over different x with the convection velocity u .

It remains to understand the possible effect of the oscillating nature coupled to the imaginary part of the conjugate eigenvalues. We shall see that this connects to the observation that stability factors decrease as the length of the mean values in time increases, which we could address to cancellation in integrals of oscillating functions. We first present a model case with a pair of conjugate imaginary eigenvalues, in which case the dual problem for each x is just the harmonic oscillator.

17.2 Rotating Flow

We consider a flow corresponding to one rotating vortex tube oriented in the x_3 -direction given by the stationary flow $\hat{u} = (u, p)$ such that

$$u(x) = \omega(-x_2, x_1, 0), \quad p = \frac{\omega}{2}(x_1^2 + x_2^2),$$

which satisfies the NS equations with $\nu = 0$ and $f = 0$, see Fig. 17.2. Here ω is a moderately large positive number which represents the angular rotational velocity of the vortex tube. We may think of the vortex tube having a diameter $1/\omega$, and we may, very loosely speaking, think of a turbulent flow as

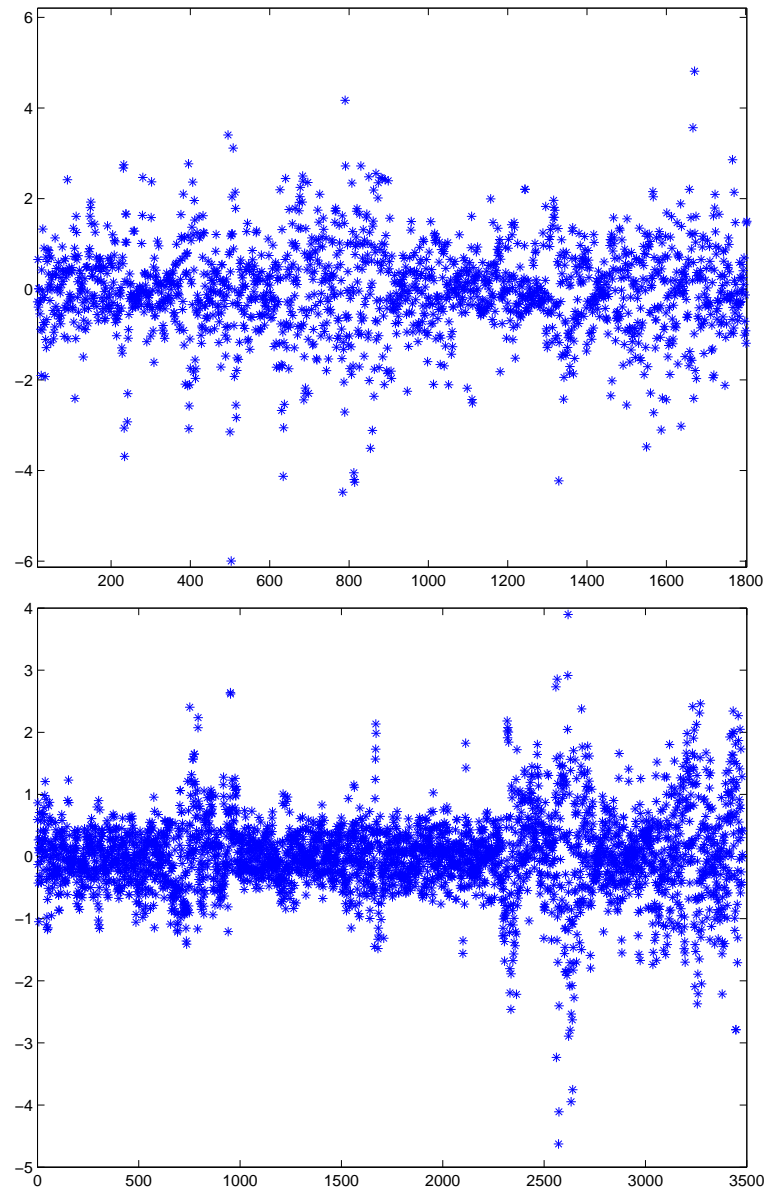


Fig. 17.1. Sum of the real parts of the eigenvalues of ∇U , for G2 solutions \hat{U} for a few thousand elements in the turbulent wake of a circular and a square cylinder, from computations presented in detail in Chapter 33.

a collection of such rotating tubes. Recalling that the velocity gradient of a turbulent flow would be of size $\nu^{-1/2}$, or $h^{-1/2}$ in a computational simulation with smallest scale h , we could expect that $\omega \sim \nu^{-1/2}$ or $\omega \sim h^{-1/2}$.

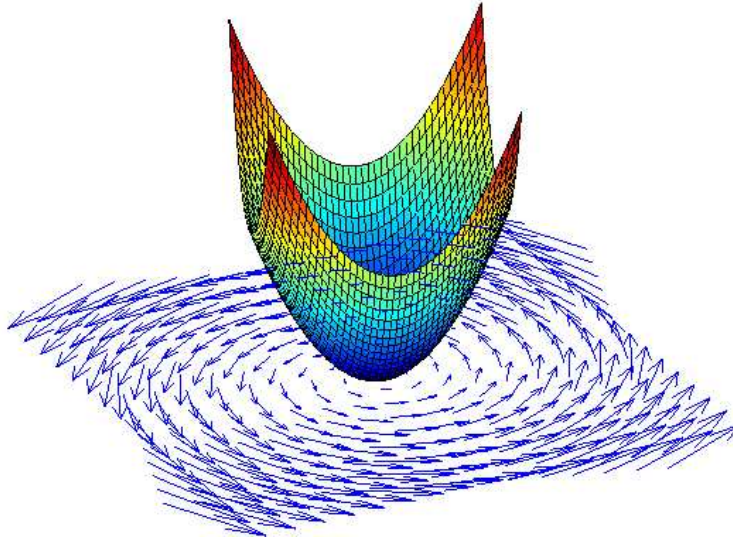


Fig. 17.2. Rotational flow $u(x) = \omega(-x_2, x_1, 0)$, and $p = \frac{\omega}{2}(x_1^2 + x_2^2)$.

17.3 A Model Dual Problem for Rotating Flow

The dual problem corresponding to rotating flow takes the following form disregarding the convection term and the φ_3 component as well as the space dependence:

$$\begin{aligned} \dot{\varphi}_1 + \omega\varphi_2 &= \psi_1 && \text{on } (0, \hat{t}], \\ \dot{\varphi}_2 - \omega\varphi_1 &= \psi_2 && \text{on } (0, \hat{t}], \\ \varphi_1(0) &= \varphi_2(0) = 0, \end{aligned} \tag{17.1}$$

where we for simplicity reversed time with the transformation $t \rightarrow \hat{t} - t$. This is the model of a harmonic oscillator with frequency ω driven by the force (ψ_1, ψ_2) . We choose $\psi_1(t) = 1/\Delta\hat{t}$ for $0 \leq t \leq \Delta\hat{t}$, $\psi_1(t) = 0$ for $\Delta\hat{t} < t \leq \hat{t}$, and $\psi_2 \equiv 0$, which (before time reversal) corresponds to the output

$$M_{\Delta\hat{t}}(u_1) = \frac{1}{\Delta\hat{t}} \int_{\hat{t}-\Delta\hat{t}}^{\hat{t}} u_1(t) dt, \tag{17.2}$$

which is a mean value in time of length $\Delta\hat{t}$.

Writing (17.1) in matrix form as $\dot{\varphi} + A\varphi = \psi$ on $[0, \hat{t}]$, $\varphi(0) = 0$, where $\varphi = (\varphi_1, \varphi_2)$ and A has a pair of imaginary eigenvalues $\pm i\omega$, we can express the solution $\varphi(t)$ as a convolution of the data $\psi(t)$ with the fundamental solution matrix $\exp(tA)$ of the homogeneous problem $\dot{\varphi} + A\varphi = 0$, as

$$\varphi(t) = \int_0^t \exp((t-s)A)\psi(s) ds.$$

Since $\exp(tA)_{11} = \cos(\omega t)$, we have for $t \leq \Delta\hat{t}$,

$$\varphi_1(t) = \frac{1}{\Delta\hat{t}} \int_0^t \cos(\omega(t-s)) ds = \frac{\sin(\omega t)}{\omega\Delta\hat{t}},$$

and for $t > \Delta\hat{t}$,

$$\varphi_1(t) = \frac{1}{\Delta\hat{t}} \int_0^{\Delta\hat{t}} \cos(\omega(t-s)) ds = \frac{\sin(\omega t) - \sin(\omega(t - \Delta\hat{t}))}{\omega\Delta\hat{t}}.$$

We now study the dependence of the magnitude of $\varphi_1(t)$ as a function of the size $\Delta\hat{t}$ of the mean value. We find that

$$|\varphi_1(t)| \approx 1 \quad \text{for } \omega\Delta\hat{t} \leq 1,$$

$$|\varphi_1(t)| \approx \frac{1}{\omega\Delta\hat{t}} \quad \text{for } \omega\Delta\hat{t} \text{ large,}$$

and we have that $\varphi_1(t)$ increases from zero with slope $1/\Delta\hat{t}$ as long as $t < \min(\Delta\hat{t}, \frac{1}{\omega})$ and then levels off into oscillations, so that for $\omega\Delta\hat{t}$ large, $\varphi_1(t)$ is much smaller than for $\omega\Delta\hat{t}$ small, see Fig. 17.3. A short mean value output thus has a larger stability factor than a long mean value, which expresses that a short mean value is more sensitive to perturbations than a long mean value output.

Obviously, the reduction in size of the dual solution going from short to long mean value comes from considerable cancellation in the integral defining $\varphi_1(t)$ as a convolution of $\psi(t)$ with the oscillating integrand $\cos(\omega t)$, which starts coming into play when $\omega\Delta\hat{t} > 1$ and becomes more pronounced as $\omega\Delta\hat{t}$ grows larger.

17.4 A Model Dual Problem for Oscillating Reaction

To model the effect of the real parts of the eigenvalues summing to zero we consider the scalar problem

$$-\dot{\varphi}(t) + \cos(t)\varphi(t) = 0, \quad \text{on } [0, \hat{t}),$$

with solution

$$\varphi(t) = \exp(\sin(\hat{t} - t))\varphi(\hat{t}).$$

Clearly, the net effect of the oscillating reaction coefficient $\cos(t)$ is very small: $\varphi(t)$ neither grows nor decays.

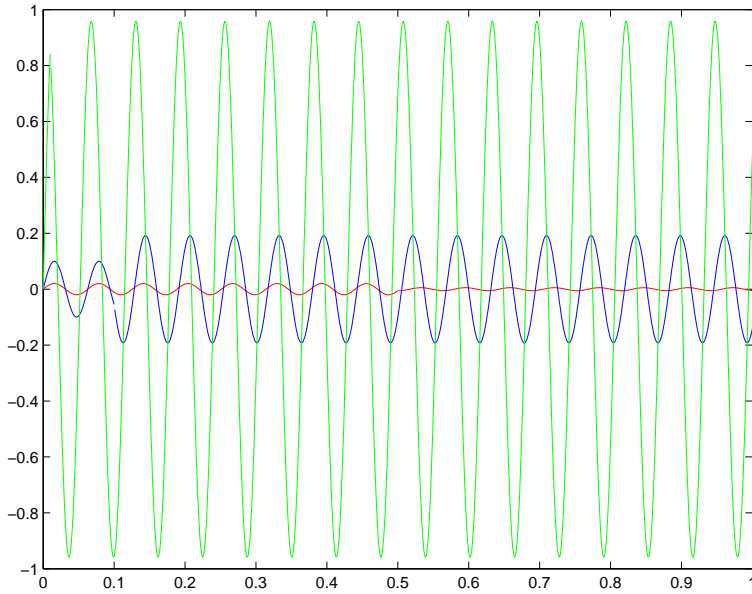


Fig. 17.3. Model dual problem for rotational flow; $\omega = 100$, $\Delta\hat{t} = 0.01, 0.1, 0.5$.

17.5 Model Dual Problem Summary

The dual problem for the NS equations is a convection-reaction-diffusion problem in space-time of the form

$$-\dot{\varphi} - u \cdot \nabla \varphi + \nabla u^\top \varphi - \nu \Delta \varphi = \psi \quad \text{on } [0, \hat{t}], \quad \varphi(\hat{t}) = 0.$$

Disregarding the diffusion and following the streamlines defined by the convection, we can view this problem as a collection of reaction problems in time of the form

$$-\dot{\varphi} + A\varphi = \psi \quad \text{on } [0, \hat{t}], \quad \varphi(\hat{t}) = 0,$$

where $A(t)$ is a 3×3 matrix which varies in time as $\nabla u^\top(x, t)$ varies along a streamline. The real parts of the eigenvalues of $A(t)$ sum to zero for each t , and the imaginary parts appear as complex conjugates. We have separately analyzed the stability properties of such a system as affected by (i) the real parts of the eigenvalues, and (ii) the imaginary parts of eigenvalues. Assuming the real parts to oscillate between negative and positive values, would give no net production. Finally the effect of the imaginary parts would by a cancellation effect make the dual solution decrease as the length of the mean value increases. The net effect would be that the stability factor is large for a small mean value output, and small for a large mean value output. We now proceed to check if we can see this type of qualitative behavior by computing the dual solution for a turbulent flow.

17.6 The Dual Solution for Bluff Body Drag

In Fig. 17.4 we plot the dual solutions for mean values of the momentary drag $D(t)$ of the surface mounted cube for different lengths of the mean values. We see that these curves behave just like the ones we just presented for the model cases of the harmonic oscillator and the oscillating reaction coefficient problem, except for the fact that in the bluff body problem the dual solution is “swept out” of the computational domain after some time resulting in a decay to zero of the dual solution for larger times. Further, in the bluff body problem we measure derivatives of the dual solution and thus the stability factors are larger than in the model problem, but their relative size follow the pattern of the model.

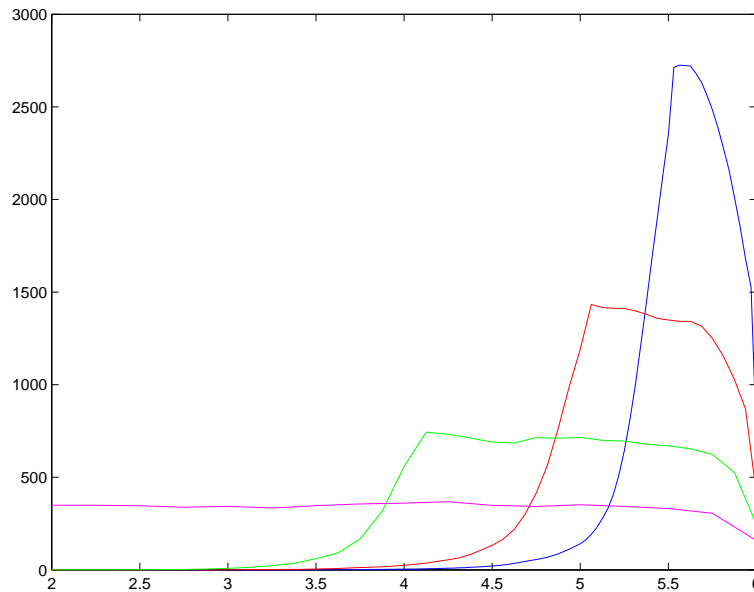


Fig. 17.4. Surface mounted cube: time series of $\|\nabla\varphi\|$ (with the time running backwards), where the dual solutions corresponds to mean values of size 0.5,1,2,4.

17.7 Duality for a Model Problem

We illustrate the use of duality for error representation in the setting of a dynamical system $\dot{u} = f(u)$ on $[0, \hat{t}]$, $u(0) = 0$, with $f : \mathbb{R} \rightarrow \mathbb{R}$. We consider two solutions $u(t)$ and $v(t)$ with different initial values $u(0)$ and $v(0)$. We want to analyze the difference in output $M_{\Delta\hat{t}}(u) - M_{\Delta\hat{t}}(v)$, where $M_{\Delta\hat{t}}(u)$ is defined

in (17.2), resulting from the difference $u(0) - v(0)$ in initial value, assuming we solve the dynamical system for $u(t)$ and $v(t)$ exactly.

By integration by parts we obtain the following representation

$$M_{\Delta\hat{t}}(u) - M_{\Delta\hat{t}}(v) = \varphi(0)(u(0) - v(0))$$

where the dual solution $\varphi(t)$ solves the linear problem

$$-\dot{\varphi} + f'(t)\varphi = \psi \quad \text{on } [0, \hat{t}], \quad \varphi(\hat{t}) = 0,$$

with $\psi = 1/\Delta\hat{t}$ on $[\hat{t} - \Delta\hat{t}, \hat{t}]$ and $\psi = 0$ else, and

$$f'(t) = \int_0^1 \frac{d}{ds} f(su(t) + (1-s)v(t)) ds.$$

Clearly $\varphi(0)$ is the stability factor expressing the sensitivity of the output mean value $M_{\Delta\hat{t}}(u)$ to changes in input initial value $u(0)$. We can compute $\varphi(0)$ by first computing the two trajectories $u(t)$ and $v(t)$ forward in time, and then solving for the dual solution $\varphi(t)$ backwards in time to the initial time $t = 0$ to get $\varphi(0)$.

17.8 Ensemble Averages and Input Variance

Although we do not in this book consider statistical approaches to turbulence, we will make a comment on ensembles of solutions corresponding to ensembles of data. We do this to exhibit an aspect of the dual problem which is of key importance to understand that a mean value output may be moderately sensitive to changes in input mean values, while it may be less sensitive to input variance. This means that if outputs are mean values, then we do not need information on input variance or the statistical distribution of input. This is crucial since usually information on input variance or distribution is lacking. The only thing we can hope for in such a case is that a mean value output such as drag is relatively insensitive to input variance.

We consider two solution ensembles $u(t; i)$ and $v(t; i)$ with initial values $u(0; i)$ and $v(0; i)$, $i = 1, \dots, N$, in the setting of a dynamical system $\dot{u} = f(u)$ on $[0, \hat{t}]$, $u(0) = 0$, with $f : \mathbb{R} \rightarrow \mathbb{R}$. For an ensemble $w(i)$, $i = 1, \dots, N$, we introduce the mean value \bar{w} and deviation $w'(i)$, $i = 1, \dots, N$, defined by

$$\bar{w} = \frac{1}{N} \sum_{i=1}^N w_i, \quad w'(i) = w(i) - \bar{w},$$

assuming a uniform density for the ensemble. Using duality we have the following representation for the time mean value $M_{\Delta\hat{t}}$ defined above:

$$\overline{M_{\Delta\hat{t}}(u)} - \overline{M_{\Delta\hat{t}}(v)} = \overline{\varphi(0)(\overline{u(0)} - \overline{v(0)})} + \frac{1}{N} \sum_{i=1}^N \varphi'(0; i)(u'(0; i) - v'(0; i))$$

where for each pair $u(t; i)$ and $v(t; i)$ the dual solution $\varphi(t; i)$ solves the linear problem

$$-\dot{\varphi} + f'(t; i)\varphi = \psi \quad \text{on } [0, \hat{t}], \quad \varphi(\hat{t}) = 0,$$

with $\psi = 1/\Delta\hat{t}$ on $[\hat{t} - \Delta\hat{t}, \hat{t}]$ and $\psi = 0$ else, and

$$f'(t; i) = \int_0^1 \frac{d}{ds} f(su(t; i) + (1-s)v(t; i)) ds.$$

Here $\overline{\varphi(0)}$ is the stability factor expressing the sensitivity of the output mean value $M_{\Delta\hat{t}}$ to changes in input mean value. Further, the deviation $\varphi'(0; \cdot)$ expresses the sensitivity of the output mean value to input deviation. We pay particular attention to problems with $\overline{\varphi(0)}$ being of moderate size and the deviation $\varphi'(0; \cdot)$ being at least one order of magnitude smaller. In such a problem output mean values would be (i) well determined from input mean values with (ii) little dependence on input deviation. In particular, (ii) signifies that the dual solution $\varphi(t; i)$ is relatively insensitive to the underlying trajectories $u(t; i)$ and $v(t; i)$.

In this book we give evidence that many cases of turbulent flow have the qualities (i) and (ii), see Chapter 15. Again, (ii) is important in order for stability aspects to be insensitive to individual trajectories. In the setting of NS equations, it is natural to view all the different solutions $u(t; i)$ (or $v(t; i)$) as members of the same set of approximate solutions W_ϵ for some $\epsilon > 0$, and we would then expect the individual outputs $M_{\Delta\hat{t}}(u(\cdot; i))$ to be close to the mean value $\overline{M_{\Delta\hat{t}}(u)}$. To compute the output it would then be sufficient to solve for only one trajectory. In this case it would not be necessary to enter into the statistics of solving for many trajectories $u(\cdot; i)$ and computing ensemble mean values.

Moreover, if (ii) is valid, then in fact all the $\varphi(0; i)$ are close to the mean value $\overline{\varphi(0)}$. We may thus expect to be able to compute a good approximation of $\overline{\varphi(0)}$, or any of the individual stability factors $\varphi(0; i)$, by solving the dual problem only once with some particular choice of linearization which would be representative.

A Convection-Diffusion Model Problem

How can it be that even if everything I do is pointwise wrong (according to my critics), yet my mean value comes out right? (Oscar Wilde)

18.1 Introduction

We discuss some basic aspects of G2 in the setting of a convection-diffusion model problem. We first comment on the fact that the residual $R(\hat{u})$ of an ϵ -weak solution \hat{u} necessarily is pointwise large where the flow is turbulent and not fully resolved. In fact, a turbulent flow is characterized by the fact that the stabilization term is not small and thus the residual large pointwise. We then show that the least squares stabilization of G2 introduces an artificial viscosity acting as a turbulent diffusion on smallest scales only and therefore does not degrade the accuracy of mean value outputs.

18.2 Pointwise vs Mean Value Residuals

We have noticed above that even though the residual $R(\hat{u})$ of an ϵ -weak solution \hat{u} of the NS equations is not small pointwise, its effect on a mean value output $M(\hat{u})$ may be small. We will now discover the same phenomenon in the following scalar linear constant coefficient stationary convection-diffusion-reaction model problem with small viscosity ν :

$$u_{,1} + u - \nu \Delta u = f \text{ in } \Omega, \quad u = 0 \text{ on } \Gamma, \quad (18.1)$$

where $\Omega = (0, 1)^2$ with boundary Γ , $u_{,1} = \frac{\partial u}{\partial x_1}$ and f is a given (smooth) function. The solution $u = u(x)$ in general has an outflow boundary layer at $x_1 = 1$ of width $\sim \nu$, and characteristic layers at $x_2 = 0$ and $x_2 = 1$ of width $\sim \sqrt{\nu}$. With an oscillating inflow value of $u(x)$ at $x_1 = 0$, the characteristic layers may fill Ω .

Let now V_h be the standard finite element space of continuous piecewise linear functions on a triangulation of Ω of mesh size h vanishing on Γ , and let $U \in V_h$ be a G2 solution defined by

$$(U_{,1} + U, v + hv_{,1}) = (f, v + hv_{,1}) \quad (18.2)$$

where (\cdot, \cdot) is the $L_2(\Omega)$ -norm, and we assume that $\nu \ll h$ so that the ν -term can be omitted in G2. Further, the stabilizing term was simplified from $h(v_{,1} + v)$ to $hv_{,1}$, as in the *streamline diffusion method* [35]. Choosing here $v = U$ gives the following basic energy estimate for U :

$$\|U\|^2 + \|\sqrt{h}U_{,1}\|^2 \leq (1 + h)\|f\|^2 \approx 1$$

where $\|\cdot\|$ is the $L_2(\Omega)$ -norm and we assume $\|f\| = 1$. We notice that in the case the exact solution u has layers, the stabilizing term $\|\sqrt{h}U_{,1}\|^2$ will not be small, because $U_{,1} \sim h^{-1}$ in an outflow layer of width $\sim h$, and $U_{,1} \sim h^{-1/2}$ in characteristic layers of width $h^{1/2}$.

Now, if $\nu \ll h$, then

$$R(U) \approx U_{,1} + U - f$$

and thus by choosing $v = U$ in (18.2)

$$-(R(U), U) \approx \|\sqrt{h}U_{,1}\|^2 \gg 0,$$

which shows that $R(U)$ cannot be pointwise small everywhere in Ω : We will argue below that $R(U) \sim h^{-1}$ in outflow layers and $R(U) \sim 1$ in characteristic layers. Note that $\|\sqrt{h}U_{,1}\|^2$ not small signifies the presence of unresolved layers where $R(U)$ is not small, which mimics the fact that in the NS equations the stabilizing term and residual are not small in unresolved (turbulent) regions.

Now, if we in the model problem take as output $M(u) = (u, \psi)$, where ψ vanishes in the layers, that is we consider only output away from the numerical layers, then it follows by the analysis of G2 in [70], that if u is smooth outside layers then

$$|M(u) - M(U)| \sim h^{3/2},$$

which shows that the error in certain outputs may be small even though the residual $R(U)$ is large pointwise in certain parts of the domain. Of course, in the model problem this is fully understandable because by the nature of the convection in the positive x_1 -direction and the smallness of the diffusion coefficients, effects in boundary layers are not propagated into the domain. Alternatively, we may as above in the case of the NS equations bound the output error in terms of

$$\|R(U)\|_{H^{-1}(\Omega)} \sim \|hR(U)\|,$$

which may be small ($\sim \sqrt{h}$), even though $R(U)$ is not small everywhere.

To understand more precisely why the residual $R(U)$ cannot be small in an outflow layer, we note that the exact solution u with f smooth there satisfies

$$u_{,1} + u - f = \nu \Delta u \sim \frac{1}{\nu} \quad (18.3)$$

if u varies between 0 and 1 in the layer, so that $R(u) = 0$ results from cancellation of the two terms $u_{,1} + u - f$ and $\nu \Delta u$ both $\sim 1/\nu$. In the numerics this cancellation cannot be realized if $h \gg \nu$, and the result is that $R(u) \approx 1/h$ in the numerical outflow layer: Roughly speaking, we have in an outflow layer

$$U_{,1} + U_1 - f \sim h U_{,11} \sim \frac{1}{h},$$

which is incompatible with (18.3) if $h \gg \nu$, and thus necessarily $R(U) \approx 1/h$ in an outflow layer. A similar argument shows that we may have $R(U) \approx 1$ in a characteristic layer. We may say that the fact that $R(U)$ cannot be small in layers, is a necessary consequence of the under resolution with $h \gg \nu$, which makes it impossible to numerically capture the cancellation of non-small viscous and non-viscous terms present in the continuous problem.

We sum up by noting that the under resolution with $h \gg \nu$ makes it impossible for $R(U)$ to be pointwise small everywhere, while the fact that $\|R(U)\|_{H^{-1}(\Omega)}$ is small opens for the possibility that the error in a mean value output is small, if the dual solution is not too large.

18.3 Artificial Viscosity From Least Squares Stabilization

The least squares stabilization in (18.2) effectively introduces the term

$$(U_{,1} + U - f, hv_{,1})$$

which involves the artificial viscosity $(U_{,1}, hv_{,1})$. The stabilizing term is obviously small where $U_{,1} + U_1 - f$ is small, that is outside layers where the solution is smooth. The net effect of the least squares stabilization thus is increased viscosity only in regions where the solution is non-smooth. Similarly the G2 stabilization in NS has the effect of a turbulent diffusion acting only on the smallest scales of the flow.

As a comparison we note that simply adding an artificial viscosity term $(U_{,1}, hv_{,1})$ without the compensating terms in $(U_{,1} + U - f, hv_{,1})$, introduces a perturbation of order h also to smooth parts of the flow, which significantly degrades the accuracy. Adding artificial viscosity in the form $(U_{,1}, hv_{,1})$ corresponds to the simplest version of the classical Smagorinsky turbulence model in NS.

The least squares stabilization in G2 thus may be viewed as a smart Smagorinsky model (see Chapter 26), effectively introducing diffusion only

on the smallest scales of the mesh. The rationale is then that the actual size of the smallest scale of the diffusion is insignificant for certain mean value outputs, and thus that certain aspects of turbulent flow can be captured on computational scales which are (much) coarser than the actual physical scales. This reflects that our World would look the same even if the “fluid particles” were much bigger than particles on atomic scales.

19

G2 for Euler

As an older friend I must advice you against it for in the first place you will not succeed, and even if you succeed, no one will believe you. (Planck to Einstein about the General Theory of Relativity)

Complex spatial structures have never been observed in numerical simulations of inviscid flow with smooth initial conditions. (Frisch in *Turbulence* 1995)

The well-posedness of the Euler equations is one of the most challenging questions of the present time for both the mathematician and the numerical analyst. (Saffman 1981)

Although this may seem a paradox, all exact science is dominated by the idea of approximation. (Bertrand Russel)

19.1 Introduction

The mathematics of existence and uniqueness for the Euler equations is even more open than for the NS equations, and is considered so difficult that not even a \$100 million Prize would seem sufficient for a solution. From mathematical point of view this is because without any viscous term, only L_2 bounds are available analytically, which are far from sufficient to prove existence and uniqueness.

Instead of attempting the impossible we compute approximate weak (turbulent) solutions by G2 including weak uniqueness and we study a basic example leading into a resolution of Loschmidt's Mystery in the setting of incompressible inviscid flow.

We recall the Euler equations (5.2) for incompressible inviscid flow:

$$\begin{aligned} \dot{u} + (u \cdot \nabla) u + \nabla p &= f, & \text{in } \Omega \times I, \\ \nabla \cdot u &= 0, & \text{in } \Omega \times I, \\ u \cdot n &= 0, & \text{on } \Gamma \times I, \\ u(\cdot, 0) &= u^0, & \text{in } \Omega. \end{aligned} \tag{19.1}$$

The Euler equations are formally reversible: Changing the sign of time t and the velocity u , obviously leave the equations unchanged. In particular, if \hat{u} is a solution to the Euler equations with initial velocity u^0 at time $t = 0$ and final value $\hat{u}(\hat{t})$ at time $t = \hat{t}$, then the function $\hat{v}(t) = (-u(\hat{t}-t), p(\hat{t}-t))$ satisfies Euler's equations for $t \in (0, \hat{t}]$ with initial data $v(0) = -u(\hat{t})$ and final velocity $v(\hat{t}) = -u(0)$. Thus, reversing the velocities $u(\hat{t})$ and letting time pass backwards, would bring back the velocities to $-u(0)$ from $-u(\hat{t})$.

The basic energy estimate (16.2) with $\nu = 0$ states that the total kinetic energy $\frac{1}{2}\|u(t)\|^2$ of a pointwise solution \hat{u} of (19.1) with $\|\cdot\|$ the $[L_2(\Omega)]^3$ -norm, stays constant if $f = 0$:

$$\frac{1}{2}\|u(\hat{t})\|^2 = \frac{1}{2}\|u(0)\|^2, \quad (19.2)$$

which follows by multiplication of the momentum equation by u and integration. Thus it appears that a system governed by the Euler equations allows the design of a *perpetuum mobile* by (somehow) reversing the velocity at $t = 0$ and $t = \hat{t}$, corresponding to a system bouncing back and forth for ever. We conclude that if the Euler equations admit a pointwise solution with pointwise zero residual, then that solution would be reversible and represent a perpetuum mobile of the first kind, which is a machine running forever without consuming any energy. On the other hand, NS equations would not allow such a design because kinetic energy would be lost to the ν -term in the energy balance (16.2), and turned into heat.

We further recall 'd'Alembert's Mystery stating that a bluff body, subject to inviscid flow described by the Euler equations, has zero drag. Both a perpetuum mobile and a bluff body with zero drag are at variance with observations, and something seems to be seriously wrong with the Euler equations. But what could it be, since they after all just express Newton's 2nd Law and incompressibility? Prandtl blamed the assumption of inviscid flow with $\nu = 0$, but we have instead pointed to the instability of any exact solutions of the Euler equations developing into turbulent approximate solutions. In particular, any conclusion made from an assumption of existence of an exact pointwise solution may be completely wrong, including the energy conservation (19.2) and d'Alembert's computations of zero drag.

We have claimed that non-existence of pointwise solutions of the Euler equations follows from the observation that solutions to the NS equations in general are turbulent if ν is small, and that it is unthinkable that these turbulent solutions could converge to a pointwise solution of the Euler equations as ν tends to zero. The reason is that as we let ν tend to zero, the corresponding NS solutions develop ever finer scales of turbulence which is incompatible with convergence to a pointwise solution of the Euler equations. If the NS solutions had stayed laminar as ν tends to zero, pointwise convergence would have been possible, but NS solutions invariably become turbulent if ν is small, and thus convergence simply cannot take place. We thus have clear evidence that in general pointwise solutions of the Euler equations are non-existent.

For an account of the analytical mathematical struggle to come to grips with the Euler equations, we refer to [30] and references therein.

19.2 EG2 as a Model of the World

If now the Euler equations lack stable pointwise solutions, does it mean that we have to regard the Euler equations as useless? In fact not; we shall see that nevertheless G2 can compute approximate weak turbulent solutions, which may supply useful information in cases of very large Reynolds numbers. G2 will thus automatically compute turbulent solutions with stable mean value output, instead of unstable pointwise solutions without meaningful output.

We remarked in Chapter 5 that the Euler equations represent an ideal Einstein model without any parameter (since the viscosity is put to zero). Thus the Euler equations combined with the solution method G2 represent and constructive model, which we refer to as *Euler/G2* or *EG2* for short, while the Euler equations without any solution method represent symbols without precise meaning. We conclude that EG2 is an example of an ideal Einstein model with the remarkable property that it may give quantitative information about e.g. the drag and heat generation of a body moving through a fluid supplying only the shape of the body, but no information on coefficients of viscosity or heat conductivity.

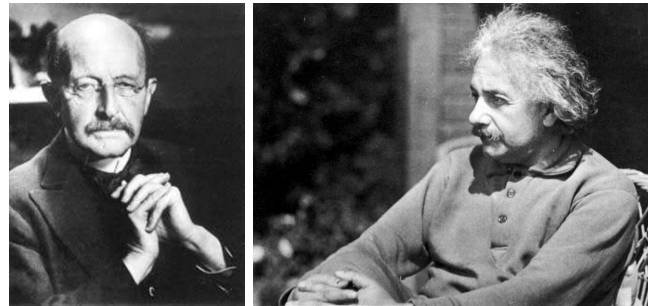


Fig. 19.1. Max Karl Ernst Ludwig Planck (1858–1947) and Albert Einstein (1879–1955).

19.3 Solution of the Euler Equations by G2

G2 for the Euler equations takes the form (16.4) with $\nu = 0$ and changing the velocity boundary conditions in \hat{V}_h from no-slip to slip boundary conditions (assuming also that $f = 0$). The basic energy estimate for the corresponding G2 solution \hat{U} reads:

$$\frac{1}{2} \|U(\hat{t})\|^2 + \|\sqrt{h}R(\hat{U})\|_Q^2 = \frac{1}{2} \|U(0)\|^2, \quad (19.3)$$

where $\|\cdot\|_Q$ is the $L_2(Q)^4$ -norm with $Q = \Omega \times I$. The least squares term $\|\sqrt{h}R(\hat{U})\|_Q^2$ corresponds to the the viscous term $D_\nu(u, \hat{t})$ in the energy estimate (16.2) for the NS equations. We shall see that in case of turbulence, the least squares term is not small, while for a laminar solution it is.

Similarly, we may obtain an a posteriori error estimate for a certain output $M(\hat{U})$ such as drag or lift. Since an exact solution \hat{u} is missing, we then estimate the difference in output of two different G2 solutions \hat{U} and \hat{W} on different meshes as follows:

$$|M(\hat{U}) - M(\hat{W})| \leq S(\|hR(\hat{U})\|_Q + \|hR(\hat{W})\|_Q),$$

where h represents the mesh size of the corresponding residual respectively, and S represents a stability factor obtained by solving a dual problem. We can thus estimate the difference in output between two different G2 solutions in terms of their residuals multiplied by a certain stability factor. Below we compute drag of a bluff body using G2 for the Euler equations, which is shown to be very close to the drag obtained using G2 for NS equations with large Reynolds number.

The evidence in G2 of non-existence of a pointwise Euler solution is that $\|R(\hat{U})\|_Q$ is not small, while $\|hR(\hat{U})\|_Q$ may be small. Typically, $\|R(U)\|_Q \sim h^{-1/2}$, reflecting that the least squares term $\|\sqrt{h}R(\hat{U})\|_Q$ has a significant contribution in the energy balance (19.3).

Notice that it is the combination of the Galerkin method and the weighted least squares stabilization that produces a reasonable compromise in the case when a pointwise solution is impossible. Using a pure least squares method will not work because the residual cannot be small in the $L_2(Q)$ -norm, and from only the knowledge that the residual is large nothing can be concluded. Further, only using the Galerkin method will not work either because the residual control is too weak to produce any sensible output. It is only the combination of the Galerkin method and the weighted least squares stabilization that works. The evidence of success is the presence of the factor h in the expression $\|hR(\hat{U})\|$ and the fact that by (16.6), we have that $\|hR(\hat{U})\| \leq \sqrt{h}$ if $\|u^0\| = 1$. In a pure least squares method the factor h in front of $R(\hat{U})$ would be missing, and in a pure Galerkin method one may have $R(\hat{U}) \sim 1/h$ and thus $\|hR(\hat{U})\| \sim 1$. Thus neither extreme case can work in general.

19.4 Drag of a Square Cylinder

As a basic example we consider the problem of computing the drag of a square cylinder of diameter $D = 0.1$ centered at $x = (0.5, 0.7, 0.2)$ and oriented in the x_3 -direction in a channel of dimension $2.1 \times 1.4 \times 0.4$ oriented in the

x_1 -direction, subject to a uniform inflow velocity $(1, 0, 0)$. We use slip boundary conditions both on the cylinder and the channel walls. We use a locally refined tetrahedral mesh with 86 904 mesh points, shown in Fig. 19.2. The advantage of using a square cylinder, instead of the circular cylinder studied in Chapter 12, is that separation occurs at the upstream corners and thus does not change position with decreasing viscosity or mesh size.

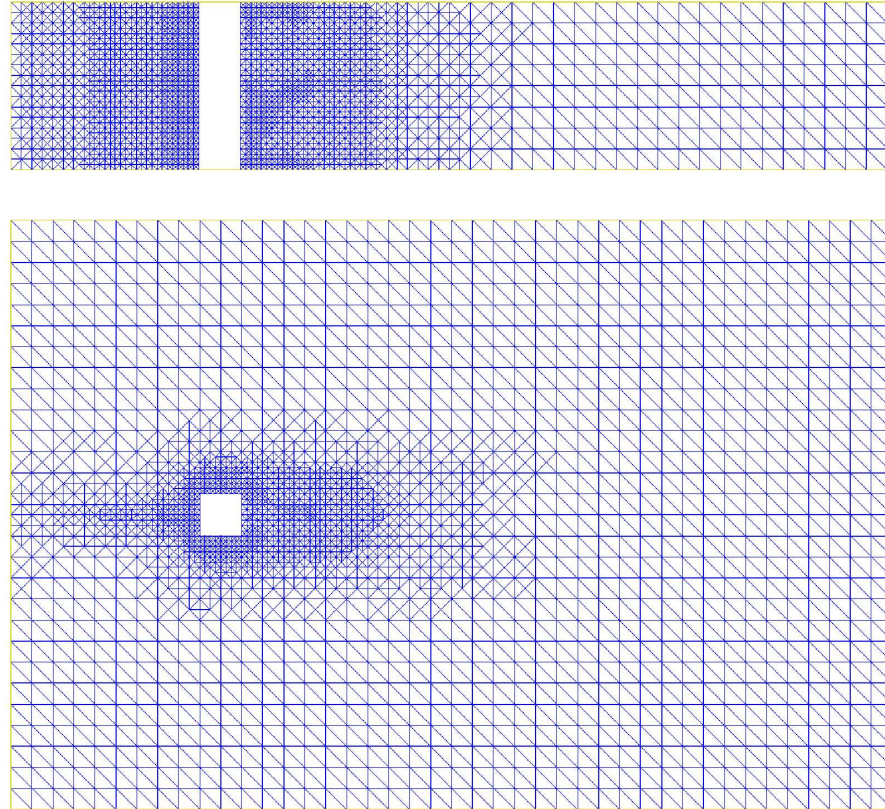


Fig. 19.2. Computational mesh in the x_1x_2 -plane (upper) and the x_1x_3 -plane (lower).

We first determine an (approximate) stationary irrotational solution, not by solving the Euler equations, but looking for a stationary velocity $u = \nabla\phi$ given by a potential $\phi(x_1, x_2, x_3)$, where $\phi = \phi(x_1, x_2, x_3)$ is constant in x_3 and solves Laplace's equation $\Delta\phi = 0$ in the domain of the fluid with $\nabla\phi \cdot n = -1$ at inflow, $\nabla\phi \cdot n = 1$ at outflow, and with homogeneous Neumann conditions $\nabla\phi \cdot n = 0$ on the channel walls and the cylinder, with n the outward unit normal. Such a velocity $u = (u_1, u_2, 0)$ is irrotational, and since the rotation

of $(u \cdot \nabla)u$ vanishes (and by symmetry the circulation $\int_{\Gamma} u \cdot ds = 0$ with Γ the intersection of the cylinder with the $x_3 = 0$ plane), there is a pressure p such that $(u \cdot \nabla)u + \nabla p = 0$. In other words, $\hat{u} = (u, p)$ is a stationary laminar solution of the Euler equations with irrotational velocity u and with $u \cdot n = 0$ on the channel walls and the cylinder surface with approximately equal inflow and outflow velocities (since u_2 and u_3 are small on inflow and outflow). The drag of \hat{u} is close to zero by the above argument.

Thus \hat{u} represents a laminar solution with pointwise residual close to zero and with close to zero drag. By increasing the length of the channel, we can reduce the pointwise residual to any size. Alternatively, by taking the inflow velocity equal to that given by the potential ϕ , we have an exact solution to Euler equations with close to zero drag.

In practice we compute ϕ by solving $\Delta\phi = 0$ using piecewise linear finite elements in the three-dimensional fluid volume, and then associate a corresponding piecewise linear velocity $U^0 = \nabla\phi$ by interpolation of the piecewise constant $\nabla\phi$ to the nodes in the mesh. This produces an approximate potential solution \tilde{U}^0 with $R(\tilde{U}^0)$ being small pointwise except close to the edges of the cylinder.

We compute an approximate solution $\hat{U} = (U, P)$ to the Euler equations with initial velocity and inflow data given by \tilde{U}^0 using G2 in the form cG(1)cG(1) with continuous linear trial functions in space-time (see Chapter 28). We find that the computed velocity $U(t)$ remains close to \tilde{U}^0 only for a few time steps, then develops non-symmetry in x_1 while maintaining two-dimensionality after which it successively develops into a fully three-dimensional turbulent solution which is far from irrotational. This turbulent solution is similar to the turbulent solution of NS equations with small viscosity and with no slip boundary conditions on the cylinder presented in [59, 53]. For the Euler equations we compute the drag coefficient, which is close to the value 2.2 obtained for the NS equations with viscosity $\nu = 10^{-6}$.

In Fig. 19.3 we plot the solution (U, P) for the first few time steps, using a very small time step of size 0.1 times the smallest element diameter in the mesh. We find that the instability of the the initial symmetric solution $U(0) = \nabla\phi$ is first expressed in a fluctuating pressure until a high pressure in front of the cylinder is established, which initializes the development of a non-symmetric velocity eventually going turbulent.

In Fig. 19.4–19.6 we show results starting with zero initial velocity, using now time steps of the same size as the finest element diameter in the mesh. We find again the potential solution during the first few time steps with the same development into a turbulent solution.

19.5 Instability of the Potential Solution

We also illustrate the instability of the potential solution by solving the dual Euler equations, linearized at the potential solution and the developed turbu-

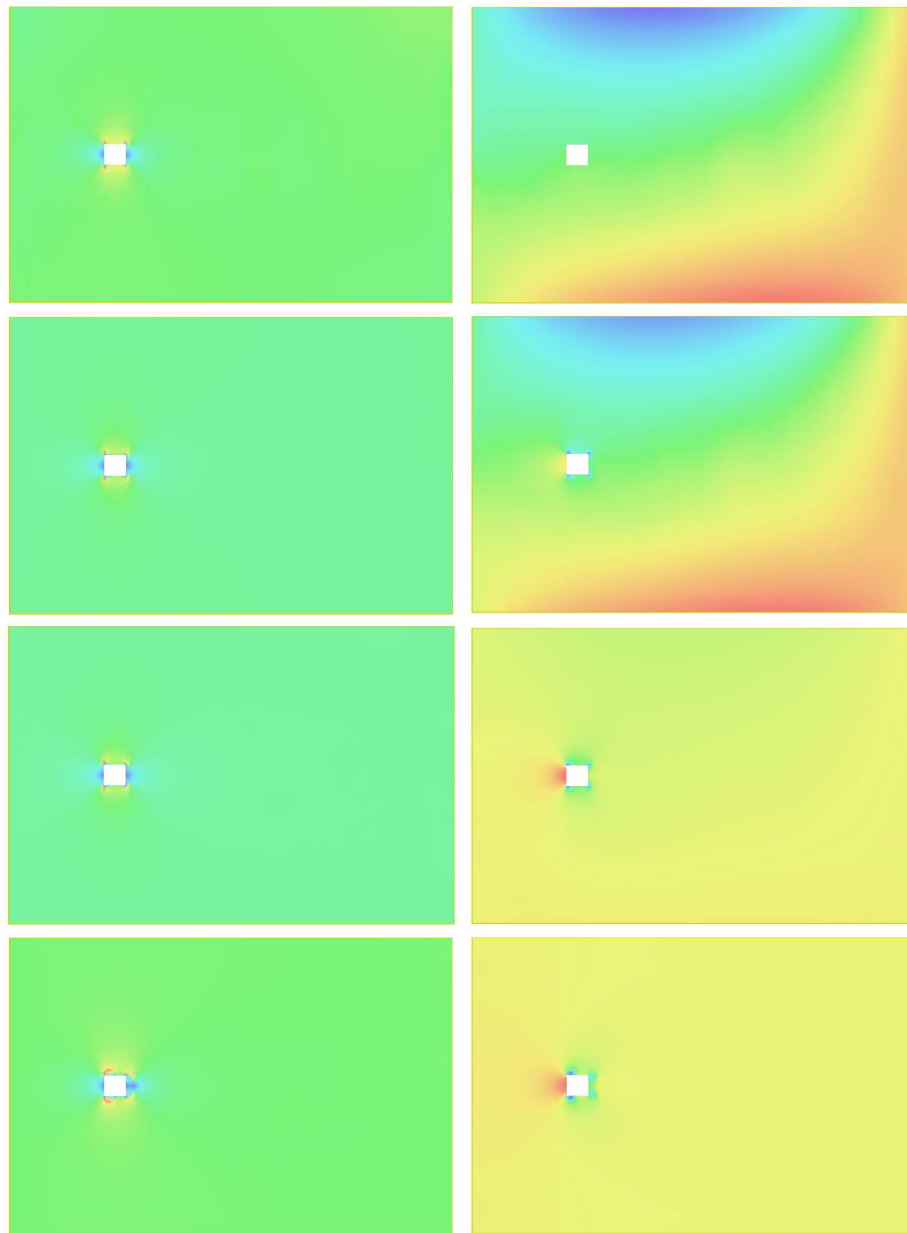


Fig. 19.3. Magnitude of the computed velocity (left) and pressure (right) from initial data $U(0) = \nabla\phi$, for time steps no 2,5,7,37.

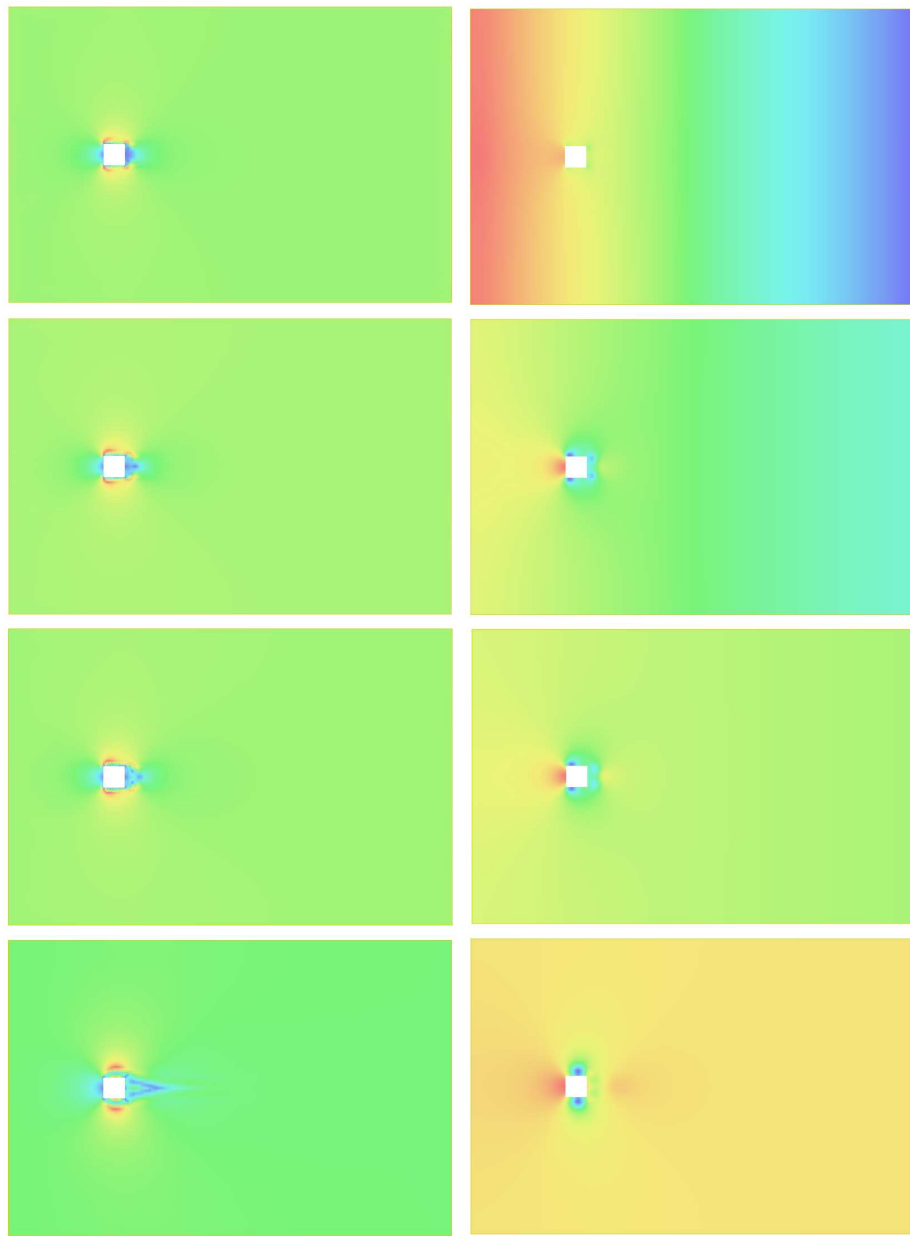


Fig. 19.4. Magnitude of the computed velocity (left) and pressure (right) corresponding to zero initial data, for time steps 4,6,8,32.

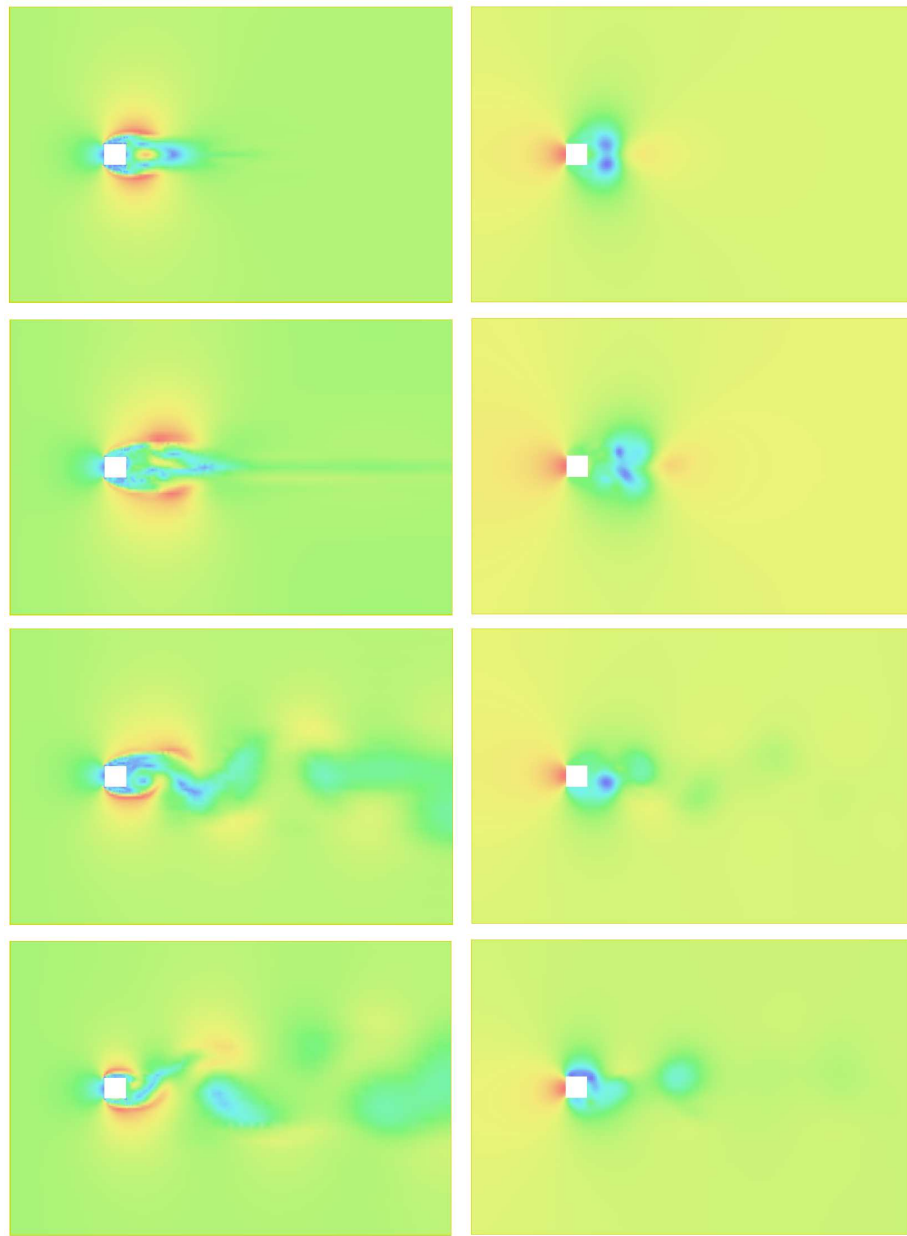


Fig. 19.5. Magnitude of the computed velocity (left) and pressure (right) corresponding to zero initial data, for time steps 64,128,256,512,1024.

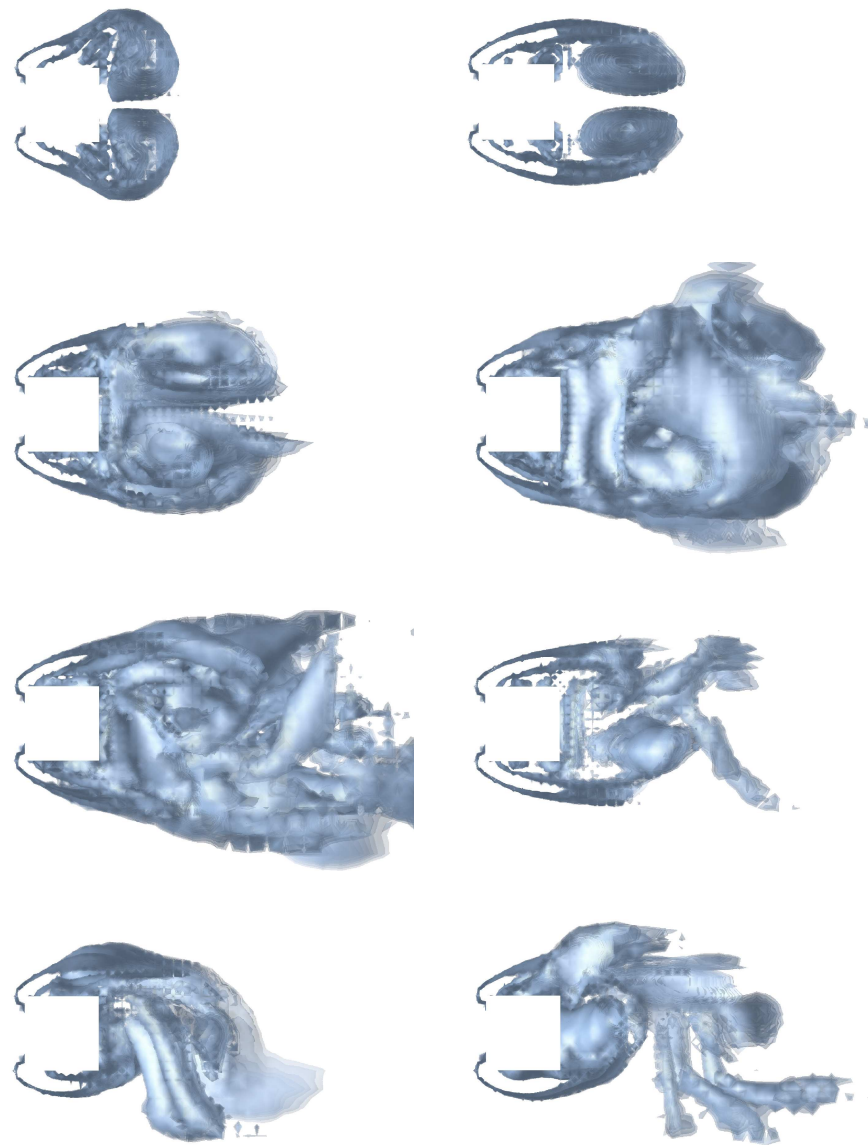


Fig. 19.6. Magnitude of the vorticity corresponding to zero initial data, for time steps 48,64,96,128,160,704,960,1024.

lent flow respectively. We use as data to the dual problem a source term in the dual velocity equation being a characteristic function over a cube in space of side length 0.025 centered at (0.6, 0.7, 0.2), times 0.025^{-4} . The source term acts over a time interval of length 0.025 from the final time (start time in the dual equation), corresponding to the computation of a small space-time mean value at final time.

In Fig. 19.8 we find that the dual solution corresponding to linearization at the potential solution grows exponentially, whereas linearized at the turbulent solution the dual solution shows a slow growth followed by decay to zero. This reflects the instability of the potential solution, being extremely sensitive to perturbations at earlier times, and the destruction of information in the turbulent flow making the solution insensitive to perturbations with respect to the mean value output. We plot the two dual solutions in Fig. 19.7.

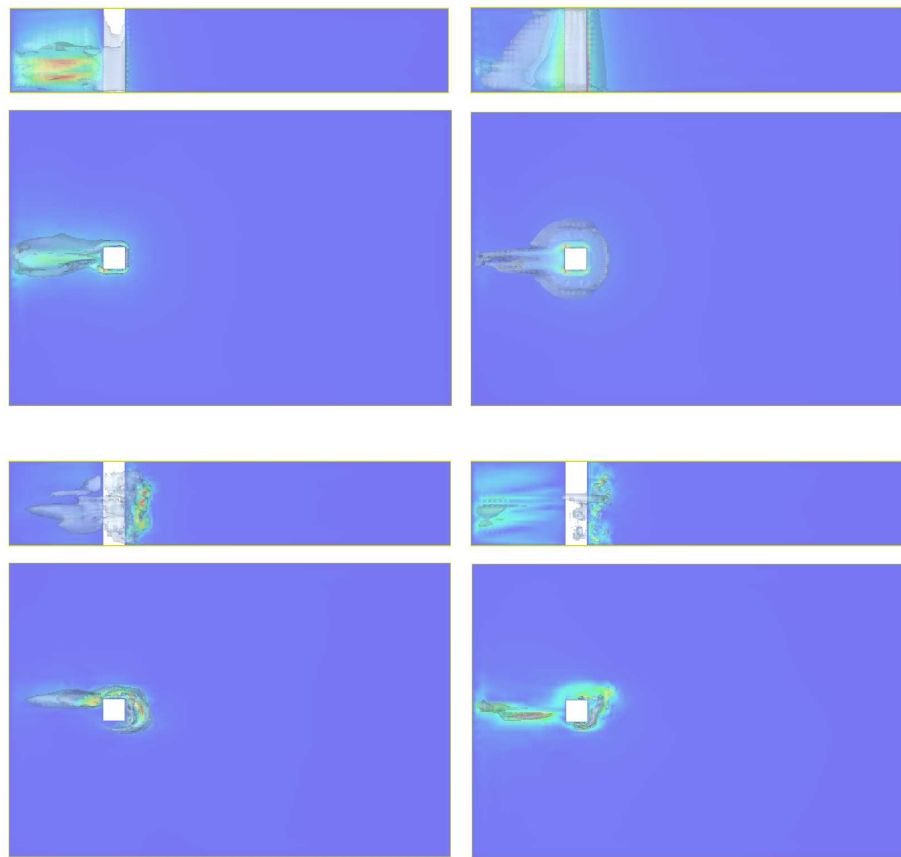


Fig. 19.7. Dual velocity $|\varphi|$, linearized at $U(0) = \nabla\phi$ (upper), and linearized at turbulent flow (lower), for time $t = 17.5, 17$.

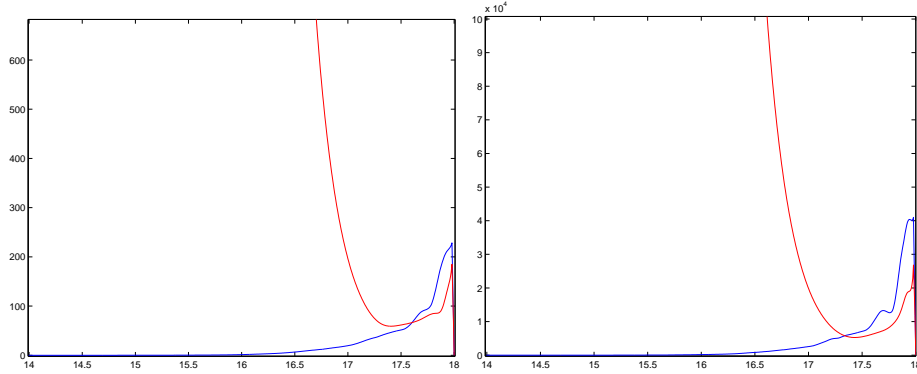


Fig. 19.8. The L_2 -norm of the dual velocity (left) and dual velocity gradient (right), linearized at $U(0) = \nabla\phi$ and turbulent flow respectively.

19.6 Temperature

We recall the general Euler equations (4.1) including the equation expressing conservation of the total energy:

$$\dot{e} + \nabla \cdot (eu + pu) = 0, \quad \text{in } Q, \quad (19.4)$$

where with $\rho = 1$ the total energy e is given by

$$e = \frac{1}{2}|u|^2 + T, \quad (19.5)$$

where T is the temperature. We can write (19.4) as

$$D_u T = -D_u \left(\frac{1}{2}|u|^2 \right) - \nabla p \cdot u \equiv E(u, p), \quad \text{in } Q, \quad (19.6)$$

where $D_u T = \dot{T} + (u \cdot \nabla)T$ is the convective derivative of T based on the velocity u . We note that for a pointwise solution (u, p) of (19.1) with $f = 0$, we have $E(u, p) = 0$, which follows by multiplication of the momentum equation by u . However, we know that (stable) pointwise solutions do not exist, so we cannot say that $E(u, p) = 0$.

Nevertheless, having computed $\hat{u} = (u, p)$ from the incompressible Euler equations, we can solve for the total energy e in the linear equation (19.4) with u and p given, to obtain the internal energy/temperature T from (19.5). Alternatively, we can solve for the internal energy T in (19.6) with the right hand side $E(u, p)$ given. In Fig. 19.9 we show the computed total energy, and the corresponding temperature starting from zero temperature at initial time and letting the inflow temperature be equal to zero. We notice that the

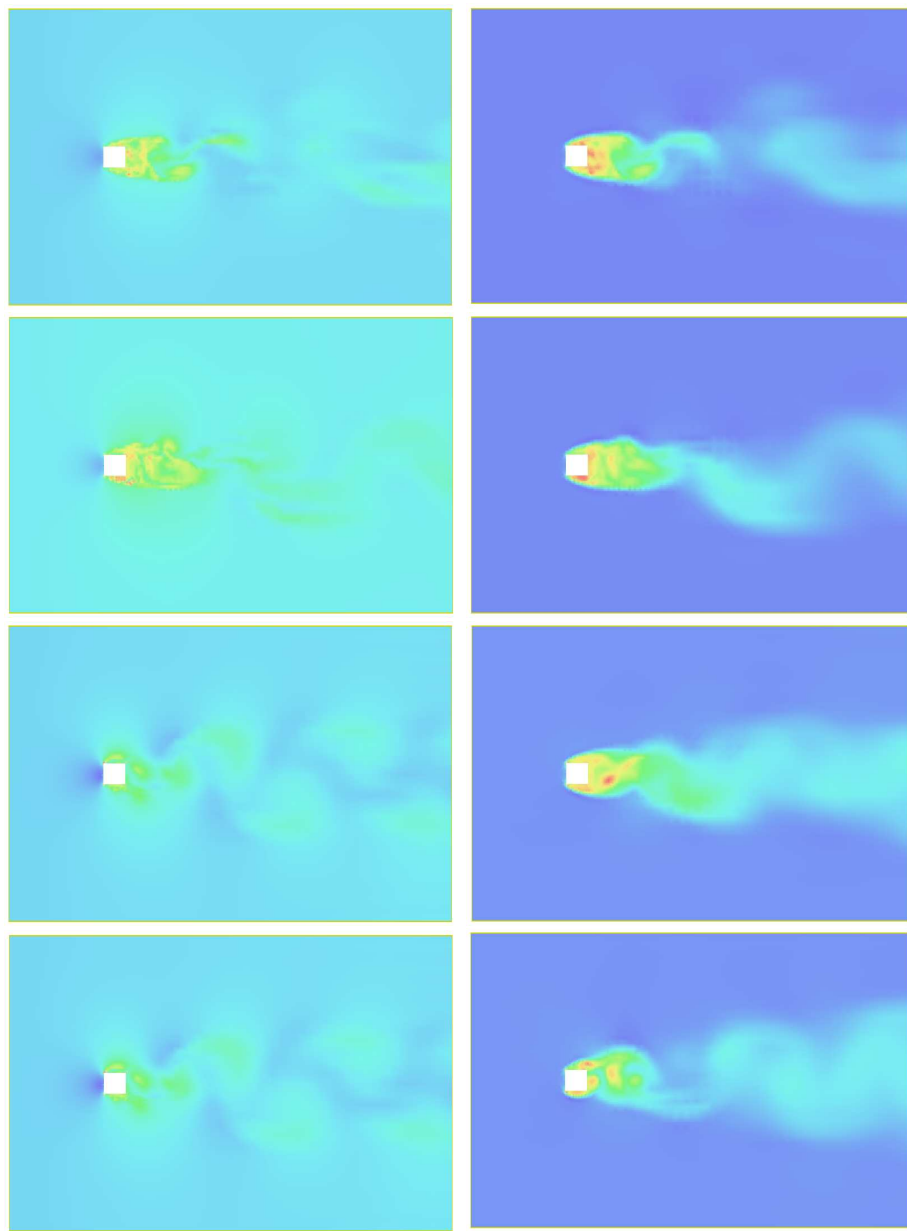


Fig. 19.9. Total energy e (left) and temperature T (right); $t = 4.5, 5.5, 11, 16$.

temperature is elevated in the turbulent wake, with the heat being generated by the turbulent dissipation (represented by the weighted least squares term in G2). We notice that the generated heat is transported by the turbulent velocity u in a process of turbulent diffusion of heat, which most likely will dominate any molecular diffusion of heat (which we effectively set to zero in the computation). We are thus able to compute a temperature distribution in a turbulent flow with the only information that the coefficients of viscosity and molecular heat diffusion are very small. This is very good news since precise quantitative determination of very small viscosities or heat conductivities is very difficult both theoretically and experimentally.

19.7 G2 as Dissipative Weak Solutions

The computations presented in Fig. 19.9 show that the temperature T is non-negative, which we may connect to the sign of the right hand side $E(u, p)$ in (19.6): If $E(u, p) \geq 0$ in $\Omega \times I$, then necessarily $T \geq 0$ in $\Omega \times I$ if $T(\cdot, 0) = T^0 = 0$. More precisely, (19.6) would then state that T can only increase following the flow. So can we guarantee that a G2 approximate weak solution (U, P) satisfies (in a suitable weak sense)

$$E(U, P) \geq 0, \quad \text{in } Q?$$

Yes, we can prove that

$$\int_Q E(U, P)\phi dxdt \geq -C\sqrt{h}, \quad (19.7)$$

for any non-negative test function ϕ , where C is a positive constant depending on ϕ . We give a proof below.

19.8 Comparison with Viscous Regularization

The same question is similarly addressed by Duchon-Robert in [32], introducing the notion of a *dissipative weak solution* (u, p) to the Euler equations, which is a function (u, p) satisfying the Euler equations in a weak sense, and in addition satisfies the positivity condition $E(u, p) \geq 0$ in Q in a weak sense. The discussion starts from the observation that a strong (pointwise) solution (u, p) satisfies $E(u, p) = 0$ pointwise, as we remarked above. Further, the observation is made that a limit (u, p) of the NS solutions (u_ν, p_ν) as the viscosity ν tends to zero, will satisfy $E(u, p) \geq 0$ weakly, as a consequence of multiplying the momentum equation in NS equations by $u_\nu \phi$ with $\phi(x, t)$ a non-negative test function and integrating, to get

$$\int_Q E(u_\nu, p_\nu)\phi dxdt = \int_Q \nu |\nabla u|^2 \phi dxdt + \sum_j \int_Q \nu u_j \nabla u_j \cdot \nabla \phi_j dxdt,$$

and noting that by the basic energy estimate (16.2)

$$\sum_j \int_Q \nu u_j \nabla u_j \cdot \nabla \phi_j \, dx dt \rightarrow 0,$$

as ν tends to zero. We thus have for small ν that

$$E(u_\nu, p_\nu) \approx \nu |\nabla u|^2, \quad \text{in } Q, \quad (19.8)$$

that is, $E(u_\nu, p_\nu)$ is in fact approximately equal to the the *intensity of the viscous dissipation* $\nu |\nabla u|^2$. In particular, we expect that $E(u_\nu, p_\nu) > 0$ for a turbulent flow with substantial turbulent dissipation.

So even if the existence of weak solutions to the Euler equations cannot be proved, Duchon-Robert propose that it may be reasonable to require a weak solution (u, p) of Euler to satisfy $E(u, p) \geq 0$ in Q in a weak sense. The rationale is that limits of solutions to the NS equations satisfy this condition, as we just demonstrated, and therefore “physical solutions” should satisfy this condition. The proof below that G2 satisfies a variant of the same condition mimics the proof for NS equations just given. As indicated above, we have strong reasons to believe that (stable) weak solutions to the Euler equations do not exist, and thus that the notion of dissipative weak solution to Euler may not be useful, but the notion of approximate dissipative weak solution is.

19.9 Finite Limit of Turbulent Dissipation

In this context, we recall Kolmogorov’s conjecture that the intensity of the turbulent dissipation should have a finite limit different from zero as ν tends to zero. Studying Fig. 19.10 where we display the dissipation intensity in G2 as a function of the mesh size (\log_{10} of the number of mesh points), we see that the intensity indeed seems to have a finite limit different from zero. Thus computation indicate that Kolmogorov was right. Of course, the alternative of a zero limit does not seem plausible as that would correspond to the existence of a (stable) smooth solution to the Euler equations, which we have seen is impossible.

19.10 The 2nd Law of Thermodynamics

We can view $D_u T = E(u, p) \geq 0$ as an expression of the *2nd Law of thermodynamics*, reflecting that kinetic energy may be turned into internal energy, that is $D_u T \geq 0$, but internal energy cannot be converted back again, that is, we can never have $D_u T < 0$ with strict inequality. Once kinetic energy has been turned into internal energy it is “lost” and cannot be retrieved. If we drop a bucket of water to the ground it will heat up, but it cannot lift itself

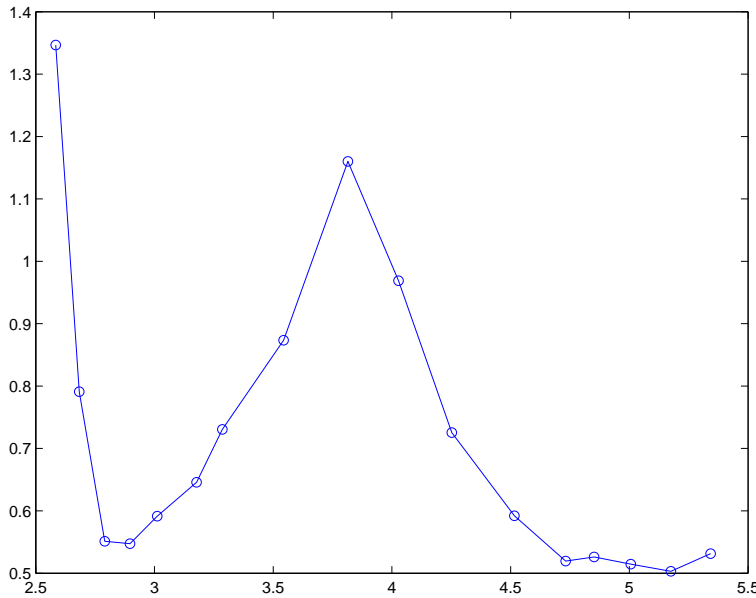


Fig. 19.10. The mean value of the dissipation intensity of G2 in the turbulent wake of the flow around a surface mounted cube (see Chapter 33), vs \log_{10} of the number of mesh points.

by cooling off. This is an example of *irreversibility* imposed by the 2nd Law, to which we will return in more detail in Part VI of this book on Loschmidt's Mystery.

We prove below that a G2 solution weakly satisfies the 2nd Law, and thus that "G2 follows Physics". We will in Part VI turn this around and ask if "Physics follows G2?".

In short, we can write the 2nd Law in the form $dT \geq 0$ with $dT = D_u T$. In Part VI we show that the 2nd Law for compressible flow generalizes to $dT + pdV \geq 0$ with dV representing change of volume. In compressible flow T may decrease under expansion with $dV > 0$.

19.11 A Global Form of the 2nd Law

Using (19.8) we can reformulate the basic energy estimate for NS equations (16.2) as the following global form of the 2nd Law:

$$\frac{1}{2} \|u_\nu(\hat{t})\|^2 + \int_Q E(u_\nu, p_\nu) dx dt \approx \frac{1}{2} \|u^0\|^2, \quad (19.9)$$

indicating that for a dissipative weak Euler solution actually

$$\frac{1}{2} \|u_\nu(\hat{t})\|^2 < \frac{1}{2} \|u^0\|^2, \quad (19.10)$$

with substantial loss of total kinetic energy for a turbulent solution. A G2 solution has the same property by the basic energy estimate (19.3). The global form of the 2nd Law states that in an isolated system without forcing the total kinetic energy can only decrease and so does for turbulent flow.

19.12 Understanding a Basic Fact

We realize that the quantities of significance and interest are turbulent dissipation and generation of heat energy. Our computations show that these quantities are largely independent of the mesh size h as soon as it is reasonably small, which may be viewed as an independence of (small) values of viscosity and heat conductivity. We presented evidence in Fig. 19.10.

We understand that the motivation to seek to determine viscosity and heat conductivity coefficients has been to compute dissipation and heat generation. If now these quantities can be directly computed, then we are relieved from the difficult (or hopeless) task of determining coefficients of viscosity and conductivity. We are led to the conclusion that the mere concept of coefficients of viscosity and heat conductivity is questionable from a scientific point of view since we can never determine relevant values of these coefficients, and even if we could they would not be useful, since they would be overshadowed by the numerical dissipation.

19.13 Proof that EG2 is a Dissipative Weak Solution

Choosing $\hat{v} = (\phi\hat{U})^h \in \hat{V}_h$ in EG2 according to (16.4), where ϕ is a positive test function and the superscript h indicates interpolation into \hat{V}_h , we get assuming \hat{U} is bounded

$$\begin{aligned} \int_Q E(\hat{U})\phi \, dxdt &= ((h\phi R(\hat{U}), R(\hat{U})) + ((R(\hat{U}), (\phi\hat{U})^h - \phi\hat{U})) \\ &\quad + ((hR(\hat{U}), R((\phi\hat{U})^h) - R(\phi\hat{U}))) + \tilde{R}, \end{aligned}$$

where $\tilde{R} \geq -C\sqrt{h}$ with $C > 0$ depending on first order derivatives of ϕ and the maximum of \hat{U} . We now use so-called *super-approximation* to obtain

$$\|\phi\hat{U} - (\phi\hat{U})^h\| \leq Ch\|\hat{U}\|,$$

with the notable feature that we gain one power of h without paying any first derivative price on \hat{U} . This is because $\phi\hat{U}$ is the product of a smooth function and a function in the finite element space \hat{V} . Combined with the basic energy estimate bounding $\|\sqrt{h}R(\hat{U})\|$, it follows that

$$\int_Q E(\hat{U})\phi \, dxdt \geq -C\sqrt{h},$$

which proves that G2 is a dissipative weak solution, as desired. This represents one of the most important proofs in the book. Notice that we assume \hat{U} to be bounded but not derivatives of \hat{U} , which would make the proof meaningless.

Summary of Mathematical Aspects

My feeling is that many mathematicians and graduate students are intrigued by what they hear about problems of the mechanics of an incompressible fluid, but don't study them because they don't know enough physics and fear to make fools of themselves. What they don't know, I think, is how abysmally little we actually know about fluids, and how it would be hard to act more the fool than many have already done. I believe the difficulty arises first, over an inflated nomenclature that burdens the subject and, second, over a lack of understanding about how ignorant we can be in our technological society and how close to the surface many problems lie.... In spite of the profound mathematical methods we use to attack the problems, we know very little about fluids, we can tell the physicist almost nothing of what he wants to know, and interesting problems abound. (Marwin Shinbrot, 1973)

Our consciousness does not reflect the molecular chaos of the phenomena but exerts an integrating function with respect both space and time, from results the apparent homogeneity and continuity of the phenomena. (Weyl)

Blind fate could never make all the planets move one and the same way in orbs concentric. (Newton)

20.1 Outputs of ϵ -weak Solutions

We have introduced the concept of ϵ -weak solutions to the NS equations. To estimate the difference in output of two ϵ -weak solutions \hat{u} and \hat{w} , $M(\hat{u}) - M(\hat{w})$, with $M(\hat{u}) \equiv ((\hat{u}, \hat{\psi}))$ defined by a function $\hat{\psi}$, we introduced a linearized dual problem with coefficients depending on u and w and estimated derivatives of the solution of the dual problem in a corresponding stability factor $S_\epsilon(\hat{\psi})$, to get

$$|M(\hat{u}) - M(\hat{w})| \leq 2\epsilon S_\epsilon(\hat{\psi}).$$

We next noted that a G2-solution \hat{U} is an $C_U \|hR(\hat{U})\|$ -weak solution, and this way we obtained an a posteriori output error estimate of the form

$$|M(\hat{u}) - M(\hat{U})| \leq (\epsilon + C_U \|hR(\hat{U})\|) S_{\epsilon_{G2}}(\hat{\psi}),$$

with $S_{\epsilon_{G2}}(\hat{\psi})$ a corresponding stability factor, and $\epsilon_{G2} = C_U \|hR(\hat{U})\|$. Simplifying, assuming ϵ small (and $C_U \leq 1$), the a posteriori error estimate took the form

$$|M(\hat{u}) - M(\hat{w})| \leq \|hR(\hat{U})\| S_0(\hat{\psi}), \quad (20.1)$$

and the corresponding stopping criterion was

$$\|hR(\hat{U})\| S_0(\hat{\psi}) \leq TOL.$$

If the stability factor $S_0(\hat{\psi})$ is not too large and the tolerance TOL not too small, then we may be able to reach the stopping criterion with available computer power.

We have pointed out a basic feature of the a posteriori error estimate resulting from the properties of G2, namely the presence of the factor h multiplying the residual $R(\hat{U})$. If $S_0(\hat{\psi})$ is not too large, this means that we may reach the stopping criterion *without the residual $R(\hat{U})$ being pointwise small*. We may thus compute an accurate mean value output from a discrete solution with a pointwise large residual. In a turbulent flow we may expect (and actually see in computations) that pointwise $R(\hat{U}) \sim h^{-1/2}$. This evidence strongly indicates that the mere idea of a pointwise solution to a turbulent flow will have to be refuted. As already pointed out above, this is in direct opposition to the Clay Institute formulation of its Prize Problem concerning existence, regularity and uniqueness of pointwise solutions to the NS equations.

20.2 Chaos and Turbulence

We have been led to the following essential aspects of a dynamical system with chaotic solutions such as the NS equations: (i) strong sensitivity of pointwise outputs, (ii) weak sensitivity of mean value outputs, and (iii) weak sensitivity of stability factors.

To identify these features for a given dynamical system, we would first compute one trajectory $u(t)$ pointwise. We would then solve the corresponding dual problem linearized at $u(t)$ with data corresponding to pointwise output to find a large stability factor, and with data corresponding to a mean value output to find a stability factor which is not large. This would give evidence of (i) and (ii). In particular we would get the information that the mean value output would be insensitive to solution perturbations, and thus that we could expect to be able to compute the mean value output from only one solution trajectory.

There would be one piece of information missing, namely (iii) which represents insensitivity of the mean value stability factor to the choice of solution trajectory underlying the linearization in the dual problem. To get evidence of this insensitivity, we would have to compute a couple of different solutions

$u(t)$ by introducing some perturbations and then solve the corresponding dual problems. The evidence would then be that the corresponding stability factors would be insensitive to the perturbations. In particular, we would get the signal that the more precise nature of the perturbations would be insignificant.

In this book we present evidence that turbulent flow has the features (i)-(iii) and thus carries the basic features of the type of chaos we suggest above. The result is that a mean-value output may be observable/computable to a tolerance of interest under statistical perturbations of input of unknown nature, while a point value is not.

In a turbulent flow a lot of detailed information is destroyed in dissipation, which thermodynamically connects to a substantial increase of entropy. In order for a mean value in turbulent flow to be well defined, it cannot have other than a weak dependence on the destroyed information, and indeed we observe this to be a real phenomenon since we find mean value aspects of turbulent flow to be computable without resolving all details of the flow. Thus certain aspects of turbulent flows may be computable, in fact, sometimes more easily computable than laminar flows, which may show a stronger dependence on details.

This is in contrast to a conventional standpoint, where turbulent flow may seem to be uncomputable without turbulence models, which are difficult if not impossible to design. In this book thus we give concrete evidence that turbulent flow is computable, in fact often computable on a PC within hours.

20.3 Computational Turbulence

We have pointed out that the secret of computational turbulence is to understand how it may be possible to compute mean value outputs, while point-value outputs are not computable. We have noted that this can be explained by the stability properties of the dual solution, which by cancellation effects is smaller for mean-value outputs than for point-values. Thus we may say that the secret lies in the cancellation in the dual problem, which may be observed to take place by simply computing the dual solution. We may also analyze the cancellation effect in simple model problems, but it seems impossible to mathematically analyze this cancellation effect in any realistic situation. Thus we may get a glimpse of the secret, but we seem to be unable to capture the whole truth by mathematical analysis. Our lives may carry a similar secret: we may observe what we experience/compute as we go along and we may understand some aspects, but the full truth will remain hidden.

20.4 Irreversibility

We have unfolded the secret of irreversibility in reversible systems in the special case of incompressible inviscid flow governed by the Euler equations

solved by G2. We have seen that the irreversibility is a necessary consequence of the non-existence of stable pointwise solutions of the Euler equations and the dissipative nature of G2 when computing approximate solutions. We may phrase our result as a proof of the 2nd Law of thermodynamics from the 1st Law combined with finite precision in the form of G2. We have remarked that EG2 is a parameter-free mathematical model of (a part of) the World in the spirit of Einstein.

Part III

Secrets

21

Secrets of Ball Sports

Football is not a matter of life and death. It is more important than that.
(Bill Shankly)

If a player is not interfering with play or seeking to gain an advantage, then he should be. (Bill Shankly)

21.1 Introduction

Major ball sports such as football, golf, tennis, and baseball, gather millions of fans at stadiums and TVs around the world every day. Can we understand the secrets of physics underlying the stunning performances of Ronaldinho, Tiger Woods, Roger Federer, Hideki Matsui and the others?

Using a moving frame of reference centered at the sphere, a ball moving through air, without any external wind load, corresponds to a stationary sphere in a uniform flow in the opposite direction of the velocity of the ball. To investigate the aerodynamics of ball sports we therefore consider the flow of air past a sphere, and in particular we focus on the resulting forces on the sphere; that is drag and lift of the sphere, with drag being the force component in the direction of the flow, and lift being the force in a direction perpendicular to the direction of the flow.

21.2 Dimples of a Golf Ball: Drag Crisis

Drag consists of the pressure drop over the sphere, referred to as *pressure drag*, and the viscous friction forces acting on the surface of the sphere, referred to as *skin friction*. We will see in Chapter 34 that the skin friction is decreasing with increasing Reynolds number, so that for high Reynolds numbers typically pressure drag is dominating. Pressure drag is connected to flow separation, see Chapter 35, where earlier separation in general leads to higher pressure drag.

The drag coefficient of a sphere for Reynolds numbers of the order $10^3 - 10^5$ is $c_D \approx 0.4$, with c_D a non dimensional normalization of the drag force F_D , defined by

$$c_D = \frac{1}{\frac{1}{2}\rho U_\infty^2 A} \times F_D, \quad (21.1)$$

with U_∞ the free stream velocity, A a representative area of the sphere, typically $A = \pi d^2/4$ with d the diameter of the sphere, and ρ is the density. The *dynamic pressure* p_{dyn} is defined as

$$p_{dyn} = \frac{1}{2}\rho U_\infty^2, \quad (21.2)$$

and we can thus express the drag coefficient $c_D = F_D/(p_{dyn}A)$ as the ratio of the drag force and the force corresponding to the dynamic pressure p_{dyn} acting on the area A .

At very high Reynolds numbers, of the order $10^5 - 10^6$, the boundary layer at the surface of the ball suddenly undergoes transition to turbulence, which leads to a delayed separation and a dramatic drop in c_D to about 0.1, referred to as *drag crisis*. It is the increased momentum near the boundary in a turbulent boundary layer that delay separation, see Chapter 35.

In golf we may want to drive the ball as far as possible, and thus we want to minimize the drag of the golf ball. As the golf ball moves through the air, the drag will lead to a reduction of its velocity, and thus also the corresponding Reynolds number. To minimize drag we would thus like the drag crisis to hold for as long part of the ball trajectory as possible, that is, for as low Reynolds numbers as possible.

Prandtl and Wieselsberger showed in a classical experiment that it is possible to induce drag crisis at a lower Reynolds number by introducing perturbations in the boundary layer, which connects to transition in a boundary layer being dependent of the product of Reynolds number and perturbation level, see Chapter 36. Thus by introducing perturbations in the boundary layer we would be able to induce drag crisis at a lower Reynolds number, which is exactly the effect of the dimples of a golf ball.

The skin friction of the boundary layer is decreasing with increasing Reynolds number, and we may computationally model drag crisis by using G2 together with a skin friction boundary condition, see Chapter 35. Decreasing skin friction then leads to delayed separation, see Fig. 21.1.

21.3 Topsin in Tennis: Magnus Effect

In a number of ball sports we are familiar with the phenomenon that a spinning ball seems to experience a force in the direction of the rotation. This is what we see in a topspin in tennis, or a curve-ball in baseball, and we refer to this phenomenon as the *Magnus effect*.

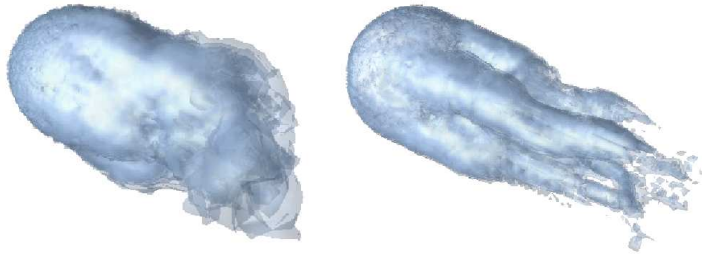


Fig. 21.1. Vorticity for a sphere before (left) and after (right) drag crisis.

The notion of the Magnus effect goes back to Lord Rayleigh, who credited Heinrich Gustav Magnus for the first explanation of the lateral deflection of a spinning ball [85]. But the phenomenon was studied already by Newton in 1672, who noted how a tennis ball is affected by spin, and by Benjamin Robins (1707–1751), referred to as “the father of science of ballistics”, who in 1742 [96] showed that a transverse aerodynamic force could be detected on a rotating sphere (therefore also referred to as the “Robins’ effect”). Robins’s book [96] attracted the interest of Euler, who was the leading expert on hydrodynamics at the time, and in 1745 Euler translated the book into German. Although excited by Robins work, Euler considered Robins findings of a side force for a spinning projectile as a mistake related to shortcomings of the experimental device. The dismissal by Euler resulted in Robins’ findings not being taken seriously, and still today Robins has not received the recognition he deserves [102].

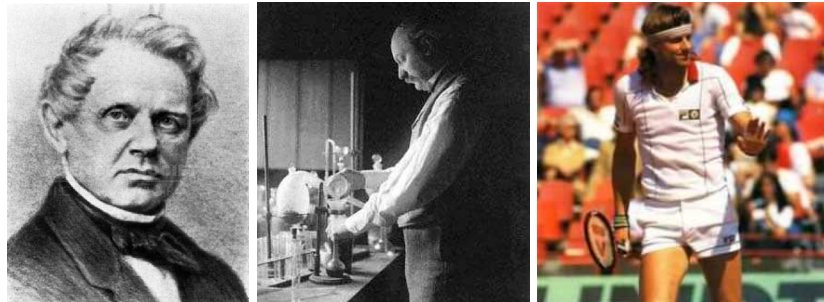


Fig. 21.2. Heinrich Gustav Magnus (1802–1870), John William Strutt/Lord Rayleigh (1842–1919), and Björn Borg.

The traditional explanation of the Magnus effect for a spinning sphere is based on Bernoulli’s Law, with the idea that the fluid velocity on one side of the sphere is enhanced by the spin of the sphere, and the velocity on the opposite side is decreased, resulting in a pressure difference over the

sphere, and thus a lift force, “the Magnus force”, should be created. However, drawing conclusions from Bernoulli’s Law in turbulent flow is risky, and so this simplistic argument may not reflect realities.

The modern explanation is instead based on boundary layer separation, where the separation is delayed on the side of the sphere that is moving in the same direction as the free stream velocity, while the separation occurs prematurely on the side moving against the free stream flow, resulting in a shift of the wake toward the side moving against the free stream velocity, causing a deflection of the flow momentum and a resulting force in the opposite direction, by conservation of momentum.

In Fig. 21.3 we give support to the modern view in a G2 simulation of a rotating sphere, where we note the asymmetric wake with a corresponding low pressure on the side moving with the free stream velocity, and asymmetric deflection of the flow creating a lift force by conservation of momentum.

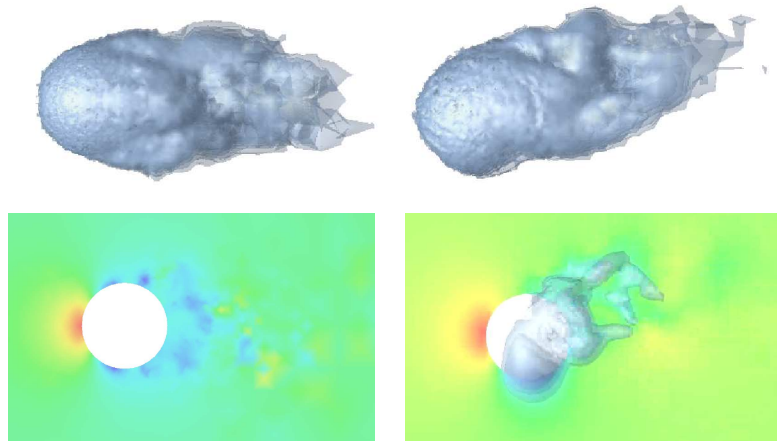


Fig. 21.3. Pressure for a still (left) and a rotating (right) sphere.

21.4 Roberto Carlos: Magnus Effect

To defend against a free-kick in football the goalkeeper is assisted by a wall of defenders, leaving the goalkeeper responsible for only a reduced part of the goal. A skilled player is able to curve the ball around the defensive wall to place the ball in the part of the goal that the goalkeeper has left to the wall to defend. The key to curving the ball is to give the ball a spin, resulting in a side force by the Magnus effect. In Fig. 21.4 we show the famous free-kick of Brazil’s Roberto Carlos against France in 1997, where the spin of the ball

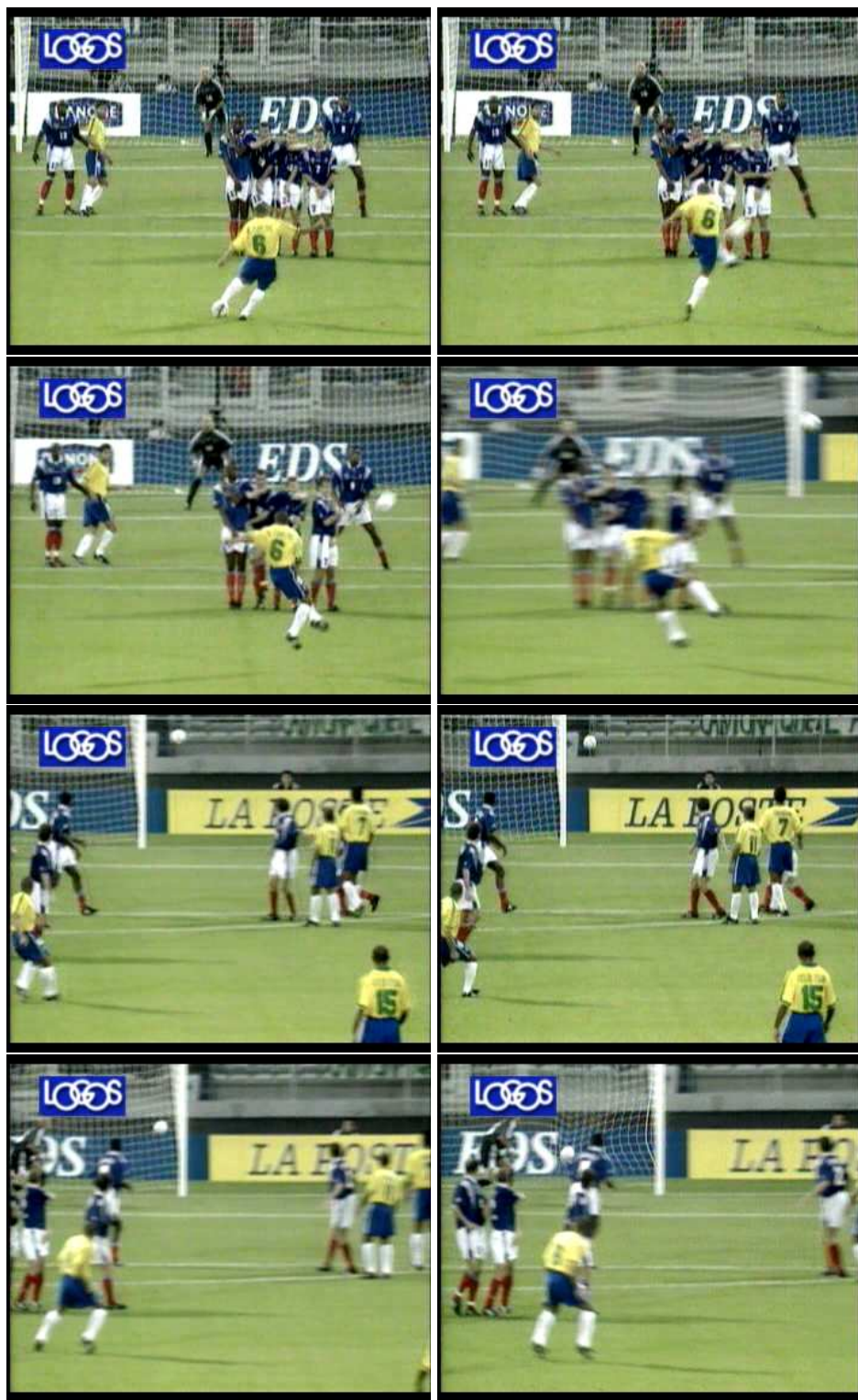


Fig. 21.4. The Brazilian Roberto Carlos' free-kick against France in 1997.

results in a very strong Magnus effect causing the ball to curve around the defenders.

At certain conditions what is known as the *reverse Magnus effect* has been noted for smooth spheres, where the resulting force is acting in the opposite direction to the “regular” Magnus force. This appears to be caused by transition in the boundary layer of the sphere on one side only, the side with the highest relative velocity, which leads to a delayed separation on that side, resulting in a shift of the wake toward the opposite direction compared to the “regular” Magnus effect. For a typical shot in football, the Reynolds number is of the order 10^5 , thus in the region close to drag crisis. It is speculated [23] in the reverse Magnus effect being involved in the free-kick of Carlos, where the ball initially appears to be moving away from the goal, clearing the wall of defenders, before curving back to end up behind the stunned French goalkeeper.

21.5 Pitching: Drag Crisis and Magnus Effect

Baseball has received a lot of attention among fluid dynamicists, see e.g. [12, 7]. When the pitcher throws the ball, assuming no wind, the only forces acting on the ball in the air is gravity and the aerodynamic forces of lift and drag. Using different spins and velocities, the pitcher has an arsenal of throws to challenge the batter.

For example, a *curve-ball* is thrown with a forward spin resulting in a Magnus force down and an exaggerated curve of the ball.

On the other hand, a *fastball* is thrown with a backward spin, resulting in a Magnus force opposite the force of gravity, minimizing the fall of the ball. There is also the *rising fastball* where supposedly the Magnus force is stronger than gravity causing the ball to rise. Although, this is considered to be a baseball myth.

A *knuckleball* is thrown with a very slow rotation, leading to a slightly wobbling trajectory of the ball which is hard to predict by the batter. One explanation of this phenomenon is that with a velocity corresponding to a flow near drag crisis, transition to turbulence in parts of the boundary layer is triggered by the seams of the ball, whereas other parts of the boundary layer remain laminar, resulting in a wobbling trajectory of the ball [109]. Recently, with the new ball design, players like the Italian Andrea Pirlo have made themselves famous for introducing the knuckleball also in football.

Secrets of Flight

Heavier than air flying machines are impossible. (Lord Kelvin (1820–1907), remark to Royal Society 1895)

I am convinced that human flight is both possible and practical. (Wilbur Wright 1899)

It will probably be many decades before computers are powerful enough to simulate in a detailed manner the fluid flows over an entire airplane. (Parviz Moin and John Kim in Scientific American in 1997)

22.1 Generation of Lift

The basic secret of flight is how to generate a lift force balancing the gravitational force acting on an airplane, while keeping the drag force so small that the velocity can be maintained. The basic question then concerns how to design a wing generating high lift with little drag.

For a symmetric flow around an object the lift oscillates around a zero mean value as we have seen in the cylinder flows in Chapters 12,19. On the other hand, the asymmetric flow around a spinning sphere generates a significant lift force by the Magnus effect, as we saw in Chapter 21. Asymmetric flow past an object can also be generated by an asymmetric shape of the object. Asymmetry of the flow around a wing can be induced by tilting the wing in the direction of motion in an *angle of attack*, and/or by an asymmetric shape of the wing. The asymmetry of the flow generates momentum and thus lift, which is also manifested by a low pressure on top of the wing and a high pressure below.

We shall see below that the lift is roughly proportional to the angle of attack below an angle of *stall*, above which the lift drops while the drag continues to increase.

Both the drag and lift force scale with the square of the velocity, which qualitatively can be motivated by Bernoulli's Law. If the take-off (and landing)

speed is 300 km/hour speed, while the cruising speed is 900 km/hour, it means that the angle of attack has to be about $3^2 = 9$ times as large at take-off than at cruising.

22.2 Simulation of Take-off

We now simulate using EG2 (see Chapter 19) the flow around a wing, increasing the angle of attack α from zero while keeping the speed constant, which simulates the critical phase of the take-off when at maximal ground speed the angle of attack suddenly is increased to generate maximal lift and take the plane off ground. For simplicity we consider a section of a long wing, which means that we here leave out the effects from the wing tips, engines and the body of the plane. The wing cross section is the NACA 0012 profile based on the NACA 4-digit series [4], which is symmetric in the vertical direction (with the wing horizontal), with a length of the wing 4 times the chord length. We shall see that we can use this model to understand basic features of lift generation under different angles of attack.

In Fig. 22.1–22.4 we present pressure, velocity and vorticity for a simulation of take-off with the increasing angles of attack $\alpha = 0, 4, 12, 14, 16, 18, 20, 22^\circ$, realized by changing the direction of the incoming free stream velocity, using a moving frame of reference centered at the wing, while keeping the wing horizontal. We see the pressure difference on top and below the wing develop as the angle of attack increases. We see that most of the lift is generated close to the leading edge of the wing for small angles, while for larger angles more of the wing is engaged. We see that the flow above the wing becomes increasingly turbulent as $\alpha \geq 12^\circ$, with considerable generation of vorticity.

We show the lift and drag forces in Fig. 22.5 as functions of α . We see that the lift increases linearly up to $\alpha \approx 16^\circ$, and then increases more rapidly up to $\approx 20^\circ$, after which the lift suddenly drops off to a about half of the maximum. The corresponding drag stays small with a linear increase until $\alpha \approx 16^\circ$, followed by a quick increase up to $\alpha \approx 20^\circ$, after which follows a slower roughly linear increase.

We may consider stall to occur at $\alpha \approx 16^\circ$, since the drag increases very quickly beyond this angle and may cause the plane to loose speed. Alternatively, with powerful engines we may consider stall to occur rather at $\alpha \approx 20^\circ$ since the lift drops off quickly beyond this angle. We see that for $\alpha \geq 22^\circ$, the lift stabilizes while the drag increases linearly, indicating that flying with larger angles of attack than 22° is not economical at all. Of course, fighter planes may occasionally violate this rule at sudden changes of direction.

A design criterion for a wing may be to maximize the lift/drag ratio at cruise. In Fig. 22.5 we find a fairly flat optimum for small angles of attack up to 10° .

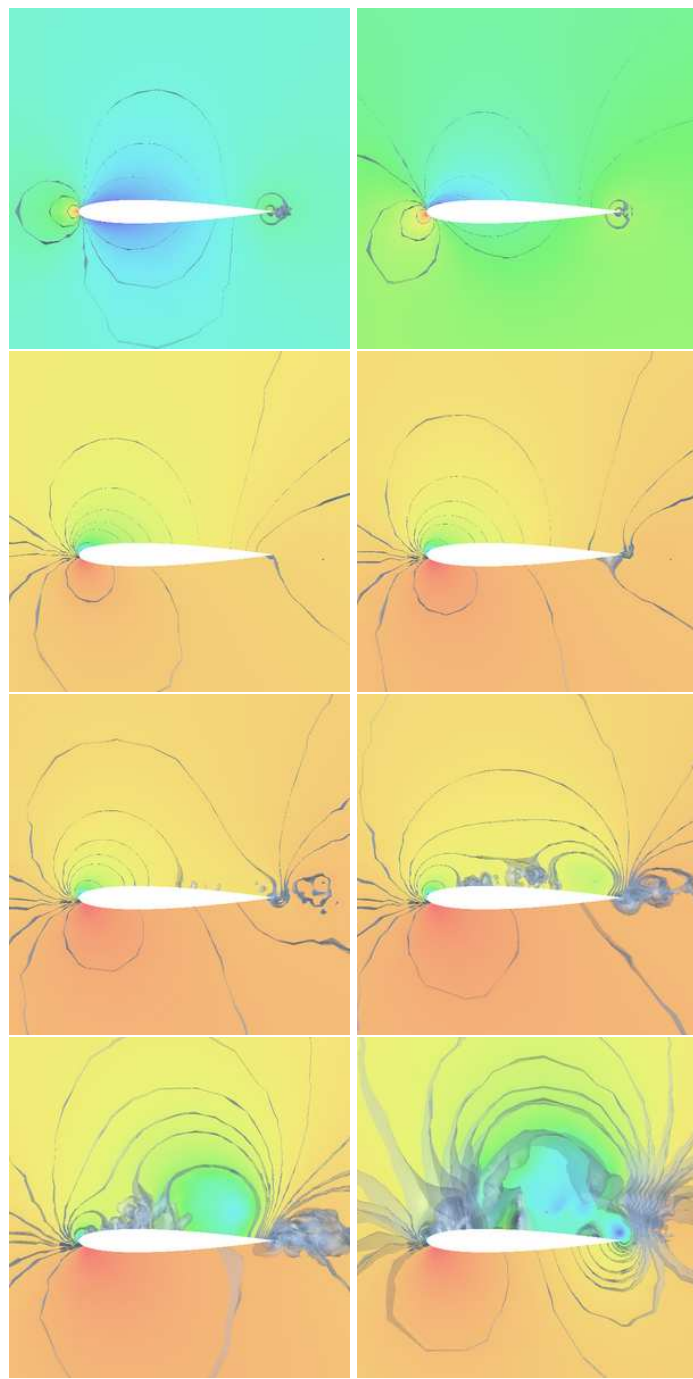


Fig. 22.1. Pressure for a 3d wing using EG2, with increasing angle of attack; 0,4,12,14,16,18,20, and 22°.

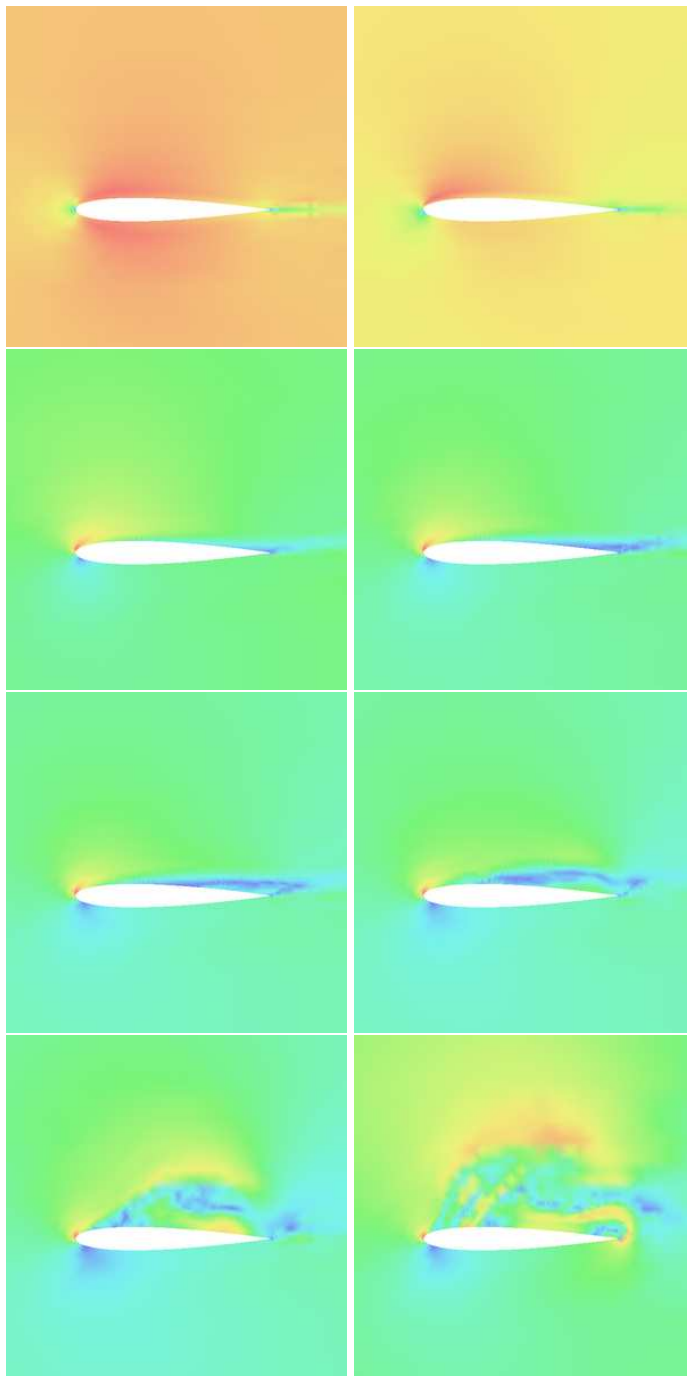


Fig. 22.2. Magnitude of the velocity for a 3d wing using EG2, with increasing angle of attack; 0,4,12,14,16,18,20, and 22° .

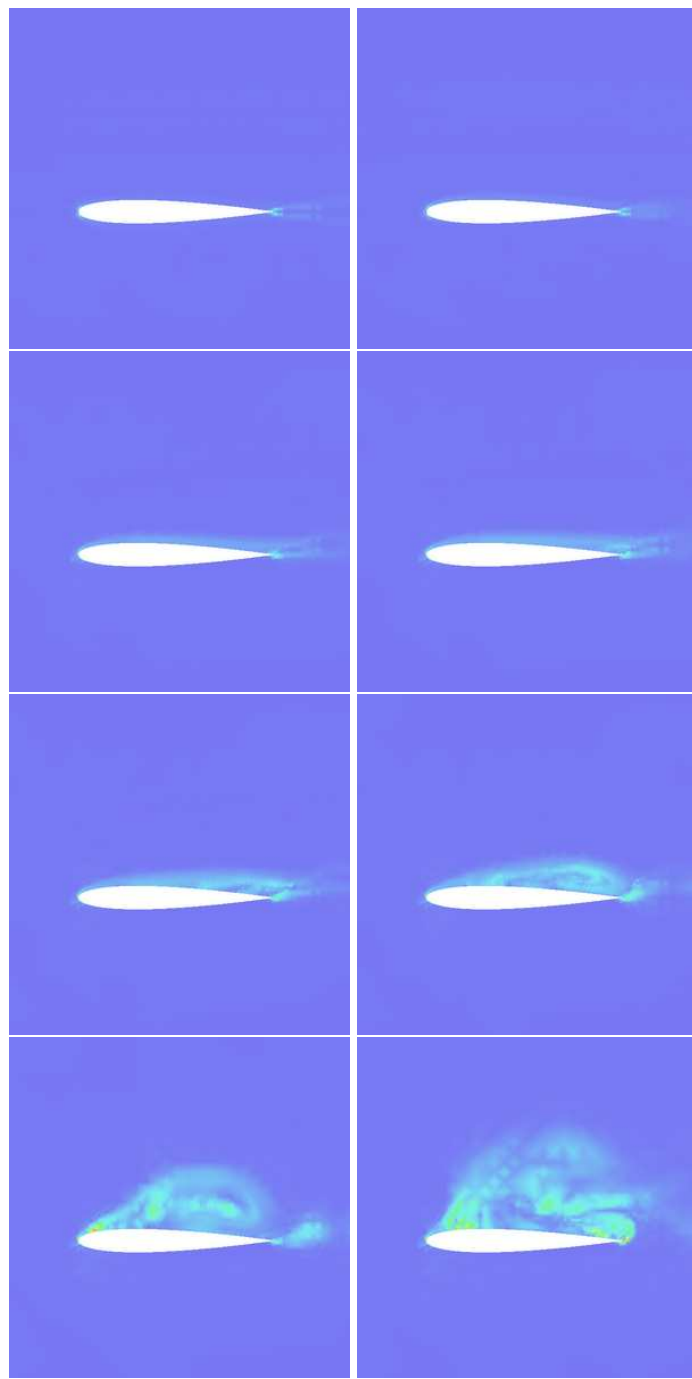


Fig. 22.3. Magnitude of the vorticity for a 3d wing using EG2, with increasing angle of attack; 0,4,12,14,16,18,20, and 22°.

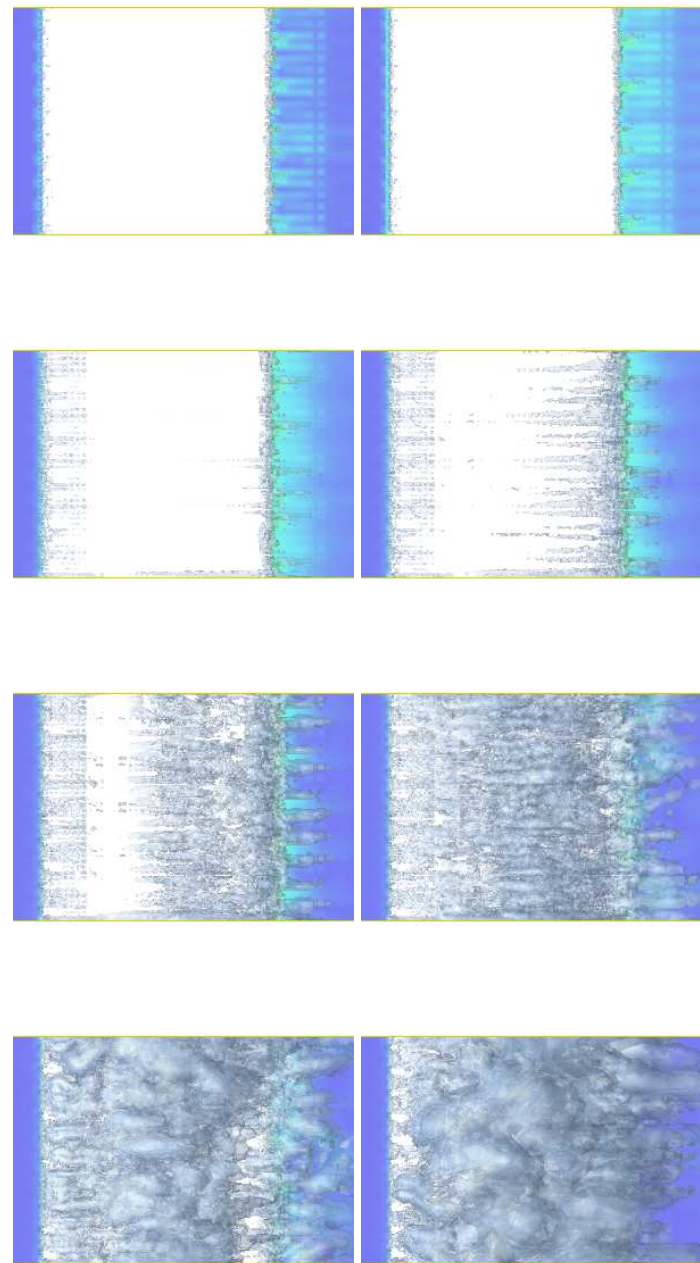


Fig. 22.4. Magnitude of first 2 vorticity components $|(\omega_1, \omega_2)|$ for a 3d wing using EG2 (with the third component in the direction of the wing), with increasing angle of attack; 0,4,12,14,16,18,20, and 22°.

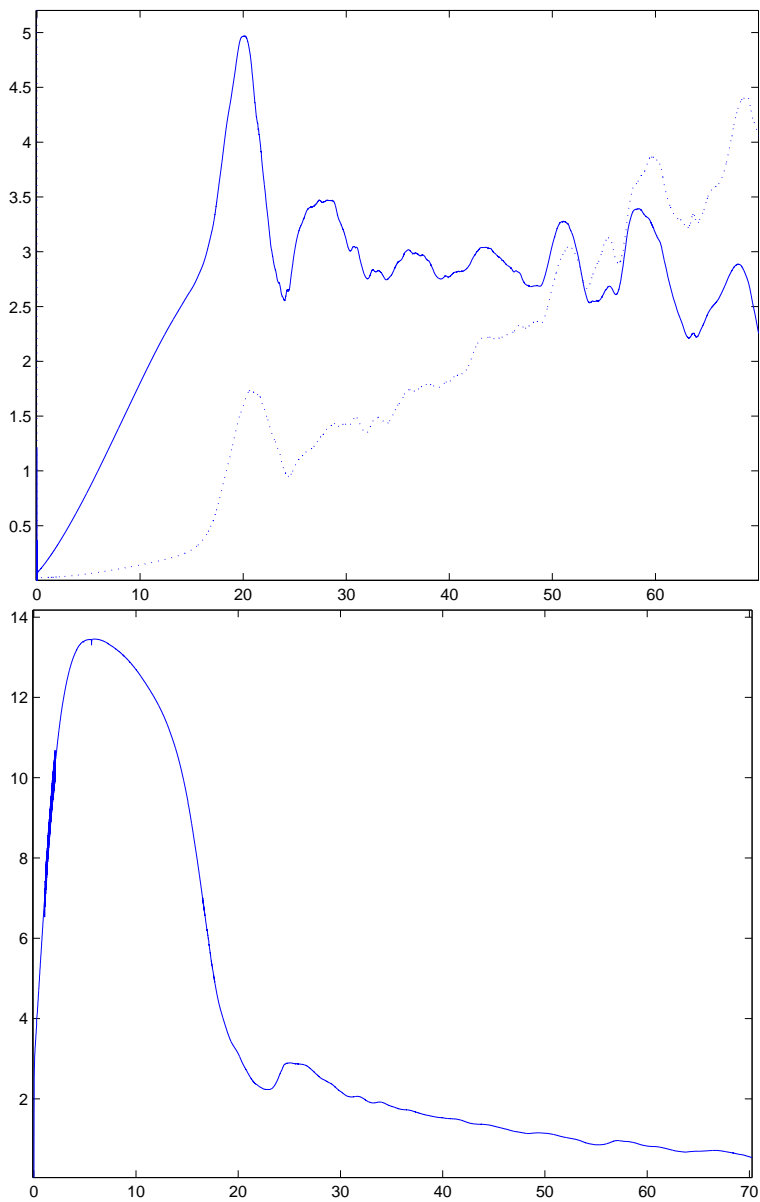


Fig. 22.5. Aerodynamics forces for a NACA 0012 profile (upper), using EG2 in a unit free stream under increasing angle of attack: lift force ('-') and drag force ('::'), not normalized with respect to wing area, and lift/drag ratio (lower).



Fig. 22.6. Take-off of full aircraft (picture from SAS Group).

22.3 More on Generation of Drag

Why is drag suddenly increasing after $\alpha \approx 16^\circ$? Well, starting at $\alpha = 0^\circ$ we see that the flow is more or less symmetric with separation at the trailing edge accompanied by tubes of streamwise vorticity generated. This is similar to the separation for the circular cylinder in Chapter 12, with the difference that for the wing the separation point is fixed at the trailing edge. As now α increases the separation point (line) on the upper surface of the wing starts to move upstream, with an associated recirculation zone developing. Vorticity streaks are generated by the acceleration of the flow in the recirculation zone, and as the recirculation zone reaches a critical point near the position of the maximum camber, turbulence is developing on the upper surface of the wing leading to increased drag.

As α is further increased the recirculation zone keeps moving upstream, to finally induce separation very near the leading edge as $\alpha \approx 20^\circ$, leading to a decreasing lift when further increasing α .

22.4 A Critical View on Kutta-Zhukovsky

Having studied the complex turbulent flow around a wing under increasing angle of attack, we understand that the modified potential flow solution suggested by Kutta and Zhukovsky has no chance to describe this phenomenon. It is possible that for small angles of attack, Kutta-Zhukovsky may reasonably well predict the lift (but not the drag), but it is clear that for larger angles

of attack the modified potential solution does not describe anything near the real flow, and thus cannot be useful.

22.5 The Challenge

The challenge is to simulate the turbulent flow around a full aircraft at take-off, including all details of the airplane, with jet engine, landing gear, wheels etc. This has apparently not been done. With friction boundary conditions in EG2 we can probably avoid the resolution of boundary layers, and thus the challenge does not seem unsurmountable. We expect to be able to compute mean value output using less than 10^8 mesh points, which is today possible and will be standard tomorrow.

23

Secrets of Sailing

Mechanics is the paradise of the mathematical sciences, because by means of it one comes to the fruits of mathematics. (Da Vinci Notebooks)

For, one day, well off the Patagonian coast, while the sloop was reaching under short sail, a tremendous wave, the culmination, it seemed, of many waves, rolled down upon her in a storm, roaring as it came. I had only a moment to get all sail down and myself up on the peak halliards, out of danger, when I saw the mighty crest towering masthead-high above me. The mountain of water submerged my vessel. She shook in every timber and reeled under the weight of the sea, but rose quickly out of it, and rode grandly over the rollers that followed...It reassured me against rude Cape Horn. (Joshua Slocum (1844–1909) in Sailing Alone Around the World)

23.1 The Sail

The main secret of sailing is how to advance against the wind. This is accomplished by *tacking*, which means that the boat moves in a direction about 45° from a direction directly against the wind, alternating from one side to the other changing the position of the sails from one side to the other, see Fig. 23.2.

Of course you know that a sail acts like an airfoil giving a lift which partly pulls the boat against the wind and partly tilts the boat away from the wind direction. The effective angle of attack may be about 20° for a good sailor when pinching at minimal tacking angle, which takes into account the motion of the boat which may change the apparent wind direction by say 15° depending on the speed of the wind and the boat, see Fig 23.1. It also accounts for a change of angle of about 10° because of the drift (leeway) with the boat pointing roughly 35° against the true wind, while effectively moving in a direction of 45° . The angle of attack 20° , change to apparent wind direction of 15° and leeway 10° , then add up to $\approx 45^\circ$. Fig 23.3 shows a stalling sail at an angle of attack of 27° from a wind tunnel test.

In the previous chapter, we found that an angle of attack of about 20° gave maximal lift for an airfoil, with one component in the direction of motion (drive) and one perpendicular component (heel), and thus seems to be optimal for drive, since the drag from the sail is small compared to the drag on the hull from the water. We understand that the air flow around the sail thus is heavily turbulent all along the back of the sail, and from the pressure distribution we understand that the whole sail is engaged in creating the drive, not only the part closest to the mast, which would be the case for a small angle of attack.

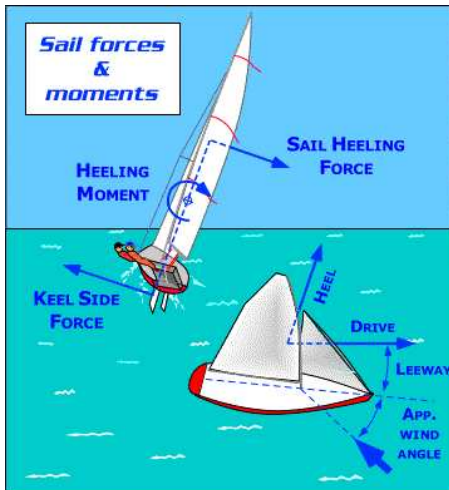


Fig. 23.1. Forces and moments acting on a sailing boat

23.2 The Keel

The keel and rudder have the shape of a symmetric air foil and gives a lift from the motion through the water, which balances the heel tilting the boat, see Fig 23.1. You cannot sail without a keel, and cannot control the boat without a rudder. The angle of attack of the keel is equal to the leeway, and thus may be about 10° , while the angle of attack of the rudder is variable giving a variable lift force, thus controlling the momentum of the combined force from keel and rudder. We have seen that for an angle of attack up to 10° , the lift force is concentrated to the leading edge of an air foil, which explains why modern boats have separated (surprisingly) deep and narrow keels and rudder combining high lift with little skin friction (and fast reaction to the rudder). Older designs have a long not so deep keel with the rudder often mounted on the keel, and are not competitive in speed but do not require the same fast and precise control of the rudder.



Fig. 23.2. Pinching at 20° of attack.



Fig. 23.3. Stall at 27° .

23.3 The Challenge

The computational challenge is to simulate the turbulent flow around a sailing boat including the air flow around the combined configuration of a jib and a main sail mounted on a mast and the motion of the hull through water and waves. This has never been done by solving the Euler/NS equations. We believe it is possible to take on the challenge using G2 and we plan to do so.

Secrets of Racing

Nevertheless, no F1 designer would ever underestimate the benefit to be gained by reducing the frontal area of the car. This prompted 1986 Williams FW11B drivers Nelson Piquet and Nigel Mansell to try and sit as low in the car as possible, each hoping to out-do each-other. Mansell discovered that by removing his seat, he lowered his position in the car by just 1.5 centimeters, which translated into an additional 25kg of downforce. (F1 Nutter [2])

24.1 Downforce

Formula One racing cars have the power to produce wheel spin for velocities higher than 100 mph. To allow the tires to transmit a greater thrust without wheel spin, and thus to increase acceleration, a major design goal for a F1 racing car is to maximize *downforce*, that is negative lift. downforce is also crucial for increasing the cornering ability.

The key to create downforce for a F1 car is the design of the front and rear wings, which are regular wing profiles turned upside down and thus generating negative lift. The front wings contribute to 25–40% of the downforce, and the rear wing to about one third [3]. Although, there is a trade-off between downforce and drag, so that increasing downforce through the design of the wings result in higher drag. Thus the specific design of the wings is frequently modified depending on the driver and the track.

Another important part of the car for downforce is the *diffuser*, which is the rear section of the car's floor where air flowing under the car exits. The exit speed of air is controlled by the design of the diffuser, with a higher speed corresponding to a lower pressure under the car, by Bernoulli's Law, and thus a higher downforce.



Fig. 24.1. Downforce and drag for F1 car.

24.2 The Wheels

The wheels of the car are considered to be the major sources of drag, and in addition the exposed wheels result in a significant lift force, reducing the downforce with about 11% for a typical F1 car [3].

Wind-tunnel testing of the wheels is associated with several problems: (i) letting air flow past a stationary car in a wind tunnel will induce a boundary layer near the floor, not present for a moving car, and (ii) the flow past a rotating wheel and a non rotating wheel is different. More advanced wind tunnels aim to overcome the difficulty (i) by trying to eliminate the boundary layer by techniques of blowing and suction, and (ii) by constructing a moving belt

so that the wheels can rotate. Even so, some problems remain and new ones are created, for example, typically a moving belt construction cannot carry the weight of a full size car leading to additional constructions supporting the car influencing the validity of the flow measurements.

The use of CFD is thus very attractive; with a reliable and efficient computational method, a computational model of the car is built in the computer for which the aerodynamic performance of various designs is easy to investigate.

In Fig. 24.2–24.3 we present results from a G2 computation of the flow of air past a model of a rotating wheel. We compare with a computation for a corresponding stationary wheel, modeling wind tunnel testing. We find that the two flows are completely different, indicating that the results from a simple wind tunnel testing may be completely misleading. We describe the computations in detail in Chapter 35.

We note that drag is significant, and that also the generated lift from the wheel is high.

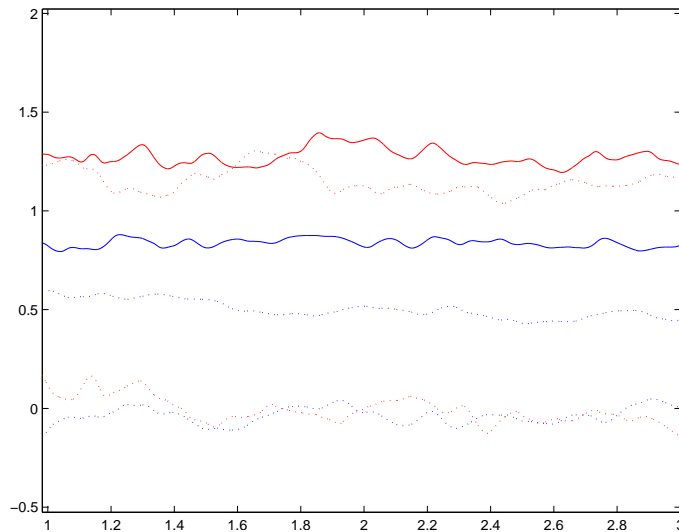


Fig. 24.2. Aerodynamic forces on the wheel: $c_D \approx 1.3$, $c_L \approx 1.2$ for the rotating wheel, and $c_D \approx 0.8$, $c_L \approx 0.5$ for the non rotating wheel. The side force is approximately zero for both cases.

24.3 Drag and Fuel Consumption

For a regular car, downforce is not the critical design criterion. On the other hand, the drag of a car directly couples to fuel consumption, and thus minimiz-

ing drag of a design is crucial for fuel economy, and reducing the environmental load from carbondioxid emission.

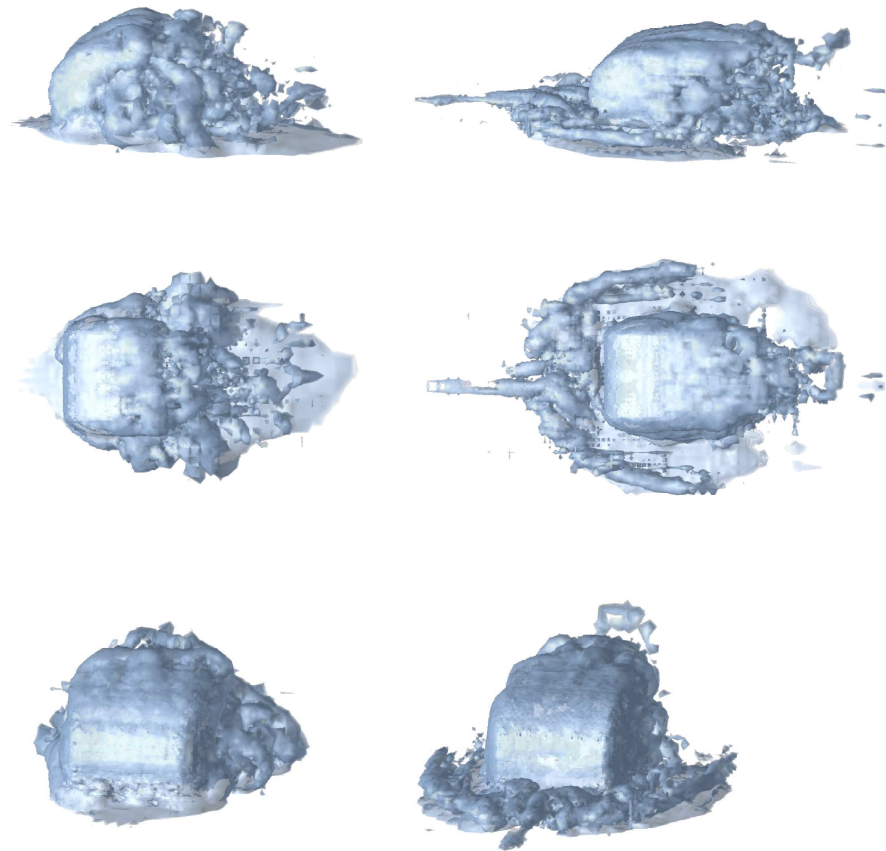


Fig. 24.3. G2 solutions of the flow past a wheel: snapshots of magnitude of the vorticity for the rotating (left) and the stationary (right) cylinder.

Part IV

Computational Method

Reynolds Stresses In and Out

[upon losing the use of his right eye] Now I will have less distraction. (Leonhard Euler)

25.1 Introducing Reynolds Stresses

The traditional approach to mathematical modeling of turbulence is to seek modified NS equations satisfied by some mean value (\bar{u}, \bar{p}) of the true velocity-pressure (u, p) . In *Reynolds Averaged Navier–Stokes equations RANS* the mean value is an ensemble mean, or a time average taken over long time, while in *Large Eddy Simulation LES* the mean value is more local in space-time. The modified equations for the mean-values are sought by taking mean values of the NS equations to get the *Averaged (or Filtered) NS equations*:

$$\frac{\partial \bar{u}_i}{\partial t} + \sum_j (\bar{u}_j \bar{u}_i)_{,j} - \nu \Delta \bar{u}_i + \bar{p}_{,i} + \sum_j \tau_{ji,j} = \bar{f}_i, \quad (25.1)$$
$$\nabla \cdot \bar{u} = 0,$$

where

$$\tau_{ji} = \overline{u_j u_i} - \bar{u}_j \bar{u}_i$$

are the so-called *Reynolds stresses*. The idea is then to seek to model the Reynolds stresses in terms of the mean-values (\bar{u}, \bar{p}) in a *turbulence model* (or *subgrid model*) to get a set of modified NS equations for the mean value (\bar{u}, \bar{p}) . Many turbulence models have been proposed in the literature, see e.g. [98], but all models only seem to cover the set of test problems they were designed for, and thus lack the generality required to be able to model new problems and make predictions.

So, designing turbulence models of the Reynolds stresses seems to be a very difficult if not an unsurmountable problem. But do we really need to model the Reynolds stresses?

25.2 Removing Reynolds Stresses

Suppose that we are interested in some output $M(u, p)$ which itself is a mean value. Using a turbulence model we would then obtain the output $M(\bar{u}, \bar{p})$ involving two mean value operations, to be compared with $M(u, p)$ with only one.

Now, averaging twice seems to be one too much, but what would be the evidence that we could live without Reynolds stresses? This would be possible if the effect of the Reynolds stresses on the output $M(u, p)$ would turn out to be small. Below we shall give computational evidence that this is true in many cases. More precisely, the computational model we use contains a stabilizing term, which may be viewed as a simple turbulence model, and we shall give evidence that the exact nature of this model has little effect on mean-value outputs. The net result is that very crude modeling of the Reynolds stresses seems to be sufficient in many cases of practical importance. We expand on this aspect in the next chapter. This means that we do not have to introduce any Reynolds stresses at all, nor model them, even if the flow is turbulent! The stabilizing term in the computational model will handle all that automatically! In particular, we settle directly for computing the mean value $M(u, p)$ and avoid introducing the double mean value $M(\bar{u}, \bar{p})$.

Obviously, avoiding Reynolds stresses greatly simplifies computational turbulence modeling, since any chosen known turbulence model could be questioned on very good grounds.

Smagorinsky Viscosity In and Out

The lateral transfer of momentum and heat by the non-linear diffusion, which parametrically is supposed to simulate the action of motions of sub-grid scale, accounts for a significant portion of the total eddy transfer. Although no direct comparison with the corresponding transfer in the real atmosphere is available, intuitively our small-scale diffusion appears to play too large a role. (Joseph Smagorinsky, 1963)

26.1 Introducing Smagorinsky Viscosity

The classical *Smagorinsky eddy viscosity* turbulence model [103] for the incompressible NS equations is obtained by replacing the given constant viscosity ν by the artificial *turbulent eddy viscosity*

$$\tilde{\nu} = \nu + Ch^2|\nabla \tilde{u}|,$$

where \tilde{u} is the velocity of the NS equations with viscosity $\tilde{\nu}$, h represents a smallest scale and $C \sim 0.01$. The Smagorinsky turbulence model thus introduces an additional non-linearity since $\tilde{\nu}$ depends on the velocity \tilde{u} . The model may also be formulated with the strain rate tensor $\epsilon(\tilde{u})$ replacing $\nabla \tilde{u}$, see Chapter 28, and the constant may be changed, possibly with feed back from \tilde{u} in a *dynamical model* [42].

The energy estimate for the NS equations with the Smagorinsky turbulence model gives a bound for the term

$$\int_0^T Ch^2 \|\nabla \tilde{u}\|^3 dt,$$

which indicates that in regions of turbulence $|\nabla \tilde{u}| \sim h^{-2/3}$, assuming dissipation ~ 1 . This is consistent with a smallest scale $\sim h$ on which the change of \bar{u} is $\sim h^{1/3}$, which fits with the Kolmogorov prediction that turbulent velocities are Hölder continuous with exponent 1/3, see e.g. [41]. Thus h would indeed

represent the smallest scale of the turbulent velocity \tilde{u} in the Smagorinsky model. Effectively, the Smagorinsky turbulence model would thus change the smallest scale from $\nu^{3/4}$ without model to h , assuming $h > \nu^{3/4}$. Further, we may expect the turbulent viscosity $\tilde{\nu} \sim h^{4/3}$ in turbulent regions with local Reynolds number $\sim h^{1/3}h/h^{4/3} \sim 1$.

The Smagorinsky model is the simplest turbulence model and as such seems to behave reasonably well, e.g. in the sense that it is consistent with the Kolmogorov estimates. The Smagorinsky model increases the effective viscosity in regions of turbulence and thereby removes the finest scales of the original flow, but it also affects coarser scales because of its action through a Laplacian. To minimize the action of the Smagorinsky model on coarser scales, variants have been contemplated with more focused action only on smallest scales [46, 66].

In Chapter 28 we introduce shock-capturing artificial viscosity in G2 which adds viscosity in the form $Ch^2|R(\hat{U})|$, which is very similar to the Smagorinsky model with $R(\hat{U})$ replacing ∇U in similarly increased viscosity in turbulent regions. This similarity is no coincidence, since Smagorinsky developed his model inspired by the work of von Neumann and Richtmyer [90] on artificial dissipation for stabilization of numerical methods [73].

Now, numerical methods for the NS equations are often augmented by e.g. the Smagorinsky turbulence model, following the idea that the numerics alone will not be capable of modeling turbulence. Doing so the parameter h in the Smagorinsky model would correspond to the smallest mesh size in the numerics. In this approach turbulence modeling and stabilization of numerics are considered as separate issues, and thus the total artificial viscosity will have a contribution from Smagorinsky artificial viscosity and a contribution from the artificial viscosity needed to stabilize the numerics. The question of the relative size of these contributions then arises; if one dominates the other the dominated viscosity could be removed.

We will now advocate that the Smagorinsky artificial viscosity is too weak to stabilize the numerics, which effectively means that the artificial viscosity from least squares stabilization usually will dominate the Smagorinsky viscosity, at least on the finest scales where dissipation is needed. Another way to see this is that shock-capturing alone is not sufficient to stabilize the numerics very well; least squares stabilization is always needed, and shock-capturing only in extreme cases. The net result is that the Smagorinsky model has a little role to play in least squares numerics, and no role at all if the numerics is augmented with shock-capturing.

26.2 Removing Smagorinsky Viscosity

We have seen that Smagorinsky viscosity may be of size $h^{4/3}$, which should be compared with h in the least squares stabilization. The Smagorinsky viscosity

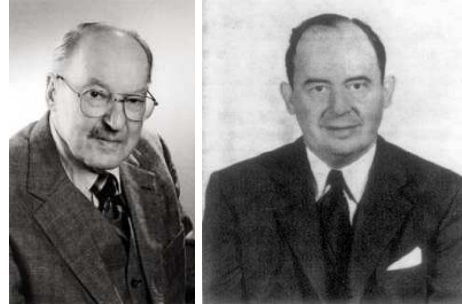


Fig. 26.1. Joseph Smagorinsky (1924–2005) and John von Neumann (1903–1957).

thus seems to be dominated by the least squares viscosity, at least on the finest scales where the dissipation is needed.

As indicated, one may pose the question if the Smagorinsky model may replace the least squares stabilization, so that Smagorinsky alone would be enough to both model turbulence and stabilize the numerics. Following this line of thought we thus consider a method for solving the NS equations based on a Galerkin method combined with the Smagorinsky model. By the analysis of G2, leaving out the least squares term, we would then be led to estimate a term of the form $\|hR(\hat{U})\|$. Using the available stability from the Smagorinsky model we would end up with an estimate of the form $\|hR(\hat{U})\| \leq Ch^{1/3}$, to be compared with the corresponding G2 estimate with instead $h^{1/2}$. Thus, it would seem that the Smagorinsky model alone could work, but not as well as G2, the difference being a factor $h^{1/6}$. This may seem pretty small but may precisely be what is needed to get that one correct decimal in the computational output which is possible to get for turbulent flow. Changing from $h^{1/2}$ to $h^{1/3}$ would increase the required number of mesh points in space for the same accuracy from N to $N^{3/2}$, thus e.g. from 10^6 to 10^9 , that is with a factor of 1000.

Our computational experience indeed shows that the Smagorinsky model alone is not sufficient to give good numerics, and that if good numerics such as G2 is used, then the Smagorinsky model has little role to play. The net result is that we see no reason to use the Smagorinsky model in conjunction with G2.

Friction Boundary Condition as Wall Model

...man will occasionally stumble over the truth, but usually manages to pick himself up, walk over or around it, and carry on. (Winston Churchill)

27.1 A Skin Friction Wall Model

An important part of the computational model for a turbulent flow is the specification of the boundary conditions. In G2 we avoid resolving all physical scales of the turbulent flow, and similarly we would like to avoid resolving the turbulent boundary layer.

To computationally resolve turbulent boundary layers would typically require many millions of mesh points and thus would be very demanding. Instead various forms of *wall modeling* have been introduced, where the turbulent boundary layer is replaced by a laminar boundary layer, modeling some aspect of the unresolved turbulent boundary layer. Traditionally, a *wall function* has been used to model the mean profile of the turbulent boundary layer, and a *wall stress model* is constructed to capture the wall stress of the turbulent boundary layer. Another approach is to use different computational models in different parts of the domain. For example, one may use RANS near the boundary and LES in the rest of the domain away from the boundary.

In G2 we use friction boundary conditions calibrated to fit a certain skin friction related to the Reynolds number, which may be viewed as a simple type of wall modeling. We thus view a turbulent boundary layer as effectively generating a certain shear force on the flow outside the boundary layer. This way we may avoid resolving the turbulent boundary layer fully, while we still open for separation without ad hoc prescribing a wall function as in traditional turbulence modeling. This model is partly inspired by the work in [67, 68], where such a boundary condition is used to study reattachment of a low Reynolds number flow past a surface mounted cube.

Our computational results in this book indicate that EG2 (see Chapter 19) with friction boundary conditions is capable of simulating a large variety of

high Reynolds number flows, for which solutions to the NS equations with resolution of boundary layers is computationally impossible. EG2 thus promises a solution to a seemingly impossible problem.

G2 for Navier-Stokes Equations

What is the Universe computing? As far as we can tell, it is not producing a single answer to a single question...Instead the Universe is computing itself. Powered by Standard Model software, the Universe computes quantum fields, chemicals, bacteria, human beings, stars and galaxies. As it computes, it maps out its own space-time geometry to the ultimate precision allowed by the laws of physics. Computation is existence. (Seth Lloyd and Y. Jack Ng in Black Hole Computers, Scientific American, Nov 2004)

28.1 Introduction

We now proceed to present G2 applied to the NS equations in detail. G2 is a weighted least-squares stabilized Galerkin finite element method in space-time. G2 is adaptive with automatic choice of the mesh in space-time based on a posteriori error estimation of outputs with stability factors/weights obtained by solving linearized dual problems. The stabilization of G2 acts as an automatic turbulence model in the form of a generalized artificial viscosity model acting selectively on the smallest scales of the mesh.

G2 may be described as an *Adaptive DNS/LES* method, where adaptively the flow is resolved in DNS in certain parts of the domain and in other parts is under resolved in a LES with an automatic turbulence model. G2 may compute mean value outputs using LES in large parts of the domain such as the turbulent wake of a bluff body, and using DNS only to capture certain critical local flow features such as boundary layer separation and transition. The adaptive combination of LES and DNS in G2 opens for a breakthrough in computational simulation of turbulent flow: With G2 Adaptive DNS/LES the number of mesh points may be orders of magnitude smaller than using non-adaptive or ad hoc refined meshes.

The a posteriori error estimation in G2 gives objective evidence that the basic idea of LES, which is to simulate turbulent flow on computational scales which are coarser than the actual physical scales using a relatively simple

turbulence model, indeed is largely functional. The reason LES works couples to a cancellation effect in the associated dual problem allowing the residual of a G2 solution to be quite large in turbulent regions. Intuitively, LES may be motivated by the fact that the actual smallest scale of dissipation of turbulent energy may be insignificant for mean value outputs: it suffices to capture the correct level of the turbulent energy dissipation which can be done on coarser scales than the physical scales. Another signal to the same effect is that quantities such as drag may change very slowly with the Reynolds number over large intervals, which opens for the possibility of correctly computing e.g. drag without fully resolving the flow and thus computing with an effective Reynolds number which is smaller than the actual one.

Altogether, G2 offers a general flexible methodology for the discretization of the NS equations applicable to a great variety of flow problems from creeping viscous flow to slightly viscous turbulent flow, including free or moving boundaries.

28.2 Development of G2

The development of stabilized space-time finite element methods, including moving meshes, is associated with Hughes, Tezduyar, and Johnson, and co-workers, see e.g. [20, 65, 70, 48, 47].

A posteriori error estimation is traditionally done with respect to an *energy-norm*, naturally induced by the underlying differential operator, resulting in estimates in terms of computable residuals. For surveys and references on this approach we refer to [108, 6]. Although, in most applications the energy-norm does not provide useful bounds on the error in quantities of real physical interest. Another approach is to use duality arguments to obtain bounds on the error in other norms, such as the L_2 -norm, or the error in various functionals of the solution, such as drag or lift forces for example. The idea of using duality arguments in a posteriori error estimation goes back to Babuška and Miller [8, 9, 10] in the context of post-processing 'quantities of physical interest' in elliptic model problems.

A framework for more general situations has since then been systematically developed, in particular by Eriksson & Johnson and Becker & Rannacher, with coworkers, see e.g. [37, 35, 14, 15, 71, 72]. For an overview of adaptive finite element methods based on duality including references, we refer to the survey articles [35, 15, 45]. For incompressible flow, applications of adaptive finite element methods based on duality have been used to compute quantities of interest such as the drag force for laminar flow in [14, 44, 50, 19].

In [58] turbulent flow is first considered, and the extension of this framework to LES is investigated in [52]. The generalization to G2 for turbulent flow by Hoffman & Johnson is first presented in [59, 53, 60], with applications to flow around a surface mounted cube and a square cylinder, followed by other applications in [56, 54, 57, 55].

28.3 The Incompressible Navier-Stokes Equations

We start by recalling the incompressible Navier-Stokes (NS) equations expressing conservation of momentum and incompressibility of a unit density Newtonian fluid with constant kinematic viscosity $\nu > 0$ enclosed in a volume Ω in \mathbb{R}^3 : Find $\hat{u} = (u, p)$ such that

$$\begin{aligned}\dot{u} + u \cdot \nabla u - \nu \Delta u + \nabla p &= f && \text{in } \Omega \times I, \\ \nabla \cdot u &= 0 && \text{in } \Omega \times I, \\ u &= w && \text{on } \partial\Omega \times I, \\ u(\cdot, 0) &= u^0 && \text{in } \Omega,\end{aligned}\tag{28.1}$$

where $u(x, t) = (u_i(x, t))$ is the velocity and $p(x, t)$ the pressure of the fluid at (x, t) , and $f, w, u^0, I = (0, \hat{t})$, is a given driving force, Dirichlet boundary data, initial data and time interval, respectively. The quantity $\nu \Delta u - \nabla p$ represents the total fluid force (modulo the external force f), and may alternatively be expressed as

$$\nu \Delta u - \nabla p = \nabla \cdot \sigma(\hat{u}),\tag{28.2}$$

where $\sigma(\hat{u}) = (\sigma_{ij}(\hat{u}))$ is the *stress tensor*, with components $\sigma_{ij}(\hat{u}) = 2\nu\epsilon_{ij}(u) - p\delta_{ij}$, composed of the *stress deviatoric* $2\nu\epsilon_{ij}(u)$ with zero trace and an isotropic pressure: Here $\epsilon_{ij}(u) = (u_{i,j} + u_{j,i})/2$ is the *strain rate tensor*, with $u_{i,j} = \partial u_i / \partial x_j$, and δ_{ij} is the usual Kronecker delta, the indices i and j ranging from 1 to 3.

A Neumann type boundary condition, corresponding to the boundary stress being prescribed, takes the form $\sigma \cdot n = g$, where $(\sigma \cdot n)_i = \sum_j \sigma_{ij} n_j$ and $g = (g_i)$ is a given boundary stress with g_i the force component in the x_i -direction, and n is the unit outward normal to Γ .

We usually seek to normalize the reference velocity and length scale in (28.1) to be of unit size, in which case the Reynolds number $Re \approx \nu^{-1}$.

28.4 G2 as Eulerian cG(p)dG(q)

We now present G2 in the special case of Eulerian tensor product space-time meshes and extend below to Lagrangian and Arbitrary-Lagrangian-Eulerian (ALE) space-time meshes. We start by presenting G2 in the form cG(p)dG(q) with continuous polynomials of degree p in space and discontinuous polynomials of degree q in time.

Let $0 = t_0 < t_1 < \dots < t_N = \hat{t}$ be a sequence of discrete time steps with associated time intervals $I_n = (t_{n-1}, t_n]$ of length $k_n = t_n - t_{n-1}$ and space-time slabs $S_n = \Omega \times I_n$, and let $W_n \subset H^1(\Omega)$ be a finite element space consisting of continuous piecewise polynomials of degree p on a finite element mesh $\mathcal{T}_n = \{K\}$ on Ω of mesh size $h_n(x)$ with W_n^0 the functions in W_n vanishing on $\partial\Omega$. We introduce for $q \geq 0$ the following spaces of finite element functions defined on the slab S_n :

$$V_n^0 = \{v \in H^1(S_n)^3 : v(x, t) = \sum_{j=0}^q (t - t_n)^j U_j(x), U_j \in [W_n^0]^3\},$$

$$Q_n = \{q \in H^1(S_n) : q(x, t) = \sum_{j=0}^q (t_n - t)^j q_j(x), q_j \in W_n\},$$

and finally introduce the velocity space $V^0 = \prod_n V_n^0$ and the pressure space $Q = \prod_n Q_n$ defined on the union of space-time slabs.

We now define G2 for (28.1) with $w = 0$ in the form of cG(p)dG(q): Find $\hat{U} = (U, P) \in V^0 \times Q$, such that for $n = 1, 2, \dots, N$,

$$(R(\hat{U}), \hat{v})_n + SD_\delta(\hat{U}; \hat{v})_n = 0, \quad (28.3)$$

for all $\hat{v} = (v, q) \in V_n^0 \times Q_n$, with the Galerkin term

$$(R(\hat{U}), \hat{v})_n \equiv (\dot{U} + (U \cdot \nabla)U, v)_n - (P, \nabla \cdot v)_n + (q, \nabla \cdot U)_n + (2\nu\epsilon(U), \epsilon(v))_n + ([U^{n-1}], v_+^{n-1}) - (f, v)_n, \quad (28.4)$$

and the stabilizing weighted least squares term

$$SD_\delta(\hat{U}; \hat{v})_n \equiv (\delta_1(\bar{R}_1(U; \hat{U}) - f), \bar{R}_1(U; \hat{v}))_n + (\delta_2(\bar{R}_2(U), \bar{R}_2(v))_n, \quad (28.5)$$

where for $\hat{v} = (v, q)$

$$\begin{aligned} \bar{R}_1(w; \hat{v}) &= \dot{v} + w \cdot \nabla v + \nabla q - \nu \Delta v, \\ \bar{R}_2(w) &= \nabla \cdot w, \end{aligned} \quad (28.6)$$

with the Laplacian defined element-wise, $\delta_1 = \kappa_1(k_n^{-2} + |U|^2 h_n^{-2})^{-1/2}$ in the convection-dominated case $\nu < Uh_n$ and $\delta_1 = \kappa_1 h_n^2$ otherwise, $\delta_2 = \kappa_2 h_n$ if $\nu < Uh_n$ and $\delta_2 = \kappa_2 h_n^2$ otherwise, with κ_1 and κ_2 positive constants of unit size, and

$$(v, w)_n = \int_{I_n} (v, w) dt, \quad (v, w) = \sum_{K \in T_n} \int_K v \cdot w dx,$$

$$(\epsilon(v), \epsilon(w)) = \sum_{i,j=1}^3 (\epsilon_{ij}(v), \epsilon_{ij}(w)).$$

Further, $[v^n] = v_+^n - v_-^n$ is the jump across the time level t_n with v_\pm^n the limit from right (+) and left (-) of $v(t)$ as $t \rightarrow t_n$, and we choose $\bar{U}_-^0 \in V_1^0$ as an interpolant of U^0 . In the case of Dirichlet boundary conditions the viscous term $(2\nu\epsilon(U), \epsilon(v))_n$ may equivalently occur in the form $(\nu \nabla U, \nabla v)_n = \sum_{i=1}^3 (\nu \nabla U_i, \nabla v_i)_n$.

28.5 Neumann Boundary Conditions

A Neumann boundary condition of the form $\sigma \cdot n = g$ on a part Γ_N of the boundary is implemented in variational form by restricting the functions in W_n^0 to vanish only where (homogeneous) Dirichlet conditions are imposed and supplementing the right hand side with an integral of $g \cdot v$ over Γ_N . This implements the Neumann boundary condition in weak form through the presence of the term $(-P, \nabla \cdot v)_n + (2\nu\epsilon(U), \epsilon(v))_n = (\sigma, \epsilon(v))_n$ on the left hand side, which when integrated by parts generates an integral over Γ_N of $(\sigma \cdot n) \cdot v$.

28.6 No Slip and Slip Boundary Conditions

The homogeneous Dirichlet velocity boundary condition $u = 0$ is referred to as a *no slip boundary condition* expressing that the fluid adheres to the boundary. A non homogeneous Dirichlet boundary condition, such as a given inflow velocity, is imposed in the velocity trial space for U , while the velocity test space is left unchanged with homogeneous Dirichlet boundary conditions.

A *slip boundary condition* corresponds to setting the normal component of the velocity $U \cdot n$ to zero at the boundary and models a boundary with negligible friction which the flow cannot penetrate.

28.7 Outflow Boundary Conditions

To simulate an outflow boundary condition we may use a Neumann condition with $g = 0$ corresponding to zero force at outflow as in outflow into a large empty reservoir. If we let the viscous term appear variationally instead in the form $(\nu \nabla U, \nabla v)_n$, then the corresponding Neumann boundary condition (with $g = 0$) takes the form $\nu \nabla u \cdot n - pn = 0$. which acts as an approximate *transparent outflow boundary condition*, attempting to let the flow leave the domain with little obstruction (also referred to as a “do nothing” boundary condition [95]).

28.8 Shock Capturing

In extreme situations with very large velocity gradients, occurring e.g. when a jet impinges on a wall, we may add residual dependent *shock-capturing artificial viscosity*, replacing ν by $\hat{\nu} = \max(\nu, \kappa_3 |R(\hat{U})| h^2)$, where $R(\hat{U}) = \sum_{i=1}^4 R_i(\hat{U})$ with

$$\begin{aligned} R_1(\hat{U}) &= |\bar{R}_1(U; \hat{U}) - f|, \\ R_2(\hat{U}) &= \nu D_2(U), \\ R_3(\hat{U}) &= |[U^{n-1}]|/k_n \quad \text{on } S_n, \\ R_4(\hat{U}) &= |\nabla \cdot U|, \end{aligned} \tag{28.7}$$

where

$$D_2(U)(x, t) = \max_{y \in \partial K} (h_n(x))^{-1} |[\frac{\partial U}{\partial n}(y, t)]| \quad (28.8)$$

for $x \in K$, with $[\cdot]$ the jump across the element edge ∂K , and κ_3 is a positive constant of unit size. $R_1(U, \hat{U}) + R_2(\hat{U})$ bounds the residual of the momentum equation, with the Laplacian term bounded by the second order difference quotient $D_2(U)$ arising from the jumps of normal derivatives across element boundaries. Note that $R_1(U, \hat{U})$ is defined element-wise and that with piecewise linears in space, the Laplacian ΔU is zero.

28.9 Basic Energy Estimate for cG(p)dG(q)

Choosing $\hat{v} = \hat{U}$ in (28.3), we obtain the following basic energy stability estimate for cG(p)dG(q) analogous to (16.2) (assuming $f = 0$):

$$\|U(\cdot, \hat{t})\|^2 + D_\nu(U, \hat{t}) + \sum_{n=0}^{N-1} \|U_+^n - U_-^n\|^2 + SD_\delta(\hat{U}; \hat{U}) = \|U^0\|^2. \quad (28.9)$$

If $q > 0$ then the term $SD_\delta(\hat{U}; \hat{U})$ gives a weighted least squares control of the residual $R(\hat{U})$ of \hat{U} . In the case $q = 0$, the residual $R(\hat{U})$ is controlled by $SD_\delta(\hat{U}; \hat{U})$ combined with the jump term giving weighted least squared control of the discrete time derivate $(U^n - U^{n-1})/k_n$. The momentum residual control is thus in the case $q = 0$ enforced by separate control of a discrete time derivative of U through the jump term combined with control of $(U \cdot \nabla U) + \nabla P - \nu \Delta U$ through the SD_δ -term.

Altogether, the basic energy estimate for cG(p)dG(q) gives control of $\|\sqrt{h}R(\hat{U})\|^2$ in terms of data, where h represents the mesh size in space-time, which expresses a fundamental property of G2.

28.10 G2 as Eulerian cG(1)dG(0)

We now specialize to G2 in the form of cG(1)dG(0) with continuous piecewise linears in space ($p = 1$) and with piecewise constants in time ($q = 0$) corresponding to the backward Euler method for time-stepping. We thus seek an approximate velocity $U(x, t)$ such that $U(x, t)$ is continuous and piecewise linear in x for each t , and $U(x, t)$ is piecewise constant in t for each x . Similarly, we seek an approximate pressure $P(x, t)$ which is continuous piecewise linear in x and piecewise constant in t . Thus we seek $U^n \in V_n^0 = W_{0n}^3$ and $P^n \in Q_n = W_n$ for $n = 1, \dots, N$, with

$$\begin{aligned} U(x, t) &= U^n(x) & x \in \Omega, \quad t \in (t_{n-1}, t_n], \\ P(x, t) &= P^n(x) & x \in \Omega, \quad t \in (t_{n-1}, t_n]. \end{aligned} \quad (28.10)$$

such that

$$\begin{aligned} & \left(\frac{U^n - U^{n-1}}{k_n}, v \right) + (U^n \cdot \nabla U^n + \nabla P^n, v + \delta_1(U^n \cdot \nabla v + \nabla q)) + (\nabla \cdot U^n, q) \\ & + (\nu \nabla U^n, \nabla v) = (f^n, v + \delta_1(U^n \cdot \nabla v + \nabla q)) \quad \forall (v, q) \in V_n^0 \times Q_n. \end{aligned} \quad (28.11)$$

where $\delta_1 = \frac{1}{2}(k_n^{-2} + |U|^2 h_n^{-2})^{-1/2}$ in the convection-dominated case $\nu < Uh_n$. Note that if $k_n \approx h_n/|U|$, which is a natural choice of time step respecting a CFL-condition, then $\delta_1 \approx h_n/|U|$. The stabilized form of the cG(1)dG(0) method is obtained by replacing v by $v + \delta_1(U^n \cdot \nabla v + \nabla q)$ in the terms $(U^n \cdot \nabla U^n + \nabla P^n, v)$ and (f^n, v) . In principle, we should make the replacement throughout, but in the present case of the cG(1)dG(0), only the indicated terms get involved because of the low order of the approximations. The perturbation in the stabilized method is of size δ_1 , and thus the stabilized method has the same order as the original method (first order in h if $k \sim h$).

Letting v vary in (28.11) while choosing $q = 0$, we get the discrete momentum equation:

$$\begin{aligned} & \left(\frac{U^n - U^{n-1}}{k_n}, v \right) + (U^n \cdot \nabla U^n + \nabla P^n, v + \delta_1 U^n \cdot \nabla v) \\ & + (\nu \nabla U^n, \nabla v) = (f^n, v + \delta_1 U^n \cdot \nabla v) \quad \forall v \in V_n^0, \end{aligned}$$

and letting q vary while setting $v = 0$, we get the discrete pressure equation:

$$(\delta_1 \nabla P^n, \nabla q) = -(\delta_1 U^n \cdot \nabla U^n, \nabla q) - (\nabla \cdot U^n, q) + (\delta_1 f^n, \nabla q) \quad \forall q \in Q_n.$$

The backward Euler first order accurate time stepping in cG(1)dG(0) in general is too dissipative for time dependent flow at high Reynolds numbers, but may be used to solve stationary problems by time-stepping.

28.11 Eulerian cG(1)cG(1)

The cG(p)cG(q) method is a variant of cG(p)dG(q) using the continuous Galerkin method cG(q) in time instead of a discontinuous Galerkin method dG(q). With cG(1) in time the trial functions are continuous piecewise linear in time and the test functions piecewise constant in time. We now present G2 in the form of cG(1)cG(1) which is less dissipative than cG(1)dG(0), and which is the method used in for all problems presented in the book.

G2 in the form cG(1)cG(1) for (28.1) with $w = 0$ reads: For $n = 1, \dots, N$, find $(U^n, P^n) \equiv (U(t_n), P(t_n))$ with $U^n \in V_0^n \equiv [W_0^n]^3$ and $P^n \in W^n$, such that

$$\begin{aligned} & ((U^n - U^{n-1})k_n^{-1} + \bar{U}^n \cdot \nabla \bar{U}^n, v) + (2\nu\epsilon(\bar{U}^n), \epsilon(v)) - (P^n, \nabla \cdot v) \\ & + (\nabla \cdot \bar{U}^n, q) + SD_\delta(\bar{U}^n, P^n; v, q) = (f, v) \quad \forall v \in V_0^n \times W^n, \end{aligned} \quad (28.12)$$

where $\bar{U}^n = \frac{1}{2}(U^n + U^{n-1})$, and

$$SD_\delta(\bar{U}^n, P^n; v, q) \equiv (\delta_1(\bar{U}^n \cdot \nabla \bar{U}^n + \nabla P^n - f), \bar{U}^n \cdot \nabla v + \nabla q) + (\delta_2 \nabla \cdot \bar{U}^n, \nabla \cdot v). \quad (28.13)$$

This method corresponds to a second order accurate Crank-Nicolson time-stepping. We note that in the stabilizing SD_δ -term the time derivative \dot{U} is missing, which is a consequence of the piecewise constancy of the test functions. This corresponds to a (small) inconsistency up to the term $\delta \dot{U}$. This inconsistency seems to be fully acceptable in the case of turbulent flow, since then the residual $R(\hat{U})$ anyway is not small.

28.12 Basic Energy Estimate for cG(1)cG(1)

To easily obtain an energy estimate for cG(1)cG(1), we assume that the non-linear term $(\bar{U}^n \cdot \nabla \bar{U}^n, v)$ in fact appears in the form

$$\frac{1}{2}((\bar{U}^n \cdot \nabla \bar{U}^n, v) - (\bar{U}^n \cdot \nabla v, \bar{U}^n)),$$

which would be equivalent if \bar{U}^n was divergence free. Choosing now $v = \bar{U}^n$ and $q = P$ on S_n in (28.12), we obtain (assuming $f = 0$):

$$\|U(\cdot, \hat{t})\|^2 + D_\nu(U, \hat{t}) + SD_\delta(\hat{U}; \hat{U}) = \|U^0\|^2. \quad (28.14)$$

As in the case of dG(0) the stabilizing term $SD_\delta(\hat{U}; \hat{U})$ does not include the time derivative \dot{U} , but in this case there is no jump term to directly give control of \dot{U} . Instead we may obtain control of $\|\sqrt{h}\dot{U}\|^2$ in terms of $SD_\delta(\hat{U}; \hat{U})$ by choosing $v = \dot{U}$ in the discrete momentum equation, and thus also cG(1)cG(1) includes the basic weighted least squares control of the residual $R(\hat{U})$ in G2.

28.13 Slip with Friction Boundary Conditions

Studied already by Navier [89] and Maxwell [86], the *slip with friction and penetration with resistance boundary condition* for a boundary Γ_{slfr} with normal n and two orthogonal tangential vectors τ_1, τ_2 takes the form

$$u \cdot n + \alpha n^T \sigma n = 0, \quad (28.15)$$

$$u \cdot \tau_k + \beta^{-1} n^T \sigma \tau_k = 0, \quad k = 1, 2, \quad (28.16)$$

with the stress tensor $\sigma = \sigma(\hat{u})$, and where we use matrix notation with all vectors v being column vectors and the corresponding row vector is denoted v^T .

Here α is a penetration parameter and β is a friction parameter, both positive functions defined on the boundary. A no slip boundary condition

corresponds to $(\alpha, \beta) \rightarrow (0, \infty)$, and a slip boundary conditions to $(\alpha, \beta) \rightarrow (0, 0)$. By increasing β we increase the resistance at the boundary, and by increasing α we increase the penetration of the boundary.

We can implement (28.15)-(28.16) weakly by decomposing the test function v into components aligned with the normal and tangent directions:

$$v = (v \cdot n)n + \sum_{k=1}^2 (v \cdot \tau_k)\tau_k, \quad (28.17)$$

see e.g. [67] for an algorithm for determining two linearly independent tangent vectors. We then have

$$\begin{aligned} \int_{\Gamma_{slfr}} (\sigma \cdot n) \cdot v \, ds &= \int_{\Gamma_{slfr}} n^T \sigma n (v \cdot n) + \sum_{k=1}^2 n^T \sigma \tau_k (v \cdot \tau_k) \, ds \\ &= - \int_{\Gamma_{slfr}} \alpha^{-1} (u \cdot n) (v \cdot n) - \sum_{k=1}^2 \beta (u \cdot \tau_k) (v \cdot \tau_k) \, ds. \end{aligned} \quad (28.18)$$

The derivation of the weak formulation of (28.1) underlying the cG(1)cG(1) method (28.12) formally involves partial integration of (28.2), resulting in the term

$$(2\nu\epsilon(U^n), \epsilon(v)) - (P^n, \nabla \cdot v) = (\sigma(U^n, P^n), \epsilon(v)), \quad (28.19)$$

in the left hand side of (28.12), together with a surface integral

$$\int_{\Gamma_{slfr}} (\sigma(U^n, P^n) \cdot n) \cdot v \, ds. \quad (28.20)$$

This surface integral is zero in (28.12), since the test function $v \in V_0^n$ satisfies a homogeneous Dirichlet condition.

To implement the boundary conditions (28.15)-(28.16), we seek a solution $(U^n, P^n) \in [W^n]^3 \times W^n$ for $n = 1, \dots, N$, satisfying (28.12) for $(v, q) \in [W^n]^3 \times W^n$, with the surface integral (28.20) subtracted from the left hand side of (28.12). Substituting the surface integral by (28.18) then corresponds to a weak implementation of the boundary conditions (28.15)-(28.16).

We stress that one has to be careful when implementing this boundary condition; one needs to use normals and tangent vectors that are defined for each node in the mesh, not for each face (or edge in 2 dimensions). The reason is that in the case the boundary Γ_{slfr} is not a flat surface, the degrees of freedom in certain nodes will be forced to satisfy conditions in too many directions. For example, in the case of a slip condition with $(\alpha, \beta) = (0, 0)$, the degrees of freedom in a node will be forced to satisfy a non penetration condition in several linearly independent directions, which may result instead in a no slip boundary condition.

By choosing $\hat{v} = \hat{U}$ in (28.12), we note that (28.18) corresponds to penalty terms for the L_2 -norms of the normal and tangential components of the velocity at the boundary, with penalty parameters α^{-1} and β , and that the energy balance (16.6) is modified by adding the time integrals of the terms

$$\|\alpha^{-1/2} u \cdot n\|_{\Gamma_{slfr}} + \sum_{k=1}^2 \|\beta^{1/2} u \cdot \tau_k\|_{\Gamma_{slfr}} \quad (28.21)$$

to the left hand side of (16.6).

We may also model friction with respect to a non zero velocity w at the boundary simply by changing $(u \cdot \tau_k)$ into $((u - w) \cdot \tau_k)$ in (28.18).

A Discrete Solver

I see no hope for the future of our people if they are dependent on the frivolous youth of today, for certainly all youth are reckless beyond words. When I was a boy, we were taught to be discrete and respectful of elders, but the present youth are exceedingly wise and impatient of restraint. (Hesiod, Father of Greek didactic poetry, 700BC)

29.1 Fixed Point Iteration Using Multigrid/GMRES

To compute a G2 solution \hat{U} , we have to solve a nonlinear system of algebraic equations for each time-step. We now briefly discuss the solution of the nonlinear system of equations generated by cG(1)cG(1).

We solve the system for (U^n, P^n) on slab S_n using fixed-point iteration with the convection velocity given by the previous iteration. Assuming the nodal values $(U^{n,j}, P^{n,j})$ in iteration j have been computed, we compute new nodal values $(U^{n,j+1}, P^{n,j+1})$ by solving a linearized version of cG(1)cG(1) of the form:

$$\begin{aligned} AU^{n,j+1} + k_n BP^{n,j+1} &= k_n F^n, \\ -B^\top U^{n,j} + CP^{n,j+1} &= G^n, \end{aligned} \tag{29.1}$$

where $A = M_n + k_n N_n - k_n \nu \Delta_n$, M_n is a mass matrix, the matrix N_n represents a discrete analog of the convection term with velocity $U^{n,j}$, Δ_n represents a discrete Laplacian, B is a discrete gradient, B^\top a discrete divergence, $C = -\delta_1 \Delta_n$, and finally F^n and G^n represent terms given by data including U^{n-1} . We here first solve for $P^{n,j+1}$ in terms of $U^{n,j}$ in the second equation using a multigrid method, and then solve for $U^{n,j+1}$ in the first equation using GMRES.

The resulting fixed point iteration converges under a CFL-condition (that is $\frac{U^n k_n}{h_n} < 1$ is small enough), and if also k_n/δ_1 is small enough. Since typically $\delta_1 \approx h_n/U^n$, convergence is thus achieved under a CFL-condition. In the

typical applications of non-stationary high Reynolds number turbulent flow presented in this book, convergence is usually obtained in a few iterations, assuming the CFL-condition is satisfied.

For further reading on solution algorithms for algebraic systems related to the discretization of NS equations, we refer to [107, 34].

G2 as Adaptive DNS/LES

I came to realize that exaggerated concern about what others are doing can be foolish. It can paralyze effort, and stifle a good idea. One finds that in the history of science almost every problem has been worked out by someone else. This should not discourage anyone from pursuing his own path. (Theodore von Kármán)

30.1 An A Posteriori Error Estimate

We now derive an *a posteriori error estimate* for cG(1)cG(1) following the route laid out in Chapter 14 with a mean value output $M(\cdot)$ defined by a given function $\hat{\psi}$. Recalling (14.5) we can express the difference in output between two ϵ -weak solutions $\hat{u} = (u, p)$ and $\hat{w} = (w, r)$ as

$$M(\hat{u}) - M(\hat{w}) = ((R(\hat{u}), \hat{\varphi})) - ((R(\hat{w}), \hat{\varphi})), \quad (30.1)$$

where $((\cdot, \cdot))$ is a space-time inner product, $\hat{\varphi}$ is the solution to the dual problem (14.4) with data $\hat{\psi}$, and we define the output by

$$M(\hat{w}) \equiv ((\hat{w}, \hat{\psi})). \quad (30.2)$$

With $\hat{w} = \hat{U}$, where \hat{U} is a cG(1)cG(1) solution given by (28.12), we may add (28.12) to (30.1), to get

$$M(\hat{u}) - M(\hat{U}) = ((R(\hat{u}), \hat{\varphi})) - ((R(\hat{U}), \hat{\varphi} - \hat{\varphi}^h)) + \int_I SD\delta(\hat{U}, \hat{\varphi}^h) dt, \quad (30.3)$$

with $\hat{\varphi}^h$ a function in the test space of cG(1)cG(1), and the stabilizing form given by (28.13).

Assuming sufficient regularity of the dual solution $\hat{\varphi}$ to satisfy the requirements of Lemma 30.2 and Lemma 30.3 below, we obtain the following a posteriori error estimate of a space-time mean value output of the form (30.2):

Theorem 30.1. If $\hat{U} = (U, P)$ solves (28.12), $\hat{u} = (u, p) \in \hat{W}_\epsilon$ is an ϵ -weak solution (with ϵ small), and $\hat{\varphi} = (\varphi, \iota)$ solves (14.4) with data $\hat{\psi}$, then we have the following error estimate for the output $M(\hat{u}) = ((\hat{u}, \hat{\psi}))$:

$$\begin{aligned} |M(\hat{u}) - M(\hat{U})| &\leq \epsilon S_\epsilon(\hat{\psi}) + \sum_{n=1}^N \left\{ \int_{I_n} \sum_{K \in \mathcal{T}_n} |R_1(\hat{U})|_K \cdot \omega_1 \, dt \right. \\ &\quad + \int_{I_n} \sum_{K \in \mathcal{T}_n} |R_2(U)|_K \omega_2 \, dt + \int_{I_n} \sum_{K \in \mathcal{T}_n} R_3(U) \cdot \omega_3 \, dt \\ &\quad \left. + \int_{I_n} \sum_{K \in \mathcal{T}_n} |SD_\delta(\hat{U}; \hat{\varphi})_K| \, dt \right\} \end{aligned}$$

with the stability factor defined by $S_\epsilon(\hat{\psi}) \equiv \|\hat{\varphi}\|_{\hat{V}}$, and the strong residuals given by

$$\begin{aligned} R_1(\hat{U}) &= \dot{U} + (U \cdot \nabla)U + \nabla P - \nu \Delta U - f, \\ R_2(U) &= \nabla \cdot U, \\ R_3(U) &= \frac{1}{2} h_{n,K}^{-1/2} \max_{S \subset \partial K} (|[[(\nu \nabla U)_1 \cdot n_S]|, \dots, |[(\nu \nabla U)_3 \cdot n_S]|), \end{aligned} \tag{30.4}$$

where $(M)_i$ denotes the i :th row of the matrix M , $SD_\delta(\cdot; \cdot)_K$ is a local version of the stabilizing form (28.13), and the dual weights are given by

$$\begin{aligned} \omega_1 &= C_{n,K}^k k_n |\dot{\varphi}|_{K,\infty} + C_{n,K}^h h_{n,K}^2 |D^2 \varphi|_K, \\ \omega_2 &= C_{n,K}^k k_n |\dot{\iota}|_{K,\infty} + C_{n,K}^h h_{n,K}^2 |D^2 \iota|_K, \\ \omega_3 &= C_{n,K}^k k_n h_{n,k}^{1/2} |\dot{\varphi}|_{\partial K \setminus \partial \Omega, \infty} + C_{n,K}^h h_{n,k}^2 |D^2 \varphi|_K, \end{aligned}$$

where $h_{n,K}$ is the diameter of element K in the mesh \mathcal{T}_n , D^2 measures second order derivatives with respect to x , and $C_{n,K}^h, C_{n,K}^k$ represent interpolation constants, $|w|_K \equiv (\|w_1\|_K, \|w_2\|_K, \|w_3\|_K)$ with $\|w\|_K = (w, w)_K^{1/2}$, and we let the dot denote the scalar product in \mathbb{R}^3 .

The stability factor $S_\epsilon(\hat{\psi})$ and the dual weights ω_i here characterize output sensitivity of the output $M(\hat{u})$. In practice we approximate $S_\epsilon(\hat{\psi})$ and ω_i by computing solutions of the corresponding dual problem linearized at \hat{U} . Taking the linearization error into consideration, we should modify the definitions of $S_\epsilon(\hat{\psi})$ and ω_i by taking the maximum over all linearizations in the corresponding spaces of ϵ -weak functions.

In Chapter 33 we derive a posteriori error estimates for the error in computing a force acting on a body in a flow, which is a special case of Theorem 30.1 for a particular choice of weight function $\hat{\psi}$.

30.2 Proof of the A Posteriori Error Estimate

To prove Theorem 30.1, we first use the definition of the ϵ -weak solution \hat{u} , to get

$$|(R(\hat{u}), \hat{\varphi}))| \leq \epsilon \|\hat{\varphi}\|_{\hat{V}}.$$

For the remaining terms in (30.3), we use partial integration to obtain a scalar product of the strong residuals (30.4) and an interpolation error in the dual solution. Integration by parts in the viscous term results in non zero boundary integrals over interior element boundaries $\partial K \setminus \partial \Omega$, for each t , since ∇U is piecewise constant in x over the elements, and thus discontinuous over interior element boundaries. This is not the case for the pressure term since the pressure is continuous in x over element boundaries, and so is the interpolation error $\varphi - \varphi^h$.

To estimate the element boundary integrals we use a standard finite element technique, where we first rewrite the sum of interior element boundary integrals as a sum of jumps of the form $[\nu \nabla U \cdot n_S]$ in normal derivative over all interior faces S in \mathcal{T}_n , with n_S being a globally defined unit normal vector associated with the face S . We then attribute half of the jump to each of the two elements sharing the face and rewrite the sum again over the elements $K \in \mathcal{T}_n$, to get

$$\begin{aligned} |M(\hat{u}) - M(\hat{U})| &\leq \epsilon S_\epsilon(\hat{\varphi}) + \sum_{n=1}^N \{|(\dot{U} + (U \cdot \nabla)U + \nabla P - \nu \Delta U - f, \varphi - \varphi^h)_n| \\ &+ |(\nabla \cdot U, \iota - \iota^h)_n| + \left| \int_{I_n} \sum_{K \in \mathcal{T}_n} \int_{\partial K \setminus \partial \Omega} \frac{1}{2} [\nu \nabla U \cdot n_S] \cdot (\varphi - \varphi^h) \, ds \, dt \right| \\ &+ \int_{I_n} \sum_{K \in \mathcal{T}_n} |SD_\delta(\hat{U}; \hat{\varphi})| \, dt \}. \end{aligned}$$

To estimate the interpolation error $\varphi - \varphi^h$ over the space-time domain $\Omega \times I_n$ we introduce $\bar{\varphi}$, a temporal average of φ over I_n , defined by

$$\bar{\varphi}(x) = \frac{1}{k_n} \int_{I_n} \varphi(x, s) \, ds. \quad (30.5)$$

Theorem 30.1 then follows from the following interpolation estimates:

30.3 Interpolation Error Estimates

Lemma 30.2. *For $(v, w) \in L_2(I_n; [L_2(\Omega)]^3 \times L_2(\Omega))$, $(\varphi, \iota) \in L_2(I_n; [H_0^2(\Omega)]^3 \times H^2(\Omega))$, with $(\dot{\varphi}, \dot{\iota}) \in C(I_n; [L_2(\Omega)]^3 \times L_2(\Omega))$, and $(\varphi^h, \iota^h) \in W_{0n}^3 \times W_n$ constant in time, we have*

$$|(v, \varphi - \varphi^h)_n| \leq \int_{I_n} \sum_{K \in \mathcal{T}_n} |v|_K \cdot (C_{n,K}^k k_n |\dot{\varphi}|_{K,\infty} + C_{n,K}^h h_{n,K}^2 |D^2 \varphi|_K) \, dt,$$

$$|(w, \iota - \varphi^h)_n| \leq \int_{I_n} \sum_{K \in \mathcal{T}_n} |w|_K (C_{n,K}^k k_n |\iota|_{K,\infty} + C_{n,K}^h h_{n,K}^2 |D^2 \iota|_K) dt,$$

where $h_{n,K}$ is the diameter of element $K \in \mathcal{T}_n$, and D^2 measures second order derivatives with respect to x .

We prove the first inequality:

$$|(v, \varphi - \varphi^h)_n| \leq |(v, \varphi - \bar{\varphi})_n| + |(v, \bar{\varphi} - \varphi^h)_n| = \mathcal{I}_1 + \mathcal{I}_2.$$

Using the mean value theorem, with $\eta, \zeta \in I_n$, we get for $(x, t) \in \Omega \times I_n$ that

$$\varphi(x, t) - \bar{\varphi}(x) = \varphi(x, t) - \varphi(x, \zeta) = \dot{\varphi}(x, \eta)(t - \eta) \leq C k_n \max_{\eta \in I_n} |\dot{\varphi}(x, \eta)|.$$

Cauchy-Schwarz inequality on each element gives

$$\mathcal{I}_1 \leq \int_{I_n} \sum_{K \in \mathcal{T}_n} |v|_K \cdot (C_{n,K}^k k_n \max_{\eta \in I_n} |\dot{\varphi}(\eta)|_K) dt.$$

For \mathcal{I}_2 , both $\bar{\varphi}$ and φ^h are constant in time. We first use Cauchy-Schwarz inequality on each element, and then a standard *interpolation error estimate* in x of the form $\|h_{n,K}^{-2}(\bar{\varphi}_i - \varphi_i^h)\|_K \leq C \|D^2 \varphi_i\|_K$, for each $t \in I_n$, to get

$$\mathcal{I}_2 \leq \int_{I_n} \sum_{K \in \mathcal{T}_n} |v|_K \cdot (C_{n,K}^h h_{n,k}^2 |D^2 \varphi|_K) dt.$$

The proof of the second inequality in the lemma is similar to the proof of the first inequality.

Lemma 30.3. For $w \in L_2(I_n; [L_2(\Omega)]^3)$, $\varphi \in L_2(I_n; [H_0^2(\Omega)]^3)$, $\dot{\varphi} \in \mathcal{C}(I_n; [H^1(\Omega)]^3)$, and $\varphi^h \in W_{0n}^3$ constant in time, we have

$$\begin{aligned} & \left| \int_{I_n} \sum_{K \in \mathcal{T}_n} \int_{\partial K \setminus \partial \Omega} w \cdot (\varphi - \varphi^h) ds dt \right| \\ & \leq \int_{I_n} \sum_{K \in \mathcal{T}_n} |w|_{\partial K \setminus \partial \Omega} \cdot (C_{n,K}^k k_n |\dot{\varphi}|_{\partial K \setminus \partial \Omega, \infty} + C_{n,K}^h h_{n,k}^{3/2} |D^2 \varphi|_K) dt, \end{aligned}$$

where $h_{n,K}$ is the diameter of element $K \in \mathcal{T}_n$, and D^2 measures second order derivatives with respect to x .

We have

$$\begin{aligned} & \left| \int_{I_n} \sum_{K \in \mathcal{T}_n} \int_{\partial K \setminus \partial \Omega} w \cdot (\varphi - \varphi^h) ds dt \right| \leq \left| \int_{I_n} \sum_{K \in \mathcal{T}_n} \int_{\partial K \setminus \partial \Omega} w \cdot (\varphi - \bar{\varphi}) ds dt \right| \\ & + \left| \int_{I_n} \sum_{K \in \mathcal{T}_n} \int_{\partial K \setminus \partial \Omega} w \cdot (\bar{\varphi} - \varphi^h) ds dt \right| = \mathcal{I}_1 + \mathcal{I}_2. \end{aligned}$$

For \mathcal{I}_1 we use the Cauchy-Schwarz inequality for each element, then (30.6), to get

$$\mathcal{I}_1 \leq \int_{I_n} \sum_{K \in \mathcal{T}_n} |w|_{\partial K \setminus \partial \Omega} \cdot (C_{n,K}^k k_n \max_{\eta \in I_n} |\dot{\varphi}(\eta)|_{\partial K \setminus \partial \Omega}) dt.$$

\mathcal{I}_2 is estimated by the Cauchy-Schwarz inequality for each element, and the standard interpolation error estimate $\|h_{n,K}^{-3/2}(\bar{\varphi}_i - \varphi_i^h)\|_{\partial K \setminus \partial \Omega} \leq C \|D^2 \varphi_i\|_K$, for each $t \in I_n$, to get

$$\mathcal{I}_2 \leq \int_{I_n} \sum_{K \in \mathcal{T}_n} |w|_{\partial K \setminus \partial \Omega} \cdot (C_{n,K}^h h_{n,k}^{3/2} |D^2 \varphi|_K).$$

30.4 G2 as Adaptive DNS/LES

To formulate an adaptive algorithm for G2 for a given output, we start from the a posteriori error estimate given by Theorem 30.1 written in the form:

$$|M(\hat{u}) - M(\hat{U})| \leq \sum_{K \in \mathcal{T}_k} \mathcal{E}_K \equiv \sum_{K \in \mathcal{T}_k} e_{D,h}^K + e_{M,h}^K \equiv e_{D,h} + e_{M,h}, \quad (30.6)$$

where $e_{D,h}$ represents the discretization error from the Galerkin part of G2, and $e_{M,h}$ represents a modeling error from the stabilization in G2. We here assume that the error contribution from the ϵ -weak solution \hat{u} is negligible compared to $e_{D,h} + e_{M,h}$.

The adaptive algorithm, which we refer to as *Adaptive DNS/LES*, can now be formulated as follows:

Algorithm 30.1. [Adaptive DNS/LES]. Given an initial coarse computational space mesh \mathcal{T}^0 , start at $k = 0$, then do

- (1) Compute approximation to the primal problem using \mathcal{T}^k .
- (2) Compute approximation to the dual problem using \mathcal{T}^k .
- (3) If $\sum_{K \in \mathcal{T}_k} \mathcal{E}_K^k < \text{TOL}$ then STOP, else:
- (4) Mark a fraction of the elements in \mathcal{T}^k for refinement, based on the size of $\mathcal{E}_{K,h}^k$.
- (5) Refine the mesh \mathcal{T}^k using a standard mesh refinement algorithm, which gives a new refined mesh \mathcal{T}^{k+1} .
- (6) Set $k = k + 1$, then goto (1).

By refining the mesh size h , also the time step k and the stabilization SD_δ are refined implicitly, since both k and δ depend on h . The stabilization may thus be thought of as being implicitly modified as we refine the mesh. But the a posteriori error estimates also allow for a direct adaptive modification

of both the time step k and the stabilization SD_δ , by locally modifying k and δ , respectively.

There are many potential optimizations of the adaptive algorithm, such as using dynamically changing meshes, adaptively refining the order of the approximation spaces in *hp-methods* [101, 50], using adaptively refined time steps, and techniques of *multi adaptivity* [82] with adaptive choice of different time steps in different parts of the domain.

A pertinent question in this context is the choice of the parameter δ in the SD_δ -term. The rule is to choose $\delta(x) \sim h(x)$, but how do we know that this is correct? It is in fact possible to choose δ to be larger, at the expense of possibly having to refine more to decrease in particular the modeling error $e_{M,h}$. However, choosing δ smaller eventually makes the numerics explode and the discretization error $e_{D,h}$ becomes large. We are thus lead to adaptively choosing δ so that both $e_{D,h}$ and $e_{M,h}$ are small, or more generally to adaptively choose the form of the stabilization SD_δ , as a form of *adaptive modeling*.

Also, the efficiency of the algorithm depend on how large fraction of the elements that are refined at each step. If we refine few elements each iteration, we may expect to avoid unnecessary refinement in areas not so crucial for the output error, but on the other hand we risk to end up with an unnecessary large number of iterations. In the computations below we refine a fraction of about 5%-30% of the elements in each iteration.

30.5 Computation of Multiple Output

Often one is interested in several different outputs from one single computation. The objective is then to construct an adaptive method to control the errors in all the different outputs, and there are various ways to achieve this. Assuming we are interested in a number of different outputs $M_k(\hat{u}) \equiv ((\hat{u}, \hat{\psi}_k))$, with $k = 1, \dots, N$, we first note that to evaluate the sum of the errors $\sum_k |M_k(\hat{u}) - M_k(\hat{U})|$, the straight forward way is to use the linearity of the dual problem (14.4) to compute solutions $\hat{\varphi}_k$ to the corresponding N dual problems

$$a(\hat{u}, \hat{U}; \hat{v}, \hat{\varphi}_k) = ((\hat{v}, \hat{\psi}_k)), \quad \forall \hat{v} \in \hat{V}_0.$$

Although, with N large this could be quite expensive. A cheaper way is to instead compute the error $\hat{e} = \hat{u} - \hat{U}$ from the *error equation*

$$a(\hat{u}, \hat{U}; \hat{e}, \hat{w}) = ((R(\hat{U}), \hat{w})), \quad \forall \hat{w} \in \hat{V}_0, \quad (30.7)$$

with $R(\hat{U})$ the residual defined by (5.3). The error equation (30.7) is independent of k , and we can then evaluate the error in each output M_k from the scalar product with the corresponding data $\hat{\psi}_k$, that is

$$M_k^{err} = M_k(\hat{u}) - M_k(\hat{U}) = M_k(\hat{e}) = ((\hat{e}, \hat{\psi}_k)).$$

For adaptive mesh refinement we need error indicators for each element individually, which is not possible to obtain only from the error M_k^{err} . Using the linearity of the dual problem we note that we obtain the sum of the output errors M_k^{err} as

$$\sum_k M_k^{err} = \sum_k M_k(\hat{u}) - M_k(\hat{U}) = ((R(\hat{U}), \hat{\varphi} - \hat{\varphi}^h)) + \int_I SD_\delta(\hat{U}; \hat{\varphi}^h) dt, \quad (30.8)$$

where $\hat{\varphi}$ is the solution to a dual problem with data $\sum_k \hat{\psi}_k$. Now, if we know the signs of the errors M_k^{err} , we may use this to avoid cancellation in (30.8) by using the linearity of the dual problem to get

$$\sum_k |M_k^{err}| = \sum_k (\operatorname{sgn} M_k^{err}) M_k^{err} = ((R(\hat{U}), \hat{\varphi} - \hat{\varphi}^h)) + \int_I SD_\delta(\hat{U}; \hat{\varphi}^h) dt, \quad (30.9)$$

where $\hat{\varphi}$ now is the solution to a dual problem with data $\sum_k (\operatorname{sgn} M_k^{err}) \psi_k$. One approach is then to solve the error equation (30.7), from which $\operatorname{sgn} M_k^{err}$ can be obtained, see [49, 45].

30.6 Mesh Refinement

In each step of the adaptive algorithm a certain fraction of the elements are marked for refinement. Depending on the geometry of the elements in the mesh, various algorithms are available for refining the mesh.

For example, in the case of a tetrahedral mesh, one may choose to subdivide each marked tetrahedron into 8 new smaller tetrahedrons, which may correspond to subdividing each triangular element face into 4 new triangles. This type of regular subdivision is not unique, and there are different ways to choose which way to subdivide. In addition, to avoid so called *hanging nodes*, one has to refine an additional number of tetrahedrons neighboring the marked elements.

The design and analysis of mesh refinement algorithms is an active area of research that we will not go into further in this book. We refer to [16] for an example of a mesh refinement algorithm for tetrahedral meshes. The algorithms used for the computations in this book are described at the homepage of FEniCS [39].

31

Implementation of G2 with FEniCS

A mythical bird that never dies, the FEniCS flies far ahead to the front, always scanning the landscape and distant space. It represents our capacity for vision, for collecting sensory information about our environment and the events unfolding within it. The FEniCS, with its great beauty, creates intense excitement and deathless inspiration. (The Feng Shui Handbook, feng shui Master Lam Kam Chuen)

31.1 The FEniCS Project

FEniCS is free software for the Automation of Computational Mathematical Modeling. G2 methods for various differential equations, including the NS equations, are implemented in FEniCS.

FEniCS was initiated in 2003 by research groups at Chalmers University, University of Chicago and Toyota Technological Institute at Chicago [33]. FEniCS builds on the earlier DOLFIN project by Hoffman and Logg [64], and Analysa by Scott [11]. FEniCS can be freely downloaded from the project homepage: www.fenics.org.

FEniCS is organized as a collection of sub projects/components, with DOLFIN [1] being the C++/Python interface of FEniCS, providing a consistent PSE (Problem Solving Environment) for solving ordinary and partial differential equations.

FEniCS currently hosts the following projects:

- *DOLFIN*: the C++/Python interface of FEniCS.
- *FFC*: automates the evaluation of variational forms.
- *FIAT*: automates the generation of finite elements.
- *FErari*: optimizes computation of element stiffness matrices.
- *Ko*: automates the simulation of mechanical systems.
- *Sieve*: data structures for parallel representation of meshes.

Features of DOLFIN today include: a simple, consistent and intuitive object-oriented API, automatic and efficient evaluation of variational forms

through FFC, automatic and efficient assembly of linear systems, support for general families of finite elements, including continuous and discontinuous Lagrange finite elements of arbitrary order on triangles and tetrahedra through FIAT, support for arbitrary mixed elements, including Taylor-Hood, high-performance parallel linear algebra through PETSc [5] with simple C++ wrappers, triangular and tetrahedral meshes, including adaptive mesh refinement and mesh hierarchies, a number of PDE solvers, multi-adaptive mcG(q)/mdG(q) and mono-adaptive cG(q)/dG(q) ODE solvers, and support for a range of output formats for post-processing, including DOLFIN XML, MATLAB, Octave, OpenDX, GiD, Tecplot and Paraview/VTK.

The method $cG(1)cG(1)$ presented in Chapter 28 is implemented in DOLFIN as a module, including demo examples.

We refer to the FEniCS homepage (www.fenics.org) for an up to date account of FEniCS and the various components.

Moving Meshes and ALE Methods

Since it was first brewed in 1777, Bass Ale has been painted by Manet, loved by Napoleon and taken into the wild by Buffalo Bill. These and many other stories, along with the famous Red Triangle that was England's first trademark, continue to ensure Bass Ale enjoys iconic status amongst beer lovers all over the world. (paid advertisement)

32.1 Introduction

The space-time formulation of G2 naturally opens the possibility of allowing the space mesh to move in time in *Lagrangian* or *Arbitrary Lagrangian Eulerian ALE* methods, as generalizations of the Eulerian method presented in Chapter 28 with the space mesh being fixed in time. Letting the nodes of the space mesh move with the fluid velocity corresponds to a Lagrangian *Characteristic Galerkin method*, while moving the space nodes with a different velocity gives an ALE method. G2 as ALE thus includes both Eulerian and Lagrangian methods as special cases.

Lagrangian or ALE methods are useful to handle problems with free or moving boundaries where the geometry in space changes with time. In such problems the space-time mesh may change continuously in time by letting the boundary nodes move according to specification and letting the internal nodes follow in ALE using *mesh smoothing*, combined with occasional re-meshing with projection into the new mesh to avoid too strong mesh distortion.

32.2 G2 Formulation

We consider the incompressible NS equations on a general space-time domain $Q = \{(x, t) : x \in \Omega(t), t \in I = (0, \hat{t}]\}$, with the space domain $\Omega(t)$ with boundary $\Gamma(t)$ occupied by the fluid at time t changing with t :

$$\begin{aligned} \dot{u} + (u \cdot \nabla) u - \nu \Delta u + \nabla p &= f && \text{in } Q, \\ \nabla \cdot u &= 0 && \text{in } Q, \\ u(\cdot, 0) &= u_0 && \text{in } \Omega(0), \end{aligned} \quad (32.1)$$

combined with boundary conditions on $\Gamma(t)$ for $t \in I$ modeling a free boundary or a boundary with prescribed motion. We start by assuming that $\Gamma(t)$ has a prescribed motion given by a prescribed velocity u on $\Gamma(t)$, and we return to the case of a free boundary below.

To define G2 for (32.1) let $0 = t_0 < t_1 < \dots < t_N = \hat{t}$ be a sequence of discrete time steps with associated time intervals $I_n = (t_{n-1}, t_n]$ of length $k_n = t_n - t_{n-1}$ and define the space-time slabs $S_n = \{(x, t) \in Q : t \in I_n\}$. Let $W_n \subset H^1(\Omega(t_{n-1}))$ be a finite element space consisting of continuous piecewise polynomials of degree p on a mesh $T_n = \{K\}$ of mesh size $h_n(x)$. Let for a given velocity field β on S_n satisfying the velocity boundary condition, the particle paths $x(\bar{x}, \bar{t})$ be defined by

$$\begin{aligned} \frac{dx}{d\bar{t}} &= \beta(x, \bar{t}) & \bar{t} \in I_n, \\ x(\bar{x}, t_n) &= \bar{x}, & \bar{x} \in \Omega(t_{n-1}), \end{aligned} \quad (32.2)$$

and introduce the corresponding mapping $F_n^\beta : \bar{S}_n \rightarrow S_n$ defined by $(x, t) = F_n^\beta(\bar{x}, \bar{t}) = (x(\bar{x}, \bar{t}), \bar{t})$, where $x = x(\bar{x}, \bar{t})$ satisfies (32.2), and $\bar{S}_n = \Omega(t_{n-1}) \times I_n$. Define for a given $q \geq 0$, the spaces

$$\begin{aligned} \bar{V}_n^\beta &= \{\bar{v} \in H^1(\bar{S}_n)^3 : \bar{v}(\bar{x}, \bar{t}) = \sum_{j=0}^q (\bar{t} - t_n)^j U_j(\bar{x}), U_j \in [W_n]^3\}, \\ \bar{Q}_n^\beta &= \{\bar{q} \in H^1(\bar{S}_n) : \bar{q}(\bar{x}, \bar{t}) = \sum_{j=0}^q (\bar{t}_n - t_n)^j q_j(\bar{x}), q_j \in W_n\}, \end{aligned}$$

together with their analogs in (x, t) -coordinates:

$$V_n^\beta = \{v : \bar{v} \in \bar{V}_n^\beta\}, \quad Q_n^\beta = \{q : \bar{q} \in \bar{Q}_n^\beta\}, \quad (32.3)$$

where $v(x, t) = \bar{v}(\bar{x}, \bar{t})$ and $q(x, t) = \bar{q}(\bar{x}, \bar{t})$ and $(x, t) = F_n^\beta(\bar{x}, \bar{t})$.

Defining finally $V^\beta \times Q^\beta = \prod_n V_n^\beta \times Q_n^\beta$, we can now formulate G2 as a generalization of (28.3) as follows: Find $\hat{U} = (U, P) \in V^\beta \times Q^\beta$ satisfying the boundary conditions, such that for $n = 1, 2, \dots, N$,

$$\begin{aligned} &(\dot{U} + (U \cdot \nabla) U, v)_n - (P, \operatorname{div} v)_n + (q, \operatorname{div} U)_n + (2\nu\epsilon(U), \epsilon(v))_n \\ &+ SD_\delta(\hat{U}; \hat{v})_n + ([U^{n-1}], v_+^{n-1}) = (f, v)_n \quad \forall \hat{v} = (v, q) \in V_{0n}^\beta \times Q_n^\beta, \end{aligned} \quad (32.4)$$

where V_{0n}^β satisfies homogeneous Dirichlet boundary conditions, and

$$SD_\delta(\hat{U}; \hat{v})_n \equiv (\delta_1(a(U; U, P) - f), a(U; v, q))_n + (\delta_2 \operatorname{div} U, \operatorname{div} v)_n \quad (32.5)$$

where $a(w; v, q) = \dot{v} + w \cdot v + \nabla q - \nu \Delta v$ with the Laplacian defined element-wise, $\delta_1 = \kappa_1(k_n^{-2} + |U|^2 h_n^{-2})^{-1/2}$ in the convection-dominated case $\nu < Uh_n$ and $\delta_1 = \kappa_1 h_n^2$ otherwise, $\delta_2 = \kappa_2 h_n$ if $\nu < Uh_n$ and $\delta_2 = \kappa_2 h_n^2$ otherwise, with κ_1 and κ_2 positive constants of unit size, and $(\cdot, \cdot)_n$ indicates integration over S_n .

The Eulerian version of G2 is obtained choosing $\beta = 0$, which means that the mesh does not move in time. G2 in the form of a *characteristic Galerkin method* is obtained by choosing $\beta = U$ which means that the mesh moves with the computed fluid velocity. Choosing β differently gives various ALE-methods, with the mesh and particle velocity being (partly) different; for example we may move the mesh with the particle velocity at a free boundary, while allowing the mesh to move differently inside the domain. In extreme situations with very large velocity gradients, we may add residual dependent shock-capturing artificial viscosity as in the Eulerian formulation (28.3). G2 for *Stokes equations* is obtained by omitting the nonlinear terms $(U \cdot \nabla)U$ and $(U \cdot \nabla)v$, and setting $\delta_1 = \kappa_1 h^2$, $\delta_2 = \kappa_2 h^2$.

Since in the local Lagrangean coordinates (\bar{x}, \bar{t}) on each slab S_n with $\beta = U$,

$$\frac{\partial \bar{U}}{\partial \bar{t}} \equiv \frac{\partial}{\partial \bar{t}} U(x(\bar{x}, \bar{t}), \bar{t}) = \dot{U} + U \cdot \nabla U,$$

the convection term $U \cdot \nabla U$ effectively disappears in the characteristic Galerkin method, when expressed in the characteristic coordinates (\bar{x}, \bar{t}) , and thus the discrete equations on each time step effectively correspond to a Stokes problem, choosing $\delta_1 = \kappa_1 h_n^2$.

32.3 Free Boundary

A *free boundary* $\Gamma(t)$ is typically specified using homogeneous Neumann boundary conditions corresponding to zero boundary stress and moves with the velocity of the fluid. Including surface tension in the model leads to a non homogeneous Neumann boundary condition. The velocity on a free boundary is thus not specified but free to vary in the variational formulation of G2. We also add a least squares stabilization of the discrete boundary stress to the left hand side of the G2 formulation (32.4), of the form

$$<\delta_3 \sigma(u, p) \cdot n, \sigma(v, q) \cdot n>_n, \quad (32.6)$$

where

$$< v, w >_n = \int_{I_n} \int_{\Gamma(t)} v \cdot w \, ds \, dt. \quad (32.7)$$

32.4 Laplacian Mesh Smoothing

In ALE methods with the mesh velocity and fluid velocity possibly being different, we may use various techniques of mesh modification to guarantee

that the space mesh does not get tangled or too distorted with negative effects on conditioning of the discrete equations and on interpolation accuracy. In a *mesh smoothing* the nodes of the mesh are moved in order to improve a certain mesh quality measure, without changing the connectivity of the mesh.

Laplacian mesh smoothing is based on solving a discrete Laplacian equation representing a spring model of the mesh, or on a diffusion model possibly with a variable diffusion coefficient. In its simplest form Laplacian mesh smoothing amounts to an iteration over the nodes in the mesh, where each node is moved to the geometric center of its neighbors.

Laplacian mesh smoothing is suitable when small deformations of the mesh suffice to improve the quality. In Section 32.6 we present a different mesh modification strategy which can handle the large deformations arising in the case of moving objects.

32.5 Mesh Smoothing by Local Optimization

We also present a mesh smoothing algorithm, where for each node we optimize the shape of the tetrahedrons surrounding the node, see e.g. [40] for similar methods. A point $x = (x_1, x_2, x_3)$ in a tetrahedron E can be written as a linear combination of the coordinates $p = (p_1, \dots, p_4)$ of the nodes (N_1, \dots, N_4) of E using *barycentric coordinates* $a = (a_1, \dots, a_4)$, as follows

$$x = a_1 p_1 + \dots + a_4 p_4, \quad (32.8)$$

with $a_1 + \dots + a_4 = 1$. We can express the barycentric coordinates a of x in the form

$$a = Ax + b, \quad (32.9)$$

where A is a 4×3 matrix. We now aim to minimize the cost functional $\mathcal{F}(N)$, given by

$$\mathcal{F}(N) = \sum_{E \in \mathcal{E}(N)} \kappa(A^T A), \quad (32.10)$$

for node N , where $\mathcal{E}(N)$ are the elements that contain the node N and $\kappa(A^T A)$ is the condition number of the 3×3 matrix $A^T A$. This loosely corresponds to minimizing the difference between the elements E and the equilateral reference element.

We now seek the entries of the matrix A . We denote by n_i the outward normal vector corresponding to the face opposite the local node N_i , given by any pairwise vector product of edge vectors on this face. The following equality

$$(x - p_i) \cdot \frac{n_i}{c_i} = (1 - a_i) = \begin{cases} 0 & x = p_i, \\ 1 & x = p_j, j \neq i, \end{cases} \quad (32.11)$$

gives the entries of matrix A in (32.9) as

$$\begin{aligned} a_1(x) &= \left(-\frac{n_1}{c_1}\right) \cdot x + \left(1 + p_1 \cdot \frac{n_1}{c_1}\right), \\ a_2(x) &= \left(-\frac{n_2}{c_2}\right) \cdot x + \left(1 + p_2 \cdot \frac{n_2}{c_2}\right), \\ a_3(x) &= \left(-\frac{n_3}{c_3}\right) \cdot x + \left(1 + p_3 \cdot \frac{n_3}{c_3}\right), \\ a_4(x) &= \left(-\frac{n_4}{c_4}\right) \cdot x + \left(1 + p_4 \cdot \frac{n_4}{c_4}\right), \end{aligned} \quad (32.12)$$

where

$$\begin{aligned} c_1 &= (p_2 - p_1) \cdot n_1, \\ c_2 &= (p_1 - p_2) \cdot n_2, \\ c_3 &= (p_1 - p_3) \cdot n_3, \\ c_4 &= (p_1 - p_4) \cdot n_4. \end{aligned} \quad (32.13)$$

Based on the cost functional $\mathcal{F}(N)$ there are various ways to set up a minimization algorithm. For example, we may use the following algorithm:
For $k = 0$ and $\mathcal{S} = \{\text{all free nodes in the mesh}\}$, do

- (1) *If $k = \max$ no iterations STOP, else*
- (2) *Find node $N \in \mathcal{S}$ with largest cost functional $\mathcal{F}(N)$*
- (3) *Find coordinates of N that minimize the cost functional $\mathcal{F}(N)$*
- (4) *Remove N from \mathcal{S}*
- (5) *Goto (1)*

To minimize $\mathcal{F}(N)$ we may use a Conjugate gradient method, where we, for example, use the *QR*-algorithm to find the eigenvalues of $A^T A$ in the evaluation of the cost functional $\mathcal{F}(N)$.

To illustrate the method we consider a simple example with a flat 3d object that we rotate slightly in a tetrahedral mesh, see Figure 32.1. We find that after only a few iterations the maximal condition numbers are reduced by a factor 10, through moving the nodes with the highest cost functional.

In Figure 32.2 we rotate the flat object $\pi/4$ radians, where we find that for this large deformation the Laplacian mesh smoothing is not enough to ensure geometric quality of the elements in the mesh. Again we find that a few iterations of the local smoothing algorithm significantly improves the mesh quality.

32.6 Object in a Box

The mesh smoothing techniques of the previous sections may be very efficient for small deformations of the mesh, but for a mesh undergoing large deformations these techniques may not be enough. We then need a strategy to handle large deformations of the mesh.

One common approach is to simply re-mesh (generate a new mesh) if the mesh deformation cannot be handled by standard mesh smoothing techniques. The downside of this approach is the cost of re-meshing, as well as the loss of accuracy from projecting the solution from the old mesh to the new mesh.

We now present a mesh moving strategy for the case of an object moving through the mesh, which we refer to as *object in a box*, where the goal is to (i)

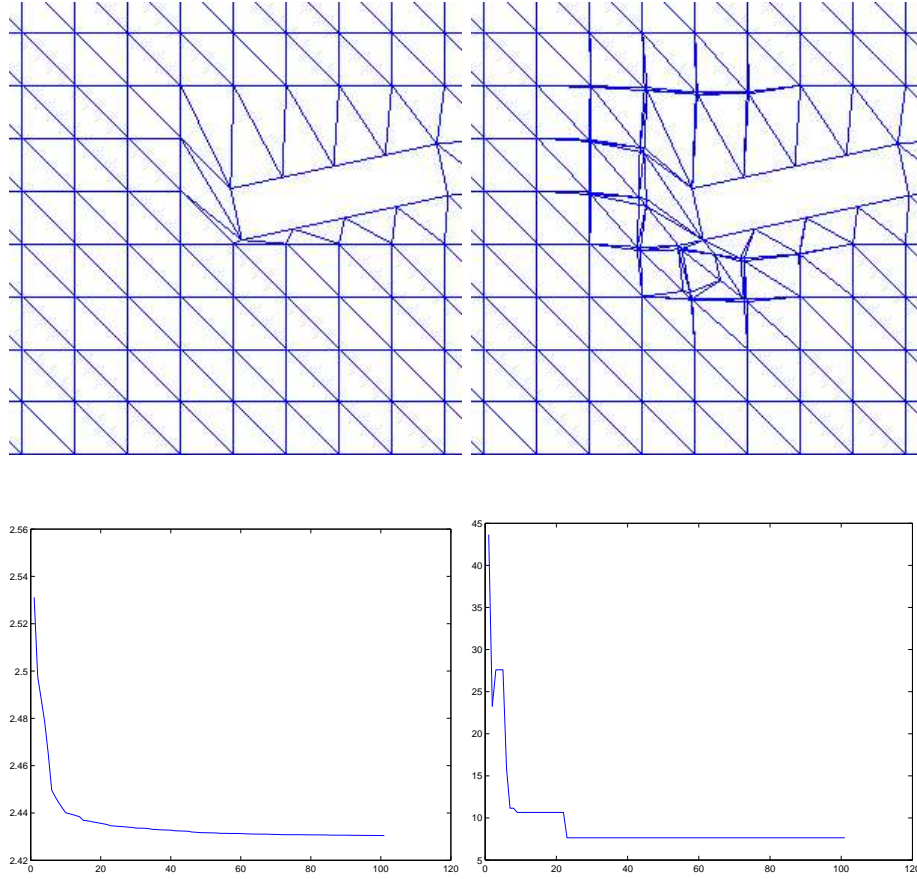


Fig. 32.1. Locally distorted mesh before (upper left) and after (upper right), 100 iterations of the local optimization algorithm. The weighted l_2 -norm (lower left) and the max-norm (lower right), of the square root of the condition numbers of $A^T A$ as functions of number of iterations.

allow for large deformations of the mesh while still keeping good mesh quality, and (ii) avoid re-meshing.

The idea is that we split the computational domain $\Omega(t)$ into two parts: (i) a box $\Omega_b(t) \subset \Omega(t)$ that fits (ii) a regular background mesh that fills the rest of the domain $\Omega(t) \setminus \Omega_b(t)$. Within the box $\Omega_b(t)$ we may have an unstructured mesh around the object. When the object moves, the main part of the mesh deformation is handled by translation of the box, or $\pi/2$ radians rotation of the box, on the regular background mesh. The remaining deformation, which then is small, is taken by the mesh inside the box and is handled through regular mesh smoothing techniques such as the ones presented above.

The key ingredients are then the algorithms for translation and rotation of the box Ω_b , which we now describe.

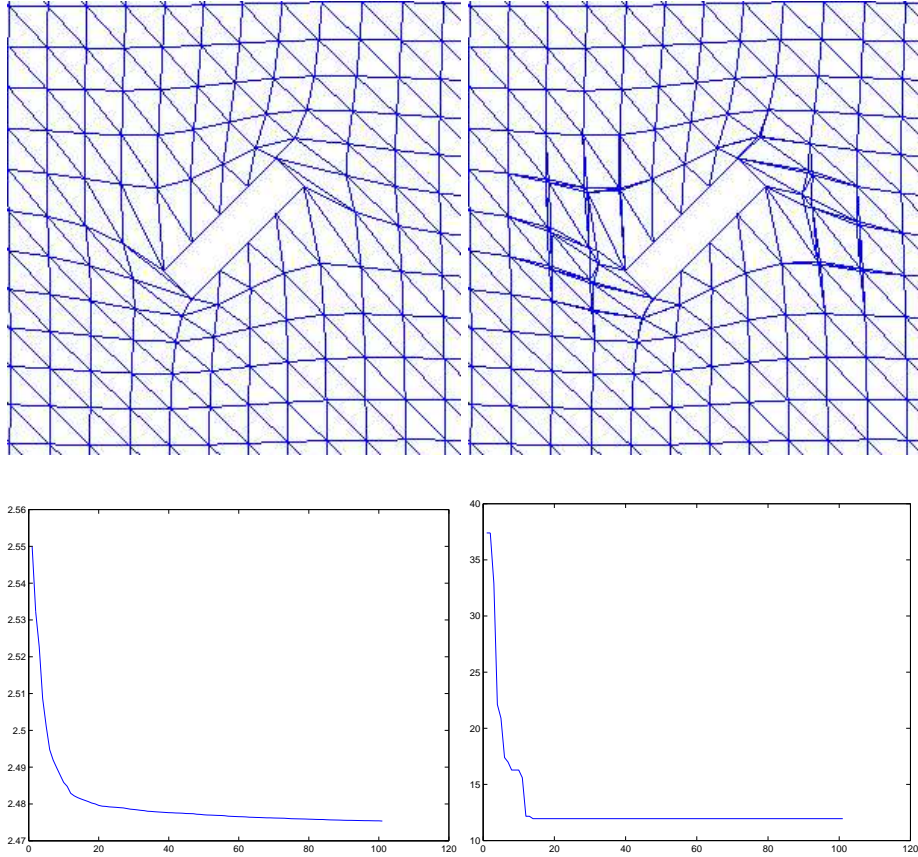


Fig. 32.2. Rotated object mesh before (upper left) with Laplacian mesh smoothing, and after 100 iterations of the local optimization algorithm (upper right). The weighted l_2 -norm (lower left), and the max-norm (lower right) of the square root of the condition numbers of $A^T A$ as functions of number of iterations.

We illustrate the box translation algorithm in Figure 32.3, where the moving object is a thin plate with dimension $1/4 \times 1/16 \times 1/4$ which is moving in negative x_2 -direction in a cubic domain $\Omega = [0, 1]^3$, within a box $\Omega_b = 0.5 \times 0.5625 \times 0.5$. We find that as the plate is moving, the box Ω_b follows and the mesh outside the box is not deformed. Inside the box the small deformations are handled through Laplacian mesh smoothing, and good mesh quality is kept. The algorithm for translation of the box in direction x_i takes the following form:

Algorithm 32.1. [Box translation in direction x_i] With a box $\Omega_b = [x_1^{min}, x_1^{max}] \times [x_2^{min}, x_2^{max}] \times [x_3^{min}, x_3^{max}]$, and with h_i^{reg} the mesh size of the regular background mesh outside the box, do
(1) For all nodes in Ω_b : $x_i = x_i + h_i^{reg}$.

- (2) For all object nodes: $x_i = x_i - h_i^{reg}$.
- (3) For all nodes in Ω_b such that $x_i = x_i^{max} + h_i^{reg}$:

$$x_i = x_i - (x_i^{max} - x_i^{min} + h_i^{reg}).$$
- (4) For all nodes in the box: apply mesh smoothing.
- (5) Update connectivity for Ω_b and the rest of the mesh.

In Figure 32.4 we illustrate box rotation using Algorithm 32.2, with Laplacian mesh smoothing, where now the box Ω_b is equal to the whole computational domain Ω .

Algorithm 32.2. [Box rotation around axis e_i] With a box $\Omega_b = [x_1^{min}, x_1^{max}] \times [x_2^{min}, x_2^{max}] \times [x_3^{min}, x_3^{max}]$, and with h_i^{reg} the mesh size of the regular background mesh outside the box, do

- (1) Rotate the object $-\pi/2$ radians around the axis e_i , using mesh smoothing inside the box Ω_b .
- (2) Rotate all nodes in Ω_b $\pi/2$ radians around the axis e_i .
- (3) Update connectivity for Ω_b and the rest of the mesh.

The update of the connectivity after rotation takes some consideration to match the two parts of the mesh. The nodes typically match, but not the elements in general. For example, with rectangular elements there is no problem, but for tetrahedrons the element faces do not match.

There are several ways to approach this. We may use special matching elements at the box boundary, such as pyramids using tetrahedrons inside the box and rectangular elements in the rest of the structured domain. Alternatively one may locally generate a new mesh in the layer at the box boundary, or use a discontinuous method locally allowing non matching element faces on the box boundary.

The global object in a box algorithm takes the form:

Algorithm 32.3. [Object in a box] At time step k do

- (1) If the global translation coordinate ϕ_i^t for the object in the direction x_i is larger than the tolerance $TOL_i^t(h_i^{reg})$, then translate the box in that direction using Algorithm 32.1.
- (2) If the global rotation coordinate for the object ϕ_i^r around the axis e_i is larger than the tolerance TOL_i^r , then rotate the box in that direction using Algorithm 32.2.
- (3) Move the object.
- (4) Smooth the mesh inside the box.
- (5) Solve the equations for time step k .

32.7 Sliding Mesh

Variants of the object in a box method are possible. For example, computing the flow in a rotating turbine, a rotating cylinder may be used, which is referred to as a *sliding mesh* method, see e.g. [13].

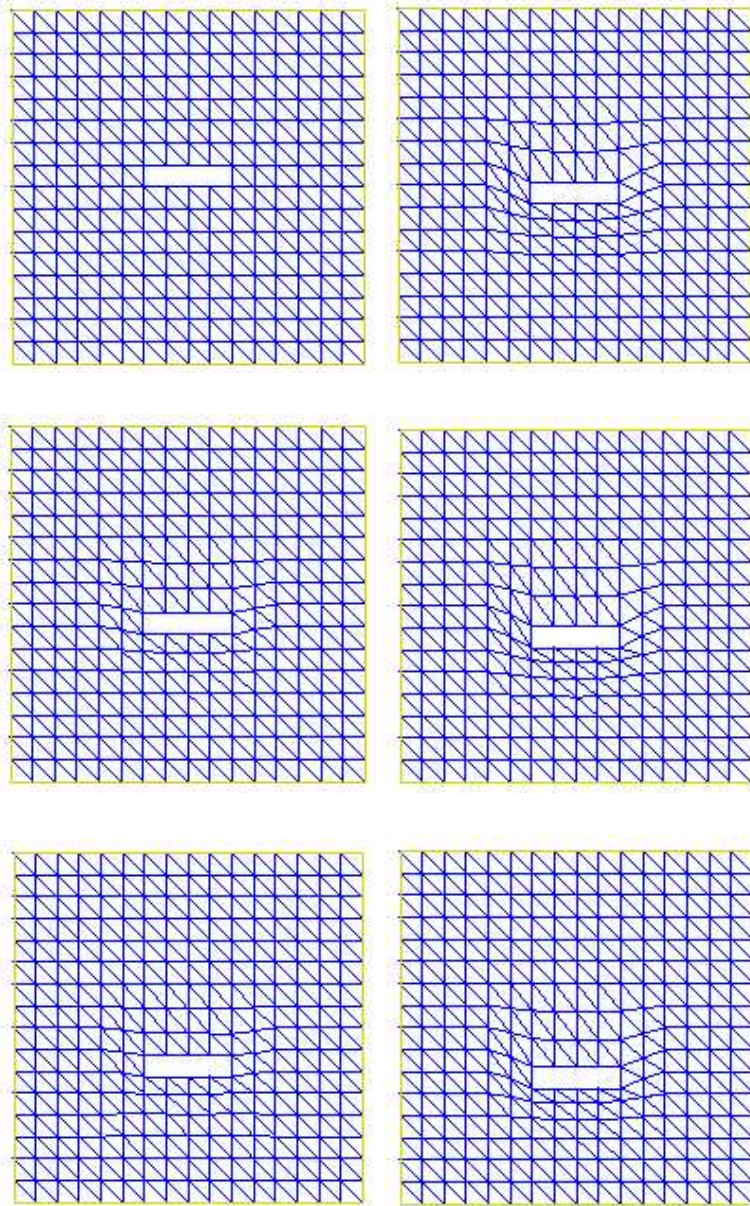


Fig. 32.3. Box translation with Laplacian smoothing, for an $0.25 \times 0.0625 \times 0.25$ object inside a $0.5 \times 0.5625 \times 0.5$ box.

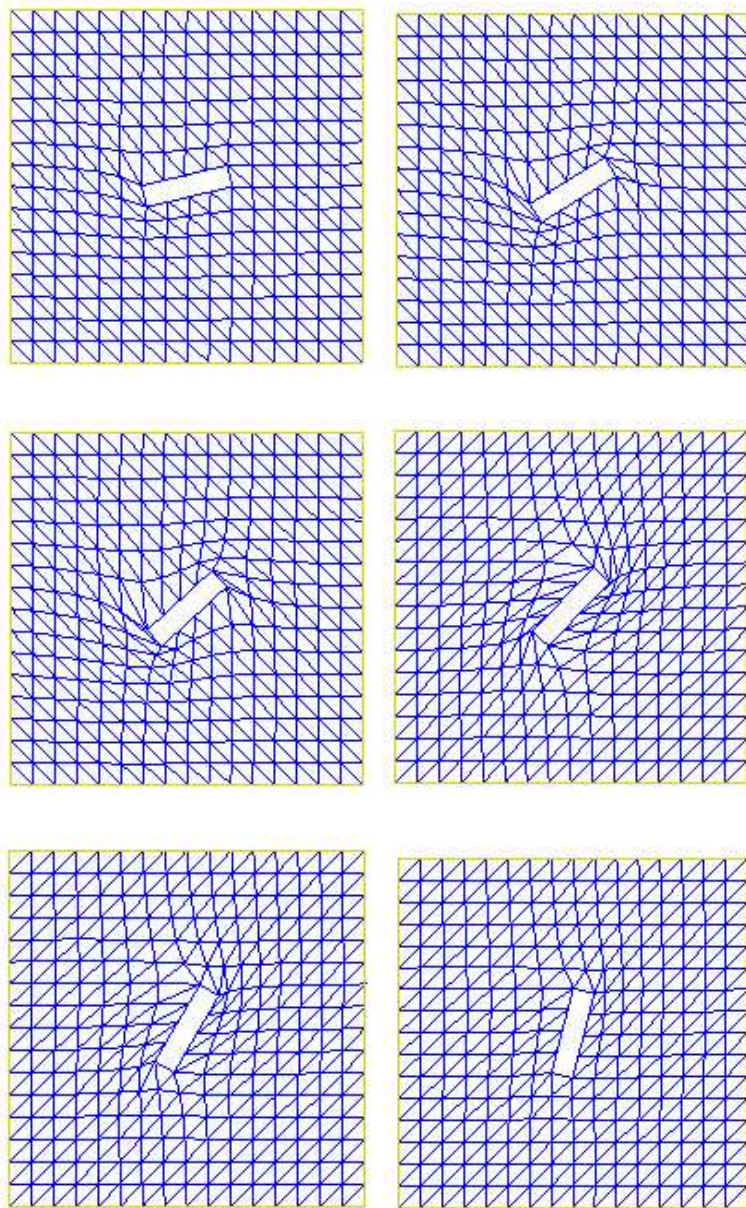


Fig. 32.4. Box rotation with Laplacian smoothing, for an $0.25 \times 0.0625 \times 0.25$ object inside a $1 \times 1 \times 1$ box.

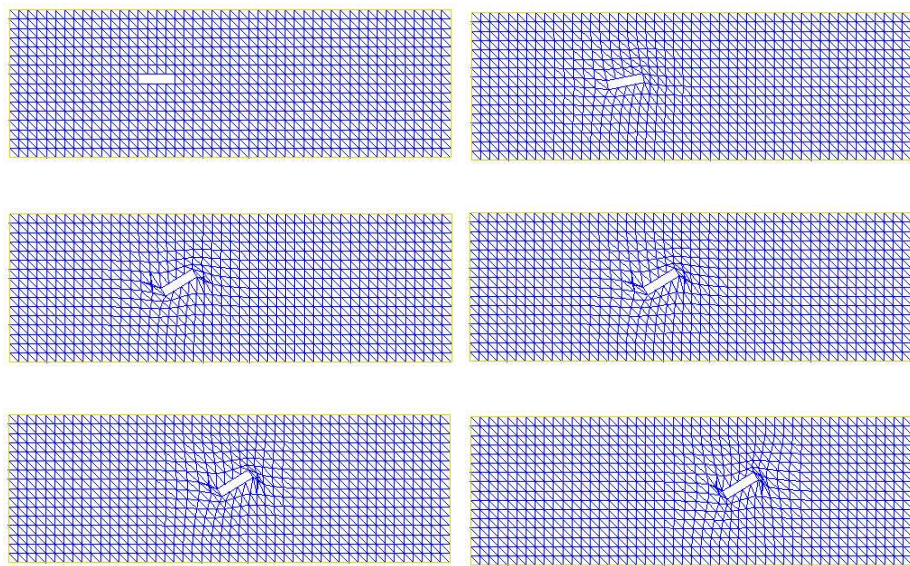


Fig. 32.5. Mesh for moving $0.25 \times 0.0625 \times 0.25$ object inside a channel.

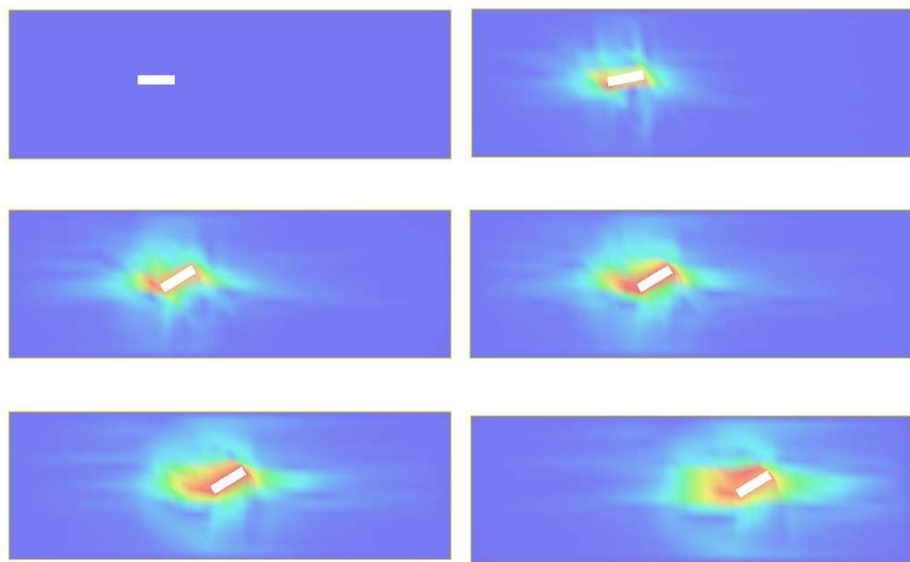


Fig. 32.6. Magnitude of the velocity $|u|$ for moving $1/4 \times 1/16 \times 1/4$ object inside a channel.

Part V

Flow Fundamentals

Bluff Body Flow

Flow visualization has from early times played an important part in research, always yielding qualitative insight, and recently also quantitative results. (Milton Van Dyke)

33.1 Introduction

A basic flow of great practical importance is *bluff body flow*, occurring in a large number of situations including vehicles moving through air/water such as cars, boats and airplanes, or flow of air/water around bodies at rest such as buildings, bridges, off-shore structures or cables. One of the basic problems of bluff body flow is to compute the *drag coefficient* c_D , which is a normalized mean value in time of the momentary *drag force* at time t , which is the total force at time t acted upon the body by the fluid. Similarly, the *lift coefficient* c_L is a normalized mean value in time of the *lift force* acting in a direction perpendicular to the flow. The drag coefficient of a car or airplane directly couples to the fuel consumption, and the lift coefficient of an airplane to its load carrying capacity, both of which are of prime concern.

The flow around a bluff body at higher Reynolds numbers is turbulent in a *wake* attaching to the rear of the body. As the shape of the body gets more streamlined, the wake gets smaller and the drag decreases. A non-streamlined body like a T-Ford may have $c_D \approx 1$, a modern more streamlined car may have $c_D \approx 0.3$, and a streamlined airfoil at subsonic speed may have $c_D \approx 0.01$. The drag has a contribution from the pressure distribution on the body surface, the *pressure drag* or *form drag*, and a contribution from the viscous forces, the *skin friction*. For a non-streamlined body skin friction is a small fraction of the total drag, while for an airfoil it may contribute up to 50 percent.

Bluff body flow exhibits basic phenomena such as *boundary layer flow*, *separation*, and *transition* from laminar to turbulent flow, to which we also devote separate chapters below.

In this chapter we present a set of benchmark problems for which experimental reference data are available, including a surface mounted cube, cylinders with square and circular cross sections and a sphere. The bluff body is placed in a channel with a given inlet flow, which may be viewed to model a wind tunnel test.

We first define the quantity of interest, drag or lift, then state an alternative expression for this quantity, and derive a corresponding a posteriori error estimate, and then we proceed to present computational results. The computational results with cG(1)cG(1) indicate that the adaptive method is very efficient in terms of the number of mesh points needed to approximate the quantity of interest to an accuracy corresponding to the precision in experiments. For further details of the computations we refer to [59, 53, 56, 54].

33.2 Drag and Lift

We consider a body with surface Γ_0 placed in a horizontal channel and surrounded by a fluid flow $\hat{u} = (u, p)$ which we assume is satisfying the NS equations, to start with in a pointwise sense. The mean value in time over a time interval $I = [0, \hat{t}]$ of the total fluid force acting on the body surface in a direction $\psi = (\psi_1, \psi_2, \psi_3)$, is given by

$$N(\sigma(\hat{u})) \equiv \frac{1}{|I|} \int_I \int_{\Gamma_0} \sum_{i,j=1}^3 \sigma_{ij}(\hat{u}) n_j \psi_i \, ds \, dt, \quad (33.1)$$

where $\sigma(\hat{u})$ is the stress on Γ_0 given by \hat{u} . If ψ is directed along the channel in the direction of the flow, then $N(\sigma(\hat{u}))$ is a mean value in time of the drag force. If ψ is directed upwards, then $N(\sigma(\hat{u}))$ is a mean value in time of the lift force. The drag and lift coefficients are normalized versions of $N(\sigma(\hat{u}))$ over a long time interval.

33.3 An Alternative Formula for Drag and Lift

Below we will use an alternative expression for the force $N(\sigma(\hat{u}))$ which naturally fits with both a weak formulation and a cG(1)cG(1) discretization, where the boundary integral over Γ_0 is replaced by a volume integral over the volume Ω surrounding the body occupied by the fluid. To this end we extend ψ to a function Φ defined in Ω and being zero on the remaining boundary $\Gamma_1 = \Omega \setminus \Gamma_0$ of the fluid volume. Multiplying the momentum equation in (28.1) by Φ and integrating by parts, we get assuming a zero Dirichlet boundary condition on Γ_1 ,

$$\begin{aligned} N(\sigma(\hat{u})) &= \frac{1}{|I|} \int_I (\dot{u} + u \cdot \nabla u - f, \Phi) - (p, \nabla \cdot \Phi) \\ &\quad + (2\nu\epsilon(u), \epsilon(\Phi)) + (\nabla \cdot u, \iota^h) \, dt, \end{aligned} \quad (33.2)$$

where we have also added an integral of $\nabla \cdot u = 0$ multiplied by a function ι^h . Obviously, this representation does not depend on ι^h , or the particular extension Φ of ψ . We note that the alternative expression (33.2) is more naturally defined for an ϵ -weak solution to the NS equations \hat{u} , than the original expression (33.1) involving derivatives of u on the boundary.

Similarly we define the drag force $N^h(\sigma(\hat{U}))$ corresponding to a computed cG(1)cG(1) approximation $\hat{U} = (U, P)$ by

$$\begin{aligned} N^h(\sigma(\hat{U})) &= \frac{1}{|I|} \int_I (\dot{U} + U \cdot \nabla U - f, \varphi^h) - (P, \nabla \cdot \varphi^h) \\ &\quad + (2\nu\epsilon(U), \epsilon(\varphi^h)) + (\nabla \cdot U, \iota^h) + SD_\delta(\hat{U}; \hat{\varphi}^h) dt, \end{aligned} \quad (33.3)$$

where now φ^h and ι^h are finite element functions with $\varphi^h = \psi$ on Γ_0 and $\varphi^h = 0$ on Γ_1 . Note in particular that we have here included the stabilization term SD_δ in (33.3) to make $N^h(\sigma(\hat{U}))$ independent of the choice of $\hat{\varphi}^h = (\varphi^h, \iota^h)$ in the finite element test space.

33.4 A Posteriori Error Estimation

We introduce the following dual problem: Find $\hat{\varphi} = (\varphi, \iota)$ with $\varphi = \psi$ on Γ_0 and $\varphi = 0$ on Γ_1 , such that

$$\begin{aligned} -\dot{\varphi} - (u \cdot \nabla)\varphi + \nabla U^\top \varphi - \nu \Delta \varphi + \nabla \iota &= 0, & \text{in } \Omega \times I, \\ \nabla \cdot \varphi &= 0, & \text{in } \Omega \times I, \\ \varphi(\cdot, \hat{t}) &= 0, & \text{in } \Omega, \end{aligned} \quad (33.4)$$

where $(\nabla U^\top \varphi)_j = \sum_{i=1}^3 U_{i,j} \varphi_i$.

For $\hat{u} \in \hat{W}_\epsilon$ an ϵ -weak solution to the NS equations, we derive a representation of the error $N(\sigma(\hat{u})) - N^h(\sigma(\hat{U}))$ by subtracting (33.3) from (33.2), with $\hat{\varphi}^h = (\varphi^h, \iota^h)$ a finite element function in the test space of cG(1)cG(1), to get

$$\begin{aligned} N(\sigma(\hat{u})) - N^h(\sigma(\hat{U})) &= \frac{1}{|I|} \int_I (\dot{u} + u \cdot \nabla u, \varphi^h) - (p, \nabla \cdot \varphi^h) \\ &\quad + (2\nu\epsilon(u), \epsilon(\varphi^h)) + (\nabla \cdot u, \iota^h) - ((\dot{U} + U \cdot \nabla U, \varphi^h) - (P, \nabla \cdot \varphi^h) \\ &\quad + (2\nu\epsilon(U), \epsilon(\varphi^h)) + (\nabla \cdot U, \iota^h) + SD_\delta(\hat{U}; \hat{\varphi}^h)) dt. \end{aligned} \quad (33.5)$$

With $\hat{\varphi}$ the solution to the dual problem (33.4), we also have, assuming Dirichlet boundary conditions for the velocity:

$$\begin{aligned} &\frac{1}{|I|} \int_I (\dot{u} + u \cdot \nabla u, \varphi) - (p, \nabla \cdot \varphi) + (2\nu\epsilon(u), \epsilon(\varphi)) + (\nabla \cdot u, \iota) \\ &\quad - ((\dot{U} + U \cdot \nabla U, \varphi) - (P, \nabla \cdot \varphi) + (2\nu\epsilon(U), \epsilon(\varphi)) + (\nabla \cdot U, \iota)) dt \\ &= \frac{1}{|I|} \int_I -(\dot{\varphi}, e) + (u \cdot \nabla e + e \cdot \nabla U, \varphi) - (p - P, \nabla \cdot \varphi) \\ &\quad + (2\nu\epsilon(e), \epsilon(\varphi)) + (\nabla \cdot e, \iota) dt = 0, \end{aligned} \quad (33.6)$$

using partial integration with $\varphi(\hat{t}) = e(0) = 0$, where $e = u - U$, and that $(u \cdot \nabla)u - (U \cdot \nabla)U = (u \cdot \nabla)e + (e \cdot \nabla)U$. By (33.5) and (33.6), we thus have that

$$\begin{aligned} N(\sigma(\hat{u})) - N^h(\sigma(\hat{U})) &= \frac{1}{|I|} \int_I (\dot{U} + U \cdot \nabla U, \varphi - \varphi^h) \\ &\quad - (P, \nabla \cdot (\varphi - \varphi^h)) + (\nabla \cdot U, \iota - \iota^h) + (2\nu\epsilon(U), \nabla(\varphi - \varphi^h)) \\ &\quad - SD_\delta(\hat{U}; \hat{\varphi}^h) - ((\dot{u} + u \cdot \nabla u, \varphi - \varphi^h) \\ &\quad - (p, \nabla \cdot (\varphi - \varphi^h)) + (\nabla \cdot u, \iota - \iota^h) + (2\nu\epsilon(u), \nabla(\varphi - \varphi^h))) dt \\ &= \frac{1}{|I|} \int_I (R(\hat{U}), \hat{\varphi} - \hat{\varphi}^h) - SD_\delta(\hat{U}; \hat{\varphi}^h) - (R(\hat{u}), \hat{\varphi} - \hat{\varphi}^h) dt, \end{aligned}$$

adding and subtracting $(f, \varphi - \varphi^h)$, where we define

$$\begin{aligned} (R(\hat{w}), \hat{v}) &\equiv (\dot{w} + w \cdot \nabla w - f, v) - (r, \nabla \cdot v) \\ &\quad + (\nabla \cdot w, q) + (2\nu\epsilon(w), \epsilon(v)), \end{aligned} \tag{33.7}$$

for $\hat{w} = (w, r)$ and $\hat{v} = (v, q)$.

We have now proved the following error representation, where we express the total output error as a sum of error contributions from the different elements K in space (assuming here for simplicity that the space mesh is constant in time), and we use the subindex K to denote integration over element K so that $(\cdot, \cdot)_K$ denotes the appropriate $L_2(K)$ inner product:

Theorem 33.1. *If $\hat{u} = (u, p)$ is an ϵ -weak solution to the NS equations, $\hat{U} = (U, P)$ is a cG(1)cG(1) solution, $\hat{\varphi} = (\varphi, \iota)$ is the dual solution satisfying (33.4), and $\hat{\varphi}^h = (\varphi^h, \iota^h)$ is a finite element function in the test space of cG(1)cG(1) satisfying $\varphi^h = \psi$ on Γ_0 and $\varphi^h = 0$ on $\Gamma_1 = \partial\Omega \setminus \Gamma_0$, then*

$$N(\sigma(\hat{u})) - N^h(\sigma(\hat{U})) = \sum_{K \in \mathcal{T}_n} \mathcal{E}_K,$$

where $\mathcal{E}_K = e_D^K + e_M^K + e_\epsilon^K$, with

$$\begin{aligned} e_D^K &= \frac{1}{|I|} \int_I (R_K(\hat{U}), \hat{\varphi} - \hat{\varphi}^h)_K dt, \\ e_M^K &= \frac{-1}{|I|} \int_I SD_\delta(\hat{U}; \hat{\varphi}^h)_K dt, \\ e_\epsilon^K &= \frac{-1}{|I|} \int_I (R_K(\hat{u}), \hat{\varphi} - \hat{\varphi}^h)_K dt, \end{aligned}$$

where $(R_K(\cdot), \cdot)_K$ is a local version of $(R(\cdot), \cdot)$, defined by (33.7).

We may here view e_D^K as a Galerkin error contribution from cG(1)cG(1) on element K , e_M^K as a modeling error contribution from stabilization in

cG(1)cG(1), and e_ϵ^K as an error contribution from the ϵ -weak solution \hat{u} characterizing the weak uniqueness of \hat{u} .

From the error representation in Theorem 33.1, there are various possibilities to construct error indicators and stopping criteria for an adaptive algorithm. Using interpolation estimates of the type presented in Chapter 28, with $\hat{\varphi}^h$ a finite element interpolant of $\hat{\varphi}$, we may estimate e_D^K as follows

$$\begin{aligned} e_D^K \leq \frac{1}{|I|} \int_I & ((|R_1(\hat{U})|_K + |R_2(\hat{U})|_K) \cdot (C_h h^2 |D^2 \varphi|_K + C_k k |\dot{\varphi}|_K) \\ & + \|R_3(\hat{U})\|_K (C_h h^2 \|D^2 \iota\|_K + C_k k \|\iota\|_K)) dt, \end{aligned}$$

where the residuals R_i are defined by

$$\begin{aligned} R_1(\hat{U}) &= \dot{U} + U \cdot \nabla U - \nu \Delta U + \nabla P - f, \\ R_2(\hat{U}) &= \nu D_2(U), \\ R_3(\hat{U}) &= \nabla \cdot U, \end{aligned} \tag{33.8}$$

with

$$D_2(U)(x, t) = \frac{1}{h_n(x)} \max_{y \in \partial K} \left| \left[\frac{\partial U}{\partial n}(y, t) \right] \right|, \tag{33.9}$$

for $x \in K$, with $[\cdot]$ the jump across the element edge ∂K , D^2 denotes second order spatial derivatives, and we write $|w|_K \equiv (\|w_1\|_K, \|w_2\|_K, \|w_3\|_K)$, with $\|w\|_K = (w, w)_K^{1/2}$, and let the dot denote the scalar product in \mathbb{R}^3 .

The next step involves replacing the exact dual solution $\hat{\varphi}$ by a computed approximation $\hat{\varphi}_h = (\varphi_h, \iota_h)$ obtained by, for example, cG(1)cG(1) on the same mesh as we use for the primal problem. Doing so we are led to the following a posteriori error estimate (omitting the ϵ -term):

$$|N(\sigma(\hat{u})) - N^h(\sigma(\hat{U}))| \approx \left| \sum_{K \in \mathcal{T}_n} \mathcal{E}_{K,h} \right| \tag{33.10}$$

where $\mathcal{E}_{K,h} = e_{D,h}^K + e_{M,h}^K$ with

$$\begin{aligned} e_{D,h}^K &= \frac{1}{|I|} \int_I ((|R_1(\hat{U})|_K + |R_2(\hat{U})|_K) \cdot (C_h h^2 |D^2 \varphi_h|_K + C_k k |\dot{\varphi}_h|_K) \\ &\quad + \|R_3(\hat{U})\|_K \cdot (C_h h^2 \|D^2 \iota_h\|_K + C_k k \|\iota_h\|_K)) dt, \\ e_{M,h}^K &= \frac{1}{|I|} \int_I S D_\delta(\hat{U}; \hat{\varphi}_h)_K dt, \end{aligned}$$

where we have replaced the interpolant $\hat{\varphi}^h$ by $\hat{\varphi}_h$. Again we may view $e_{D,h}^K$ as the error contribution from the Galerkin part of cG(1)cG(1) on element K , and $e_{M,h}^K$ as the contribution from the stabilization in cG(1)cG(1) on element K .

Note that we may view the ϵ -weak solution \hat{u} as an approximate solution using maximal computational resources, and we may thus assume that $e_\epsilon^K \ll$

$e_D^K + e_M^K$, and therefore drop e_ϵ^K . With this interpretation the term e_ϵ^K in Theorem 33.1 characterizes a best possible accuracy for the output $N(\sigma(\cdot))$ with the available computational resources.

In the computations below we use $C_k = 1/2$ and $C_h = 1/8$ as constant approximations of the interpolation constants in Theorem 33.1. These values are motivated by a simple analysis on reference elements, using Taylor's formula. More detailed approximation of interpolation constants is possible using a computational approach for each element individually.

Non-Dirichlet boundary conditions, such as slip boundary conditions at lateral boundaries and transparent outflow boundary conditions, introduce additional boundary terms in the error representation in Theorem 33.1, but since the dual solution in the bluff body examples in this chapter is small at such non-Dirichlet boundaries, we neglect the corresponding boundary terms in the computations below.

We use Algorithm 30.1 for adaptive mesh refinement in space (with for simplicity the same space mesh for all time steps) based on the a posteriori error estimate (33.10).

33.5 Surface Mounted Cube

The flow past a surface mounted cube may serve as a very simple model of the flow of air around a moving car, or the flow past a building, for example. In this model the incoming flow is laminar time-independent forming a horse shoe vortex upstream the cube, and a laminar boundary layer on the front surface, which separates and develops a turbulent wake attaching to the rear face of the cube. The flow is thus very complex with a combination of laminar and turbulent features including boundary layers and a large turbulent wake, see Figure 33.1.

In the model problem the cube side length is $H = 0.1$, and the cube is centrally mounted on the floor of a rectangular channel of length $15H$, height $2H$, and width $7H$, at a distance of $3.5H$ from the inlet. The cube is subject to a Newtonian flow governed by the NS equations with kinematic viscosity $\nu = 2.5 \times 10^{-6}$ and a unit inlet bulk velocity corresponding to a Reynolds number of 40 000, using the dimension of the cube as characteristic dimension. The inlet velocity profile is interpolated from experiments, we use no slip boundary conditions on the cube and the vertical channel boundaries, slip boundary conditions on the lateral channel walls, and a transparent outflow boundary condition.

33.5.1 The drag coefficient c_D

The drag coefficient c_D is a long-time mean value of a normalized drag force. We seek an approximate drag coefficient \bar{c}_D over a finite time interval $I = [0, \hat{t}]$ with fully developed flow \hat{u} , defined by

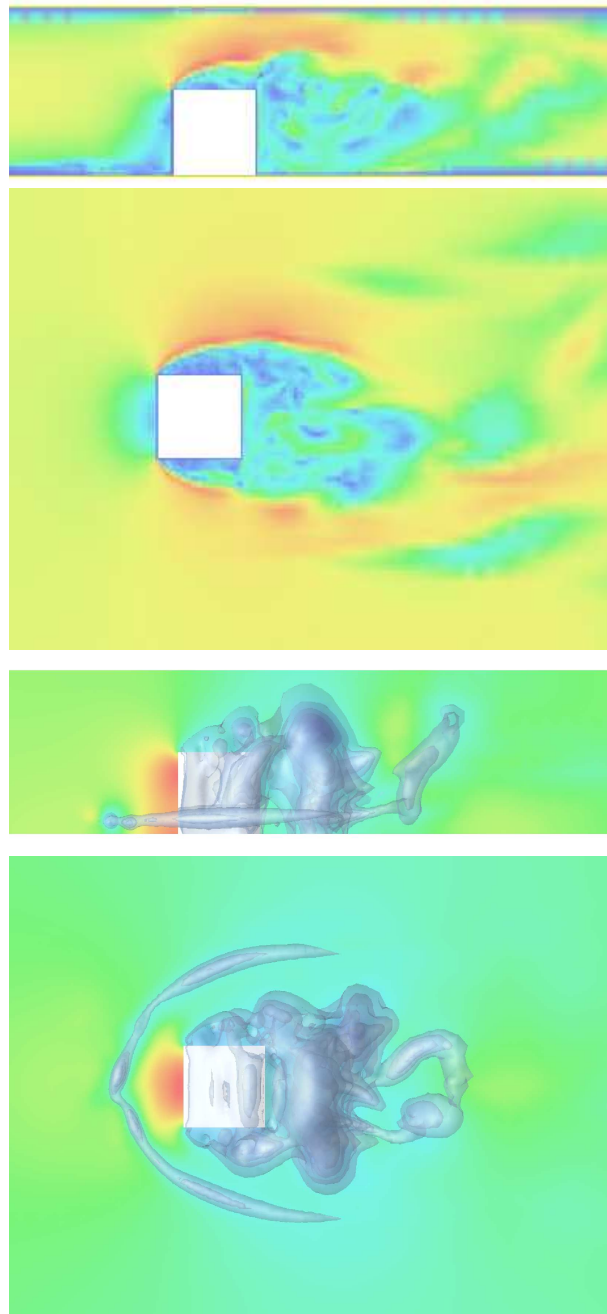


Fig. 33.1. Surface mounted cube: Magnitude of velocity (upper), and pressure color map, with iso-surfaces for negative pressure, illustrating the horse shoe vortex.

$$\bar{c}_D \equiv \frac{1}{\rho^{\frac{1}{2}} U_{\infty}^2 A} \times N(\sigma(\hat{u})), \quad (33.11)$$

where $\hat{t} = 40H$, $U_{\infty} = 1$ is a bulk inflow velocity, $A = H \times H = H^2$ is the cube area facing the flow, $N(\sigma(\hat{u}))$ is defined by (33.1), and we assume constant unit density $\rho = 1$. We compute an approximate drag coefficient

$$\bar{c}_D^h = \frac{1}{\rho^{\frac{1}{2}} U_{\infty}^2 A} \times N^h(\sigma(\hat{U})), \quad (33.12)$$

with $N^h(\sigma(\hat{U}))$ defined by (33.3) and \hat{U} a cG(1)cG(1) approximate solution. We use an adaptive algorithm based on a normalized version of the a posteriori error estimate (33.10).

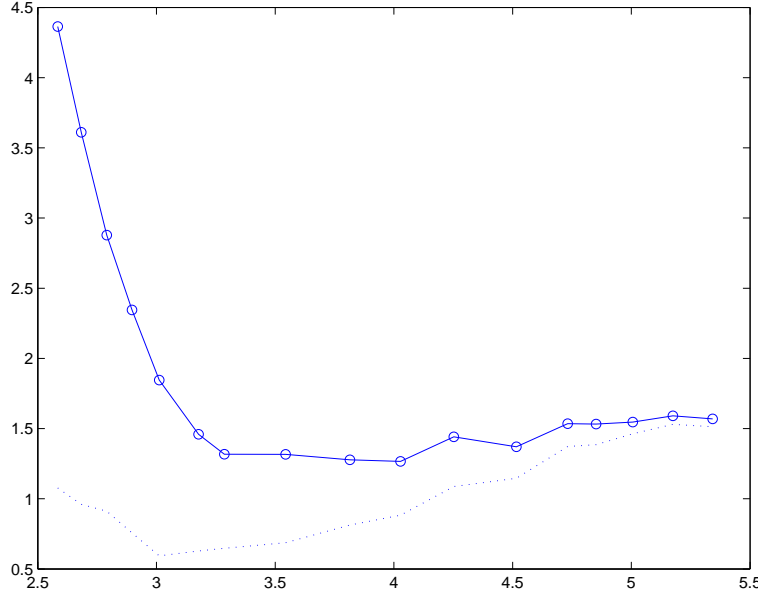


Fig. 33.2. Surface mounted cube: \bar{c}_D^h ('o'), and the corresponding approximations without the contribution from the stabilizing term (':'), as functions of the 10-logarithm of the number of mesh points.

In Figure 33.2 we display c_D^h as a function of the number of mesh points in space. We obtain $c_D^h \approx 1.55$, with the value seemingly being well captured up to ± 0.03 already using less than 10^5 mesh points. In each step of the adaptive process we refine roughly 30% of the space elements. The drag contribution from the stabilizing terms in (33.3) is notable on coarse meshes but decreases to less than 5% on the finer meshes. The a posteriori error estimate gives a tolerance of ± 0.3 , which seems to be an over-estimate by a factor of 10, which can be attributed to the presence of absolute values in the error estimation.

33.5.2 Dual solution and a posteriori error estimates

Snapshots of the dual solution and the adaptively refined computational mesh are shown in Figure 15.3 and in Figure 33.3. The initial mesh is uniform and very coarse, 384 mesh points, and we find that the adaptive method automatically captures the turbulent wake and the horse-shoe vortex.

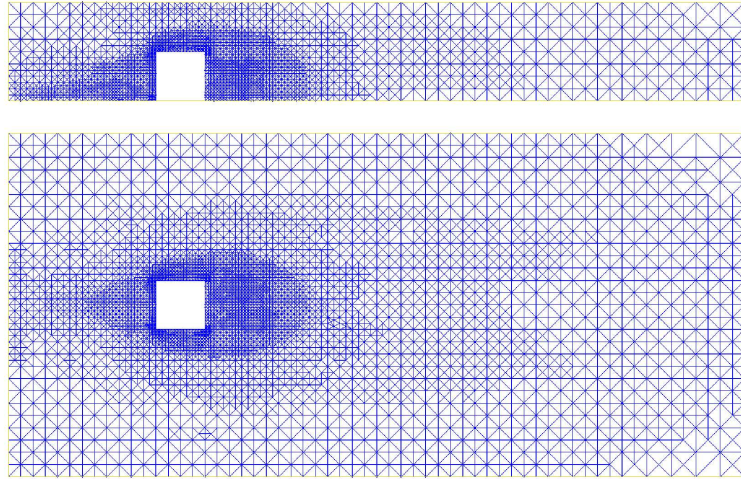


Fig. 33.3. Surface mounted cube: computational mesh refined with respect to mean drag, in the x_1x_2 -plane at $x_3 = 3.5H$ and in the x_1x_3 -plane at $x_2 = 0.5H$.

In Figure 33.4 we plot the a posteriori error estimates $e_{D,h} = \sum_K e_{D,h}^K$ and $e_{M,h} = \sum_K e_{M,h}^K$ from (33.10), as well as the true error based on the computational approximation on the finest mesh. For the modeling error $e_{M,h}$ we use a conservative estimate where we have set the absolute values inside the sums in space and time.

We find that once the value for \bar{c}_D^h is stabilized, the a posteriori error estimates indicate that it may be hard to further increase the precision in c_D , which couples to the discussion above of a lower bound on the tolerance.

33.5.3 Comparison with reference data

We know of no experimental reference values of c_D , but in [21] a DNS using about 70×10^6 degrees of freedom gives $c_D \approx 1.42$ with the same data as in our computations using cG(1)cG(1). The stabilizing terms in (33.3) is not used in the evaluation of c_D , and the result should thus be compared to the curve of somewhat lower values in Figure 33.2, resulting in a good agreement.

In [77] results using LES are reported where the computational setup is similar to the one we use here, except the numerical method, the length of

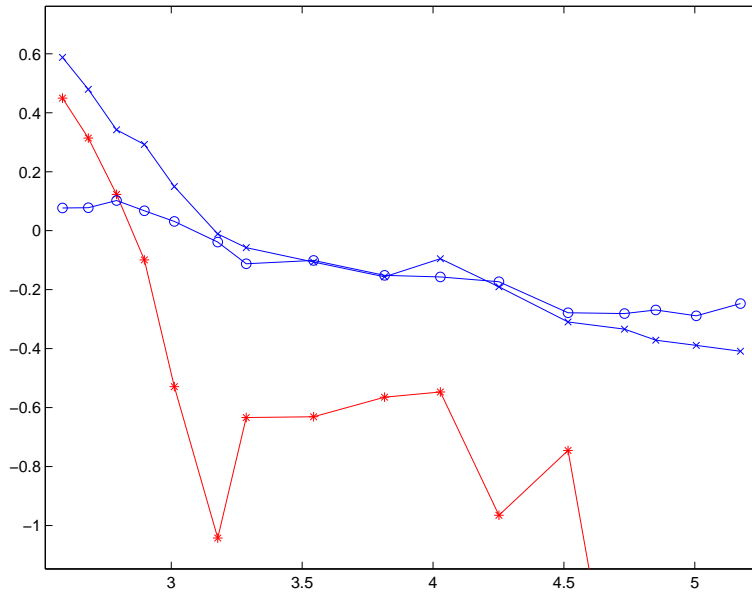


Fig. 33.4. Surface mounted cube: \log_{10} - \log_{10} plot of the a posteriori error estimates $e_{D,h}$ ('o') and $e_{M,h}$ ('x'), and the true error ('*') based on $c_D = 1.55$ (the solution on the finest mesh), as functions of the number of mesh points in space.

the time interval, and the length of the channel. Using LES with different meshes and subgrid models, approximations of c_D in the interval [1.14, 1.24] are reported, thus significantly lower values.

We note that we reach the stable value of $c_D \approx 1.5$ using about 50 000 mesh points in space, which means that the adaptive method is very efficient in terms of the number of degrees of freedom, making the computations possible using a standard PC. In addition, we have an estimated accuracy from the a posteriori error estimates, and a set of results for a hierarchy of refined computational meshes reflecting convergence in output.

33.6 Flow Past a Car

The surface mounted cube may represent a simple model of a building experiencing a wind load, or a very simple model of the flow past a moving car. In Fig. 33.5-33.6 we present a G2 computation of the flow past a full model of a car and an associated dual solution providing sensitivity information with respect to computing drag.

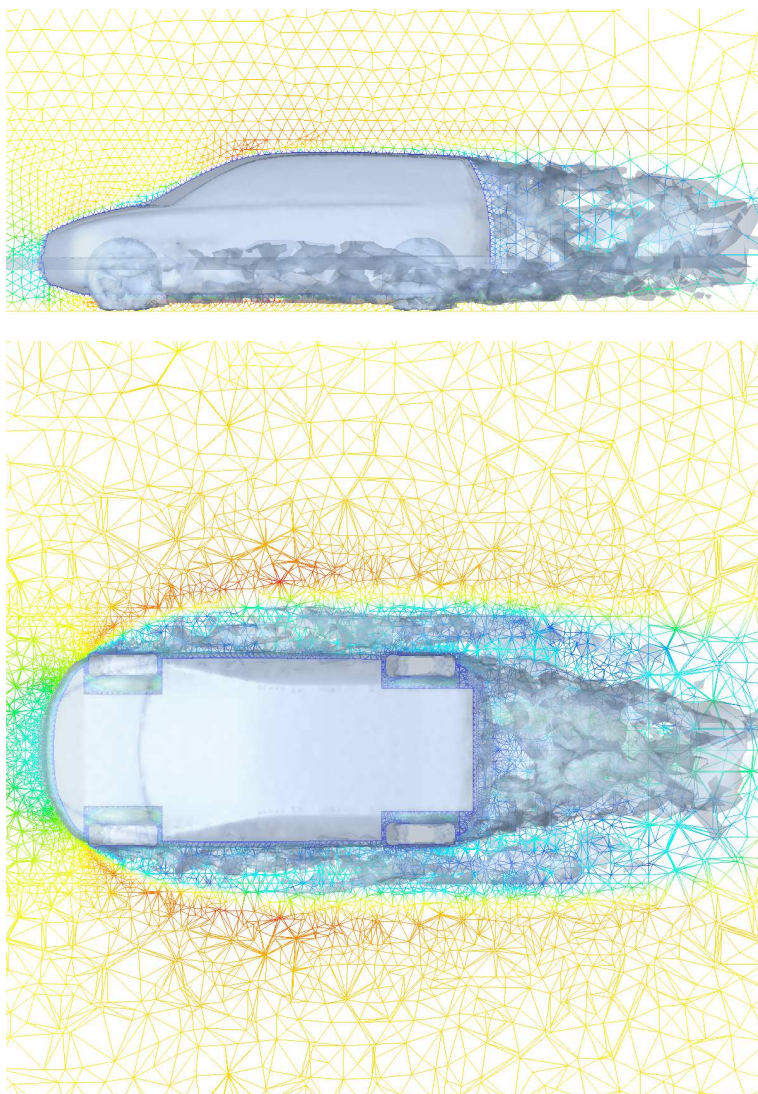


Fig. 33.5. G2 solution of the turbulent flow around a car (geometry courtesy of Volvo Car Corporation).

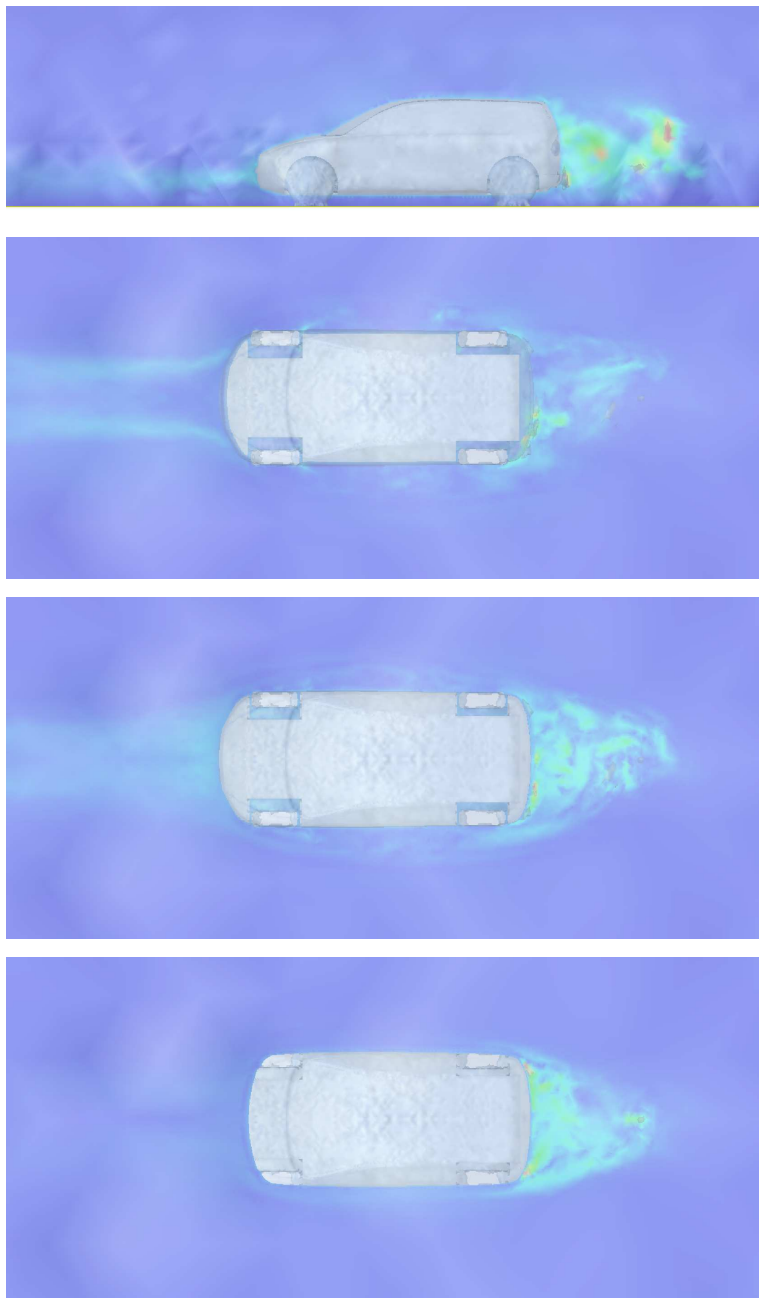


Fig. 33.6. Dual solution with respect to drag around a car (geometry courtesy of Volvo Car Corporation).

33.7 Square Cylinder

We now consider a square cylinder at Reynolds number 22 000, based on the cylinder diameter $D = 0.1$ and the unit inflow velocity in the streamwise direction. The computational domain is a channel of size $21D \times 14D \times 4D$ in the x_1 -direction with the cylinder directed in the x_3 -direction and centered at $(x_1, x_2) = (5D, 7D)$. We use no slip boundary conditions on the cylinder, slip boundary conditions on the lateral channel walls, and a transparent outflow boundary condition.

Characteristics of this flow are a turbulent wake of approximate diameter $1D$ attached to the trailing face of the cylinder, and two opposite shear layers periodically shedding vortices, see Figure 33.7. In addition, we have a cycle-to-cycle variation, so called *phase jitter*, due to turbulence and 3D instabilities in the shear layers, which is illustrated in Figure 33.8 as a time series of the vorticity showing the changing wake, with the shorter wake, with more pronounced vortex shedding, corresponding to high drag in Figure 33.9.

33.7.1 Computing mean drag: time vs. phase averages

We seek to compute the mean drag force $N(\sigma(\cdot))$ of the square cylinder, and we here choose an averaging time interval of length $100D$, starting at fully developed flow. The length of the time interval directly couples to computability and output uniqueness of $N(\sigma(\cdot))$, with a longer time interval resulting in a more well determined mean drag force which is cheaper to compute from an accuracy point of view. On the other hand, for a longer time interval the computational cost of course increases for each iteration of the adaptive algorithm.

Phase jitter complicate the computation of time averages, since the time averages are highly dependent of the size and location of the time interval, and thus a very long time interval is needed for a well determined mean drag force. This has lead to alternative ways to represent averages. For example, one may consider so called *phase averages*, where a number of shedding cycles are chosen as “typical” for the flow, over which mean values are computed.

We now seek the drag coefficient c_D , which we approximate by \bar{c}_D , defined by (33.11), with its computational version \bar{c}_D^h given by (33.12), where we set $U_\infty = 1$ based on the inflow velocity, and the area $A = 4D \times D = 4D^2$. In Figure 33.9 we plot computed approximations \bar{c}_D^h as we refine approximately 30% of the elements in the mesh each iteration, where we also include approximations without the stabilizing term in (33.3). For the finer meshes we get a \bar{c}_D^h in the interval 2.0–2.4, and a value about 5% lower for the formulation without the stabilizing term. The large variation in \bar{c}_D^h can be explained by effects of phase jitter and a relatively short time interval, as noted above. In Figure 33.9 we plot the trajectory of the normalized drag force for the finest mesh, where we notice the variations in amplitude and local mean of the drag.

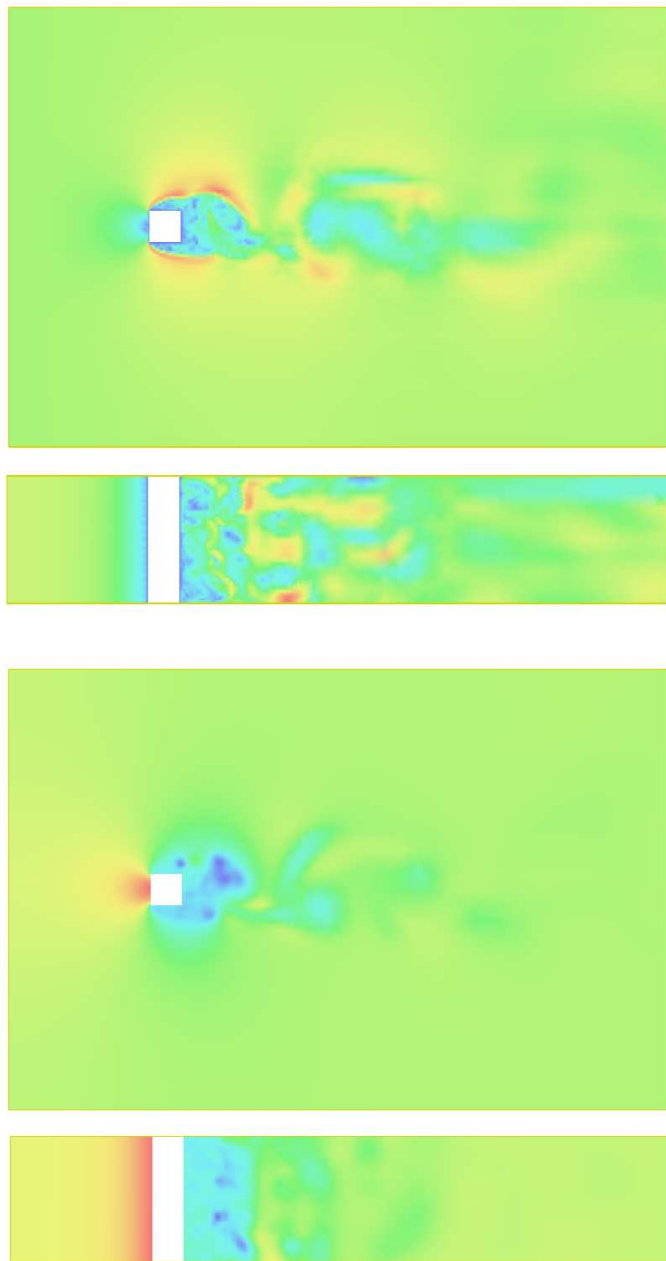


Fig. 33.7. Velocity $|U|$ (upper), and pressure P (lower), in the x_1x_2 -plane at $x_3 = 2D$.

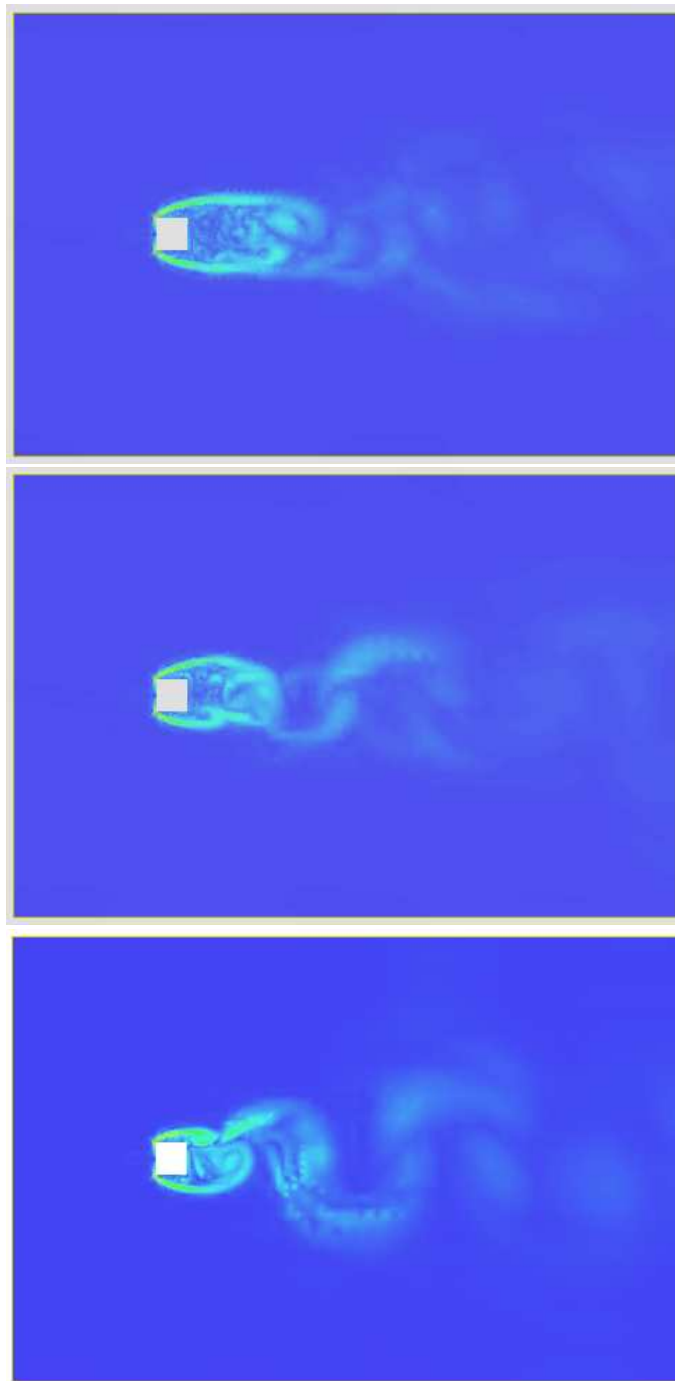


Fig. 33.8. Time evolution of vorticity $|\nabla \times U|$, in the x_1x_2 -plane at $x_3 = 2D$.

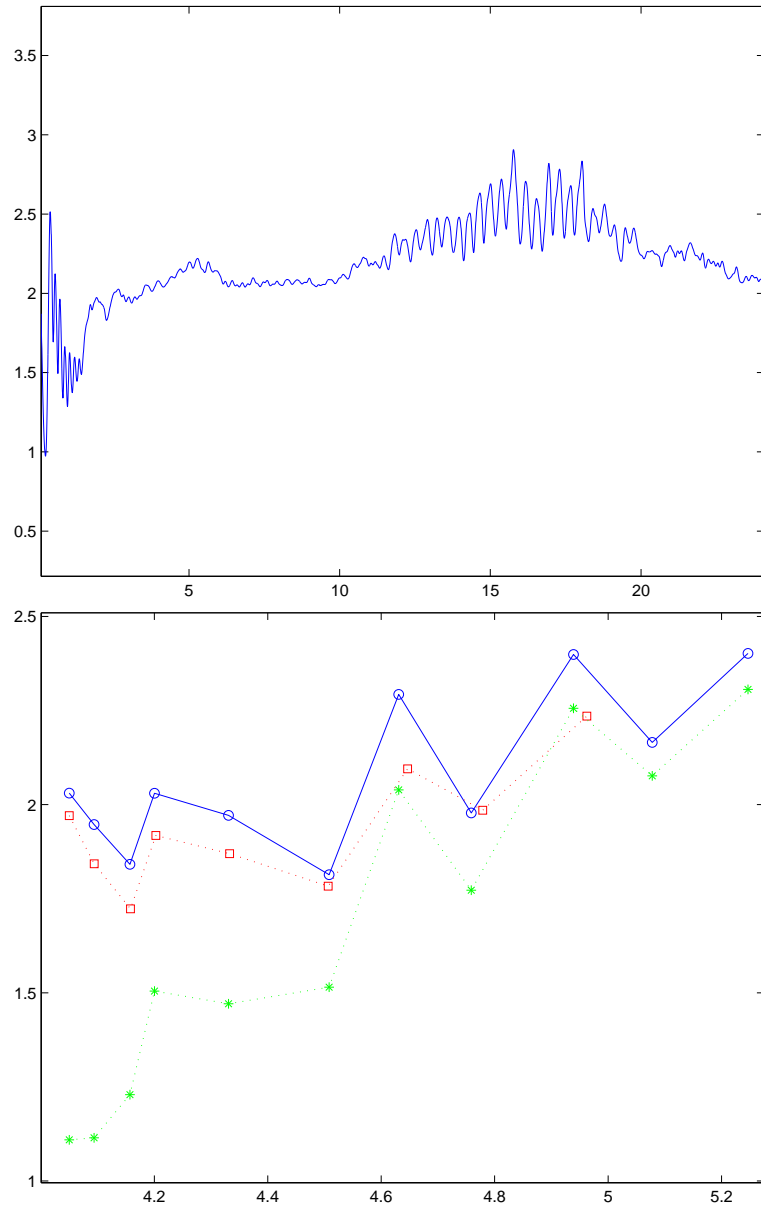


Fig. 33.9. Square cylinder: Normalized drag force as a function of time after 9 mesh refinements (upper), and \bar{c}_D^h ('o'), the corresponding approximations without the contribution from the stabilizing term in (33.3) ('*'), and the approximation with 2% white noise in inflow velocity (' \square '), as functions of the 10-logarithm of the number of mesh points in space (lower).

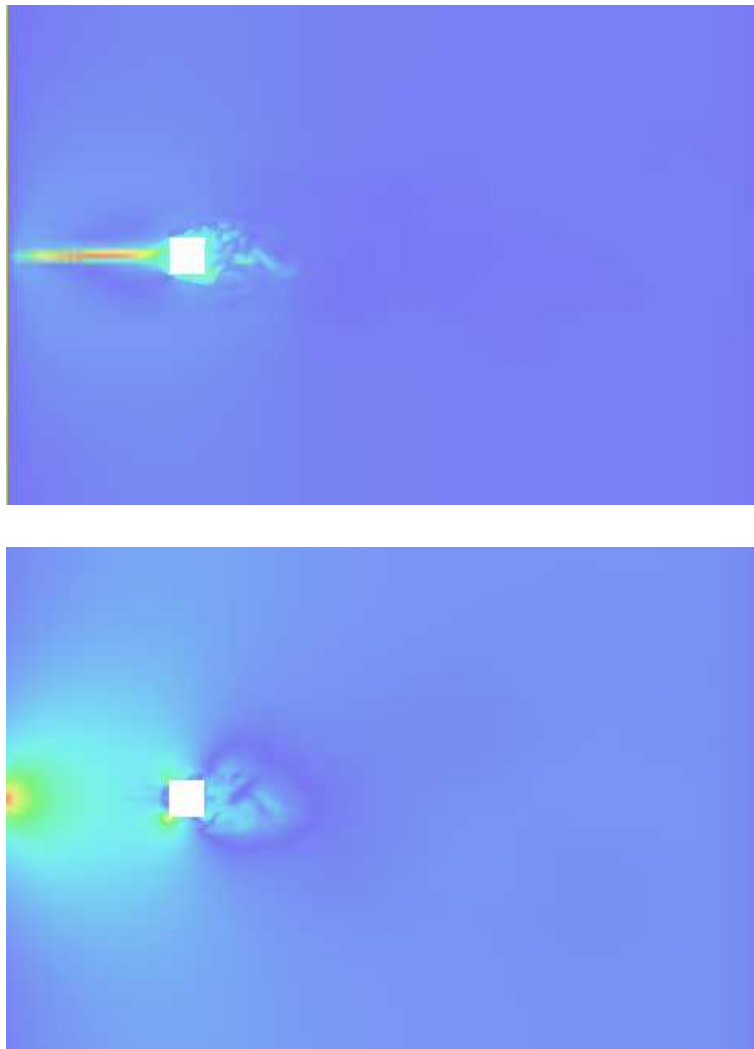


Fig. 33.10. Square cylinder: dual velocity $|\varphi_h|$ (upper), and dual pressure $|\iota_h|$ (lower), in the x_1x_3 -plane at $x_2 = 7D$ and in the x_1x_2 -plane at $x_3 = 2D$.

33.7.2 Dual solution and a posteriori error estimates

A snapshot of the dual solution is shown in Figure 33.10. We note that the dual solution, with velocity boundary data on the cylinder in the streamwise direction, is of moderate size, and in particular is not exploding as pessimistic worst case analytical estimates may suggest, but rather seems to behave as if the net effect of the crucial reaction term (with large oscillating coefficient ∇U)

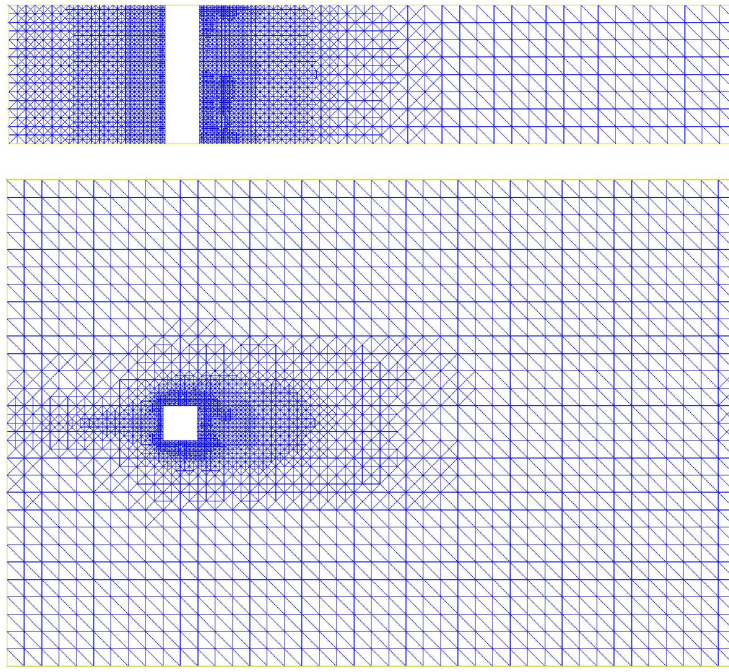


Fig. 33.11. Square cylinder: computational mesh after 9 adaptive mesh refinements with respect to mean drag, in the x_1x_3 -plane at $x_2 = 7D$ and in the x_1x_2 -plane at $x_3 = 2D$.

is only a moderate growth. We also note that $\hat{\varphi}_h = (\varphi_h, \iota_h)$ is concentrated in space, thus significantly influencing the adaptive mesh refinement.

The resulting computational mesh after 9 adaptive mesh refinements is shown in Figure 33.11. The initial space mesh is uniform and coarse, and without the dual weights in the a posteriori error estimate the mesh would come out quite differently. We notice in particular that the adaptive method automatically captures the turbulent wake, which is essential for accurately computing drag.

In Figure 33.12 we plot the a posteriori error estimates $e_{D,h}$ and $e_{M,h}$ from (33.10), as well as an estimate of the true error based on the computational approximations on the finest meshes, suggesting that 2.2 may be a good candidate for a representative value of c_D . The modeling error $e_{M,h}$ consists of sums in space and time of integrals over the space-time elements, and in the evaluation of $e_{M,h}$ in Figure 33.12 we have set the absolute values inside the sums in space and time. The same goes for the discretization error, and thus error cancellation is not possible, leading to conservative error estimates.

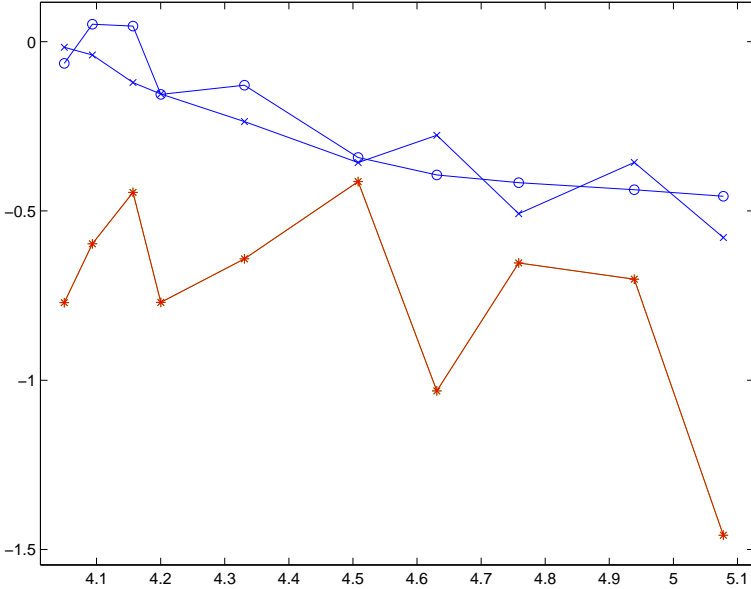


Fig. 33.12. Square cylinder: $\log_{10}-\log_{10}$ plot of the a posteriori error estimates $e_{D,h}$ ('o') and $e_{M,h}$ ('x'), and the true error ('*') based on $c_D = 2.2$, as functions of the number of mesh points in space.

33.7.3 Comparison with reference data

Various reference values for this problem are reported, including mean drag. Experimental reference values for c_D are reported in the interval 1.9-2.1, where the experiments are carried out under slightly different conditions than the computations, such as a slightly lower Reynolds number, a longer cylinder, and a turbulence level of 2% in the inflow velocity. In a collection of results from different research groups [97], LES results are reported in the interval 1.66-2.77, and RANS results in the interval 1.6-2.0.

To test the sensitivity in inflow data, we compare our results with a computation with 2% white noise added to the inflow velocity. These results are plotted in Figure 33.9, giving similar values for c_D , although somewhat lower, closer to the experimental results.

We find that apart from drag we are also able to capture the correct frequency of the oscillating wake, characterized by the *Strouhal number* St , defined as the dimensionless number

$$St = \frac{fL}{U_\infty}, \quad (33.13)$$

where f is the frequency, L is a length scale (here equal to the cylinder diameter: $L = D$), and U_∞ is a velocity scale (here $U_\infty = 1$).

In this study, the computation of c_D^h corresponds to the interval [10, 20] in Figure 33.9. We can see that translating this interval suitably would result in a lower c_D^h , within the tolerance of the experimental reference values. We note that again we reach the targeted value for the drag coefficient using very few mesh points.

33.8 Circular Cylinder

The flow past a circular cylinder is a classical problem of fluid dynamics. In our model we consider a circular cylinder of diameter D and length $4D$, in the direction of the x_3 -axis, subject to a unit streamwise velocity inflow condition in a channel along the x_1 -axis of length $21D$ and height $14D$. We use no slip boundary conditions on the cylinder, slip boundary conditions on the lateral walls of the channel, and a transparent outflow boundary condition at the end of the channel.

The character of the flow past a circular cylinder depends on the Reynolds number: For Re very low (Re less than 4-5) we have *creeping flow* without separation and with high viscous drag, increasing the Reynolds number the flow separates to form a steady, symmetric wake of recirculating flow, and further increasing Re beyond 30-48 leads to the onset of an oscillation of the wake that periodically sheds alternating vortices gradually developing downstream, a so called *von Kármán vortex street*. Theodore von Kármán in 1911 investigated the stability of two rows of vortices, showing that such vortices are generally unstable and that the only stable arrangement is that with $h/l = 0.281$, with h and l being the vertical and streamwise distances between the center of the vortices, see Fig. 33.13.

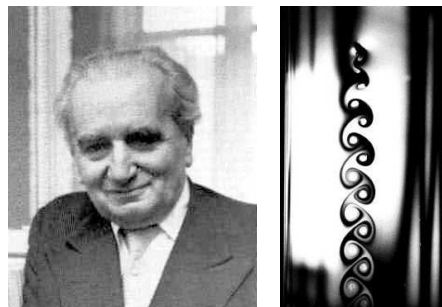


Fig. 33.13. Theodore von Kármán (1881–1963), and a von Kármán vortex street for $Re = 100$.

The flow for higher Reynolds numbers is characterized by transition to turbulence in different parts of the flow: First the wake undergoes transition, then the shear layers, and finally the boundary layers. The different regimes

are characterized by different separation and different shedding frequencies. For $Re < 100$, c_D is proportional to Re^{-1} , for $100 < Re < 10^5$ we have $c_D \approx 1$, while for $Re > 10^5$ we find that the c_D first drops significantly and then rises back again. The drag reduction near $Re = 10^5$ is commonly referred to as *drag crisis*, where the boundary layer undergoes transition, leading to a delayed separation with a smaller wake, corresponding to a drastic reduction of the drag. We come back to the problem of simulating drag crisis in Chapter 35.

A cG(1)cG(1) approximation of the flow past a circular cylinder is plotted in Fig. 33.14 for $Re = 100$. We find that the flow is two dimensional for this low Reynolds number, and we clearly see the vortex shedding. For $Re = 3900$, we find in Fig. 33.15 that we still have vortex shedding, but now the flow is three dimensional, and we have a large turbulent wake attached to the cylinder, see Fig. 33.16.

33.8.1 Comparison with reference data

The flow past a circular cylinder at various Reynolds numbers is probably the most well documented bluff body flow, with an extensive amount of experimental and computational results available, see e.g. [110, 99].

In Fig. 33.17 we plot computational approximations of the drag coefficients using cG(1)cG(1) for Reynolds numbers 100 and 3900, where we refine 10% and 5% of the elements in each iteration, respectively. The normalization is now $U_\infty = 1$ and $A = 0.1 \times 0.4 = 0.04$. For $Re = 100$ we get a \bar{c}_D^h somewhat lower than 1.5, which is within the tolerance of experimental results, and for $Re = 3900$ we have \bar{c}_D^h slightly less than 1.0, which is consistent with experiments. We also capture the correct Strouhal numbers, with $St \approx 0.16$ for $Re = 100$ and $St \approx 0.22$ for $Re = 3900$, where we average over a time interval $I = 35D/U_\infty$.

We study the surface pressure on the cylinder as a function of an angle starting from the upstream stagnation point of the cylinder, in the form of a *pressure coefficient* c_p , defined by

$$c_p = \frac{p - p_\infty}{\rho \frac{1}{2} U_\infty^2}, \quad (33.14)$$

where U_∞ and p_∞ are the *free stream velocity magnitude* and the *free stream pressure*, respectively, and we assume constant unit density $\rho = 1$.

The normalization of c_p in (33.14) couples to *Bernoulli's Law*, stating that for an incompressible irrotational inviscid fluid at steady state, we have

$$\rho \frac{1}{2} |u|^2 + p = C, \quad (33.15)$$

with C a constant. If Bernoulli's Law is valid, we have $c_p = 0$ in the free stream, and $c_p = 1$ at the upstream stagnation point with zero velocity. Typically, upstream the cylinder the flow is almost steady, and thus Bernoulli's

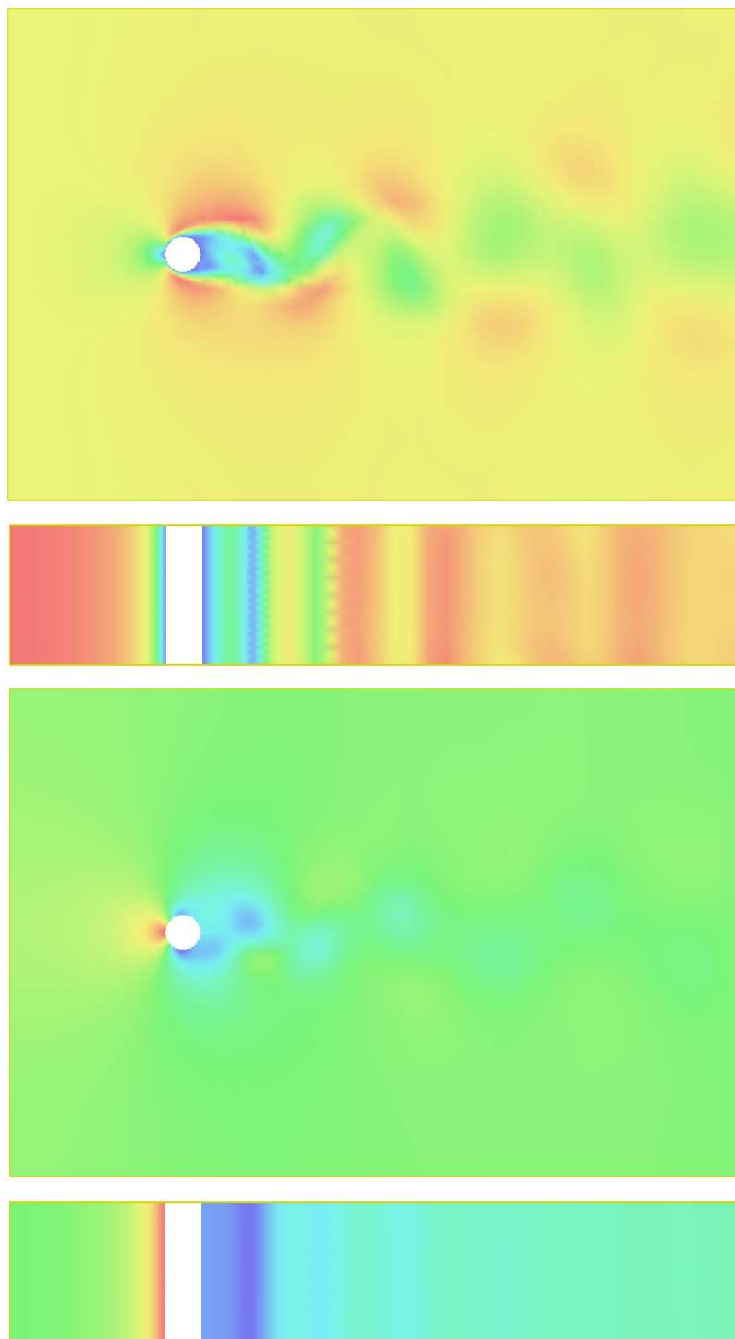


Fig. 33.14. Circular cylinder at $Re = 100$: magnitude of velocity $|U|$ (upper), and pressure P (lower).

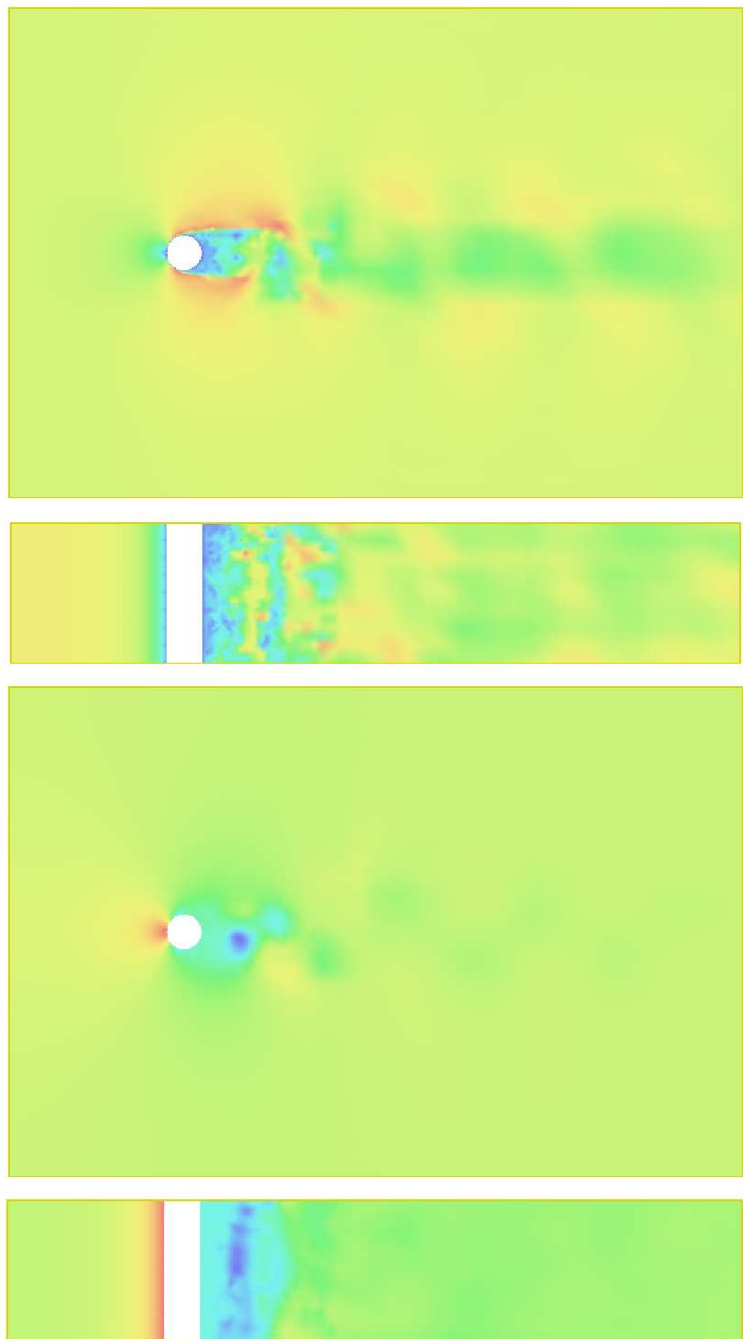


Fig. 33.15. Circular cylinder at $Re = 3900$: magnitude of velocity $|U|$ (upper), and pressure P (lower).

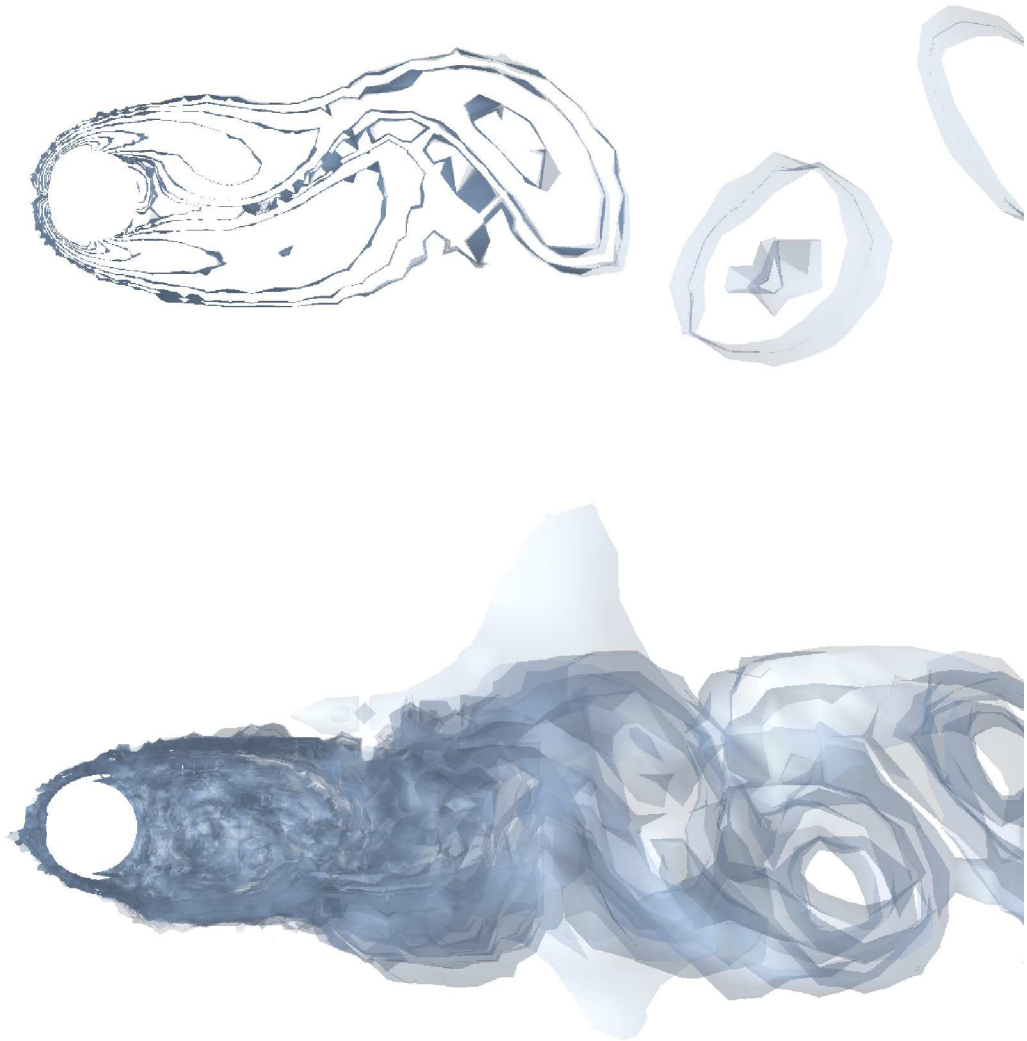


Fig. 33.16. Magnitude of vorticity iso-surfaces for 3,5,10,20,...,100, for a circular cylinder at $Re = 100$ (upper), and $Re = 3900$ (lower).

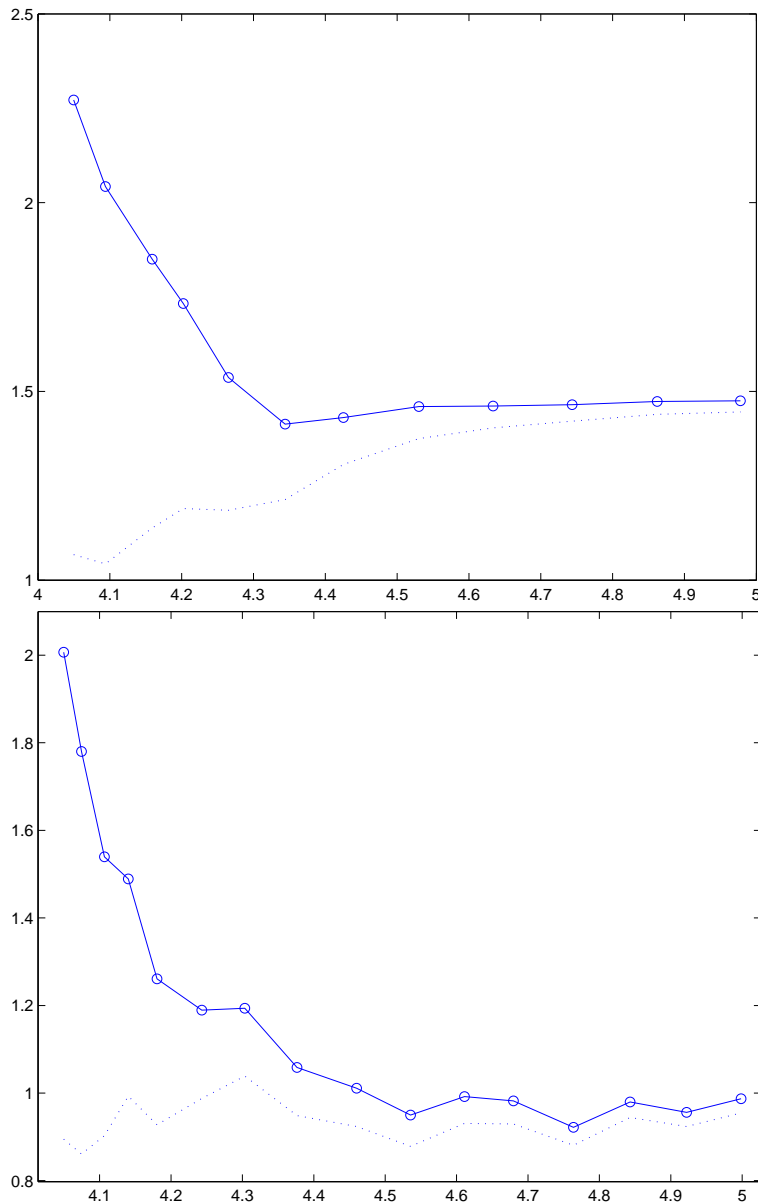


Fig. 33.17. Circular cylinder: approximative drag coefficient as a function of the 10-logarithm of the number of mesh points in space, for $Re = 100$ (upper) and $Re = 3900$ (lower).

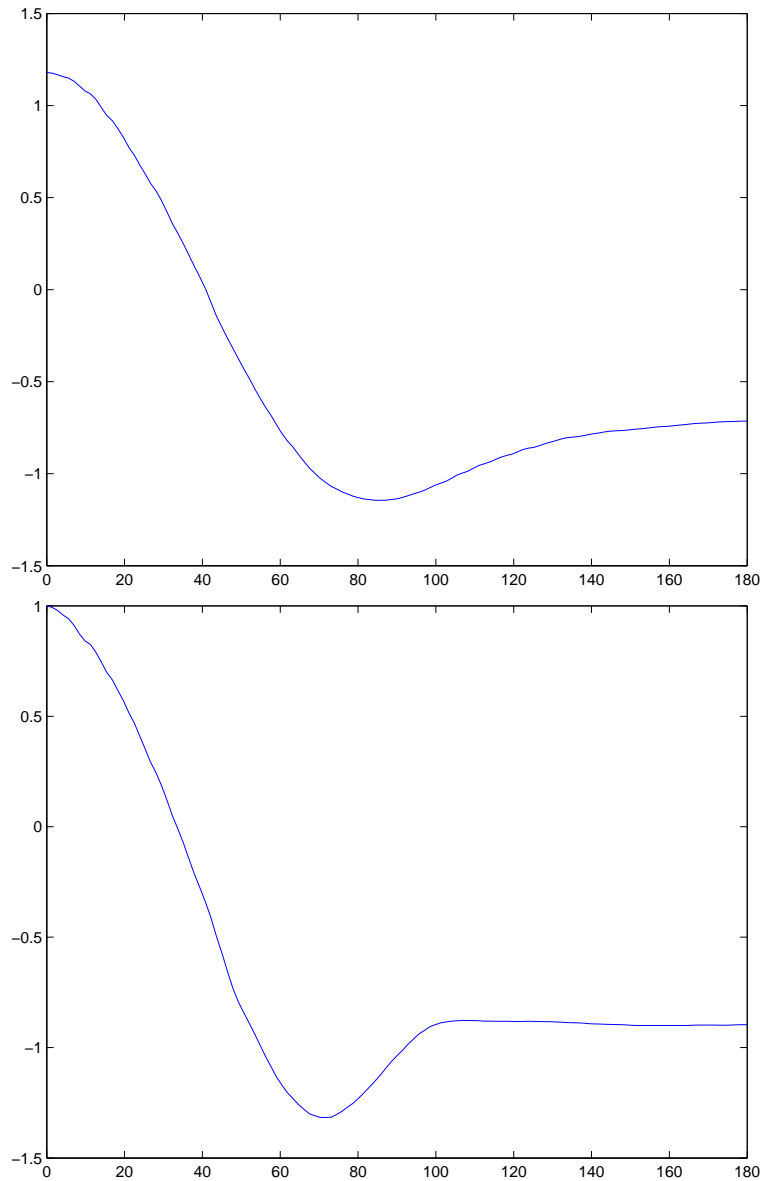


Fig. 33.18. Circular cylinder: Pressure coefficient c_p as a function of an angle starting at the stagnation point, for $Re = 100$ (upper) and $Re = 3900$ (lower).

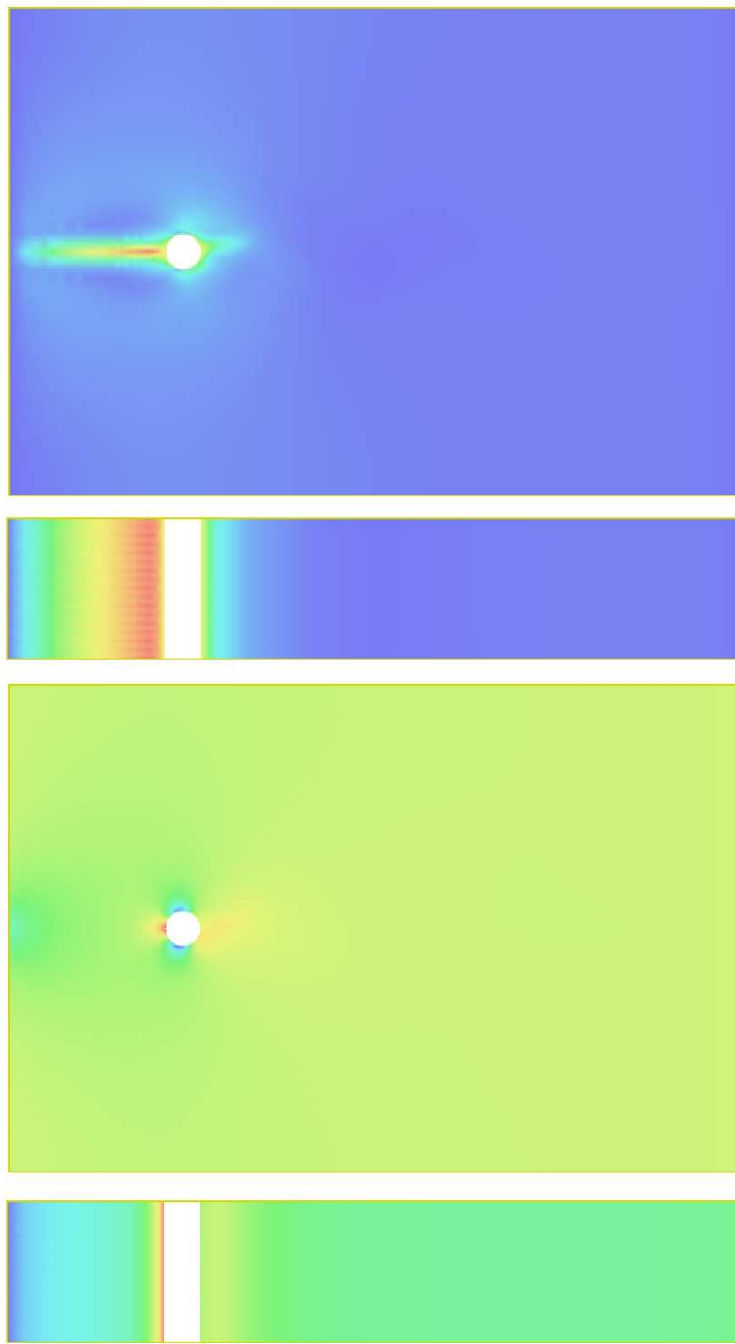


Fig. 33.19. Circular cylinder at $Re = 100$: magnitude of dual velocity $|\varphi_h|$ (upper), and dual pressure $|\iota_h|$ (lower).

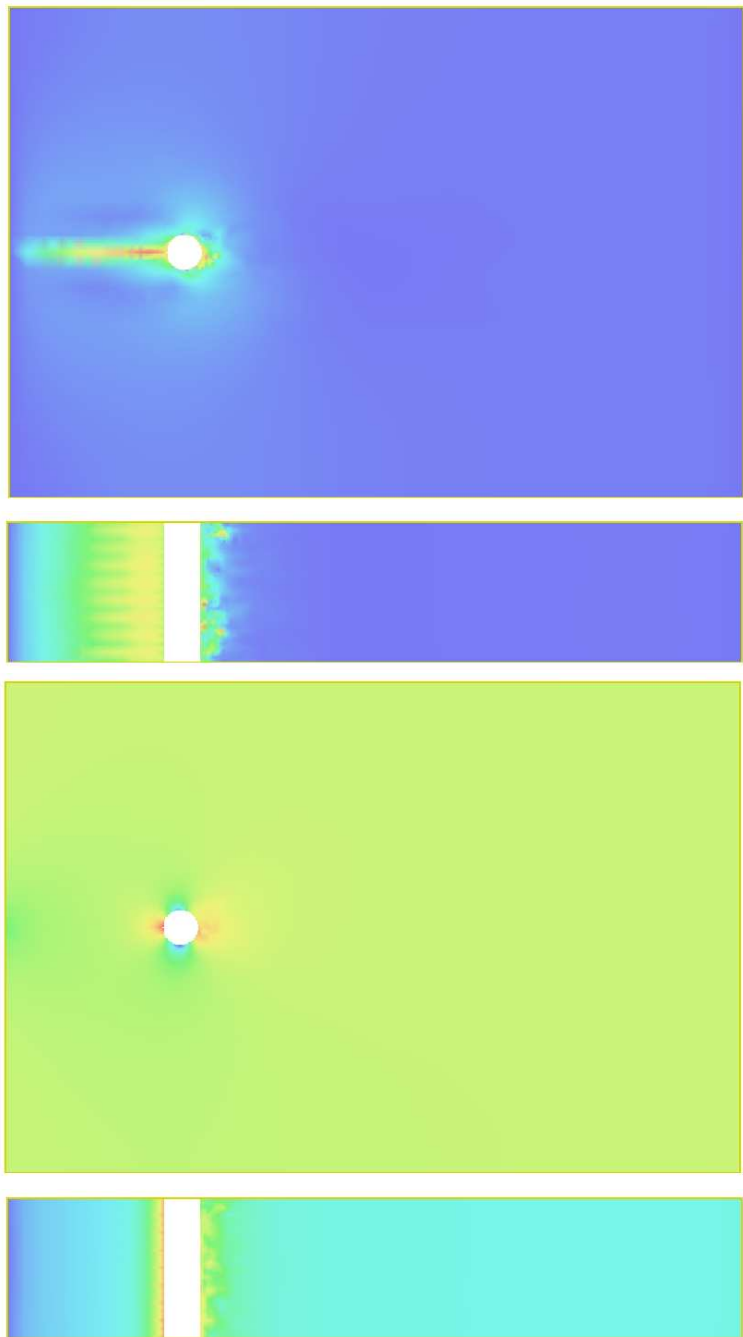


Fig. 33.20. Circular cylinder at $Re = 3900$: magnitude of dual velocity $|\varphi_h|$ (upper), and dual pressure $|\iota_h|$ (lower).

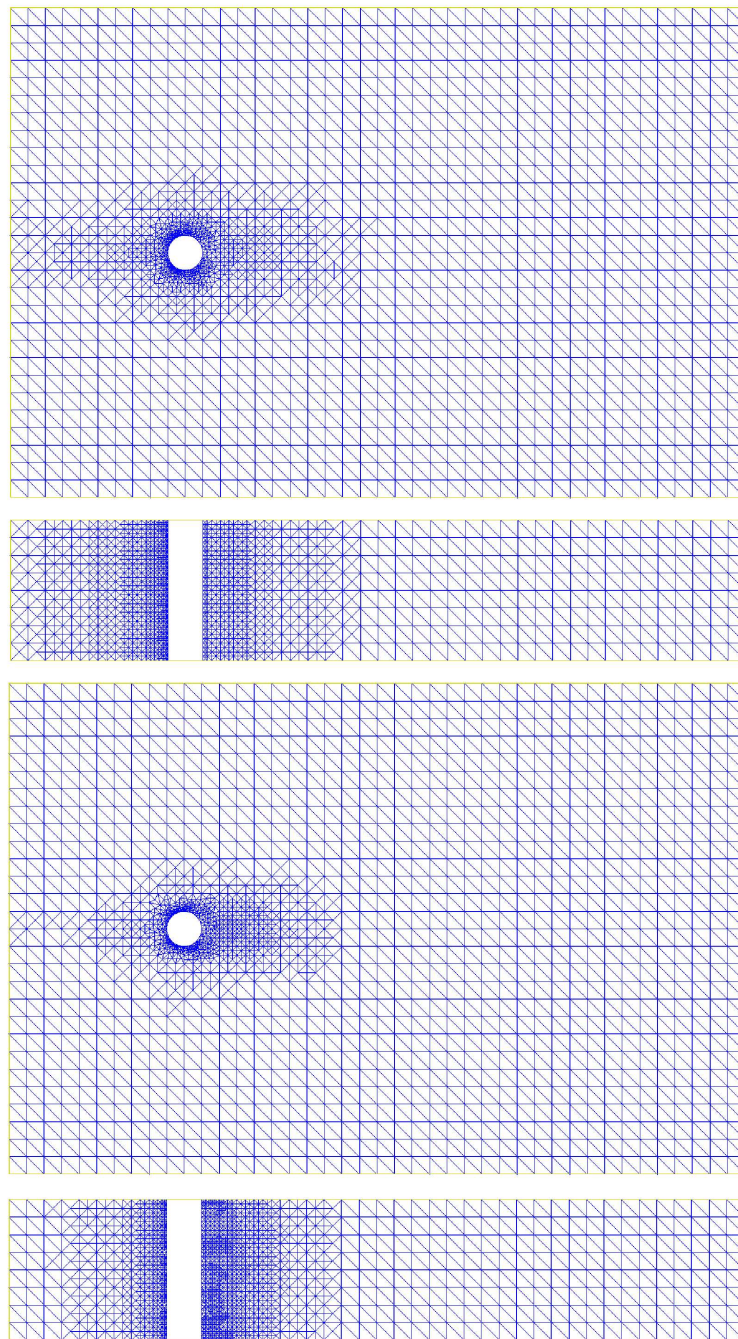


Fig. 33.21. Circular cylinder: Computational mesh for $Re = 100$ (upper), and $Re = 3900$ (lower).

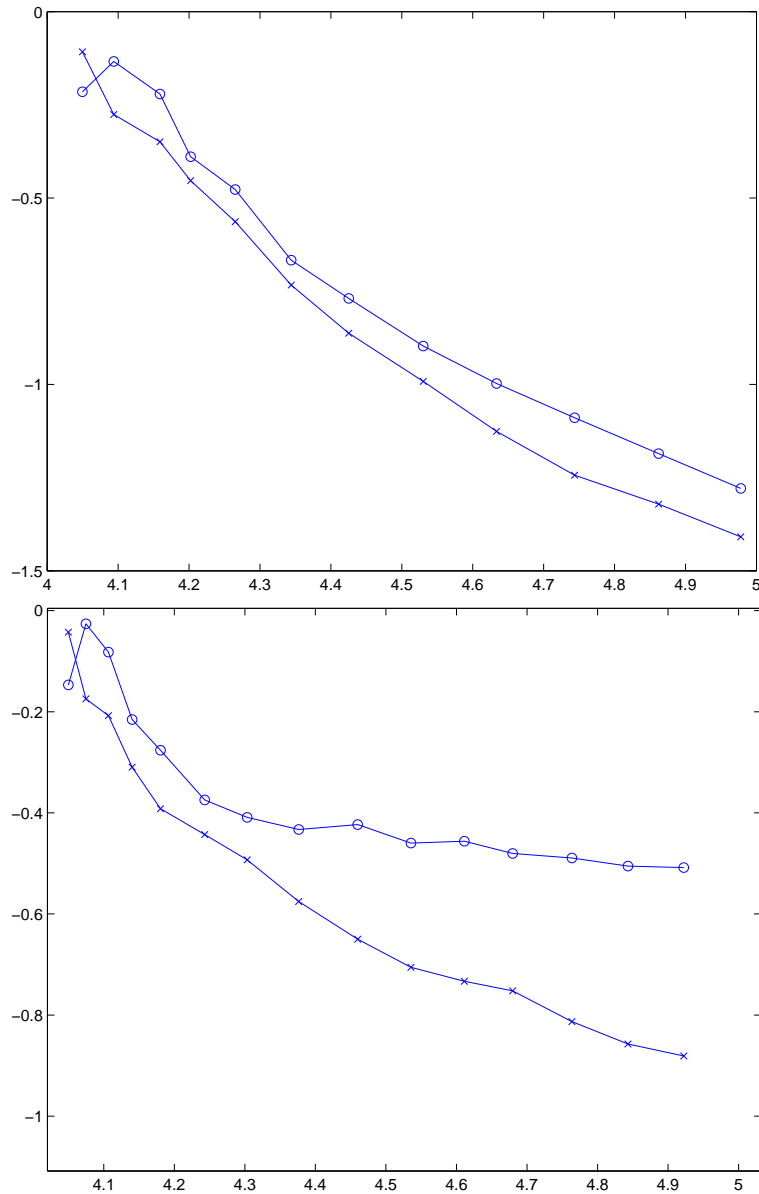


Fig. 33.22. Circular cylinder: A posteriori error estimates e_D ('o') e_M ('x'), for $Re = 100$ (upper) and $Re = 3900$ (lower).

Law should be valid for ν small. On the other hand, for ν large, corresponding to small Reynolds numbers, Bernoulli's Law may not be valid, and thus c_p may differ from 1. In Figure 33.18 we plot the pressure coefficients for $Re = 100$ and $Re = 3900$, both matching experimental results.

33.8.2 Dual solution and a posteriori error estimates

In Fig. 33.19–33.20 we plot the dual solutions corresponding to approximation of drag, and in Fig. 33.21 we plot the resulting computational meshes.

Studying the different meshes, we note that the mesh corresponding to $Re = 100$ is almost symmetric in the streamwise direction, and that the mesh refinement is spread wider vertically for this laminar flow than for the turbulent flow corresponding to $Re = 3900$. For $Re = 3900$, the mesh refinement is concentrated to the boundary layer of the cylinder and to the turbulent wake.

Overall, the mesh refinement is more localized for the higher Reynolds number, which is consistent with the dual problem being convection dominated, whereas the dual problem for the lower Reynolds number is more viscous and thus spreads the data more. For example, this results in a larger sensitivity to boundary conditions for low Reynolds numbers than for large.

In Fig. 33.22 we plot the a posteriori error estimates, where we find that the convergence rate is faster for $Re = 100$ than for $Re = 3900$, in particular the convergence with respect to the discretization error is slower for $Re = 3900$.

33.9 Sphere

The next example is the flow around a sphere with diameter $D = 0.1$, centered at $(5.5D, 7.5D, 7.5D)$, in a channel of dimension $10D \times 15D \times 15D$. We use no slip boundary conditions on the sphere, unit streamwise inflow velocity, slip boundary conditions on the lateral walls, and a transparent outflow boundary condition at the end of the channel.

A typical benchmark problem for turbulent flow in the literature concerns the case of $Re = 10\,000$, and here the experiences from using cG(1)cG(1) is very much the same as for the circular cylinder. We plot the solution in Fig. 33.24, and in Fig. 33.23 we plot the approximation of c_D as we refine 5% of the elements in each iteration of the adaptive algorithm.

For the sphere we have $c_D \approx 0.40$, which thus is less than half the drag of the cylinder, and in Fig. 33.24 we find that the wake behind the sphere is smaller than for the cylinder, consistent with lower drag.

33.9.1 Comparison with reference data

Using less than 30 000 nodes we capture the experimental reference value $c_D \approx 0.40$, and for the finer meshes using less than 10^5 nodes we capture

the correct frequency $St \approx 0.20$. Compared to LES computations with *ad hoc* mesh refinement [27, 26, 28], cG(1)cG(1) is very cheap in terms of the number of mesh points needed for accurate approximation of mean values.

33.9.2 Dual solution and a posteriori error estimates

In Fig. 33.24 we plot snapshots of a dual solution and in Fig. 33.25 we plot the resulting computational mesh, where we note that again mesh refinement is concentrated to the boundary layers and the turbulent wake.

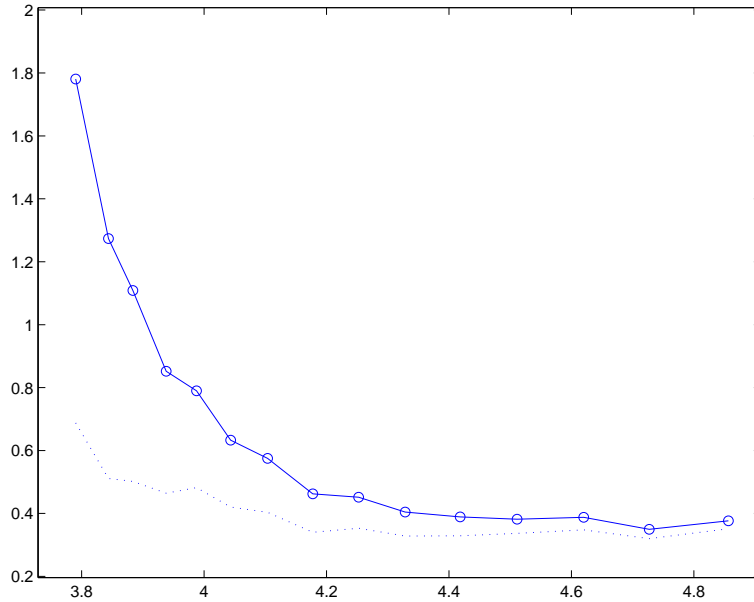


Fig. 33.23. Sphere: approximative drag coefficient as a function of the 10-logarithm of the number of mesh points in space.

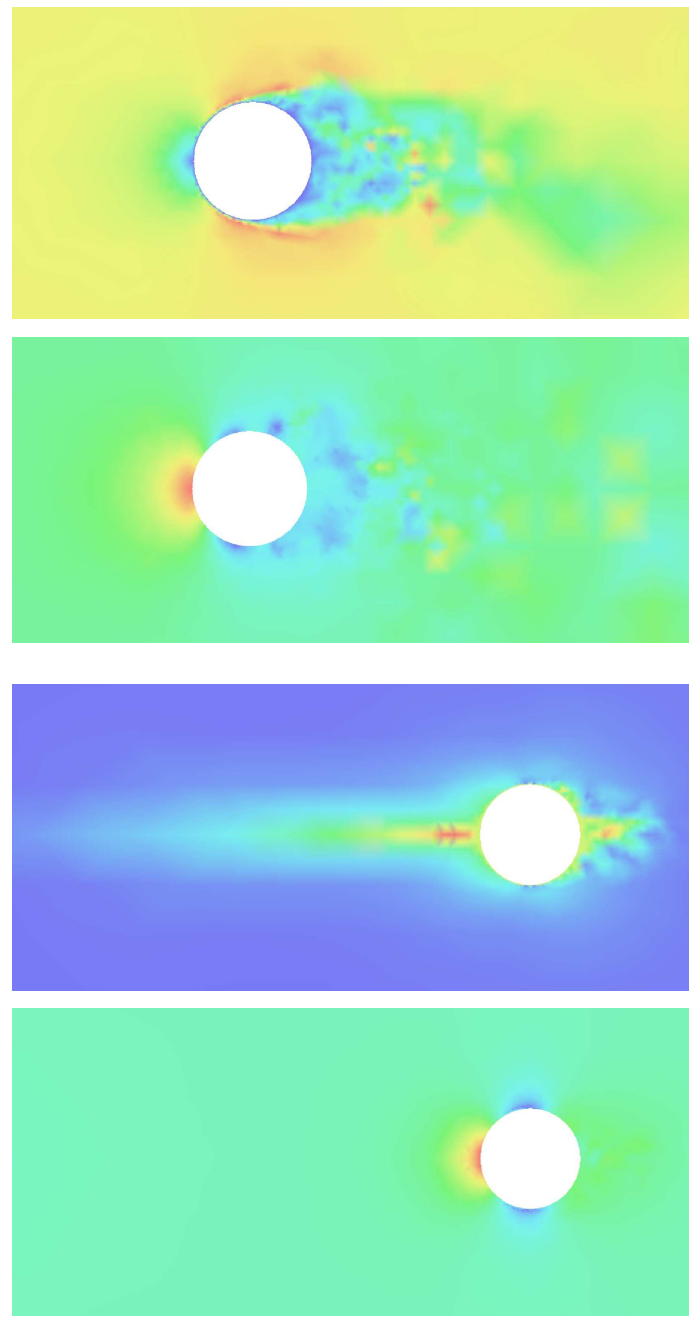


Fig. 33.24. Sphere: magnitude of velocity and pressure (upper), and magnitude of dual velocity and pressure (lower).

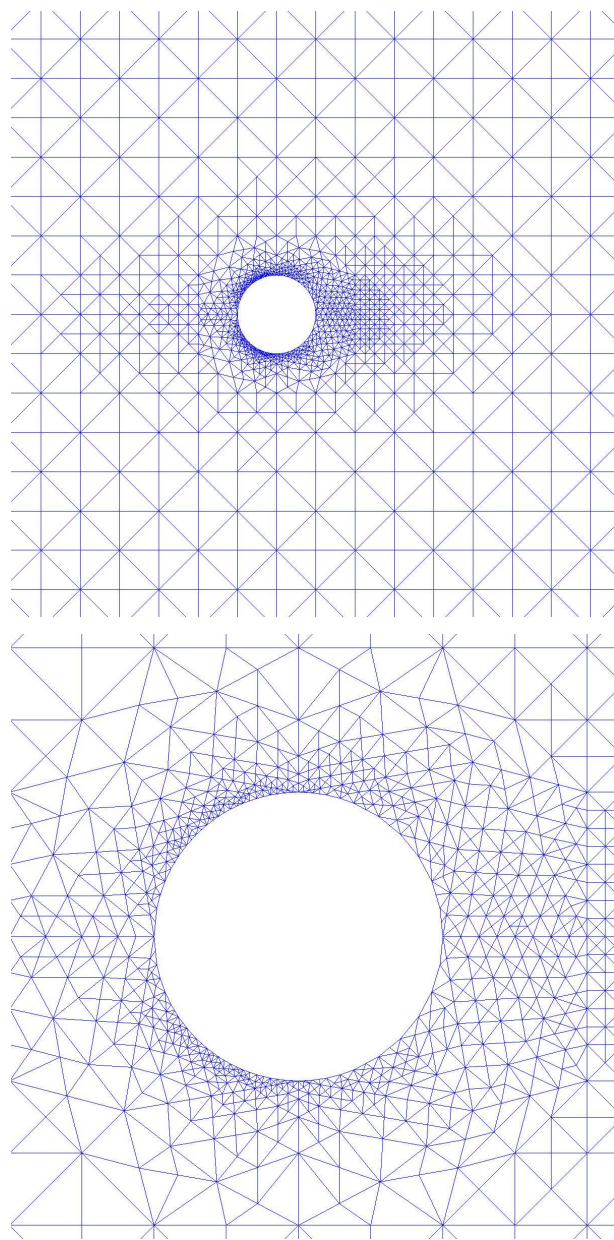


Fig. 33.25. Sphere: computational mesh refined with respect to drag.

Boundary Layers

“Prandtl’s contribution of the boundary layer was to realize that we can view the flow as being divided into two regions. The bulk of the flow can be regarded as a potential flow essentially the same as that studied by the mathematicians. Only in a small region near the body do viscous effects dominate.” (On Ludwig Prandtl)

34.1 Introduction

A common feature of fluid flow is the appearance of *boundary layers*, which are thin regions adhering to the boundary where the tangential fluid velocity rapidly changes from being zero at the boundary to taking on a non-zero value inside the fluid volume. Boundary layer flow represents *shear flow*, notably with strong shear because the tangential velocity gradient is large in the direction normal to the boundary. In Chapter 36 we shall see that laminar flows with strong shear are unstable and turn turbulent in a process of *transition* from laminar to turbulent flow. This process takes some time and therefore a boundary layer may stay laminar over some distance in the direction of the flow before transition. Boundary layers thus may be laminar or turbulent and the precise location in space-time for transition may be sensitive to surface roughness or inflow perturbations.

The generic model case of boundary layer flow is represented by flow over a (horizontal) flat plate with no-slip velocity boundary conditions. In this chapter we briefly recall some of the material concerning this model problem usually presented in texts on fluid dynamics based on heuristics of qualitative dimensional analysis or experiments. A goal of this heuristics has been to design *wall models* which can be used in conjunction with the NS equations instead of no-slip conditions to model the flow in turbulent boundary layers without resolving the flow. The design of wall models is a part of turbulence modeling and carries the same difficulties, see [98] for an overview.

We compare the heuristics with some computational results using G2 without using any wall model. We find that we can simulate the transition in the boundary layer from laminar to turbulent flow on a PC, and we are able to compute the correct drag in the turbulent boundary layer found in experiments.

For bluff body flow, the contribution to drag from skin friction of the boundary layer is small, since drag is dominated by the pressure drop. However, the general flow pattern including the size and form of the turbulent wake and the location of boundary layer separation may significantly influence the drag. In Chapter 33 we found that we were able to compute the correct drag and capture the large scale features of the flow, such as the separation, without resolving the boundary layers to their physical width.

Although, the problems in Chapter 33 are all flows with laminar separation, that is the boundary layer stays laminar before separation. For very high Reynolds numbers the boundary layer undergoes transition to turbulence before separation, which delays the separation of the boundary layer. We discuss this phenomenon further in Chapter 35, where we offer a solution with a very simple wall model, based on a friction boundary condition. Transition to turbulence is further discussed in Chapter 36.

34.2 Flat Plate Laminar Boundary Layer

We consider fluid flow of viscosity ν over a flat horizontal plate with a leading edge facing a constant inflow velocity U_∞ . We estimate the thickness δ of a laminar boundary layer at a distance l from the leading edge assuming balance of the inertia and viscous forces estimated by

$$\begin{aligned} F_{viscous} &= |\nu \Delta u| \approx \frac{\nu U_\infty}{\delta^2}, \\ F_{inertia} &= |u \cdot \nabla u| \approx \frac{U_\infty^2}{l}, \end{aligned} \tag{34.1}$$

which gives $\delta \sim (\nu l / U_\infty)^{1/2}$, or more precisely with a heuristic constant,

$$\delta = 5 \sqrt{\frac{\nu l}{U_\infty}}. \tag{34.2}$$

We see that qualitatively speaking, the boundary layer thickness increases as the viscosity and the distance from the leading edge increase, and decreases as the inflow velocity increases.

34.3 Skin Friction for Laminar Boundary Layers

We noted in Chapter 33 that a bluff body drag force has a contribution from *skin friction*, which is the friction force from the viscous stresses at the boundary, and from *pressure drag*, which relates to the pressure drop over the bluff

body. For a flat horizontal plate the pressure does not contribute to the drag, and the drag is then equal to the skin friction, which we normalize to a *skin friction coefficient* c_f by dividing by $\rho \frac{1}{2} A U_\infty^2$, with constant unit density $\rho = 1$, and $A = bl$ the area of the plate with b the width and l the length. We note the difference compared to Chapter 33, where we normalized the bluff body drag coefficient c_D by an area based on the cross section of the object normal to the flow.

The shear stress τ_0 on the plate is given by

$$\tau_0 = \nu \left(\frac{\partial u_1}{\partial x_2} \right)_0 \quad (34.3)$$

with x_2 the direction perpendicular to the plate, and u_1 the streamwise velocity component. Estimating $(\partial u_1 / \partial x_2)_0 \sim U_\infty / \delta$, we obtain $\tau_0 \sim \nu U_\infty / \delta$, and using (34.2) we get

$$\tau_0 \sim \sqrt{\frac{\nu U_\infty^3}{l}}. \quad (34.4)$$

The total drag force D on the plate is then $\tau_0 bl$, which, with b the width of the plate, would then be

$$D \sim b \sqrt{\nu U_\infty^3 l}, \quad (34.5)$$

with the total drag being proportional to b , $\nu^{1/2}$, $U_\infty^{3/2}$ and $l^{1/2}$. For the skin friction coefficient (or drag coefficient) for laminar boundary layer flow, we then obtain with a heuristic constant

$$c_f = \frac{D}{\frac{1}{2} bl U_\infty^2} = 1.328 \sqrt{\frac{\nu}{U_\infty l}}. \quad (34.6)$$

34.4 Skin Friction for Turbulent Boundary Layers

There are various attempts to derive models for the boundary layer thickness and skin friction for turbulent boundary layers, where the models are typically based on assumptions on the turbulent mean velocity profile and fit to experimental data.

For a flat plate, one may introduce a type of Reynolds number

$$Re_l = U_\infty l / \nu, \quad (34.7)$$

which is based on the length of the plate l , and typically one finds in experiments that the skin friction c_f for a turbulent boundary layer is proportional to $Re_l^{-0.2}$ [99], that is a very weak dependence on Re_l .

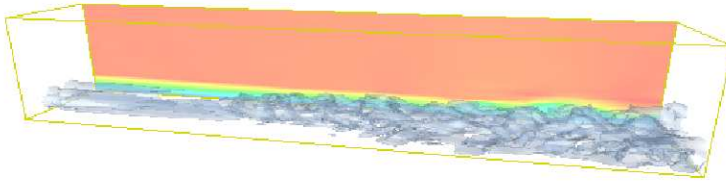


Fig. 34.1. Transition to turbulence in a boundary layer computation, introducing Taylor-Görtler type perturbations (see Chapter 36) of amplitude 0.1 at the inflow.

34.5 Computing Skin Friction by G2

As an example, we consider flow over a flat plate with $U_\infty = 1$, $b = 1$, and $\nu = 10^{-4}$. We assume a laminar boundary layer thickness $\delta = 0.2$, which corresponds to

$$l = \left(\frac{\delta}{5}\right)^2 \frac{U_\infty}{\nu} = \left(\frac{0.2}{5}\right)^2 \frac{1}{10^{-4}} = 16, \quad (34.8)$$

using (34.2), corresponding to a Reynolds number $Re_l = 1 \times 16/10^{-4} = 1.6 \times 10^5$. The corresponding skin friction of the laminar boundary layer would be

$$c_f = 1.328 \sqrt{\frac{10^{-4}}{1 \times 16}} \approx 3.3 \times 10^{-3}.$$

We note that this is orders of magnitude lower than the drag for the bluff body problems in Chapter 33, for which the pressure drop dominates. For a turbulent boundary layer, one finds in experiments that c_f at $Re_l \approx 10^5$ is about 5×10^{-3} [99].

We now compute a boundary layer flow in a channel of dimension $12 \times 1 \times 1$ using cG(1)cG(1), with no slip boundary conditions on the channel floor, and slip boundary conditions on the other walls. We initialize the computation with a linear streamwise velocity profile in a boundary layer of thickness 0.2 at the floor of the channel, given by initial and inflow data. The mesh is of dimension $129 \times 33 \times 33$ mesh points, 21 vertically for $0 < x_2 \leq 0.2$ and 12 vertically for $0.2 < x_2 \leq 1$. We introduce small rotational perturbations of size 0.1, and notice transition from laminar to turbulent flow at a certain distance from the inlet. Perturbations of this type are referred to as *Taylor-Görtler* type perturbations. We will come back to the problem of transition to turbulence in more detail in Chapter 36.

We now use the techniques of Chapter 33 to compute the drag (here equal to skin friction) over the floor of the channel viewed as a plate. Using (33.3) to approximate drag gives a drag force $D \approx N^h(\sigma(\hat{U}))$, and normalizing with the relevant plate area, we have

$$c_f \approx \frac{N^h(\sigma(\hat{U}))}{\frac{1}{2} U_\infty^2 b l}, \quad (34.9)$$

where we get $c_f \approx 3 \times 10^{-3}$ for the laminar part of the boundary layer and $c_f \approx 5 \times 10^{-3}$ for the turbulent part, thus in accordance with experimental findings [99].

34.6 Summary

We have in this chapter given a glimpse into laminar/turbulent boundary layer flow including transition from laminar to turbulent flow. Using G2 we were able to simulate transition to turbulence in a flat plate boundary layer, where we found that our approximations of the skin friction coefficient c_f was in accordance with experimental data, both in the case of a laminar and a turbulent boundary layer.

Separation

The scientist describes what is; the engineer creates what never was.
(Theodore von Kármán 1881–1963)

35.1 Introduction

Separation in a boundary layer occurs where the tangential flow velocity changes sign and *recirculation* occurs. Similarly, a separated flow may *reattach* where the tangential velocity changes sign in the opposite direction. Alternatively, we may define separation/reattachment to occur where the streamwise shear stress at the boundary changes sign. Separation is caused by a positive pressure gradient in the streamwise direction, resulting in a force opposing the flow with a retarding effect. If the opposing pressure force is strong enough over a sufficiently long time, the tangential velocity may change sign and separation will occur. We note that there is no separation in a flow over a flat plate, since the streamwise pressure gradient is negative.

In bluff body flow the drag depends critically on the location of separation, with an earlier separation (following the direction of the flow) increasing the drag because of a lower pressure in the wake and a larger pressure drop over the body. If the boundary layer undergoes transition to turbulence before separation, the separation is delayed, corresponding to *drag crisis*, with a significant reduction of the drag.

Separation is also connected to the *Magnus effect* causing a tennis ball with top spin to curve down (as skillfully exploited by Björn Borg).

35.2 Simulation of Blood Flow

The main part of the examples in this book are external flows past bodies of different shapes. Other important examples are internal flows, such as flow in a pipe, which currently receive a lot of interest in medical research as a model

of blood flow. There are many challenges in modeling blood flow, including the non-Newtonian properties of the blood plasma, fluid-structure interaction with the vessel wall, and under certain conditions simulation of turbulent flow.

Simulation of blood flow may help to get a better understanding of the causes for cardiovascular diseases. For example, the correlation of regions of low wall shear stress and recirculation with atherosclerosis may be studied from such simulations [94].

In Fig. 35.2 we show a simulation of the flow in a realistic geometric model of a human carotid bifurcation, where we find that the flow may locally separate from the wall after the bifurcation. We refine the mesh with respect to the error in wall shear stress, based on the information we obtain from solving an associated dual problem. To increase the realism in the model we should include effects of fluid-structure interaction, which we will return to elsewhere.

35.3 Drag Reduction for a Square Cylinder

For the bluff body problems with sharp corners in Chapter 33, the surface mounted cube and the square cylinder, the flow separates at the sharp leading edge of the body, to form a large turbulent wake resulting in high drag, as compared to the rounded geometries of the circular cylinder and the sphere with smaller wakes. For the surface mounted cube we have $c_D \approx 1.5$ and for the square cylinder $c_D \approx 2.2$.

But why is the drag so much lower for the surface mounted cube than for the square cylinder? One main difference between the two is the no-slip boundary condition on the channel floor for the surface mounted cube, implying that the difference in drag should connect to the presence of a boundary layer upstream the surface mounted cube, which has no equivalent for the cylinder. The presence of the boundary layer leads to separation and the formation of a horse-shoe vortex upstream the surface mounted cube, see Fig. 33.1, with less pressure build-up on the leading face of the cube compared to the cylinder.

To check the validity of this explanation of the difference in drag, we artificially introduce a boundary layer ahead of the square cylinder flow by inserting a horizontal plate in front of the cylinder. As expected the plate makes the flow separate ahead of the cylinder, causing c_D to drop from 2.2 to 1.4, see Fig. 35.2–35.3. The plate also causes the frequency in the wake oscillation to increase from $St \approx 0.14$ to $St \approx 0.16$.

35.4 Drag Crisis

In Fig. 35.4 we plot the drag coefficient c_D of a circular cylinder as a function of Reynolds number, as obtained from experimental results presented in the literature. We note that for $Re < 100$, c_D is proportional to Re^{-1} , for $100 < Re < 10^5$ we have $c_D \approx 1$, while for $Re > 10^5$ we find that c_D first drops

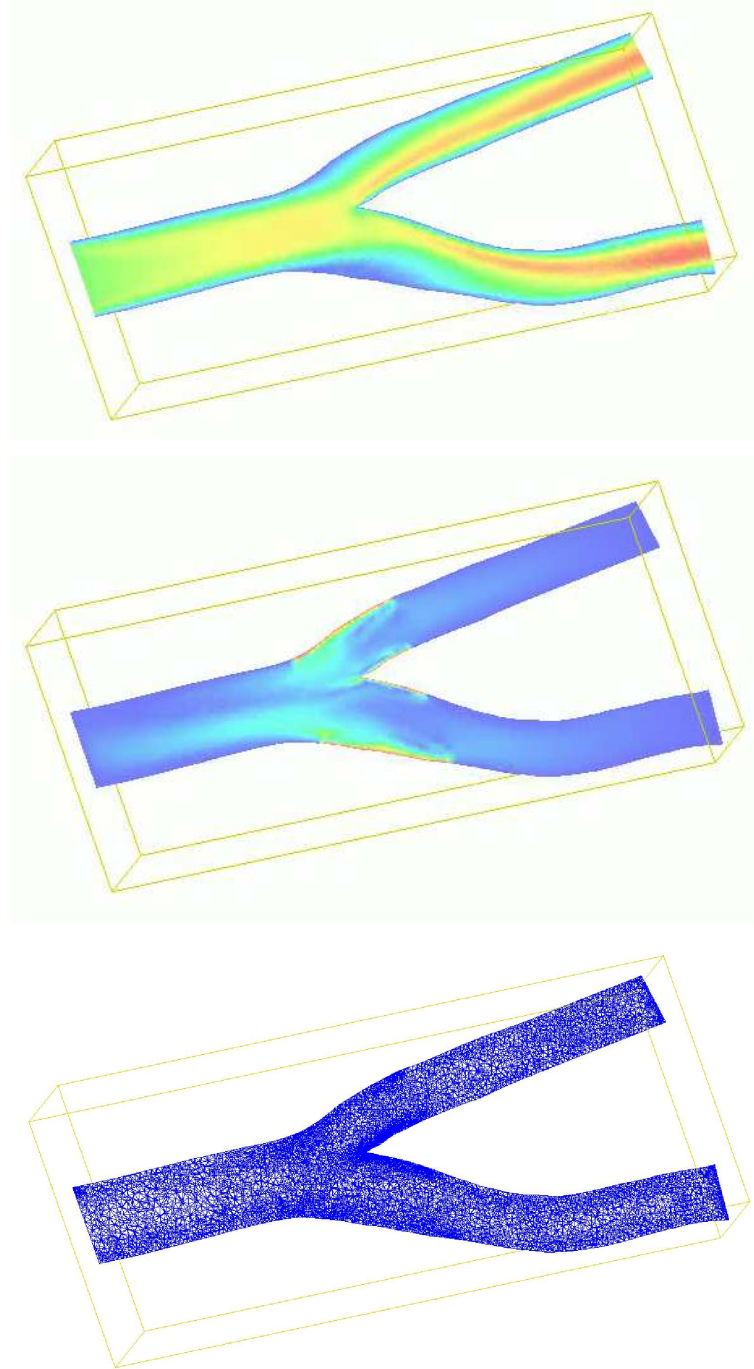


Fig. 35.1. From Chapter 35: Midsections showing snapshots of a G2 simulation of the blood flow in a realistic bifurcation model of a human carotid bifurcation (upper), the dual solution corresponding to the computational error in wall shear stress (middle), and the corresponding mesh (lower). Geometrical model produced by K. Perktold, TUG Graz, developed from an experimental cast (D. Liepsch, FH Muenich).

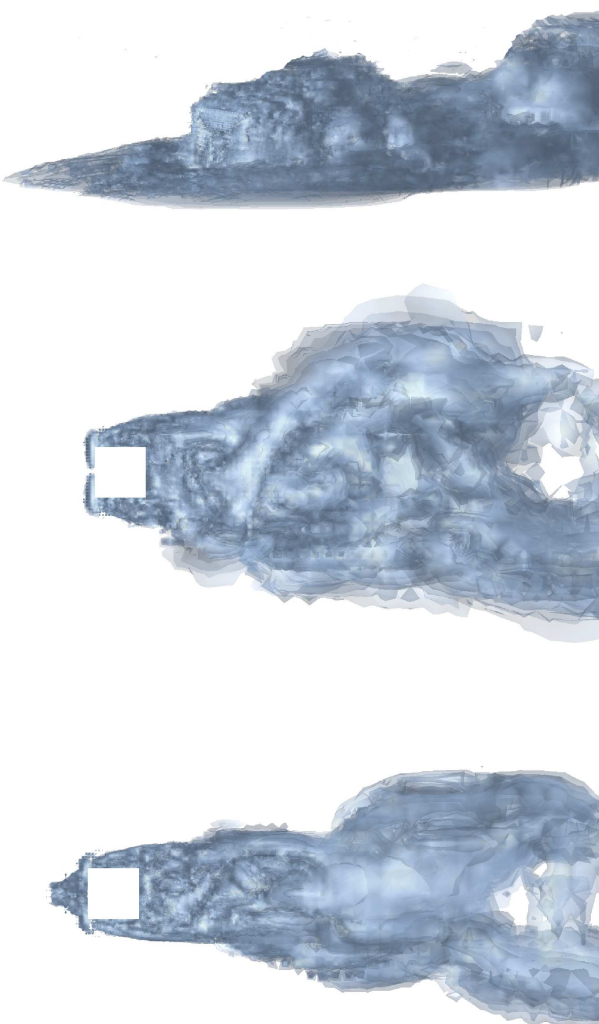


Fig. 35.2. Iso-surfaces for the magnitude of the vorticity for the cube (upper), the cylinder (middle), and the cylinder with a plate (lower).

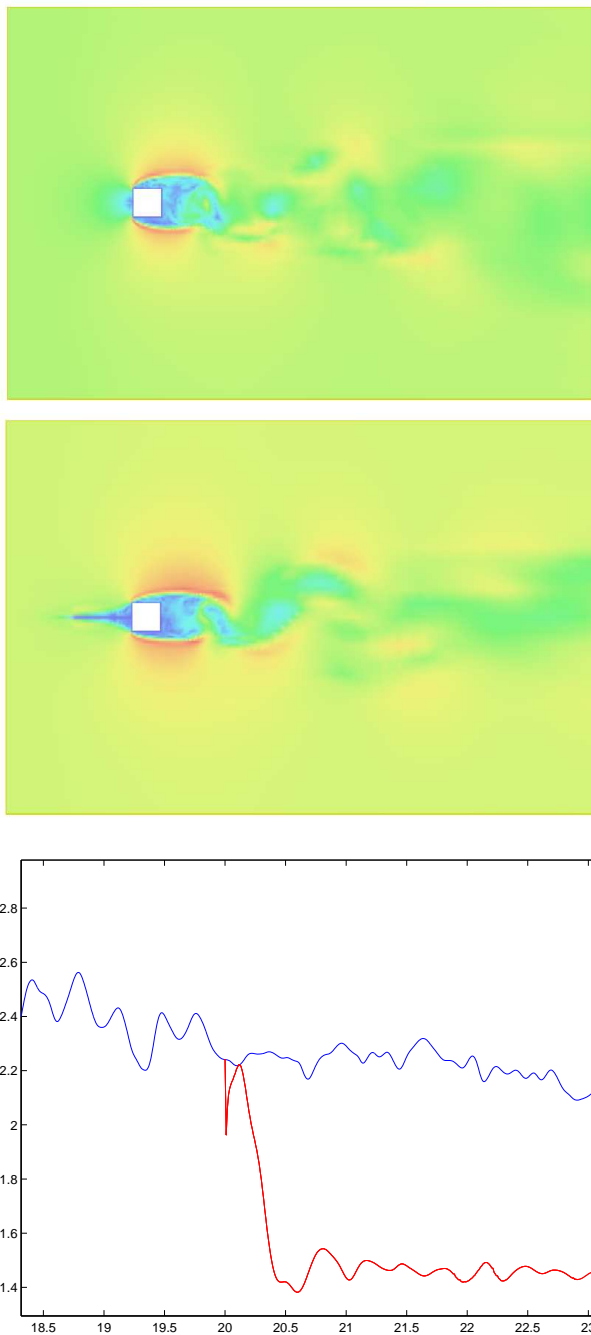


Fig. 35.3. Magnitude of the velocity for the cylinder with and without the plate (upper), and a time series of the corresponding (normalized) drag forces when introducing the plate (lower).

significantly and then rises back again. The drag reduction near $Re = 10^5$ is commonly referred to as *drag crisis*, which is related to transition to turbulence in the boundary layers causing a delayed separation. Simulation of drag crisis is a major challenge of turbulence simulation.

To resolve the very thin boundary layer of a high Reynolds number flow is too expensive, and thus many different wall-models have been proposed to capture the effect of the boundary layer without resolving it to its physical scale, see [98] for an overview.

Assuming the main effect of the boundary layer on the flow is the skin friction, we propose in [55] a simple approach to model the effect of the unresolved boundary layer, based on a slip with friction boundary condition, see Chapter 28, which may be viewed as a very simple wall-model. The problem is then to choose a suitable friction coefficient β , and we now go on to present results from [55] using friction boundary conditions for simulating drag crisis.

In [67, 68] such a boundary condition is used to study reattachment of a low Reynolds number flow past a surface mounted cube in 2d and 3d as a function of the friction parameter β , and it is found that the reattachment is delayed with decreasing friction, as could be expected.

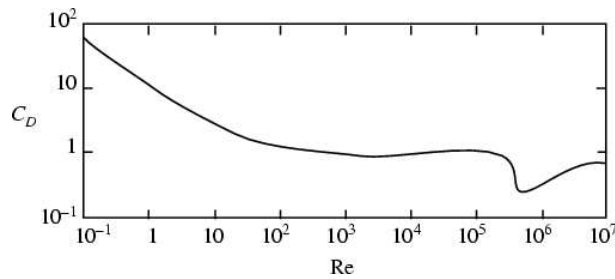


Fig. 35.4. c_D for a circular cylinder as a function of Reynolds number.

35.5 Drag Crisis for a Circular Cylinder

We now turn to the issue of modeling drag crisis for a circular cylinder of diameter D and length $4D$, with the cylinder in the direction of the x_3 -axis, subject to a unit streamwise velocity inflow boundary condition (in the x_1 -direction) in a channel of length $21D$, width $4D$ and height $14D$. We use slip boundary conditions on the lateral walls of the channel, and a transparent outflow boundary condition at the end of the channel.

For very high Reynolds numbers the viscous ν -term in the computational method (28.12) is negligible if we do not resolve the finest scales of the flow, and may be dropped from the equation, corresponding to a cG(1)cG(1)

method for the Euler equations. Apart from the boundary conditions, the dissipation in the flow is then only due to the stabilizing term in (28.12), with the energy dissipation expressed in (16.6).

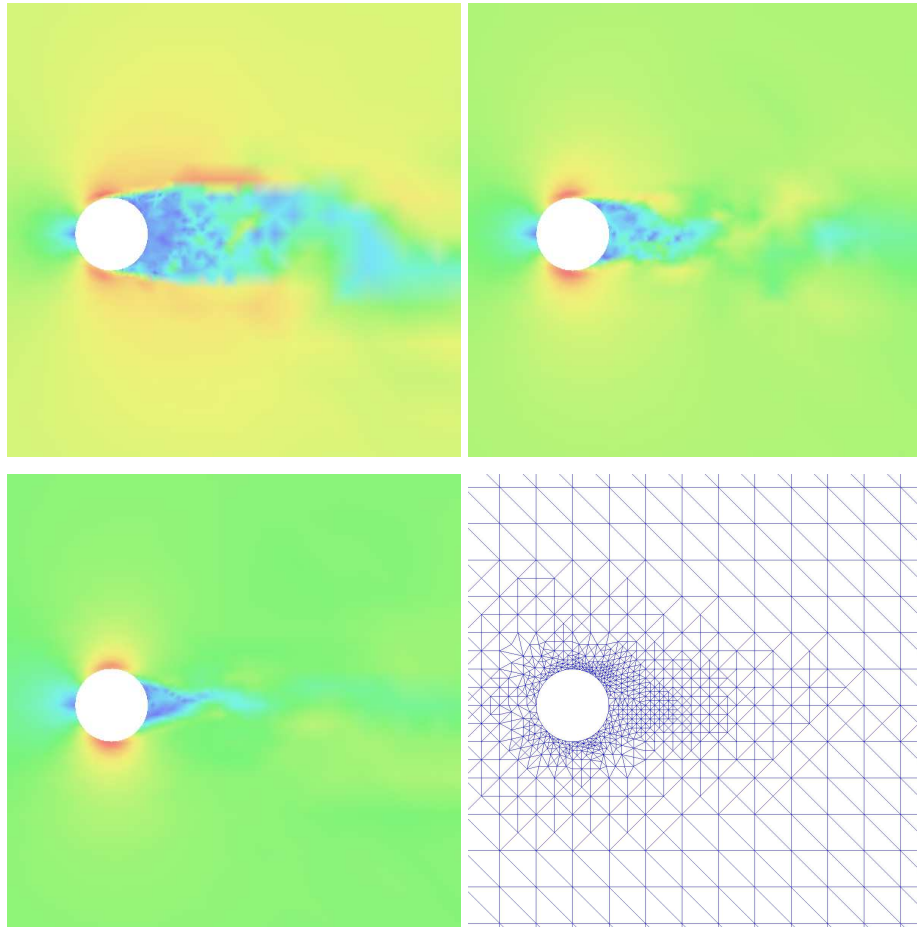


Fig. 35.5. Drag crisis for a circular cylinder: magnitude of the velocity for G2 solutions for $\nu = 0$; $\beta = 2 \times 10^{-2}$ with $c_D \approx 0.7$ (upper left), $\beta = 1 \times 10^{-2}$ with $c_D \approx 0.5$ (upper right), $\beta = 5 \times 10^{-3}$ with $c_D \approx 0.45$ (lower left), and the mesh with 80 000 mesh points (lower right), in the x_1x_2 -plane for $x_3 = 0.2$.

The main computational challenge is here to capture the correct separation of the flow and the correct dissipation in the boundary layer. Flow separation is determined by the force balance in the momentum equation, where an adverse pressure gradient in the flow direction results in a force in the opposite direction which reduces the momentum. When this retarding force has reduced

the momentum to zero near the boundary the flow separates. The skin friction of the boundary layer is reducing the momentum near the boundary, and thus high skin friction leads to an earlier separation. And conversely, when the skin friction decreases with the Reynolds number, the separation is delayed since the momentum near the boundary increases.

The idea underlying the model of the boundary layer is here that for flow separation, the important characteristic of the boundary layer is skin friction, and thus that it should be possible to capture a correct separation of the boundary layer as long as we have correct skin friction.

For the problems in Chapter 33 the flow separates from a laminar boundary layer, corresponding to a relatively high skin friction, where it is possible to capture the separation using no slip boundary conditions (corresponding to $\beta = \infty$).

The criterion for choosing β should be that the skin friction in the computation should be the same as in the physical problem. In Chapter 34 we found that experimental results indicate that skin friction has a very weak dependence on the Reynolds number, proportional to $Re^{-0.2}$ in the case of a flat plate, and thus a certain value for β should be characteristic for a rather wide range of Reynolds numbers. Experimental results also indicate that once we have drag crisis the separation is again rather stable for a range of Reynolds numbers. The exact Reynolds number for when the separation point starts to move downstream seems to be hard to determine, which is probably due to its relation to transition to turbulence in the boundary layers, which in turn depends on the level of perturbations in the boundary layer, which is very hard to determine in a realistic problem, see Chapter 36. Thus, there is a range of Reynolds numbers, close to where transition in the boundary layers occur, for which the separation of the flow is very hard to predict. From an engineering point of view it is then important to take both the sub-critical and the super-critical scenario into account.

Our model is here a cG(1)cG(1) method for the Euler equations together with a slip with friction boundary condition. Letting the friction parameter β go from large to small values, we find that the separation point is moving downstream. For $\beta = 10^{-2}$ we are able to capture the delayed separation of a drag crisis with $c_D \approx 0.4$, see Fig 35.5.

35.6 EG2 and Turbulent Euler Solutions

We now turn to the question of what happens as $\beta \rightarrow 0$, corresponding to the Reynolds number $Re \rightarrow \infty$.

Our computational model then reduces to G2 for the Euler equations with slip boundary conditions, which we refer to as an *EG2 model* (see Chapter 19). We note that in this model the only parameter is the discretization parameter h , and we show that some mean value output (such as drag) may be indepen-

dent of h , making EG2 a completely parameter-free model of turbulent flow with respect to that output.

The EG2 solution corresponds to a physical flow with a very high Reynolds number, and we find solutions with similar characteristics of separation in one point and turbulent vortex shedding e.g. in studying geophysical bluff body problems. We note that the need of a reliable computational model for the case $Re \rightarrow \infty$ will increase, due to the large dimensions of civil-, offshore and wind engineering structures of today.

35.7 The Dual Problem for EG2

We recall that in computing the drag for a body, the mesh is refined using the a posteriori error estimate (33.10) based on a discrete approximation of the continuous dual problem (14.4), with unit boundary data for the dual velocity in the streamwise direction on the surface of the body.

The underlying error representation is based on the continuous dual problem, and thus we have to be careful so that the discrete (G2) approximation of the dual problem is a good enough approximation of the continuous dual problem. For the problems in Chapter 33 we used no slip boundary conditions for the primal problem, and we found that after some mesh refinement the approximate dual weight in (33.10) is (approximately) independent of the mesh refinement, which is taken as an indication of the validity of (33.10).

Since the normal component of the convection velocity field (the primal velocity) in the dual problem is zero, the boundary data in the dual problem is only transported into the interior of the domain by diffusion. Although, with EG2 we have that $\nu = 0$ and thus it is not obvious how the boundary data is to be transported into the interior of the domain. In irregular parts of the flow, the stabilization will act as a numerical diffusion that will spread the data, but with the slip boundary condition in the primal problem the flow near the boundary will be smooth since there is no boundary layer, and thus the diffusion at the boundary will be very small.

With $\nu = 0$, the skin friction is zero and the mean drag F_D of a body with surface Γ_0 is solely due to the pressure:

$$F_D = \frac{1}{|I|} \int_I \int_{\Gamma_0} p n_1 \, ds \, dt, \quad (35.1)$$

with n_1 the streamwise x_1 -component of the normal.

For EG2, we propose in [55] to study instead the following quantity:

$$\tilde{F}_D = \frac{1}{|I|} \frac{|\Gamma_0|}{|\tilde{\Gamma}_0|} \int_I \int_{\tilde{\Gamma}_0} p \tilde{n}_1 \, dx \, dt, \quad (35.2)$$

with \tilde{n}_1 a piecewise linear finite element function which is equal to n_1 at all nodes on Γ_0 and zero at all other nodes. We define $\tilde{\Gamma}_0 \subset \Omega$ as the union of

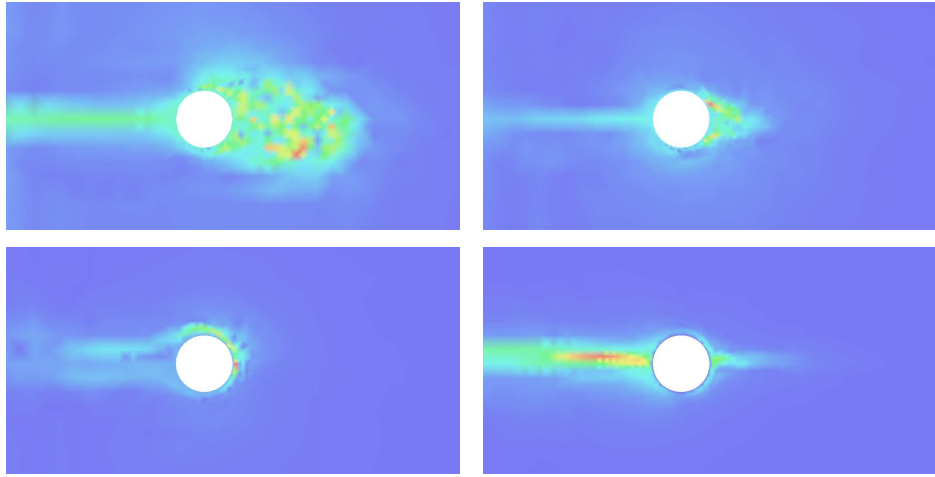


Fig. 35.6. Magnitude of the dual velocity for $\beta = 0.1$ (upper left), 0.01 (upper right), 0 (lower left), using velocity boundary data, and for $\beta = 0$ using pressure data (lower right), in the x_1x_2 -plane for $x_3 = 0.2$.

all cells in the mesh with at least one vertex on the surface Γ_0 . The quantity \tilde{F}_D is then defined in (35.2) as a weighted average of the pressure p , which is of the same order of magnitude as F_D . For example, for Γ_0 a straight line segment in 2d which is normal to the x_1 -axis, piecewise linear approximation on uniform triangles, or bilinear approximation on uniform quadrilaterals, gives that $\tilde{F}_D = 1/2 F_D$.

Formulating an adaptive method for the computation of \tilde{F}_D instead of F_D leads to the same a posteriori error estimate (33.10), but now with a different set of data for the dual problem. Instead of the boundary data for the dual velocity leading to an error representation for F_D , we are now lead to choose the data in the dual problem as a force in the dual continuity equation; that is we use homogeneous velocity boundary data, and the source term $\hat{\psi} = (\psi_1, \psi_2)$ in (14.4) we choose to be

$$\psi_1 = 0, \quad \psi_2 = \frac{|\Gamma_0|}{|\tilde{\Gamma}_0|} \tilde{n}_1. \quad (35.3)$$

With this data the issue of the missing boundary layer for $\nu = 0$ is avoided. Instead the data (35.3) establishes a pressure difference over the body in the dual problem, resulting (as expected) in a similar dual flow field as for the dual problems at lower Reynolds number with a boundary layer, see Fig. 35.6. Here we find that the dual solution with pressure data (35.3) to a large extent resembles the dual solutions for $\beta = 0.1, 0.01$ (modulo the different sizes of the turbulent wake), whereas the dual solution with velocity boundary data is not able to transport the boundary data into the interior of the domain,

but only transports the data at the downstream separation point upstream. Similarly we find that the corresponding adaptive mesh refinement algorithms result in different meshes.

We believe that the data (35.3) for the dual problem is more appropriate also at lower Reynolds numbers, when a turbulent boundary layer is not fully resolved.

35.8 EG2 for a Circular Cylinder

When studying the flow past a circular cylinder we find that as $\beta \rightarrow 0$ the separation points (lines) move downstream until they collapse into only one separation point (line), resembling the potential solution with zero drag. As we noted in Chapter 12, the potential solution is not stable and the single separation point (line) starts to oscillate, leading to vortex shedding and turbulence downstream, and for this solution the drag is high, momentarily even higher than for the laminar separation at lower Reynolds numbers, see Fig. 12.6.

That is, we have the following scenario as the friction parameter $\beta \rightarrow 0$ (corresponding to $Re \rightarrow \infty$) for the cylinder: (i) the laminar separation is stable for a range of Reynolds numbers ($Re \approx 10^3 - 10^5$) with drag $c_D \approx 1.0$, (ii) we then for a range of Reynolds numbers have drag crisis with a reduced wake and $c_D \approx 0.4$, when the separation points have moved downstream, and then (iii) the separation points collapse into one separation point which starts to oscillate resulting in vortex shedding and turbulence downstream, corresponding to high drag, with $c_D \approx 1$.

The case of $Re \rightarrow \infty$ for a circular cylinder is in [110] referred to as the *ultimate regime* or the *T2 regime*. In the recent book [110] this regime is described as the least known and understood state of flow, and the main reason is the lack of data. Experimental results for the circular cylinder is only available up to $Re \approx 10^7$ [99, 110], for which drag is low, corresponding to drag crisis. In wind tunnels there is an upper limit on the size of the cylinder, and increasing the velocity eventually will make the incompressible flow model invalid, due to effects of compressibility and cavitation. To find much higher Reynolds numbers we have to consider flow problems with very large dimensions, such as geophysical flows.

Indeed, studying geophysical bluff body problems, such as the flow of air past the Guadalupe Island or the Canary Islands in Fig. 35.7, it is clear that the flow separates in one point, which is consistent with the EG2 solution, rather than in two points with a wake in between, which is the case for a standard von Karman vortex street at low Reynolds numbers [88].

We note that this model is cheap since we do not have to resolve any boundary layers. The only parameter in the EG2 model is the discretization parameter h , and after some mesh refinement the EG2 solution is independent of h with respect to certain mean value output, such as drag for example. In particular, this means that we are able to determine the dimensionless number

c_D (up to a tolerance) using a computational model without any empirical constants.

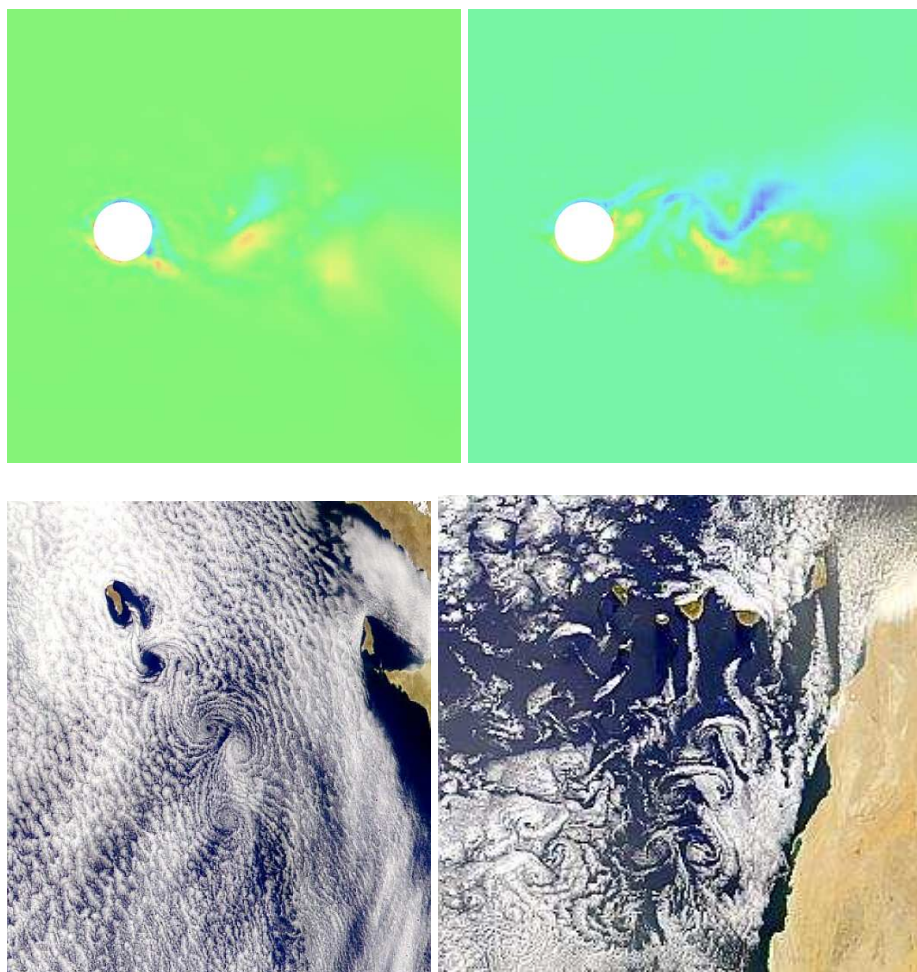


Fig. 35.7. EG2: x_3 -vorticity at two different times, in two different sections parallel to the x_1x_2 -plane (upper), and Clouds over the Guadalupe Islands and the Canary Islands (lower).

35.9 The Magnus Effect

We consider the circular cylinder, now rotating counter-clockwise with an angular velocity corresponding to a unit magnitude of the velocity at the

surface. The result of a cG(1)cG(1) computation using 62 000 nodes is shown in Fig. 35.8, where we clearly see an asymmetric separation of the flow, and an asymmetric pressure distribution, resulting in a downward force component, with $c_L \approx -1.5$ and $c_D \approx 1$.

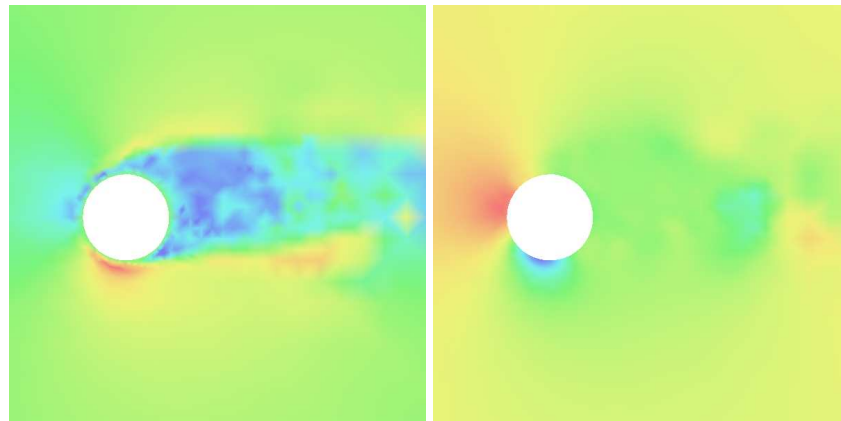


Fig. 35.8. Asymmetric separation of a rotating cylinder (with the rotation counter-clockwise).

This phenomenon of a rotation of an object in a flow resulting in a transversal force, is referred to as the *Magnus effect*. The Magnus effect has been given different explanations, with the traditional one being that the velocity at the surface of the cylinder is enhanced on one side of the cylinder and decreased on the other side, which by Bernoulli's Law leads to an asymmetric pressure and a resulting transversal force. A more recent explanation is based on an asymmetric boundary layer separation, with a delayed separation on the side which rotates in the same direction as the free stream velocity, and an earlier separation on the opposite side. The resulting asymmetric wake is then redirecting flow momentum downstream the cylinder, resulting in a corresponding momentum on the cylinder in the opposite direction due to the law of conservation of momentum. Of course, also in this mode of explanation we can invoke Bernoulli's Law for the resulting velocity to explain the transversal pressure difference.

Observations of a *reverse Magnus effect* are reported for high Reynolds numbers, where the resulting transversal force acts in the opposite direction. An explanation of this phenomenon is a situation with transition to turbulence in the boundary layer on one side only, the side with the largest relative velocity, which leads to a delayed separation on that side resulting in an asymmetric wake, now in the other direction.

35.10 Flow Past an Airfoil

The asymmetric separation of the flow past a rotating cylinder causes a lift force in the Magnus effect, and similarly a lift force is induced by the asymmetric separation of the flow past an airfoil, now caused by the geometry of a tilted airfoil. In Fig. 35.10 we show an EG2 simulation of the flow past an airfoil NACA 0012 with an angle of attack of 14° , and an associated dual solution representing sensitivity information related to the computation of lift and drag.

35.11 Flow Due to a Cylinder Rolling Along Ground

We now consider the problem of computing the flow due to a cylinder rolling along ground. A typical application comes from the automotive industry, where the flow of air past the wheels of a car or other vehicle is of much concern, since the drag of the wheels is a significant part of the total drag.

In [57] we use a computational model where we assume uniform rotation of a circular cylinder on flat ground, with the length of the cylinder being equal to its diameter. In a coordinate frame moving with the constant speed of the center of the cylinder, the problem is to determine the flow past a uniformly rotating circular cylinder with a fixed center and in contact with the ground moving with the same velocity as the oncoming free stream. The Reynolds number based on the free stream velocity and the cylinder diameter is set to $Re = 10\,000$. We compare our results with a stationary cylinder on a stationary surface in a free stream, modeling a stationary wheel in a wind tunnel. In Fig. 35.11–35.13 we plot the solutions, the adaptively refined meshes, and the approximations of the drag coefficients as we refine the mesh, with $c_D \approx 1.3$ for the rotating cylinder and $c_D \approx 0.8$ for the stationary cylinder.

We note that since the ground is moving with the same speed as the flow for the rotating cylinder, we have no boundary layer, and thus no separation of the flow upstream the cylinder, which makes the flow very different from the flow past the stationary cylinder, where we have separation upstream the cylinder due to the presence of a boundary layer, similar to the flow around a surface mounted cube. We also have an earlier separation of the flow for the rotating cylinder. These differences have important practical implications, illustrating limitations of wind tunnel testing.

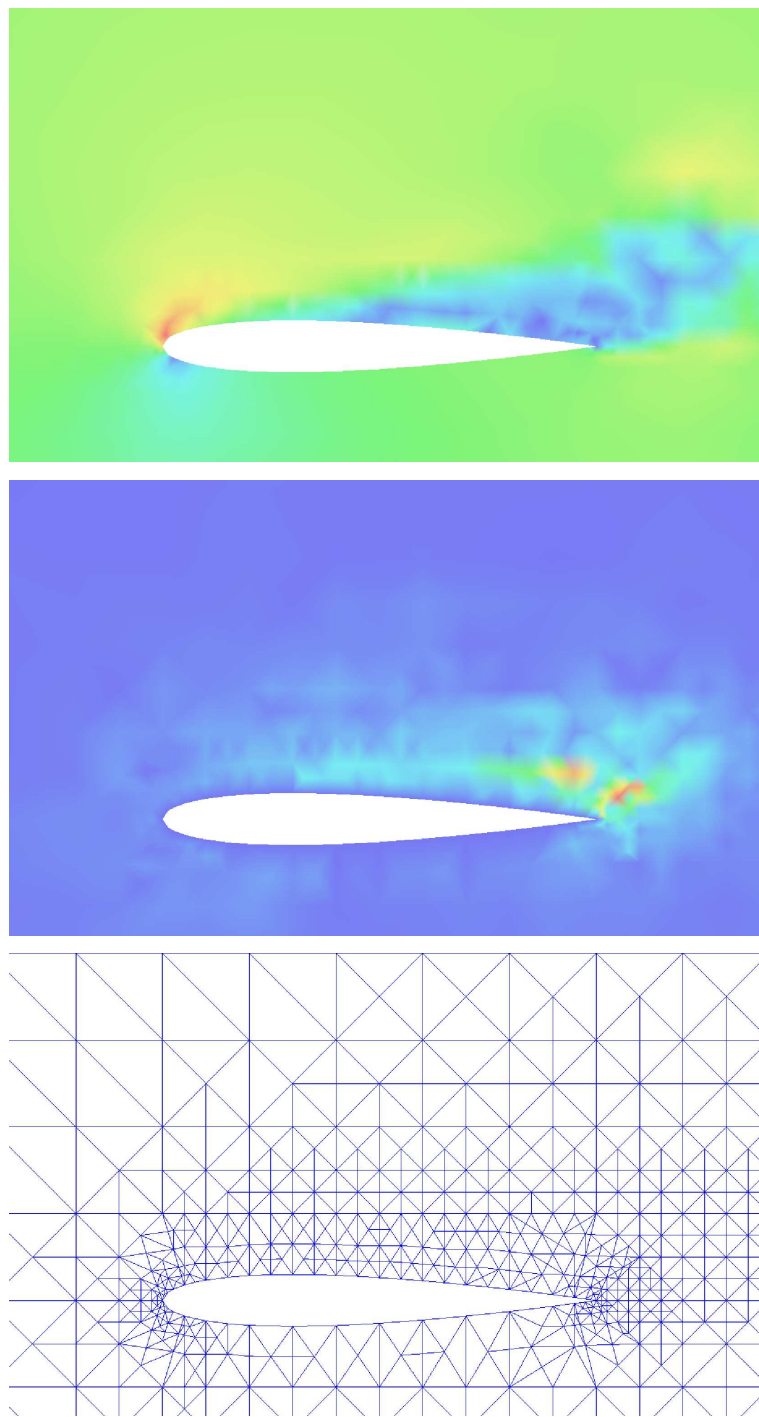


Fig. 35.9. Adaptive mesh refinement in an EG2 simulation of the flow past a NACA 0012: magnitude of the velocity (upper), dual solution (lower) representing sensitivity information related to the computation of lift and drag, and a corresponding (coarse) mesh under refinement.

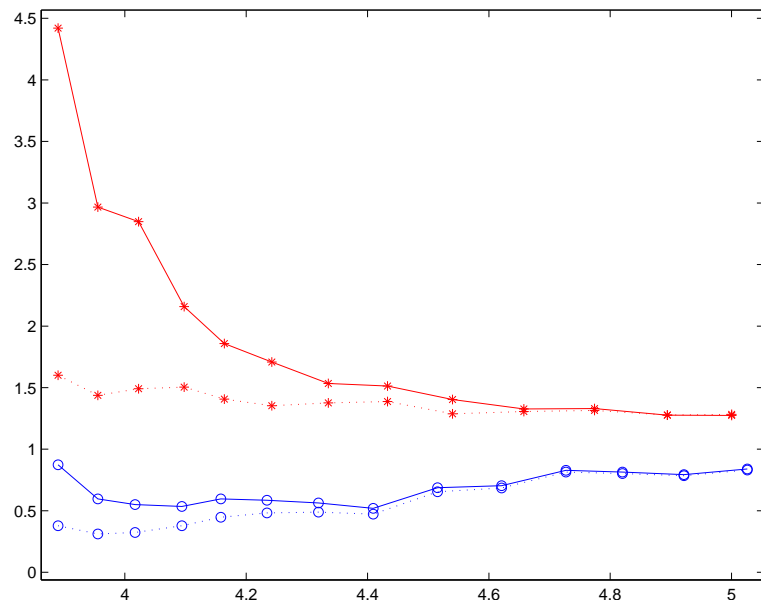


Fig. 35.10. \bar{c}_D^h vs $\log_{10} \#$ mesh points for the rotating ('*') and the stationary ('o') cylinder.

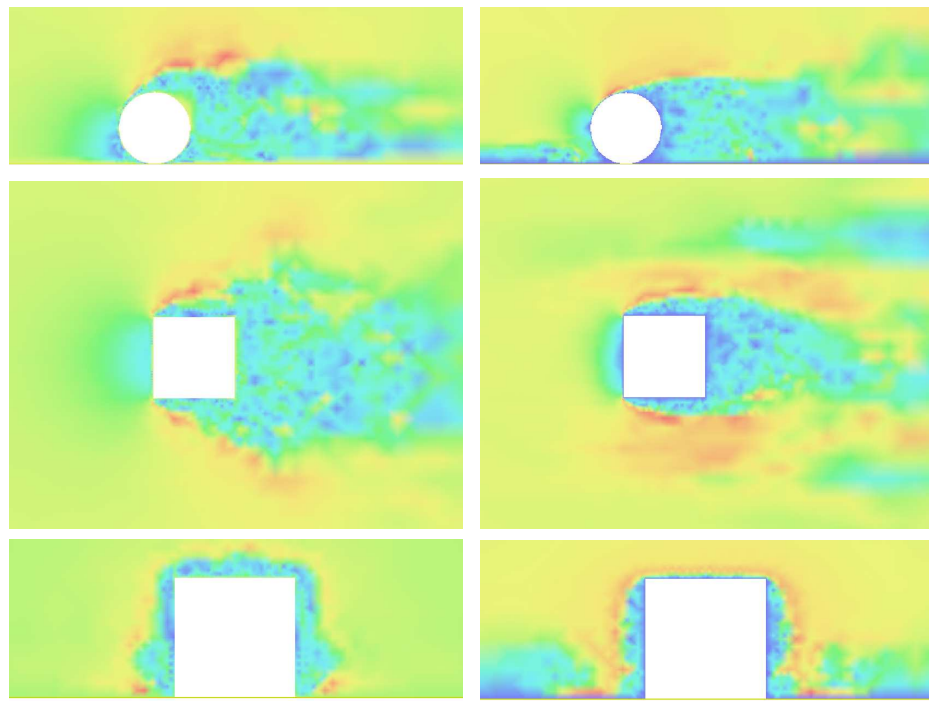


Fig. 35.11. Snapshots of magnitude of velocity, for rotating (left) and stationary (right) cylinder, in the x_1x_2 -, x_1x_3 -, and x_2x_3 -planes, through the center of the cylinder.

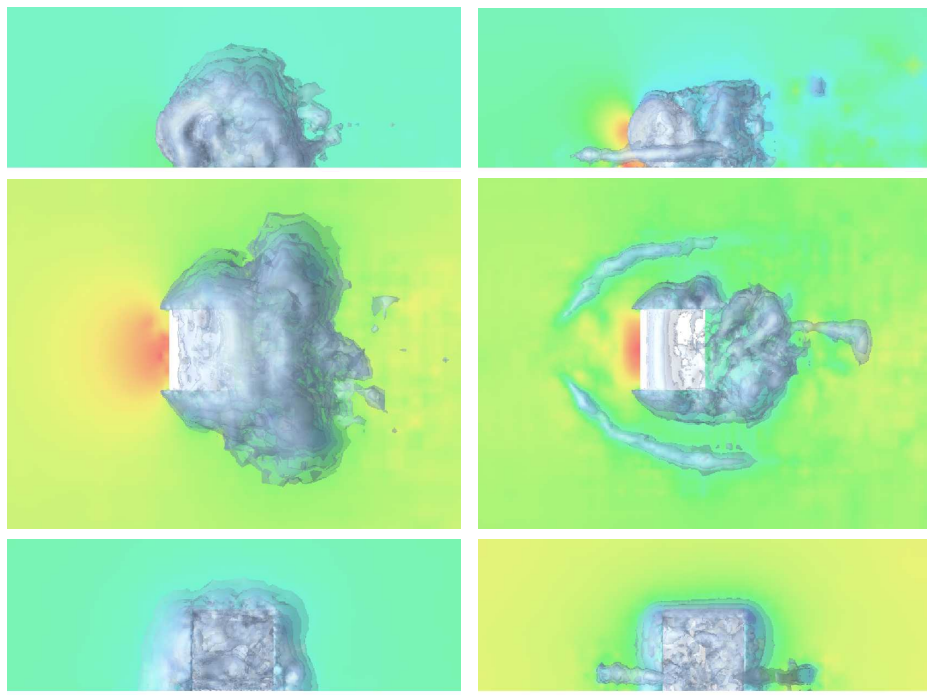


Fig. 35.12. Snapshots of pressure and iso-surfaces of negative pressure, for rotating (left) and stationary (right) cylinder, in the x_1x_2 -, x_1x_3 -, and x_2x_3 -planes, through the center of the cylinder.

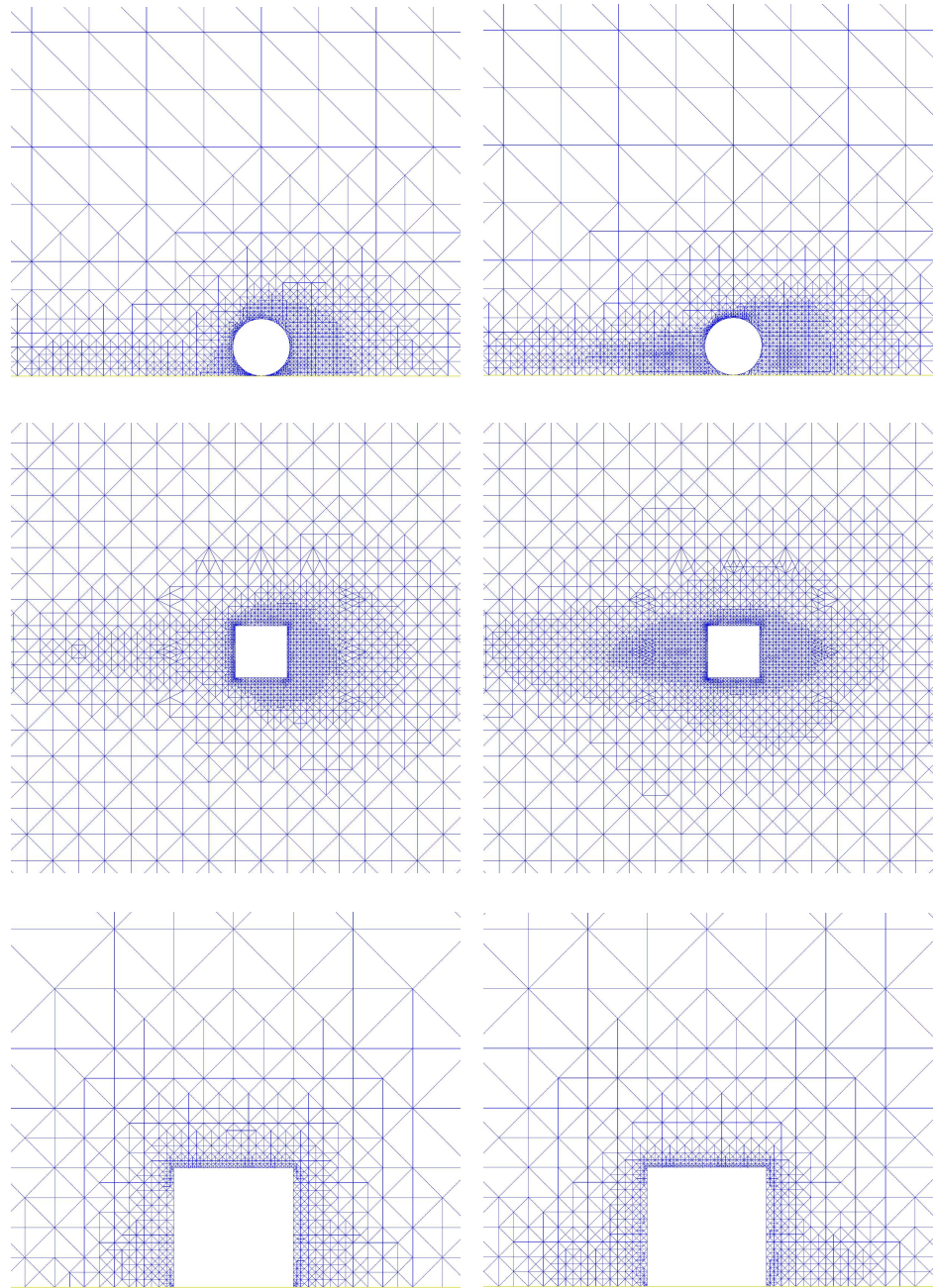


Fig. 35.13. Refined mesh for the rotating (left) and the stationary (right) cylinder, in the x_1x_2 -, x_1x_3 -, and x_2x_3 -planes.

Transition to Turbulence

The scientist should listen to every reasonable suggestion, but judge objectively. He should not be biased by appearances; have a favorite hypothesis; be of a fixed school of thought; or have a master in matters of knowledge. He should remember constantly that the progress of knowledge is often hampered by the tyrannical influence of dogma. (G.A. Tokaty)

The sudden transition from smooth, laminar flow to turbulence as the fluid velocity is gradually increased remains one of the least adequately explained phenomena in all of classical physics (James Case, SIAM News, 2002).

36.1 Modal and Non-Modal Schools

We now return to a more detailed study of the phenomenon of *transition* to turbulence in laminar parallel shear flow, such as Couette and Poiseuille pipe flow, which we have touched in Chapter 7 and 9. We recall that Reynolds in extensive studies of pipe flow in the 1880s without result tried to find a critical Reynolds number above which transition would take place, but not below. We have indicated that Reynolds did not realize that transition takes place if the product of perturbation growth and perturbation level is above a certain threshold level, where the perturbation growth typically is proportional to the Reynolds number. For large Reynolds numbers the perturbation growth thus may be large and thus a small perturbation may cause the flow to turn from laminar to turbulent.

To understand transition to turbulence in a given laminar flow we thus need to study perturbation growth, while we may assume that the perturbation level is given by inflow or boundary data. To study perturbation growth we are led to a linearized problem, with given data representing data perturbations, and the solution of the linearized problem representing the perturbation growth in space-time. For simplicity, we start with the simplest of all flows, namely Couette flow with a stationary linear velocity profile, which is a solution to NS equations for all Reynolds numbers.

We recall that Sommerfeld erroneously predicted that in Couette flow there would be no perturbation growth, and thus Couette flow would be stable for all Reynolds numbers. Sommerfeld showed that the eigenvalues of the linearized operator were non-positive and (correctly) draw the conclusion that there were no eigenmodes with exponential growth in time, but then (incorrectly) forgot that the linearized problem is not symmetric and thus may have a non-modal solution growing linearly in time causing large perturbation growth.

We have noted that the presence of non-modal linear growth in transition in parallel flows such as Couette and Poiselle flow, is far from an accepted truth in the fluid dynamics literature. The debate still goes on between a traditional “modal” school based on the work by Sommerfeld and Schlichting and a new “non-modal” school based on the work initiated by Mårten Landahl [78] in the early 1980s, continued by his student Dan Henningson and presented in the recent monograph [100].

We now enter this debate on the non-modal side, with a combined analytical and computational analysis of transition in Couette flow. We believe that without any doubt only the non-modal analysis describes the initial completely crucial phase of the transition, a phase which Reynolds could not detect in his experiments because the streamlines of the injected ink remain straight, as if nothing happens before the sudden transition. But it does, as we shall see...



Fig. 36.1. Arnold Sommerfeld (1868–1951) and Mårten Landahl (1927–1999) (Landahl picture from M.I.T. News Office: <http://web.mit.edu/newsoffice>).

36.2 Difficulties of Experimental Transition Studies

Reynolds unsuccessful experiments show a main difficulty of experimental studies of transition: If we initialize a stationary laminar flow which is stable, then nothing will happen. If we try to initialize an unstable flow then we will not succeed. In both cases the experiment will be a failure. What we want to do is to initialize a stationary laminar flow which is initially stable, so that we can initiate it, and then watch the flow becoming unstable turbulent

after some time. This is what Reynolds sought, and sometimes he did observe transition and sometimes not, but he could not understand what made the difference and thus could not give transition a scientific explanation supported by reproducible experiments.

36.3 Possibilities of Computational Transition

We shall now show that computation opens to controlled experiments of transition, including the quantitative perturbation growth, which concerns the crucial question of the specific growth in time of specific initial perturbations. By computation we can thus redo Reynold's experiments and thereby unravel what seemed so mysterious to Reynolds. We can do this, either by solving the linearized equations with different initial perturbations, or the Euler/NS equations with different data. The latter simulation directly exhibits the full transition process, while the linearized problem only describes the initial, but completely crucial, phase; without initial growth there will be no growth and no transition.

The problem of transition to turbulence in shear flow has mathematical features which seem to be present in a range of phenomena outside fluid dynamics, sharing the aspects of transition from order to chaos, occurring in e.g. crashes of stock markets, long-lasting marriages, superpowers, or sudden deaths of living organisms et cet. All these cases share the features of non-modal perturbation growth and have perturbation threshold levels for transition, as explained in Chapter 49 "The Crash Model", in Body&Soul Vol 3 [36].

36.4 The Challenge

We seek to explain transition in stationary Poiseuille pipe flow with parabolic velocity profile studied by Reynolds and Couette flow between two parallel plates with linear profile, both representing parallel shear flow. We thus consider flows which remain stationary laminar if the perturbation level (in initial/boundary conditions or forcing) is below a certain (small) threshold level, and which undergo transition to turbulent flow for perturbations above the threshold level. We refer to this type of flow as *conditionally stable*. Depending on the perturbation level, pipe flow may undergo transition for Reynolds' numbers in wide range from 1000 to 20 000, and Couette flow in the range 300-10 000, depending on the perturbation level. For sufficiently small Reynolds' numbers, the flow stays stationary laminar even under large perturbations.

Sommerfeld's analysis predicts Poiseuille flow to be stable for Reynolds numbers smaller than 5772, and Couette flow for all Reynolds numbers, which is clearly at variance with observations. Sommerfeld's analysis thus cannot be correct, and we have indicated that the mistake is to forget non-modal growth.

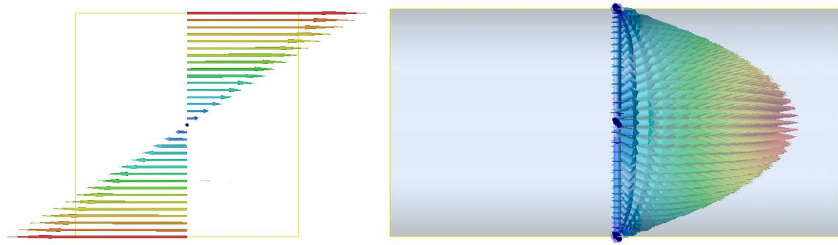


Fig. 36.2. Couette flow (left) with a linear velocity profile, and Poiseuille flow (right) with a parabolic velocity profile.

36.5 Modal and Non-Modal Perturbation Growth

Since the base flow is conditionally stable, the linearized equations cannot have any exponentially unstable eigenmodes, that is all eigenvalues of the linearized stationary equations have positive (stable) real part: There is no exponential modal growth of small perturbations. The only possibility of perturbation growth is then *non-modal growth* connecting to the non-symmetric nature of the linearized equations. Typically, non-modal growth is of the form $t \exp(-\nu t)$ which takes on a maximum of size $1/\nu$ for $t \approx 1/\nu$, thus representing large perturbation growth proportional to the Reynolds number. Typically, ν represents the real part of the eigenvalue with smallest real part, and with the corresponding eigenmode having the slowest exponential decay.

With perturbation growth proportional to the Reynolds number, the Euler equations will formally exhibit infinite perturbation growth, which is one of the indications that the Euler equations lack (stable) exact solutions.

We shall see that the non-modal perturbation growth may change the velocity profile substantially, while streamlines remain straight and thus is not detected in Reynolds' ink experiment. We will refer to the reorganization as resulting from the *Taylor-Görtler mechanism* (or *lift-up* in Landahl's terminology) through which small transversal velocity perturbations after some time result in large perturbations in the streamwise velocity, which is the initial and crucial phase of the transition process. This reorganization will occur as soon as the streamwise velocity has a gradient in a transversal cross-flow direction, that is in shear flows with fluid particles moving with different speed in the same direction, which occur unless all particles move with the same velocity.

36.6 Different Perturbations and Threshold Levels

The basic problem of transition is thus perturbation growth: if a small perturbation may have a big effect on the flow, it may change the base flow to a new base flow with potentially exponentially unstable modes which in a secondary step may develop into a turbulent flow. The study of transition of

stationary shear flow thus must be the study of *threshold levels for different types of perturbations*, with the threshold level being defined as the smallest level of a particular type of perturbation that leads to transition. We may call this a *special threshold level* characteristic of a specific type of perturbation. Correspondingly, we may define a *general threshold level* as the smallest level above which there is *some* perturbation leading to transition, so that no perturbation below the general threshold level leads to transition.

Different perturbations may have very different perturbation growth, and the perturbations with largest perturbation growth, referred to as *optimal perturbations*, with correspondingly smallest threshold, define the general threshold level.

The mathematical analysis of initial transition concerns perturbation growth in the linearized NS equations, with focus on identifying optimal perturbations. In particular one may expect to search for optimal perturbations among eigenmodes which decay slowly.

The detailed analysis of threshold levels for transition can only be made computationally by testing the effect of different perturbations, for example with a focal objective to find optimal perturbations.

We present below a computational study of transition with different types of perturbations and techniques to identify perturbations with strong growth and the corresponding general threshold levels. We start with an analytical study identifying key features. Of course the linearized NS equations and the dual linearized NS equations express similar features of stability. The linearized NS equations are useful for studies of perturbation growth, while the dual linearized NS equations are used to study effects on outputs of perturbations. Here we thus focus on the linearized NS equations.

36.7 Analytical Stability of the Linearized NS

Let \hat{u} be a solution of the NS equations (28.1) with initial data u_0 and right hand side f , and $\hat{u} + \hat{\varphi} = (u + \varphi, p + \iota)$ the solution with the perturbed initial data $u^0 + \varphi^0$ and right hand side $f + g$. Subtracting the two versions of the NS equations and omitting the quadratic perturbation term $(\varphi \cdot \nabla)\varphi$, we are led to the linearized NS for the perturbation $\hat{\varphi}$:

$$\begin{aligned}\dot{\varphi} + u \cdot \nabla \varphi + (\varphi \cdot \nabla)u - \nu \Delta \varphi + \nabla \iota &= g, & \text{in } \Omega \times I, \\ \nabla \cdot \varphi &= 0, & \text{in } \Omega \times I, \\ \varphi &= 0, & \text{on } \partial\Omega \times I, \\ \varphi(\cdot, 0) &= \varphi^0, & \text{in } \Omega,\end{aligned}\tag{36.1}$$

where $(\varphi \cdot \nabla)u = (\sum_{j=1}^3 \varphi_j u_{i,j})_{i=1}^3$ with $v_{i,j} = \partial v / \partial x_j$.

The growth of small perturbations is governed by the stability of (36.1) and can be measured as *stability factors* estimating various norms of (φ, ι) in terms of certain norms of the data (g, φ_0) . A basic example is given by the

weak stability factor $S_0(u, \hat{t}, \varphi^0)$ depending on the base flow \hat{u} , final time \hat{t} and the perturbation φ^0 , defined by

$$S_0(u, \hat{t}, \varphi^0) = \frac{\|\varphi\|_I}{\|\varphi^0\|}, \quad (36.2)$$

or the factor $S_0(u, \hat{t})$ depending on the base flow u and the final time \hat{t} with a maximization over all perturbations, defined by

$$S_0(u, \hat{t}) = \sup_{\varphi^0 \in L_2} \frac{\|\varphi\|_I}{\|\varphi^0\|}, \quad (36.3)$$

where φ is the solution of (36.1) with $g = 0$ and initial data $\varphi^0 \neq 0$, and $\|v\| = \|v\|_{L_2(\Omega)}$, $\|v\|_I = \sup_{0 < t < \hat{t}} \|v(\cdot, t)\|$. The factor $S_0(u, \hat{t}, \varphi^0)$ measures the growth over the time interval $(0, \hat{t}]$ of the perturbation φ^0 of initial data, related to a special perturbation threshold, and the factor $S_0(u, \hat{t})$ measures the maximal growth over the time interval $(0, \hat{t})$ of a perturbation of initial data, related to a general perturbation threshold. We refer to these stability factors as *weak* because we measure the solution itself and not derivatives thereof (as we do for solutions to the dual NS equations).

We now give estimates of the stability factor $S_0(u, \hat{t})$ in two extreme cases: a *worst case* with exponential dependence in $G\hat{t}$, where G is a measure of the modulus of the maximum velocity gradient ∇u , related to an unstable flow with exponentially growing eigenmodes, and a *best case* with linear dependence in $G\hat{t}$ related to a conditionally stable flow with no exponentially growing eigenmodes. Assuming that $G = 1$ and $\hat{t} = \nu^{-1} = Re$, the dependence can be expressed as an exponential or linear dependence in the Reynolds' number Re , with the exponential dependence indicating instability even for moderately large Reynolds' numbers, while the linear dependence corresponds to a smooth laminar flow with strong growth for large Reynolds numbers.

36.7.1 Worst Case Exponential Perturbation Growth

Multiplying the first equation of (36.1) by φ and integrating over $\Omega \times (0, t)$, using the incompressibility of both u and φ , one gets for $t > 0$:

$$\|\varphi(\cdot, t)\|^2 \leq -2 \int_0^t \int_\Omega (\varphi \cdot \nabla) u \cdot \varphi \, dx ds + \|\varphi^0\|^2 \leq CG \int_0^t \|\varphi\|^2 \, ds + \|\varphi^0\|^2,$$

with $C \approx 1$, from which follows that

$$S_0(u, \hat{t}) \leq \exp(CG\hat{t}). \quad (36.4)$$

This is a worst case exponential estimate. We note that the exponential growth is generated by the presence of the zero order term $(\varphi \cdot \nabla) u$, as in the simple scalar ode $\psi' = G\psi$ with solution $\psi(t) = \psi(0) \exp(Gt)$. A flow with such a

very strong perturbation growth cannot exist as a stable flow. Since there are some more or less stable flows observable in nature, it must be possible in special cases to obtain reduced growth rates by using particular features of the zero order coupling term $(\varphi \cdot \nabla)u$. A basic such case arises in shear flow, with a particular coupling of the perturbations of the velocities in streamwise and transversal directions, which we now turn to.

36.7.2 Linear perturbation growth in shear flow

We consider (almost) parallel shear flow, where the streamlines are (almost) parallel straight lines and the transversal variation of the streamwise flow velocity corresponds to a streamwise shear force. We now show that for such flows the weak stability factor $S_0(u, \hat{t})$ defined by (36.3) satisfies $S_0(u, \hat{t}) \approx CG\hat{t}$, with $C \approx 1$. This estimate underlies the first crucial step in the scenario of transition to turbulence in shear flow to be presented, showing that a perturbation growth $\approx \nu^{-1}$ over time intervals of length $\hat{t} = \nu^{-1}$ is possible even for smooth flows with $G = 1$, indicating that a small initial perturbation (of size ν say) in fact may cause the base flow to change significantly, if we only wait long enough (over a time interval $\approx \nu^{-1}$).

We consider a smooth parallel stationary base flow (u, p) in an infinitely long straight pipe $\Omega = \mathbb{R} \times \omega$, where ω in the (x_2, x_3) -plane is the cross-section (with smooth boundary) of the pipe of diameter of size 1. The axis of the pipe is oriented along the x_1 -axis, and u vanishes on the boundary of the pipe. We assume that the base flow (u, p) is independent of x_1 and satisfies the following assumptions

$$\|u_1\| \approx 1, \quad \|\bar{\nabla}u_1\|_\infty = C, \quad \|\bar{u}\|_\infty + \|\bar{\nabla}\bar{u}\|_\infty \leq c\nu, \quad (36.5)$$

where $\|\cdot\|_\infty$ denotes the maximum norm, $\bar{u} = (u_2, u_3)$, and $\bar{\nabla}$ is the gradient with respect to (x_2, x_3) . Here and below, c and C denote positive constants of moderate size, which are independent of ν . The assumption (36.5) including a smooth streamwise velocity $u_1 \approx 1$ in the x_1 direction being independent of x_1 , and smooth small transversal velocities \bar{u} of size $\approx \nu$, may be viewed as a basic characteristic of shear flow. A further characteristic may be that the derivatives in the streamwise direction x_1 are one order smaller in ν , so that $u_{1,1} \sim \nu$ and $u_{2,1}, u_{3,1} \sim \nu^2$. We will return to this feature below in the presentation of the scenario of transition to turbulence. We further assume as already indicated that $\hat{t} \sim 1/\nu = Re$.

Assuming that also the perturbations (φ, q) are independent of x_1 , the linearized equations (36.1) take the following form:

$$\begin{aligned} \dot{\varphi}_1 + u \cdot \nabla \varphi_1 + (\bar{\varphi} \cdot \bar{\nabla})u_1 - \nu \Delta \varphi_1 &= 0 && \text{in } \omega \times I, \\ \dot{\varphi} + u \cdot \nabla \bar{\varphi} + (\bar{\varphi} \cdot \bar{\nabla})\bar{u} + \bar{\nabla} \iota - \nu \Delta \bar{\varphi} &= 0 && \text{in } \omega \times I, \\ \bar{\nabla} \cdot \bar{\varphi} \equiv \varphi_{2,2} + \varphi_{3,3} &= 0 && \text{in } \omega \times I, \\ \varphi &= 0 && \text{on } \partial\omega \times I, \\ \varphi(\cdot, 0) &= \varphi_0 && \text{on } \omega. \end{aligned} \quad (36.6)$$

These equations have a very particular structure. First, the equations for the transversal velocity $\bar{\varphi}$ are fully decoupled from the equation for the streamwise velocity φ_1 , and have zero order terms with small coefficients because $|\bar{\nabla}\bar{u}| \leq c\nu$. Secondly, the zero order term $(\bar{\varphi} \cdot \bar{\nabla})u_1$ in the equation for φ_1 does not contain φ_1 , because $u_{1,1} = 0$. This means that the zero order terms in (36.6) have a special form, which makes it possible to reduce the general worst case exponential growth (36.4) of $S_0(\hat{t})$, to a linear growth.

The basic structure of the equations (36.6) is present in the system of ordinary differential equations $\dot{\varphi}_1 - \varphi_2 = 0$, $\dot{\varphi}_2 = 0$, for $t > 0$, $\varphi^0 = (0, \varphi_2^0)$ with solution $\varphi_1(t) = t\varphi_2^0$, $\varphi_2(t) = \varphi_2^0$, showing a linear growth of φ_1 . The growth in this system, which we met already in the stability analysis of Chapter 8, is very different from the exponential growth obtained by changing the first equation to $\dot{\varphi}_1 - \varphi_1 = 0$, with the exponentially growing solution $\varphi_1(t) = \exp(t)\varphi_1^0$, assuming now $\varphi_1^0 \neq 0$. Clearly, the change from linear to exponential growth is related to the nature of the coupling, with the direct coupling $\dot{\varphi}_1 = \varphi_1$ being much stronger than the indirect coupling $\dot{\varphi}_1 = \varphi_2$, where $\dot{\varphi}_2 = 0$.

We now prove a basic estimate giving a linear growth bound in time of the streamwise velocity perturbation φ_1 generated by a small transversal perturbation $\bar{\varphi}^0$. We refer to the physical phenomena causing this perturbation growth as the *Taylor-Görtler mechanism*, which has a crucial role in transition to turbulence. The bound is based on an energy estimate using the decoupling of φ_1 and $\bar{\varphi}$, resulting from the fact that $q_{,1} = 0$ and $\varphi_{1,1} = 0$. Below we present computations showing that the bound is sharp and that linear perturbation growth actually occurs.

Theorem 36.1. *The stability constant $S_0(u, \hat{t})$, defined by (36.3) in the context of x_1 -independent pipe flow (u, p) satisfying (36.5), satisfies the following bound for $\hat{t} = \nu^{-1}$:*

$$S_0(u, \hat{t}) \leq C\nu^{-1}, \quad (36.7)$$

where C depends on the constant c in (36.5). If the constant c is small enough, then the estimate (36.7) holds for $\hat{t} \geq \nu^{-1}$ with ν^{-1} replaced by \hat{t} .

Proof: First, multiplying the equation for $\bar{\varphi}$ by $\bar{\varphi}$, and integrating over ω using the fact that $\bar{\nabla} \cdot \bar{u} = \bar{\nabla} \cdot \bar{\varphi} = 0$, shows that

$$\frac{1}{2} \frac{d}{dt} \|\bar{\varphi}\|^2 + \nu \|\bar{\nabla} \bar{\varphi}\|^2 \leq c\nu \|\bar{\varphi}\|^2,$$

from which follows that

$$\|\bar{\varphi}(\cdot, t)\|^2 \leq \exp(C\nu t) \|\bar{\varphi}^0\|^2, \quad 0 < t \leq \hat{t}.$$

Next, multiplying the equation for φ_1 by φ_1 and using again the fact that $\bar{\nabla} \cdot \bar{u} = \bar{\nabla} \cdot \bar{\varphi} = 0$, we get

$$\frac{1}{2} \frac{d}{dt} \|\varphi_1\|^2 + \nu \|\bar{\nabla} \varphi_1\|^2 \leq C\left(\frac{1}{2}\nu \|\varphi_1\|^2 + \frac{1}{2}\nu^{-1} \|\bar{\varphi}\|^2\right),$$

from which the desired estimate follows by integration. The modification with c sufficiently small is straight forward. \square

A challenge is to extend the above result to different base flows $\hat{u} = (u, p)$ with slight x_1 -dependence. As a small contribution to this problem we present the following example: we assume in addition to (36.5) that

$$\|u_{1,1}\|_\infty \leq c\nu, \quad \|\bar{u}_{,1}\|_\infty \leq c\nu^2, \quad (36.8)$$

where c is a positive constant, and we allow the perturbation velocity φ to depend on x_1 , but we assume for the pressure part q that $q_{,1} = 0$ and that correspondingly the incompressibility condition reduces to $\varphi_{2,2} + \varphi_{3,3} = 0$, which corresponds to a slight compressibility of the original fluid with a pressure perturbation q , which is constant in the x_1 -direction. In this case the linearized perturbation equations take the form:

$$\begin{aligned} \dot{\varphi}_1 + u \cdot \nabla \varphi_1 + (\varphi \cdot \nabla) u_1 - \nu \Delta \varphi_1 &= 0 && \text{in } \Omega \times I, \\ \dot{\bar{\varphi}} + u \cdot \nabla \bar{\varphi} + (\varphi \cdot \nabla) \bar{u} + \bar{\nabla} \iota - \nu \Delta \bar{\varphi} &= 0 && \text{in } \Omega \times I, \\ \varphi_{2,2} + \varphi_{3,3} &= 0 && \text{in } \Omega \times I, \\ \varphi &= 0 && \text{on } \partial\Omega \times I, \\ \varphi(\cdot, 0) &= \varphi_0 && \text{on } \Omega, \end{aligned}$$

which again decouples and thus is amenable to analysis as above.

The *Orr-Sommerfeld equations* are the linearized NS equations linearized at x_1 -directed parallel flow $u = (u_1(x_2), 0, 0)$ between two parallel plates with normal in the x_2 direction, assuming the perturbations are independent of the transversal direction x_3 parallel to the plates and also that $\varphi_3 = 0$: find $(\varphi(x_1, x_2, t), p(x_1, x_2, t))$ such that for $|x_2| < d$, $x_1 \in \mathbb{R}$, $t > 0$,

$$\begin{aligned} \dot{\varphi}_1 + u \cdot \nabla \varphi_1 + u_{1,2} \varphi_2 - \nu \Delta \varphi_1 + p_{,1} &= 0, \\ \dot{\varphi}_2 + u \cdot \nabla \varphi_2 - \nu \Delta \varphi_2 + p_{,2} &= 0, \\ \varphi_{1,1} + \varphi_{2,2} &= 0, \end{aligned} \quad (36.9)$$

with $\varphi(x_1, \pm d) = 0$, and the initial condition $\varphi(x_1, x_2, 0) = \varphi^0(x_1, x_2)$, and where $2d$ is the distance between the plates. In the case of Couette flow $u_1(x_2) \propto x_2$ and for Poiseuille flow $u_1(x_2) \propto (1 - (x_2/d)^2)$, the stability factor $S_0(u, \hat{t})$ turns out to be much smaller than the corresponding factor for the linearized problem (36.6) with x_1 independent perturbations. We conclude that x_3 -independent perturbations seem to be less significant than x_1 -independent perturbations, and we thus conclude that the Orr-Sommerfeld equations are not relevant in initial transition to turbulence in shear flow, while the classical stability analysis is based on these equations [99].

36.8 Computational Transition in Shear Flows

In Section 36.7 we showed that linear perturbation growth proportional to the Reynolds' number is possible in parallel shear flow. We will now investi-

gate this linear perturbation growth computationally, for conditionally stable Couette and Poiseuille flows.

We thus present computational results for Couette flow and Poiseuille flow in a pipe along the x_1 -axis with square cross section 1×1 , assuming periodicity in the streamwise direction. We use cG(1)cG(1) on the unit cube with a regular tetrahedral mesh with $65 \times 65 \times 65$ nodes, and we set the viscosity to $\nu = 1/10\,000$.

We further consider jet flow with periodic boundary conditions in all directions, with initial streamwise velocity one in the jet and zero streamwise velocity outside the jet, on a computational domain $2 \times 1 \times 1$ using cG(1)cG(1) on a tetrahedral mesh with $65 \times 33 \times 33$ nodes, again with the viscosity set to $\nu = 1/10\,000$.

36.9 Couette Flow

The Couette base flow $u = (u_1, 0, 0)$ has a linear streamwise velocity profile $u_1 = 2x_2 - 1$, with streamwise velocity ± 1 on the top and bottom. In the streamwise and span-wise directions we use periodic boundary conditions. We are interested in conditionally stable flows, and we thus first show that Couette flow is conditionally stable.

We present computational results for Couette flow with a random initial perturbation of maximal size 1, centered in $(0.5, 0.5, 0.5)$. That is, for each velocity component we add a random perturbation, uniformly distributed in $(-1, 1)$, times a weight function $64 \times x_1(1-x_1)x_2(1-x_2)x_3(1-x_3)$. The random perturbation may be considered to include contributions from all modes, and in Fig 36.3–36.5 we find that most of these modes are quickly damped out and leaves only a combination of a few modes with a slow decay.

A small streamwise perturbation increases very slowly, but only as long as the decreasing transversal perturbations are above a certain threshold. This streamwise perturbation growth, caused by the Taylor-Görtler mechanism, is here too weak to cause transition to turbulence.

Evidently this computational model of Couette flow is conditionally stable, since there exist perturbations for which the flow is stable.

36.9.1 Linear Perturbation Growth

Since Couette flow is conditionally stable there exist no exponentially growing eigenmodes, but in Section 36.7 we showed that in parallel shear flow, perturbation growth proportional to the Reynolds' number is possible. We will now show that this linear perturbation growth may be strong enough to cause the flow to undergo transition to turbulence, by taking the original stable base flow, without any exponentially growing eigenmodes, to a new unstable flow with exponentially growing eigenmodes.

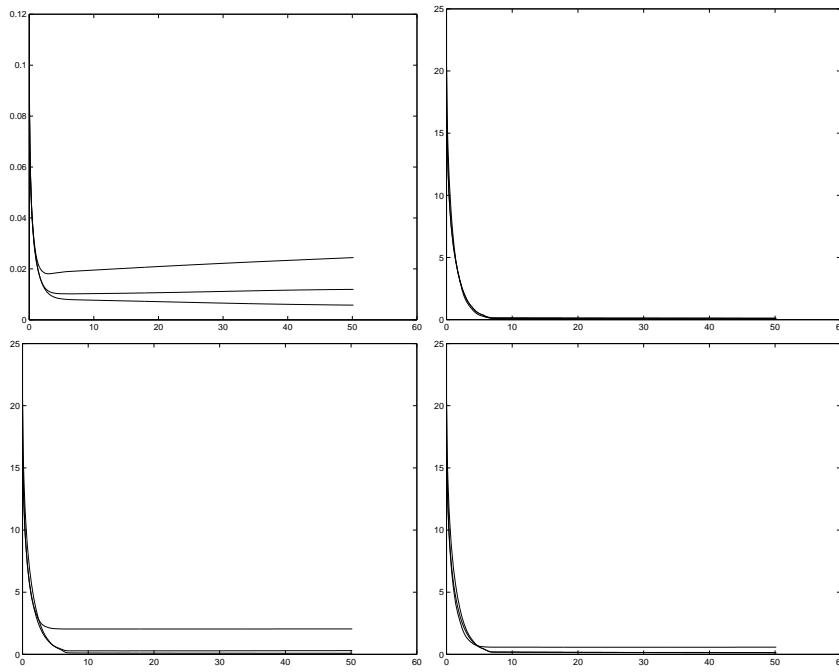


Fig. 36.3. Couette flow (random initial perturbation): Perturbations $\|\varphi_i\|$ as functions of time (upper left), derivatives $\|\partial u_i / \partial x_1\|$ (upper right), $\|\partial u_i / \partial x_2\|$ (lower left), and $\|\partial u_i / \partial x_3\|$ (lower right) as functions of time.

Not only the size of perturbations matter, but also the nature of the perturbations. In the case of a random perturbation we did not get transition even for large perturbations, but since transition is observed in experiments (starting at Reynolds' numbers at around 300) there must be other types of perturbations that leads to transition. It is intuitively clear that a large scale rotational perturbation results in large perturbation growth through the Taylor-Görtler mechanism, slowly shifting particles with different streamwise velocity transversally.

We now present computational results using an initial transversal, x_1 -independent, rotational perturbation $\varphi^0 = (0, \varphi_2^0(x_2, x_3), \varphi_3^0(x_2, x_3))$, of the type

$$\begin{aligned}\varphi_2^0(x_2, x_3) &= \kappa\nu \sin(2\pi x_2) \cos(\pi x_3), \\ \varphi_3^0(x_2, x_3) &= -\kappa\nu \cos(2\pi x_2) \sin(\pi x_3),\end{aligned}$$

where $\kappa\nu = 0.5$. We also apply a very small x_1 -dependent driving force $f = (0, f_2(x_1), f_3(x_1))$, with $f_2(x_1) = f_3(x_1) = 10^{-3} \sin(10\pi x_1)$, creating and sustaining a very small streamwise variation. We use slip boundary conditions in the span-wise direction, and periodic boundary conditions in the streamwise direction.

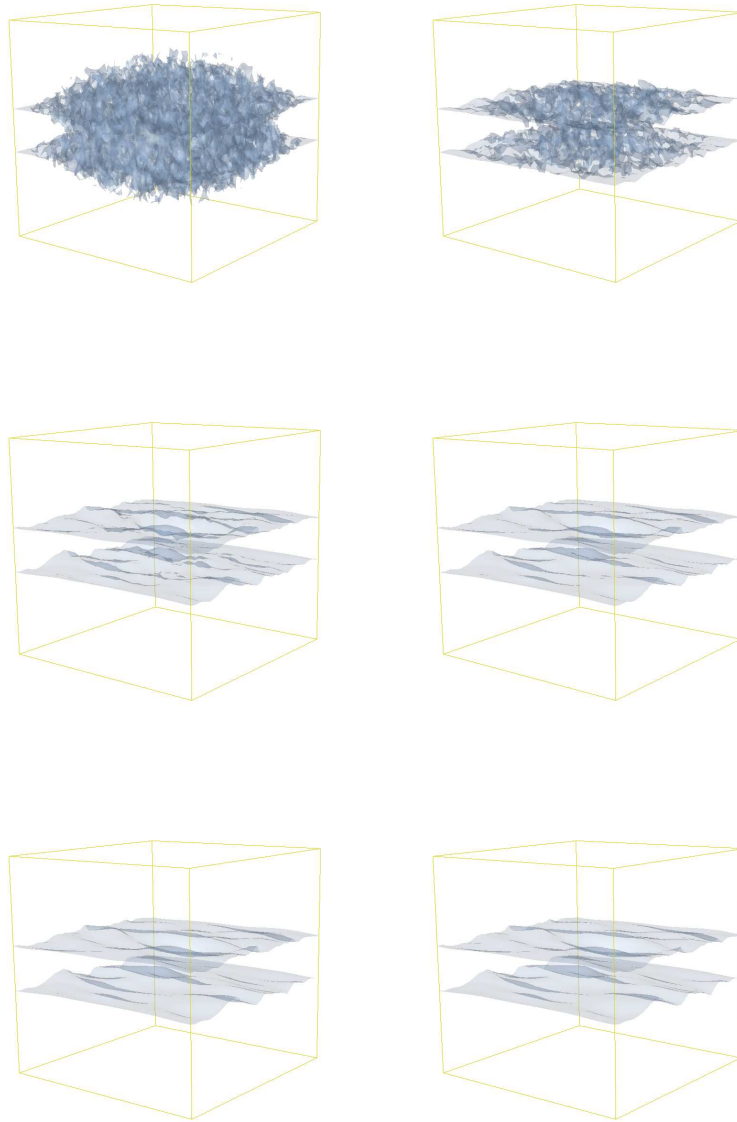


Fig. 36.4. Streamwise velocity iso-surfaces for $|u_1| = 0.2$ in Couette flow (random initial perturbation) for $t = 0, 1, 4, 5, 7, 10$

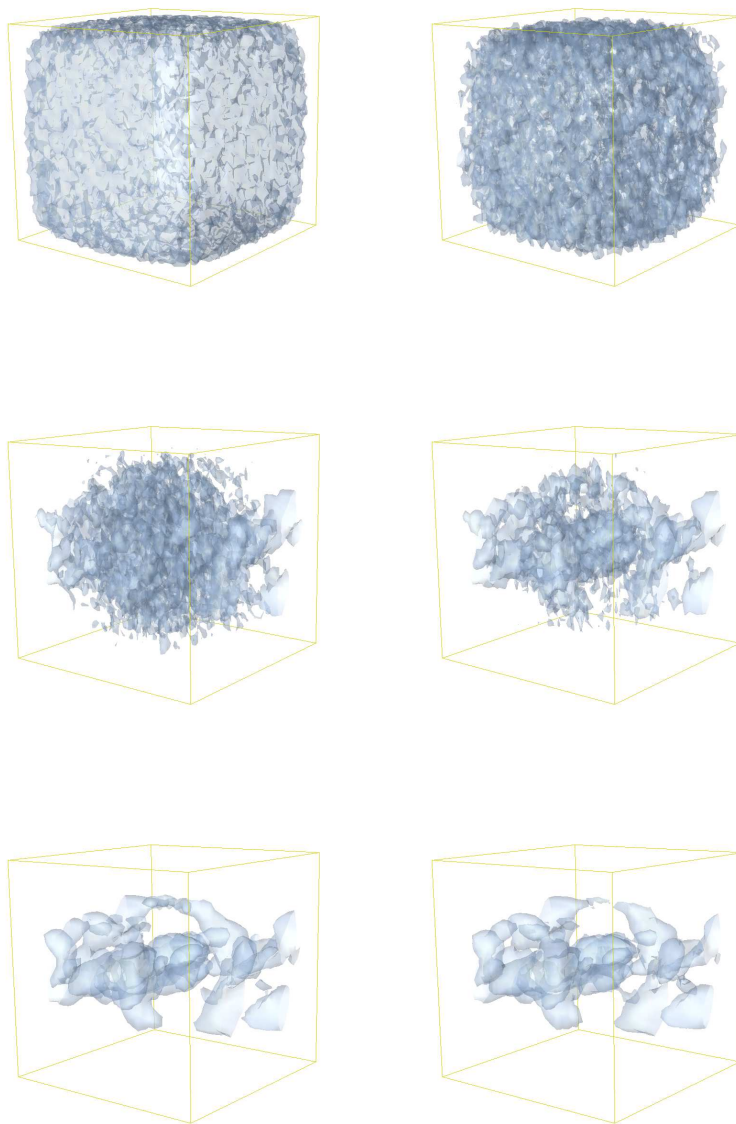


Fig. 36.5. Transversal velocity iso-surfaces for $|u_2| = 0.015$ in Couette flow (random initial perturbation) for $t = 0, 1, 4, 5, 7, 10$

Initially, the streamwise perturbation φ_1 grows linearly through the action of the Taylor-Görtler mechanism, causing the formation of high and low velocity streaks, see Fig 36.6–36.9, and the perturbations φ_2 and φ_3 decrease initially. In the same way, transversal derivatives with respect to x_2 and x_3 grow linearly for u_1 , and decrease for u_2 and u_3 . This linear growth is easy to observe in Fig 36.7, where the iso-surfaces for the absolute value of the streamwise velocity is shown for $|u_1| = 0.2$. In Fig 36.6 we see that near $t = 10$ we get a sudden burst, where all x_1 -derivatives increase by a factor 100 over a short time interval, corresponding to initial transition when the base flow loses stability. A key observation is that this initial transition is not possible until the perturbation φ_1 , and the transversal derivatives $\partial u_1 / \partial x_2$ and $\partial u_1 / \partial x_3$, has reached a certain threshold. Another important observation, which is not obvious from studying the global norms in Fig 36.6, is that the perturbations of course vary in space, and that the threshold is a local condition that has to be satisfied.

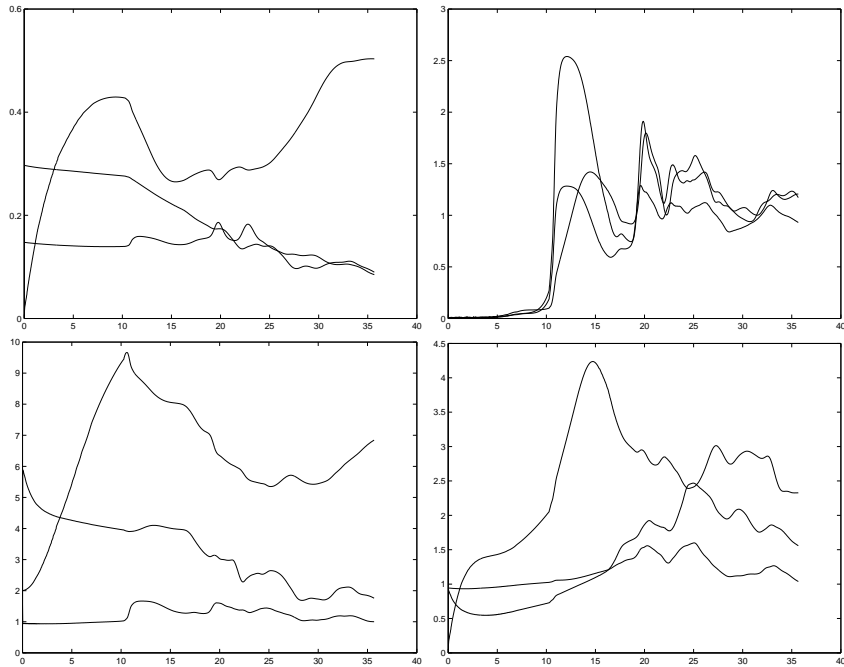


Fig. 36.6. Couette flow ($\kappa\nu = 0.5$): Perturbations $\|\varphi_i\|$ as functions of time (upper left), derivatives $\|\partial u_i / \partial x_1\|$ (upper right), $\|\partial u_i / \partial x_2\|$ (lower left), and $\|\partial u_i / \partial x_3\|$ (lower right) as functions of time.

To test the dependence of the size of the perturbation, we present computational results for a smaller initial perturbation $\kappa\nu = 0.1$, instead of $\kappa\nu = 0.5$,

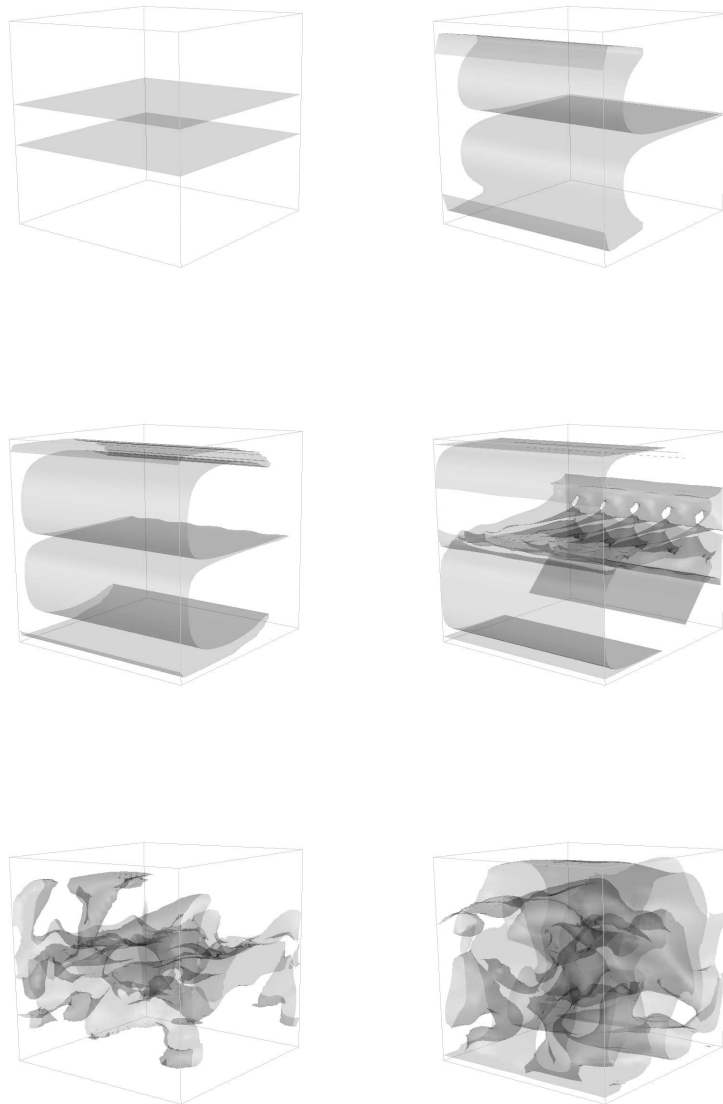


Fig. 36.7. streamwise velocity iso-surfaces for $|u_1| = 0.2$ in Couette flow ($\kappa\nu = 0.5$) for $t = 0, 5, 10, 15, 20, 30$

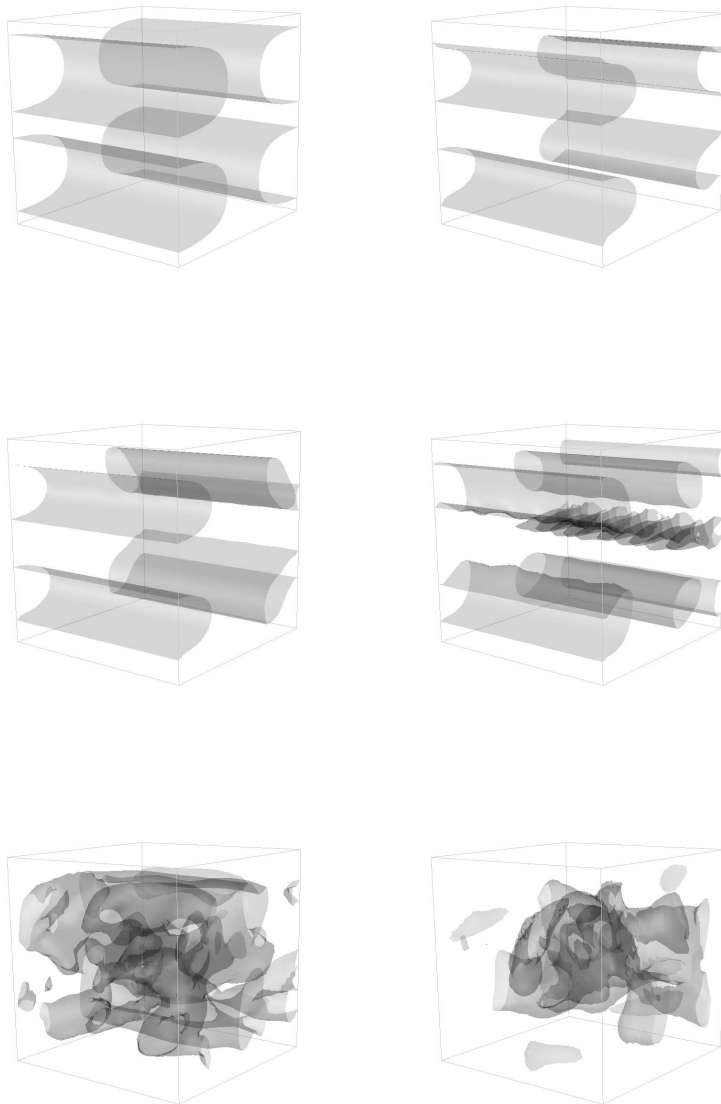


Fig. 36.8. Transversal velocity iso-surfaces for $|u_2| = 0.2$ in Couette flow ($\kappa\nu = 0.5$) for $t = 0, 5, 10, 15, 20, 30$

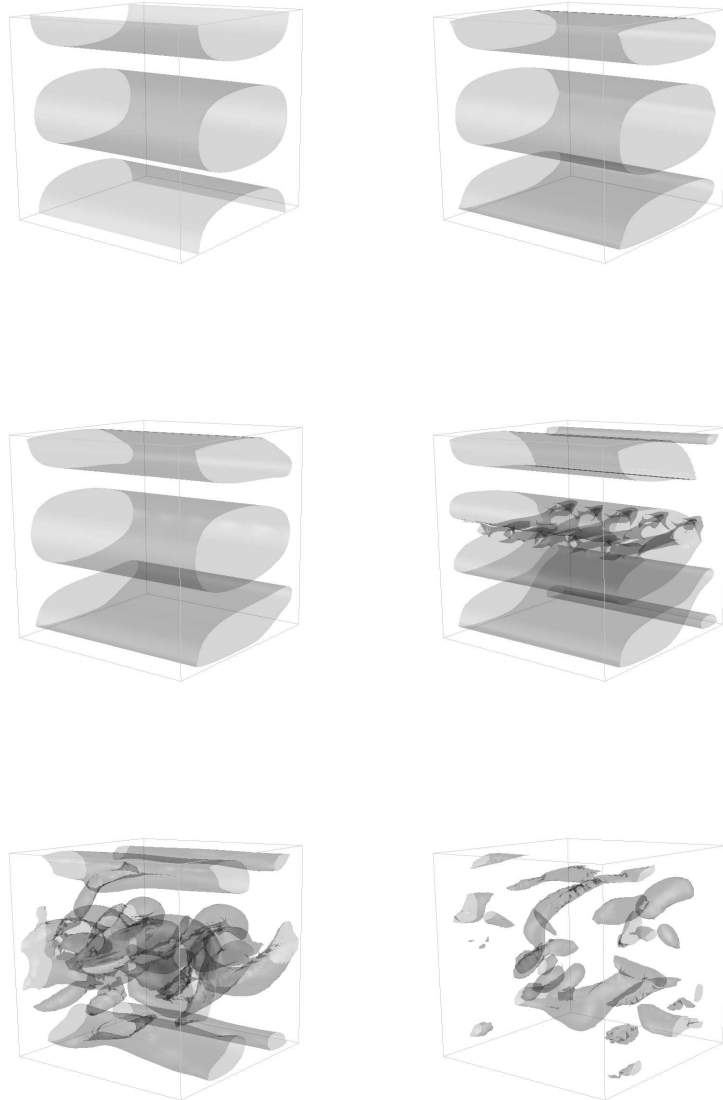


Fig. 36.9. Transversal velocity iso-surfaces for $|u_3| = 0.2$ in Couette flow ($\kappa\nu = 0.5$) for $t = 0, 5, 10, 15, 20, 30$

in Fig 36.10. We get a similar scenario also in this case, although the time scale is longer. We can see that the burst in the x_1 -derivatives now takes place at $t \approx 25$, instead of $t \approx 10$ as in the case a with larger initial perturbation. We can see the linear growth of $\|\partial u_i / \partial x_2\|$, $\|\partial u_i / \partial x_3\|$, and $\|\varphi_i\|$, until a threshold is reached and the base flow loses stability.

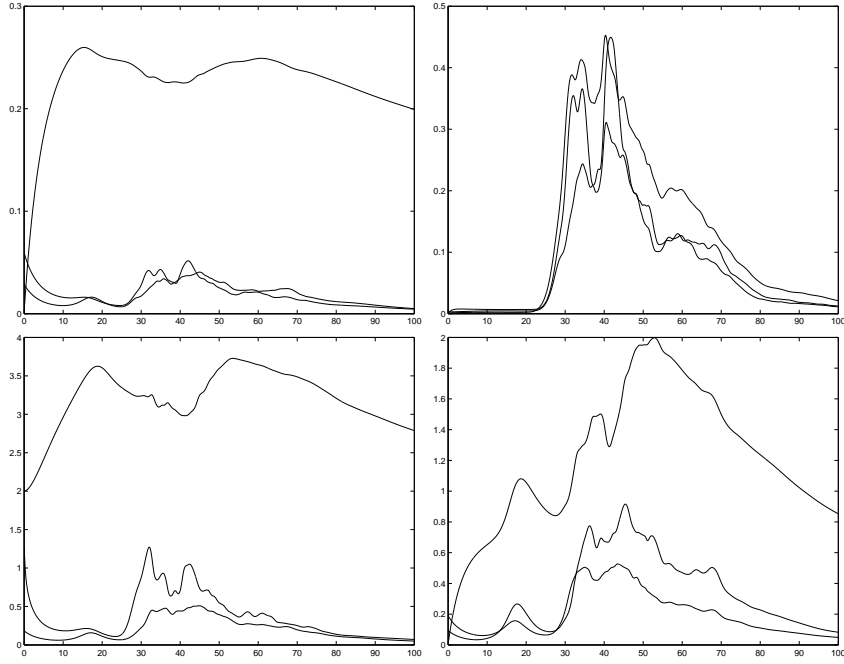


Fig. 36.10. Couette flow ($\kappa\nu = 0.1$): Perturbations $\|\varphi_i\|$ as functions of time (upper left), derivatives $\|\partial u_i / \partial x_1\|$ (upper right), $\|\partial u_i / \partial x_2\|$ (lower left), and $\|\partial u_i / \partial x_3\|$ (lower right) as functions of time.

There exist a threshold value for the size of this type of perturbation for the (conditionally stable) Couette flow. For $\kappa\nu = 0.01$ we do not get transition since the linear growth is then too weak, and thus the special threshold value for this type of perturbation is somewhere in the interval $(0.01, 0.1)$.

36.9.2 Periodic Span-wise Boundary Conditions

In Section 36.9.1 we used slip boundary conditions in the span-wise x_3 -direction. Alternatively, we may use periodic boundary in the span-wise direction. The results for the initial perturbation $\kappa\nu = 0.5$ and periodic boundary conditions in the span-wise direction are presented in Fig 36.11. We have basically the same scenario also in this case, although there are slight differences

in the times scales. In the x_3 -periodic case the linear growth of φ_1 is somewhat steeper, and the initial burst takes place earlier.

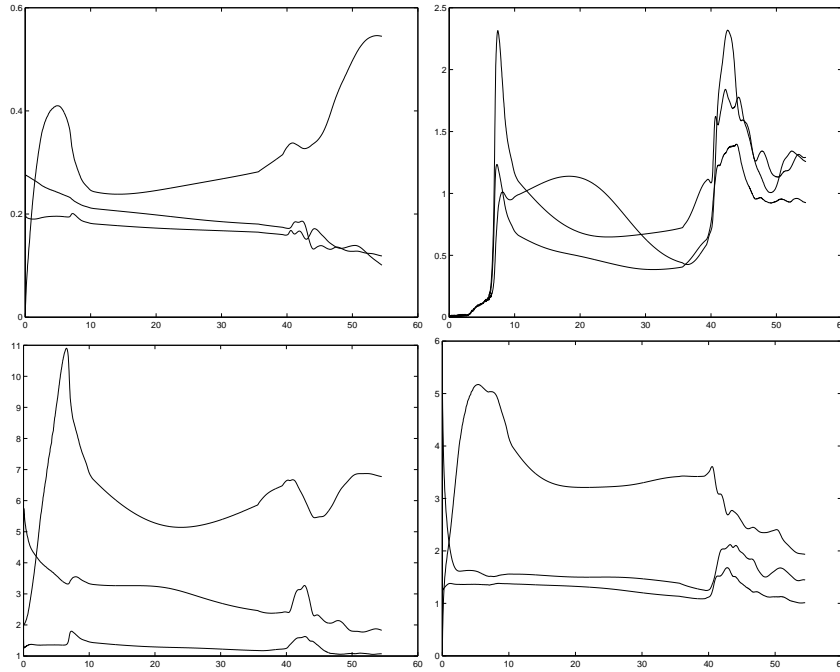


Fig. 36.11. x_3 -periodic Couette flow ($\kappa\nu = 0.5$): Perturbations $\|\varphi_i\|$ as functions of time (upper left), derivatives $\|\partial u_i / \partial x_1\|$ (upper right), $\|\partial u_i / \partial x_2\|$ (lower left), and $\|\partial u_i / \partial x_3\|$ (lower right) as functions of time.

36.9.3 Random Force Perturbation

In Fig 36.7-Fig 36.9 we make the observation that when the initial base flow loses stability, the flow does not go immediately into an irregular turbulent flow. Instead we have an intermediate state, a new base flow, that later loses stability and goes turbulent, also referred to as a *secondary instability*. The x_1 -period for the intermediate base flow is 0.2, that is 5 periods over the computational domain, and this periodic flow is likely to be triggered by the small force perturbation $f_2(x_1) = f_3(x_1) = 10^{-3} \sin(10\pi x_1)$ with the same period.

We now present results from computations using a small random perturbation of size 10^{-3} instead. That is, at each time step we add a perturbation $10^{-3} \times w(x)$ to each velocity component, where $w(x)$ is equally distributed in $(-1, 1)$. The results of the computations are presented in Fig 36.15-Fig 36.14,

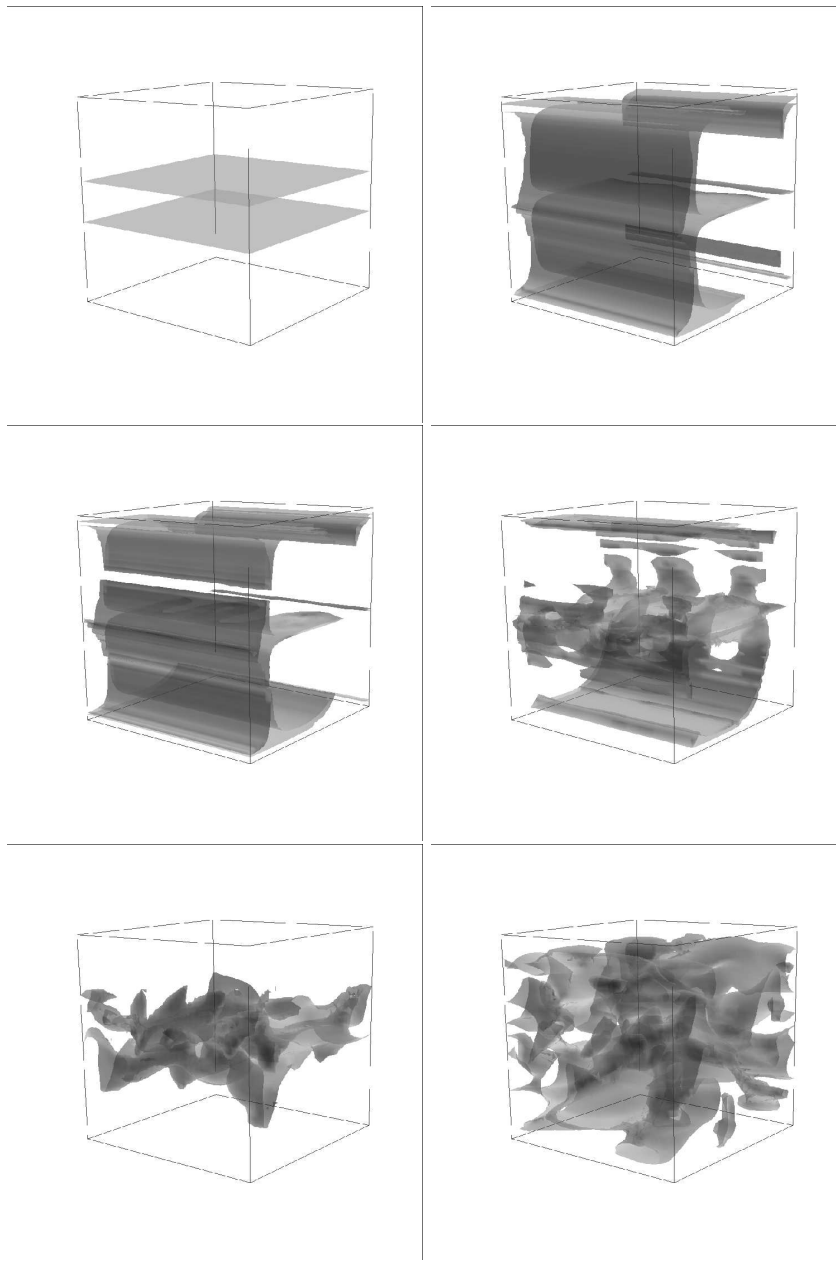


Fig. 36.12. streamwise velocity iso-surfaces for $|u_1| = 0.2$ in x_3 -periodic Couette flow ($\kappa\nu = 0.5$, random force perturbation) for $t = 0, 5, 6, 7, 10, 20$

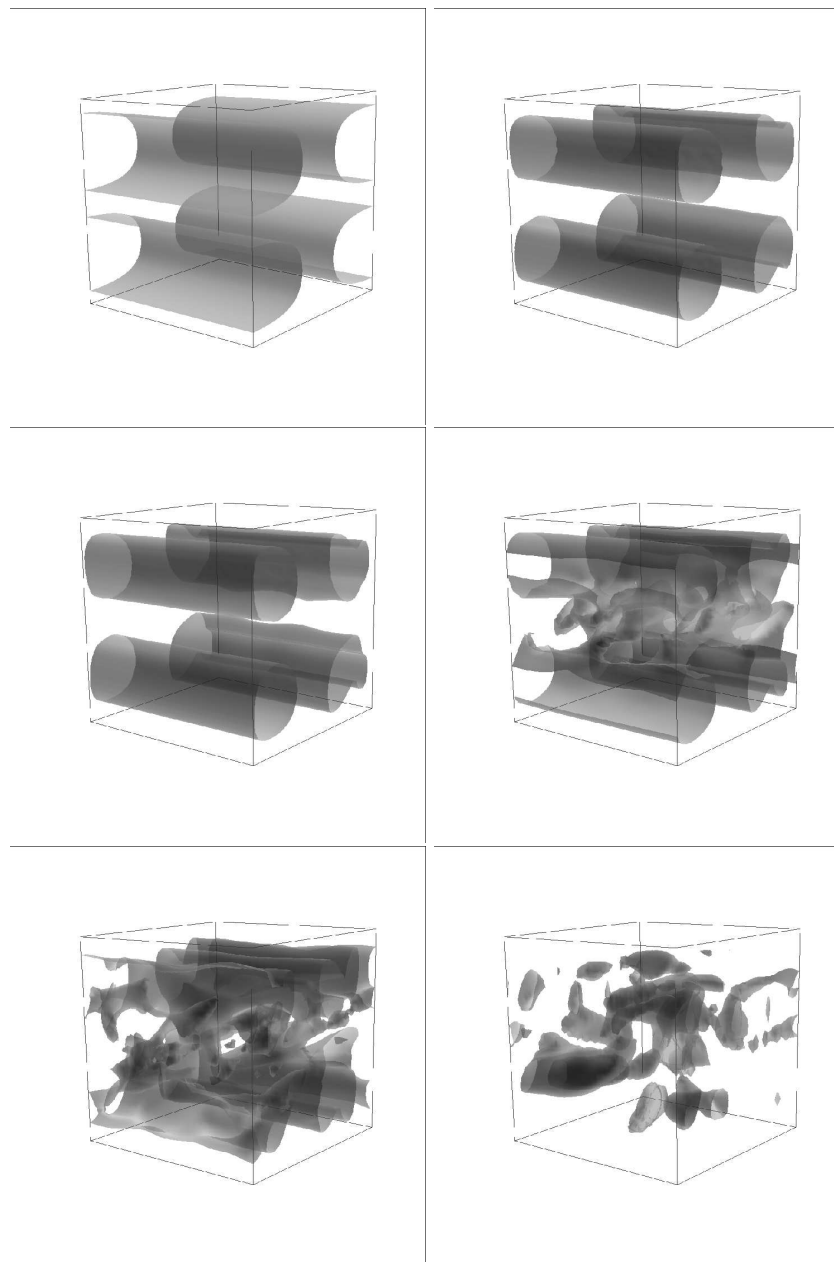


Fig. 36.13. Transversal velocity iso-surfaces for $|u_2| = 0.2$ in x_3 -periodic Couette flow ($\kappa\nu = 0.5$, random force perturbation) for $t = 0, 5, 6, 7, 10, 20$

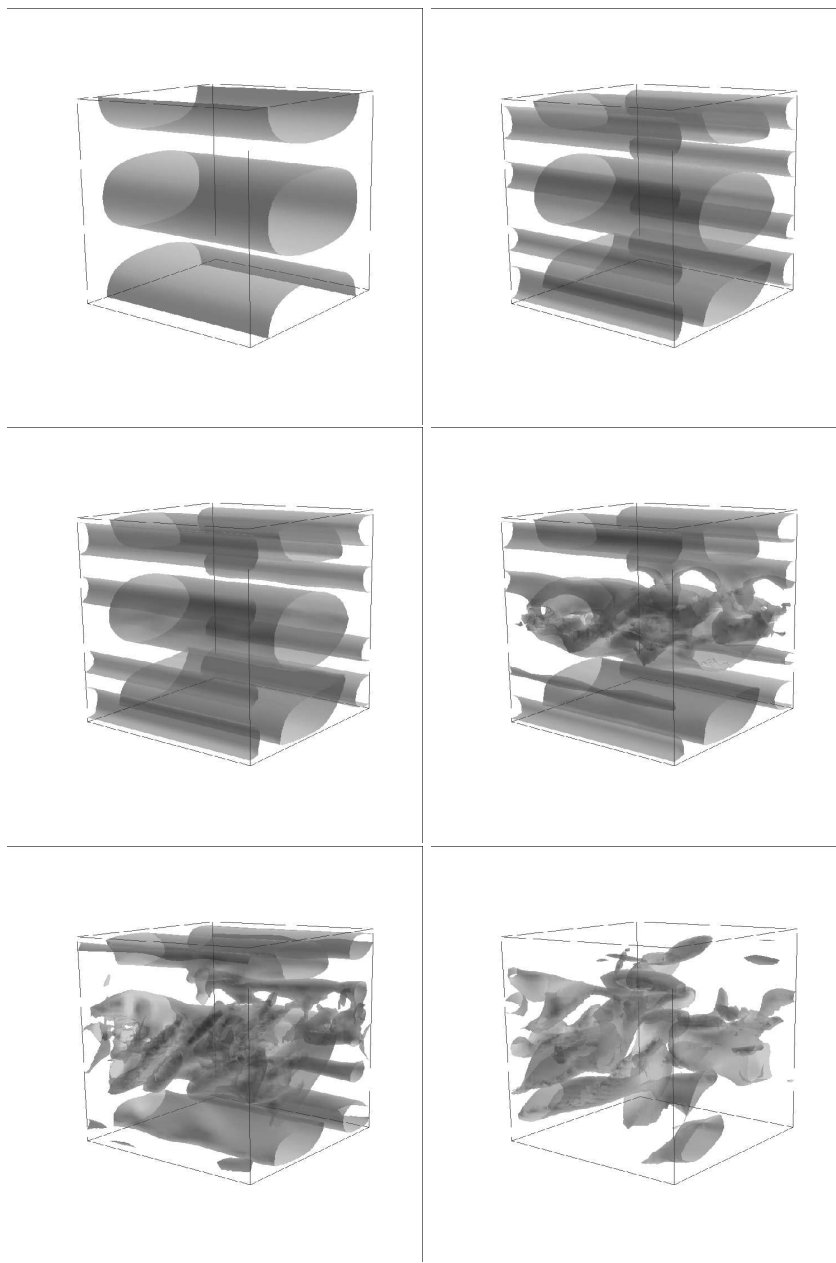


Fig. 36.14. Transversal velocity iso-surfaces for $|u_3| = 0.2$ in x_3 -periodic Couette flow ($\kappa\nu = 0.5$, random force perturbation) for $t = 0, 5, 6, 7, 10, 20$

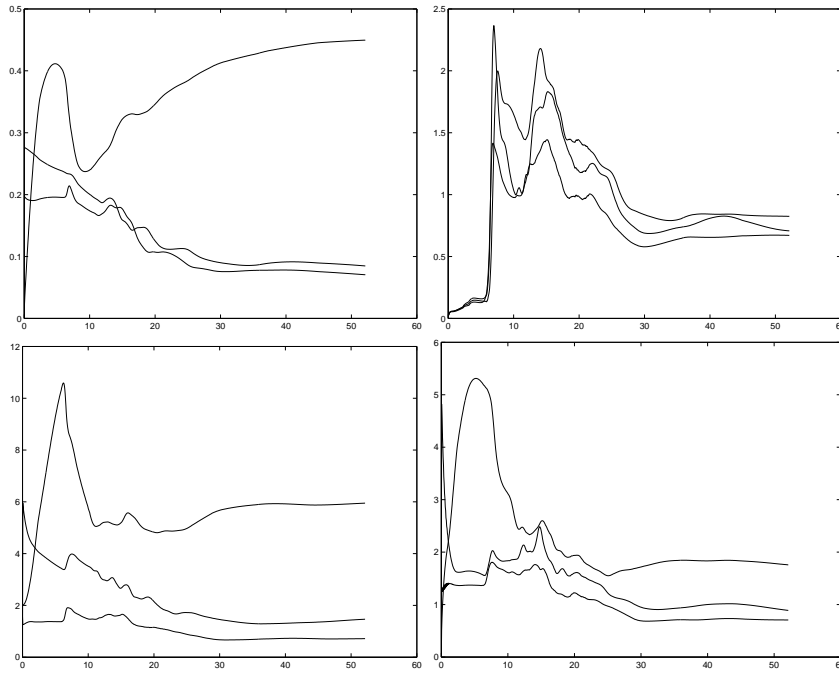


Fig. 36.15. x_3 -periodic Couette flow ($\kappa\nu = 0.5$, random force perturbation): Perturbations $\|\varphi_i\|$ as functions of time (upper left), derivatives $\|\partial u_i / \partial x_1\|$ (upper right), $\|\partial u_i / \partial x_2\|$ (lower left), and $\|\partial u_i / \partial x_3\|$ (lower right) as functions of time.

where we cannot observe any periodic mode after the initial transition, instead we have a lower mode that quickly loses stability before the flow goes into an increasingly unstable turbulent flow.

We conclude that in the case of the secondary stability, many different transition scenarios are possible and the actual scenario may depend on the nature of the perturbations.

36.10 Poiseuille Flow - Reynolds Experiment

We now present results for the conditionally stable Poiseuille flow in a pipe, which is a model of Reynolds original experiments. The Poiseuille base flow has a streamwise velocity profile $u_1(x_2, x_3) = 16x_2(1 - x_2)x_3(1 - x_3)$ in a square channel with no slip walls and a force term $f = (32(x_2(1 - x_2) + x_3(1 - x_3)), 0, 0)$, where we use periodic boundary conditions in the streamwise direction. In Fig36.17 we note a linear growth in the streamwise perturbation corresponding to the Taylor-Görtler mechanism, whose action is shown in Fig36.16, slowly shifting particles with different streamwise velocity transversally resulting in a considerable reorganization of the streamwise

velocity. Fig36.17 also shows the x_1 -derivatives as a function of time, with a sudden increase near $t = 6$, similar to the case of Couette flow. Again we note that this increase is not possible until the x_1 -perturbation φ_1 (and the transversal derivatives of the streamwise velocity, $\partial u_1 / \partial x_2$ and $\partial u_1 / \partial x_3$) are large enough.

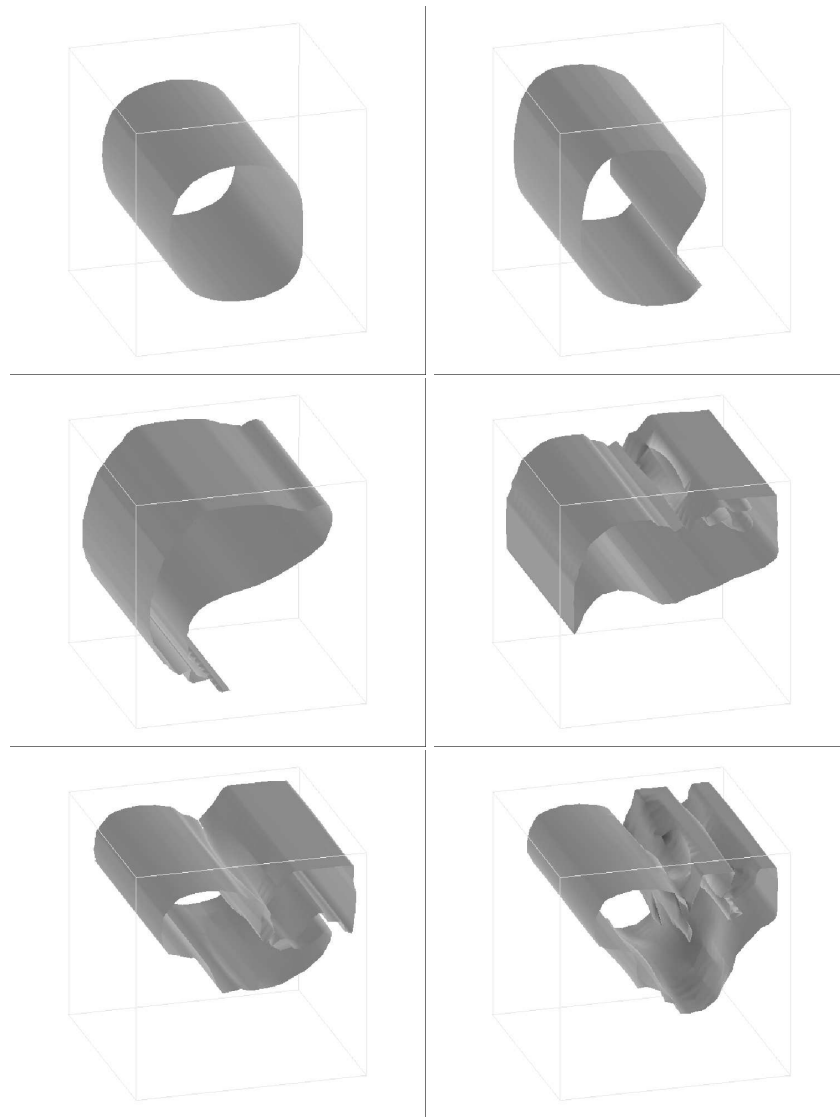


Fig. 36.16. Velocity iso-surfaces in Poiseuille flow ($\kappa\nu = 0.1$) at $t = 1, 3, \dots, 15$, illustrating the Taylor-Görtler mechanism

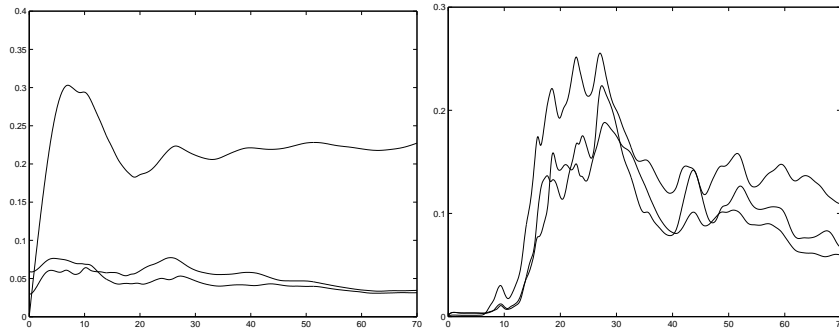


Fig. 36.17. Poiseuille flow ($\kappa\nu = 0.1$): Perturbations $\|\varphi_i\|$ (left) and x_1 -derivatives $\|\partial u_i / \partial x_1\|$ (right).

36.11 Taylor-Görtler Perturbations

Rotational perturbations of Taylor-Görtler type used in the previous sections occur naturally. For example, a small object (say a stone) on the bottom of the channel could trigger such a perturbation. To illustrate this, in Fig36.18 we plot the velocity field downstream the surface mounted cube i Chapter 33, where we see the formation of cigar-shaped structures of high transversal (rotational) velocity after the obstacle, that is perturbations of Taylor-Görtler type.

36.12 Unstable Jet Flow

As an example of an unstable flow, with exponentially growing eigenmodes, we consider a periodic jet flow, with initial streamwise velocity one in the jet and zero streamwise velocity outside the jet on a computational domain $2 \times 1 \times 1$. We set $\nu = 1/10\,000$, and we apply a small random perturbation of maximal size 0.1. That is, for each velocity component we add a random perturbation uniformly distributed in $(-0.1, 0.1)$, times a weight function $16 \times x_1(2 - x_1)x_2(1 - x_2)x_3(1 - x_3)$. In Fig36.22-Fig36.21 we see that most modes in the random initial perturbation are quickly damped out, but a low unstable mode is exerted and grows exponentially causing the flow to go unstable. We note that in this case there is no growth in the transversal derivatives of the streamwise velocity before transition.

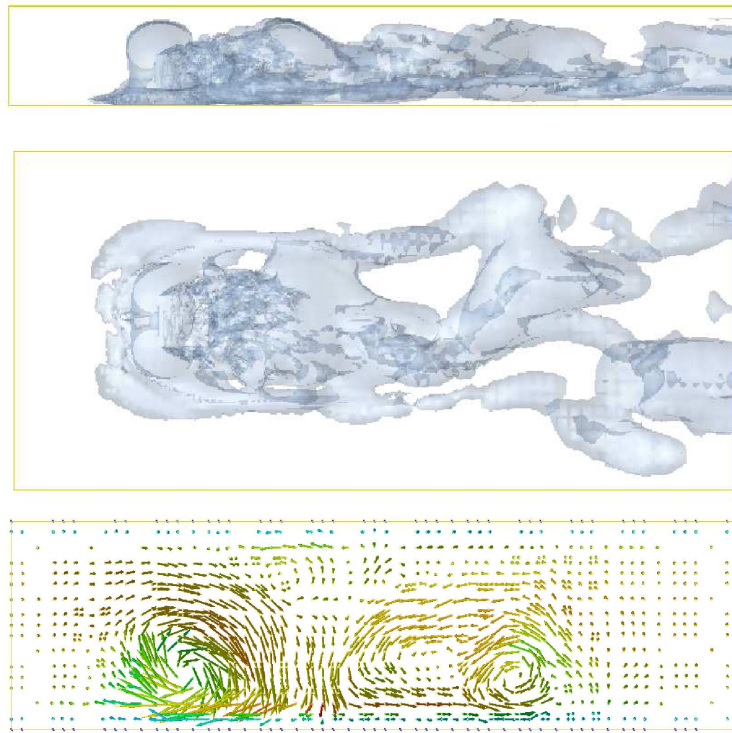


Fig. 36.18. Surface mounted cube: iso-surfaces for $|(\mathbf{u}_2, \mathbf{u}_3)|$ in the x_1x_2 -plane (upper), in the x_1x_3 -plane (middle), and the velocity field in the x_2x_3 -plane downstream the cube (lower).

36.13 Test for Optimal Perturbations

In Section 36.9 we found, by applying a random perturbation, that our computational model of Couette flow is conditionally stable: there exist no exponentially unstable modes. The only way this flow may go unstable from a small perturbation is through linear perturbation growth. We now propose a test for finding optimal perturbations, that is perturbations that may lead to large linear perturbation growth.

For a perturbation to be able to lead to any significant perturbation growth it must not be damped out too quickly, since the linear perturbation growth typically is rather slow. We thus seek the optimal perturbations among the modes that have the slowest decay. A way to do this is to apply a random perturbation as in In Section 36.9. In Fig 36.4-Fig 36.5 the response of a random initial perturbation is shown, and whereas most modes are quickly damped out a few modes decay very slowly. These modes, shown in Fig 36.23,

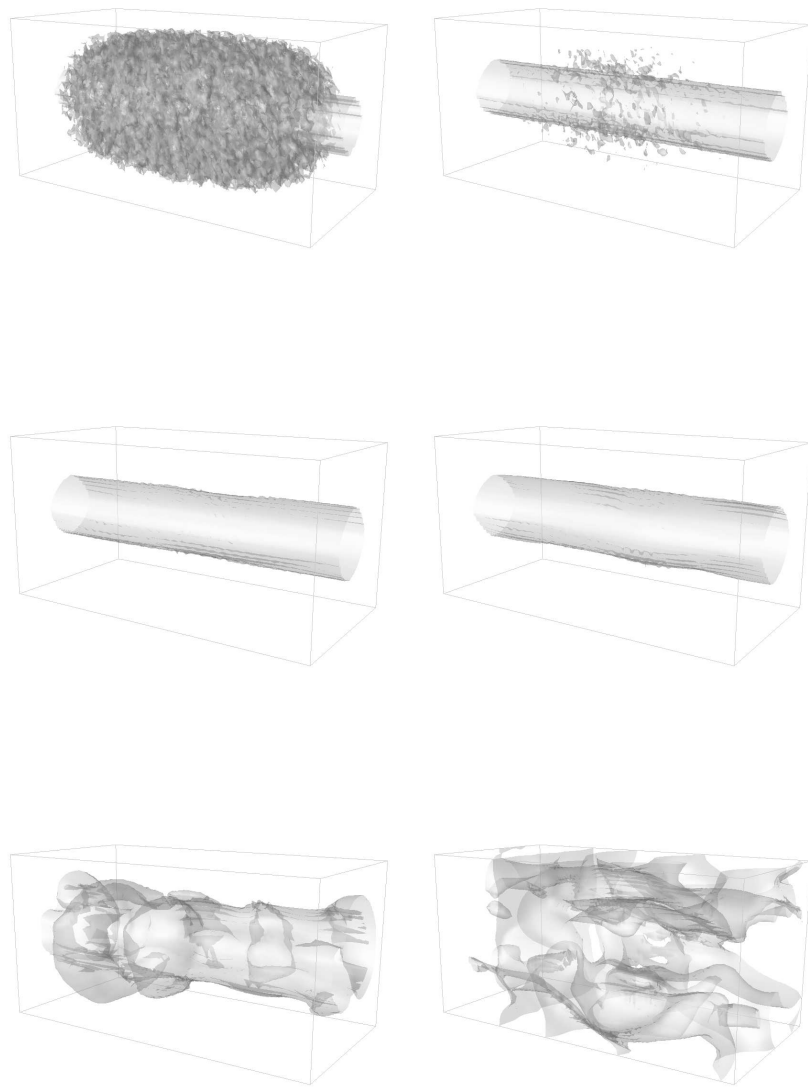


Fig. 36.19. streamwise velocity iso-surfaces for $|u_1| = 0.02$ in jet flow (random initial perturbation) for $t = 0, 2, 5, 7, 10, 15$

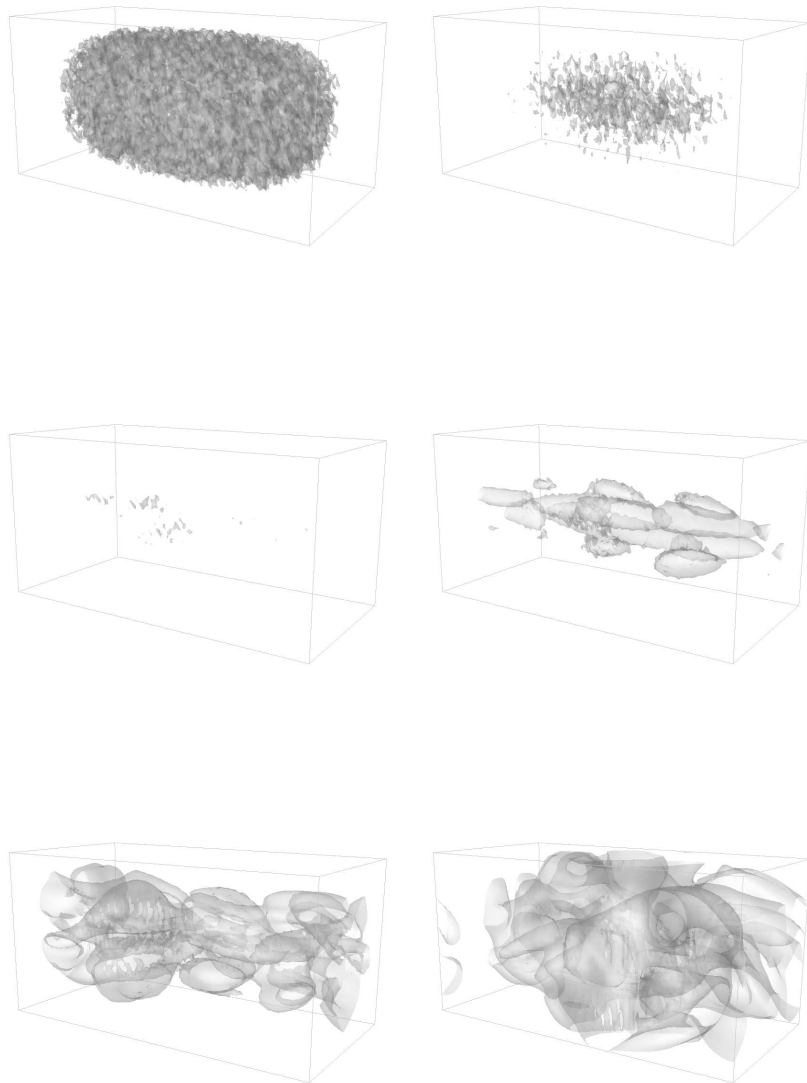


Fig. 36.20. Transversal velocity iso-surfaces for $|u_2| = 0.02$ in jet flow (random initial perturbation) for $t = 0, 2, 5, 7, 10, 15$

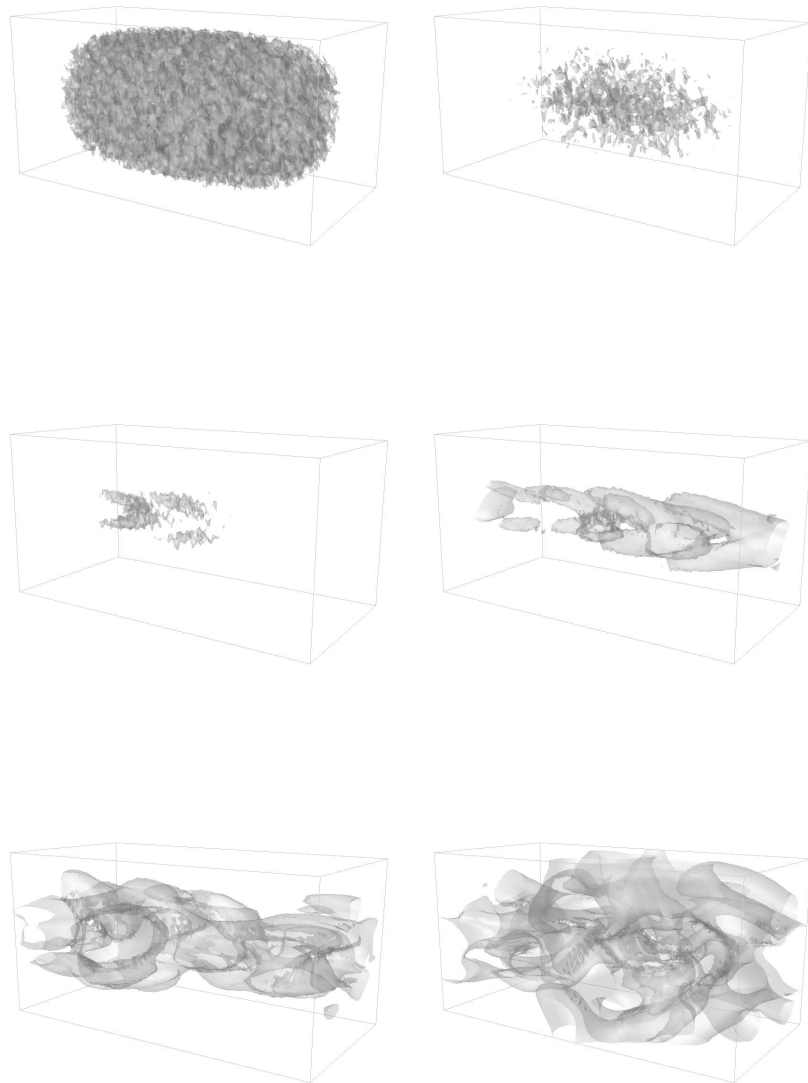


Fig. 36.21. Transversal velocity iso-surfaces for $|u_3| = 0.02$ in jet flow (random initial perturbation) for $t = 0, 2, 5, 7, 10, 15$

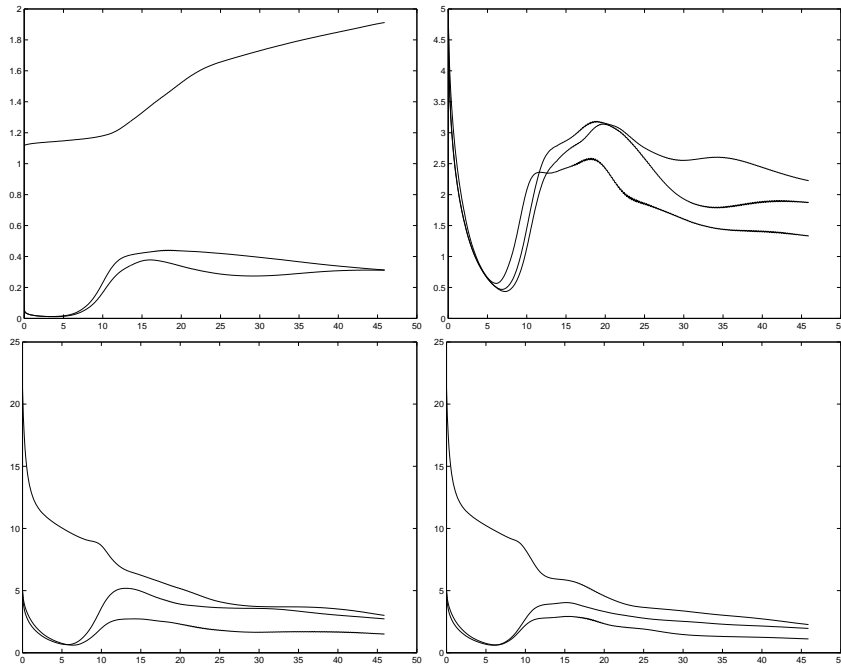


Fig. 36.22. Jet flow (random initial perturbation): perturbations $\|\varphi_i\|/\|u\|$ (upper left) as functions of time, derivatives $\|\partial u_i / \partial x_1\|/\|u\|$ (upper right), $\|\partial u_i / \partial x_2\|/\|u\|$ (lower left), and $\|\partial u_i / \partial x_3\|/\|u\|$ (lower right).

are rotational perturbations of Taylor-Görtler type, shaped as cigars oriented in the streamwise x_1 -direction.

Since the amount of these modes in the white noise random perturbation is too small they are unable to take the flow into transition. On the other hand, if we take a cross section at say $x_1 = 0.5$ and apply the transversal components of the modes multiplied by a factor 10 to a Couette flow, we get transition at $t \approx 100$.

36.14 A Critical Review of Classical Theory

The classical research on transition to turbulence in fluid flow has been focused on finding a relation between Reynolds number and transition, with ideally a so called critical Reynolds number for each type of flow, identified by the fact that transition to turbulence takes place if and only if the actual Reynolds number is larger than the critical Reynolds number. This approach was initiated by Reynolds, although judging from his experiments he had little reason to believe in the existence of such critical Reynolds numbers.

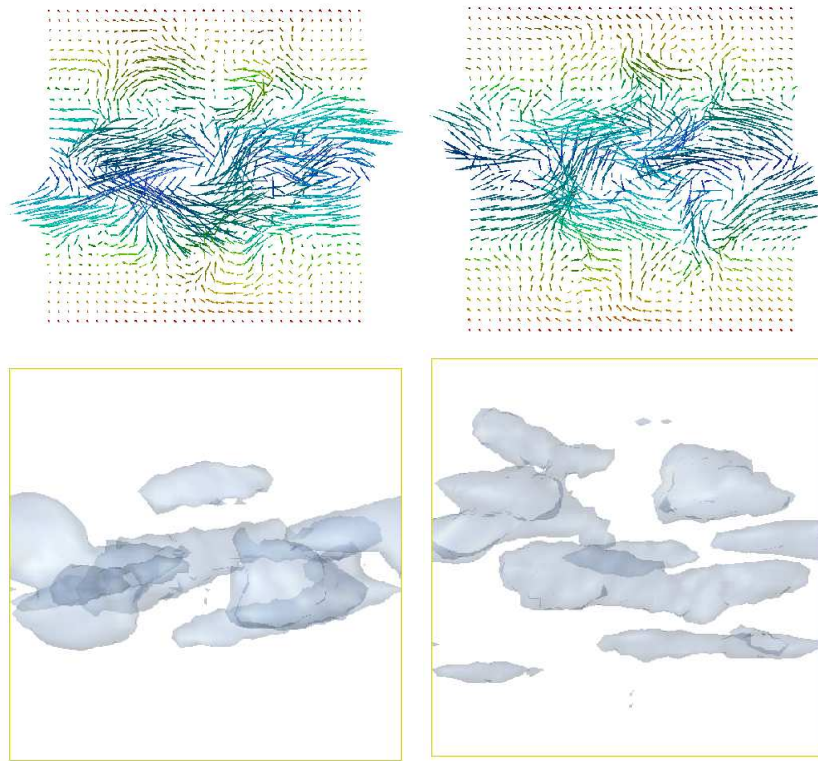


Fig. 36.23. Slowest decaying modes from a uniformly distributed random perturbation, in the x_2x_3 -plane at $x_1 = 0.25$ (upper left) and $x_1 = 0.75$ (upper right), iso-surfaces for $|u| = 0.015$ in the x_1x_2 -plane (lower left) and in the x_1x_3 -plane (lower right).

Nevertheless, most text books in fluid mechanics still today present “critical Reynolds numbers” for various flows, such as 5772 for Poiseuille flow between two parallel fixed plates (with parabolic velocity profile), and ∞ for Couette flow between two moving parallel plates (with linear velocity profile), both however at severe variance with experiments. The stated critical Reynolds numbers come out of a normal mode stability analysis of 2d linearized equations, referred to as the Orr-Sommerfeld equations, based on identifying exponentially growing eigenmodes, so-called Tollmien-Schlichting waves. The striking difference in the theoretical predictions and the practical experiments for transition in parallel flow, has driven the classical study of transition into a severe crisis, with scientifically impossible concepts like “sub-critical Reynolds number” and “bypass transition” to handle the disagreement of theoretical predictions and actual observations.

We now give a couple of citations describing the crisis, recalling also Schlichtings standpoint as expressed in the initial citation of Chapter 2:

For a circular Poiseuille flow (pipe flow), as well as Couette flow, the classical linear-instability analysis leads to stability, whatever the Reynolds number and the wavenumber of the perturbation. Experimentally, one observes also turbulent spots in these flows. (Lesieur [80])

Apparently, the asymptotic stability of a shear flow to infinitesimal disturbances cannot fully characterize its stability. (Blossey [17])

Further, transition scenarios based on Tollmien-Schlichting waves are irrelevant because of the large perturbation levels needed to exert these modes. (Henningson-Schmid [100])

In this book I have tried to bring together into a coherent account what I have learnt of hydrodynamic stability. Perhaps the most serious omission is the absence of any reference to viscous shear flow....in the last an author chooses to write only about those matters in which he has some confidence of his understanding. (Chandrasekhar, [24])

The standpoint of Schlichting as expressed in the initial citation in Chapter 2 is from a scientific point of view completely stunning: If the proposed theory does not pass a most simple and basic test, the conclusion is not that there must be something seriously wrong with the theory, but instead that the test should be discarded because of its simplicity! The remark by Chandrasekhar (Nobel Prize in Physics 1983) shows another attitude towards science, but does not give any information.

We next give a couple of citations indicating the new view of non-modal 3d linear perturbation growth opening a way out of the crisis:

Shortly before his death 1999 Mårten Landahl completed research on the basic theoretical problem of how a 3-D initial disturbance within a shear flow evolves over time. He felt certain his work would form a new fundamental approach to the transition problem (tackled by many in the past 100 years) as opposed to the classical Orr-Sommerfeld equation, and he had planned further research on completing the asymptotic long-time evolution of a 3-D disturbance in a parallel shear flow. He then planned to use this work as the basis for a new transition theory as well as a new turbulence model. (M.I.T. News, 1999)

It should be finally mentioned that the growth of the quasi-linear non-normal longitudinal mode considered in section 2.3 (algebraic (linear) perturbation growth) might be important for the transition in these unconditionally stable shear flows, as well in sub-critical situations. (Lesieur [80])

Thus in a flow that is asymptotically stable to infinitesimal disturbances, transient growth (non modal algebraic perturbation growth) is necessary if finite amplitude disturbances are to lead to transition to turbulence. (Blossey [17])

Summing up, it is clear that the classical “modal” stability theory is completely inadequate for explaining the necessary initial phase of transition in shear flow, and there is a new “non-modal” analysis emerging showing the crucial role of the Taylor-Görtler mechanism with linear growth of 3d perturbations.

36.15 Comparison with Bifurcation towards Stability

A possible reason for the survival of the classical misleading modal stability analysis for parallel shear flow, despite its lack of experimental support, is probably the fact that there are some other cases where the same type of analysis in fact is correct and conforms with experiments, namely the *bifurcating* Bernard and Taylor-Couette flows, changing from one configuration to another at a certain well defined Reynolds number. The bifurcation of Bernard flow involves the development of organized patterns of convective rolls of fluid in motion. A bifurcation involves a change from one configuration losing stability, to a new stable configuration, which is different from the process of transition to turbulence, with the new configuration being increasingly unstable. Now, a bifurcation in general may be detected through a normal mode analysis based on finding for the linearized equations an eigenvalue with zero real part. In particular, the critical Reynolds number for the first bifurcations in Taylor-Couette and Bernard flow, may be found analytically this way. As indicated this approach does however not work for parallel Couette or Poiseuille flow, which do not bifurcate to find new stable configurations, but instead go into turbulent unstable motion.

This is because in linearizations of Taylor-Couette or Bernard flow, linear perturbation growth is dominated by slow exponential decay, whereas in parallel Couette or Poiseuille flow, linear perturbation growth dominates. It appears that the success of the mathematical theory in the bifurcating cases, has overshadowed the failure in the non-bifurcating cases. We discuss these ideas below in the setting of simple ode-models.

36.16 An ODE-Model for Transition

We consider the following initial value problem for a system of two ordinary differential equations: find $w(t) = (w_1(t), w_2(t))$ such that

$$\begin{aligned}\dot{w}_1 + \nu w_1 - \lambda w_1 w_2 &= \nu & t > 0, \\ \dot{w}_2 + 2\nu w_2 - \nu w_2 w_1 &= 0 & t > 0, \\ w_1(0) = 1, \quad w_2(0) &= \kappa \nu,\end{aligned}\tag{36.10}$$

where ν is a small positive parameter, and λ and κ are positive parameters of moderate size. The system (36.10) models almost parallel shear flow with w_1 representing the flow velocity in the main direction of the flow, and w_2 the small velocities transversal to the main flow, and the stationary solution $w = (1, 0)$ corresponds to Couette flow between two plates or Poiseuille flow in a pipe. We shall use the model to describe how the small perturbation $\kappa \nu$ of w_2 may cause the base solution $(1, 0)$ to become unstable if $\lambda \kappa$ is larger than some critical value of moderate size.

We shall see that the model (36.10) contains an essential part of the secret of transition to turbulence in shear flow. The equations for w_1 and w_2 in (36.10) are coupled through the quadratic terms $\lambda w_1 w_2$ and $\nu w_1 w_2$, and model the following selection of terms from the NS equations

$$\begin{aligned}\dot{u}_1 - \nu \Delta u_1 + \bar{u} \cdot \bar{\nabla} u_1 &= \nu & t > 0, \\ \dot{\bar{u}} - \nu \Delta \bar{u} + u_1 \partial \bar{u} / \partial x_1 &= 0 & t > 0,\end{aligned}\tag{36.11}$$

from the momentum equations for the main flow velocity u_1 and the transversal velocity \bar{u} . The nonlinear coupling terms $\bar{u} \cdot \bar{\nabla} u_1$ and $u_1 \partial \bar{u} / \partial x_1$ are modeled in the form $\lambda w_1 w_2$ and $\nu w_2 w_1$, corresponding to assuming that $u_{1,i} = -\lambda u_1$, for $i = 2, 3$, and $\partial \bar{u} / \partial x_1 = -\nu \bar{u}$, connecting transversal derivatives of u_1 with u_1 through the parameter λ , and the streamwise derivative of the transversal velocity \bar{u} with \bar{u} through the small parameter ν . The relation $\partial \bar{u} / \partial x_1 = -\nu \bar{u}$ models a basic feature of parallel flow with the streamwise variations being small. Since we assume initially that $\bar{u} \approx w_2 \approx \nu$, it corresponds to assuming $\partial \bar{u} / \partial x_1 \sim \nu^2$, which is indeed very small. On the other hand, the assumption that $u_{1,i} = -\lambda u_1$, for $i = 2, 3$, with λ of moderate size corresponds to a natural transversal variation of moderate size of the streamwise velocity in a shear flow.

Note that the coupling term $u_{1,1} u_1$ in the equation for u_1 is not modeled in the form of some multiple of w_1^2 . This is because (a) assuming $u_{1,1} \approx \nu^2$, with a corresponding very small term $-\nu^2 w_1^2$ in the model, has no destabilizing effect, and (b) assuming $u_{1,1} = -C\nu$ with a corresponding larger term $-C\nu w_1^2$, which may cause exponential growth through self-resonance in w_1 , is not realistic. In fact, (b) is more or less the classical scenario based on the 2d Orr-Sommerfeld equations, which require artificially generated perturbation levels in experiments, for example through heavily vibrating ribbons.

In the transition model, we thus seek to build in realistic features of shear flow including realistic perturbation levels. If we assume zero perturbations, then the model reduces to $\dot{w}_1 + \nu w_1 = 0$, $\dot{w}_2 + 2\nu w_2 = 0$, which has no chance of going unstable. If we assume large perturbation levels, then instability may result immediately. However, none of these scenarios occur in reality, and the role of the model is to explain how small but realistic size perturbations, indeed may cause the initially stable base flow to go unstable after some time.

Our model builds on the presence of a very small perturbation of order ν^2 of the transversal velocity in the streamwise direction, which naturally may be introduced through the roughness of the pipe. The model does not build on a larger variation of order ν of the streamwise velocity in the streamwise direction, which only seems to be possible with artificially generated perturbations.

The model (36.10) contains the two basic parameters λ and κ , both of moderate size, λ being related to the transversal geometry of the flow such as pipe cross section, $\kappa\nu$ representing a perturbation level in transversal velocities, and $\kappa\nu^2$ a perturbation level in streamwise derivatives of transversal velocities, including both transversal and streamwise perturbations levels. We will see that if $\lambda\kappa$ is larger than some critical value of moderate size, then transition to instability will take place in the model. This indicates that transition in shear flow builds on a combination of features related the transversal geometry and levels of perturbations in both transversal and streamwise direction. The presented computational results for transition to turbulence in Couette and Poiseuille flow presented supports this picture.

The system (36.10) has two stationary solutions $w = (1, 0)$ and $w = (2, \nu/(2\lambda))$, with $(1, 0)$ representing the basic Couette or Poiseuille flow. A classical stability analysis based on the eigenvalues of the corresponding linearized system, indicates that $(1, 0)$ is stable and $(2, \nu/(2\lambda))$ is unstable. For example, the linear system obtained linearizing at $(1, 0)$, takes the form

$$\begin{aligned}\dot{\varphi}_1 + \nu\varphi_1 - \lambda\varphi_2 &= \nu & t > 0, \\ \dot{\varphi}_2 + \nu\varphi_2 &= 0 & t > 0, \\ \varphi_1(0) &= \varphi_{10}, & \varphi_2(0) &= \varphi_{20},\end{aligned}\tag{36.12}$$

where the coefficient matrix $A = [\nu - \lambda, 0 \ \nu]$ has a double positive eigenvalue ν . The corresponding coefficient matrix linearizing at $(2, \nu/(2\lambda))$, has one positive (stable) and one negative (unstable) eigenvalue. A classical stability analysis shows that $(1, 0)$ is stable under sufficiently small perturbations, and that $(2, \nu/(2\lambda))$ is unstable even under small perturbations. As a result $(1, 0)$ is unstable under large perturbations bringing the initial value sufficiently close to the unstable solution $(2, \nu/(2\lambda))$. However, the classical eigenvalue stability analysis is unable to explain the intriguing fact that $(1, 0)$ may become unstable even under a small perturbation of the initial data $(1, 0)$, if we just have patience to wait! We will now present such a scenario of transition, where the stationary solution $(1, 0)$ of (36.10) goes unstable under a small perturbation of initial data of the form $(0, \kappa\nu)$, where κ is a parameter of moderate size, and the scaling with ν makes the perturbation small (since we assume ν to be small). We shall see that if the product $\lambda\kappa$ is above a certain threshold of moderate size, then transition to instability will take place, if we wait over a period of time of length ν^{-1} .

We thus consider the problem (36.10) with the initial data $(1, \kappa\nu)$ close to $(1, 0)$, and we ask if the corresponding solution $\bar{w}(t)$ may become unstable after some time. We see that $\dot{w}_1(0)/\bar{w}_1(0) = \lambda\kappa\nu$, while $\dot{w}_2(0)/\bar{w}_2(0) = -\nu$,

which shows that initially \bar{w}_1 grows and \bar{w}_2 decays at rates $\propto \nu$. Now, \bar{w}_1 will continue to grow at that rate as long as $\lambda\bar{w}_2 > \nu$, and further \bar{w}_2 will start to grow as soon as $\bar{w}_1 > 2$. Thus, if \bar{w}_1 manages to become larger than 2, before \bar{w}_2 has decayed below ν/λ , then both components will propel each other to infinity, corresponding to instability. We shall see that this will occur if $\lambda\kappa$ is above a certain threshold. We notice that the time scale for significant changes in both \bar{w}_1 and \bar{w}_2 is $\sim \nu^{-1}$, which is a long time since ν is small. The scenario is thus that \bar{w}_1 grows slowly at the rate ν over a long time, and if $\lambda\kappa$ is above the threshold, then \bar{w}_1 may reach the value 2, where also \bar{w}_2 starts to grow after which a blow up follows on a usually somewhat shorter time scale (though still $\propto \nu^{-1}$). This scenario is easy to grasp intuitively, and conforms with the every-day experience of a sudden blow-up, as a result of an accumulation of small events over a long period.

Solving the linearized equation (36.12) approximately describing the evolution of $\bar{w} - (1, 0)$, we find that

$$\bar{w}_1(t) \approx 1 + \varphi_1 = 1 + \lambda\kappa t\nu \exp(-t\nu), \quad \bar{w}_2(t) \approx \varphi_2 = \kappa\nu \exp(-t\nu), \quad (36.13)$$

which shows the slow growth of \bar{w}_1 and slow decay of \bar{w}_2 over the long time scale prior to the blow up, occurring if $\lambda\kappa$ is above the threshold. The linear growth in time of φ_1 may be viewed as a consequence of the non-normality of the coefficient matrix A . A classical stability analysis focusing on the double positive eigenvalue ν of $A = [\nu \ -\lambda, 0 \ \nu]$, states that the factor $t \exp(-\nu t)$ eventually will decay to zero as $t \rightarrow \infty$, but misses the substantial transient growth to the level $\propto \nu^{-1}$ after time $\propto \nu^{-1}$ prior to decay. This perturbation growth of size $\propto \nu^{-1}$ is capable of bringing a solution from the point $(1, \kappa\nu)$ very close to $(1, 0)$, into a neighborhood of the unstable point $(2, \nu(2\lambda))$ with ensuing blow up.

In Chapter 49 The Crash Model in Body&Soul Vol 3 [36], we give several interpretations of the ode-model (36.10) relating to economy, politics and human relations, sharing similarities of transition in shear flow.

36.17 A Bifurcating ODE-Model

We now consider the following ode-model modeling aspects of Taylor-Couette flow between two rotating cylinders:

$$\begin{aligned} u_{1,t} + u_1 u_2 + \nu u_1 - \gamma u_1 &= 0, & t > 0, \\ u_{2,t} - \nu u_1^2 + \nu u_2 &= 0, & t > 0, \\ u(0) &= u^0, \end{aligned} \quad (36.14)$$

where γ is a parameter, and u_1 represents a streamwise velocity (modulo a base flow) and u_2 a transversal velocity. This problem admits the *stationary trivial base solution* $(u_1, u_2) = (0, 0)$ for all γ . If $\gamma > \nu$, then also $(\pm\sqrt{\gamma - \nu}, \gamma - \nu)$ is a stationary solution and thus $(u_1, u_2, \gamma) = (0, 0, \nu)$ is a *bifurcation*

point with $(\pm\sqrt{\gamma-\nu}, \gamma-\nu)$ the two *bifurcated branches* for $\gamma > \nu$. This is the standard scenario in a *pitchfork bifurcation*. The eigenvalues of the (symmetric) Jacobian $J_0(\gamma)$ at the trivial solution $(0, 0)$ are $\nu - \gamma$ and ν , and thus the trivial branch is stable for $\gamma < \nu$ and unstable for $\gamma > \nu$. The eigenvalues of the Jacobian $J_{\pm}(\gamma)$ at a bifurcated branch $(\pm\sqrt{\gamma-\nu}, \gamma-\nu)$ for $\gamma > \nu$ are $\frac{1}{2}\nu \pm \sqrt{\frac{1}{4}\nu^2 - 2\nu(\gamma-\nu)}$ and have positive real part, and thus perturbations of the bifurcated branches exhibit exponential decay.

If we follow a transient behavior of solutions of (36.14) with γ slowly increasing with time starting from zero and initial data u^0 small, we will stay close to the trivial branch as long as $\gamma < \nu$, while we will shift to follow close to one of the non-trivial branches when $\gamma > \nu$ depending on the sign of the initial data u_1^0 . We will thus always stay close to an exponentially stable branch, and the corresponding Jacobian will always have real parts with positive (stable) real part. The bifurcation point is detected by finding a value of γ_c of γ such that the Jacobian $J_0(\gamma_c)$ has an eigenvalue which is zero (or has zero real part), which in our case is the value $\gamma_c = \nu$. We may call this value a *critical value* of γ . If $\gamma < \gamma_c$, then solutions of (36.14) with u^0 small are stable. However, it is not correct to say that for $\gamma > \gamma_c$, solutions will become unstable, because as we said the solution will then stay close to one of the exponentially stable bifurcated branches. We conclude that detection of a bifurcation point is not a sign of emerging instability, but rather an indication that the flow will seek a new stable configuration with the old (trivial) configuration becoming unstable.

Taylor-Couette flow between two rotating cylinders may bifurcate at a well determined Reynolds' number identified by an eigenvalue with zero real part of the corresponding Jacobian. However this Reynolds' number, which we may refer to as a critical Reynolds number, has nothing to do with transition to turbulence. Above this critical Reynolds number the flow will find a new stable bifurcated configuration represented by the easily observable rolls in the Taylor-Couette experiments.

We conclude that much of the trouble in classical hydrodynamic stability theory comes from a severe confusion concerning the use of the term *critical Reynolds' number* referring to both (i) bifurcation with a Jacobian having an eigenvalue with zero real part, and to (ii) transition to turbulence with transition occurring above the critical Reynolds number. We have just indicated that (i) and (ii) have very little connection and we have shown above that in fact (ii) cannot have any meaning. So, eliminating (ii) gives a clear definition of a critical Reynolds' number which is then not connected to transition.

We finally remark that the Reynolds experiment is a “hands off” experiment: we just sit and watch the flow suddenly undergo transition to turbulence without any intervention. In the bifurcating Taylor-Couette case on the other hand, we change the speed of at least one of the cylinders slowly through the bifurcation.

36.18 Summary

We sum up our experience from analysis and computation as follows: We consider a given initial laminar highly organized shear flow such as Couette flow between two parallel plates, Poiseuille flow in a pipe or a single jet, at a certain Reynolds number Re of the order of 10000 for Couette and Poiseuille flow, and jet flow. We ask the question if the given flow may undergo transition into a highly fluctuating disorganized turbulent flow under perturbations of initial data and/or driving forces of a certain small magnitude δ with a suitable measure. We may view this as a question of perturbation growth, with a perturbation growth of order $1/\delta$ being necessary for the transition from laminar to turbulent flow, assuming the flow velocity is normalized to be of unit size. Now, perturbation growth in general may couple to exponentially growing eigenmodes in a normal mode analysis, or to linear growth because the linearized system is non-symmetric. To test exponential growth we may use white noise perturbations containing all modes, while the non-modal linear growth typically is related to the special perturbations of the Taylor-Görtler mechanism.

We find computationally that the jet undergoes transition under small white noise perturbations of initial data. The jet is thus exponentially unstable. We find computationally that Couette flow does not undergo transition under even large white noise perturbations, but does so under small Taylor-Görtler perturbations. We analyze Couette flow analytically and find that linear perturbation growth proportional to the Reynolds number is possible. This resolves the dilemma of traditional hydrodynamic stability analysis claiming that Couette flow is stable based on a modal eigenvalue analysis, and shows that Couette flow may undergo transition under perturbations proportional to the inverse of the Reynolds number. More precisely, we find transition if the product of a small transversal, streamwise constant, perturbation (of size $\nu \sim 1/Re$) and a very small streamwise perturbation (of size ν^2), is large enough. In particular it follows that the concept of a critical Reynolds number for Couette flow cannot have any meaning: transition or not depends of the size and the type of the perturbations. The experience with Poiseuille flow is similar to that of Couette flow just reported. Concerning the unstable jet flow, we remark that computationally we may set up this problem and study transition, while experimentally it may be very difficult to form the unstable initial jet to be studied.

Of course we may expect to see exponentially growing modes once the transition has been initiated, but we cannot hope to explain the initial phase of transition by the presence of exponentially growing modes. For the (obviously critical) initial phase, we need linear growth which is offered by the Taylor-Görtler mechanism in shear flow.

Once again: we focus on the initial most critical phase of transition with large perturbation growth offered by the Taylor-Görtler mechanism, which may change an initially exponentially stable base flow into a new possibly

exponentially unstable base flow which may develop into a turbulent flow in a secondary phase. It is also of interest to study this secondary phase with again computational methods as the only feasible technique because the new base flow may be quite complex, although the original base flow was very simple.

In the computational experiments for Couette and Poiseuille flow we use a 64^3 uniform mesh on the unit cube assuming periodicity in the streamwise direction, with slip or periodic boundary conditions in the horizontal transversal direction. The periodicity in the streamwise direction corresponds physically to recirculation, like in the Taylor-Couette flow between two cylinders.

The periodic boundary conditions may be convenient when studying slow perturbation growth, since a simulation of a channel of say a length 100 is very expensive. A computation of transition to turbulence in a boundary layer, see Fig 36.24, serves as an example of linear perturbation growth in a non-periodic case. When we introduce Taylor-Görtler perturbations of different amplitude at the inflow, where we find that transition is delayed for the perturbation of lower amplitude, again confirming the idea that transition is not a phenomenon determined solely by the Reynolds number, but is a question of perturbation growth, determined by the size and type of perturbations.

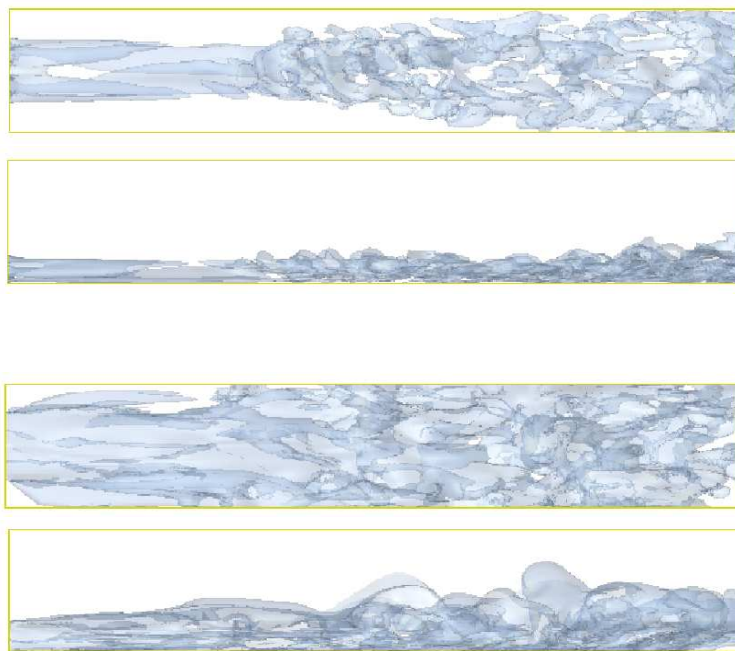


Fig. 36.24. Iso-surfaces for $|(u_2, u_3)| = 0.06$ for transition to turbulence in a boundary layer computation from Chapter 34, for $\nu = 10^6$, $l = 6$, and $b = 1$, introducing Taylor-Görtler type perturbations at the inflow of amplitude 0.1 (upper) and 0.5 (lower), resulting in transition further downstream for the smaller perturbation.

Part VI

Loschmidt's Mystery

Thermodynamics

There are great physicists who have not understood it. (Einstein about Boltzmann's statistical mechanics)

...the whole procedure was an act of despair because a theoretical interpretation had to be found at any price, no matter how high that might be...
(Planck on the statistical mechanics basis of his radiation law)

There is apparently a contradiction between the law of increasing entropy and the principles of Newtonian mechanics, since the latter do not recognize any difference between past and future times. This is the so-called reversibility paradox (Umkehrreinwand) which was advanced as an objection to Boltzmann's theory by Loschmidt 1876-77. (Translators foreword to Lectures on Gas Theory by Boltzmann).

37.1 Objective

In this concluding part we present a new approach to resolving Loschmidt's Mystery of the origin of irreversibility in reversible Hamiltonian systems, which we touched upon in Chapter 19 in the form of the 2nd Law of thermodynamics. Our resolution invites to form a new foundation of thermodynamics based on finite precision computation in the form of G2 instead of the standard approach of statistical mechanics. In the new foundation the 2nd Law is a consequence of the 1st Law combined with finite precision computation, which eliminates the mystery of the 2nd Law in the standard approach. We develop the new foundation in detail in Body&Soul Vol 5 on Computational Thermodynamics, and here give only a short account.

We thus stay within a deterministic Hamiltonian framework and only add a restriction of finite precision G2 computation. A World governed by Hamiltonian mechanics combined with finite precision G2 computation, follows the laws of mechanics as far as possible taking the finite precision into account, but is not based on any microscopic game of roulette as statistical mechanics. The difference of scientific paradigm is fundamental.

We are thus led to a model of the World as a giant *Clock with Finite Precision* [62], replacing the classical Laplace Clock with infinite precision, which has shown to be too good to be true.

37.2 What is Thermodynamics?

Thermodynamics is fundamental in a wide range of phenomena from the astronomical scales of cosmology and Big Bang over the macroscopic scales of geophysics and meteorology to the microscopic scales of microbiology and quantum mechanics. Thermodynamics essentially concerns the interplay between heat energy and kinetic energy. We shall see that the 2nd Law allows kinetic energy to transform to heat energy by compression or friction, and also allows heat energy to transform to kinetic energy by expansion. But the 2nd Law forbids reversal of transformation of kinetic energy to heat energy by friction. The industrial society of the 19th century was built on the use of steam engines, and the initial study of thermodynamics was motivated by the need to increase the efficiency of steam engines to convert heat to kinetic energy. Thermodynamics is closely connected to the dynamics of compressible gases, since substantial expansion can occur in a gas, but not in a solid.

The Big Bang Model postulates that 12 to 14 billion years ago, the portion of the universe we can see today was only a few millimeters across, and has since expanded from this hot dense state into the vast and much cooler cosmos we currently inhabit. We can see remnants of this hot dense matter as the now very cold cosmic microwave background radiation, visible to microwave detectors as a uniform glow across the entire sky. The 2nd Law states that an expansion generated from a hot dense initial state, cannot be reversed, and thus from a thermodynamical point of view it would appear that the Universe can only continue to expand.

37.3 EG2 as a Model of Thermodynamics

As a model of thermodynamics we consider the Euler equations (4.1), which is a one-species model, where the total energy has contributions from kinetic and internal heat energy, but not from chemical reactions, combined with finite precision computation in the form of G2. We refer to the resulting model as EG2.

Note that the Euler equations without a (constructive) solution method such as G2, do not themselves represent a true model, since after all they are just some symbols on a piece of paper. This observation is of particular relevance here, since the Euler equations lack pointwise solutions because of the appearance of turbulence and also *shocks*, which represent phenomena with very strong gradients, such as breaking water waves or the air bang from a supersonic airplane. The only exact pointwise solutions to the Euler

equations, which do exist, are trivial solutions with constant velocity and pressure.

37.4 The Classical Laws of Thermodynamics

Classical thermodynamics is based on two laws, the 1st Law and the 2nd Law. The 1st Law states conservation of total energy or that the increase in the energy of a closed system is equal to the amount of energy added to the system by heating, minus the amount lost in the form of work done by the system on its surroundings. The 1st Law is easy to understand and reflects that energy is defined so that it cannot be destroyed neither created and thus is conserved. There are different forms of energy like kinetic energy, potential energy, heat energy, chemical energy and nuclear energy, which sum up to the total energy which thus is conserved.

The 2nd Law has several forms, all cryptic as we will see:

- Carnot 1824 [22]: No heat engine can be more efficient than a *Carnot engine* with efficiency $1 - t_{cold}/t_{hot}$ operating between two temperatures $t_{cold} < t_{hot}$.
- Clasius 1850: It is impossible for heat to flow from a colder body to a warmer body without any work having been done to accomplish the flow. Energy will not flow spontaneously from a low temperature object to a higher temperature object.
- Kelvin-Planck 1851 [105]: It is impossible to obtain a process that, operating in cycle, produces no other effect than the subtraction of a positive amount of heat from a reservoir and the production of an equal amount of work.
- Clausius 1865: In any (cyclic) process the entropy cannot decrease.

The Clausius, Kelvin-Planck and Carnot formulations express impossibilities which are tricky to decipher: If somebody claims having constructed an engine more efficient than a Carnot engine, then Carnot would say that it is not a heat engine. Or if we observe heat flow from a cold to a warm body, then Clausius would say that it is not spontaneous. We understand that in the end this runs the risk of being an empty play with words, where a heat engine is an engine which is not more efficient than a Carnot engine and spontaneous heat flow occurs spontaneously.

The only statement of the above versions of the 2nd Law which is positive in form, is the last one about *entropy*. But this formulation requires a definition of what entropy is and its physical significance, and this has shown to be very difficult, if not impossible. In particular, nobody has found any sensor of entropy in Nature, and thus the mechanism preventing entropy from decreasing, is completely unknown, if there is any.

37.5 What is the Role of the 2nd Law?

If now the 2nd Law is so difficult to formulate and justify, why has it been formulated at all? The reason is that it is a common belief that without a 2nd Law of some form or the other, there would be no *arrow of time* pointing forward in time. All processes would seem to be reversible and there would seem to be no limitation on the possibilities of transforming one form of energy to another, as long as the total energy is constant. But this is not what we observe; time is always moving forward and transforming heat energy generated by friction from kinetic or potential energy, back to kinetic or potential energy, seems impossible: We may observe that a stone dropped to the ground heats up, but nobody has ever observed a stone on the ground lifting itself by cooling off.

On the other hand, classical Newtonian or Hamiltonian mechanics appear to be reversible, and the question then comes up what the mechanics behind irreversibility might be, if it is not Newtonian? This is Loschmidt's Mystery.

To resolve this mystery, scientists of the late 19th century were searching for a foundation of thermodynamics in the form of a 2nd Law expressing that a certain quantity named entropy could never decrease and when increasing strictly would signify irreversibility. The scientific challenge became to justify the 2nd Law by giving the entropy a physical molecular-mechanistic meaning. This turned out to be very difficult, and as a last resort Boltzmann introduced statistical methods. Many prominent scientists including Einstein could never understand Boltzmann's arguments, and statistical mechanics was initially viewed with considerable suspicion. Although, during the 20th century the critics and their criticism gradually faded, and statistical mechanics is today often presented as an accepted truth questioned by few.

Below we shall revive Einsteins criticism of statistical mechanics and present a constructive alternative resolving Loschmidt's Mystery without resorting to any form of statistics.

Joule's 1845 Experiment

The total energy of the universe is constant; the total entropy is continually increasing. (Rudolf Clausius)

I know that most men, including those at ease with problems of the highest complexity, can seldom accept even the simplest and most obvious truth if it be such as would oblige them to admit the falsity of conclusions which they have delighted in explaining to colleagues, which they have proudly taught to others, and which they have woven, thread by thread, into the fabric of their lives. (Tolstoy)

38.1 The Experiment

For illustration, we recall Joule's experiment [105] from 1845 with a gas initially at rest with temperature $T = 1$ at a certain pressure in a certain volume immersed into a container of water, see Fig. 38.1. At initial time a valve was opened and the gas was allowed to expand into the double volume while the temperature change in the water was carefully measured by Joule. To the great surprise of both Joule and the scientific community, no change in the temperature of the water could be detected, in contradiction with the expectation that the gas would cool off under expansion. Moreover, the expansion was impossible to reverse; the gas had no inclination to contract back to the original volume.

We now simulate Joule's experiment using an EG2 model where the two volumes are connected by a small channel which is opened at $t = 0$. At initial time $t = 0$ the gas is at rest with density $\rho = 1$ in the left container and $\rho = 0.1$ in the right container, and the temperature $T = 1$ in both containers. The difference in density causes the gas to flow from the left to the right container for $t > 0$.

Results from the EG2 computation are displayed in Fig. 38.1–38.3, where we discover the following scenario: The mean temperature in the left container drops below 1 as the gas expands into the right container with increasing

velocity, and shocks/turbulence appearing which heat the gas in the right container, increasing the mean temperature in the right container. The total energy is, of course, conserved by the 1st Law, and in the final state with the gas at rest in the two containers, corresponding to zero kinetic energy, the temperature is back to $T = 1$. We can also understand that the rapidity of the expansion process makes it difficult to detect any temperature drop in the water in the initial phase.

Altogether, using EG2 we can first simulate and then understand Joule's experiment, and we thus see no reason to be surprised. We shall see below as a consequence of the 2nd Law that reversal of the process with the gas contracting back to the original small volume, is impossible because the only way the gas can be put into motion is by expansion, and thus contraction is impossible.

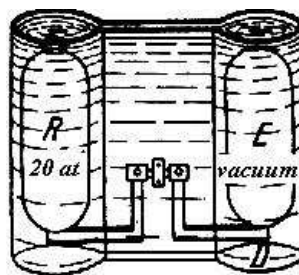


**Fig. 358 Concerning overflowing experiment of Joule (Scientific Papers).
R contains at first air compressed to 20 atm, E is initially a vacuum, D the tube**

Fig. 38.1. The Joule-Thomson experiment

We now compare with an analysis of the experiment using classical thermodynamics based on statistical mechanics. We then recall that classical thermodynamics only considers systems in equilibrium, that is we start with the gas at rest in the initial volume and we end up with the gas at rest in the double volume. By energy conservation, we understand that the temperature cannot change, so Joule's observation is after all not surprising even with a classical perspective. But how can we explain the irreversibility? Well, the basic idea of classical thermodynamics is to say that there is something, the entropy, which has increased from initial to final state. Boltzmann would say that because the volume of the final state is larger, the final state is "less ordered" or "more probable", and this would make the reverse process with the gas contracting back to the initial small volume, if not completely impossible, so at least very improbable. Of course, from a scientific point of view this is

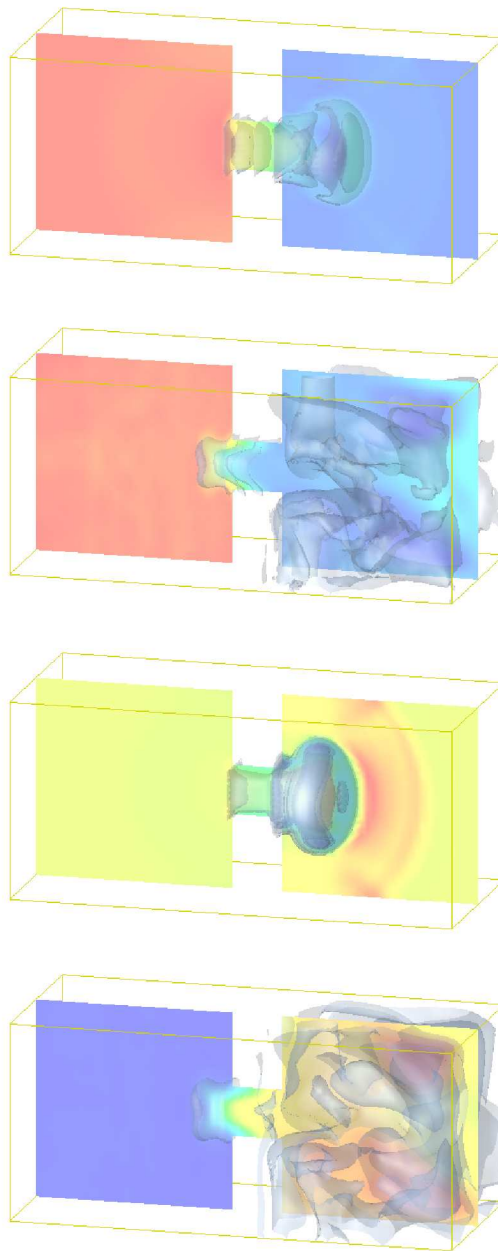


Fig. 38.2. EG2 simulation of the Joule-Thomson experiment: snapshots of density (upper 2 figures) and temperature (lower 2 figures) at 2 different time instants.

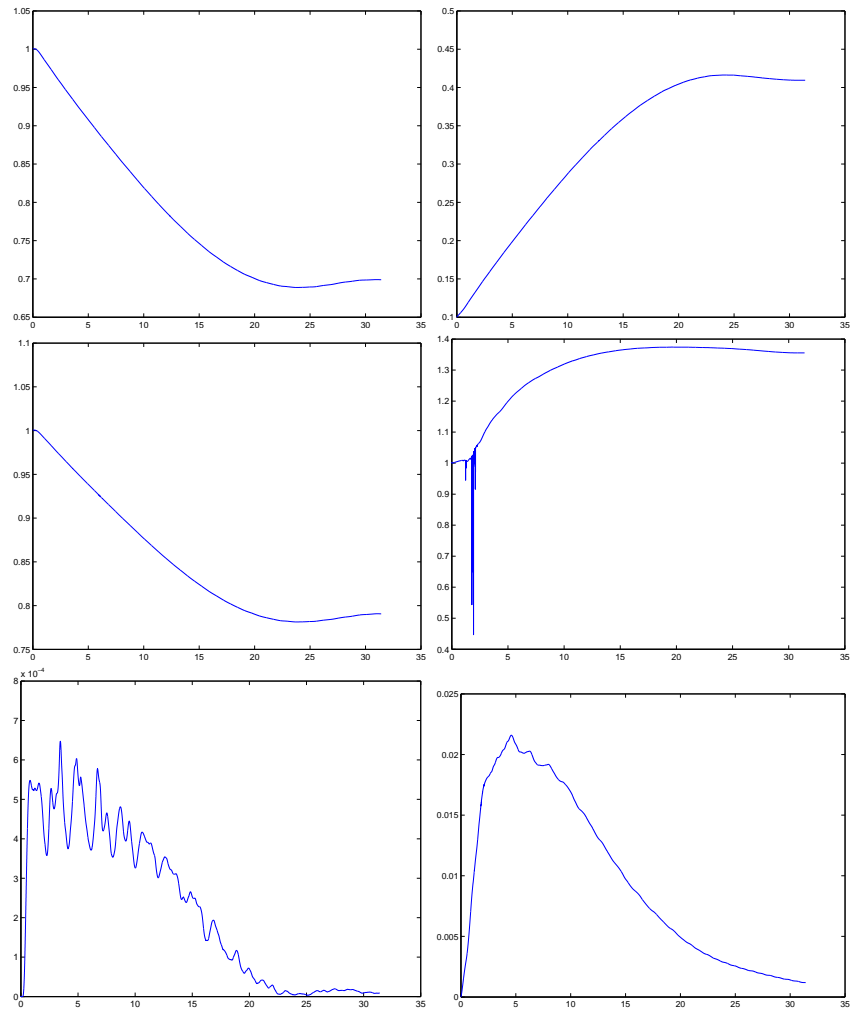


Fig. 38.3. The Joule-Thomson experiment: mean density (upper), mean temperature (middle) and mean kinetic energy (lower), for the left (left) and right chamber (right) in the initial phase of the EG2 simulation in Fig. 38.1.

not easy to make sense of, and we would still wonder *why* the gas would be willing to expand but not contract. To say that expansion is “more probable” does not explain anything, as far as we can see at least.

Another attempt of classical explanation would be to say that there is something like the “total amount of temperature”, which has increased from initial to final state with the increase in volume under constant temperature, but again the physical significance would be unclear. We are thus led to the impression that classical thermodynamics lacks a solid scientific foundation,

which is also reflected by the well-known difficulty to learn and teach this subject.

In contrast, taking the true dynamics of the process into account including in particular the heat generation from shocks and/or turbulence, we can easily intuitively understand the observation of constant temperature and irreversibility in a deterministic fashion without using any concept of entropy ultimately based on statistics.

Compressible Euler in 1d

Everyone knows that heat can produce motion. That it possesses vast motive power no one can doubt, in these days when the steam engine is everywhere so well known. The study of these engines is of great interest, their importance is enormous, their use is continually increasing, and they seem designed to produce a great revolution in the civilized world. (Sadi Carnot in “Reflections of the motive power of fire and on machines fitted to develop that power”, 1824).

By 2045 one thousand dollars’ worth of computation will be equal to 10^{26} cps, so the intelligence created per year (at a total cost of about $\$10^{12}$) will be about one billion times more powerful than all human intelligence today (Ray Kurzweil in “The Singularity Is Near”, 2005)

39.1 The Compressible Euler Equations in 1d

We now proceed to formulate a deterministic form of the 2nd Law and then verify that EG2 satisfies the 2nd Law. For definiteness we may assume the gas to be perfect, but the 2nd Law will take the same form for a general state equation.

To get some familiarity with the compressible Euler equations, we start considering the case of one space dimension. We thus consider a compressible inviscid perfect gas enclosed in a tube represented by the interval $\Omega = (0, 1)$ in space over a time interval $I = (0, \hat{t}]$ with zero as initial time and final time \hat{t} and we assume that the force $f = 0$. The compressible Euler equations take the form: Find $\hat{u} = (\rho, m, e)$ depending on $(x, t) \in Q = [0, 1] \times [0, \hat{t}]$ such that

$$\begin{aligned}\dot{\rho} + (\rho u)' &= 0, & \text{in } Q, \\ \dot{m} + (mu + p)' &= 0, & \text{in } Q, \\ \dot{e} + (eu + pu)' &= 0, & \text{in } Q, \\ u(0, t) &= u(1, t) = 0, & t \in I, \\ \hat{u}(\cdot, 0) &= \hat{u}^0, & \text{in } \Omega,\end{aligned}\tag{39.1}$$

where $v' = \frac{\partial v}{\partial x}$, ρ is density, u velocity and $m = \rho u$ momentum, the total energy $e = k + \theta$ is the sum of the kinetic energy $k = \rho u^2/2$ and internal heat energy $\theta = \rho T$, the pressure $p = (\gamma - 1)\rho T$ and $\gamma > 1$. For a mono-atomic gas $\gamma = 5/3$.

We may express the 1st Law of thermodynamics as conservation of mass, momentum and total energy. We may then say that the Euler equations (39.1) express the 1st Law. Strictly speaking, the 1st Law in classical form expresses conservation of total energy, while conservation of momentum corresponds to Newton's 2nd law and conservation of mass reflects that mass cannot be destroyed. However, it is convenient to let the 1st Law express conservation of both mass, momentum and total energy, so that in short the Euler equations express the 1st Law.

39.2 Euler is Formally Reversible

The Euler equations (39.1) are formally *reversible*: Changing the sign of the velocity u and the direction of time (the sign of the time-derivative \dot{u}), the Euler equations obviously remain unchanged. This means that if $\hat{u}(t)$ is a solution to the Euler equations in forward time on $[0, \hat{t}]$ taking the initial value $\hat{u}(0)$ to the final value $\hat{u}(\hat{t})$, we obtain a solution in backward time taking $\hat{u}(\hat{t})$ back to $\hat{u}(0)$ by reversing the velocity at time \hat{t} . Of course we can view this solution as proceeding in forward time by just continuing counting time forward after the velocity reversal.

We conclude that, formally, the Euler equations admit a perpetuum mobile, which is a machine running forever without consuming any energy, for ever bouncing back and forth by repeated reversal of the velocity at two given time instances.

39.3 All Wrong

The problem with the above argument showing reversibility of Euler solutions, is that it is all wrong. How come? We shall answer this question below by showing that the trouble is that the Euler equations do not admit exact solutions, which can be reversed as indicated. In contrast approximate EG2 solutions do exist, but these solutions turn out to be irreversible as we will see.

We sum up: the exact solutions which would have been reversible if they had existed, do not exist. The approximate EG2 solutions which do exist, are not reversible. This is the main lesson of this part of the book, and resolves the main open problem of classical thermodynamics: Loschmidt's Mystery.

39.4 The 2nd Law in Local Form

We now present a formal argument leading to the 2nd Law. We then start from the following viscous version of the momentum equation

$$\dot{m} + (mu + p)' - \nu u'' = 0, \quad \text{in } Q, \quad (39.2)$$

where ν is a positive viscosity, which we will let tend to zero. The basic operation is then to multiply the viscous momentum equation (39.2) by $u\phi$, with ϕ a *non-negative smooth test function*. We then obtain integrating over the space-time domain Q , and performing an integration by parts in the viscous term,

$$\begin{aligned} & \int_Q (\rho \dot{u}u + \dot{\rho}uu + u\rho u'u + u\rho'uu + u'\rho uu + p'u)\phi \, dxdt \\ &= - \int_Q \nu(u')^2 \phi \, dxdt - \int_Q \nu u' u \phi' \, dxdt, \end{aligned} \quad (39.3)$$

where $\nu(u')^2$ is the intensity of the *viscous dissipation*. Assuming now that $\int_Q \nu(u')^2 \, dxdt$ stays bounded as ν tends to zero, and further that the velocity u stays bounded, we see using Cauchy's inequality that the second term in the right hand side of (39.3) tends to zero as ν tends to zero. We conclude that for all non-negative smooth test functions ϕ ,

$$\int_Q (\rho \dot{u}u + \dot{\rho}uu + u\rho u'u + u\rho'uu + u'\rho uu + p'u)\phi \, dxdt = - \int_Q \delta \phi \, dxdt,$$

where

$$\delta = \lim_{\nu \rightarrow 0} \nu(u')^2, \quad (39.4)$$

and since ϕ is variable,

$$\rho \dot{u}u + \dot{\rho}uu + u\rho u'u + u\rho'uu + u'\rho uu + p'u = -\delta, \quad \text{in } Q.$$

Using next mass conservation in the form $\frac{u^2}{2}(\dot{\rho} + (\rho u)') = 0$, this equality can be written

$$\frac{\partial}{\partial t} \left(\rho \frac{u^2}{2} \right) + u \left(\rho \frac{u^2}{2} \right)' + u' \rho \frac{u^2}{2} + p'u = -\delta,$$

or

$$\dot{k} + (ku)' + up' = -\delta. \quad (39.5)$$

Combined with the energy equation written in the form

$$\dot{k} + \dot{\theta} + (ku)' + (\theta u)' + p'u + pu' = 0,$$

this gives

$$\dot{\theta} + (\theta u)' + pu' = \delta, \quad (39.6)$$

or, using again mass conservation,

$$\dot{T} + uT' + \frac{pu'}{\rho} = \frac{\delta}{\rho}. \quad (39.7)$$

We have now formally derived the 2nd Law in local form in any of the equivalent expressions (39.5)-(39.7), where $\delta \geq 0$. For a shock with a discontinuous velocity, the viscous dissipation $\delta > 0$ is of the size of the discontinuity squared and thus is not small. We understand that for a shock there is a significant transfer of kinetic energy to internal heat energy corresponding to the δ -term reflecting viscous dissipation in the shock.

We note that the basic ingredient in the proof of the 2nd Law in any of the forms (39.5)-(39.7) is multiplication of the momentum equation by the velocity u , or more precisely $u\phi$, and using the sign of the viscous dissipation in the momentum equation. The key observation is that the intensity of the viscous dissipation has a non-zero limit as ν tends to zero, and that $\delta > 0$ for a shock.

39.5 The 2nd Law in Global Form

By partial integration in space we have

$$\int_{\Omega} pu' dx = - \int_{\Omega} p'u dx,$$

using that $u(0, t) = u(1, t) = 0$. Integrating (39.5) and (39.6) in space, we thus obtain the following global form of the 2nd Law:

$$\begin{aligned} \dot{K} - W &= -\Delta, \\ \dot{\Theta} + W &= \Delta, \end{aligned} \quad (39.8)$$

where a capital letter indicates integration in space so that

$$K = \int_{\Omega} k dx, \quad \Theta = \int_{\Omega} \theta dx, \quad \Delta = \int_{\Omega} \delta dx,$$

and

$$w = pu', \quad W = \int_{\Omega} w dx,$$

represents local and global *work* performed by the pressure p on the velocity u , and where $\Delta > 0$ for solutions with shocks. We note that $w > 0$ under expansion with $u' > 0$.

In particular, we have by summation the global form of the 1st Law

$$\dot{E} \equiv \frac{d}{dt} \int_{\Omega} e dx = \dot{K} + \dot{\Theta} = 0, \quad (39.9)$$

stating that the integral (or totality) in space of the total energy e is constant in time.

39.6 Irreversibility by the 2nd Law

We understand that the global 2nd Law (39.8) for solutions with shocks with $\Delta > 0$, states an irreversible transfer of kinetic energy to heat energy. On the other hand, the sign of W is variable and thus the corresponding energy transfer may go in either direction. In a cyclic process, Δ represents heat lost in cooling.

To couple to the above argument with velocity and time reversal at final time, suppose we formally perform these operations on a given forward solution and denote the time reversed solution by $u(t)$. The global 2nd Laws (39.8) would then transform to

$$\begin{aligned}\dot{K} - W &= \Delta, \\ \dot{\Theta} + W &= -\Delta,\end{aligned}\tag{39.10}$$

with a change of sign of the Δ -term resulting from reversing the sign of velocity and time. This is a false 2nd Law as we will see.

We now compare with the true 2nd Law for a process starting at final time with the initial value $u(\hat{t})$ and going backward in time (thus forgetting the forward solution producing the value $u(\hat{t})$). The true 2nd Law for this process takes the form:

$$\begin{aligned}\dot{K} - W &= -\Delta, \\ \dot{\Theta} + W &= \Delta.\end{aligned}\tag{39.11}$$

We understand that the difference between the two processes from \hat{t} to 0 is the sign of the Δ -terms. In a real process satisfying the true 2nd Law (39.11), there is transfer from kinetic to internal heat energy, while in the fictitious process satisfying the false 2nd Law (39.10), the transfer would be from heat to kinetic energy, thus violating the true 2nd Law. We conclude that the formally reversed process and the true reversed process both starting with the value $u(\hat{t})$ and going backward in time, would be different for $t < \hat{t}$ since the true solution would satisfy the true 2nd Law (39.11), while the false formally reversed process would satisfy the false 2nd Law (39.10).

39.7 Compression and Expansion

We see from the 2nd Law (39.8) that there is a transfer of kinetic energy to heat energy if $W < 0$, that is under compression with $u' < 0$, and a transfer from heat to kinetic energy if $W > 0$, that is under expansion with $u' > 0$. In addition, there is always a transfer from kinetic to heat energy since always $\Delta \geq 0$ with $\Delta > 0$ for shocks.

Returning to Joule's experiment, we see by the 2nd Law that contraction back to the original volume from the final rest state in the double volume is impossible, because the only way the gas can be set into motion is by expansion.

Burgers' Equation

I feel sure that you do not understand how I came by my lonely ways.
(Einstein about the statistical interpretation of quantum mechanics)

Some physicists, among them myself, cannot believe that we must abandon, actually and forever, the idea of direct representation of physical reality in space and time; or that we must accept then the view that events in nature are analogous to a game of chance. (Einstein, On Quantum Physics, 1954)

If God has made the world a perfect mechanism, He has at least conceded so much to our imperfect intellects that in order to predict little parts of it, we need not solve innumerable differential equations, but can use dice with fair success. (Born, on Quantum Physics)

40.1 A Model of the Euler Equations

As a simple model of the Euler equations, with the particular intention to display the nature of shocks, we consider Burgers' equation: Find the scalar function $u = u(x, t)$ such that

$$\begin{aligned}\dot{u} + (f(u))' &= 0, \quad x \in \mathbb{R}, \quad t \in \mathbb{R}_+, \\ u(x, 0) &= u^0(x), \quad x \in \mathbb{R},\end{aligned}\tag{40.1}$$

where $f(u) = u^2/2$, and we assume that $u(t, x)$ tends to zero as $x \rightarrow \pm\infty$.

Burgers' equation (40.1) takes the pointwise form $\dot{u} + uu' = 0$ for a smooth solution u , which expresses that $u(x, t)$ is constant with values $u^0(\bar{x})$ along straight lines $x = st + \bar{x}$ with slope $s = u^0(\bar{x})$. If $u^0(x)$ is increasing with increasing x and is smooth, then there is a smooth solution $u(t, x)$ for all time given by this formula. However, if the initial data $u^0(x)$ is strictly decreasing, then characteristics cross in finite time, and then a *shock* necessarily develops, which is a discontinuous solution $u(x, t)$ satisfying Burgers' equation in the weak sense:

$$\int_{\mathbb{R} \times \mathbb{R}_+} (-u\dot{\phi} - f(u)\phi') dx dt - \int_{\mathbb{R}} u^0(x)\phi(x, 0) dx = 0, \quad (40.2)$$

for all differentiable test functions φ such that $\varphi(x, t)$ vanishes for large (x, t) , which is obtained from (40.1) by multiplication by ϕ and integration by parts.

40.2 The Rankine-Hugoniot Condition

A discontinuous function $u(x, t)$ defined by $u(x, t) = u_+$ if $x > st$ and $u(x, t) = u_-$ if $x < st$, where u_+ and u_- are two constant states and s is a constant, corresponding to a discontinuity propagating with speed s , is a weak solution to Burgers' equation according to (40.2), if the shock speed satisfies the *Rankine-Hugoniot condition*

$$s = \frac{[f(u)]}{[u]},$$

where $[u] = u_+ - u_-$ and $[f(u)] = f(u_+) - f(u_-)$. With $f(u) = u^2/2$ as in Burgers' equation, we have

$$s = (u_+ + u_-)/2. \quad (40.3)$$

The Rankine-Hugoniot condition (40.3) expresses Burgers' equation in weak form for a piecewise constant discontinuous function u .

40.3 Rarefaction wave

The solution to Burgers' equation with the increasing discontinuous initial data $u^0(x) = 0$ for $x < 0$, and $u^0(x) = 1$ for $x > 0$, is a *rarefaction wave* given by

$$\begin{aligned} u(x, t) &= 0, & \text{for } x < 0, \\ u(x, t) &= x/t, & \text{for } 0 \leq x/t \leq 1, \\ u(x, t) &= 1, & \text{for } 1 < x/t. \end{aligned} \quad (40.4)$$

This is a continuous function for $t > 0$, differentiable off the lines $x = 0$ and $x = t$, which satisfies (40.1) pointwise for $t > 0$. In a rarefaction wave, an initial discontinuity separating two constant states develops into a continuous linear transition from one state to the other of width t in space, corresponding to "fan-like" level curves in space-time, see Fig 40.1.

The stability of a rarefaction wave $u(x, t)$ is governed by the linearized equation

$$\dot{w} + (uw)' = 0, \quad \text{in } \mathbb{R} \times \mathbb{R}_+, \quad (40.5)$$

where w represents a (small) perturbation (tending to zero for $|x|$ tending to infinity). Multiplying by w and integrating in space, we obtain by a simple

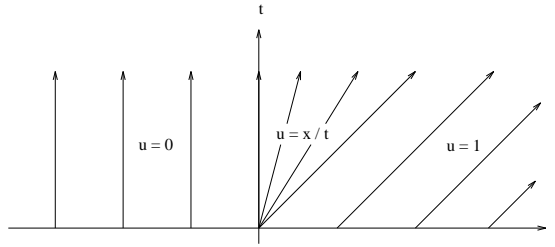


Fig. 40.1. Characteristics of a rarefaction wave.

computation using the fact that $u'(x, t) = 1/t$ for $0 \leq x \leq t$ and $u'(x, t) = 0$ else,

$$\frac{d}{dt} \int_{\mathbb{R}} w^2(x, t) dx + \int_0^t w^2(x, t) \frac{1}{t} dx = 0, \quad \text{for } t > 0,$$

from which follows that

$$\int_{\mathbb{R}} w^2(x, t) dx \leq \int_{\mathbb{R}} w^2(x, 0) dx, \quad \text{for } t > 0. \quad (40.6)$$

This inequality shows that the L_2 -norm in space of a perturbation of initial data does not grow with time, which proves stability of a rarefaction wave. Note that this argument builds on the fact that the rarefaction wave $u(x, t)$ is increasing in x so that u' is non-negative.

40.4 Shock

The solution with decreasing discontinuous initial data $u^0(x) = 1$ for $x < 0$, and $u^0(x) = 0$ for $x > 0$, is a discontinuous *shock wave* moving with speed $1/2$:

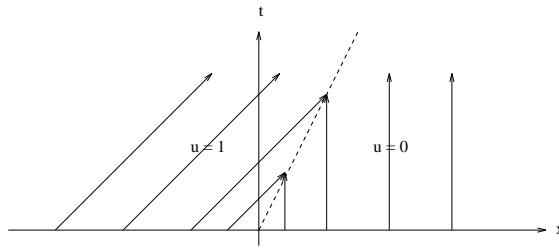
$$\begin{aligned} u(x, t) &= 1, & \text{for } x < t/2, \\ u(x, t) &= 0, & \text{for } x > t/2, \end{aligned}$$

see Fig 40.2. The stability proof used above to prove stability of a rarefaction wave, does not work the same way for a shock, since in this case $u(x, t)$ is decreasing with x . In fact a shock does not satisfy an L_2 stability estimate of the form (40.6). However, one may prove instead an L_1 -bound of the form

$$\int_{\mathbb{R}} |w(x, t)| dx \leq \int_{\mathbb{R}} |w(x, 0)| dx, \quad \text{for } t > 0. \quad (40.7)$$

This follows by multiplying (40.5) by $\text{sgn}(w) = +1$ if $w > 0$ and -1 if $w < 0$, to get by integration by parts:

$$\frac{d}{dt} \int_{\mathbb{R}} |w(x, t)| dx + (u_- - u_+)|w(\frac{t}{2}, t)| = 0, \quad (40.8)$$

**Fig. 40.2.** Characteristics of a shock

and using the fact that for a shock $u_+ < u_-$. Thus, a shock is a stable phenomenon.

40.5 Weak solutions may be non-unique

The rarefaction wave initial data $u^0(x) = 0$ for $x < 0$ and $u^0(x) = 1$ for $x > 0$, also admits the alternative discontinuous weak solution

$$\begin{aligned} u(x, t) &= 0, \quad \text{for } x < t/2, \\ u(x, t) &= 1, \quad \text{for } x > t/2, \end{aligned} \tag{40.9}$$

corresponding to a discontinuity $\{(x, t) : x = st\}$ moving with speed $s = 1/2$. This solution is obviously different from the rarefaction wave solution (40.4), which since it is a classical solution, also is a weak solution. Thus, we have in this case two different weak solutions, and thus we have an example of non-uniqueness of weak solutions.

We saw above that the rarefaction wave solution is stable, and we now study the stability of the alternative weak solution (40.9). By the same argument as used to prove (40.8) we obtain

$$\frac{d}{dt} \int_{\mathbb{R}} |w(x, t)| dx = (u_+ - u_-) |w(\frac{t}{2}, t)|, \tag{40.10}$$

where now $u_+ > u_-$. In this case, $\int_{\mathbb{R}} |w(x, t)| dx$ can grow arbitrarily fast, since the positive right hand side in (40.10) in no way can be controlled by the left hand side, and we thus conclude that the alternative weak solution is unstable. We may thus discard the alternative weak solution on the ground that it is unstable and thus not physical, because physics would of course prefer to realize a stable solution before an unstable. We may refer to the alternative unstable weak solution, as a non-physical shock.

We shall now disqualify the alternative weak solution as a physical solution also because it violates the 2nd Law. We thus have two methods to single out physical weak solutions, one based on stability, and the other based on the 2nd Law. This shows that ultimately the 2nd Law expresses a stability condition, reflecting that Nature only can realize phenomena which are not unstable.

40.6 The 2nd Law for Burgers' Equation

The 2nd Law for Burgers' equation is obtained by multiplication by u with viscous regularization, which gives the following local form:

$$\frac{\partial}{\partial t} \left(\frac{u^2}{2} \right) + \left(\frac{u^3}{3} \right)' = -\delta, \quad (40.11)$$

with corresponding global form

$$\dot{K} = -\Delta,$$

where as above $k = u^2/2$, $K = \int_{\mathbb{R}} k dx$ and $\Delta = \int_{\mathbb{R}} \delta dx$. We see that a weak Burgers' solution satisfying the 2nd Law cannot gain total kinetic energy (as an incompressible flow).

For a discontinuous solution consisting of two constant states u_+ and u_- separated by the line $\{x = st\}$, the 2nd Law (40.11) takes the form

$$s \left[\frac{u^2}{2} \right] - \left[\frac{u^3}{3} \right] \geq 0,$$

from which by a simple computation, we get

$$0 \leq \frac{1}{2}(u_- + u_+) \frac{1}{2}[u^2] - \frac{1}{3}[u^3] = (u_- - u_+) \frac{1}{12}(u_- - u_+)^2.$$

We conclude that the 2nd Law for a discontinuous weak solution can be stated as $u_- \geq u_+$, that is,

$$u_- \geq s \geq u_+.$$

A physical shock solution is thus characterized by the condition $u_- > u_+$ with shock speed $(u_- + u_+)/2$, in which case the 2nd Law is satisfied with strict inequality reflecting that a shock dissipates kinetic energy into heat.

40.7 Destruction of Information

The 2nd Law states that the characteristics of a physically admissible discontinuous weak solution of the inviscid Burgers equation “converge into” the shock, corresponding to $u_- > u_+$. This eliminates the discontinuous weak solution to the rarefaction initial data as an unphysical weak solution violating the 2nd Law, since in this case $u_- < u_+$, and the characteristics appear to “emerge from” the discontinuity. This reflects that the 2nd Law states that in a closed system, information may get destroyed (as in a shock with converging characteristics), but not created (as in an unphysical rarefaction with diverging characteristics): Burning a ground-breaking mathematics manuscript into ashes is easy, while restoring it is virtually impossible.

41

Compressible Euler in 3d

Where does irreversibility come from? It does not come from Newton's laws. Obviously there must be some law, some obscure but fundamental equation, perhaps in electricity, maybe in neutrino physics, in which it *does* matter which way time goes. (The Feynman Lectures on Physics 1963)

You believe in the God who plays dice, and I in complete law and order in a world which objectively exists, and which I, in a wild speculative way, am trying to capture. I hope that someone will discover a more realistic way, or rather a more tangible basis than it has been my lot to find. Even the great initial success of Quantum Theory does not make me believe in the fundamental dice-game, although I am well aware that younger colleagues interpret this as a consequence of senility. No doubt the day will come when we will see those instinctive attitude was the correct one. (Einstein to Born, 1944)

41.1 The 2nd Law in Local Form

We now extend to the compressible Euler equations (4.1) in 3d, which read:

$$\begin{aligned} \dot{\rho} + \nabla \cdot (\rho u) &= 0, & \text{in } Q, \\ \dot{m}_i + \nabla \cdot (m_i u) + p_{,i} &= 0, & \text{in } Q, \quad i = 1, 2, 3, \\ \dot{e} + \nabla \cdot (eu + pu) &= 0, & \text{in } Q, \\ u \cdot n &= 0, & \text{on } \Gamma \times I, \\ \hat{u}(\cdot, 0) &= \hat{u}^0, & \text{in } \Omega, \end{aligned} \tag{41.1}$$

with again $f = 0$, and we recall that $e = k + \theta$ with $k = \rho \frac{|u|^2}{2}$ and $\theta = \rho T$, and $p = (\gamma - 1)\rho T$.

We shall formally prove the following local forms of the 2nd Law:

$$\dot{k} + \nabla \cdot (ku) + \nabla p \cdot u = -\delta, \tag{41.2}$$

$$\dot{\theta} + \nabla \cdot (\theta u) + p \nabla \cdot u = \delta, \tag{41.3}$$

$$\dot{T} + u \cdot \nabla T + \frac{p}{\rho} \nabla \cdot u = \frac{\delta}{\rho}, \quad (41.4)$$

where

$$\delta = \lim_{\nu \rightarrow 0} \sum_{i=1}^3 \nu |\nabla u_i|^2,$$

with $\delta > 0$ for shocks/turbulence. The proof starts by scalar multiplication of the momentum equation by u_i and assuming the presence of a dissipative term now of the form $-\nu \Delta u_i$, and that $u_i = 0$ on Γ , to give (using the convention that repeated indices indicate summation from 1 to 3):

$$\rho \dot{u}_i u_i + \dot{\rho} u_i u_i + u_j \rho u_{i,j} u_i + u_j \rho_{,j} u_i u_i + u_{j,j} \rho u_i u_i + \nabla p \cdot u = -\delta,$$

which using mass conservation in the form $\frac{|u|^2}{2}(\dot{\rho} + \nabla \cdot (\rho u)) = 0$, can be written

$$\frac{\partial}{\partial t} \left(\rho \frac{|u|^2}{2} \right) + u \cdot \nabla \left(\rho \frac{|u|^2}{2} \right) + \nabla \cdot u \rho \frac{|u|^2}{2} + \nabla p \cdot u = -\delta,$$

which is (41.2). Combined with the energy equation written in the form

$$\frac{\partial}{\partial t} \left(\rho \frac{|u|^2}{2} \right) + \dot{\theta} + u \cdot \nabla \left(\rho \frac{|u|^2}{2} \right) + u \cdot \nabla \theta + \nabla \cdot u \left(\rho \frac{|u|^2}{2} \right) + \theta \nabla \cdot u + \nabla p \cdot u + p \nabla \cdot u = 0,$$

this gives (41.3), and using mass conservation we obtain (41.4).

41.2 Incompressible Flow

For incompressible flow with $\nabla \cdot u = 0$, the 2nd Law takes the form

$$D_u T = \dot{T} + u \cdot \nabla T = \frac{\delta}{\rho} \geq 0,$$

which is the form of the 2nd Law derived in Chapter 19, and which expresses that the internal heat energy density cannot decrease and will increase strictly for turbulence/shocks.

41.3 The 2nd Law in Global Form

By partial integration we have

$$\int_{\Omega} p \nabla \cdot u dx = - \int_{\Omega} \nabla p \cdot u dx,$$

using that $u \cdot n = 0$ on Γ . Integrating (41.2) and (41.3) in space, we thus obtain the following global form of the 2nd Law:

$$\begin{aligned}\dot{K} - W &= -\Delta, \\ \dot{\Theta} + W &= \Delta,\end{aligned}\tag{41.5}$$

where

$$K = \int_{\Omega} k \, dx, \quad \Theta = \int_{\Omega} \theta \, dx, \quad \Delta = \int_{\Omega} \delta \, dx,$$

and

$$w = p \nabla \cdot u, \quad W = \int_{\Omega} w \, dx,$$

represents local and global work performed by the pressure p on the velocity u , and where $\Delta > 0$ for solutions with shocks/turbulence. We note that $w > 0$ under expansion with $\nabla \cdot v > 0$.

In particular, we have by summation the global form of the 1st Law

$$\dot{E} \equiv \frac{d}{dt} \int_{\Omega} e \, dx = \dot{K} + \dot{\Theta} = 0, \tag{41.6}$$

stating that the integral (or totality) in space of the total energy e is constant in time.

For incompressible flow with $\nabla \cdot u = 0$, the 2nd Law in global form reads

$$\begin{aligned}\dot{K} &= -\Delta, \\ \dot{\Theta} &= \Delta,\end{aligned}\tag{41.7}$$

stating that for turbulent flow the total kinetic energy K is strictly decreasing and the total internal heat energy Θ is strictly increasing.

41.4 Irreversibility by the 2nd Law

We note as above that the global 2nd Law (41.5) for solutions with shocks or turbulence with $\Delta > 0$, states an irreversible transfer of kinetic energy to heat energy. The sign of W is variable and thus the corresponding energy transfer may go in either direction. In a cyclic process, Δ represents heat lost in cooling.

41.5 Trend Towards Equilibrium by the 2nd Law

The 2nd Law implies a trend towards equilibrium with zero velocity and constant pressure, since the transfer from kinetic energy to heat energy will continue as long as there are velocity gradients generating shocks/turbulence. We thus conclude that an isolated system will have a trend towards equilibrium with zero velocity and constant pressure.

41.6 Comparison with Classical Entropy

We compare the local form (41.4) of the 2nd Law in T with the classical basic relation of thermodynamics usually written in the form:

$$TdS = dT + pdV = dT - p \frac{d\rho}{\rho^2}, \quad (41.8)$$

where dS represents change of *entropy* S , and the 2nd Law is expressed as $dS \geq 0$. Further, $dV = d(1/\rho) = -d\rho/\rho^2$ represents volume change with ρdV corresponding to $\nabla \cdot u$, $\dot{T} + u\nabla T$ to dT , and finally (41.4) reflecting $TdS \geq 0$ expresses the same inequality as $dS \geq 0$. We note that by mass conservation, we have $D_w\rho = -\rho\nabla \cdot w$ so that formally $d\rho = -\rho\nabla \cdot w$.

Integrating the classical relation

$$dS = \frac{dT}{T} + \frac{p}{T}dV = \frac{dT}{T} + (1 - \gamma)\frac{d\rho}{\rho},$$

we obtain $S = \log T\rho^{1-\gamma} = \log(p\rho^{-\gamma})$ up to a constant.

Thus, the entropy $S = S(\hat{u})$ is a simple function of \hat{u} , but its physical meaning as well as the physical significance of the 2nd Law in the form $dS \geq 0$, has remained a mystery of classical thermodynamics ever since it was introduced by Clausius in 1865 based on the relation $TdS = dT + pdV$. Since $dS \geq 0$ and the 2nd Law in the form (41.4) express the same inequality, the mystery of $dS \geq 0$ will disappear along with a justification of the 2nd Law. We have given a formal justification of the 2nd Law based on viscous regularization, and we will give a real justification for EG2 below.

We emphasize again that the 2nd Law in the local forms (41.2)-(41.4) or the global forms (41.5) do not involve the quantity S , and as indicated come out as consequences of the 1st Law expressing conservation of mass, momentum and energy combined with viscous regularization. We shall prove below that EG2 automatically satisfies the 2nd Law, because the stabilization in G2 introduces a form of viscous regularization. The net result is that we can simply forget about the entropy S which relieves us from the hopeless task of finding a mechanism in Nature guaranteeing that S does not decrease. EG2 will automatically have this property and we may expect that Nature in its own analog computation similarly satisfies the 2nd Law without knowing anything about entropy.

41.7 Heat Capacities and the Gas Constant

We connect to the previous section by deriving the classical relation $c_p - c_v = \gamma - 1$ for a perfect gas from the 1st Law expressed as $dQ = c_vdT + pdV$, with dQ an increment of energy added to a system being equal to the sum of the increment of internal energy c_vdT and work pdV performed, where c_p is the

heat capacity at constant pressure and c_v that at constant volume. Clearly $c_v = dQ/dT$ if $dV = 0$. Further, since $p = (\gamma - 1)\rho T$, we have assuming $dp = 0$, i.e. $d\rho T + \rho dT = 0$, that

$$dQ = c_v dT + (\gamma - 1)\rho T d\left(\frac{1}{\rho}\right) = c_v dT + (\gamma - 1)\left(-\frac{T d\rho}{\rho^2}\right) = c_v dT + (\gamma - 1)dT,$$

which shows that $c_p - c_v = \gamma - 1$.

EG2 for Compressible Flow

The 2nd Law cannot be derived from purely mechanical laws. It carries the stamp of the essentially statistical nature of heat. (Bergman in Basic Theories of Physics 1951)

The theory (quantum mechanics) yields a lot, but it hardly brings us closer to the secret of the Old One. In any case I am convinced that *He* does not throw dice. (Einstein to Born 1926)

Shut up and calculate. (Dirac on quantum mechanics)

42.1 G2 for the Compressible Euler Equations

We now present EG2 for the compressible Euler equations written in a system as follows: Find $\hat{u}(x, t)$ such that

$$\begin{aligned} R(\hat{u}) &\equiv \frac{\partial \hat{u}}{\partial t} + \sum_{i=1}^3 f_i(\hat{u}),_i = 0, & \text{in } Q, \\ u(x, t) \cdot n(x, t) &= 0, & \text{in } \Gamma \times I, \\ \hat{u}(\cdot, 0) &= \hat{u}^0, & \text{in } \Omega, \end{aligned} \tag{42.1}$$

where

$$\hat{u} = \rho \begin{bmatrix} 1 \\ u_1 \\ u_2 \\ u_3 \\ e/\rho \end{bmatrix}, \quad f_i(\hat{u}) = u_i \hat{u} + p \begin{bmatrix} 0 \\ \delta_{1i} \\ \delta_{2i} \\ \delta_{3i} \\ u_i \end{bmatrix},$$

with $\delta_{ii} = 1$, and $\delta_{ij} = 0$ if $i \neq j$.

EG2 takes the general form: Find $\hat{u} \in V_h$ such that for all $\hat{v} \in V_h$

$$\begin{aligned} &((R(\hat{u}), \hat{v})) + ((hR(\hat{u}), R_u(\hat{v}))) \\ &+ ((\hat{v} \nabla u_i, \nabla v_i)) + (u(\cdot, 0) - u_0, v(\cdot, 0)) = 0, \end{aligned} \tag{42.2}$$

where V_h is a finite element space of mesh size h in space-time of functions \hat{v} with velocity components v satisfying the boundary condition $v \cdot n = 0$ on Γ , $((\cdot, \cdot))$ and (\cdot, \cdot) represent $L_2(Q)$ and $L_2(\Omega)$ scalar products, $R_u(\hat{v})$ is the linearization of $R(\hat{u})$ obtained by freezing the convective velocity at u noting that $R_u(\hat{u}) = R(\hat{u})$, and $\hat{\nu} = h^2|R(\hat{u})|$ is a shock-capturing artificial viscosity. EG2 combines a weak satisfaction of the Euler equations with a weighted least squares control of the residual $R(\hat{u})$ and thus represents a midway between the Scylla of weak solution and Carybdis of least squares strong solution.

42.2 EG2 Satisfies the 2nd Law

We can show in the same way as we proved the 2nd Law for incompressible flow in Chapter 18 that EG2 satisfies a weak form of the 2nd Law expressed in any of the local forms (41.2)-(41.4) or global form (41.5). We give the detailed proof in Body&Soul Vol 5 on Computational Thermodynamics, with the prototype of the proof presented in [69].

We conclude that EG2 produces approximate solutions to the Euler equations which are irreversible in the general case of shocks and turbulence. Thus EG2 produces approximate solutions which are irreversible, to be compared with exact solutions, which would have been reversible had they existed, but they don't.

42.3 EG2 and the Classical Entropy

The classical entropy S can be obtained from the defining relation $TdS = dT + pdV$ to get $S = \log(T\rho^{1-\gamma})$. The 2nd Law can be expressed in classical form as $\dot{S} + \nabla \cdot (wS) \geq 0$, and we can prove that EG2 weakly satisfies the 2nd Law in this form. As indicated, we prefer not to introduce S , since its physical meaning is unclear. Nevertheless, we can as in [69] obtain choosing as test function v in (42.2) an interpolant of the gradient $-S'(\hat{u})$ of $-S(\hat{u})$ with respect to \hat{u} , the following global bound

$$-\int_{\Omega} S(\hat{u}(T))dx - ((hR(\hat{u}), R(\hat{u})S'')) \leq \int_{\Omega} -S(\hat{u}(0))dx,$$

where $-S''(\hat{u}) > 0$ is the Hessian of $-S(\hat{u})$, which gives a weighted bound of the least squares term $((hR(\hat{u}), R(\hat{u})))$ in terms of logarithms effectively being bounded. The proof that EG2 weakly satisfies $\dot{S} + \nabla(wS) \geq 0$ is similar multiplying by $-S'(\hat{u})\phi$ with ϕ a non-negative test function. We can thus use the classical entropy to obtain an a priori global bound for the stabilization term, but that is the only useful role of the entropy we see. Of course a posteriori we may check if the stabilization term is bounded, so in practice the a priori bound may not be needed, and thus we may entirely forget about S and expect that Nature does the same, since a sensor for S seems to be missing.

Philosophy of EG2

Originally I viewed it as the function of the abstract machine to provide a truthful picture of the physical reality. Later, however, I learned to consider the abstract machine as the *true* one, because that is the only one we can *think*; it is the physical machine's purpose to supply a *working model*, a (hopefully) sufficiently accurate physical simulation of the true, abstract machine. (Dijkstra)

Since the theory of general relativity implies representations of physical reality by a continuous field, the concept of particles or material points cannot have a fundamental part, nor can the concept of motion. (Einstein)

I consider it quite possible that physics cannot be based on the field concept, i.e., on continuous structures. In that case, nothing remains of my entire castle in the air, gravitation theory included, and of the rest of physics. (Einstein 1954)

43.1 Dijkstra's Vision

Following the idea cited above by the famous computer scientist Dijkstra, we conjecture that Nature may conform to a good computational model (true abstract machine), rather than the opposite, reflecting a modern form of the idealism of Plato. What a wonderful victory this would be for a science, if it was true! But can it be true?

Well, we have seen that EG2 is a good computational model of thermodynamics including the 2nd Law, and it is conceivable that Nature in its own analog computation thus will choose to be close to EG2. As Dijkstra suggests, only EG2 is open to inspection, while the true physics of Nature's analog computation may for ever be hidden to us. By studying EG2 we may thus learn about Nature, at least this is the principle behind this book.

So what may be the physical realization of G2? Well, the least squares stabilization corresponds to controlling the residual pointwise, which corresponds to setting a limit to the *non-equilibrium* of the conservation laws, if we refer

to equilibrium as pointwise satisfaction of conservation of mass, momentum and energy. We then expect the non-equilibrium to be most pronounced in the momentum equation, since it is here the dissipation from turbulence and shocks is present, with the dissipated energy being captured as internal energy in the energy equation. We know that the pointwise residual in the momentum equation may be of size $h^{-1/2}$ in turbulent regions, and for shocks it may be even larger of size h^{-1} .

The Galerkin part of G2 is more delicate to interpret in physical terms, since it reflects that local mean values of possibly large pointwise residuals are small. It is conceivable that a large, say positive, residual at some point may be compensated by a large negative value nearby, so that their mean-value is small. However it remains to discover the physics of taking local mean values and guaranteeing that the mean values are kept small.



Fig. 43.1. Edsger Wybe Dijkstra (1930-2002).

43.2 The Role of Least Squares Stabilization in G2

We have seen that the weighted least squares control of the residual in G2 adds a dissipative term which effectively makes the system irreversible. This is like a fine or cost arising from not following the law pointwise. It is thus the appearance of turbulent/shock small scales and the resulting impossibility of computing solutions with pointwise small residuals, which necessarily introduces the irreversibility. By necessity, a fine has to represent a positive cost; if we would get paid by breaking the law, society would quickly collapse. Or if there would be a negative cost (gain) in changing currency, the monetary system would explode.

Facing the impossibility of pointwise solution, the system thus reacts by producing an approximate solution in which some of the kinetic energy is lost in a dissipative least squares term implying irreversibility. Moreover, the size of the dissipation and the energy loss does not decrease with increasing precision: In turbulence the dissipation always occurs on the finest scales available, but the total amount of the turbulent dissipation (turning into heat), stays (approximately) constant under scale refinement. A shock in compressible flow has a similar nature. Mean value outputs thus may show an independence of the scale of resolution in the computation, while pointwise solution is impossible even if the computational scale is refined indefinitely. The more you refine, the more scales you find and there is no end to this process.

The basic idea is thus that in certain Hamiltonian processes necessarily small scale features in the form of turbulence/shocks appear, and when faced with these small unresolvable scales, which physically generate heat, the system reacts by introducing a dissipative least squares control of the residual, which implies irreversibility. Thus, in turbulence/shocks, large scale mechanical energy may be turned into small scale motion, corresponding to generation of heat, and this process is irreversible since the details of the small scales cannot be kept and thus cannot be recovered: To smash a valuable Chinese vase into pieces does not require much of precision, but to restore the vase by assembling the pieces may require too much of precision to be realized.

The key here is to realize that the dissipative stabilization (i) is necessary, (ii) is substantial, (iii) is not a numerical artifact which can be diminished by increasing the precision. The key new fact behind (i)-(iii) is the non-existence of solutions to the Hamiltonian equations! The appearance of turbulence/shocks in inviscid compressible flow is an example of an irreversible process satisfying (i)-(iii), where inevitably and irreversibly energy is turned into heat.

In G2 the irreversibility arises from the presence of the least squares control of the residual, which corresponds to a loss of the kinetic energy which cannot be recovered; reversing time and velocities at final time in G2 and computing backwards in time will bring in a new least squares term only adding to the losses already made in the forward computation. This reflects the difficulty of getting a refund of an already paid fine.

43.3 Aspects of Irreversibility

The Euler equations for inviscid flow may be viewed to model a very large collection of “fluid particles” following Newton’s 2nd Law subject to a pressure force maintaining incompressibility.

The Euler equations represent a formally reversible system, which as we have seen in general lacks pointwise solutions. This is because the laminar pointwise solutions, which do exist, turn out to be unstable without physical realization, and because the turbulent solutions, which do appear, are not

pointwise solutions but only approximate weak solutions. Thus, both computation and Nature will have to go for suitable approximate solutions of the Euler equations. Computation will then rely on G2, with presumably Nature resorting to something similar, which inevitable (because of the least squares residual control in G2) will introduce a dissipative effect implying irreversibility.

We have thus met a situation, where the equations we want to solve do not have exact pointwise solutions, (or if they have, then they are unstable), while the turbulent/shock solutions which do exist in fact only are approximate weak solutions and not pointwise solutions, and moreover these approximate solutions necessarily have a dissipative character resulting in irreversibility. It is important to notice that the dissipation is substantial and does not tend to zero with decreasing mesh size, as it would have done if a smooth exact solution had existed. The paradox of irreversibility in a formally reversible Hamiltonian system is thus a consequence of the non-existence of a stable laminar pointwise (strong) solutions to the Euler equations, which would have been reversible if they had only existed, and the dissipative nature of the turbulent approximate weak solutions, which do exist computationally and for which mean value outputs can be accurately computed.

We note that the non-existence of (stable) exact solutions, changes the way mathematics for the Euler equations can be presented: With non-existent exact solutions, the attention has to move to existing approximate solutions, and thus the computational aspect takes a prime position before analytical mathematics.

The non-existence of pointwise solutions to the Euler equations, which may be viewed as a failure of mathematics, in fact may be turned around into an advantage from a computational point of view: If there were an exact solution, one could always ask for more precision in computing this solution requiring finer resolution and higher computational cost, but if there is no exact solution, then we could be relieved from this demand beyond a certain point. A key feature in this situation is that the absolute size of the fine scales no longer are important, and this could save computational work. In turbulence this means that mean value outputs may be computed on meshes which do not resolve the turbulent vortices to their actual physical scale.

In order for a Hamiltonian system to develop turbulence, it has to be rich enough in degrees of freedom. In particular, the incompressible or compressible Euler equations in less than three space dimensions are not rich enough, even if the mesh is very fine. On the other hand, turbulence invariably develops in three dimensions once the mesh is fine enough. Our experience with turbulent solutions of the incompressible Navier–Stokes equations indicates that a mesh with 100 000 mesh points in space may suffice in simple geometries, while in more complex geometries millions, but not billions, of mesh points may be needed.

43.4 Imperfect Nature and Mathematics?

How are we to handle the fact that the Euler equations do not have pointwise solutions in general? Does this express an imperfection of mathematics? And what is the consequence in physics? Is Nature simply unable to satisfy the basic laws laid down in the form of e.g. Newton's 2nd Law? Does this mean that also Nature is imperfect? And if now both mathematics and Nature indeed are imperfect, what is the degree of imperfection and how does it show up?

We may make a parallel with the square root of two $\sqrt{2}$, which is the length of the diagonal in a square with side length 1. We know that the Pythagoreans discovered that $\sqrt{2}$ is not a rational number. This knowledge had to be kept secret, since it indicated an imperfection in the creation by God formed as relations between natural numbers according the basic belief of the Pythagoreans. Eventually this unsolvable conflict ruined their philosophical school and gave room for the Euclidean school based on geometry instead of natural numbers. Civilization did not recover until Descartes resurrected numbers and gave geometry an algebraic form, which opened for Calculus and the scientific revolution.

But how is the Pythagorean paradox of non-existence of $\sqrt{2}$ as a rational number handled today? Well, we know that the accepted mathematical solution since Cantor and Dedekind is to extend the rational numbers to the real numbers, some of which like $\sqrt{2}$ are called irrational, and which can only be described approximately using rational numbers. We may say that this solution in fact is a kind of non-solution, since it acknowledges the fact that the equation $x^2 = 2$ cannot be solved exactly using rational numbers, and since the existence of irrational numbers (as infinite decimal expansions or Cauchy sequences of rational numbers) has a different nature than the existence of natural numbers or rational numbers. The non-existence is thus handled by expanding the solution concept until existence can be assured.

We handle the non-existence of pointwise solutions to the Euler equations similarly, that is, by extending the solution concept to approximate solutions in a weak sense combined with some control of pointwise residuals. Doing so we necessarily introduce a dissipation causing irreversibility. In this case, the non-existence of solutions thus has a cost: irreversibility. In the perfect World, pointwise solutions would exist, but this World cannot be constructed neither mathematically nor physically, and in a constructible World necessarily there will exist irreversible phenomena as a consequence of the non-existence of pointwise solutions. The non-existence of pointwise solutions reflects the development of complex solutions with small scales, and thus the non-existence also reflects a complexity of the constructible World. The perfect World would lack this complexity, so in addition to being non-existent it would also probably be pretty non-interesting. The World we live in thus does not seem to be perfect, but it surely is complex and interesting.

What is the reason that the resolution of Loschmidt's Mystery we are proposing has not been presented before, if it indeed uncovers the mystery? We believe it can be explained by the Ideal Worlds that both mathematicians and physicists assume as basis of their science. In the Ideal World of mathematics, exact solutions to differential equations exist as well as infinite sets, not just approximate solutions and finite sets, and the World of physics is supposed to follow laws of physics exactly, not just approximately, unless a resort to statistics is made (which is a very strong medication with severe side effects). It thus appears that an imperfect World of mathematics or physics, where equations cannot be solved exactly or laws of physics cannot be exactly satisfied, classically is unthinkable at least as a deterministic World, and thus has received little attention by mathematicians and physicists with little background in computational mathematics. Yet, such an imperfect World seems to be a reality in both mathematics and physics, and thus should be studied.

43.5 A New Paradigm of Computation

From a philosophical point of view, we may say that the traditional paradigm of both mathematics and physics is Platonistic in the sense that it assumes the existence of an Ideal World, where equations/laws are satisfied exactly. We may say that this is an Ideal World of infinities because exact satisfaction of e.g. the equation $x^2 = 2$ requires infinitely many decimals. This is the mathematical Ideal World of Cantor, which represents a formalist/logicist school. In strong opposition to this school of infinities, is the constructivist school, which only deals with mathematical objects that can be constructed or computed in a finite number of steps. In the constructivists Constructible World, the set of natural numbers does not exist as a completed mathematical object as in Cantors Ideal World, but only as a never-ending project where always a next natural number can be constructed if needed, which follows the suggestions of e.g. Aristotle and Gauss. The Constructible World is finitary and thus inherently computational, while Cantors Ideal World is non-finitary and non-computational. We give our vote to the Constructible World, which today can be explored using the computer, which is the leading theme of the Body&Soul project.

43.6 The Clay Prize Problem Again

We have noted that one of the seven Clay Institute Millennium \$1 Million Prize Problems asks for a proof of existence of a pointwise solution to the Navier-Stokes equations for incompressible fluid flow, a formulation which fits into an Ideal World paradigm. We argue that the formulation of the Prize Problem is unfortunate, and propose instead a reformulation of the Prize Problem in constructive terms, since in general pointwise solutions do not exist, while turbulent approximate solutions do.

Does God Really Play Dice?

Der liebe Gott würfelt nicht. God does not play dice. (Einstein)

I still believe in the possibility of giving a model of reality which shall represent events themselves and not merely the probability of their occurrence. (Einstein in his Spenser lectures 1933)

Neither Herr Boltzmann nor Herr Planck has given a definition of W . (Einstein)

Usually W is put equal to the number of complexions. In order to calculate W , one needs a *complete* (molecular-mechanical) theory of the system under consideration. Therefore it is dubious whether the Boltzmann principle has any meaning without a *complete* molecular-mechanical theory or some other theory which describes the elementary processes (and such a theory is missing). (Einstein)

44.1 Einstein and Modern Physics

In this concluding chapter we give some more perspectives on statistical mechanics, which today is considered as the foundation of thermodynamics.

Einstein could never accept the idea that physics ultimately is based on microscopic games of dice as in Boltzmann's gas dynamics and the Copenhagen interpretation of quantum mechanics. Einstein's criticism can be given the following paraphrase in politics: Consider a politician who states that he firmly believes that each individual voter plays dice when deciding how to vote, and claims that his belief is based on the observation that he cannot predict how individual voters will vote. Would you believe that this politician has any contact with realities? Wouldn't you say that most voters probably try to make a rational choice based on the arguments in the election debate, instead of simply playing dice?

Or on observing people walking around in a city, would you say that their apparent erratic and unpredictable paths would be the results of playing dice

at each foot step? Would you say that it at least looks *as if* people are playing dice, even if they don't *really* do that, and that this would be a useful model? Or would you say that you see no good reason to use such a model?

Well, if you believe that dice-playing voters belong to fiction (although there may be some cynics using this approach), then you may also join Einstein in his criticism of physics based on the idea that individual particles like molecules, atoms or electrons play dice when deciding what to do next, based on the observation that it is difficult to predict the position and velocity of individual particles.

But from where does the idea come that physics is based on dice-playing particles, which is a physics against the principles of Newtonian mechanics based on cause-effect and which Einstein questioned long before his criticism was dismissed as a sign of senility. Well, we know that the idea came out of a need to develop a foundation of thermodynamics including the 2nd Law in the late 19th century. In Newton's mechanistic world the 2nd Law and arrow of time is missing since Newton's laws are time reversible, and so the scientists had to come up with something: Large values were at stake, both scientific and economical.

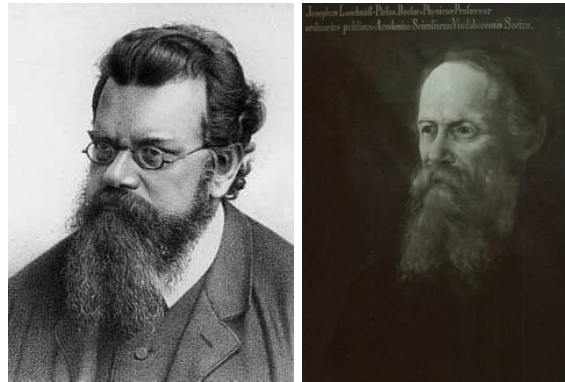


Fig. 44.1. Ludwig Boltzmann (1844–1906) and Jan Josef Loschmidt (1821–1895).

44.2 Boltzmann and Statistical Mechanics

The German mathematician and physicist Ludwig Boltzmann took up the challenge to give thermodynamics a scientific mathematical basis including an explanation of the 2nd Law of irreversibility [18]. Boltzmann started with a molecular-deterministic model of a gas consisting of a very large number of molecules colliding elastically following Newton's laws. Boltzmann of course understood that this model is time reversible, so he had to modify it to make it

irreversible. His modification was to let the molecules play dice *before* collision to decide how to collide, but not after, which broke the time reversibility of Newton's laws and thus led to irreversibility. This was the birth of statistical mechanics, which inspired Planck in the early evening of Sunday October 7 1900, in an "act of despair", to invent a solution to the outstanding open problem of *black-body radiation*, based on statistics of quanta. This opened the way to *quantum mechanics* with its statistical interpretation of the Schrödinger wave function as the probability of finding a particle like an electron at a specific location in space-time. In short, this led into forms of *modern physics* based on various forms of statistical mechanics, which Einstein could never accept, even under strong pressure from the scientific community.

Using particle statistics Boltzmann could demonstrate a version of the 2nd Law stating that a certain quantity S named entropy could never decrease and when increasing strictly would signify irreversibility and give the arrow of time a direction forward: Reversal of a process with strictly increasing entropy would violate the 2nd Law and thus be impossible. On Boltzmann's tombstone the famous formula

$$S = k \log(W) \quad (44.1)$$

is engraved, where k is Boltzmann's constant ($k \approx 10^{-23}$ joules/kelvin) and W denotes the probability of a certain state representing the number of "complexions" corresponding to the state. Increasing entropy would then reflect that Nature would tend to move from less probable to more probable states or towards states with more complexions. Einstein could not accept these ideas as healthy science, and the questions *why* and *how* Nature would seek to increase entropy, was left without any answer. Modern physics has not brought much of understanding, as is clear from the above citation of the Nobel physics laureate Richard Feynman.

But is statistical mechanics scientific in the sense of Popper, so that it can be falsified and is it based on sound scientific logic? Or is Einstein's criticism in fact relevant? After all, Einstein is considered to be the greatest scientist of the 20th century, so how probable is it that he was on a completely wrong track, all through the later half of his long life? We believe that he was not.

Is it possible to falsify statistical mechanics? Probably not, as it would require a full molecular-mechanical model according to Einstein. Concerning scientific logic, we recall that there are many particle systems based on Newtonian deterministic mechanics with a very complex dynamics, like a turbulent gas in an diesel engine or a galaxy of interacting stars, and also a game of roulette or dice. In such complex systems the positions in space-time of the particles are very sensitive to small perturbations, and thus are impossible to predict or compute (although mean values in space-time may be as we have seen in this book). We may refer to such systems as (macroscopic) games of roulette, which thus are very complex. Now, statistical mechanics is based on microscopic games of roulette, which leads to microscopics of microscopics in a never-ending chain, which is against scientific logic: By definition micro-

scopics is simple, because what is complex has its own microscopics and thus is not microscopic. Further, to say that Nature seeks to move towards more probable states, is a truism without scientific interest: How probable could it be that a system moves towards a less probable state instead of a more probable? We conclude that statistical mechanics is neither scientific nor logical, and we present an alternative based on deterministic computation with finite precision, without any form of statistics, which includes the 2nd Law and irreversibility.

Note that we do not claim that it is impossible to set up models of elections based on dice-playing voters, or models of thermodynamics based on dice-playing particles, which sometimes may produce reasonable results. What we say is that we see no reason to do so, since more precise results may be obtained from a deterministic computational model.

We also recall that statistical mechanics grew out of a necessity to handle a scientific dilemma without any computers available, and that with computers Boltzmann probably would have chosen a solution based on computation less open to criticism, to which he was very sensitive.

We claim that from a scientific point of view EG2 is better than Boltzmann's statistical mechanics, since the basic assumptions of Euler of conservation of mass, momentum and energy can hardly be disputed and the G2 computational methodology is transparent, while the basic assumptions of statistical mechanics are both illogical and virtually impossible to either prove or disprove.

44.3 Summary

We have outlined a new foundation of thermodynamics based on the 1st Law in the form of the inviscid Euler equations expressing conservation of mass, momentum and energy, combined with finite precision computation in the form of G2, and we have shown that the resulting EG2 model satisfies a 2nd Law implying irreversibility and an arrow of time. Further we have shown that the irreversibility is a consequence of the impossibility to solve the Euler equations exactly, and the necessary occurrence of shocks/turbulence in inviscid flow corresponding to G2 approximate weak solutions.

Thus we have resolved the main mystery of classical thermodynamics of formulation and justification of the 2nd Law, by showing that the 2nd Law is a consequence of the 1st Law and finite precision computation. We have thus mathematically justified the 2nd Law, without using any form of statistics or by referring to some property of physical systems to always increase entropy, both of which have shown to be impossible to rationalize.

We have shown that if Nature follows the weak/strong midway of EG2 in its own analog computation, then Nature will automatically (without knowing it) satisfy the 2nd Law, which opens to a scientific understanding of irreversibility and the arrow of time.

We may view the 2nd Law to reflect an interplay between stability and finite precision stating that only processes which are stable under finite precision computation can be realized and thus exist. In particular, reversing a transformation of kinetic energy to heat energy by friction or turbulent dissipation is impossible, because it would require infinite precision.

In Vol 5 we develop further aspects of thermodynamics by applying EG2 to a variety of concrete problems. We also make a fresh attack on the famous problem of black-body radiation based on computation, with quantum mechanics remaining as a veritable challenge.

References

1. *Dolfin*, <http://www.fenics.org/dolfin>.
2. *F1 Nutter aerodynamics*, <http://www.flnutter.co.uk/tech/aero.php>.
3. *F1 Country aerodynamics*, <http://www.fl1-country.com/f1-engineer/aerodynamics/f1-aerodynamics.html>.
4. *Naca airfoil series*, <http://www.aerospaceweb.org/question/airfoils/q0041.shtml>.
5. *PETSc*, <http://www-unix.mcs.anl.gov/petsc>.
6. M. AINSWORTH AND J. T. ODEN, *A posteriori error estimation in finite element analysis*, Computat. Meth. Appl. Mech. Eng., 142 (1997), pp. 1–88.
7. L. W. ALAWAYS, *Aerodynamics of the curve-ball: and investigation of the effects of angular velocity on baseball trajectories*, PhD thesis, University of California Davis, 1998.
8. I. BABUŠKA AND A. D. MILLER, *The post-processing approach in the finite element method, i: Calculation of displacements, stresses and other higher derivatives of the displacements.*, Int. J. Numer. Meth. Eng., 20 (1984), pp. 1085–1109.
9. ———, *The post-processing approach in the finite element method, ii: The calculation stress intensity factors.*, Int. J. Numer. Meth. Eng., 20 (1984), pp. 1111–1129.
10. ———, *The post-processing approach in the finite element method, iii: A posteriori error estimation and adaptive mesh selection*, Int. J. Numer. Meth. Eng., 20 (1984), pp. 2311–2324.
11. B. BAGHERI AND L. R. SCOTT, *Analysa*, <http://people.cs.uchicago.edu/ridg/al/aa.html>.
12. A. T. BAHILL, D. G. BALDWIN, AND J. VENKATESWARAN, *Predicting a baseball's path*, American Scientist, 93 (1980), pp. 218–225.
13. A. BAKKER, R. D. LAROCHE, M.-H. WANG, AND R. V. CALABRESE, *Sliding mesh simulation of laminar flow in stirred reactors*, The Online CFM Book (<http://www.bakker.org/cfm>), (1998).
14. R. BECKER AND R. RANNACHER, *A feed-back approach to error control in adaptive finite element methods: Basic analysis and examples*, East-West J. Numer. Math., 4 (1996), pp. 237–264.
15. ———, *A posteriori error estimation in finite element methods*, Acta Numer., 10 (2001), pp. 1–103.
16. J. BEY, *Tetrahedral grid refinement*, Computing, 55 (1995), pp. 355–378.

17. P. BLOSSEY, *Book review of stability and transition in shear flows*, SIAM Review, 44(1) (2002).
18. L. BOLTZMANN, *Lectures on Gas Theory*, Dover, 1964.
19. M. BRAACK AND T. RICHTER, *Solutions of 3d Navier-Stokes benchmark problems with adaptive finite elements*, Computers and Fluids, 35(4) (2006), pp. 372–392.
20. A. BROOKS AND T. HUGHES, *Streamline upwind/Petrov-Galerkin formulations for convection dominated flows with particular emphasis on the incompressible Navier-Stokes equations*, Computer methods in applied mechanics and engineering, 32 (1982), pp. 199–259.
21. S. BUIJSSEN AND S. TUREK, University of Dortmund, private communication, (2004).
22. S. CARNOT, *Reflections of the motive power of fire and on machines fitted to develop that power*, 1824.
23. M. J. CARRÉ, T. ASAI, T. AKATSUKA, AND S. J. HAAKE, *The curve kick of a football ii: flight through the air*, Sports Engineering, 5 (2002), pp. 193–200.
24. S. CHANDRASEKHAR, *Hydrodynamic and Hydromagnetic Stability*, Dover, 1981.
25. B. A. CHIPRA, *Tossed coins and troubled marriages: mathematical highlights from aaas 2004*, SIAM News (<http://www.siam.org/pdf/news/217.pdf>), 37(4) (2004).
26. G. CONSTANTINESCU, M. CHAPELET, AND K. SQUIRES, *Turbulence modeling applied to flow over a sphere*, AIAA Journal, 41(9) (2003), pp. 1733–1742.
27. G. CONSTANTINESCU, R. PACHECO, AND K. SQUIRES, *Detached-eddy simulation of flow over a sphere*, AIAA, 2002-0425 (2002).
28. G. CONSTANTINESCU AND K. SQUIRES, *Numerical investigations of flow over a sphere in the subcritical and supercritical regimes*, Physics of Fluids, 16(5) (2004), pp. 1449–1466.
29. J. d'ALEMBERT, *Essai d'une nouvelle théorie de la résistance des fluides*, Paris, <http://gallica.bnf.fr/anthologie/notices/00927.htm>, 1752.
30. J. DENG, T. HOU, AND X. YU, *Geometric properties and nonblowup of 3d incompressible Euler flow*, Comm. in Partial Differential Equations, 30 (2005), pp. 225–243.
31. P. DIACONIS, S. HOLMES, AND R. MONTGOMERY, *Dynamical bias in the coin toss*, SIAM Review, (to appear).
32. J. DUCHON AND R. ROBERT, *Inertial energy dissipation for weak solutions of incompressible euler and Navier-Stokes solutions*, Nonlinearity, (2000), pp. 249–255.
33. T. DUPONT, J. HOFFMAN, C. JOHNSON, R. KIRBY, M. LARSON, A. LOGG, AND R. SCOTT, *The fenics project*, Chalmers Finite Element Center Preprint 2003-21, Chalmers University of Technology, (2003).
34. H. ELMAN, D. SILVESTER, AND A. WATHEN, *Finite elements and fast iterative solvers: with applications in incompressible fluid dynamics*, Oxford University Press, Oxford, 2005.
35. K. ERIKSSON, D. ESTEP, P. HANSBO, AND C. JOHNSON, *Introduction to adaptive methods for differential equations*, Acta Numer., 4 (1995), pp. 105–158.
36. K. ERIKSSON, D. ESTEP, AND C. JOHNSON, *Applied Mathematics Body and Soul: Vol I-III*, Springer-Verlag Publishing, 2003.
37. K. ERIKSSON AND C. JOHNSON, *An adaptive finite element method for linear elliptic problems*, Math. Comp., 50 (1988), pp. 361–383.

38. L. EULER, *Principes généraux du mouvements des fluides*, l'Academie de Berlin, 1755.
39. FENICS, *Fenics project*, <http://www.fenics.org>, (2003).
40. L. FREITAG AND P. KNUPP, *Tetrahedral mesh improvement via optimization of the element condition number*, *Intl. J. Numer. Meth. Engr.*, 53 (2002), pp. 1377–1391.
41. U. FRISCH, *Turbulence - The Legacy of A. N. Kolmogorov*, Cambridge University Press, 1995.
42. M. GERMANO, U. POIMELLI, P. MOIN, AND W. CABOT, *A dynamic subgrid scale eddy-viscosity model*, *Phys. Fluids A*, 3 (1991), p. 1760.
43. J. W. GIBBS, *On the Equilibrium of Heterogeneous Substances (1875)*, The Scientific Papers by J W Gibbs, Dover, 1961.
44. M. GILES, M. LARSON, M. LEVENSTAM, AND E. SÜLI, *Adaptive error control for finite element approximations of the lift and drag coefficients in viscous flow*, Technical Report NA-76/06, Oxford University Computing Laboratory, (1997).
45. M. GILES AND E. SÜLI, *Adjoint methods for pdes: a posteriori error analysis and postprocessing by duality*, *Acta Numer.*, 11 (2002), pp. 145–236.
46. J. L. GUERMOND, *Stabilization of Galerkin approximations of transport equations by subgrid modeling*, *M2AN*, 33(6) (1999), pp. 1293–1316.
47. P. HANSBO, *A Crank-Nicolson type space-time finite element method for computing on moving meshes*, *Journal of Computational Physics*, 159 (2000), pp. 274–289.
48. P. HANSBO AND A. SZEPESSY, *A velocity-pressure streamline diffusion finite element method for the incompressible Navier-Stokes equations*, *Computer methods in applied mechanics and engineering*, 84 (1990), pp. 175–192.
49. R. HARTMANN AND P. HOUSTON, *Goal-oriented a posteriori error estimation for multiple target functionals*, in *Hyperbolic problems: theory, numerics, applications*, (T.Y. Hou and E. Tadmor, editors), pp. 579–588, Springer, 2003.
50. V. HEUVELINE AND R. RANNACHER, *Duality-based adaptivity in the hp-finite element method*, *J. Numer. Math.*, 11(2) (2003), pp. 95–113.
51. J. HEYWOOD, *Remarks on the possible global regularity of solutions of the three-dimensional Navier-Stokes equations*.
52. J. HOFFMAN, *On duality based a posteriori error estimation in various norms and linear functionals for les*, *SIAM J. Sci. Comput.*, 26(1) (2004), pp. 178–195.
53. ———, *Computation of mean drag for bluff body problems using adaptive DNS/LES*, *SIAM J. Sci. Comput.*, 27(1) (2005), pp. 184–207.
54. ———, *Adaptive simulation of the turbulent flow past a sphere*, *J. Fluid Mech.*, (accepted).
55. ———, *Computation of turbulent flow past bluff bodies using adaptive general galerkin methods: drag crisis and turbulent euler solutions*, *Comput. Mech.*, 38 (2006), pp. 390–402.
56. ———, *Efficient computation of mean drag for the subcritical flow past a circular cylinder using General Galerkin G2*, *Int. J. Numer. Meth. Fluids*, (accepted).
57. ———, *Adaptive simulation of the turbulent flow due to a cylinder rolling along ground*, (in review).
58. J. HOFFMAN AND C. JOHNSON, *Adaptive finite element methods for incompressible fluid flow*, Error Estimation and Solution Adaptive Discretization in Computational Fluid Dynamics (Ed. T. J. Barth and H. Deconinck), Lecture

- Notes in Computational Science and Engineering, Springer-Verlag Publishing, Heidelberg, 2002, pp. 97–158.
59. ———, *A new approach to computational turbulence modeling*, Comput. Methods Appl. Mech. Engrg., (in press).
 60. ———, *Stability of the dual Navier-Stokes equations and efficient computation of mean output in turbulent flow using adaptive DNS/LES*, Comput. Methods Appl. Mech. Engrg., (in press).
 61. ———, *Finally: Resolution of d'alembert's paradox*, Finite Element Center preprint (www.femcenter.org), (2006).
 62. ———, *Is the world a clock with finite precision?*, Finite Element Center preprint (www.femcenter.org), (2006).
 63. J. HOFFMAN, C. JOHNSON, AND A. LOGG, *Dreams of Calculus: Perspectives on Mathematics Education*, Springer-Verlag Publishing, 2004.
 64. J. HOFFMAN AND A. LOGG, *Dolfin - dynamic object oriented library for finite element computation*, Chalmers Finite Element Center Preprint 2002-06, Chalmers University of Technology, (2002).
 65. T. HUGHES AND T. TEZDUYAR, *Finite element methods for first-order hyperbolic systems with particular emphasis on the compressible Euler equations*, Computer methods in applied mechanics and engineering, 45 (1984), pp. 217–284.
 66. T. J. R. HUGHES, L. MAZZEI, AND K. E. JANSEN, *Large eddy simulation and the variational multiscale method*, Computer methods in applied mechanics and engineering, 3 (2000), pp. 47–59.
 67. V. JOHN, *Slip with friction and penetration with resistance boundary conditions for the Navier-Stokes equations - numerical tests and aspects of the implementation*, J. Comp. Appl. Math., 147 (2002), pp. 287–300.
 68. V. JOHN AND A. LIAKOS, *Time dependent flow across a step: the slip with friction boundary condition*, accepted for publication in Int. J. Numer. Meth. Fluids, (2005).
 69. C. JOHNSON, *Adaptive Finite Element Methods for Conservation Laws*, Advanced Numerical Approximation of Nonlinear Hyperbolic Equations, Springer Lecture Notes in Mathematics, Springer Verlag, 1998, pp. 269–323.
 70. C. JOHNSON, U. NÄVERT, AND J. PITKÄRANTA, *Finite element methods for linear hyperbolic equations*, Comput. Methods Appl. Mech. Eng., 45 (1984), pp. 285–312.
 71. C. JOHNSON AND R. RANNACHER, *On error control in CFD*, Int. Workshop Numerical Methods for the Navier-Stokes Equations (F.K. Hebeker et.al. eds.), Vol. 47 of *Notes Numer. Fluid Mech.*, Vierweg, Braunschweig, 1994, pp. 133–144.
 72. C. JOHNSON, R. RANNACHER, AND M. BOMAN, *Numerics and hydrodynamic stability: Toward error control in CFD*, SIAM J. Numer. Anal., 32 (1995), pp. 1058–1079.
 73. G.-S. KARAMANOS AND G. E. KARNIADAKIS, *A spectral vanishing viscosity method for large-eddy simulations*, Journal of Computational Physics, 163 (2000), pp. 22–50.
 74. A. N. KOLMOGOROV, *Dissipation of energy in locally isotropic turbulence*, Dokl. Akad. Nauk SSSR, 32 (1941), pp. 16–18.
 75. ———, *The local structure of turbulence in incompressible viscous fluid for very large Reynolds number*, Dokl. Akad. Nauk SSSR, 30 (1941), pp. 299–303.

76. ———, *On degeneration (decay) of isotropic turbulence in an incompressible viscous liquid*, Dokl. Akad. Nauk SSSR, 31 (1941), pp. 538–540.
77. S. KRAJNOVIĆ AND L. DAVIDSON, *Large-eddy simulation of the flow around a bluff body*, AIAA Journal, 40 (2002), pp. 927–936.
78. M. LANDAHL, *A note on an algebraic instability of inviscid parallel shear flows*, J. Fluid Mech., 252 (1980), p. 209.
79. J. LERAY, *Sur le mouvement d'un liquide visqueux emplissant l'espace*, Acta Mathematica, 63 (1934), pp. 193–248.
80. M. LESIEUR, *Turbulence in Fluids*, Kluwer Academic Publishers, London, England, 1997.
81. J. LIONS, *Quelques méthodes de résolution des problèmes aux limites non linéaires*, Etudes mathématiques, Dunod Gauthiers-Villars, 1969.
82. A. LOGG, *Automation of Computational Mathematical Modeling*, PhD thesis, Chalmers, 2004.
83. E. LORENZ, *Deterministic nonperiodic flow*, J. Atmospheric Sciences, 20 (1963).
84. J. LOSCHMIDT, *Sitzungsber. kais. akad. wiss. wien, math.*, Naturwiss. Classe 73, (1876), pp. 128–142.
85. H. G. MAGNUS, *On the derivation of projectiles; and on a remarkable phenomenon of rotating bodies*, Memoirs of the Royal Academy, Berlin, Edited by John Tyndall and William Francis, (1852), p. 210.
86. J. C. MAXWELL, Phil. Trans. Royal Society, (1879).
87. P. MOIN AND J. KIM, *Tackling turbulence with supercomputers*, Scientific American, (1997).
88. NASA, *Various views of von karman vortices*, http://disc.gsfc.nasa.gov/oceancolor/scifocus/oceanColor/vonKarman_vortices.shtml, (2005).
89. C. L. M. H. NAVIER, *Mémoire sur les lois du mouvement des fluïdales*, Mém. Acad. Royal Society, 6 (1823), pp. 389–440.
90. J. V. NEUMANN AND R. D. RICHTMYER, *A method for the numerical calculation of hydrodynamic shocks*, J. Appl. Phys., 21(3) (1950).
91. H. POINCARÉ, *Science and Method*, 1903, Dover 1982.*aux limites non linéaires*, Dunod, Paris, 1969.
92. PRANDTL, *Prandtl standard view*, www.fluidmech.net/msc/prandtl.htm, (2006).
93. L. PRANDTL, *On motion of fluids with very little viscosity*, Third International Congress of Mathematics, Heidelberg, <http://naca.larc.nasa.gov/digidoc/report/tm/52/NACA-TM-452.PDF>, (1904).
94. A. QUARTERONI, *What mathematics can do for the simulation of blood circulation*, EMS Proc. of the ICM 2006 Conference, Madrid. EMS 2006, (in press).
95. R. RANNACHER, *Finite element methods for the incompressible Navier–Stokes equations*, Preprint Institute of Applied Mathematics, Univ. of Heidelberg, (1999).
96. B. ROBINS, *New principles of gunnery containing the determination of the force of gunpowder and investigation of the difference in the resisting power of the air to swift and slow motion*, 1742.
97. W. RODI, J. H. FERZIGER, M. BREUER, AND M. POURQUIÉ, *Status of large eddy simulation: Results of a workshop*, ASME Journal of Fluids Engineering, 119 (1997), pp. 248–262.

98. P. SAGAUT, *Large Eddy Simulation for Incompressible Flows*, Springer-Verlag, Berlin, Heidelberg, New York, 2001.
99. H. SCHLICHTING, *Boundary Layer Theory*, McGraw-Hill, 1955.
100. P. SCHMID AND D. HENNINGSON, *Stability and Transition in Shear Flows: Applied Mathematical Sciences 142*, Springer, 2001.
101. C. SCHWAB, *p- and hp- Finite Element Methods Theory and Applications to Solid and Fluid Mechanics*, Oxford University Press, 1999.
102. T. K. SENGUPTA AND S. B. TALLA, *Robins-maguns effect: a continuing saga*, Current Science, 86(7) (2004), pp. 1033–1036.
103. J. SMAGORINSKY, *General circulation experiments with the primitive equations, part i: The basic experiment*, Mon. Wea. Rev., 91 (1963), p. 99.
104. A. SOMMERFELD, *Ein Beitrag zur hydrodynamischen erklärung der turbulenten flüssigkeitsbewegungen*, Atti del 4. Congr. Internat.dei Mat. III, Roma, (1908), pp. 116–124.
105. W. THOMSON, *On the dynamical theory of heat; with numerical results deduced from mr. Joule's equivalent of a thermal unit and M. Regnault's observations on steam*, Math. and Phys. Papers, 1 (1851), p. 179.
106. D. J. TRITTON, *Physical Fluid Dynamics*, 2nd ed. Oxford, Clarendon Press, 1988.
107. S. TUREK, *Efficient Solvers for Incompressible Flow Problems: An Algorithmic and Computational Approach*, Springer, Berlin, 1999.
108. R. VERFÜRTH, *A Review of A Posteriori Error Estimation and Adaptive Mesh Refinement Techniques*, Wiley/Teubner, New York/Stuttgart, 1996.
109. WIKIPEDIA, *Baseball pitches*, http://en.wikipedia.org/wiki/Baseball_pitches.
110. M. M. ZDRAVKOVICH, *Flow around circular cylinders: a comprehensive guide through flow phenomena, experiments, applications, mathematical models, and simulations. Vol.1 [Fundamentals]*, Oxford Univ. Press, Oxford, 1997.

Index

- ϵ -weak solution, 109
1st Law, 343, 354
2nd Law, 159, 343, 353, 363
- a posteriori error estimate, 129, 243
ACMM, VII
adaptive algorithm, 219
Adaptive DNS/LES, 203, 219
adiabatic index, 34
ALE, 225
angle of attack, 176
approximate weak solution, 53
- Bernoulli, 68
Bernoulli's Law, 68, 70, 175, 291
bluff body flow, 239
Boltzmann, 378
boundary layer, 53, 273
- Carnot, 343
Cayley, 28
CC, VII
 $cG(1)cG(1)$, 209
chaos, 91
chaotic dynamical system, 92
circular cylinder, 258
Clausius, 343
Clay Mathematics Institute, 107
compressible Euler, 351, 363
computability, 56
convective derivative, 36
Couette flow, 63, 307, 308
- d'Alembert's Mystery, 23, 27, 68
- density, 33
deterministic chaos, 91
Dijkstra, 371
Direct Numerical Simulation, 51
dissipative weak solution, 157
DNS, 51
DOLFIN, 223
downforce, 189
drag coefficient, 52, 239
drag crisis, 170, 284
dual problem, 54, 113, 131, 241, 287
dynamical system, 41
- eddy viscosity, 197
EG2, 105, 147, 286, 342, 345
Einstein, 377
entropy, 343
error representation, 115
Euler, 4, 171
Euler equations, 33, 37, 67, 145
existence, 107
- FEniCS, 223
flat plate, 275
form drag, 239
free boundary, 227
friction boundary condition, 201, 210
Functional Analysis, 109
- G2, 128, 147, 203
gas constant, 34
General Galerkin, 128
- Hadamard, 109
harmonic oscillator, 95

- heat capacity, 34
- heat conductivity, 40
- horse shoe vortex, 244
- ideal fluid, 33
- ideal of Einstein, 41
- incompressibility, 34, 36, 37, 205
- internal energy, 34
- inviscid fluid, 33
- irreversibility, 341, 374
- irrotational, 44
- Joule's experiment, 345
- Kelvin-Planck, 343
- Kolmogorov, 47
- Kutta, 28
- Kutta condition, 28
- Kutta-Zhukovsky, 182
- laminar boundary layer, 274
- laminar flow, 45
- Landahl, 300
- Large Eddy Simulation, 195
- Leonardo da Vinci, 27
- Leray, 54, 107
- LES, 195
- lift coefficient, 52, 239
- lift generation, 176
- Lilienthal, 28
- linearized Euler equations, 59
- Lorenz, 91, 101
- Loschmidt's Mystery, 23, 105, 341
- Mach number, 34
- Magnus, 171
- Magnus effect, 170, 291
- mesh refinement, 221
- mesh smoothing, 228
- modal, 300
- momentum, 33
- Navier, 4
- Navier-Stokes equations, 38, 108, 205
- Neumann boundary condition, 207
- Newton, 27
- Newtonian, 4, 38, 205
- no slip boundary condition, 207
- non-modal, 64, 300
- non-Newtonian fluids, 4
- NS, 38, 108, 205
- object in a box, 229
- optimal perturbations, 325
- outflow boundary condition, 207
- output sensitivity, 113, 115
- paradox, 23
- phase averages, 251
- phase jitter, 251
- Planck, 379
- Poiseuille flow, 307, 319
- Poisson, 4
- potential flow, 44, 70
- Prandtl, 28, 75
- predictability, 56
- pressure, 33
- pressure drag, 169, 239
- Prize Problem, 107
- probability, 97
- randomness, 91
- RANS, 195
- rarefaction, 358
- reattach, 279
- recirculation, 279
- regularity, 107
- residual, 108, 148
- reverse Magnus effect, 173
- Reynolds, 45, 300
- Reynolds number, 45
- Reynolds stresses, 195
- Robins, 171
- Robins' effect, 171
- Saint-Venant, 4
- Schlichting, 300
- separation, 279
- shock, 359
- shock-capturing, 198, 207, 370
- skin friction, 169, 239, 274
- sliding mesh, 232
- slip boundary condition, 207
- Smagorinsky, 197
- Smagorinsky model, 198
- Sommerfeld, 300
- Sommerfeld's Mystery, 23, 64
- speed of sound, 34
- sphere, 269

- square cylinder, 251
stability factor, 54, 109
stabilized Galerkin method, 127
state equation, 34
statistical mechanics, 105, 379
Stokes, 4
strain rate tensor, 205
stress tensor, 205
surface mounted cube, 244
Taylor-Görtler mechanism, 319
temperature, 34, 155
test function, 108, 205, 209
thermodynamics, 342
total energy, 33
transition, 45, 299
turbulent boundary layer, 170, 275
turbulent flow, 45
uniqueness, 107
velocity, 33
velocity potential, 44
viscosity, 38
von Kármán, 258
von Kármán vortex street, 258
vorticity, 72
wall modeling, 201
weak uniqueness, 54, 115, 119
well-posed, 110
Wright, 29
Zhukovsky, 29